

IPNS Progress Report 2001 – 2006

In celebration of the 25th Anniversary of IPNS



About Argonne National Laboratory

Argonne is a U.S. Department of Energy laboratory managed by UChicago Argonne, LLC under contract DE-AC02-06CH11357. The Laboratory's main facility is outside Chicago, at 9700 South Cass Avenue, Argonne, Illinois 60439. For information about Argonne, see www.anl.gov.

Availability of This Report

This report is available, at no cost, at <http://www.osti.gov/bridge>. It is also available on paper to the U.S. Department of Energy and its contractors, for a processing fee, from:

U.S. Department of Energy

Office of Scientific and Technical Information

P.O. Box 62

Oak Ridge, TN 37831-0062

phone (865) 576-8401

fax (865) 576-5728

reports@adonis.osti.gov

Disclaimer

This report was prepared as an account of work sponsored by an agency of the United States Government. Neither the United States Government nor any agency thereof, nor UChicago Argonne, LLC, nor any of their employees or officers, makes any warranty, express or implied, or assumes any legal liability or responsibility for the accuracy, completeness, or usefulness of any information, apparatus, product, or process disclosed, or represents that its use would not infringe privately owned rights. Reference herein to any specific commercial product, process, or service by trade name, trademark, manufacturer, or otherwise, does not necessarily constitute or imply its endorsement, recommendation, or favoring by the United States Government or any agency thereof. The views and opinions of document authors expressed herein do not necessarily state or reflect those of the United States Government or any agency thereof, Argonne National Laboratory, or UChicago Argonne, LLC.

I would like to congratulate the entire staff of the Intense Pulsed Neutron Source, past and present, on 25 years of outstanding achievement in creating and operating what has become the nation's most reliable source of neutrons, a mainstay of the accelerator community, and above all, a place where outstanding science is done.

The first beam was delivered at Argonne's Intense Pulsed Neutron Source in 1981. That fledgling facility had been developed and built on an extremely tight budget that was stretched by scavenging equipment from a decommissioned accelerator. This determination to succeed, in combination with pioneering work in spallation science, created the nation's first major pulsed neutron source.

Outstanding scientific and administrative leadership under directors John Carpenter, David Price, Gerard Lander, Bruce Brown, and Ray Teller added an array of specialized concepts and instruments to create a leading national user facility and an invaluable tool in conducting outstanding science in such fields as physics, chemistry, materials science and biology.

Today, the IPNS sets the national standards for service and availability that allow its users to maximize the effectiveness of their time there and to conduct cutting-edge scientific research. The depth and breadth of the IPNS' user community testifies to its success: More than 7,000 experiments have been performed there by nearly 5,000 researchers from hundreds of universities, government laboratories and industrial firms from the United States and other nations. At the same time, the IPNS has become the nation's foremost facility for training scientists in the art of using neutron scattering as a research tool.

Again, congratulations to everyone at IPNS on 25 successful years! All of us at Argonne National Laboratory and everyone in the community appreciate the job you have done so well. During the coming years, we look forward to maintaining these high standards of excellence, and we anticipate that the IPNS will be a continuing source of outstanding scientific achievement.



Robert Rosner

Director

Argonne National Laboratory

Foreword

The 25th Anniversary Edition of the IPNS Progress Report is being published in recognition of the Intense Pulsed Neutron Source's first twenty-five years of successful operation as a user facility.

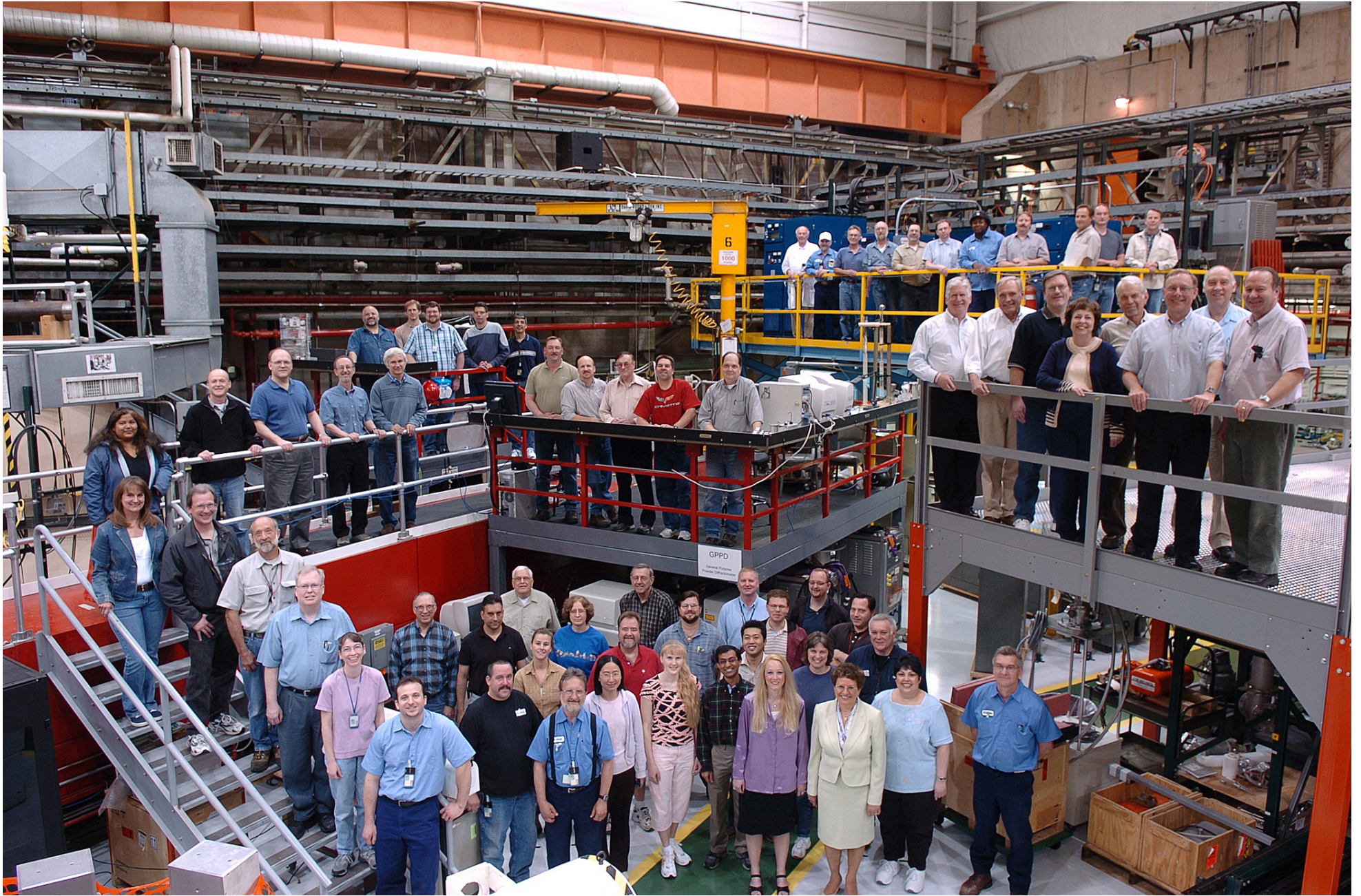
For this report, authors were asked to prepare articles that highlighted recent scientific accomplishments at IPNS, from 2001 to present; to focus on and illustrate the scientific advances achieved through the unique capabilities of neutron studies performed by IPNS users; to report on specific activities or results from an instrument; or to focus on a body of work encompassing different neutron-scattering techniques. Articles are also included on the accelerator system, instrumentation, computing, target, and moderators.

A list of published and "in press" articles in journals, books, and conference proceedings, resulting from work done at IPNS since 2001, was compiled. This list is arranged alphabetically according to first author. Publication references in the articles within this report are listed by last name of first author and year of publication. Other references not part of the IPNS publications list are listed at the end of each article.

From the startup of IPNS in 1981, our goal has been the optimization of research opportunities for the neutron user community. IPNS has led the world in many of the important developments at spallation neutron sources. We are playing a major role in the development of the target, moderator, and instrument systems for the Spallation Neutron Source (SNS), the world's most powerful future neutron source.

The accomplishments described in the pages of this report are a tribute to the people who work at IPNS. Our enviable record of accelerator performance and scientific and technical achievements could not have been sustained without the hard work and dedication of all members of the IPNS team. We are proud of the accomplishments at IPNS over the past twenty-five years and look forward to a productive future.





Contents

1 Introduction

2 Instrumentation and Scientific Highlights (2001-2006)

Crystallography

Nuclear and Magnetic Structures of $\text{La}_{1-x}\text{Sr}_x\text{MnO}_3$

Role of Local Structure in Understanding Functional Electronic Oxides

Neutron Diffraction Investigations of H_2 Storage in Clathrate Hydrates

Evidence of Inter- and Intra-Granular Strains Induced by Cyclic Deformation

Chemical Diffusion and Oxygen Vacancy Distribution in $\text{Ce}_{0.8}\text{Y}_{0.2}\text{O}_{1.9-\delta}$
Electrolytes

Single Crystal Neutron Diffraction Studies of Thermoelectric Materials

A Pressure-Switchable Jahn-Teller Distortion in $(\text{ND}_4)_2[\text{Cu}(\text{D}_2\text{O})_6](\text{SO}_4)_2$

Linear M-H-M Bonding in Simple Dinuclear Metal Complexes

Disordered Materials

The Glass Liquids and Amorphous Materials Diffractometer in IPNS 2001-2006

The Glacial State of Triphenyl Phosphite

Structural Investigations of Superacids and Superacidic Solutions

The First Sharp Diffraction Peak in Binary Selenide Glasses

Experiments with Transformation Processes in Amorphous Ice

Combined Levitation and Neutron Diffraction at High Temperatures

Soft Materials and Large Scale Structures

Structural Arrest Transition in L64/ D_2O Triblock Copolymer Micellar Solutions

Nanoscale Effects Illuminated by Neutron Scattering and Reflectivity

Solvation and Aggregation of Asphaltenes in Model Petroleum Mixtures

Mechanism and Energetics of Third Phase Formation in TBP Solvent Extraction
of Metal Salts

MISANS (Modulated Intensity Small Angle Neutron Scattering)

Structural Transitions of Block Copolymers in Liquid Crystal Solvent

Neutron Reflectometry

Magnetic Profiles in Ferromagnetic/Superconducting Superlattices

Contents (continued)

Spectroscopy

The Proton Density of States Study of Deeply Supercooled Water near the Second Critical Point

Phonon Density of States of Model Ferroelectrics

Modeling of Negative Thermal Expansion in ZrW_2O_7 and ZrMo_2O_8 Using Lattice Dynamics and Interelastic Neutron Scattering

Dynamic Magnetic Susceptibility of $\text{Gd}_5\text{Si}_2\text{Ge}_2$ and $\text{Gd}_4\text{YSi}_{1.9}\text{Ge}_{2.1}$

Observations of Water-Framework Interactions in a Hydrated Microporous Aluminum Phosphate

Experimental Evidence of a Liquid-Liquid Transition at 240 K in Interfacial Water

Hydroxyl Group Content of Bone Mineral

Water in Carbon Nanotubes: Neutron Spectroscopy and MD Simulations

Lattice Vibrations

Investigation of Porous Materials for Hydrogen Storage

Computing Developments

Instrument Hardware and Software Upgrades at IPNS at ANL

3 Accelerator and Target Systems

The IPNS Accelerator System

Fabricating Neutrons

IPNS Moderator Status

4 Future Plans

A Very Cold Neutron Source (VCNS)

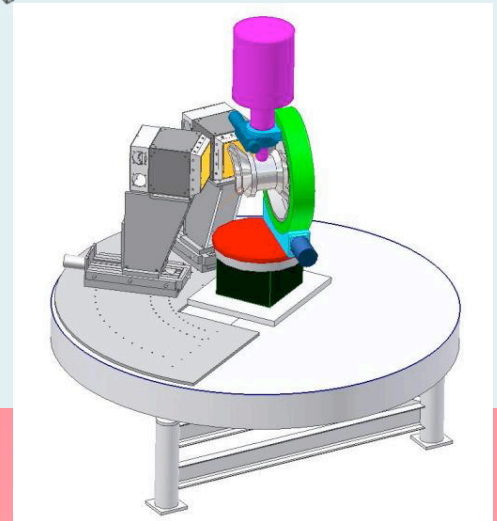
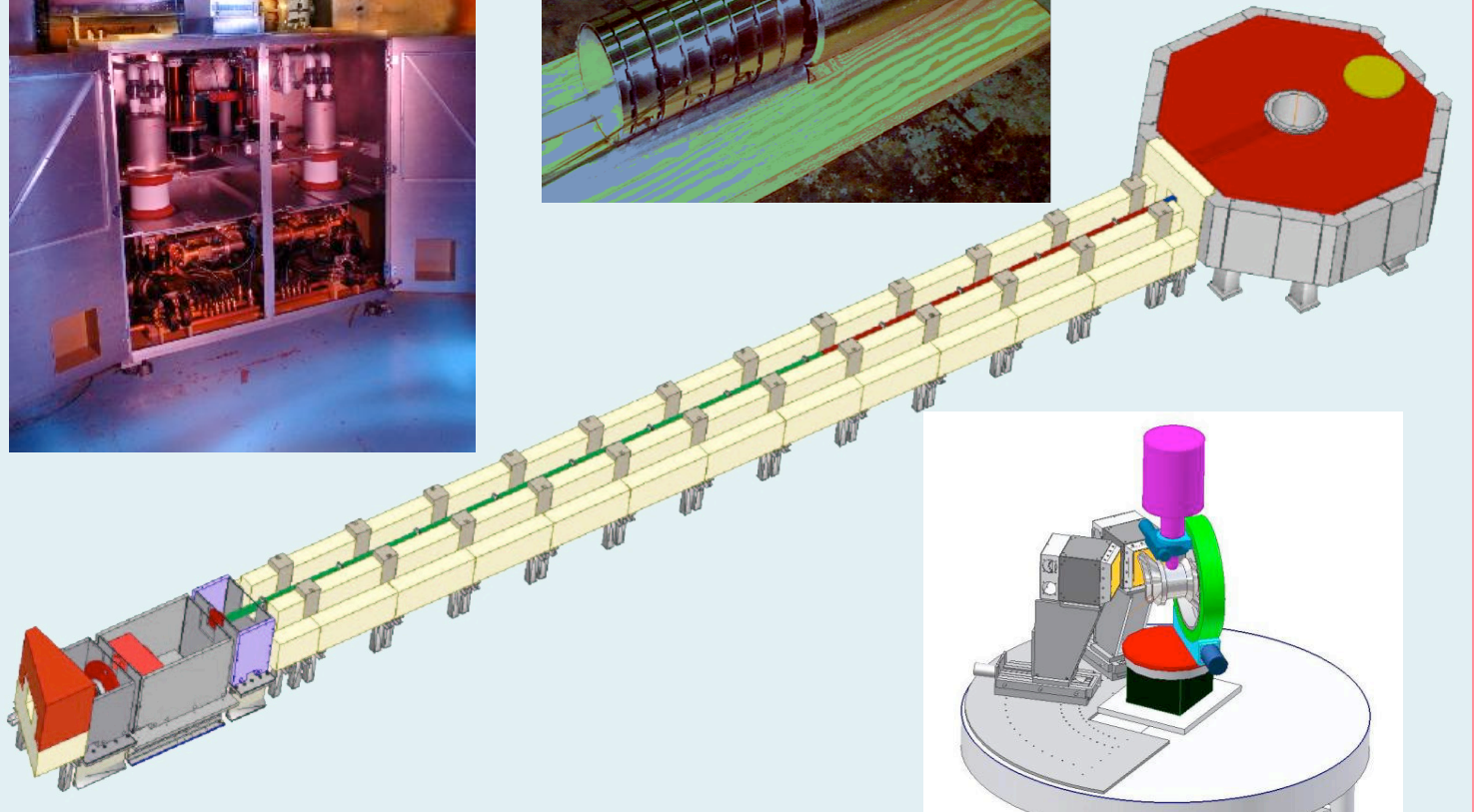
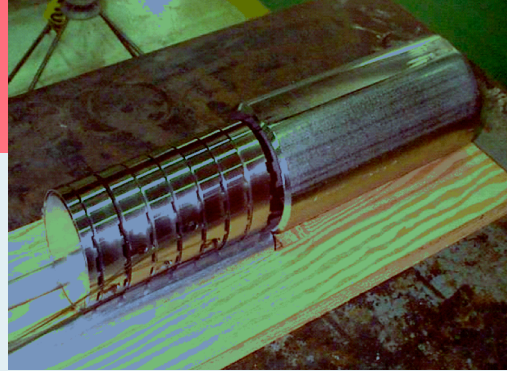
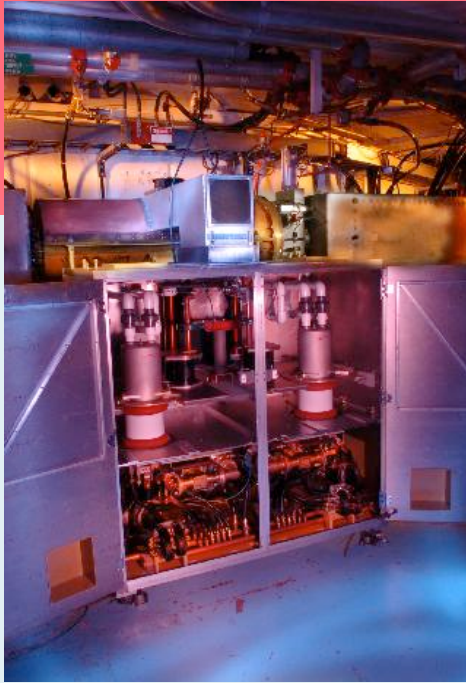
5 User Program and Organization

IPNS-Sponsored Workshops

6 Awards and Recognitions

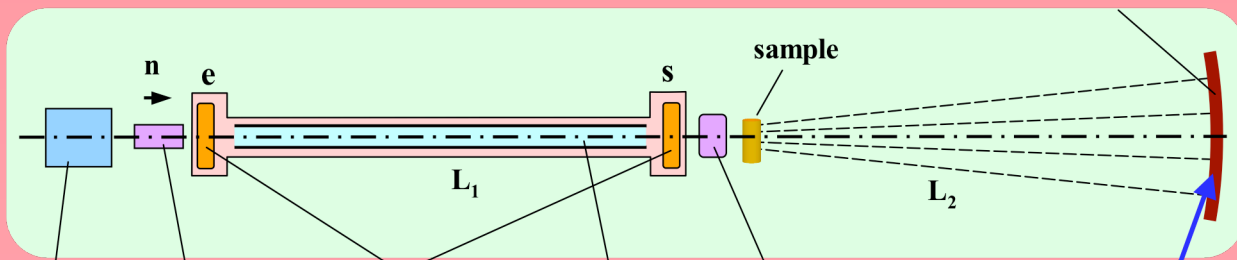
7 Publications (2001-2006)

1. Introduction



MISANS

detector with space and time resolution



selector
 $\Delta\lambda/\lambda \approx 10\%$
 or:
 operation at
 pulsed source

polariser

NRSE coils in
 magnetic screen

R.Gaehler

guide with low angle
 for total reflection

³He polariser or
 high precision bender

Intensity varies sinusoidally
 with a frequency up to 2 MHz.
 Its contrast is a measure of the
 quasielastic scattering.

Introduction

Raymond G. Teller, Director

In August 1981, the proton beam from the rapid cycling synchrotron (RCS) was first delivered to the Intense Pulsed Neutron Source (IPNS) neutron scattering target and now, in June 2006, it is with great joy that we celebrate the impending 25th anniversary of this event. This edition of the IPNS Progress Report will focus on the development and scientific accomplishments of the past 5 years, since our last Progress Report, but with some mention of the 25 years of IPNS experience.

It is appropriate at this anniversary date to recall some of the more significant historic events that have led to the present IPNS and discuss some of the plans that will lead to even more successes. Below is a brief chronology that captures some of the developments of IPNS.

- 8/4/81 - First beam delivered to the neutron scattering target
- 6/10/84 - IPNS produced its one billionth neutron pulse
- 1/10/85 - Installed world's first solid methane moderator
- 6/30/87 - 1000th experiment performed at IPNS
- 9/19/87 - IPNS produced its two billionth neutron pulse
- 11/20/91 - 2000th experiment performed at IPNS
- 4/17/04 - IPNS produced its eight billionth neutron pulse
- 8/19/05 - 7000th experiment performed at IPNS

During the past 5 years, several significant source and instrument developments have taken place. Most of these are discussed in more detail elsewhere in the report, but three of the ones most visible to users are mentioned here.

Revitalization of IPNS Accelerator Systems To Ensure Reliable Operation

A third rf cavity and amplifier system has been completed and is in operation. The original two cavities could provide about 22 kV/turn of rf voltage at the bunch-rotation frequency that varies from about 2 to 5 MHz during the acceleration from 50 to 450 MeV. This new system will add second harmonic rf (4-6 MHz) during the capture and early acceleration process, reducing capture losses by a factor of 2 to 3. It will then be switched back to the same frequency as the existing systems to increase the kV/turn during the mid-point of the acceleration cycle. This additional fundamental voltage will provide improved bunch handling and should assist in suppressing the beam instabilities that presently limit current in the synchrotron.

Upgrades of IPNS instruments continue

The IPNS continues to make major instrument upgrades to maintain world class science capabilities for US users 1) More than one half of the user instruments

have been migrated to a new data acquisition system that enables faster and more flexible data binning, 2) installation of neutron guides and frame definition choppers has boosted flux on sample for some instruments by 2-20 times and 3) improved detectors and collimation and larger detector coverage have significantly reduced the time required to collect neutron data, enabling parametric studies.

GLAD – Glass Liquid and Amorphous Materials Diffractometer: Radial collimators were installed in FY02 and the in-line horizontal and vertical Soller collimators were replaced with a coarser honeycomb collimator in FY06. The result was a three fold increase in flux on the sample with a negligible change in background level. In FY05 and FY06 new GLAD data analysis software was written in ISAW, reducing data processing times from hours to minutes. The pixel-by-pixel analysis has extended the low-Q limit of GLADs' already wide Q range to $Q_{\min}=0.175 \text{ \AA}^{-1}$ ($Q_{\max}=40 \text{ \AA}^{-1}$). Considerable effort has also gone into the development of sophisticated neutron sample environment equipment on GLAD, including aerodynamic levitation, piston anvil pressure cells and containment of corrosive liquids.

GPPD – General Purpose Powder Diffractometer: By moving GPPD from 20 to 25 m and fully equipping it with a neutron guide and extended groups of detectors, intensity gain factors of 6-15 have been achieved, with no loss in resolution. The T_0 and frame-definition choppers allow routine measurements with wavelengths up to 8-10 Å. Conversion to a new data acquisition system (DAS) completed the upgrade of this instrument.

In its final form this instrument is truly optimized for the IPNS source. It is an excellent instrument for *in situ* diffraction experiments where good instrumental resolution is required, as well as conventional diffraction experiments where subtle crystallographic features must be resolved. This instrument, with a cold liquid methane spectrum further “cooled” by a neutron guide and wavelengths up to 10 Å, is now well suited to large-cell crystallography problems. In these applications there is a premium on good resolution at large d-spacings. This can be accommodated with high-angle detectors using long wavelength neutrons.

MISANS – Modulated Intensity Small Angle Neutron Spectrometer: The development of this unique hybrid small angle scattering instrument – having the ability to monitor both structure and dynamics – that takes advantage of the spin precession of the neutron in magnetic fields is ongoing at IPNS. This instrument will provide unique measuring capabilities for nanoscience. The MISANS instrument takes advantage of the Neutron Resonance Spin Echo technique (NRSE) to provide an extremely high degree of energy resolution without sacrificing intensity like in other quasi-elastic neutron

techniques. Successful tests of MISANS were conducted at IPNS in 2005, representing the first demonstration of this technique at any pulsed source in the world. Since NSE spectrometers would hugely benefit from the broad wavelength band and the time structure of every neutron pulse, several attempts, most of them led by IPNS scientists, are under development worldwide in order to adapt this technique to a modern pulsed neutron source such as the Spallation Neutron Source (SNS).

POSY I - Polarized Neutron Reflectometer: An XYZ cryomagnet has been installed which allows the magnetic field to be directed in any spatial direction. The maximum fields are 0.8T, 0.8T, and 2T. A wide angle polarization analyzer, which allows simultaneous polarization analysis of both the specular as well as the offspecular reflection, has been installed. The analyzer covers a solid angle that matches that of the position sensitive detector.

QENS - Quasielastic Neutron Spectrometer: A supermirror guide in the incident beam was successfully installed in the summer of 2003 resulting in a ~2.5-fold increase of the flux of long-wavelength neutrons at sample. The net effect, coupled with the upgrade of detector arms already completed, is a data rate gain factor of >30 and the ability to collect data simultaneously for all Q values. This major increase in data rate has allowed new science to be done on QENS. The ability to collect a complete data set in less than 1 hour (much less in some cases) means that it will now be practical to obtain a detailed map of the behavior of a chemical system as one or more external parameters (e.g., temperature, partial pressure, composition) are varied. It will also be possible to follow the progress of chemical reactions and phase transitions in real time.

SAND - Small Angle Neutron Diffractometer: Conversion to the new data acquisition system (DAS) on the SAND instrument during FY04 has enabled simultaneous measurement of high quality low Q data using the position sensitive area detector and the high resolution diffraction data extending to a d_{\min} of 1 Å with the wide angle bank of linear position sensitive detectors. This feature of providing scattering data in a wide Q range of 0.0035 to 6 Å⁻¹ in a single measurement at higher resolution makes SAND unique in the world, as systems that undergo phase separation and crystallization can be probed *in situ* in a single setting. During FY07, we propose to develop a T_0 chopper and replace the cryogenic MgO single crystal filter in order to increase the flux at the short wavelength region for the measurement of the diffraction data.

SCD - Single Crystal Diffractometer: - The SCD instrument was completely upgraded by replacing the old detector and data acquisition system with two new position-sensitive area detectors and with a completely new data acquisition system. The new detectors are smaller and more compact, such that the total solid angle is twice as large compared to before the upgrade. This permits data collection in half the time than previously

required. In addition, the new data acquisition system is capable of handling larger histograms permitting larger range of wavelengths (0.5–10.0 Å) at higher resolution ($\Delta\lambda/\lambda = 0.01$) in one measurement. An optical table has been installed upstream from the sample for test of a compact helium-3 polarizer. Accompanying the hardware upgrades, new software based on ISAW has been developed for data display and analysis.

SEPD - Special Environment Powder Diffractometer: The conversion to the new data acquisition system (DAS) and installation of linear position sensitive detectors (LPSD) in the forward scattering directions has improved the data quality for powder diffraction from SEPD by reducing the geometric instrument broadening at low angles and allowing for a data binning scheme that closely matches instrument resolution. A 7 Tesla superconducting magnet system was installed and tested in FY05, which promises to bring new capabilities for studies of magnetic materials.

The IPNS neutron-generating target

Through the combined efforts of three divisions at Argonne, a rebuilt neutron scattering target has been completed and is in use at IPNS. The project was a close collaboration of IPNS engineering and operations, CMT and PFS personnel. The rebuilt target was assembled from usable uranium discs removed from old IPNS targets, a method which has resulted in substantial cost savings. Successful commissioning of a new IPNS target from recycled disks recovered from end-of-life targets has provided a cost effective alternative to the construction of entirely new IPNS targets and enables IPNS operations for an additional six years. The additional results of this project were a cost deferment of \$1M and the reduction of \$10K in radioactive waste disposal cost.

This effort led to IPNS being the recipient of the DOE Spirit Award for waste minimization and pollution prevention and, in addition, IPNS was cited with an Office of Science “Notable Practice” for this work in a letter from Energy Secretary Bodman.

Operations at IPNS continue to be outstanding

For the last five consecutive years IPNS has exceeded its goal of offering at least 95% reliable operations. This is a remarkable achievement and sets the standard by which other accelerator-based neutron facilities can be judged.

Nuclear Historic Landmark

At their November 2001 meeting in Reno, Nevada, the American Nuclear Society (ANS) announced the designation of Argonne’s Intense Pulsed Neutron Source as a Nuclear Historic Landmark. IPNS celebrated this significant event on Monday, May 13, 2002. ANS President, Dr. Gail Marcus, formally presented the award. Attendees included important contributors to the development of IPNS, and others holding stake and having interests in IPNS.

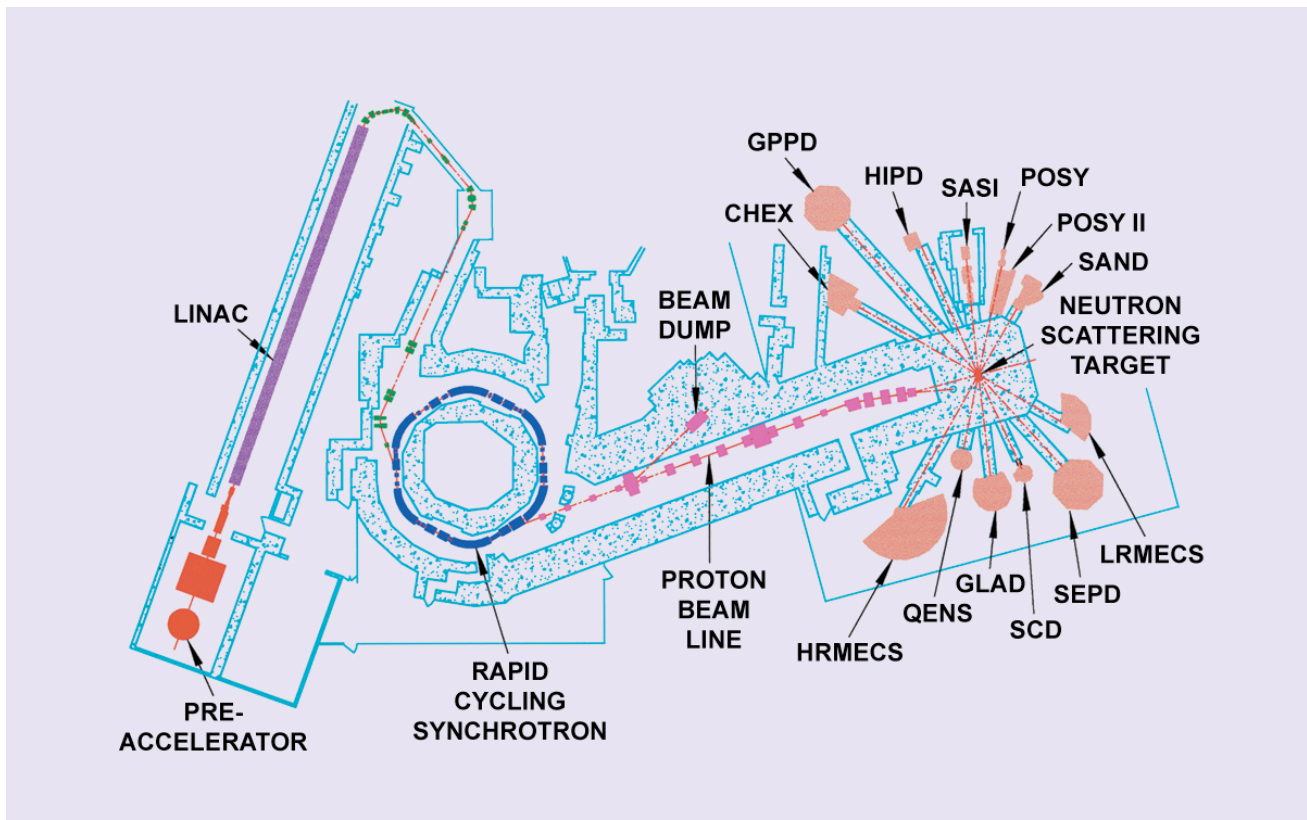
Interactions with the Spallation Neutron Source (SNS)

IPNS will continue to play a critical role as the community prepares for the unprecedented scientific capabilities of the Spallation Neutron Source (SNS), which is preparing for proton beam on target as I am penning this introduction. Jack Carpenter (IPNS Technical director) has been a senior advisor for the Experimental Systems and has had a major role in the development of the target/moderator and instrument systems. Early in the construction of the SNS, IPNS also had the lead responsibility for the instruments at the SNS.

After departure of the SNS instrument team to Oak Ridge, IPNS personnel have continued to stay heavily involved in developing instruments at SNS. In addition to participating in development teams of numerous instruments currently under construction there, IPNS personnel have spearheaded efforts for several novel instruments. These instruments are: MaNDi, the Macromolecular Neutron Diffractometer that is expected to revolutionize the structural biology field by finding the

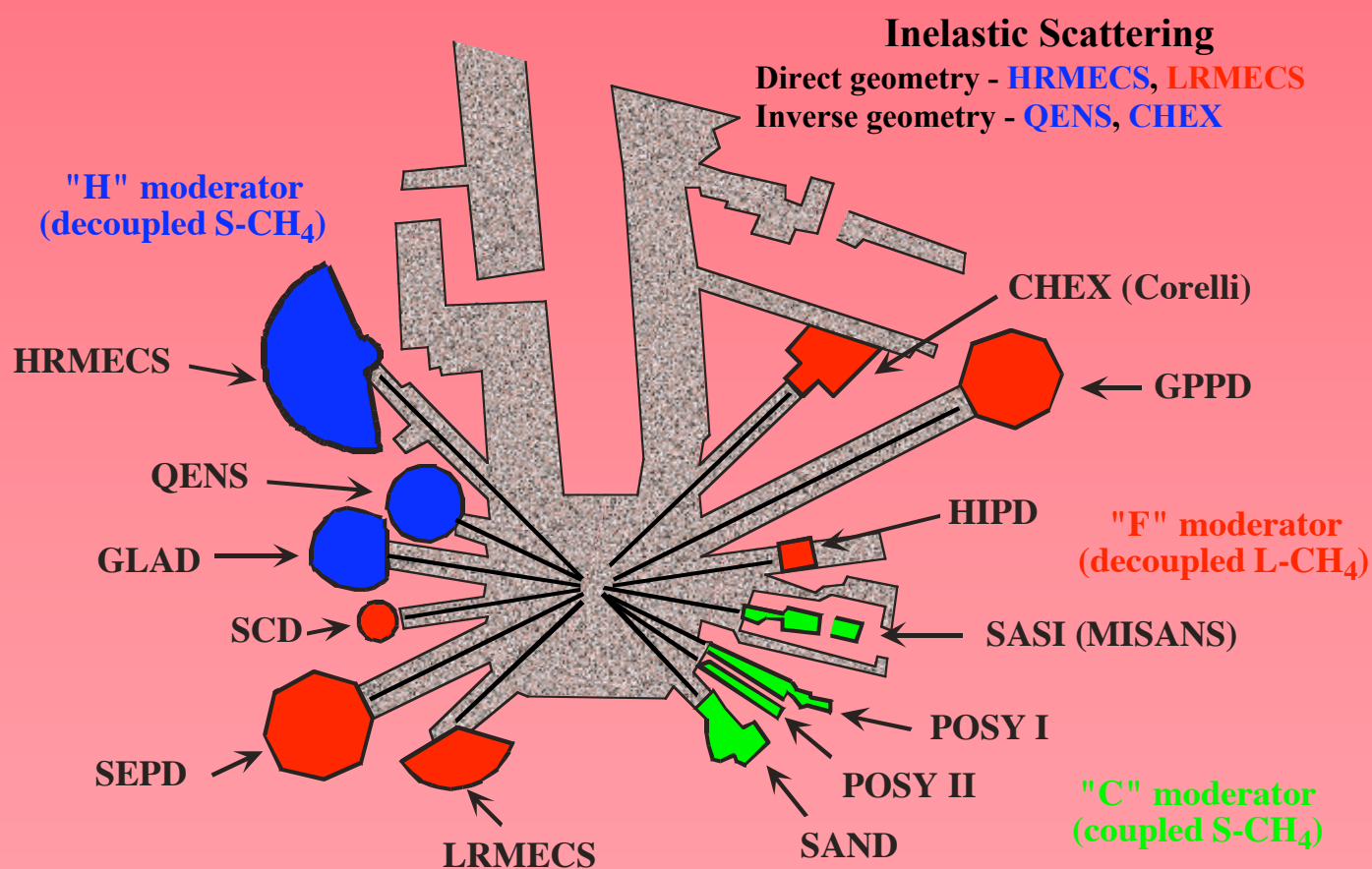
locations of hydrogen atoms in macromolecular structures; USANS, an Ultra-Small Angle Neutron Scattering instrument capable of characterizing structures in the 5 to 10,000 nm range; MISANS, a sister instrument similar to that described above with extended q and ω ranges; and Topaz, a single crystal diffractometer that will revolutionize small molecule single crystal neutron diffraction.

We are proud of the accomplishments at IPNS over the past twenty-five years and look forward to a productive future. IPNS has led the world in many of the important developments at spallation neutron sources and we continue playing a major role in the world's most powerful future source, the SNS. This enviable record of accelerator performance and scientific and technical achievements could not have been made without the hard work and dedication of all members of the IPNS team. It has been a pleasure and honor to work with this group and I am certain that there are many successes ahead for IPNS.



IPNS Facility layout

2. Instrumentation and Scientific Highlights (2001-2006)



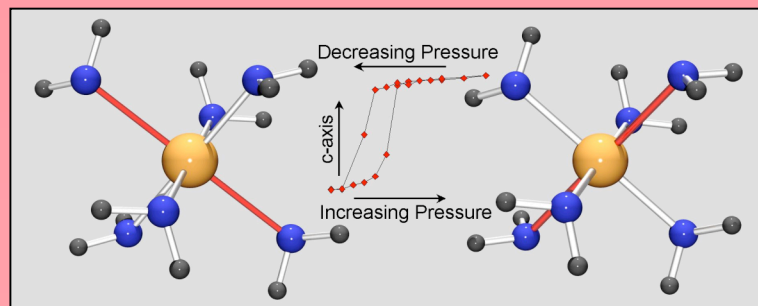
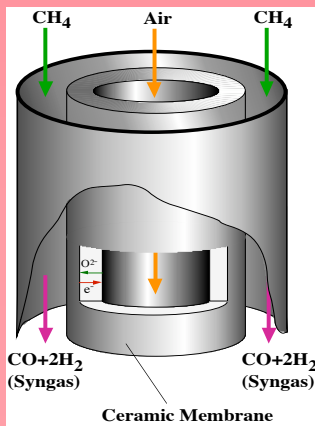
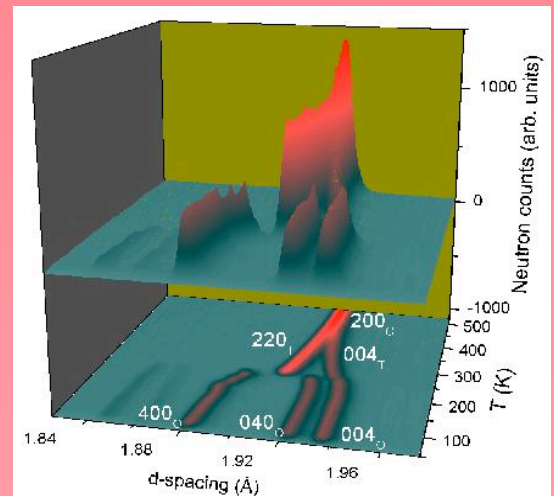
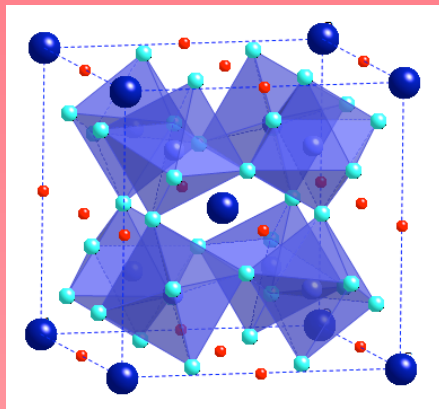
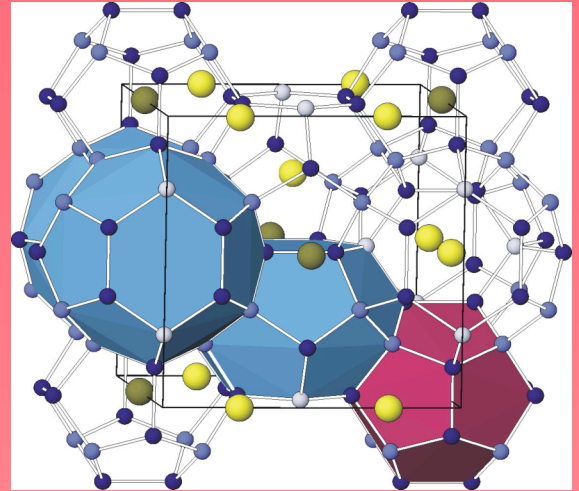
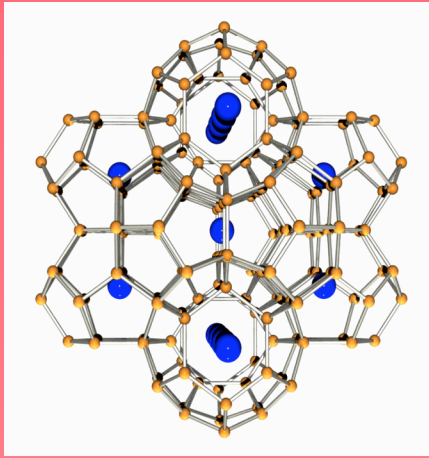
Diffraction

Powder diffraction - **SEPD, GPPD, HIPD**
 Single crystal - **SCD**
 Liquids and Amorphous Materials - **GLAD**

Large Scale Structures

Small Angle Scattering - **SAND, SASI**
 Reflectometry - **POSY I, POSY II**

Crystallography



SINGLE CRYSTAL DIFFRACTOMETER (SCD)

A. J. Schultz, P. M. De Lurgio, J. P. Hammonds, M. E. Miller, I. Naday,
P. F. Peterson, P. M. B. Piccoli, R. R. Porter, T. G. Worlton
Argonne National Laboratory

D. J. Mikkelson, R. L. Mikkelson,
University of Wisconsin-Stout

Abstract

During the past five years the SCD has undergone a major upgrade involving replacement of most of the hardware and software. In particular, two new position-sensitive scintillator area detectors based on the Anger camera concept were designed, fabricated and installed on the SCD. Each of these detectors has active areas of $15 \times 15 \text{ cm}^2$ with a spatial resolution of better than 2 mm. A new data acquisition system permits the use of larger data files with a larger wavelength bandwidth at higher time-of-flight resolution. Software developed with tools in the ISAW workbench provides graphical manipulation of three-dimensional arrays of data in histogram coordinates and in reciprocal space, and user-friendly wizards for routine data analysis.

Introduction

Since the early 1980's with the advent of pulsed spallation neutron sources, the single crystal neutron time-of-flight (TOF) Laue technique has been shown to be a highly useful tool in studies ranging from chemical structure and bonding to superlattice formation in high- T_c superconductors. As described in detail elsewhere [1-3], the TOF Laue technique at a pulsed spallation neutron source can gather data from a solid volume of reciprocal space with a stationary sample and area detectors. The IPNS single crystal diffractometer (SCD) became opera-

tional in 1981 with a neutron Anger camera which was designed and fabricated at Argonne [4]. The detector, with an active area of $30 \times 30 \text{ cm}^2$ and spatial resolution of $\sim 3.5 \text{ mm}$, had performed well for over 20 years, but relied on currently outdated analog electronics which were becoming unreliable. A few years ago it was decided to replace the original detector with two new $15 \times 15 \text{ cm}^2$ detectors with resolution of $< 2 \text{ mm}$. At the same time, a completely new data acquisition system was installed as part of a general IPNS upgrade project.

Instrument Configuration

A schematic drawing of the instrument is shown in Figure 1 and instrument parameters are provided in Table 1. This configuration is similar to the previous one except that a single $30 \times 30 \text{ cm}^2$ detector at 2θ of 90° has been replaced by two $15 \times 15 \text{ cm}^2$ detectors. These detectors now sit on pedestals which are mounted on translators with computer-controlled stepping motors to vary the sample to detector distances. In addition, an aluminum plate with a radial array of tapped holes permits the detectors to be manually moved to other scattering angles if required or to add additional detectors.

The detectors are at sample-to-detector distances on a locus of equal resolution as described by Carpenter [5].

Table 1. Instrument parameters.

Moderator	liq. methane at 105 K
Source frequency	30 Hz
Sample-to-moderator dist.	940 cm
Detectors:	
Number of detectors	2
Detector active area	$155 \times 155 \text{ mm}^2$
Scintillator	GS20 ^6Li glass
Scintillator thickness	2 mm
Efficiency @ 1 Å	0.86
Typical detector channels	100 x 100
Detector 1:	
angle	75°
sample-to-detector dist.	23 cm
Detector 2:	
angle	120°
sample-to-detector dist.	18 cm
Typical TOF range	1–25 ms
wavelength range	0.4–10 Å
d -spacing range	~ 0.3 –8 Å
TOF resolution, $\Delta t/t$	0.01

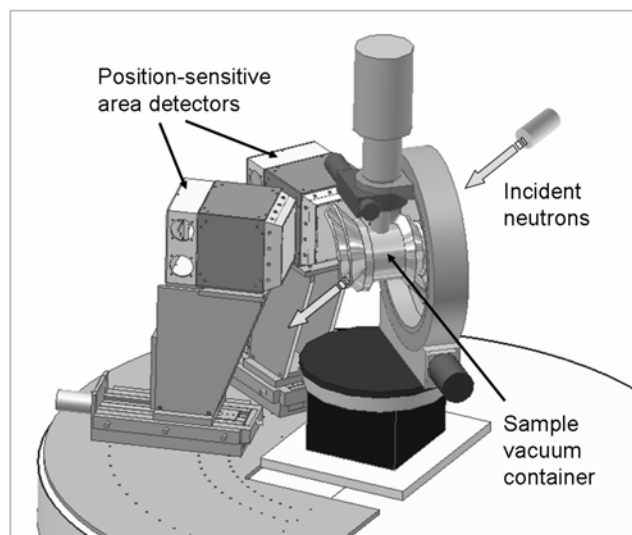


Figure 1. Schematic drawing of the SCD without shielding.

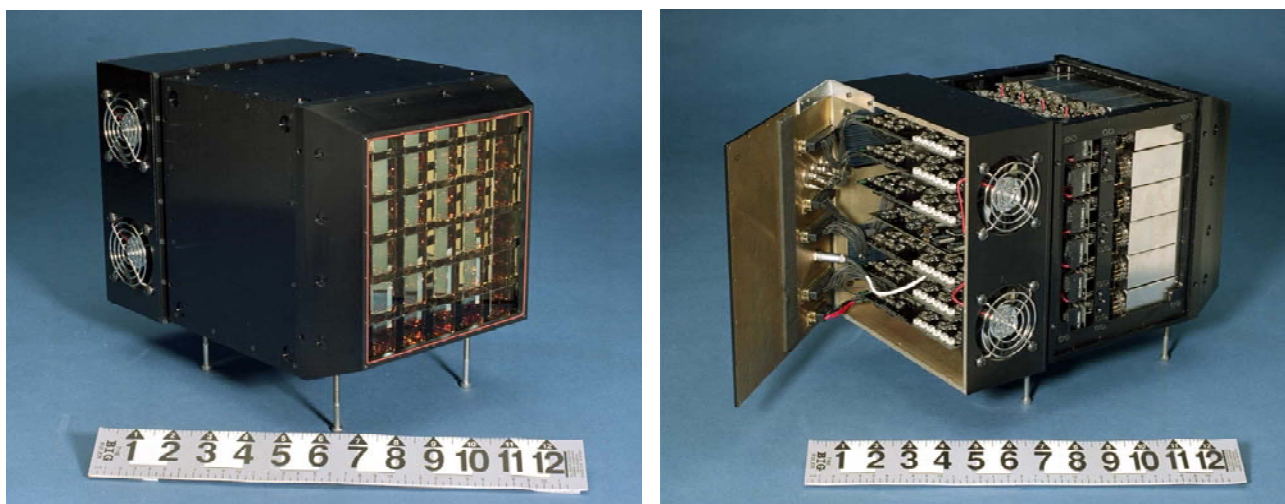


Figure 2. Two photographs of the neutron Anger detectors. Left: front view with the scintillator and front cover panel removed. Right: back view with side panels removed.

One of the detectors is centered at a scattering angle of 75° and a crystal-to-detector distance of 23 cm, and the second detector is at 120° and 18 cm. With this arrangement, each detector also subtends a similar solid angle in reciprocal space, which results in a more efficient data collection. The 22 settings are half of the number of settings previously required with the larger detector at 32 cm, thus reducing the data collection time by a factor of two.

Detector Design

In the original detector, four $15 \times 15 \text{ cm}^2$ ^6Li -glass scintillators were epoxied together to form a $30 \times 30 \text{ cm}^2$ active area [4]. Behind the scintillators was a light coupler and then a 7 by 7 array of 2 inch square photomultiplier tubes. The detector, which was rebuilt in 1993, worked well for over 20 years although the seams where the four scintillators were joined were clearly visible in the data. In addition, the aging analog electronic components were beginning to fail.

Photographs of the new detectors are shown in Figure 2. The detectors were designed to be smaller and more compact, and with better spatial resolution than the previous detector, so that they could be situated closer to the sample [6]. Thus, the two new detectors, each with an active area of $155 \times 155 \text{ mm}^2$, provide twice the solid angle coverage of the old $300 \times 300 \text{ mm}^2$ detector. Spatial resolution for the new detectors is $\sim 1.5 \text{ mm}$. The new design incorporates optimized optics with a 6 by 6 array of 28 mm square small pitch photomultiplier tubes (PMTs) coupled to tapered light concentrators which reflect light to the photocathode of the appropriate PMT that would otherwise fall between PMTs.

Also incorporated are newly developed software controlled electronics and a new position extraction algorithm (PEA) which achieves spatial resolution better than 2 mm full width at half maximum over the entire active area. The position is calculated in real-time by a

microprocessor using the new PEA which fits a two-dimensional light spread function to the observed light spread response of the PMTs to obtain parameters describing the event position. Essentially, the PEA provides an analytical equivalent of a numerical maximum-likelihood position determination for each event. This new method improves the spatial resolution and uniformity of the flood field response. The new PEA can determine the position of events at the edge of the scintillator when a portion of the light spread function falls beyond the edge of the PMT array. The detector enclosure incorporates attached shielding plates that minimize the surface area needed to shield the detector.

Data Acquisition System

The old data acquisition system (DAS) utilized a DEC MicroVAX computer. User control of starting and stopping runs, scheduling runs, controlling stepping motors and temperature, etc., was accomplished through Fortran programs with line command input.

In the new system, the user computer is a PC running the Linux operating system [7]. The EPICS control system provides a graphical user interface (GUI) for controlling the instrument hardware. In addition, run file setup and visualization (see below) is performed using the ISAW scripting language with GUI's for input from the user.

ISAW Developments for SCD Data

ISAW is the acronym for the Integrated Spectral Analysis Workbench software developed at IPNS and at the University of Wisconsin-Stout, with the support of the National Science Foundation [8]. ISAW is constructed from a large collection of individual components that provide data access, analysis and visualization operations for neutron scattering data. ISAW is implemented in Java for portability and is freely available from the IPNS web site at <http://www.pns.anl.gov/>, then click on Controls and

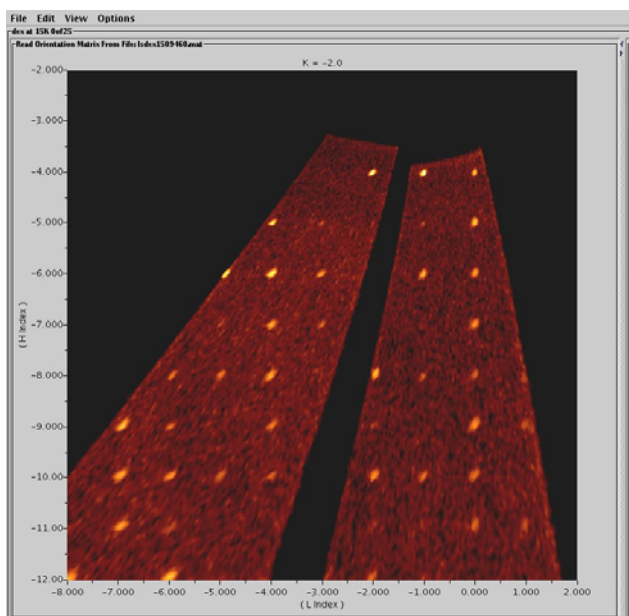


Figure 3. A 2D slice through the data. The image shows data from the two detectors from a single run file.

Computing > ISAW.

ISAW is built around a few fundamental concepts, DataSets, Operators, viewers and retrievers. "DataSet" objects hold raw and partially processed collections of spectra, along with meta-data needed for analysis of the data, such as detector positions, initial flight path length and sample orientation. A DataSet can be viewed in several different ways using "DataSetViewer" objects. Various data analysis steps can be carried out by applying self-describing "Operator" objects to DataSets. These individual steps can be invoked manually from the ISAW

GUI, or a sequence of operations can be carried out using a script written in ISAW's scripting language or in Jython. Sequences of operations can also be combined in a Wizard to allow the user to adjust parameters and to step forward or backward through a sequence of Operators.

To support the upgraded SCD, operators were implemented to carry out essential analysis steps such as finding, indexing and integrating peaks in the 3D data volume. In addition, user-friendly Wizards were implemented to help the user step through these operations. Interactive viewers were designed and implemented to display arbitrary slices through reciprocal space (Fig. 3) and to provide a 3D view of reciprocal space (Fig. 4) to help index twinned crystals and observe diffuse scattering. Finally, a new calibration system was developed to adjust instrument parameters such as the nominal detector positions, orientations and sizes.

Tutorial

A tutorial has been developed which leads the user step by step through the data analysis from initial peak finding and autoindexing to integration and data reduction, after which the structure can be analyzed and refined with programs such as GSAS and SHELX. The tutorial is available for downloading along with the raw data files (70 Mb) from a crystal of oxalic acid dihydrate from the web site <http://www.pns.anl.gov/instruments/scd/>, then click on Software and Procedures > Manuals, Users Guides and Tutorials. A web version of just the tutorial can be viewed online with a web browser. The tutorial is continuously modified as additions and modifications to the software are instituted. The SCD web site also contains links to other useful information and software for new and returning users.

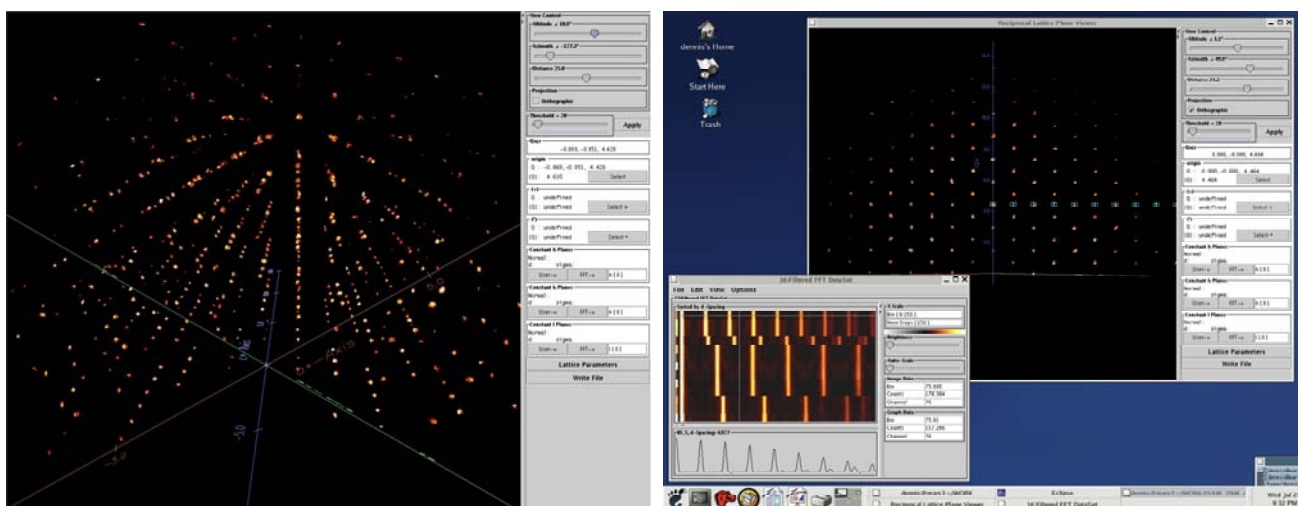


Figure 4. The 3D reciprocal lattice view of data from several run files combined from a quartz crystal. The left view is a perspective view of the reciprocal lattice. The right view is orthographic and also shows the lattice planes from the FFT application.

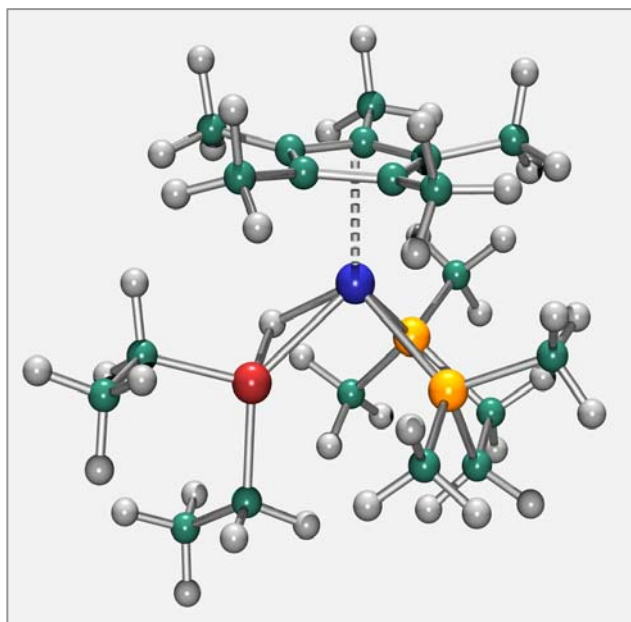


Figure 5. Molecular structure of a molybdenum silylene hydride complex with a three center Si–H–Mo bond (Mo, blue; Si, red; H, gray; P, orange; C, green).

Recent Results

Several data collections and analyses have been completed with the new upgraded SCD instrument and software. In one example, the structures of two binuclear nickel complexes with linear Ni–H–Ni bonds recently derived from data obtained with the new system are described by Vicic and coworkers from the University of Arkansas in an accompanying article in this *Progress Report* and in a publication of one of the molecules [9].

Another recent example is the structure of the molybdenum silylene hydride complex shown in Figure 5 [10]. Just as the search for stable, multiple-bonded, transition metal–carbon complexes (alkylidene complexes) was of great interest for 20–30 years in investigations, Mork and Tilley at the University of California at Berkeley have recently been investigating complexes with multiple bonding between silicon and transition metals. One of these complexes, $(C_5Me_5)Mo(SiHEt_2)(Me_2PCH_2CH_2P-Me_2)$, was isolated, and its neutron structure provides a snapshot of the intermediate in the oxidative addition of a Si–H bond to a metal. The structure can be described as having the form of a three-legged piano stool with one leg consisting of a Si–H σ -bond complex with the molybdenum. The molecule formally contains a 16-electron system in the absence of the Si–H σ -bond interaction with the metal center. As observed previously, formation of a 3-center, 2-electron, σ -complex bond achieves a stable 18-electron configuration.

Summary

In summary, the IPNS SCD single-crystal neutron Laue diffractometer has recently been upgraded with two new

position-sensitive detectors and new data acquisition hardware and software. The improvements to the SCD described in this article provide more accurate data in half the time of the previous system. Additional detectors can be added incrementally as permitted by funding and effort resources.

REFERENCES

- [1] A. J. Schultz and P. C. W. Leung (1986). "Analysis of Spallation Time-of-Flight (TOF) Neutron Data from a 2-D Position-Sensitive Detector." *J. de Physique Colloque C5* **47**, 137-142.
- [2] A. J. Schultz (1986). "Chemical Crystallography" in *Neutron Scattering, Part A*, edited by K. Sköld and D. L. Price, Academic Press, Orlando, FL, pp 339-367.
- [3] C. C. Wilson (2005). "Neutron single crystal diffraction: techniques and applications in molecular systems." *Z. Kristallogr.* **220**, 385-398.
- [4] M. G. Strauss, R. Brenner, F. J. Lynch and C. B. Morgan (1981). "2-D Position-Sensitive Scintillation Detector for Neutrons." *IEEE Trans. Nucl. Sci.* **NS-28**, 800-806.
- [5] J. M. Carpenter (1967). "Extended detectors in neutron time-of-flight diffraction experiments." *Nucl. Instrum. Methods* **47**, 179-180.
- [6] P. M. De Lurgio, K. A. Farrar, A. S. Kreps, T. J. Madden, I. Naday, J. T. Weizeorick, J. P. Hammonds, M. E. Miller and A. J. Schultz (2005). "2-D scintillation position-sensitive neutron detector." *IEEE Nuclear Science Symposium*, in press.
- [7] J. P. Hammonds, R. R. Porter, A. Chatterjee, T. G. Worlton, P. F. Peterson, J. W. Weizeorick, P. M. D. Lurgio, I. Naday, D. J. Mikkelsen and R. L. Mikkelsen (2002). "Developments for the IPNS Data Acquisition System Upgrade." NOBUGS 2002, NIST, Gaithersburg, MD, November 4-6, <http://www.arxiv.org/abs/physics/0210075>.
- [8] D. Mikkelsen, A. J. Schultz, R. Mikkelsen and T. Worlton (2005). "Visualization and analysis of single crystal time-of-flight neutron scattering data using ISAW." *IUCr Commission on Crystallographic Computing Newsletter No. 5*, edited by S. Billinge, G. Chapuis, L. Cranswick and R. Lifshitz, pp 32-39, <http://www.iucr.org/iucr-top/comm/ccom/newsletters/>.
- [9] D. A. Vicic, T. J. Anderson, J. A. Cowan and A. J. Schultz (2004). "Synthesis, structure, and reactivity of a dinuclear metal complex with linear M–H–M bonding." *J. Am. Chem. Soc.* **126**, 8132-8133.
- [10] B. V. Mork, T. D. Tilley, A. J. Schultz and J. A. Cowan (2004). "Silylene Hydride Complexes of Molybdenum with Silicon-Hydrogen Interactions. Neutron Structure of $(\eta^5-C_5Me_5)(Me_2PCH_2CH_2P-Me_2)Mo(H)(SiEt_2)$." *J. Am. Chem. Soc.* **126**, 10428-10449.

SINGLE CRYSTAL NEUTRON DIFFRACTION STUDIES OF THERMOELECTRIC MATERIALS

B. B. Iversen, A. Bentien, M. Christensen, N. Lock, Department of Chemistry, University of Aarhus, DK-8000 Denmark
A. J. Schulz, IPNS, Argonne, IL 60439, U.S.A.

Abstract

The crux of modern thermoelectric materials is their very low lattice thermal conductivities (κ_L), and the origin of the glass-like behavior of κ_L in some highly crystalline clathrates has been intensely discussed. Guest atom tunnelling, resonant scattering, anharmonicity, and disorder has been used to explain the very low κ_L , but these models all lack the ability to explain the fundamental difference in κ_L between the almost identical crystal structures of *n*- and *p*-type $\text{Ba}_8\text{Ga}_{16}\text{Ge}_{30}$. Clathrates have presented a particularly challenging case for studying the relation between structure and property. In a series of studies, we have used IPNS single crystal neutron diffraction data to accurately establish crystal structures of thermoelectric clathrates, and to quantify disorder, and harmonic as well as anharmonic thermal motion contributions.

INTRODUCTION

Thermoelectric materials had their main blooming in the 50s, where many of the materials used commercially even today were developed. Due to the discovery of promising new materials, the scientific interest in TE materials has been revitalized in recent years. These materials are based on a design strategy named the “phonon-glass – electron crystal” concept [1]. Briefly, this means that a good thermoelectric should conduct heat like an amorphous material and electricity like a crystal. The basic hypothesis for the thermoelectric properties of the new materials is that a semi-conducting host structure results in a high Seebeck coefficient (S) and electric conductivity (σ), while extreme thermal motion of the loosely bonded guest atoms gives a large reduction of the thermal conductivity (κ) through scattering of the heat carrying phonons. This results in a large thermoelectric “figure of merit”, $ZT = TS^2\sigma/\kappa$. The two most studied examples of the new host-guest thermo-electric materials are skutterudites and inorganic clathrates.

Most studies of clathrates have concerned the type I clathrate structure, $(\text{M}^{2+})_8\text{III}_{16}\text{IV}_{30}$, which can be formed with a large number of elemental compositions (roman numeral refer to group number in the periodic table), Fig. 1. There are many structural aspects, which are important for understanding the thermoelectric properties of clathrates. For the guest atoms it is especially the exact position and the atomic motion that is of importance. In other words, are the atoms located in the centers of the cages or are they displaced towards the cage wall and statistically disordered (static or dynamic) over several sites? Are the atoms rattling with low frequency motion

that can hybridize with the acoustic phonons? How large is the anharmonic contribution to the atomic motion? With regard to the framework atoms, the exact positions of the group III atoms in the framework can greatly influence the thermoelectric properties [2]. This makes it important to establish whether the group III atoms are randomly distributed or prefer certain framework sites [3]. Furthermore, the overall stoichiometry of the clathrates is decisive for the charge carrier concentration. In the case of $\text{M}_8\text{Ga}_{16-x}\text{Ge}_{30+x}$ clathrates, $\text{Ga} > 16$ gives a *p*-type system, whereas $\text{Ga} < 16$ gives an *n*-type system [4, 5].

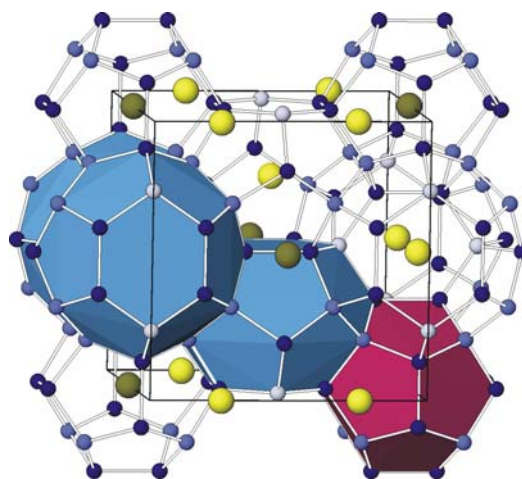


Figure 1: The type I clathrate structure with the cubic unit cell marked by a black solid line. Framework atoms are located on 6*c* (light blue), 16*i* (dark blue) and 24*k* (blue) sites forming two types of cages. The red cage is surrounding an M1 guest atom on the 2*a* site, and the larger blue cage surrounds an M2 guest atom on the 6*d* site.

GUEST ATOMS

Chakoumakos *et al.* reported multi-temperature single crystal as well as powder neutron diffraction data on $\text{Sr}_8\text{Ga}_{16}\text{Ge}_{30}$, which showed that the guest atom in the large cage, Sr2, had unusually large Atomic Displacement Parameters (ADPs) [6, 7]. The features of difference Fourier nuclear density maps lead Chakoumakos *et al.* to suggest a four site disorder model for Sr2. The complex nature of the Sr2 atom in $\text{Sr}_8\text{Ga}_{16}\text{Ge}_{30}$ and of Ba2 in $\text{Ba}_8\text{Ga}_{16}\text{Ge}_{30}$ was also revealed by maximum entropy method (MEM) analysis of single crystal X-ray data by Bentien *et al* [3]. The advantage of the MEM electron densities is that they are model free and the problem with

Fourier termination ripples is much reduced. However, a direct plot of the thermally smeared electron density distribution only showed a very diffuse M2 atomic density with no “peaks” to define possible disorder. For this reason Bontien *et al* introduced MEM deformation densities which show the combined effects of chemical bond deformation, charge transfer and structural disorder. The analysis suggested that the disorder is more complex than a four-site model, but similar for Sr2 and Ba2. However, the inherent problem in X-ray analysis of disorder is the superimposed diffuse features of the electron density distribution, and such studies are best done with neutrons.

We therefore carried out a benchmark multi-temperature single crystal neutron diffraction study of Ba₈Ga₁₆Si₃₀ [8]. Extensive data were collected at SCD at 15, 100, 150, 200, 250, 300, 450, 600, 900 K. In Fig. 2 the MEM nuclear deformation density in the (100) plane of Ba2 is shown at 15 K, 300 K and 900 K together with the total MEM nuclear density at 15 K. The MEM nuclear density is broad and centered at the center of the cage (lower right in Fig. 2). The Ba2 nuclear density becomes much more diffuse with increasing temperature, but there is no clear evidence of disorder. However, just as the subtle details of an electron density distribution are better revealed through deformation densities, subtle disorder features are best revealed by nuclear deformation densities. In the MEM nuclear deformation density a reference model based on a Ba2 atom centered in the cage has been subtracted from the final MEM density. The map provides direct evidence that the Ba2 atom in Ba₈Ga₁₆Si₃₀ is either disordered or exhibits high order anharmonic motion even at 15 K. The data furthermore show that also the Ba1 atom in the small cavity has disorder and/or anharmonicity even at 15 K

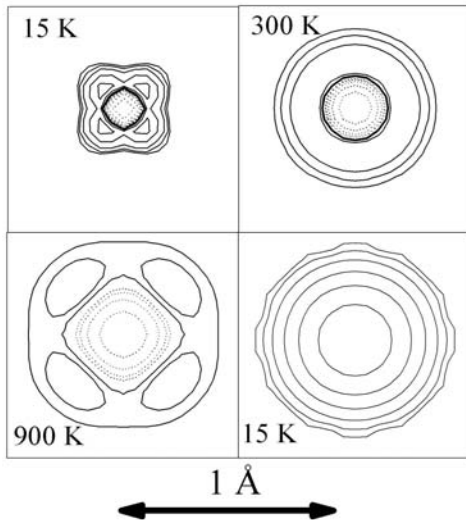


Figure 2: MEM difference densities, $\rho(\text{MEM}) - \rho(\text{reference})$, in the (100) plane through Ba(2) in Ba₈Ga₁₆Si₃₀ at 15 K, 300 K and 900 K. The difference densities are plotted on a logarithmic scale, 0.0125×2^N ($N = 0, \dots, 6$), and solid contours are positive, dotted

contours are negative. The plot at the lower right is the total MEM nuclear density at 15 K.

In two new IPNS SCD studies multi-temperature single crystal neutron data have been collected on both *p*-type and *n*-type Ba₈Ga₁₆Ge₃₀ [9]. Data were recorded to extremely high resolution ($d_{\text{min}} < 0.25 \text{ \AA}$), and the non-elliptical features obtained for Ba in Ba₈Ga₁₆Si₃₀ are also observed for Ba in these two types of Ba₈Ga₁₆Ge₃₀ structures. Another key result is that the *p*-type and *n*-type Ba₈Ga₁₆Ge₃₀ crystal structures are virtually identical, and this seriously challenges current models for explaining the glass-like κ in some clathrates.

The disorder on the guest atom sites also can be probed indirectly by modeling the temperature dependence of the refined ADPs with an Einstein model,

$$\langle u^2 \rangle = d^2 + \frac{\hbar^2}{2mk_B \Theta_E} \coth \frac{\Theta_E}{2T}$$

In this equation, Θ_E is the Einstein temperature. Figure 2 shows the guest atom ADPs of Ba₈Ga₁₆Si₃₀ as a function of temperature. A good modelling is only obtained if both a disorder parameter (d) and a Gruneisen parameter γ_G is included in the fit [8]. The latter can be done if the temperature dependence of the cell volume is known so that $\Theta_E(T)$ can be rewritten as $\Theta_E(T_0)(1 - \gamma_G \Delta V(T)/V(T_0))$.

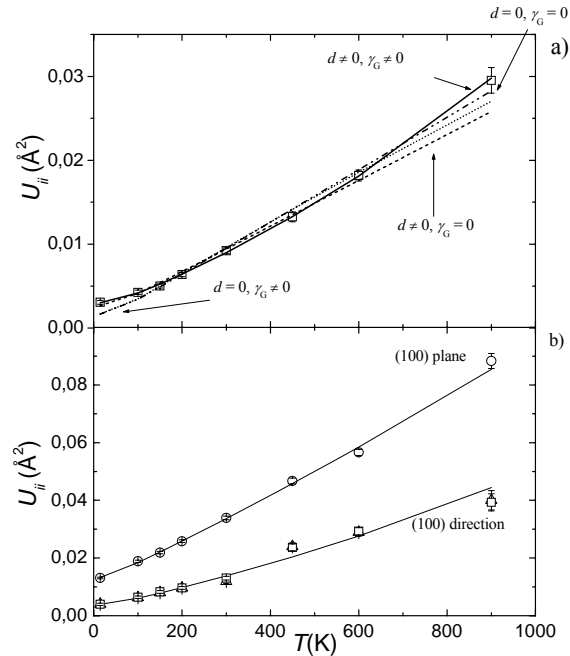


Figure 3: Guest atom ADPs in Ba₈Ga₁₆Si₃₀ as a function of temperature. In (a) $U_{11} = U_{22} = U_{33}$ (\square) is plotted for Ba(1), and in (b) U_{11} (\square) and $U_{22} = U_{33}$ (\circ) for Ba(2).

It is interesting that higher values of the guest atom resonance frequencies are obtained from diffraction

experiments and specific heat data on one side than from inelastic neutron scattering, Raman spectroscopy and acoustic attenuation on the other [10]. This discrepancy has recently been explained by the presence of strong phonon charge carrier scattering, which is also believed to be the origin of the glass-like behavior of κ [11]

To model anharmonic motion one can use the Gram-Charlier expansion of the harmonic temperature factor [12]. In X-ray structure factor refinements it can be difficult to separate anharmonic thermal motion from aspherical bonding effects, and neutron data are therefore preferable.

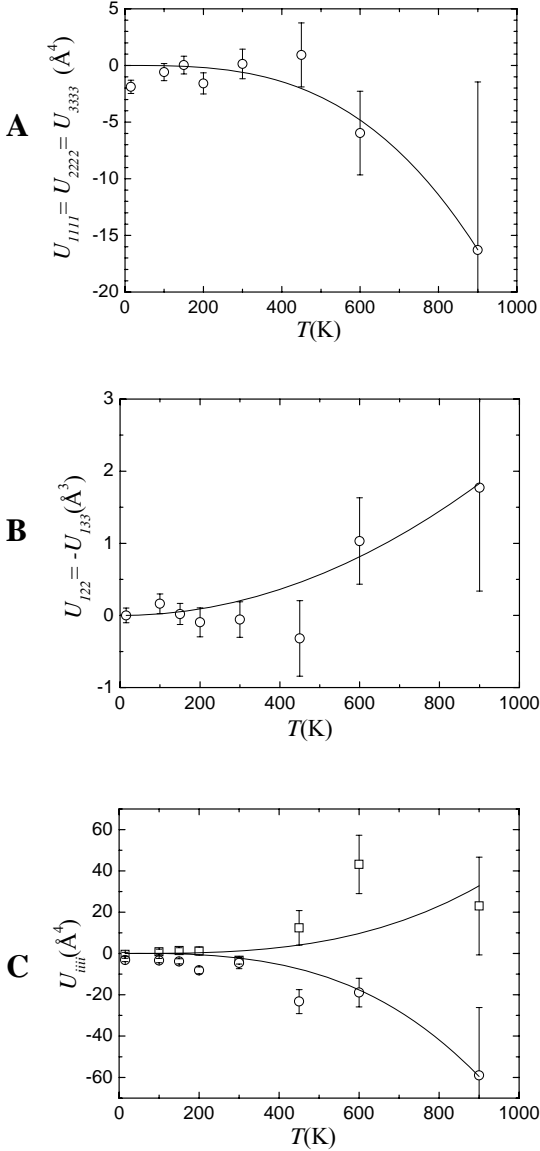


Figure 4: (a) The $U_{1111} = U_{2222} = U_{3333}$ anharmonic Gram-Charlier parameter for Ba(1), (b) the cubic anharmonic Gram-Charlier parameter for Ba(2), (c) the U_{1111} (\square) and $U_{2222} = U_{3333}$ (\circ) anharmonic Gram-Charlier

parameters for Ba(2). The lines represent a T^3 dependence in (a) and (c), and a T^2 dependence in (b).

The Gram-Charlier expansion contains no explicit model for the temperature dependence of the anharmonic parameters, since they are not related to a physical model, but merely mathematical parameters describing deviations from a Gaussian distribution. In Figure 5 refined anharmonic parameters are plotted as a function of temperature. For both Ba1 and Ba2, anharmonicity becomes visible above 450 K. A T^2 dependence has been fitted to the cubic parameter, whereas T^3 dependencies are fitted to the fourth order parameters. Such temperature dependencies are expected for anharmonic One Particle Potential parameters (see below), but not necessarily for Gram-Charlier parameters [13]. Nevertheless, the fits are quite good, and they isolate the 450 K point as an outlier. The values of the anharmonic parameters are almost an order of magnitude larger than the anharmonic parameters observed in metallic magnesium [14].

An alternative scheme for quantifying the anharmonicity is direct space fitting of the MEM nuclear densities [8, 14]. The MEM nuclear density is proportional to the nuclear probability density function ($P(\mathbf{u})$). If we approximate the Ba2 guest atom as an Einstein oscillator then, in the classical limit, $P(\mathbf{u})$ is given by the Boltzman equation $P(\mathbf{u}) = \exp(-V(\mathbf{u})/kT)$, where $V(\mathbf{u})$ is the one-particle potential of the oscillator in the local displacement coordinate \mathbf{u} . If Ba2 is disordered at the $24j$ position in the large cage, we can approximate the probability density function as a weighted sum of the $P(\mathbf{u})$'s for each disorder site, $P_{\text{tot}}(r) = P[V(r_1, r_2-\lambda, r_3-\lambda)] + P[V(r_1, r_2+\lambda, r_3-\lambda)] + P[V(r_1, r_2-\lambda, r_3+\lambda)] + P[V(r_1, r_2+\lambda, r_3+\lambda)]$, where λ models the off-center location. Taking the site symmetry of Ba2 in space group 223 into account we fitted a potential expression up to fourth order to the MEM nuclear density.

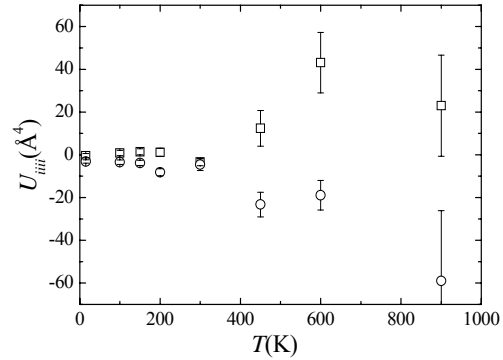


Figure 5: Fourth order anharmonic force constants for Ba(2) in $\text{Ba}_8\text{Ga}_{16}\text{Si}_{30}$ (δ_{1111} and $\delta_{2222} = \delta_{3333}$). The values were obtained using the classical OPP model for least squares fitting to MEM nuclear densities.

In Figure 5 the MEM derived fourth order anharmonic parameters are plotted. As for the reciprocal space fitting,

the anharmonicity becomes significant above the Debye temperature (387 K). The magnitude of the fitted parameters is again much larger than parameters obtained for metallic magnesium using the same approach [15]. It is noteworthy that the refined disorder parameter, λ , is increasing with temperature, which means that the atoms move closer to the framework at elevated temperatures. This presumably is an effect of moving up in an asymmetric potential.

FRAMEWORK

In $M_8Ga_{16}Ge_{30}$ clathrates it is difficult to determine the exact host structure due to the very similar scattering powers of Ga and Ge for both X-rays and neutron. For neutrons the scattering lengths are $b(Ga) = 0.73$ fm and $b(Ge) = 0.81$ fm, whereas for X-rays the contrast is even worse with Ga having 31 electrons and Ge 32 electrons. In many crystallographic studies of Ga/Ge clathrates the 16 Ga atoms are assumed to be randomly distributed over the 46 framework sites [6, 7]. However, early on MEM analysis of X-ray diffraction data on $Sr_8Ga_{16}Ge_{30}$ and $Ba_8Ga_{16}Ge_{30}$ actually found a preference for Ga at the 6c site and that Ga avoids the 16i site [3]. This result was later supported by the framework positions observed in clathrates such as $Ba_8Ga_{16}Si_{30}$ where the scattering contrast is much larger [8, 10]. More recently resonant powder diffraction measurements on $Sr_8Ga_{16}Ge_{30}$ have also supported the result of the MEM analysis but a reliable quantitative assessment could not be given for the host structure ordering [15]. Thus, refined occupancies from the $Sr_8Ga_{16}Ge_{30}$ resonant powder diffraction data sum to give a strongly p -type material for a crystal that is n -type. The new SCD data on p - and n -type $Ba_8Ga_{16}Ge_{30}$ have very high resolution such that stable refinements of occupancies can be carried out [9]. The refinements once again support the Ga preference for the 6c site, but also indicate that the framework is more ordered in n -type $Ba_8Ga_{16}Ge_{30}$ than in p -type $Ba_8Ga_{16}Ge_{30}$.

REFERENCES

- [1] G. A. Slack (1995) *CRC Handbook of Thermoelectrics*, edited by D. M. Rowe, pp. 407, Boca Raton, Florida: CRC Press
- [2] N. P. Blake, D. Bryan, S. Lattner, L. Møllnitz, G. D. Stucky and H. Metiu, *J. Chem. Phys.* **114** (2001), 10063
- [3] A. Bentien, A. E. C. Palmqvist, J. D. Bryan, S. Lattner, G. D. Stucky, L. Furenlid and B. B. Iversen, *Angew. Chem. Int. Ed.* **39** (2000) 3613
- [4] J. D. Bryan, N. P. Blake, H. Metiu, G. D. Stucky, B. B. Iversen, R. D. Poulsen and A. Bentien, *J. Appl. Phys.* **92** (2002), 7281
- [5] A. Bentien, M. Christensen, J. D. Bryan, A. Sanchez, S. Paschen, F. Steglich, G. D. Stucky and B. Iversen, *Phys. Rev. B* **69** (2004), 045107
- [6] B. C. Chakoumakos, B. C. Sales, D. G. Mandrus and G. S. Nolas, *J. Alloys Compd.* **296** (2000), 80.
- [7] V. Keppens, B. C. Sales, D. Mandrus, B. C. Chakoumakos, C. Laermans, *Philos. Mag. Lett.* **80** (2000), 807.
- [8] Bentien, A.; Iversen, B. B.; Bryan, J. D.; Stucky, G. D.; Palmqvist, A. E. C.; Schultz, A. J.; Henning, W. *J. Appl. Phys.* **2002**, *91*, 5694-5699
- [9] M. Christensen, N. Lock, J. Overgaard, B. B. Iversen, in preparation
- [10] A. Bentien, E. Nishibori, S. Paschen and B. B. Iversen, *Phys. Rev. B.* **71** (2005) 144107-1-18.
- [11] A. Bentien, S. Johnsen and B. B. Iversen, *Phys. Rev. B.* (2005), submitted.
- [12] W. F. Kuhs, *Acta Crystallogr. Sect. A* **48** (1992), 80
- [13] P. Coppens (1997) *X-ray Charge Densities and Chemical Bonding*, Oxford University Press
- [14] B. B. Iversen, S. K. Nielsen and F. K. Larsen, *Philos. Mag. A.* **72** (1995) 1357
- [15] Zhang, Y. G., Lee, P. L., Nolas, G. S. & Wilkinson, A. P. *Appl. Phys. Lett.* **80**, 2931-2933 (2002)

LINEAR M-H-M BONDING IN SIMPLE DINUCLEAR METAL COMPLEXES

D. A. Vicic, T. J. Anderson, University of Arkansas, Fayetteville, AR 72701
J. A. Cowan, P. M. B. Piccoli, A. J. Schultz, IPNS, Argonne, IL 60439.

Abstract

Single crystal neutron diffraction structures of $[(\text{dippm})_2\text{Ni}_2\text{Br}_2](\mu\text{-H})$ (**1**) and $[(\text{dippm})_2\text{Ni}_2\text{Cl}_2](\mu\text{-H})$ (**2**, $\text{dippm} = \text{bis}(\text{di-}i\text{-propylphosphino})\text{methane}$) were obtained and detailed the first examples of linear M-H-M bonding in simple dinuclear metal complexes.

Introduction

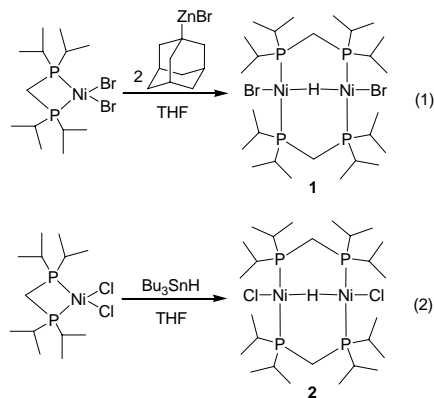
A number of years ago, the X-ray crystal structure of the unsupported bridging hydride complex $[\text{HCr}_2(\text{CO})_{10}]^-$ was reported by Dahl and co-workers [2]. The position of the bridging hydride could only be inferred to have a linear relationship with the two chromium atoms based on the D_{4h} symmetry of the anion and the eclipsed positions of the equatorial carbonyl groups. However, it was later revealed by neutron diffraction that, because of the presence of a crystallographic center of inversion in the middle of the anion, the hydrogen atom did not lie at the predicted position but rather was disordered over two bent Cr-H-Cr positions [1]. Low temperature neutron diffraction analysis of the $[\text{K}(\text{crypt-222})]^+$ salt (which has no symmetry-imposed restraints) later confirmed the bent nature of the Cr-H-Cr bond [4]. Since then, a plethora of neutron diffraction studies on transition metal hydrides suggest that the M-H-M linkage is inherently bent [6,8] (Table 1 shows the largest M-H-M bond angles thus far reported in single hydrogen bridged systems). Here we report two dinuclear nickel complexes, each containing a single bridging hydride, that is found to lie co-linearly with the two metal centers and shows no disorder in the neutron diffraction studies.

Synthesis of Compounds

Compound **1** was formed unexpectedly in 48% yield by the reaction of 1-adamantylzinc bromide with $(\text{dippe})\text{NiBr}_2$ according to the reaction described in eq 1 [10]. Because of the difficulty in preparing 1-adamantylzinc chloride, an alternate method was developed to prepare compound **2** (eq 2). Reaction of $(\text{dippe})\text{NiCl}_2$ with excess tributyltin hydride afforded **2** in only 22% [13], but provided enough material for crystals suitable for neutron diffraction.

Description of Structures

The ORTEP diagram of **1** is shown in Figure 1, and clearly shows linear nature of the bridging hydride ligand. Instead of adopting a conventional "A-frame" structure that is normally seen in dimers containing the



bis(dialkylphosphino)methane ligand [3], the geometry is constrained with the two bromides occupying the endpoints of a linear axis. The Ni-H-Ni bond angle was found to be $177.9(10)^\circ$, much larger than the previously reported dinuclear metal complex having the largest bridging hydride ligand (Table 1) [6,8]. Moreover, the structure is dramatically different than that found for the closely related compound $[(\text{dcpm})_2\text{Ni}_2\text{Cl}_2](\mu\text{-H})$ (**3**, $\text{dcpm} = \text{bis}(\text{dicyclohexylphosphino})\text{methane}$), which has an M-H-M bond angle of $128(8)^\circ$ [14].

The difference in geometry between **1** and **3** prompted us to prepare the chloride derivative **2** to see if electronic effects were responsible for change to linearity in the Ni-H-Ni linkage of **1**. It seemed reasonable that electronic differences between Cl and Br could effect the occupancy of the Ni antibonding orbital, leading to stronger Ni-Ni repulsions and a linear Ni-H-Ni bridge in the case of the bromide analogue. However, since **1** and **3** contained

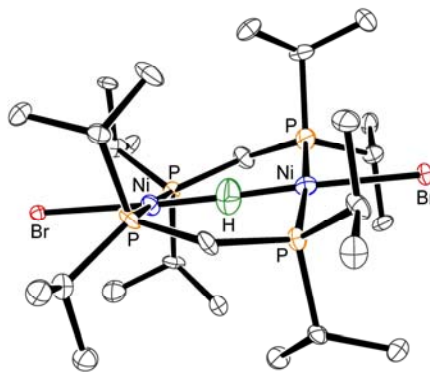


Figure 1. ORTEP diagram of **1** (50 % ellipsoids). All hydrogens except the bridging hydride are omitted for clarity.

Table 1. Largest M-H-M Bond Angles (°) Reported for Bimetallic Compounds and Characterized by Neutron Diffraction

Compound	M-H-M <	Ref.
1	177.9(10)	this work
2	177.5(11)	this work
[Cr ₂ (μ-H)(CO) ₁₀][NEt ₄]	158.9(6)	[1]
[Cr ₂ (μ-D)(CO) ₁₀][PPN]	155.8(9)	[3]
[Cr ₂ (μ-H)(CO) ₁₀][K(C ₁₈ H ₃₆ N ₂ O ₆)]	145.2(3)	[4]
(CO) ₅ Re(μ-H)Mn(CO) ₄ Mn(CO) ₅	138.5(3)	[5]
[W ₂ H(CO) ₁₀][NEt ₄]	137.1(10)	[6]
W ₂ H(CO) ₈ NO[P(OMe) ₃]	129.4(3)	[7]
β-W ₂ H(CO) ₉ NO	125.4(4)	[9]
α-W ₂ H(CO) ₉ NO	125.0(2)	[9]
[W ₂ H(CO) ₁₀][PPh ₄]	123.4(5)	[11]
[MoCp(CO) ₂] ₂ H[PMe ₂]	122.9(2)	[12]

different supporting ligands, it was necessary to prepare **2** to more rigorously rule out competing steric effects. Figure 2 shows the ORTEP diagram of **2**. The data show that the change of the ancillary ligand from bromide to chloride does not effect the preference of the bridging hydride to be linear.

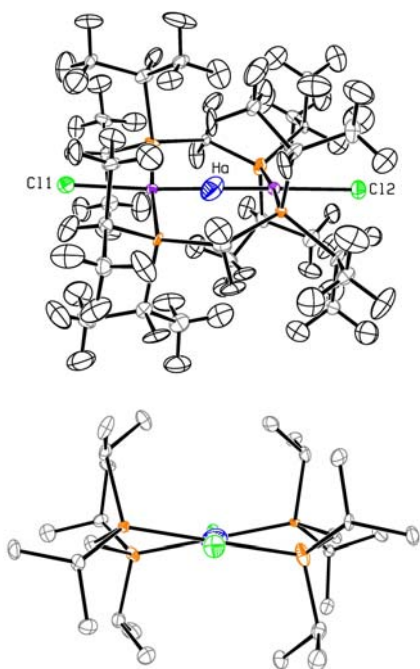


Figure 2. ORTEP diagram of **2** (50% ellipsoids). Top plot shows full structure. Bottom plot shows a side-on view with all hydrogens except the bridging hydride omitted for clarity.

So what are the forces responsible for the linear geometry in **1** and **2**? A reinvestigation of the structure of **3** by neutron diffraction techniques is currently being pursued in order to determine what role the phosphine ligand

plays in this unique type of bonding. Perhaps the ability of the *i*-propyl groups to interact with the halogen ligands coaxes the geometry to be linear (Figure 3). Indeed, contacts shorter than the sum of the van der Waals radii for C and X were observed for both **1** and **2**.

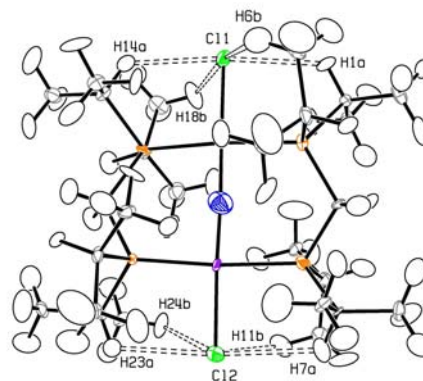


Figure 3. ORTEP diagram of **2** (50% ellipsoids) showing the intramolecular H...Cl contacts.

REFERENCES

- [1] Roziere, J.; Williams, J. M.; Stewart, R. P., Jr.; Petersen, J. L.; Dahl, L. F. *J. Am. Chem. Soc.* **1977**, *99*, 4497-4499.
- [2] Handy, L. B.; Ruff, J. K.; Dahl, L. F. *J. Am. Chem. Soc.* **1970**, *92*, 7312-7326.
- [3] Petersen, J. L.; Brown, R. K.; Williams, J. M.; McMullan, R. K. *Inorg. Chem.* **1979**, *18*, 3493-3498.
- [4] Petersen, J. L.; Brown, R. K.; Williams, J. M. *Inorg. Chem.* **1981**, *20*, 158-165.
- [5] Bullock, R. M.; Brammer, L.; Schultz, A. J.; Albinati, A.; Koetzle, T. F. *J. Am. Chem. Soc.* **1992**, *114*, 5125-5230.
- [6] Bau, R.; Teller, R. G.; Kirtley, S. W.; Koetzle, T. F. *Acc. Chem. Res.* **1979**, *12*, 176-183.
- [7] Love, R. A.; Chin, H. B.; Koetzle, T. F.; Kirtley, S. W.; Whittlesey, B. R.; Bau, R. **1976**, *98*, 4491-4498.
- [8] Bau, R.; Drabnis, M. H. *Inorg. Chim. Acta* **1997**, *259*, 27-50.
- [9] Olsen, J. P.; Koetzle, T. F.; Kirtley, S. W.; Andrews, M.; Tipton, D. L.; Bau, R. *J. Am. Chem. Soc.* **1974**, *96*, 6621-6627.
- [10] Vicic, D. A.; Anderson, T. J.; Cowan, J. A.; Schultz, A. J. *J. Am. Chem. Soc.* **2004**, *126*, 8132-8133.
- [11] Hart, D. W.; Bau, R.; Koetzle, T. F. *Organometallics* **1985**, *4*, 1590-1594.
- [12] Petersen, J. L.; Dahl, L. F.; Williams, J. M. *J. Am. Chem. Soc.* **1974**, *96*, 6610-6620.
- [13] Vicic, D. A. unpublished results, 2005.
- [14] Kriley, C. E.; Woolley, C. J.; Krepps, M. K.; Popa, E. M.; Fanwick, P. E.; Rothwell, I. P. *Inorg. Chim. Acta* **2000**, *300-302*, 200-205.

A PRESSURE-SWITCHABLE JAHN-TELLER DISTORTION IN $(\text{ND}_4)_2[\text{Cu}(\text{D}_2\text{O})_6](\text{SO}_4)_2$

M. A. Hitchman, H. Stratemeier, University of Tasmania, Hobart, Australia
C. J. Simmons, University of Hawaii, Hilo, HI, U.S.A.
A. J. Schultz, ANL, Argonne, IL, U.S.A.

Abstract

The Jahn-Teller effect plays a pivotal role in determining the structures of copper(II) and chromium(II) compounds, and may underlie the activity of the former metal ion in high temperature superconductors and biologically active molecules. The fact that the direction of the Jahn-Teller distortion in the copper and chromium ammonium Tutton salts may be switched by deuteration, the application of pressure, or doping with zinc ions, means that these compounds provide a unique opportunity to study the interplay of electronic and crystal packing forces in a Jahn-Teller system.

Introduction

The stereochemistry of Cu^{2+} complexes is generally interpreted in terms Jahn-Teller vibronic coupling, with this being termed ‘dynamic’ when the geometry changes as a function of temperature. The ammonium copper Tutton salt $(\text{NH}_4)_2[\text{Cu}(\text{H}_2\text{O})_6](\text{SO}_4)_2$ is of particular interest because on deuteration it adopts a structure (Form *A*) in which the long axis of the Jahn-Teller distorted $\text{Cu}(\text{D}_2\text{O})_6^{2+}$ ion occurs to a different pair of water molecules from those in the hydrogenous salt (Form *B*), with the change being accompanied by slight alterations in the hydrogen bonding and disposition of the counterions. Moreover, both $(\text{NH}_4)_2[\text{Cu}(\text{H}_2\text{O})_6](\text{SO}_4)_2$ and its deuterated analogue undergo a thermal equilibrium involving the alternative direction of the elongated Jahn-Teller distortion [1].

Pressure-Temperature Dependence

The present research has built upon the observation using the IPNS SCD that the structure of perdeuterated ammonium copper sulfate changes from Form *A* to Form *B* upon application of pressure [2], the first known exam-

ple of such a pressure-induced Jahn-Teller switch. The influence of pressure and temperature on the structural phase transition of $(\text{ND}_4)_2[\text{Cu}(\text{D}_2\text{O})_6](\text{SO}_4)_2$ has been looked at in greater detail using pulsed neutron powder diffraction on the SEPD and HIPD diffractometers [3,4]. At various temperatures between 260 K and 325 K the compound was found to change from Form *A* to *B* as the pressure was progressively increased from 1 to 700 bar, with the pressure needed to cause the switch decreasing as the temperature increased.

At 315 K and 325 K the structural change was gradual, smooth and reversible. At lower temperatures the change became sharp and below 307 K the pressure at which Form *B* changed to Form *A* as the pressure was slowly released was lower than that when the pressure was raised, *i.e.*, a pressure hysteresis occurred. For temperatures below ~ 298 K the sample remained ‘frozen’ in Form *B* when the pressure returned to 1 bar. On slowly warming a sample in this metastable state it changed to Form *A* between 296 K and 298.5 K.

As Form *B* is slightly less dense than Form *A*, the unit cell volume V was found to decrease as the thermal equilibrium developed. In the temperature range where the pressure switch was sharp and shows hysteresis the phase-change approximates to a first-order transition. The enthalpy or latent heat ΔH of the transformation may then be obtained from the rate of change of the pressure P as a function of the temperature T via the Clapeyron equation: $dP/dT = \Delta H/(T \Delta V)$.

Substitution of the observed changes in unit cell volume ΔV yields enthalpy changes decreasing from 259 cm^{-1} at 260 K to 29 cm^{-1} at 303 K. The low-temperature value is consistent with estimates of the energy difference between the two Jahn-Teller orientations of the $\text{Cu}(\text{D}_2\text{O})_6^{2+}$ ion [5]. The dramatic fall in ΔH as the

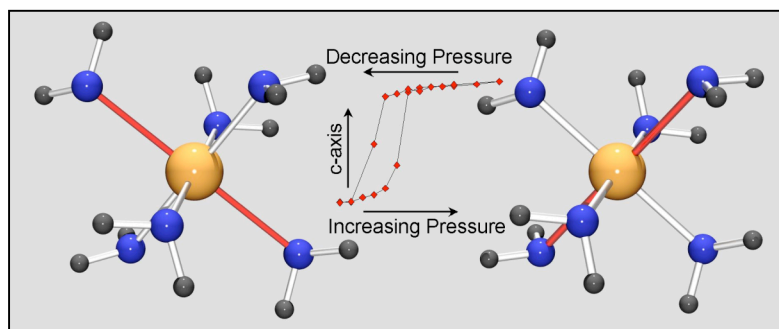


Figure 1. The Jahn-Teller elongation of two trans Cu–O bonds (shown in red) in $(\text{ND}_4)_2[\text{Cu}(\text{D}_2\text{O})_6](\text{SO}_4)_2$ switches by 90° with the application of pressure as observed by single crystal neutron diffraction [2]. The switch leads to a cooperative structural phase transition transmitted by a hydrogen bonding network. At 303 K, hysteresis is observed by following the changes in lattice constants by neutron powder diffraction [4].

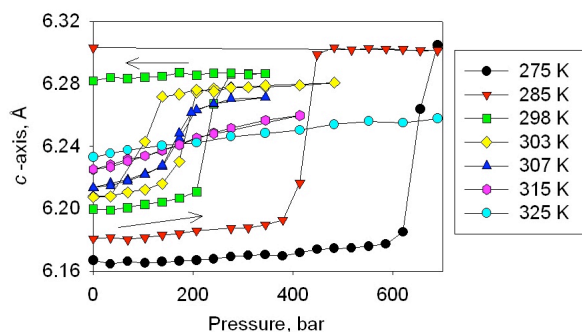


Figure 2. Pressure dependence of the unit cell c -axis at various temperatures. Pressure was applied to samples initially in Form A . Note the hysteresis loop for the 303 K data and that at temperatures of 298 K and lower the samples remain in the B phase even after the applied pressure was decreased to zero. Data at 50, 230 and 260 K are not shown for clarity [4].

temperature increases is to be expected because the basic structural difference between the two Forms decreases with the development of the thermal equilibrium.

Partial Deuteration and Zn Doping

A second recent line of inquiry has involved the sensitivity of the structure of $(\text{ND}_4)_2[\text{Cu}(\text{D}_2\text{O})_6](\text{SO}_4)_2$ to doping with other species. In an earlier study we found that the structure does not change gradually from Form A to Form B if deuterium is progressively replaced by hydrogen [6]. Rather, Form A is maintained until $\sim 50\%$ replacement, with Form B occurring for a lower fraction of deuterium. Perhaps surprisingly, the position of the thermal equilibrium was found to be unaffected by the substitution. The $\text{Cr}(\text{H}_2\text{O})_6^{2+}$ ion has a similar Jahn-Teller distortion to the copper complex and it was observed that $(\text{NH}_4)_2[\text{Cr}(\text{H}_2\text{O})_6](\text{SO}_4)_2$ switched from Form A to B when 22% of the Cr^{2+} ions were substituted by Zn^{2+} [7]. An investigation by X-ray diffraction suggested that a similar change could be induced in $(\text{ND}_4)_2[\text{Cu}(\text{D}_2\text{O})_6](\text{SO}_4)_2$ by substituting as little as 3.4% of the Cu^{2+} sites by Zn^{2+} [8]. The most recent SCD study confirmed this by examining the structure of a single crystal of 3.4% Zn-doped $(\text{ND}_4)_2[\text{Cu}(\text{D}_2\text{O})_6](\text{SO}_4)_2$ by single crystal neutron diffraction at 20 K [9]. The structure was found to be Form B and within the limits of experimental uncertainty the geometry of the $\text{Cu}(\text{D}_2\text{O})_6^{2+}$ ion was found to be identical to that of the $\text{Cu}(\text{H}_2\text{O})_6^{2+}$ ion in this Form in $(\text{NH}_4)_2[\text{Cu}(\text{H}_2\text{O})_6](\text{SO}_4)_2$. When in Form A , the $\text{Cu}(\text{D}_2\text{O})_6^{2+}$ ion has a slightly larger Jahn-Teller distortion than the $\text{Cu}(\text{H}_2\text{O})_6^{2+}$ ion in Form B and it was suggested that this might be due to an isotope effect [2]. The most recent result implies that this is not the case, so that the difference in distortion must be caused by an inequivalence of the lattice interactions in the two Forms. In addition, the atomic displacement parameters for Zn-doped $(\text{ND}_4)_2[\text{Cu}(\text{D}_2\text{O})_6](\text{SO}_4)_2$ showed no evidence for disorder,

in contrast to $(\text{NH}_4)_2[\text{Cr}_{0.78}\text{Zn}_{0.22}(\text{H}_2\text{O})_6](\text{SO}_4)_2$ at 15 K which indicated disorder for the aqua ligands [7].

REFERENCES

- [1] M. A. Hitchman, W. Maaskant, J. van der Plas, C. J. Simmons and H. Stratemeier (1999). "Cooperative Jahn-Teller interaction in dynamic copper(II) complexes. Temperature dependence of the crystal structure and EPR spectrum of deuterated ammonium copper(II) sulfate hexahydrate." *J. Am. Chem. Soc.* **121**, 1488-1501.
- [2] C. J. Simmons, M. A. Hitchman, H. Stratemeier and A. J. Schultz (1993). "High-Pressure, Low-Temperature, Single-Crystal Study of Deuterated and Hydrogenous Ammonium Hexaaquacopper(II) Sulfate (Tutton's Salt): A Pressure-Switchable Jahn-Teller Distortion." *J. Am. Chem. Soc.* **115**, 11304-11311.
- [3] A. J. Schultz, M. A. Hitchman, J. D. Jorgensen, S. Lukin, P. G. Radaelli, C. J. Simmons and H. Stratemeier (1997). "Hysteresis of the Pressure-Induced Jahn-Teller Switch in Deuterated Ammonium Copper(II) Tutton Salt, $(\text{ND}_4)_2[\text{Cu}(\text{D}_2\text{O})_6](\text{SO}_4)_2$." *Inorg. Chem.* **36**, 3382-3385.
- [4] A. J. Schultz, R. W. Henning, M. A. Hitchman and H. Stratemeier (2003). "Influence of pressure and temperature on the crystal structure of deuterated ammonium copper Tutton salt, $(\text{ND}_4)_2[\text{Cu}(\text{D}_2\text{O})_6](\text{SO}_4)_2$." *Cryst. Growth Des.* **3**, 403-407
- [5] W. Rauw, H. Ahsbahs, M. A. Hitchman, S. Lukin, D. Reinen, A. J. Schultz, C. J. Simmons and H. Stratemeier (1996). "Pressure Dependence of the Crystal Structures and EPR Spectra of Potassium Hexaaquacopper(II) Sulfate and Deuterated Ammonium Hexaaquacopper(II) Sulfate." *Inorg. Chem.* **35**, 1902-1911.
- [6] R. W. Henning, A. J. Schultz, M. A. Hitchman, G. Kelly and T. Astley (2000). "Structural and EPR Study of the Dependence on Deuteration of the Jahn-Teller Distortion in Ammonium Hexaaquacopper(II) Sulfate, $(\text{NH}_4)_2[\text{Cu}(\text{H}_2\text{O})_6](\text{SO}_4)_2$." *Inorg. Chem.* **39**, 765-769.
- [7] F. A. Cotton, L. M. Daniels, L. R. Falvello, C. A. Murillo and A. J. Schultz (1994). "Solid Solutions of a Jahn-Teller Compound in an Undistorted Host. 4. Neutron and X-ray Single-Crystal Structures of Two Cr/Zn Tutton Salt Solid Solutions and the Observation of Disorder by Low-Temperature Neutron Diffraction." *Inorg. Chem.* **33**, 5396-5403.
- [8] C. Simmons, M. A. Hitchman, H. Stratemeier and T. Astley (2000). "Effect of Zn Substitution upon the Crystal Structure of $(\text{ND}_4)_2[\text{Cu}[\text{Zn}](\text{D}_2\text{O})_6](\text{SO}_4)_2$." *Inorg. Chem.* **39**, 4651-4653.
- [9] A. J. Schultz, J. A. Cowan, M. A. Hitchman and H. Stratemeier (2005). "Single crystal neutron diffraction study at 20 K of Zn-doped (3.4%) $(\text{ND}_4)_2[\text{Cu}(\text{D}_2\text{O})_6](\text{SO}_4)_2$." *Acta Cryst. C* **61**, m234-m236.

NEUTRON DIFFRACTION INVESTIGATIONS OF H₂ STORAGE IN CLATHRATE HYDRATES

K.C. Hester, T.A. Strobel, C.A. Koh, E.D. Sloan, Center for Hydrate Research, Colorado School of Mines, Golden, CO 80401, US

A.J. Schultz, IPNS, Argonne National Laboratory, Argonne, IL 60439, US

Abstract

Hydrogen storage in clathrate hydrates has recently received increasing attention. Two hydrate systems containing hydrogen were studied using powder neutron diffraction: tetrahydrofuran-d8 (TDF) + D₂ and cyclohexanone-d10 (CHone) + D₂. The crystal structure was determined to be sII for both systems. This is the first crystallographic evidence that CHone forms sII. Additionally, a single guest hydrate is not known to form with CHone. Therefore, to the best of our knowledge, this is the first report of hydrogen stabilizing a double hydrate, where a second guest is required.

Observed Fourier maps were used to determine the disordered guest locations. In both structures at 20 K, the hydrogen was found to occupy the small (5¹²) cavity of the sII hydrate with the nuclear density centered in the middle of the 5¹² cavity. While further model refinements are still in progress, D₂ occupancy in the 5¹² cavity varied from around 0.5 molecules/cavity (0.5 wt%) for the CHone system, and around 1 molecule/cavity (1.1 wt%) for the TDF system. Also, the thermal expansivity of the two hydrate systems, which is greater than that of ice, was measured over a range of 20-270 K for various pressures up to 70 MPa.

INTRODUCTION

Clathrate hydrates are non-stoichiometric crystalline inclusion compounds [1] composed primarily of water. When combined with small (< 9 Å), typically non-associating, “guest” molecules at high pressures and low temperatures, the “host” water crystallizes into molecular cavities trapping the guest. Three common crystalline phases form generally as a function of the guest size: sI, sII, and sH. The smallest of hydrate formers (H₂, He) and larger molecules (C₃H₈, THF) form sII, a *Fd3m* lattice (*a* ~ 17 Å). This structure has two cavity types: eight 5¹² and sixteen 5¹²6⁴ (X^Y, where X = vertices of a cavity face, Y = number of faces per cavity). Molecules of in between sizes (CH₄, C₂H₆) form sI, a *Pm3n* lattice (*a* ~ 12 Å). This structure also has two cavity types: two 5¹² and six 5¹²6². The structure containing the largest of guest molecules is sH, where two molecules are needed to form this *P6/mmm* hexagonal lattice (*a* ~ 12.3, *c* ~ 10.2 Å). To form sH, a large guest, such as methylcyclohexane, must occupy the 5¹²6⁸ cavity (one per unit cell)

combined with a guest that will fill the smaller 4³5⁶6³ (two per unit cell) and 5¹² (three per unit cell) cavities.

It is well-established that hydrates have the ability to highly concentrate gas in the lattice. For example, this high energy density material can store around 172 volumes of methane (STP) per volume of hydrate. The concept of storing H₂ in hydrates was popularized in 2002 after spectroscopy work suggested quadruple occupancy of the 5¹²6⁴ cavity and double occupancy of the 5¹² cavity in a sII hydrate [2]. This would provide a material with slightly over 5 wt% storage of hydrogen. Even after neutron diffraction studies showed that the 5¹² cavity was in fact only singly occupied [3], suggesting a storage capacity of ~ 3.8 wt%, interest still remained in this storage material whose only by-product is liquid water. While storage in the pure hydrogen hydrate has many advantages, high pressure conditions are required to stabilize the material (200 MPa at 280 K [2]). This required pressure can restrict the practical application of the pure H₂ hydrate as a storage material. By the addition of stoichiometric (5.6 mol%) THF, we found that the necessary pressure conditions can be reduced by about two orders of magnitude [4] (6 MPa versus 200 MPa for the pure hydrogen hydrate at 280 K). However, with this reduction in pressure, there is also a reduction in storage capacity, as THF occupies the 5¹²6⁴ cavities of the sII hydrate.

Powder neutron diffraction has been successfully previously used at IPNS [5-7] and elsewhere [3, 8-10] to determine the position of disordered guest molecules in the hydrate cavities, and to quantify the fractional occupancy of guest molecules in the hydrate cavities. In this study, we examine two systems: tetrahydrofuran-d8 (TDF) + D₂ and cyclohexanone-d10 (CHone) + D₂. In both systems, the change in lattice parameter was determined as a function of pressure (up to 70 MPa), for temperatures from 20-270 K. Also, the position and an estimate of the occupancy of the D₂ in the hydrate was determined.

EXPERIMENTAL

All measurements were performed using the General Purpose Powder Diffractometer (GPPD) at IPNS at the Argonne National Laboratory. All high pressure work was performed in an aluminum pressure cell, described elsewhere [5]. This cell was masked with cadmium to reduce the contribution of the Al to the diffractogram in the 90° detector bank. Due to background from the

pressure cell, for both systems, only data from the 90° detector bank was analyzed.

Sample Preparation

TDF, D₂ hydrate

THF-d8 was mixed in a stoichiometric ratio (~5.6 mol%) with D₂O and placed in a freezer at 253 K for up to around 12 hours. A solid formed, which we later confirmed to be TDF hydrate containing less than 1 wt.% Ih. Pure TDF hydrate is stable at 281 K at ambient pressure [11]. The TDF hydrate was then crushed under liquid nitrogen, sieved to < 200 μm, and loaded into the pressure cell. The sample was then pressurized with D₂ gas at 270 K and given time to convert to the binary hydrate. After around two hours, no further pressure drop was observed and the system was assumed to be fully formed TDF + D₂ hydrate.

CHone, D₂ hydrate

Unlike the TDF system, there is no known pure CHone hydrate, and a second guest is required to stabilize the hydrate lattice. In order to form the hydrate, CHone was added in a stoichiometric ratio (~5.6 mol% for sII) with D₂O in a container. This solution was then shaken vigorously to emulsify the immiscible CHone into the aqueous phase and then quenched in liquid nitrogen. This ensured that the CHone was distributed homogeneously throughout the sample. This frozen sample was crushed under liquid nitrogen, sieved to < 200 μm, and loaded into the pressure cell. The sample was then pressurized at 160 K with D₂, below the melting point of CHone (~220 K). The system was then slowly heated above the pure CHone melting point. Upon melting the CHone, noticeable hydrate formation was detected in the diffractograms. The system was heated to 265 K and left to convert further to hydrate. Formation was determined by the decrease of the ice Bragg reflections compared to the increase in reflections for sII hydrate. After eight hours, 95 wt.% of the sample was sII with 5 wt.% Ih. Since no further change in the composition was observed, the system was assumed to have reached the maximum obtainable conversion.

Data Analysis

Rietveld analysis was performed using GSAS [12] with EXPGUI [13]. Initial atom positions for the host atoms in the sII hydrate were obtained from a previous study of the THF + H₂S hydrate [14]. The guests in the 5¹²6⁴ cavities were modeled using a spherical Bessel function, similar to the approach taken by Mak and McMullan [14]. In both cases, the effective radius of the Bessel function was adjusted to ensure the occupancy of the 5¹²6⁴ cavity refined to unity (*cf.* [10]).

Observed Fourier maps were used to determine the location of the D₂ molecules in the 5¹² cavity. Fig. 1 shows a representative FOBS map for both systems, at 20 K, centered at (0,0,0). The D₂ molecule was modeled as a D atom slightly offset in the 5¹² cavity, similar to others modeling diatomic molecules in hydrates [8].

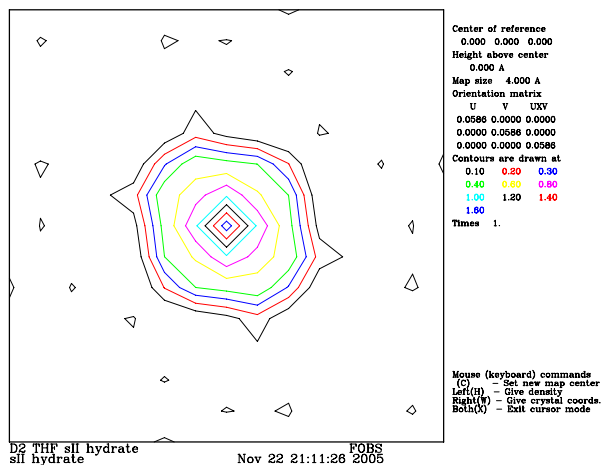


Figure 1: FOBS map centered at (0,0,0). D₂ nuclear density is shown to be centered in middle of the 5¹² cavity. Map size: 2 Å center to edge, cavity atoms not shown.

Additionally, Al (only present in the TDF system) and Ih phases were included in the refinement. The sII phase was found to contribute greater than 85% of the overall amount of the phases present in both systems. Using *d*-spacing data between 0.5 and 3.15 Å, the lattice parameter, host atom positions, isotropic thermal parameters, peak profile, and guest occupancies were all refined. Additionally, the background was modeled for diffuse scattering contributions.

RESULTS AND DISCUSSION

TDF + D₂ System

Neutron patterns were collected over approximately twelve hours. Fig. 2 shows a representative diffraction pattern for the TDF + D₂ hydrate system.

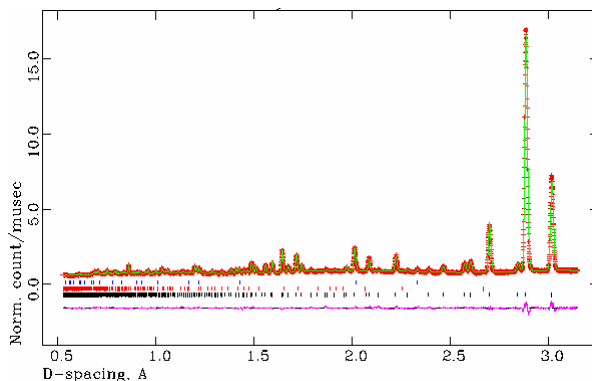


Figure 2: Diffraction pattern for TDF + D₂ hydrate at 20 K and 0.1 MPa.

For the 20 K data, the statistics obtained were $wRp = 4.16\%$ and $\chi^2 = 5.809$. Using this current model, D_2 occupancy was refined to around 1 molecule per 5^{12} cavity (Fig. 3). This is similar to the result obtained for the pure D_2 hydrate system [3].



Figure 3. Representation of TDF-8/ D_2 hydrate with 1 D_2 molecule per 5^{12} cavity, and large cavity filled with TDF-d8.

CHone + D_2 System

Neutron diffraction patterns were collected between fifteen minutes and twelve hours. Fig. 4 shows a representative diffraction pattern for the CHone + D_2 hydrate system.

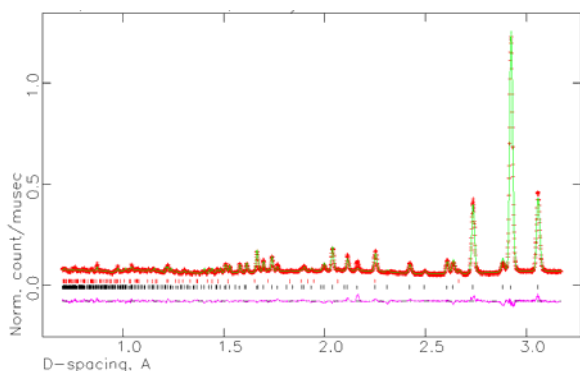


Figure 4: Diffraction pattern for CHone + D_2 hydrate at 20 K and 0.1 MPa.

For the 20 K data, the statistics obtained were $wRp = 5.36\%$ and $\chi^2 = 4.566$. CHone requires a second guest to form. Because a double hydrate with CHone + D_2 was formed, there is further evidence that hydrogen behaves as any other hydrate guest. Therefore, there is no reason not to expect a sH system to be possible with hydrogen.

Two points of interest arose from the CHone + D_2 system. Firstly, using this current model, D_2 occupancy was refined to around 0.5 molecules per 5^{12} cavity. We found this result surprising. Unlike TDF, which exists as a pure hydrate, D_2 is necessary to form a hydrate with CHone. Therefore, one might intuitively expect the occupancy to be greater in the CHone system versus the TDF system. Further work is being

performed to determine the cause of this lower hydrogen occupancy compared to the TDF system.

Secondly, the effective radius of the Bessel function required to fit the CHone in the $5^{12}6^4$ cavity is less than that for TDF. Because the CHone molecule is physically larger than TDF, this may be an artifact of the spherical Bessel function model used. We are currently investigating the effect of using a rigid body refinement to model the CHone and TDF molecules in the $5^{12}6^4$.

Lattice Parameters

The thermal expansivity of hydrates is known to be greater than that of ice [15]. Lattice parameters for both systems were determined as a function of temperature from 20-270 K for various pressures.

Fig. 5 shows the changes in lattice parameter for the TDF + D_2 system. Fig. 6 shows the changes in lattice parameter for the CHone + D_2 system. Note that the CHone system has a much larger lattice parameter when compared to the TDF system. This is due to the large size of the CHone relative to the $5^{12}6^4$ cavity. CHone is one of the largest known sII formers. Its size causes the lattice volume to expand by over 4%.

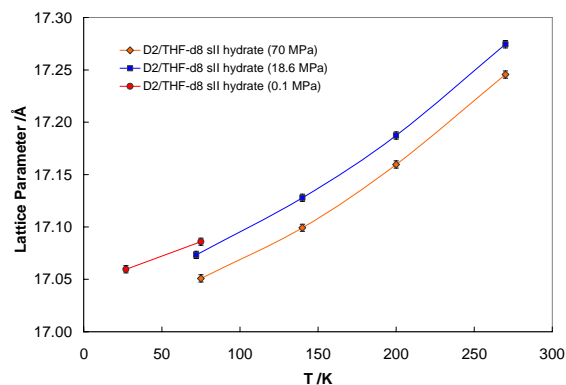


Figure 5. Lattice parameter versus temperature for the TDF + D_2 system at various pressures.

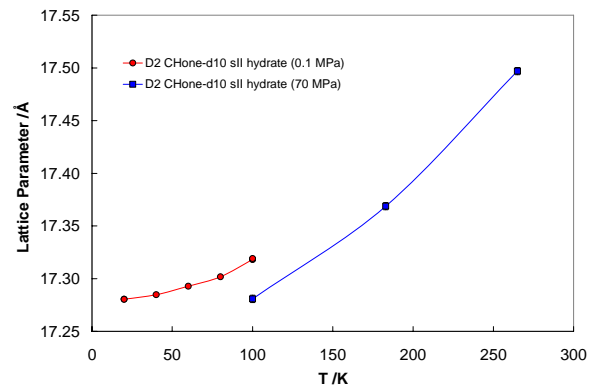


Figure 6. Lattice parameter versus temperature for the CHone + D_2 system at various pressures.

CONCLUSIONS

Neutron diffraction was performed on two systems containing hydrogen: TDF + D₂ and CHone + D₂. In both systems, D₂ was found centered in the 5¹²6⁴ cavity at the low temperature conditions. Initial refinements show that the D₂ occupancy ranged from 0.5 to 1 molecule/cavity as a function of the second guest molecule.

Lattice parameters for both systems show that the size of the guest can have a significant effect of the size of the lattice. In this case, there was over a 4% increase going from TDF to CHone.

Further work on the refinements will be focused on the model used for the large guest in the 5¹²6⁴ cavity. The results will be compared to that using the spherical Bessel function approach for these disordered systems.

Overall, this work shows that more research is needed to understand the behavior of hydrogen in hydrates. As hydrogen storage materials, the systems investigated in this study have storage capacities between 0.5-1 wt% hydrogen. However, these results could be used to provide new insight into the search for other hydrate systems which can offer improved storage capacities.

Acknowledgments

K. Hester is supported by NURP grant UAF03-0098. Work at Argonne was supported by the U.S. Department of Energy, Basic Energy Sciences–Materials Sciences, under Contract W-31-109-Eng-38. We thank James Richardson, Ashfia Huq, and Arvind Gupta for experimental advice and assistance. E. Maxey, K. Volin, and J. Fieramosca are thanked for their tireless efforts with the all of the experimental apparatus on GPPD.

REFERENCES

1. Sloan, E.D., Jr., *Clathrate Hydrates of Natural Gases, Second Edition*. 1998, NY: Marcel Dekker. 754 pp.
2. Mao, W.L., et al., *Hydrogen clusters in clathrate hydrate*. *Science*, 2002. **297**(5590): p. 2247-2249.
3. Lokshin, K.A., et al., *Structure and Dynamics of Hydrogen Molecules in the Novel Clathrate Hydrate by High Pressure Neutron Diffraction*. *Physical Review Letters*, 2004. **93**(12): p. 125503-1.
4. Florusse, L.J., et al., *Stable Low-Pressure Hydrogen Clusters Stored in a Binary Clathrate Hydrate*. *Science*, 2004. **306**(5695): p. 469-471.
5. Henning, R., et al., *Neutron diffraction studies of CO₂ clathrate hydrate: Formation from Deuterated Ice*. *J. Phys. Chem.*, 2000. **104**: p. 5066.
6. Halpern, Y., et al., *Time-Resolved in Situ Neutron Diffraction Studies of Gas Hydrate: Transformation of Structure II (sII) to Structure I (sI)*. *Journal of the American Chemical Society*, 2001. **123**(51): p. 12826-12831.
7. Wang, X., A.J. Schultz, and Y. Halpern, *Kinetics of Methane Hydrate Formation from Polycrystalline Deuterated Ice*. *Journal of Physical Chemistry A*, 2002. **106**(32): p. 7304-7309.
8. Chazallon, B. and W.F. Kuhs, *In situ structural properties of N₂-, O₂-, and air-clathrates by neutron diffraction*. *Journal of Chemical Physics*, 2002. **117**(1): p. 308-320.
9. Gutt, C., et al., *The structure of deuterated methane hydrate*. *Experimental Physik*, 2000: p. 1.
10. Jones, C.Y., et al., *Structure and Thermal Expansivity of Tetrahydrofuran Deuterate Determined by Neutron Powder Diffraction*. *Journal of physical Chemistry B*, 2003. **107**: p. 6026-6031.
11. Hanley, H.J.M., et al., *The Melting Curve Tetrahydrofuran Hydrate in D₂O*. *International Journal of Thermophysics* 1989. **10**(4).
12. Larson, A.C. and R.B. Von Dreele, *General Structure Analysis System (GSAS)*. Los Alamos National Laboratory Report LAUR, 2000: p. 86-748.
13. Toby, B.H., *EXPGUI, a graphical user interface for GSAS*. *J. Appl. Cryst.*, 2001. **34**: p. 210-213.
14. Mak, C.W. and R.K. McMullan, *Polyhedral Clathrate Hydrates. X. Structure of the Double Hydrate of Tetrahydrofuran and Hydrogen Sulfide*. *Joun. Chem. Phys.*, 1965. **42**, No. 8: p. 2732-2737.
15. Tse, J.S., *Thermal Expansion Of The Clathrate Hydrates Of Ethylene Oxide And Tetrahydrofuran*. *Journal De Physique*, 1987. **48 C1**: p. 543-549.

CHEMICAL DIFFUSION AND OXYGEN VACANCY DISTRIBUTION IN $\text{Ce}_{0.8}\text{Y}_{0.2}\text{O}_{1.9-\delta}$ ELECTROLYTES

Yaping Li, Evan R. Maxey and James W. Richardson Jr., IPNS

Beihai Ma, Tae H. Lee and Sun-Ju Song, Energy Technology Division, Argonne National Laboratory, Argonne, Illinois 60439

1. Introduction

CeO_2 -based solid electrolytes exhibiting good oxygen ionic conductivities are of great interest for applications in various electrochemical devices such as solid oxide fuel cells (SOFCs), oxygen separation membranes, and sensors, etc. [1-3]. Although ideal electrolytes are electronic insulators, the anode (fuel) sides of CeO_2 -based electrolytes, when subjected to strongly reducing atmospheres, will undergo Ce^{4+} to Ce^{3+} reduction resulting in mixed-conducting properties. The exact extent of this has not been fully understood, in particular in the presence of high oxygen partial pressure on the cathode (air) sides of the electrolytes. Such an exact description of the spatial distribution of oxygen vacancy concentration in electrolytes/membranes is needed to develop a better understanding (mechanical and electrochemical) of ionic conducting ceramics as electrochemical devices [4].

Although several attempts have been made to derive such a profile on the basis of defect chemistry models (e.g. Duncan et al. [4], Atkinson et al. [5], and Godicke-

meier et al. [6]), independent experimental data are still lacking to verify and examine these models. Neutron powder diffraction has shown promise to elucidate the profile of oxygen defect concentration $V(x)$ in mixed conducting ceramic membranes [7], and our previous results suggested that the bulk materials studied (membranes based on perovskite and related structures in the Sr(La)-Fe-Co-O system) have a uniform oxygen vacancy concentration corresponding to that in air, significantly dropping near the reducing-side surface of the membrane (i.e., $V(x) \approx V(0)$ for $0 \leq x \leq L$, and $V(x) \rightarrow V(L)$ as $x \rightarrow L$, where $x=0$ and $x=L$ represent the air- and reducing-side surfaces, respectively). Here we extend our previous work to a pure ionic conductor (in air/oxygen atmosphere), and examine the $V(x)$ profile expected to be quite different than those of perovskite-derived membranes, as suggested by Atkinson et al. [5].

The change in oxygen vacancy concentration following the change in $p\text{O}_2$ is governed by the reaction between the oxide and oxygen from the gas phase. Both surface-

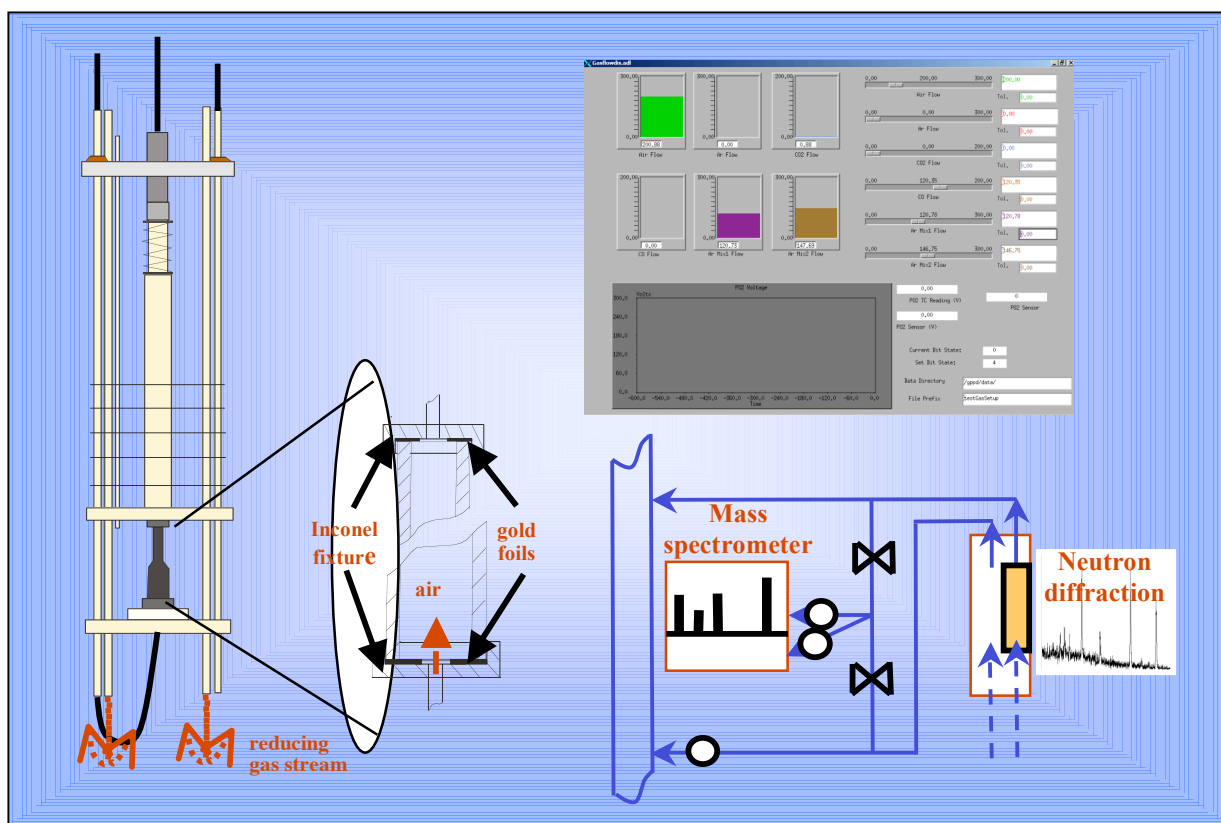


Figure 1. Schematic illustration of experimental set-up including sample holder with gold foil seals, EPICS control of gas flows, and mass spectrometry sampling of exhaust gases.

oxygen exchange and bulk-oxygen diffusion are involved in the defect transport, and identifying the rate-limiting step is a prerequisite for improving the performance of SOFC's. We took advantage of the upgraded GPPD for time-resolved diffraction studies exploring kinetic phenomena. We are particularly interested in developing a new method to study oxygen diffusion in Y-doped ceria, consisting of determining the correlation between lattice parameter and oxygen content - the most direct quantity for macroscopic scale oxygen diffusion - after an abrupt change in oxygen partial pressure.

Experimental

The $\text{Ce}_{0.8}\text{Y}_{0.2}\text{O}_{1.9-8}$ sample was formed into a tube about 3-inch long with wall thickness $\sim 1\text{mm}$ in the manner reported elsewhere [8], and loaded into a specially designed sample holder, equipped with a device to provide a gas-tight seal between the electrolyte and the gas handling system (described in more detail in [9]). The $p\text{O}_2$ value on the reducing side was monitored with a solid zirconia electrolyte oxygen sensor.

The required oxygen partial pressures for both sides of the electrolyte were achieved by flowing gas mixtures involving Air, Ar, CO_2 , CO, 1.2%CO/Ar, He and O_2 . The conditions for measurements in $p\text{O}_2$ gradients are described by $p\text{O}_2'$ (inside |CY20 electrolyte| $p\text{O}_2''$ (outside). Control of flow rates of gases were integrated into the data collection software. An on-line mass spectrometer was installed in the exhaust lines from the inside and outside for leakage evaluation (leakage was determined to be negligible) and gas composition analysis when necessary. Data were recorded at 15-min intervals at 900°C in the $2\theta = \pm 90^\circ$ detector banks, and Rietveld profile analysis was performed with GSAS [10]. The experimental set-up is illustrated in Figure 1.

Results and Discussion

Initial measurements were made in a static mode where the gas mixtures on the inside and outside of the tube were the same. At the completion of the static runs, with $p\text{O}_2 \sim 10^{-14}$ atm (I) and $\sim 10^{-18}$ atm (II) (Fig. 2), data collection was continued under $p\text{O}_2$ gradients by flowing oxidizing gases (40sccm He and 10sccm O_2 , $p\text{O}_2 \sim 10^{-0.7}$ atm) (III) and less reducing gas (50 sccm He with $\text{O}_2 < 5\text{ppm}$, $p\text{O}_2 \sim 10^{-5.3}$ atm) (IV) through the inside of the electrolyte while the low $p\text{O}_2$ of $\sim 10^{-18}$ atm was maintained on the outside of the electrolyte. Sequential Rietveld analysis of diffraction data was performed in a similar fashion as described before [9].

As the electrolyte was exposed to reduced $p\text{O}_2$, oxygen sub-stoichiometry δ was created in the structure (Fig. 3) accompanied by chemically-induced lattice expansion (Fig. 2). The refined lattice parameter and oxygen content follow an approximately linear relationship, with ϵ_c/δ of 0.08 ($\epsilon_c = \Delta a/a$) (Fig. 4).

Since $p\text{O}_2$ -dependent ionic and n-type conductivity have been well understood for doped ceria, some conclusions on transport properties could be drawn from analy-

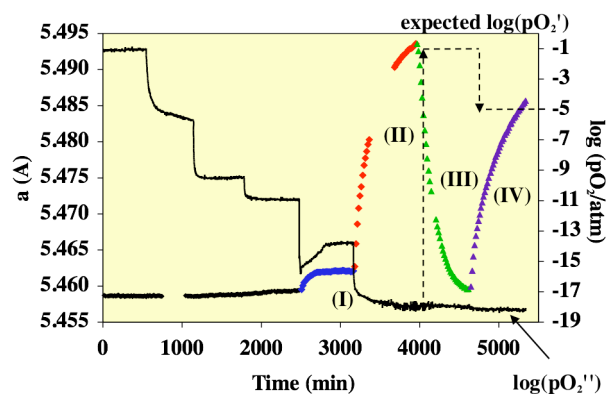


Figure 2. Variation in lattice parameter with time during progressive reduction in static mode (I) and (II), and in dynamic mode (III) and (IV).

sis of structural data for the electrolyte under $p\text{O}_2$ gradients. As $p\text{O}_2$ on the inside was increased from $\sim 10^{-18}$ atm to $\sim 10^{-0.7}$ atm (III), both the average lattice parameter (Fig. 2) and oxygen non-stoichiometry (Fig. 3) were decreased to corresponding values similar to those observed for $p\text{O}_2$ in the electrolytic region, suggesting that the electronic domain at the reducing side (due to Ce^{4+} partial reduction) was at least partially suppressed by $p\text{O}_2'$ of $\sim 10^{-0.7}$ atm on the oxidizing side of the electrolyte. However, as $p\text{O}_2$ on the oxidizing side was reduced to $\sim 10^{-5.3}$ atm (IV), the average lattice parameter (Fig. 2) and δ (Fig. 3) subsequently increased to values corresponding to the prevailing $p\text{O}_2$ of $\sim 10^{-18}$ atm in the electrolyte. Therefore, the electrochemical properties of the electrolyte can be tuned by changing oxygen partial pressure on the one side from electrolytic domain using the conditions $p\text{O}_2' = \sim 10^{-0.7}$ atm |CY20| $p\text{O}_2'' = \sim 10^{-18}$ atm to electronic domain using the conditions $p\text{O}_2' = \sim 10^{-5.3}$ atm |CY20| $p\text{O}_2'' = \sim 10^{-18}$ atm.

Oxygen diffusion kinetics in CY20 electrolytes

A number of different techniques have been used to study oxygen chemical diffusion kinetics in doped ceria and related ceramic materials, including electrical conductivity relaxation [11-13], gravimetric relaxation [14-16], etc. In this work, oxygen diffusion was studied us

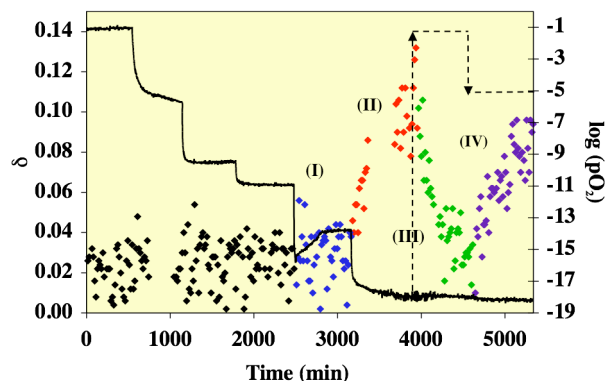


Figure 3. $\log(\Delta a/a)$ vs. $\log(p\text{O}_2/\text{atm})$ in low $p\text{O}_2$ regime compared with straight line with slope of $-1/4$.

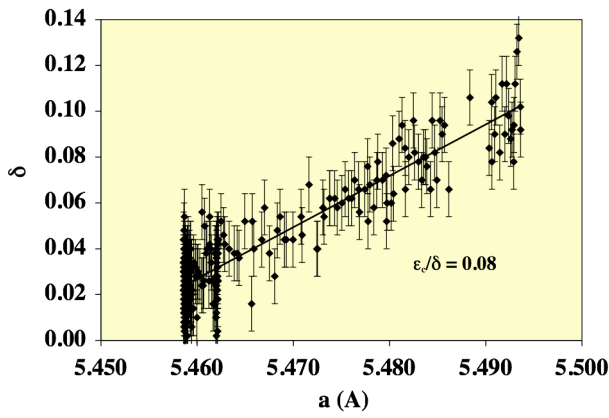


Figure 4. Correlation between lattice parameter and refined oxygen sub-stoichiometry δ for CY20.

ing lattice relaxation, relying on the fact that the lattice parameter is a direct measure of oxygen content based on the linear relationship described above (Fig. 5).

The sample geometry is a thin hollow cylinder with average inner and outer radii $a=0.33$ cm and $b=0.44$ cm, respectively, and can be considered a planar sheet, with sheet thickness $b-a \approx 0.11$ cm. Since the length is $\gg a$ and b , diffusion along the length of the electrolyte can be neglected. Oxygen diffusion coefficients were obtained by fitting the lattice relaxation data using the Fick equation with appropriate boundary conditions and involving both bulk diffusion and surface exchange kinetics [17]:

$$\frac{M_t - M_0}{M_\infty - M_0} = 1 - \sum_{n=1}^{\infty} \frac{2L^2 \exp(-\beta_n Dt / l^2)}{\beta_n (\beta_n^2 + L^2 + L)} \quad (1)$$

where M_0 , M_t , and M_∞ are oxygen content values at $t=0$, t and ∞ , respectively; l half the electrolyte thickness (cm); D the oxygen chemical diffusion coefficient ($\text{cm}^2 \cdot \text{s}^{-1}$); t the diffusion time (s); β_n s positive roots of $\beta \tan \beta = L$, and $L = lk/D$; k the linear rate constant of oxygen exchange ($\text{cm} \cdot \text{s}^{-1}$) and L a dimensionless parameter. Large values of L correspond to bulk-diffusion-controlled and small ones to surface-oxygen exchange-controlled processes.

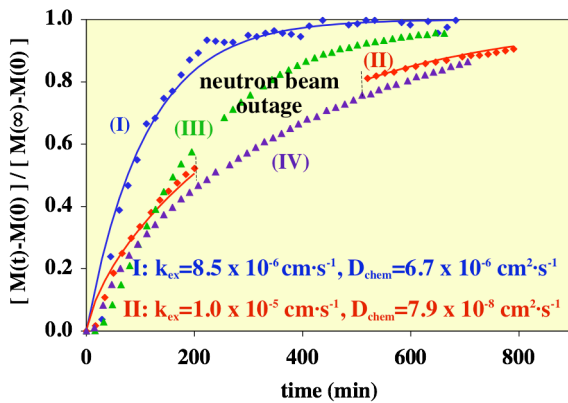


Figure 5. Experimental lattice relaxation data in terms of fractional change of oxygen contents as function of time, and fitted curve from which both surface exchange constant and chemical diffusion coefficient were extracted.

Non-linear least-square fitting using equation (1) was performed by varying only two parameters D and k , resulting in D and k values for (I) and (II) (Fig. 5). The obtained diffusion coefficients in the two relaxation runs – $D_{\text{chem}} = 6.7 \times 10^{-6}$ and $7.9 \times 10^{-8} \text{ cm}^2 \cdot \text{s}^{-1}$, $K_{\text{ex}} = 8.5 \times 10^{-6}$ and $10.0 \times 10^{-6} \text{ cm} \cdot \text{s}^{-1}$, for (I) and (II) respectively – indicated that D_{chem} increased with increasing $p\text{O}_2$, while K_{ex} remained basically unchanged. The surface exchange constant becomes important at $p\text{O}_2$ of $\sim 10^{-14}$ atm. These results are in good agreement with the literature [15,16]. Included in Fig. 5 are relaxation data for (III) and (IV) with experimental data only; no attempt was made to fit these data before finding the appropriate analytical solution to model chemical diffusion where the surface conditions on the two sides of the membrane are different.

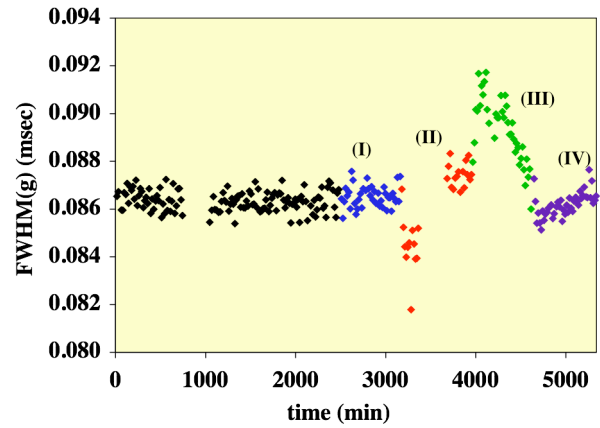


Figure 6. Variation of Gaussian FWHM for (220) reflection obtained from single peak fitting in GSAS.

Oxygen vacancy concentration profile $V(x)$

As illustrated above, at the end of the static mode measurements, the inside of the electrolyte was exposed to an oxidizing atmosphere while the $p\text{O}_2$ on the reducing side remained unchanged. As we have already seen, the increase in oxygen partial pressure on the inside of the electrolyte led to a decrease in lattice parameter. At this point when the $p\text{O}_2$ gradient was imposed, we examined diffraction peak profiles, from which information about $V(x)$ could be extracted. Since neutron diffraction reflects the spatial average of material, peak profiles contain complete information about structural or chemical inhomogeneities in the sample, namely oxygen vacancy distribution $V(x)$ across the electrolyte thickness, in this case assuming that δ is a function of radial position only.

To measure the peak profile variation as the electrolyte was exposed to different $p\text{O}_2$'s and $p\text{O}_2$ gradients, single peak fitting was employed for two reflections (220) and (111). Gaussian broadening, along with the peak position and intensity, was allowed to vary.

As shown in Figure 6, there is minimal variation in peak width down to $p\text{O}_2 \sim 10^{-13}$ in the static measurements. The initial peak sharpening at $p\text{O}_2 \sim 10^{-18}$ in zone (II) is not clear at this point. As the $p\text{O}_2$ gradient was applied in (III), peaks initially broadened and eventually returned to original values. The fractional change in

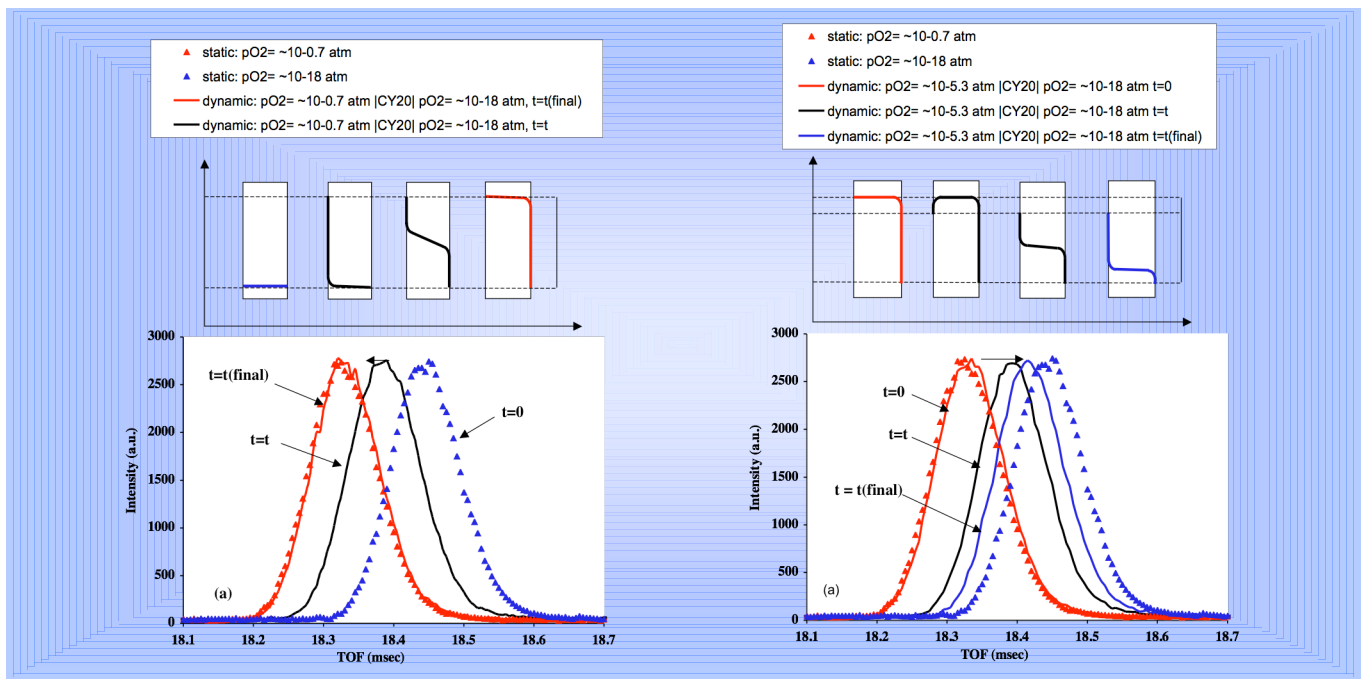


Figure 7. Schematic illustration of oxygen content profile change when electrolyte is exposed to pO_2 gradients (III) and (IV). On the left, starting from 10^{-18} |CY20| 10^{-18} , i.e., highly reducing on both sides then switching to $10^{-0.7}$ |CY20| 10^{-18} induces a small gradient across the membrane as the bulk switches to an oxidized condition, with a strong gradient at the reducing surface. On the right, the starting condition is $10^{-0.7}$ |CY20| 10^{-18} switching to $10^{-5.3}$ |CY20| 10^{-18} where there is minimal gradient across the membrane and the bulk switches to a highly reduced form near that of the reducing side, and the strongest gradient is at the oxidizing surface.

peak breadth is consistent with only a very minor variation in oxygen content $V(x)$ across the electrolyte, with a slope estimated to be $\leq 1/8$ the slope expected from linear variation between the most oxidizing and most reducing extremes. The observed variation in peak breadth throughout zone (III) indicates that the oxygen distribution $V(x)$ varies with time. At the same time, the lattice parameter varied smoothly as shown in Figure 2. There was much less peak broadening in zone (IV) suggesting that the $V(x)$ is very flat during this transition.

Acknowledgments

We are grateful to the Energy Technology Division Ceramics Section of ANL for access to the facilities of ceramic processing.

References

- [1] S. Wang, T. Kakehisa, M. Dokiya, T. Hashimoto, *J. of Electrochem. Soc.* 147 (2000) 3606.
- [2] J.F.Q. Rey, E.N.S. Muccillo, *J. of the Euro. Ceram. Soc.* 24 (2004) 1287.
- [3] L. Navarro, F. Marques, J. Frade, *J. Electrochem. Soc.* 144 (1997) 267.
- [4] K.L. Duncan, E.D. Wachsman, *Proceedings of the International Symposium, Solid State Ionic Devices*, 1999.
- [5] A. Atkinson, T.M.G.M. Ramos, *Solid State Ionics* 129 (2000) 259.
- [6] M. Godickemeier, L.J. Gauckler, *J. Electrochem. Soc.* 145 (1998) 414.

- [7] Y. Li, E.R. Maxey, J.W. Richardson, Jr., *Solid State Ionics* (in press).
- [8] Y. Li, E.R. Maxey, J.W. Richardson, Jr., B. Ma, T. H. Lee, S-J Song, *J. Am. Ceram. Soc.* (in press).
- [9] Y. Li, E.R. Maxey, J.W. Richardson, Jr., *J. Am. Ceram. Soc.* 88 (2005) 1244.
- [10] A.C. Larson, R.B. Von Dreele, *General Structure Analysis System (GSAS)*. Report No. LA-UR-86-748, Los Alamos National Laboratory, Los Alamos, NM, 1987.
- [11] J.A. Lane, J.A. Kilner, *Solid State Ionics* 136-137 (2000) 997.
- [12] S. Wang, A. Verma, Y.L. Yang, A.J. Jacobson, B. Abeles, *Solid State Ionics* 140 (2001) 125.
- [13] W. Preis, E. Bucher, W. Sitte, *Solid State Ionics* 175 (2004) 393.
- [14] M. Katsuki, S. Wang, M. Dokiya, T. Hashimoto, *Solid State Ionics* 156 (2003) 453.
- [15] K. Yashiro, S. Mnuma, A. Kaimai, Y. Nigara, T. Kawada, J. Mizusaki, K. Kawamura, T. Horita, H. Yokokawa, *Solid State Ionics* 152-153 (2002) 469.
- [16] M. Katsuki, S. Wang, K. Yasumoto, M. Dokiya, *Solid State Ionics* 154-155 (2002) 589.
- [17] J. Crack, *The Mathematics of Diffusion*, 2nd ed., Oxford Univ. Press, New York, 1975.
- [18] A. Atkinson, S.A. Baron, N.P. Brandon, *J. of Electrochem. Soc.* 151 (2004) E186.

NUCLEAR AND MAGNETIC STRUCTURES OF $\text{La}_{1-x}\text{Sr}_x\text{MnO}_3$ *

O. Chmaissem[#], B. Dabrowski, S. Kolesnik, J. Mais, Physics Department, Northern Illinois University, DeKalb, IL 60115

J. D. Jorgensen, S. Short, Argonne National Laboratory, Argonne, IL 60439

Abstract

Using neutron powder diffraction, we constructed the full nuclear and magnetic phase diagram for the $\text{La}_{1-x}\text{Sr}_x\text{MnO}_3$ system. In this paper, we describe the delicate balance between the various magnetic states that coexist in very narrow composition ranges for $x \sim 0.5$ and 0.95 . We show that $\text{La}_{0.5}\text{Sr}_{0.5}\text{MnO}_3$ and $\text{La}_{0.45}\text{Sr}_{0.55}\text{MnO}_3$ undergo a series of paramagnetic, ferromagnetic and A-type antiferromagnetic phase transitions. For $x = 0.5$, phase separation occurring below 135 K results in the coexistence of ferromagnetic and antiferromagnetic phases over a wide temperature range. Orbital ordering is associated with the low temperature A-type AFM phase. On the other hand, a very steep boundary line separates the C-type and G-type antiferromagnetic phases in the composition range 0.9-0.95. For $x = 0.94$, both antiferromagnetic types coexist at low temperatures.

INTRODUCTION

Manganese-based $\text{La}_{1-x}\text{A}_x\text{MnO}_3$ ($\text{A} = \text{Ca}, \text{Sr}, \text{or Ba}$) materials exhibiting colossal magnetoresistive properties have been at the center of intense research over the last few years. Interest in this system arises from the exotic behavior of the different members of the series and the corresponding complex nuclear and magnetic phase diagram. Indeed, several studies demonstrated the existence of complex charge ordered and/or orbital ordered patterns in Ca substituted LaMnO_3 observed for compositions with special $\text{Mn}^{3+}/\text{Mn}^{4+}$ nominal ratios (e.g., 1/2, 1/4, 1/8, etc).

The structures and properties of $\text{La}_{1-x}\text{Sr}_x\text{MnO}_3$ with strontium content (x) less than 0.5 are well understood [1–4]. However, structural and transport properties of $\text{La}_{1-x}\text{Sr}_x\text{MnO}_3$ materials with $x > 0.5$ remained less understood because of the inherent difficulty in synthesizing single phase materials with $x > 0.5$ [5-10]. In this paper, we show the full phase diagram of $\text{La}_{1-x}\text{Sr}_x\text{MnO}_3$ and focus our attention on compositions near the phase boundaries that separate different magnetically ordered states.

MATERIALS SYNTEHSIS AND EXPERIMENTAL DETAILS

A two-step solid-state synthesis method was employed to obtain high quality $\text{La}_{1-x}\text{Sr}_x\text{MnO}_3$ perovskite samples

using stoichiometric mixtures of pre-fired La_2O_3 , SrCO_3 , and MnO_2 . In a first step, oxygen-deficient perovskite materials were produced by firing the mixtures in flowing gas of argon (10 ppm O_2 or less) at temperatures up to 1400 °C. In the second step, the precursors were fully oxidized by simple post-annealing in air at 500 °C and the final oxygen content was carefully monitored using thermogravimetric analysis. X-ray and neutron powder diffraction confirmed the single phase quality of all samples under investigation.

NEUTRON POWDER DIFFRACTION

Extensive studies have been performed in the composition range of $0 \leq x \leq 0.5$ [1-4, 11]. In previous work [1], we demonstrated that LaMnO_3 assumes several structural symmetries (AFM orthorhombic, FM orthorhombic, monoclinic, or rhombohedral) depending on the synthesis conditions and final oxygen stoichiometry (see also ref. [12]). For $0.1 \leq x \leq 0.2$, we demonstrated the presence of two characteristic temperatures: a Curie temperature T_C that increases linearly with increasing Sr content and an orbital-ordered Jahn-Teller distorted transition temperature T_{JT} that decreases with increasing Sr content. The two transition temperature curves cross at $x = 0.145$ and $T = 210$ K. In the same composition range, additional structural regions have been identified in which the materials exhibit large or small coherent and incoherent Jahn-Teller distortions. In the $0.16 \leq x \leq 0.45$ composition range, the materials are energetically stable and crystallize in a rhombohedral symmetry with no structural competition ever observed or reported. The full phase diagram of $\text{La}_{1-x}\text{Sr}_x\text{MnO}_3$ is presented in Fig. 1 in which additional structural types are identified for different compositions and/or temperatures in the $0.5 \leq x \leq 1$ composition range, namely, cubic $\text{Pm}\bar{3}\text{m}$, tetragonal I4/mcm , and orthorhombic Fmmm .

SrMnO_3

SrMnO_3 crystallizes in a simple cubic $\text{Pm}\bar{3}\text{m}$ structure in which undistorted corner-sharing MnO_6 octahedra are arranged three dimensionally, thus, forming cavities suitable for the Sr ions. The cubic $\text{Pm}\bar{3}\text{m}$ structure extends to lower x values and a room temperature transformation to a tetragonal symmetry for $x = 0.7$ is observed. The tetragonal I4/mcm structure results from a subtle distortion of the cubic symmetry with the elongation of the MnO_6 octahedra and their rotation around the c -axis. The orthorhombic Fmmm structure is observed at low temperatures for $x \sim 0.5-0.6$. In this structure, more degrees of freedom are introduced with

*Work at NIU was supported by the DARPA/ONR, Grant No. NSF-DMR-0105398, and by the State of Illinois under HECA. At ANL, this work was also supported by the U.S. Department of Energy, Division of Basic Energy Science-Materials Sciences, under contract No. W-31-109-ENG-38 (the operation of IPNS).

[#]Chmaissem@physics.niu.edu

three independent pairs of oxygen atoms forming the MnO_6 octahedra.

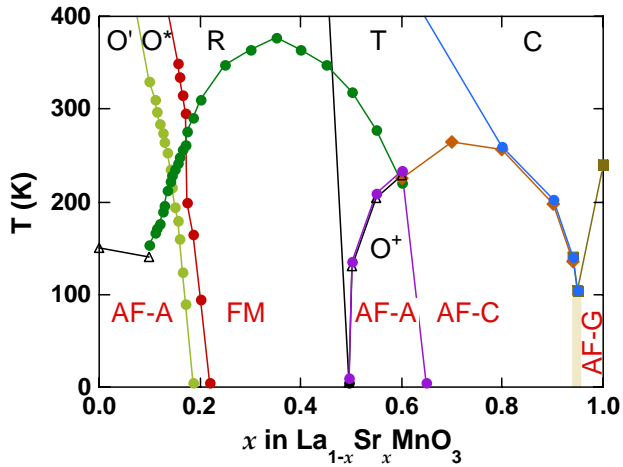


Figure 1: Magnetic and structural phase diagrams for $\text{La}_{1-x}\text{Sr}_x\text{MnO}_3$. Structural and magnetic transition boundaries are shown as solid and dashed lines, respectively. The symbols C, T, R, and O refer to cubic, tetragonal, rhombohedral, and orthorhombic symmetries, respectively. Coherent and incoherent Jahn-Teller distortions are present in the O' and O^* Pbnm structures, respectively. O^+ represents the Fmmm orthorhombic symmetry (see text for more details).

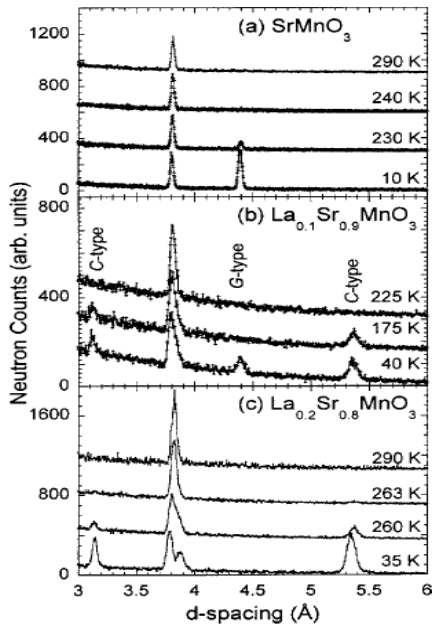


Figure 2: Raw neutron diffraction data showing magnetic peaks of the C-type for $x = 0.8$, of the G-type for $x = 1.0$ and of the C- and G-types for $x = 0.9$.

The $x = 0.9$ – 0.95 samples are particularly interesting because they lie near or at the bottom of a valley on the phase diagram that separates the C-type and G-type antiferromagnetic states by a sharp and nearly vertical boundary line. As shown in Fig. 2, neutron diffraction data collected for $x = 0.8$, 0.9 , and 1 in the d -spacing

range of 3 to 6 Å clearly demonstrate the strong competition between the C- and G-types and the coexistence of the two states for $x = 0.9$.

This observed phase coexistence is in agreement with several theoretical models [13-17] suggesting that electronic phase separation into different magnetic domains results from unstable canted antiferromagnetic structures. The tendency to phase separation was explained by Yunoki *et al.* [16, 17] to be an intrinsic property of the double exchange model. Recent neutron scattering [18-20] and NMR [21] measurements gave experimental evidence for phase separation in $\text{La}_{1-x}\text{Ca}_x\text{MnO}_3$ with $0.92 < x < 0.97$, for example [20], in the form of ferromagnetic droplets embedded within the host AFM structure. We should note, however, that such a FM phase is not observed in the $\text{La}_{1-x}\text{Sr}_x\text{MnO}_3$ system at the cubic (G-type)/tetragonal (C-type) phase boundary but as will be seen in the next paragraph phase separation of FM-AFM domains does occur for $x = 0.5$.

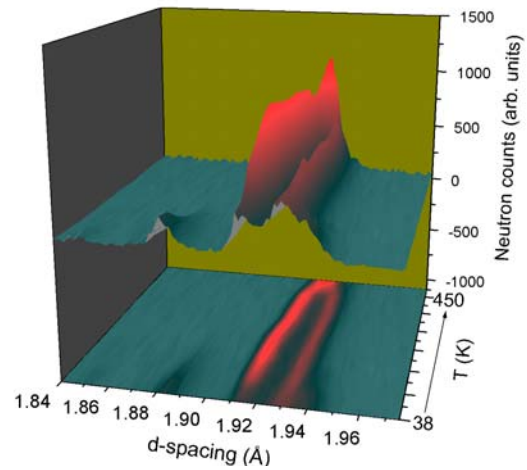


Figure 3: Splitting of the tetragonal 220 and 004 peaks into orthorhombic peaks below 150 K for $\text{La}_{0.5}\text{Sr}_{0.5}\text{MnO}_3$.

$\text{La}_{0.5}\text{Sr}_{0.5}\text{MnO}_3$

Paramagnetic $\text{La}_{0.5}\text{Sr}_{0.5}\text{MnO}_3$ crystallizes in a tetragonal $I4/mcm$ symmetry between the temperatures of 450 and 320 K. Below 320 K, the material undergoes a paramagnetic to ferromagnetic phase transition with the nuclear tetragonal structure remaining unchanged. Between 320 and 135 K, the ferromagnetic ordering of the Mn magnetic moments occurs in the direction of the long tetragonal c -axis. Below 135 K, a significant number of additional diffracted intensities that appear in the neutron patterns indicate the occurrence of phase separation and the existence of a low temperature phase with reduced symmetry. In fact, the high temperature ferromagnetic remained present (in lesser amounts) and coexisted with the low temperature phase at all measured temperatures between 38 and 135 K. The low temperature phase was determined to be orthorhombic of space group Fmmm and found to accommodate an A-type antiferromagnetic ordering of the Mn spins. The A-type magnetic structure consists of parallel ferromagnetic sheets that are antiferromagnetically coupled in a specific

direction. As such, in this structure, orbital ordering is supported and clearly observed as indicated by the measured ordered Mn-O bond-lengths. Fig. 3 shows a three dimensional portion of neutron diffraction patterns as a function of temperature in which the low temperature coexistence of the two phases is clearly visible.

$La_{0.45}Sr_{0.55}MnO_3$ and $La_{0.4}Sr_{0.6}MnO_3$

A similar sequence of nuclear phase transitions has been observed for $La_{0.45}Sr_{0.55}MnO_3$ and $La_{0.4}Sr_{0.6}MnO_3$. Similarly, similar magnetic states have been identified for the $x=0.55$ sample but not for $x=0.6$. The ferromagnetic phase was absent in the $La_{0.4}Sr_{0.6}MnO_3$ material and the transition from paramagnetic to antiferromagnetic occurred fairly quickly in a very narrow temperature range near 200 K as shown in Fig. 4.

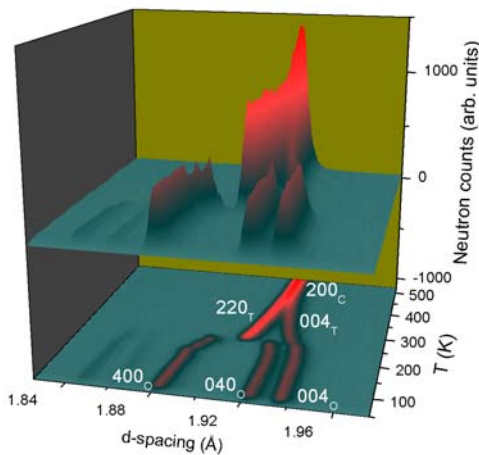


Figure 4: Evolution of the Bragg peaks between 1.8 and 2 Å as a function of temperature for $La_{0.4}Sr_{0.6}MnO_3$. Cubic to tetragonal to orthorhombic phase transitions are clearly observed.

CONCLUSIONS

$La_{1-x}Sr_xMnO_3$ samples with $0.5 < x < 1$ were synthesized and studied in their stoichiometric single-phase perovskite form. Using neutron powder diffraction, we constructed the full structural and magnetic phase diagram for $La_{1-x}Sr_xMnO_3$ and demonstrated the presence of a strong competition between ferromagnetism and antiferromagnetism for $x \sim 0.5$ and a similar competition between C-type and G-type AFM states for $x \sim 0.95$. It is also important to mention that first order transitions were observed when nuclear and magnetic structural transitions coincided for $0.8 < x < 0.95$ [22], whereas, second-order phase transitions occurred for compositions in which the structural and magnetic transitions are decoupled and happen at different temperatures. Examining the various AFM configurations, we find that the A-type magnetic structure is favored when the MnO_6 octahedra possess two short Mn-O (compressed) and four long bond lengths, thus, giving rise to the observed orthorhombic Fmmm symmetry and to AFM interactions in the direction of the short bonds.

REFERENCES

- [1] B. Dabrowski, X. Xiong, Z. Bukowski, R. Dybzinski, P. W. Klamut, J. E. Siewenie, O. Chmaissem, J. Shaffer, and C. W. Kimball, Phys. Rev. B 60, (1999) 7006.
- [2] H. Kawano, R. Kajimoto, M. Kubota, and H. Yoshizawa, Phys. Rev. B 53, (1996) R14 709.
- [3] M. C. Martin, G. Shirane, Y. Endoh, K. Hirota, Y. Moritomo, and Y. Tokura, Phys. Rev. B 53, (1996) 14 285.
- [4] J. F. Mitchell, D. N. Argyriou, C. D. Potter, D. G. Hinks, J. D. Jorgensen, and S. D. Bader, Phys. Rev. B 54, (1996) 6172.
- [5] C. Martin, A. Maignan, M. Hervieu, B. Raveau, Z. Jirak, A. Kurbakov, V. Trounov, G. Andre, and F. Bouree, J. Magn. Mater. 205, (1999) 184.
- [6] C. Martin, A. Maignan, M. Hervieu, and B. Raveau, Phys. Rev. B 60, (1999) 12 191.
- [7] F. Damay, C. Martin, M. Hervieu, A. Maignan, B. Raveau, G. Andre, and F. Bouree, J. Magn. Mater. 184, (1998) 71.
- [8] K. Kikuchi, H. Chiba, M. Kikuchi, and Y. Syono, J. Solid State Chem. 146, (1999) 1.
- [9] S. L. Yuan, Y. Jiang, X. Y. Zeng, W. Y. Zhao, Y. P. Yang, J. P. Qian, G. Q. Zhang, F. Tu, and C. Q. Tang, Phys. Rev. B 62, (2000) 11 347.
- [10] L. Rormark, K. Wiik, S. Stolen, and T. Grande, J. Mater. Chem. 12, (2002) 1058.
- [11] X. Xiong, B. Dabrowski, O. Chmaissem, Z. Bukowski, S. Kolesnik, R. Dybzinski, and J. D. Jorgensen, Phys. Rev. B 60, (1999) 10 186.
- [12] Q. Huag, A. Santoro, J. W. Lynn, R. W. Erwin, J. A. Borchers, J. L. Peng, and R. L. Greene, Phys. Rev. B 55, (1997) 14 987.
- [13] E. L. Nagaev, Sov. Phys. Usp. 39, (1996) 781.
- [14] E. L. Nagaev, Phys. Rev. B 58, (1998) 2415.
- [15] L. P. Gor'kov, Sov. Phys. Usp. 41, (1998) 589.
- [16] S. Yunoki, J. Hu, A. L. Malvezzi, A. Moreo, N. Furukawa, and E. Dagatto, Phys. Rev. Lett. 80, (1998) 845.
- [17] S. Yunoki, A. Moreo, and E. Dagatto, Phys. Rev. Lett. 81, (1998) 5612.
- [18] M. Hennion, F. Moussa, J. Rodriguez-Carvajal, L. Pinsard, and A. Revcholevski, Phys. Rev. Lett. 81, (1998) 1957.
- [19] M. Hennion, F. Moussa, G. Biotteau, J. Rodriguez-Carvajal, L. Pinsard, and A. Revcholevski, Phys. Rev. B 61, (2000) 9513.
- [20] J. J. Neumeier and J. L. Cohn, Phys. Rev. B 61, (2000) 14 319, and the references therein.
- [21] G. Allodi, R. de Renzi, G. Guidi, F. Licci, and M. W. Pieper, Phys. Rev. B 56, (1997) 6036; G. Allodi, R. de Renzi, and G. Guidi, ibid. 57, (1998) 1024.
- [22] O. Chmaissem, B. Dabrowski, S. Kolesnik, J. Mais, J. D. Jorgensen, S. Short, Phys. Rev. B 67, (2003) 094431.

ROLE OF LOCAL STRUCTURE IN UNDERSTANDING FUNCTIONAL ELECTRONIC OXIDES

E. S. Božin, X. Qiu, S. J. L. Billinge, Michigan State University, East Lansing, MI 48824, U.S.A.
P. M. Woodward, Ohio State University, Columbus, OH 43210, U.S.A.
J. F. Mitchell, MSD, ANL, Argonne, IL 60439, U.S.A.

Abstract

We describe atomic pair distribution function (PDF) measurements of the local structure of a number of topical electronic oxide materials. This total scattering approach utilizes spallation neutrons to obtain precise, quantitative structural information from local structures, going beyond crystallography. We report recent results on colossal magnetoresistant manganites and giant dielectric titanate materials. We also report PDF measurements from the recently upgraded GPPD instrument and compare them to GPPD before the upgrade.

INTRODUCTION

Functional oxides with interesting electronic properties are important systems due to their potential in technological applications and for extending our understanding of the complex physics of correlated systems. They comprise a wide spectrum of materials such as manganites, titanates, and cuprates, all of which exhibit novel, and still not fully understood, phenomena such as colossal magnetoresistance (CMR), giant dielectric constant response, and high temperature superconductivity (HTS). Electron-lattice coupling in these systems plays an important, and poorly understood, role. In particular, elucidating the subtle *local* structural details, often very different from the crystallographic structure and usually involving the oxygen sublattice, could prove crucial for understanding the properties. Local structural information is accessible by means of the atomic pair distribution function (PDF) technique [1], which, as a total scattering technique, includes both Bragg and diffuse scattering information, and yields both the average crystalline structure and local deviations from it. The PDF is defined as

$$G(r) = \frac{2}{\pi} \int_0^{\infty} Q(S(Q) - 1) \sin(Qr) dQ,$$

where $S(Q)$ is the total scattering structure function. To obtain accurate information on the oxygen sublattice it is necessary to use neutrons as a probe, and to access the high momentum transfers, essential for PDF study, neutron spallation sources are required. The PDF approach is seeing increasing use in the study of nanostructured materials and disorder in crystals [1].

GIANT DIELECTRIC TITANATES

Recently there has been considerable interest in the dielectric properties of the cubic perovskite related to

$\text{CaCu}_3\text{Ti}_4\text{O}_{12}$ (CCTO). This material exhibits a giant dielectric constant (GDC) response with a highly unusual temperature dependence. It has a high and relatively temperature independent low frequency dielectric constant over a wide temperature range between 100 and 600 K. However, below 100 K its value drops abruptly by almost three orders of magnitude, an effect that is not accompanied by a long range structural phase transition [2-4]. The crystal structure of CCTO is shown in Figure 1. Various competing proposals have been put forward to explain this phenomenon [4-6]. The discussion revolves

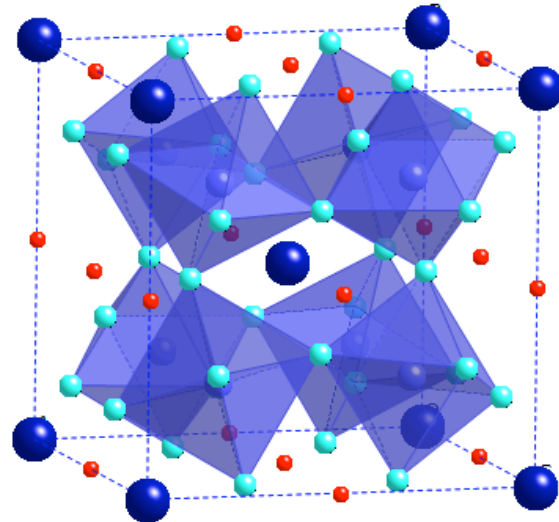


Figure 1: $\text{CaCu}_3\text{Ti}_4\text{O}_{12}$ structure is cubic (s.g. $Im-3$): TiO_6 octahedra, Ca atoms (light spheres), and Cu atoms (dark spheres).

around whether the interesting behavior is extrinsic, due to domain boundary effects, or intrinsic in the lattice. To distinguish these possibilities it is necessary to characterize the local structure. In the PDF work local structural properties of the CCTO system were investigated as a function of temperature within a range from 50 K up to room temperature [7].

We performed a complementary neutron diffraction and x-ray diffraction study on finely pulverized samples of $\text{CaCu}_3\text{Ti}_4\text{O}_{12}$. The neutron diffraction part of the study used time-of-flight experiments carried out at the Special Environment Powder Diffractometer (SEPD) at the IPNS at Argonne National Laboratory (ANL). About 10 g of polycrystalline sample was sealed in a cylindrical vanadium tube with helium exchange gas. The sample

was cooled using a closed-cycle He refrigerator, and data collected at 50, 100, 150, 200, and 290 K.

Typical PDFs of CCTO both from neutron diffraction and from x-ray diffraction experiments are shown in Figure 2. It should be noted that the *neutron* PDFs of CCTO exhibit peculiar behavior: contributions of Ti–O and Cu–O to the first PDF peak cancel out, so the first peak is ‘missing’. This is due to the negative scattering length of Ti for neutrons, *and* due to almost identical component distances of Ti–O and Cu–O. Inspecting the PDF profiles (figures 2(a) and (b)), one sees that the neutron scattering properties of Ti cause both positive and negative PDF peaks, i.e., peaks and valleys, respectively. This is in contrast to the case of x-ray diffraction PDFs where all the peaks contribute positive intensity (figure 2(c)). This perfect cancellation of the Cu–O and Ti–O intensities will only occur for selected peaks in the structure. Other peaks contain information about the relative positions of these ions and so a refinement over a wide range of r will provide accurate structural information on these species.

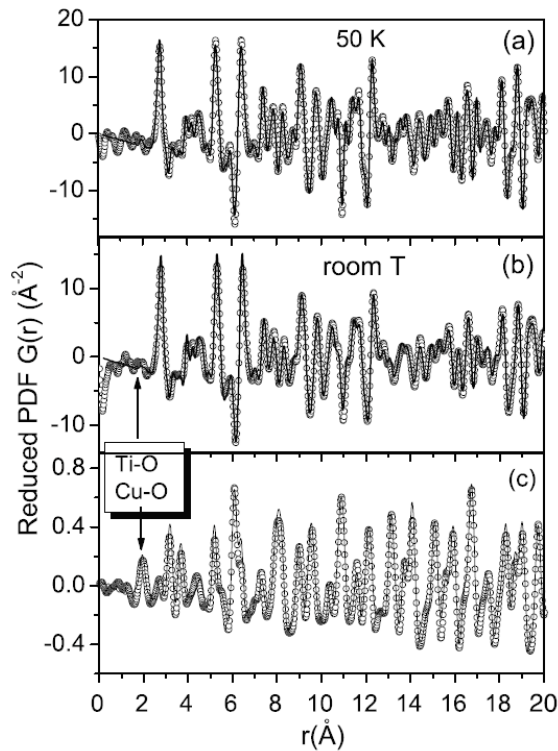


Figure 2: The reduced atomic PDF of CCTO. Experimental data (open circles) and fits (solid curves) are shown for: (a) data obtained from neutron diffraction at 50 K and (b) at room temperature; (c) data obtained from x-ray diffraction at room temperature (collected on X7A at NSLS at Brookhaven National Laboratory). Arrows mark the nearest neighbor PDF peak: in CCTO it contains two contributions, coming from Ti–O and Cu–O distances.

In agreement with earlier studies, no signature of a structural phase change was observed. The temperature dependence of the nearest neighbor Cu–O distance (not shown) is very flat, supporting the idea that this is bracing the structure. No evidence for nanoscale octahedral tilting, or off-centre Ti displacements, is found. However, the isotropic Ca displacement parameter (Figure 3(a)), has a significant static offset compared to the expected Debye behavior.

Simple modeling based on bond valence concepts supported the local structural observations. The temperature at which both the Ca and Cu environments are optimal was estimated to be in the vicinity of 260 K.

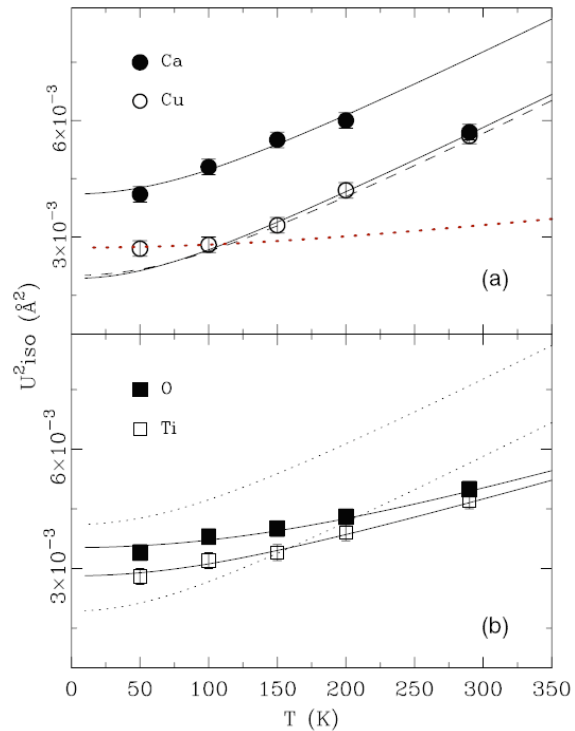


Figure 3: (a) Evolution with temperature of the isotropic displacement parameters of Ca and Cu. Solid curves show the Debye model for Ca and Cu, with parameters as specified in Table 3 of Reference [7]. The dashed curve is a Debye curve of Ca corresponding to the same Debye temperature, but with offset parameter set to zero. The thick dotted curve shows a Debye model for Cu using a higher Debye temperature of 785 K. (b) Isotropic displacement parameters of Ti and O as a function of temperature, with Debye model curves superimposed (solid curves). Debye model curves for Ca and Cu (dotted curves) are also shown for comparison.

At lower temperatures the Ca becomes *underbonded*. This is generally accompanied by a reduction in site symmetry and may result in off-center displacements of Ca ions. If these displacements do not become long range ordered because of the braced structure, this would explain the

absence of a structural phase transition and the static offset of the Ca thermal parameters. This would be consistent with the presence of local domains of coherently polarized displaced Ca ions at low temperature and which could explain the enhanced values of far IR lattice dielectric constant, a parameter playing an important role in intrinsic and extrinsic boundary layer capacitance models for the large dielectric response [7].

CMR MANGANITES

The neutron probe is a particularly useful tool for studying systems with strong charge-lattice coupling. As a matter of fact, often the mere existence of such coupling is revealed from neutron diffraction studies. The possibility of the isotopic enrichment option represents an integral component of this type of study.

Isotopic substitution has a dramatic effect on the properties of the CMR material $\text{Pr}_{0.525}\text{La}_{0.175}\text{Ca}_{0.3}\text{MnO}_3$. In this system the ferromagnetic metallic (FM) phase is marginally stable. Simply replacing ^{18}O with ^{16}O has the dramatic effect of destroying the low-temperature FM phase [8-10]. PDF studies of these isotopically substituted samples clearly showed the important structural response to the appearance of the FM phase. The height of the PDF peak at 2.75 \AA is an order parameter for the FM phase as is clearly evident in Fig. 4.

Neutron powder diffraction experiments were carried out on SEPD instrument at the IPNS. We find from the

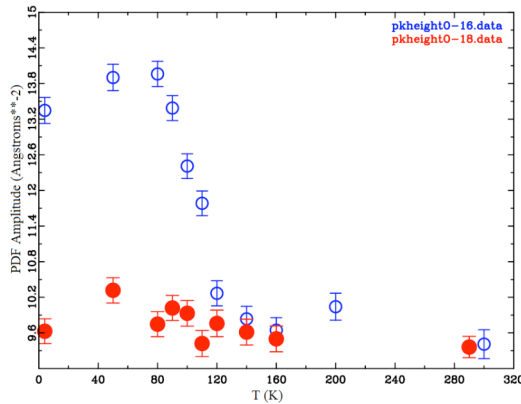


Figure 4: Plot of PDF peak-height of the $r = 2.75 \text{ \AA}$ O-O peak vs. temperature for two samples of $\text{La}_{0.525}\text{Pr}_{0.175}\text{Ca}_{0.3}\text{MnO}_3$ enriched with ^{16}O (open circles) and ^{18}O (filled circles) respectively. In the ^{18}O the transition to a FM ground-state is suppressed and the sample remains an AF insulator to low temperature. This clearly shows that the excess PDF peak-height is coming from the appearance of undistorted octahedra in the metallic phase.

the PDF that the shape of the MnO_6 octahedra changes from being elongated, due to a Jahn-Teller distortion, to a more regular shape below the IM transition in the ^{16}O

sample, whereas the ^{18}O sample remains distorted at all temperatures. This local structural result, which was possible to obtain only by neutron powder diffraction experiment, emphasizes the important role that lattice plays in the CMR effect and the IM transition in manganites [11].

Bilayer Manganites

The atomic PDF technique has been employed to probe the atomic local structural responses in naturally double layered manganites $\text{La}_{2-2x}\text{Sr}_{1+2x}\text{Mn}_2\text{O}_7$ in the doping range $0.54 \leq x \leq 0.80$. This system has a rich and interesting, but not fully understood phase diagram, shown in Figure 5 [12, 13]. The low temperature neutron powder diffraction

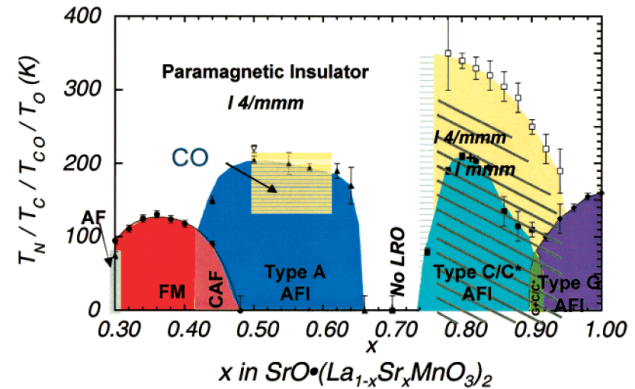


Figure 5: Structural and magnetic phase diagram of the bilayer manganite $\text{La}_{2-2x}\text{Sr}_{1+2x}\text{Mn}_2\text{O}_7$ in the range $0.3 \leq x \leq 1.0$ determined by neutron powder diffraction. Solid markers represent the magnetic transition temperature (T_C or T_N); open squares delineate the tetragonal to orthorhombic transition. Several magnetic phases are identified: ferromagnetic metal (FM), canted antiferromagnetic (CAF), and A-, C-, and G-type antiferromagnetic insulators (AFI). The region marked 'No LRO' has no magnetic diffraction peaks at $T \geq 5 \text{ K}$. Samples in the region marked 'CO' exhibit long-range charge ordering reflections in x-ray and/or electron diffraction.

measurements, performed on SEPD at IPNS at ANL, suggest the coexistence of two different Jahn-Teller (JT) distorted MnO_6 octahedra when its ordered magnetic structure crosses over from type A ($0.54 \leq x \leq 0.66$) to type C/C* ($0.74 \leq x \leq 0.90$) ordering. At all doping levels at low temperature the doped holes reside predominantly in the plane of the bilayer. In the type A magnetic ordering regime, the e_g electrons appear to be significantly delocalized in the plane resulting in undistorted octahedra, while in type C/C* regime, elongated JT distorted octahedra are apparent.

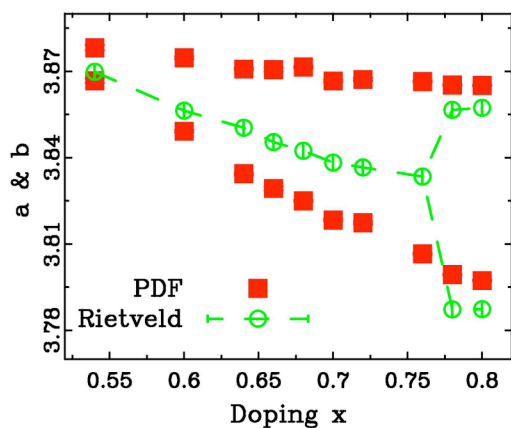


Figure 6: Solid circles are the in-plane lattice constants a and b from PDF refinements with orthorhombic models, while open circles are from Rietveld refinements on the same data with tetragonal and orthorhombic models in $0.54 \leq x \leq 0.76$ and $0.78 \leq x \leq 0.80$, respectively.

This is consistent with the presence of inhomogeneous coexisting delocalized and localized electronic states. No evidence of macroscopic phase separation has been observed. Such nanoscale inhomogeneities may explain the magnetically frustrated behavior observed in the spin disordered ‘gap’ region ($0.66 \leq x \leq 0.74$). The pulsed neutron diffraction based PDF study revealed that what crystallographically appears as an orthorhombic to tetragonal phase transition, is actually an order-disorder type transition with the underlying structure locally always being orthorhombic, as demonstrated in Figure 6 [14].

Reciprocal space effects on PDF

In addition to experiments with primarily scientific context, we carried out several more technical experiments dedicated to further develop the PDF technique at IPNS. These projects included efforts in establishing improved measures of quality for the atomic PDF [15], and extensive studies of the reciprocal-space instrumental effects on the real-space neutron atomic PDF [16]. Recently, the importance of the Q -space resolution has been understood in studies of nanocrystalline materials and disordered crystals. In these studies reported here we used SEPD and General Purpose Powder Diffractometer (GPPD), rather than the Glass, Liquid, and Amorphous Materials Diffractometer (GLAD) to take advantage of the higher resolution. Here we note that GPPD was recently upgraded with a neutron wave guide. We recently tested the upgraded GPPD instrument to benchmark its performance and suitability for PDF studies, using a set of standard samples. A qualitative comparison of the results is shown in Figure 7, where the real-space resolution of the upgraded GPPD is compared to that of the same instrument prior the upgrade, as well as to the NPDF diffractometer of LANSCE at Los Alamos National Laboratory. The upgraded GPPD is a highly suitable and reliable instrument for carrying out atomic

PDF studies. The data-rates of the upgraded GPPD are improved with a data collection time of 6 hours compared to 8 hours for the instrument prior to the upgrade.

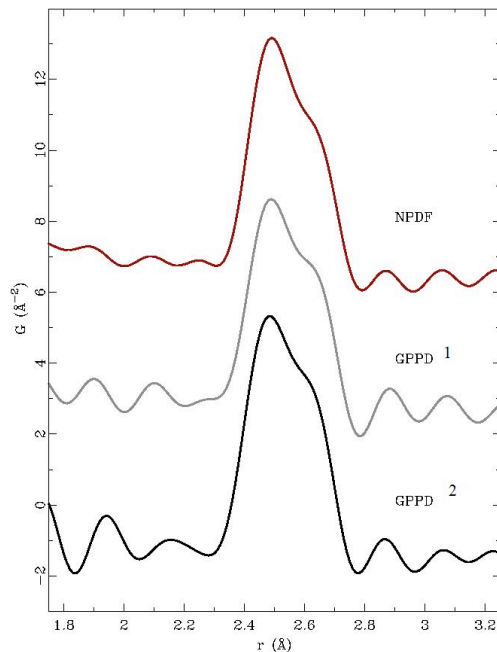
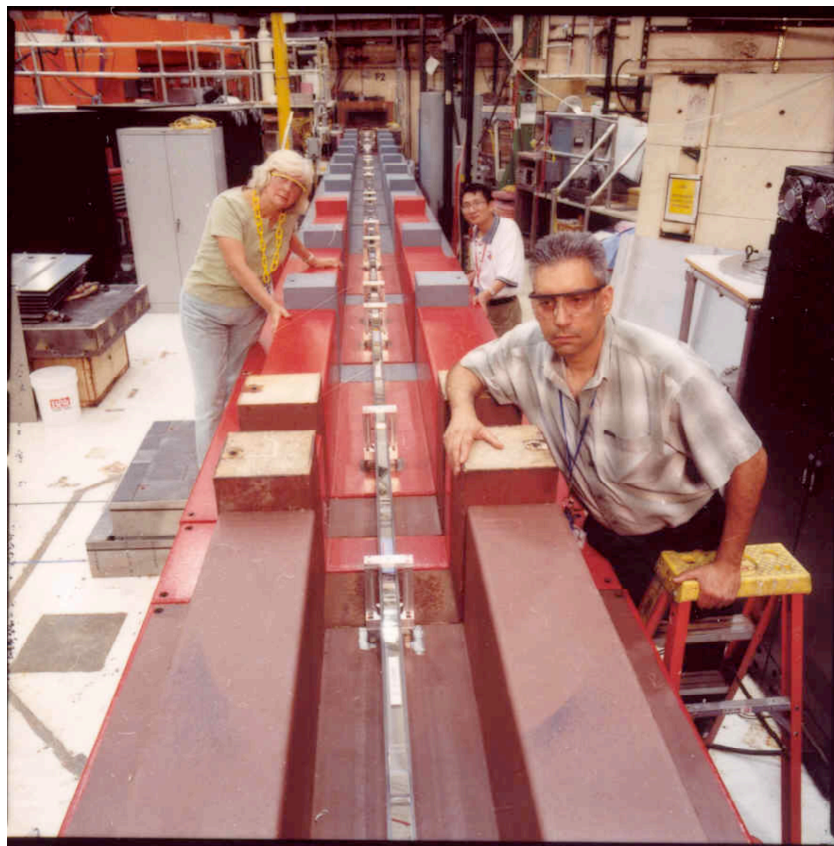


Figure 7: The reduced atomic PDF $ZnSe_{0.5}Te_{0.5}$ at 10K, obtained through a sine Fourier transform of $F(Q)$ using data up to $Q_{max}=35\text{\AA}^{-1}$; focus on the low- r region and the nearest neighbor peak splitting. The figure features the same r -region for the three measurements, with PDFs obtained under identical conditions. From top to bottom: at the NPDF at LANSCE at Los Alamos National Laboratory, at the GPPD at IPNS at Argonne National Laboratory before the upgrade (1), and after the recent upgrade (2).

REFERENCES

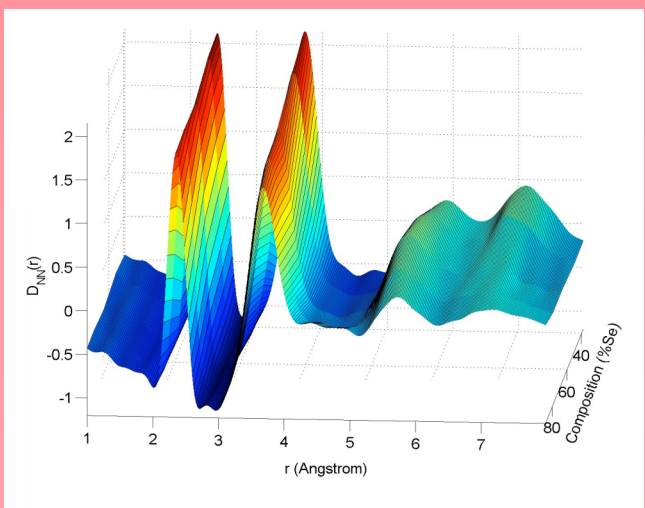
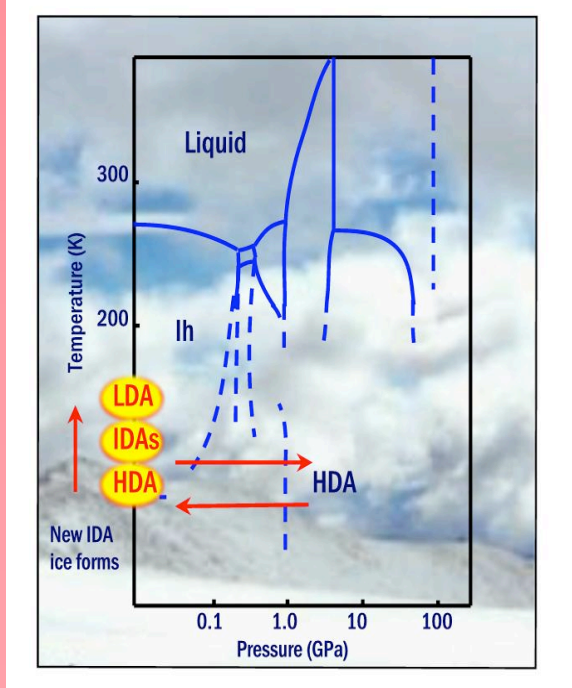
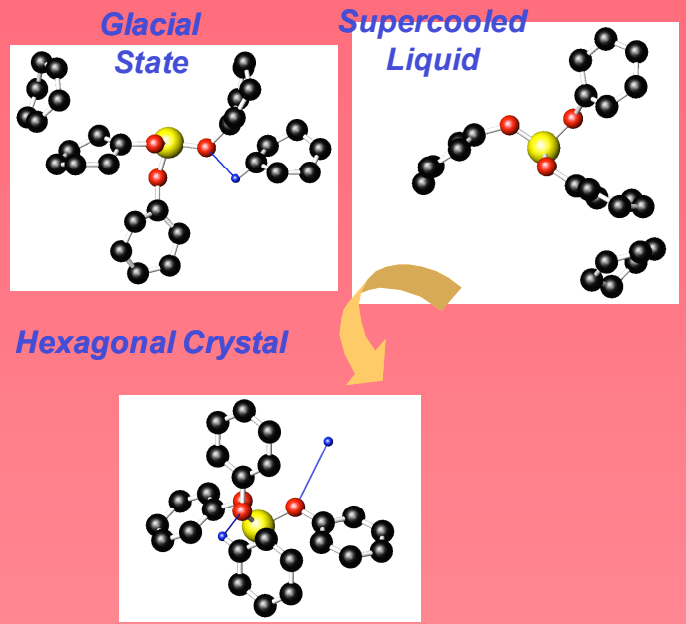
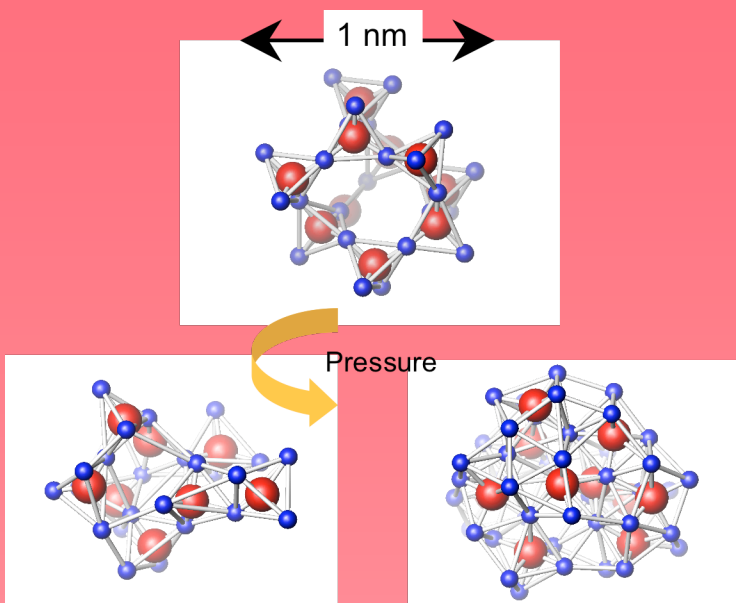
- [1] S.J.L. Billinge and M. Kanatzidis, *Chem. Comm.*, 174, 2004; T. Egami and S.J.L. Billinge, “*Underneath the Bragg Peaks: Structural Analysis of Complex Materials*”, Pergamon/Elsevier, Oxford (2003).
- [2] M.A. Subramanian, D. Li, N. Duan, B.A. Reisner, and A. Sleight, *J. Solid State Chem.* **151** (2000) 323.
- [3] A.P. Ramirez, M.A. Subramanian, M. Gardel, G. Blumberg, D. Li, T. Vogt, and S. Shapiro, *Solid State Commun.* **115** (2000) 217.
- [4] C.C. Homes, T. Vogt, S. Shapiro, S. Wakimoto, and A.P. Ramirez, *Science* **293** (2001) 673.
- [5] A.P. Ramirez, G. Lawes, V. Butko, M.A. Subramanian, and C. M. Varma, *cond-mat/0209498*.
- [6] L. He, J.B. Neaton, M.H. Cohen, D. Vanderbilt, and C.C. Homes, *Phys. Rev. B* **65** (2002) 214112.

- [7] E.S. Božin, V. Petkov, P.W. Barnes, P.M. Woodward, T. Vogt, S.D. Mahanti, and S.J.L. Billinge, *J. of Phys.: Cond. Matt.* **16** (2004) 5091.
- [8] A.M. Balagurov, V.Yu. Pomjakushin, D.V. Sheptyakov, V.L. Aksenov, N.A. Babushkina, L.M. Belova, A.N. Taldenkov, A.V. Inyushkin, P. Fischer, M. Gutmann, L. Keller, O.Yu. Gorbenko, and A.R. Kaul, *Phys. Rev. B* **60**, (1999) 383.
- [9] G.M. Zhao, H. Keller, J. Hofer, A. Shengelaya, and K.A. Müller, *Solid State Comm.* **104**, (1997) 57.
- [10] N.A. Babushkina, L.M. Belova, O.Yu. Gorbenko, A.R. Kaul, A.A. Bosak, V.I. Ozhogin, and K.I. Kugel, *Nature* **391**, (1998) 159.
- [11] M. Gutmann, E.S. Božin, S.J.L. Billinge, N.A. Babushkina, L.M. Belova, A.R.Kaul, O.Yu. Gorbenko, *Appl. Phys. A* **74**, (2002) 892.
- [12] M. Kubota, H. Fujioka, K. Hirota, Y. Morimoto, and H. Yoshizawa, *J. Phys. Chem. Solids* **60**, (1999) 1161.
- [13] C.D. Ling, J.E. Millburn, J.F. Mitchell, D.N. Argyriou, J. Linto, *Phys. Rev. B* **62**, (2000) 15096.
- [14] X. Qiu, S.J.L. Billinge, C.R. Kmety, J.F. Mitchell, *Phys. J. Phys. Chem. Solids* **65**, (2004) 1423.
- [15] P.F. Peterson, E.S. Božin, Th. Proffen, and S.J.L. Billinge, *J. Appl. Cryst.* **36**, (2003) 53.
- [16] X. Qiu, E.S. Božin, P. Juhas, Th. Proffen, and S.J.L. Billinge, *J. Appl. Cryst.* **37**, (2004) 110.



Evan Maxey (GPPD), Simine Short (SEPD) and Yaping Li (GPPD) "inspect" the supermirror guide in the upgraded GPPD

Disordered Materials



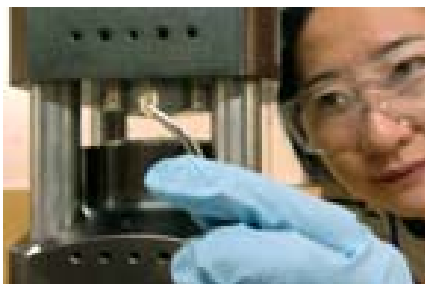
THE GLASS LIQUIDS AND AMORPHOUS MATERIALS DIFFRACTOMETER AT IPNS 2001-2006.

Chris .J. Benmore
Argonne National Laboratory, Argonne, IL 60439.

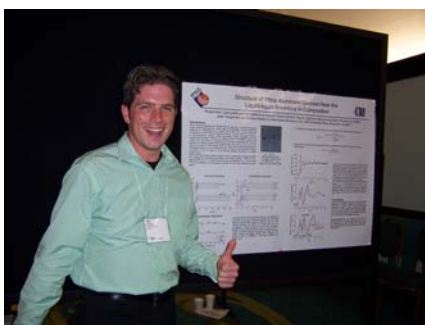
INTRODUCTION

It has been a productive five years for GLAD which has been spurred on by the surge of interest in polyamorphism as well as liquid-liquid and amorphous-amorphous transitions in general. Substantial progress has also been made by combining data from spallation neutron diffractions new 'sister' technique high energy x-ray diffraction. Measurements at extreme conditions have been a primary theme during these past few years, with experiments at high pressures up to 6GPa using piston anvil cells, the development of containerless melting techniques with laser heating up to 3050°C, and last but by no means least, structural measurements on liquid hydrogen fluoride. However user experiments are often remembered for the actions or comments of characters that worked on them. So I will start this report with a word of thanks to all the postdocs and students associated with GLAD who have worked with us during this time.

PERSONNEL

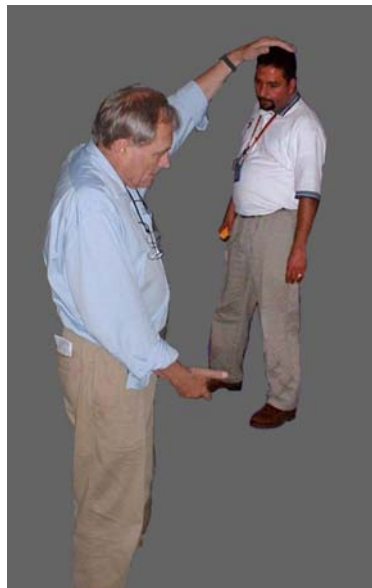


Qiang Mei (U. Wyoming) squashing glass in the Paris-Edinburgh cell. Mei has accepted an offer to stay at GLAD as an Argonne postdoc for 2006.

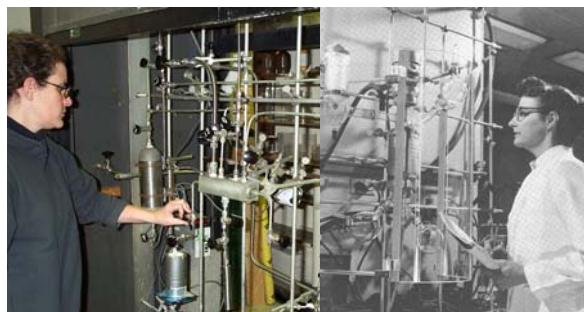


Rob Hart proving he really did attend at least some of the glass and optical materials meeting in Florida. Rob left in the summer of 2005 to go into industry.

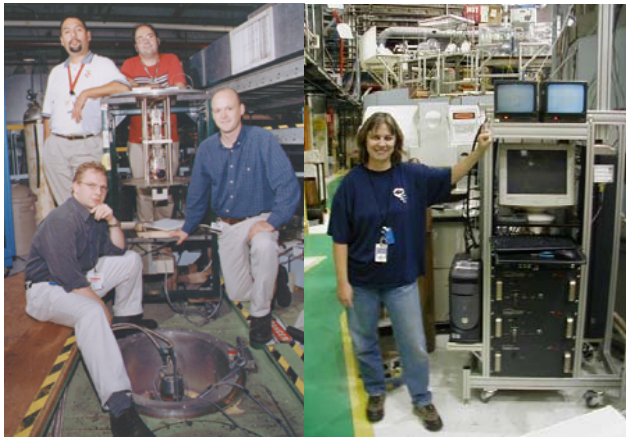
Sujatha Sampath left in 2002 to take up a postdoc position at U. Wisconsin but has recently returned as a visiting adjunct professor from Arizona State University.



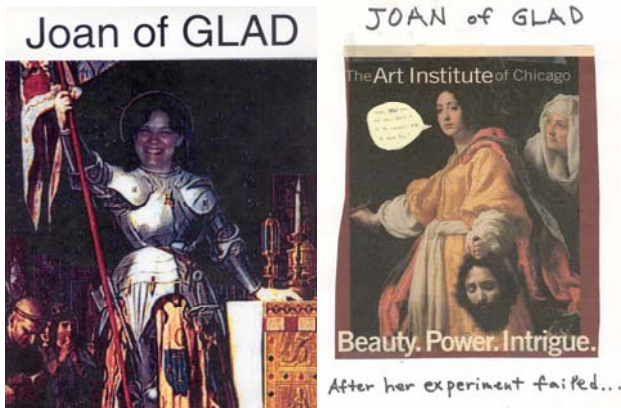
Jack defines a new way of measuring postdocs - in units of Urquidi's. Photo courtesy of Evan Maxey. Jacob left in 2002 to take up a joint professorship at New Mexico State University and LANSCE.



Sylvia McLain (left or is it right ?) making something hazardous to put on GLAD. Sylvia was awarded an international NSF postdoc in 2004 and is serving her time at ISIS.



The hot and cold of it. **Left:** Clockwise from bottom left: Chris Tulk (SNS), Jacob Urquidi (IPNS), Joerg Neuefeind (ANL, now SNS), Chris Benmore (IPNS) during an ice experiment on GLAD. **Right:** Joan at the laser controls.



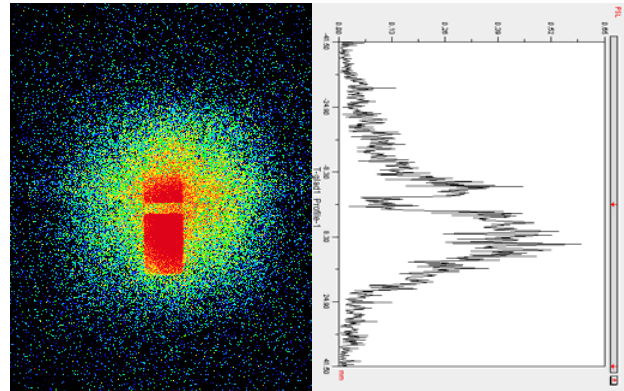
The bubble reads 'OK, now tell me how easy it is to correct for hydrogen'.

Joan Siewenie has been busy modeling GLAD data using the Reverse Monte Carlo technique with trips to U. Tennessee and U. Littoral, France, to help set up simulations for GLAD users. In 2005 Joan was awarded an Argonne pacesetter award as an acknowledgement for this work. She has now started a part time physics Ph.D. at Northern Illinois University (on computer modeling of glass and liquid neutron data of course) in addition to her work on GLAD.

INSTRUMENT

GLAD stability and backgrounds have greatly improved over the years making it suitable for accurate measurements. Extensive work and tests have been carried out on a new incident honeycomb Soller collimator system and this should be put into place permanently in 2006, with a some increase in incident flux. In 2005, after being squeezed either side by instrument upgrades on QENS and SCD, we expanded away from the monolith by means of a large deck extension. The final one hundred ^3He position sensitive

detectors, needed to bring the GLAD detector bank up to its' full design capacity, were procured in 2005 and GLAD is scheduled to undergo a major detector upgrade in the summer shutdown of 2006. At the same time the data acquisition system will be upgraded and the old Atlas/Genie GLAD analysis software completely replaced. In fact GLAD recently reached run number 10,000 which forced an early switch to the new software for some users.

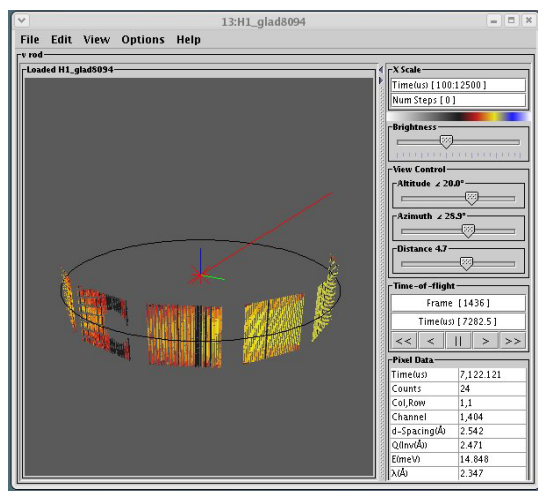


Measured image of the GLAD beam profile. The horizontal strip is a BN mask placed at the sample position. Usually for powdered samples in a Vanadium can the main neutron intensity falls on the sample at the bottom of the can.

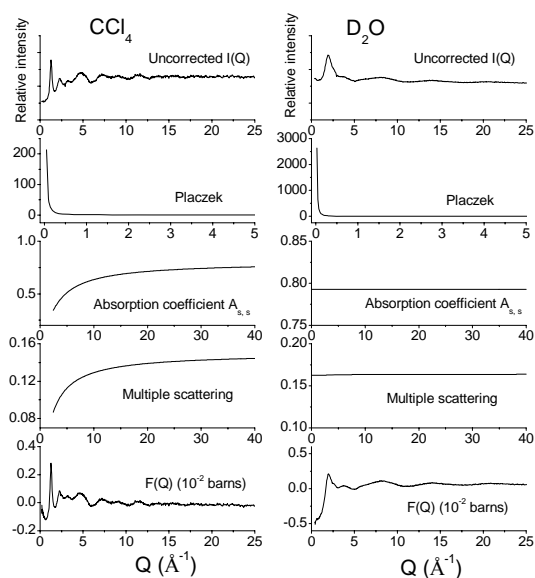
SOFTWARE

Analyzing Time-of-Flight neutron total scattering data involves many instrument dependent corrections, including: detector deadtime, normalization of detector counts to beam monitor counts, time-of-flight to momentum transfer Q rebinning, use of vanadium data for both calibration and data merging purposes, as well as attenuation, multiple scattering, and inelastic effects. The implementation of these in the Integrated Spectra Analysis Workbench (*ISAW*) software suite has been achieved through the efforts of Julian Tao (IPNS) to whom I and many users are indebted. Extensive details on the corrections and their implementation have been documented in reference [1].

The fastest I could probably analyze a raw GLAD data set using the old *Atlas* software was about an hour. The new Java based software rather than grouping into 19 angular groups, performs the corrections pixel-by-pixel (1.6 million of them) and creates an $S(Q)$ in approximately 3 minutes. In addition the low Q limit of GLAD has been extended from 0.325 \AA^{-1} to 0.175 \AA^{-1} .



A 3-D view of GLAD and measured intensities as a function of time-of-flight in ISAW.



Examples of the measured intensity and correction factors associated with analyzing data from CCl_4 and D_2O . **From top to bottom** : sample scattering intensity vs. Q before corrections; calculated Placzek effect in terms of a dimensionless ratio between the Placzek corrected scattering cross section and the uncorrected one; calculated coefficient of neutrons scattered by sample then attenuated by sample calculated multiple scattering in terms of secondary scattering fraction; corrected sample scattering intensity vs. Q . Corrections were calculated at the scattering angle $2\theta = 113.6^\circ$.

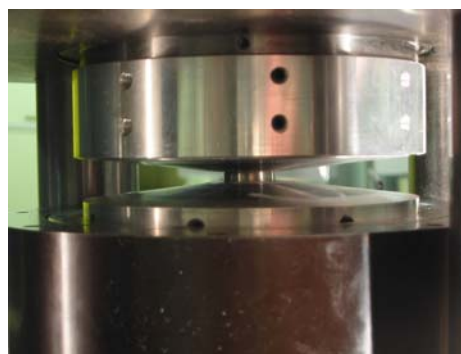
I would like to point out that the GLAD computer which now runs the new software is called *Perseus*. The choice of this name comes from Greek mythology and I quote an email message from Rob Hart below for the reason :

Atlas fought on the side of his father, Chronos, against Zeus and the Olympians. Upon the eventual victory of the

Olympians, he was banished. But an oracle prophesied that a son of Zeus would kill his mortal body. Perseus was Zeus's son who killed the gorgon Medusa, and as a result had something of an award tour. But Atlas would not host him, and out of displeasure over this fact, Perseus showed Atlas the head of Medusa, which turned his body into stone. The legend goes that this is the creation of the Atlas mountains. As if this were not enough, in the afterlife, he is punished by Zeus to eternally bear the earth on his back to keep it separate from the heavens. So while our new software will be the mortal death of Atlas, it remains the foundation of our data analysis. Thus a fitting name for the new computer is Perseus.

SAMPLE ENVIRONMENT

As mentioned in the introduction GLAD has specialized in experiments at extreme conditions in the past few years, whether it was pressure, temperature or acidity. With help from Chris Tulk, Malcom Guthrie (both SNS) and Darren Locke (Stonybrook) a considerable amount of knowledge of how (and how not) to perform high pressure experiments on amorphous materials has been obtained. A phase II small business initiative grant in collaboration with Rick Weber (CRI Inc.) helped adapt a containerless levitation system with laser heating for use in wide angle neutron diffraction experiments. Meanwhile John Turner and Sylvia McLain (U. Tennessee) fabricated Teflon and monel sample containers for diffraction measurements on superacidic solutions.



A photograph of a TiZr gasket between two anvils in the Paris-Edinburgh cell.



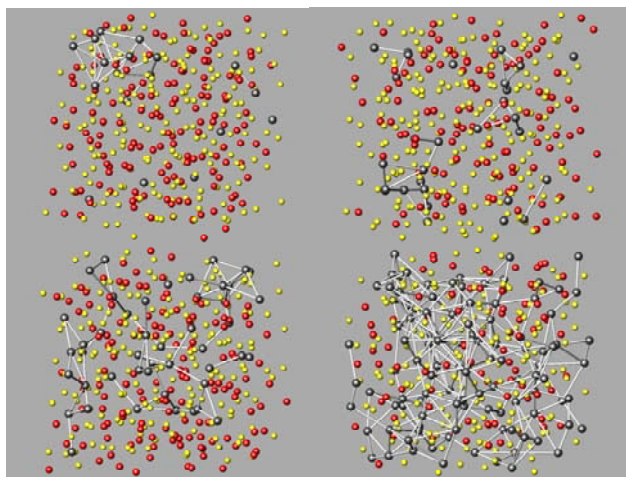
A flat plate Teflon can manufactured for a diffraction experiment on liquid hydrogen fluoride.



Jim Rix (CRI Inc.) lines up the 240W CO₂ laser on GLAD for a levitation experiment.

MODELING AND VISULIZATION

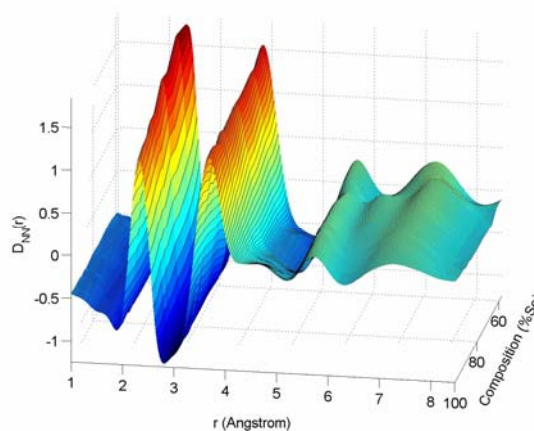
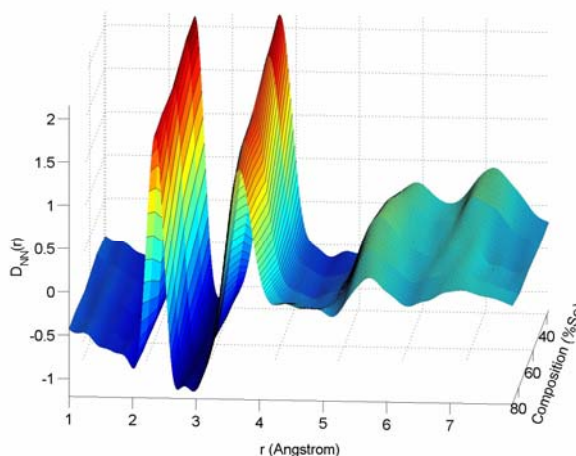
Structural modeling of diffraction data continues to be an important but often time consuming aspect of data interpretation. Several groups of users have used MD packages such as DL_POLY to model their neutron data with literature potentials with much success. For RMC (or EPSR), the use of both neutron and high energy x-ray diffraction data is usually a necessity for generating a realistic model. Isotopic substitution data also provides an important constraint. Joan Siewenie ran a course in 2003 for users wanting to get started with RMC called 'Make it Go'.



Clustering occurring in AgGeS glass as a function of Ag₂S composition produced using RMC modeling and constrained by two Ag isotope neutron measurements and a high energy diffraction data set.

For many systems several data sets have been collected, and a popular way to show several radial distribution functions is to plot the D(r) data as a real space contour plot. **Top:** The example of glassy AsSe as a function of

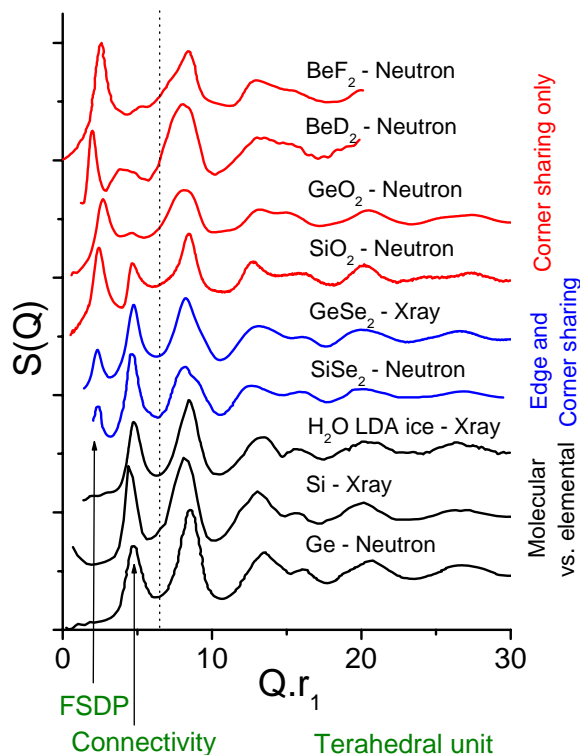
composition is shown above representing the formation of As₄Se₄ molecular-type units. **Bottom :** The formation of tetrahedral in GeSe₂ – in this case the neutron spectra represents the topology of the glass.



SCIENCE HIGHLIGHTS

Adrian Wight has remarked that it is futile for researchers performing structural studies on glasses to search for a universal theory of the first sharp diffraction peak (FSDP) [2]. Nonetheless, taken for a single system as a function of some variable (pressure, composition etc.) useful local information on changes the intermediate range order and local structure may be obtained. Such studies on the FSDP have formed a large part of the research on GLAD in recent years. Martin *et al* [3] have had success in indexing FSDP's by comparing to known crystalline templates in layered systems. Elliott and co-workers [4] have modeled the first huge principal peak in VHDA ice by positionally disordering mixtures of high density crystalline phases. Tulk *et al* [5] have tracked the position of the FSDP as a function of time and anneal temperature to access a myriad of intermediate amorphous ice forms. They have also begun to relate changes on the local structural level to network formation on the intermediate

range order length scale in amorphous ice. An empirical formulae for this relation has already recently been derived for binary selenide glasses by Bychkov *et al* [6]. All we now need is an explanation.

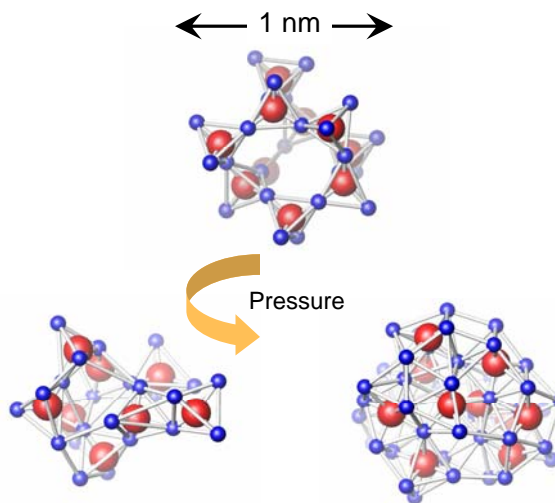


A comparison of $S(Q)$ is made for several tetrahedral glasses, scaled by the first peak in the radial distribution function r_1 . The first sharp diffraction peak, often associated with intermediate range order, the chemical ordering peak related to the connectivity of units and the region of the spectra dominated by details of the tetrahedral unit are also marked. Note the similarity of the x-ray spectra (oxygen-oxygen partial) for low density amorphous ice, amorphous Si and amorphous Ge, compared to that of classic AX_2 type glasses which include a well defined FSDP due to the existence of open regions in the network [7].

SPALLATION NEUTRON AND HIGH ENERGY X-RAY DIFFRACTION COMBINED

Probably one of the most significant advances in glass structure determination in recent years is the development of the high energy x-ray diffraction technique, which allows high momentum transfers to be accessed. Beamlines at 11-ID and 1-ID at the APS now cover a comparable Q-range to the GLAD diffractometer at IPNS and several neutron users now regularly apply for time at both facilities to study the same sample. Kohara *et al* [8] and Wilding *et al* [9] have successfully exploited the spallation neutron/high energy x-ray combination in the case of geological glasses. Whereas Sampath *et al* [10] and Guthrie *et al* [11] have used the combination to

observe the effects of high pressure on glass structure. Turner and co-workers [12] have combined isotopic neutron diffraction with high energy x-ray data to make a full partial structure factor analysis of liquid HF for the first time.



Formation of a dense Octahedral glass [9].

REFERENCES

- [1] *Time-of-Flight Neutron Total Scattering Data Analysis implemented in the software suite ISAW*, J. Tao, C.J. Benmore, T.G. Worlton, J.M. Carpenter, D. Mikkelson, R. Mikkelson, J. Hammonds, A. Chatterjee, *Nuclear Instruments and Methods*, submitted.
- [2] C. Wright *J. Non-Cryst. Solids* 179 (1994) 84-115.
- [3] J.D. Martin, S.J. Goettler, N. Fossé, and L. Iton, *Nature* 419, 381–384 (2002).
- [4] J.K. Christie, M. Guthrie, C.A. Tulk, C.J. Benmore, D.D. Klug, S.N. Taraskin, and S.R. Elliott, *Phys. Rev. B* 72, 012201 (2005)
- [5] C. A. Tulk, C. J. Benmore, J. Urquidi, D. D. Klug, J. Neuefeind, B. Tomberli and P. A. Egelstaff, *Science* 297 (2002) 1320-1323.
- [6] E. Bychkov, C.J. Benmore, and D.L. Price, *Phys. Rev. B*, 72, 172 107 (2005).
- [7] C.J. Benmore, R.T.Hart, Q.Mei, D.L.Price, J.Yarger, C.A.Tulk and D.D.Klug. *Phys. Rev. B.* 72 132201 (2005).
- [8] S. Kohara, K. Suzuya, K. Takeuchi, C-K. Loong, M. Grimsditch, J.K.R. Weber, J.A. Tangeman and T.S. Key, *Science*, 303, 1649-52 (2004).
- [9] M. C. Wilding, C. J. Benmore, J. A. Tangeman and S. Sampath. *Europhysics Lett.*, 67 (2004) 212.
- [10] S. Sampath, C.J. Benmore, K.Z. Lanszky, J. Neuefeind, D.L. Price and J. Yarger. *Phys. Rev. Lett.*, 90, 11 (2003) 115502
- [11] M. Guthrie, C.A. Tulk, C.J. Benmore, J. Xu, J.L. Yarger H-K. Mao and R.J. Hemley. *Phys. Rev. Lett.*, 93 (2004) 115502.
- [12] S.E. McLain, C.J. Benmore, J.E. Siewenie, J. Urquidi and J.F.C. Turner. *Angewandte Chemie Int. Ed.* 43 (2004) 1951-1955.

THE GLACIAL STATE OF TRIPHENYL PHOSPHITE

Q. Mei^{1,2}, P. Ghalsasi³, C.J. Benmore², and J.L. Yarger^{1,3}

¹ Arizona State University, Department of Chemistry and Biochemistry, Tempe, AZ 85287.

² Argonne National Laboratory, Argonne, IL 60439.

³ University of Wyoming, Laramie, WY 82071.

INTRODUCTION

Kivelson and co-workers have discovered a low-temperature rigid state in the fragile glass former triphenyl phosphite (TPP) [1]. It was discovered by annealing the low temperature glassy phase at 220K. The annealed (high density) form was initially reported to be amorphous and named as the “glacial state”. They argue that the locally preferred structure (glacial) and ideal crystal structures are expected to be slightly different. The glacial phase could provide the first experimental evidence of topological frustration in super-cooled liquid, and the investigation of polyamorphism of TPP would contribute to the understanding of the supercooled liquid state and the subsequent glass formation. However, the nature of the glacial state is a matter of debate and several different interpretations have now been proposed. Hedoux et al. [2] have performed Raman, X-ray diffraction and inelastic neutron scattering experiments, and argue that the glacial state is not amorphous but formed by nanocrystallized domains of the stable crystalline phase, mixed with a fraction of under-cooled liquid. The relative fractions of these components depend on the aging temperature. Raman spectra have shown that there exists a weak C-H...O hydrogen bond in the glacial state at 222K~226K, which has been used to support the nanocrystalline-supercooled liquid mixture interpretation.

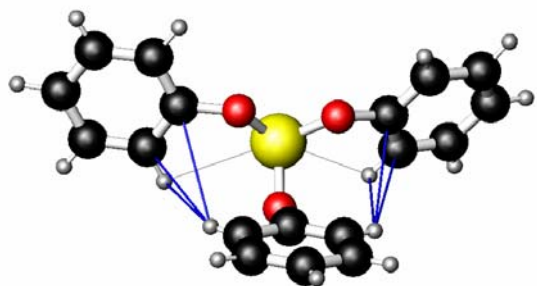


Figure 1. The molecular conformation of TPP in the hexagonal crystal state. The nearest neighbour HH and CH interactions to which neutrons are most sensitive are shown.

EXPERIMENTAL DETAILS

Neutron scattering experiments were performed at low temperature (190 K – 250 K using a liquid nitrogen cryostat) on a fully deuterated $P(OC_6D_5)_3$ (D-TPP) sample and 67% fully deuterated 33% fully hydrogenated mixture $P_{2/3}(OC_6D_5)_2 + P_{1/3}(OC_6H_5)$ sample using the Glass Liquid

and Amorphous materials Diffractometer at Argonne National Laboratory, USA. The TPP samples were loaded into 9.5mm outer diameter (D-TPP) and 6.3mm (Mixture TPP) vanadium cans of 0.1mm wall thickness in an inert glove box. Sample temperatures for these experiments were stable to within ~ 0.2 K. The 67:33 mixture was chosen to give 15 atomic% hydrogen content, balancing the requirements of performing manageable inelastic scattering corrections on a 6.3mm diameter cylindrical sample, obtaining good statistics in a reasonable period of time (between 2 and 8 hours) and providing a measurable isotopic contrast to extract the hydrogen related interactions [3].

RESULTS AND DISCUSSION

Figure 2 shows the neutron diffraction patterns for the crystal, glacial, super-cooled liquid, glass and liquid of D-TPP. These spectra are dominated by C-H, C-C and H-H interactions. Evidence of Bragg peak formation in the glacial state is observed in the neutron data and absent in X-ray structure factor, suggesting the Bragg peaks may be dominated by hydrogen lattice interactions.

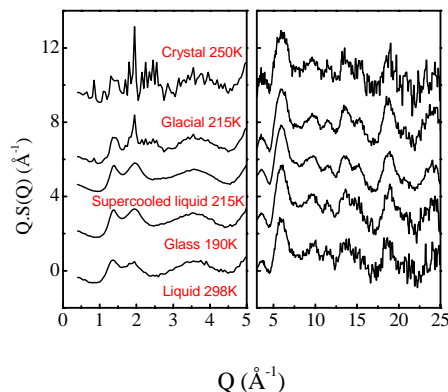


Figure 2 Measured total neutron structure factors for the fully deuterated TPP in different forms.

In order to differentiate between intra- and inter-phenyl ring hydrogen interactions in first order difference distribution function $\Delta D_H(r)$ (not shown), a simple model phenyl ring, was calculated based on a modified version of the published x-ray crystal structure. It is found that the

intra-phenyl ring hydrogen distances H-C₁ (hydrogen to the first adjacent carbon atom), H-C₂ and H-C₃ in the neutron spectra are ~0.15 Å longer relative to the published x-ray crystal structure data. The bond distances from neutron data are considered to be more accurate and reliable since neutron scattering is extremely sensitive in probing hydrogen (deuterium) positions. The simple model phenyl ring was constructed from Gaussian peaks in which the C-H bond length was fixed to 1.08 Å, in agreement with the neutron data (see figure 3). Consequently the neutron 2.17 Å distance is assigned to H-C₂, the 3.37 Å distance to H-C₃, and the shoulder at 2.40 Å to intra-ring H-H correlations. The comparison of the modeling and experimental data suggests that the two smaller hydrogen correlation peaks around ~2.8 and ~3.0 Å in TPP crystal are most likely due to inter-phenyl (C-H and/or H-H) ring interactions. It is not possible from the isotopic substitutions made in this experiment to ascertain whether or not these correlations are between phenyl rings in the same molecule or between different molecules. From the modified structural model of the TPP molecule we find six intramolecular H-C and H-H distances below 3.4 Å which are very sensitive to the orientation of the phenyl rings, in particular the ‘inverted’ ring. Two distinct C(H)-O intermolecular hydrogen bond distances at 2.81 and 2.97 Å (between neighbouring molecules) have been identified in the hexagonal crystal structure which lead to H-H and C-H correlations with minimum approach distances of 2.89 Å and 3.15 Å, respectively. These are illustrated in figures 4 and 5.

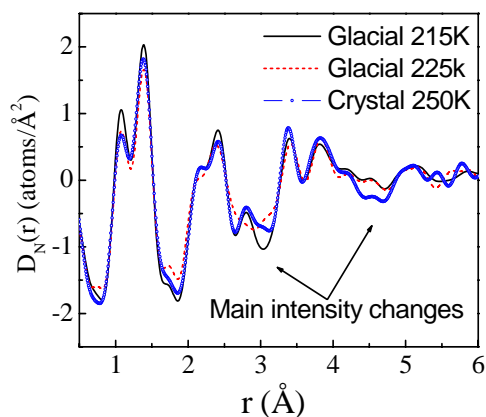


Figure 3. Total neutron correlation functions for the fully deuterated sample in the early glacial stage at 215K, later glacial stage at 225K, and crystal at 250K. The data were truncated at $O_{max}=25 \text{ \AA}^{-1}$.

Total neutron correlation functions for the glacial state formed at 215 K, 225 K and the crystal at 250 K for the fully deuterated TPP sample are shown in figure 3. These data show significant structural re-arrangements in the

glacial state have to occur in the 2.8-3.0 Å and 4.5 Å regions before longer-range crystallization can take place. In addition, since the 225 K glacial state data cannot be simply reproduced from a linear combination of the 215 K glacial state and the crystalline structures, the results suggest that the glacial state is not a simple two-component mixture of the nanocrystalline and supercooled liquid phases. Based on the neutron and x-ray results we suggest slight variations in molecular conformation as well as changes in the next nearest neighbour interactions are responsible for the longer range structural differences between the glacial and crystalline states. Therefore the glacial state may well originate from a frustration effect caused by a competition between optimal molecular conformation (in the glacial form) and weak intermolecular hydrogen bonding effects (in the crystal, as shown in Figure 3).

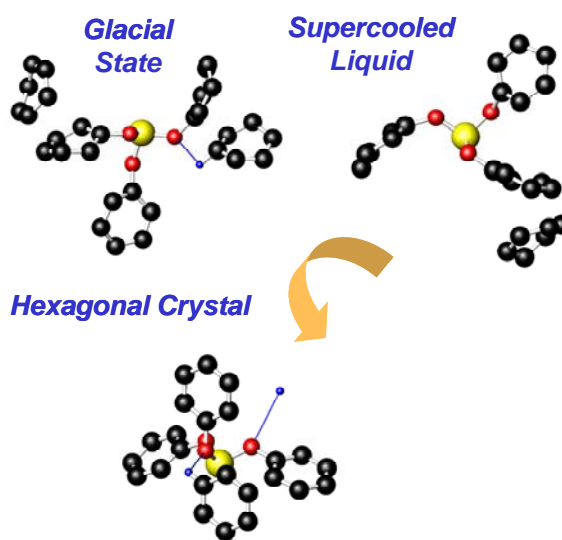


Figure 4. A schematic model of the nearest neighbour interactions in the supercooled liquid, glacial state and hexagonal crystal state of TPP. Hydrogen bonds are shown in blue.

The concept of “locally preferred structure” (LPS) has been proposed by Kivelson and co-workers to interpret the structural changes and the metastable glacial phase [4]. A LPS is loosely defined as an arrangement of molecules which, in a given region of the pressure-temperature phase diagram, minimizes some local free energy [4]. It is assumed that there are (at least) two different LPS in TPP. In the suggested scenario the first LPS is a TPP molecule cluster which has a low local free energy because it can assume an optimal molecular conformation. The second type of LPS is a TPP molecule cluster linked by two inter-molecular hydrogen bonds, which slightly alters the molecular conformation.

Reverse Monte Carlo simulations are in progress to help determine the possible orientational correlations between neighbouring molecules in TPP. Preliminary results show

a high degree of parallel, 'T' and 'L' type structural configurations are associated with the supercooled liquid and glacial states.

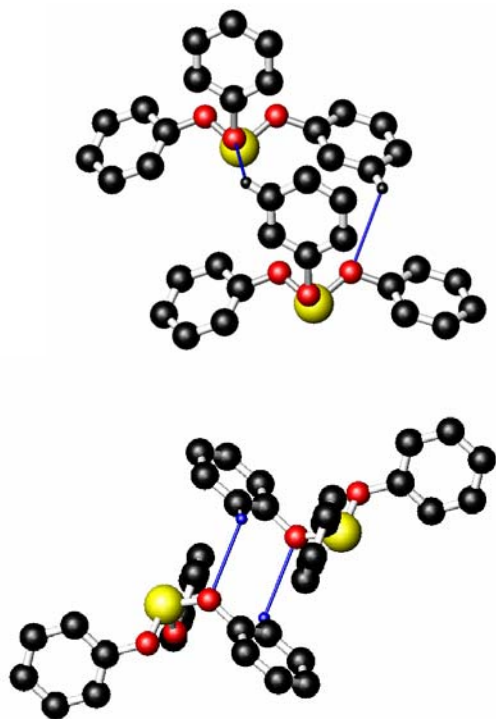


Figure 5. An example of different locally preferred structures. Intermolecular hydrogen contacts between TPP molecules in the hexagonal crystal (top) and monoclinic crystal (bottom). Only hydrogens involved in intermolecular bonding are shown for clarity as small open spheres. The oxygen atoms are shown as red spheres. The thin solid line represents weak intermolecular hydrogen bonds.

REFERENCES

- [1] A. Ha, I. Cohen, X. Zhao, M. Lee, and D. Kivelson, *J. Phys. Chem.* 1996, 100, 1.
- [2] Hedoux A. Guinet Y., Derollez P., Hernandez O., Lefort R. And Descamps M. *Phys. Chem. Chem. Phys.*, 2004, 6, 3192-3199.
- [3] Q. Mei, P. Ghalsasi, C.J. Benmore, and J.L. Yarger *J. Phys. Chem. B*, 2004, 108, 20076-20082.
- [4] G. Tarjus, C. Alba-Simionesco, M. Grousson, P. Viot, D. Kivelson, *J.Phys.:Condens. Matter*. 2003, 15, 1077.

STRUCTURAL INVESTIGATIONS OF SUPERACIDS AND SUPERACIDIC SOLUTIONS

John F. C. Turner,¹ Sylvia E. McLain,^{2,3,4} Jamie J. Molaison,²
Joan E. Siewenie⁴ and Chris J. Benmore⁴

¹ Neutron Sciences Consortium and Department of Chemistry,
University of Tennessee, Knoxville, TN, 37996

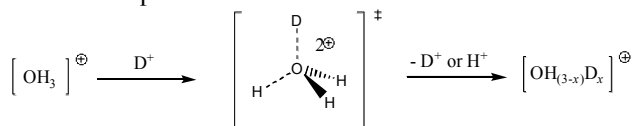
² Department of Chemistry, University of Tennessee, Knoxville, TN, 37996

³ ISIS Facility, Rutherford-Appleton Laboratory, Chilton, UK

⁴ Argonne National Laboratory, Argonne, IL 60439.

INTRODUCTION

Superacids are a class of fluid that show extreme acidity due to the presence of 'superelectrophilic' hydrogen. The reactivity is such that conventional bases, such as ammonia and hydroxide ion are augmented by hydrocarbons, including methane, the hydronium ion the presence of which in a conventional solution is the sole criterion for a Brønsted acid and the ammonium ion. By indirect spectroscopic techniques, it is well-established that these species exchange hydrogen for deuterium in superacidic media with the only mechanistic pathway being associative, meaning that H_3O^+ is itself protonated in certain superacids.



Superacids are used widely in both academic and industrial contexts. The ability to protonate hydrocarbons is exploited in the cracking of crude oil and almost all the hydrocarbons used for fuel and fine chemical synthesis is the product of superacidic or acidic catalysis.

A program to investigate the structure and dynamics of superacids and superacidic solutions began in 2000 and has resulted in the structural characterization of the major materials in this class, including anhydrous hydrogen fluoride, fluorosulfuric acid, antimony pentafluoride and boron trifluoride. All of these materials are either archetypes for superacidity or for Lewis acidity. Support for this work has been provided by IPNS, the Department of Chemistry and the Neutron Sciences Consortium of the University of Tennessee, the National Science Foundation and the Petroleum Research Fund.

HYDROGEN FLUORIDE

The study of the structure of anhydrous HF has provided, for the first time, the structure of the strongest hydrogen-bonded fluid at the pair correlation function level. The partial pair correlation function for each interaction, derived from neutron diffraction and high energy X-ray data is shown in Figure 1 along with the subsequent fits from the RMC model to the data.

These results [1-3], important and interesting in their own right, are also a critical test of calculation methods

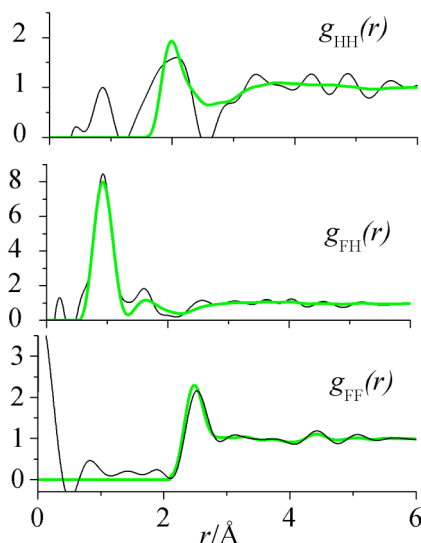


Figure 1: Partial pair correlation function for HF; data (black line), RMC fits (green line.)

short strong hydrogen bond in condensed phase. In contrast to prior calculational predictions, the structure at the boiling point of the fluid is comprised of short, unbranched oligomers of $\sim 8 - 10$ molecules with very short, bent hydrogen bonds. Representative chains from the RMC modeling box are shown in Figure 2.

At the freezing point, the chains are functionally infinite and the hydrogen bonds are linear and even shorter. A highly surprising result is the constancy of the shortest F-F distance in the fluid, which is invariant with temperature. Moreover, the breadth of the H-H pair correlation function implies that the hydrogen atom in this system is not behaving classically, a feature that has been included in the most recent calculations by others. This points to the fact that HF is a truly remarkable fluid.

FLUOROSULFURIC ACID

One of the acids, besides HF, which shows the highest acidity, is the molecular superacid, FSO_3H . FSO_3H was studied [4] and it was revealed that this liquid contained two intermolecular hydrogen bonds, which are not known, to date, in any other acidic system.

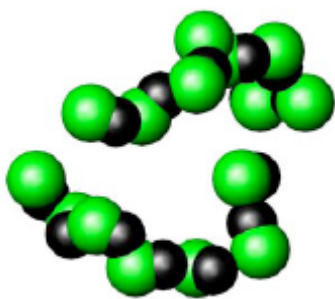


Figure 2: An average structure of an HF chain at 298 K from a reverse Monte Carlo model of the X-ray and neutron diffraction data.

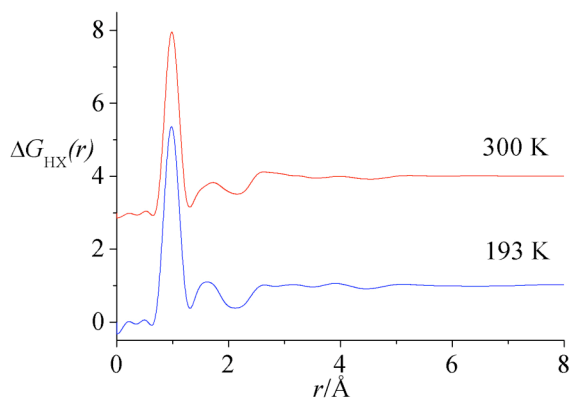


Figure 3: Pair correlation functions for only the hydrogen containing correlations in FSO_3H .

Figure 3 shows the pair correlation functions for only the hydrogen-containing correlations at two different temperatures, where the first peak in each of the data shown here corresponds to the molecular O-H peak, whereas the second peak corresponds to the intermolecular hydrogen bonding peak.

Close inspection of the hydrogen bonding peak showed that this peak was asymmetric at both temperatures measured, indicating the presence of two rather than one hydrogen bonding interaction. For this reason, the DFT calculations were performed to determine if there was a possibility that one of the hydrogen bonds seen could be a O-H \cdots F interaction along with the expected O-H \cdots O interaction. Figure 4 shows the results of the DFT calculations with two dimers; one is bonded through O-H \cdots O interactions and one through O-H \cdots F interactions. In each case the dimers converged to give an acceptable minimal energy.

BORON TRIFLUORIDE

Boron trifluoride is a molecular Lewis acid and an interesting fluid in its own right. The strength of the Lewis acidity of the boron trihalides has often been assumed to increase with the atomic number of the halide, with BF_3 being atypically weak.

The rationale for this chemical behavior is usually

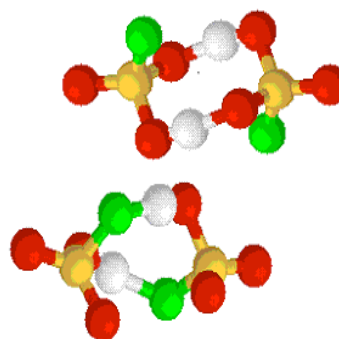


Figure 4: Hydrogen bonded FSO_3H dimers. The white atoms represent hydrogen, the red atoms oxygen and the green atoms fluorine.

based on the assumed decreasing strength of $p\pi$ - $p\pi$ “back-bonding” interactions (between the filled p-orbitals in the ligating halide and the boron center) with increasing halide atomic number. In order to determine the amount of $p\pi$ - $p\pi$ “back-bonding” seen in liquid and supercritical BF_3 , neutron diffraction measurements were performed on $^{11}\text{BF}_3$ in two liquid and three supercritical states and subsequently modeled using RMC analysis. $T(r)$ for BF_3 at each state measured is shown in Figure 5.

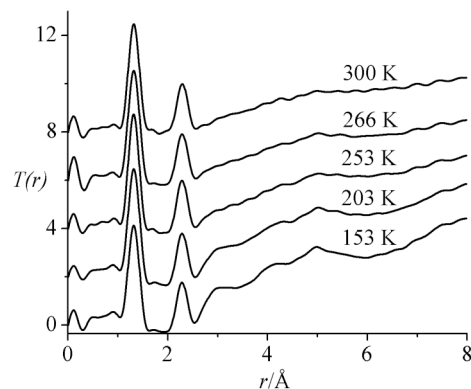


Figure 5: $T(r)$ for $^{11}\text{BF}_3$ at five measured state points.

It was clear from the measurements that the molecular symmetry of the BF_3 remained in tact at each pressure and temperature as the first and second peaks- B-F (1.3 Å) and F-F (2.4 Å) are unchanged at each state point [5]. In order to understand the degree of interactions, RMC modeling was performed and a degree of intermolecular interactions, albeit weak interactions, were detected in the liquid at 153 K. A model of these interactions is shown in Figure 6. The model showed that a proportion of molecules were canted toward each other indicating that there is indeed some preferred orientation in BF_3 in the liquid state between molecules. This refutes the claim that BF_3 is a weak molecular acid by virtue of its intra-molecular interactions, but instead supports the view that intermolecular interactions at least partially determine the structure of this fluid.

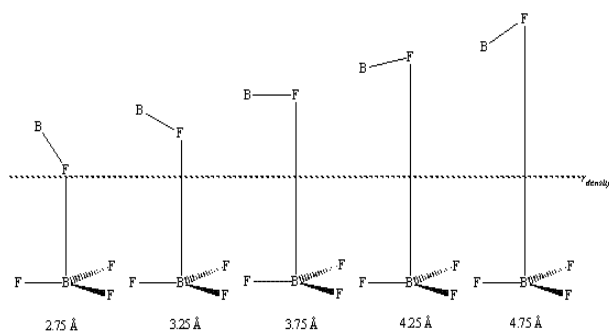


Figure 6: Axial interactions in liquid and supercritical BF_3 , showing the density derived radius to scaled relative to the BF bond length, and the orientation of a proportion of the intermolecular interactions.

ANTIMONY PENTAFLUORIDE

In condensed phases, SbF_5 is highly associated; it also serves as an archetype for associated fluids that are bound by 3 center – 4 electron (3c-4e) interactions. SbF_5 is the strongest simple fluoride acceptor on the Lewis acidity and the associated nature of SbF_5 represents an ‘autoamphoteric’ interaction in that in the pure fluid SbF_5 acts both as a fluoride donor and acceptor. In fact the addition of SbF_5 to the superacids FSO_3H and HF leads to an increase in the acidity by 10 – 15 orders of magnitude. Measurements were taken on SbF_5 in the liquid phase using both neutron and high-energy X-ray diffraction the total pair correlation functions from each of these measurements are shown in Figure 7.

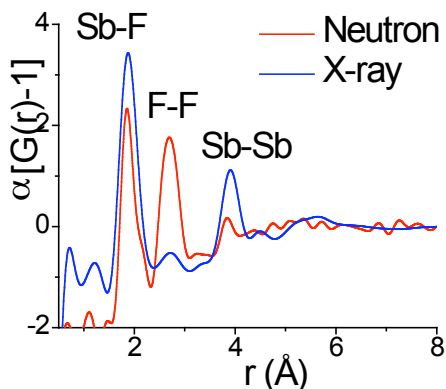


Figure 7: Total pair correlation functions for SbF_5 at 298 K from neutron and high energy X-ray diffraction measurements.

Previous measurements using ^{19}F NMR suggested the presence of a polymeric form of SbF_5 linked by bridging fluorine atoms in the fluid. In order to reproduce the structure of SbF_5 in the liquid state the Empirical Structure Refinement (EPSR) was used. EPSR was specifically designed for creating a model of the disordered materials which is consistent with the diffraction measurements. By using EPSR, the structure of SbF_5 which is comprised of fluorine linked individual

molecules was seen [6]. A representative sample from the diffraction box is shown in Figure 8.

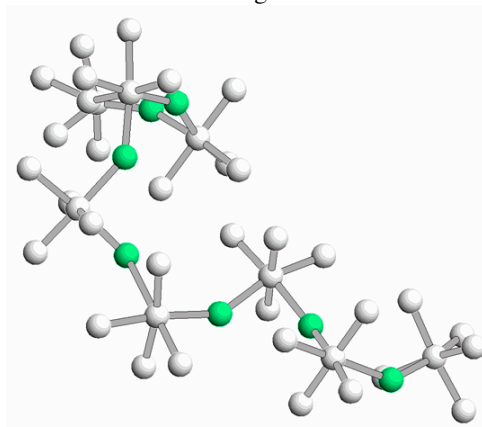
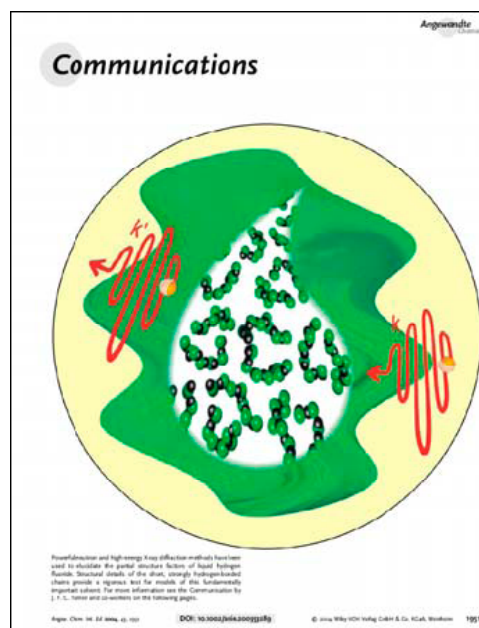


Figure 8: SbF_5 chains generated from the EPSR fits to the neutron and high energy X-ray data. The green atoms show the bridging fluorines.



REFERENCES

- [1] J.F.C. Turner, S.E. McLain, T.H. Free, C.J. Benmore, K.H. Herwig and J.E. Siewenie. *Rev. Sci. Instr.*, 74 (2003) 4410-4417.
- [2] S.E. McLain, C.J. Benmore, J.E. Siewenie, J. Urquidi and J.F.C. Turner. *Angewandte Chemie Int. Ed.* 43 (2004) 1951-1955.
- [3] S.E. McLain, C.J. Benmore, J. Siewenie, J.J. Molaison and J.F.C. Turner. *J. Chem. Phys.*, 121 (2004) 6448.
- [4] S.E. McLain, C.J. Benmore and J.F.C. Turner. *J. Chem. Phys.*, 117 (2002) 3816-3821.
- [5] S.E. McLain, J.E. Siewenie, C.J. Benmore and J.F.C. Turner. *J. Chem. Phys.*, 119 (2003) 6671-6679
- [6] S.E. McLain, A.K. Soper, J.J. Molaison, C.J. Benmore, M.R. Dolgos, J.L. Yarger and J.F.C. Turner. *J. Mol. Liq.*, submitted.

THE FIRST SHARP DIFFRACTION PEAK IN BINARY SELENIDE GLASSES

E. Bychkov¹, C.J. Benmore², and D.L. Price³

¹ Université du Littoral, 59140 Dunkerque, France.

² Argonne National Laboratory, Argonne, IL 60439.

³ Oak Ridge National Laboratory, Oak Ridge TN 37831, USA

INTRODUCTION

Compositional changes of the first sharp diffraction peak (FSDP) in the measured structure factor have been studied for several binary selenide glasses using pulsed neutron and high-energy x-ray diffraction techniques. The observed variations in the FSDP (factor of 10 in the amplitude and $\approx 0.5 \text{ \AA}^{-1}$ in the peak position) reflect multiple aspects in the glass network on both the short- and intermediate-range scale and are also correlated with macroscopic properties. An empirical relation has been discovered relating the compositional dependence of the FSDP position to the local coordination number of the guest atom.

The first sharp diffraction peak (FSDP), a prominent low- Q feature in the structure factor $S(Q)$ of network glasses, has been a subject of extended interest in the last two decades. Nevertheless, the origin of the FSDP is still a matter of debate, although it is clear that it can arise for different reasons in different systems [1,2]. Neutron diffraction with isotopic substitution [3,4] and anomalous x-ray scattering [5] clearly show that the main contribution to the FSDP usually comes from network-forming cation-cation (NFC) correlations. The FSDP shows at least two anomalies: (i) it remains invariant or even becomes more intense and narrow with increasing temperature in contrast to usual broadening of peaks in $S(Q)$ [6,7], and (ii) it decreases in amplitude with increasing pressure [8,9]. The NFC correlations reflect an intermediate-range ordering (IRO) in the glass network since a characteristic length scale deduced from the FSDP position, $L_1 \approx 2\pi/Q_1 = 3.5\text{-}8 \text{ \AA}$, covers usually 2-3 interatomic distances [2]. In contrast to extensive studies of the FSDP as a function of temperature and to a lesser extent pressure, surprisingly very little attention has been paid to the compositional dependence of the FSDP parameters except for previous works on binary selenide systems P-Se [10] and Si-Se [11].

EXPERIMENTAL DETAILS

The selenide binaries $A_x\text{Se}_{1-x}$, where A is an element of Group IV, V or VI, are very suitable model materials for these studies since they exhibit a very large glass-forming range from pure vitreous Se ($x = 0$) to $x = 0.4\text{-}0.7$. In addition, $A_x\text{Se}_{1-x}$ glasses remain homogeneous on mesoscopic scale over the entire vitreous domain on the contrary to phase-separated S-rich binaries. In this study we have carried out time-of-flight neutron and high-energy x-ray diffraction measurements on complementary

binary selenide glassy systems (Ge-Se, As-Se, Te-Se) as well as additional P-Se glass compositions and compared to literature data on Si-Se glass.

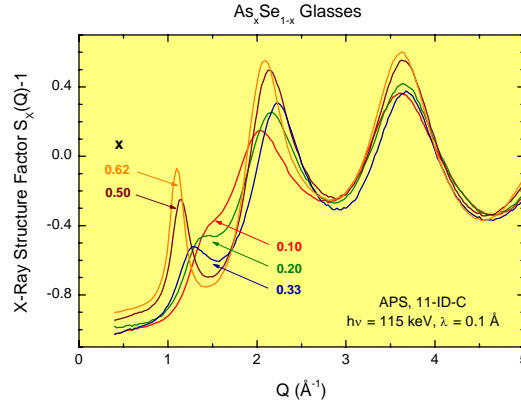


FIG. 1. Low- Q part of the x-ray structure factor $S_X(Q)$ for selected compositions in the $\text{As}_x\text{Se}_{1-x}$ system.

The low- Q part of the $S(Q)$ for the binary glasses exhibits remarkable changes with composition (Fig. 1). With increasing NFC content, the FSDP becomes a factor of 10 more intense and shifts to lower Q by 0.5 \AA^{-1} . Such an enormous change is not exhibited by any other peak in the structure factor. Plotting the FSDP amplitude (Fig. 2) and position (Fig. 3) as a function of the NFC concentration, several characteristic composition regions appear for the Group-IV ($\text{Ge}_x\text{Se}_{1-x}$, $\text{Si}_x\text{Se}_{1-x}$) and Group-V ($\text{As}_x\text{Se}_{1-x}$, $\text{P}_x\text{Se}_{1-x}$) alloys. On the other hand, the chain-like Group-VI alloy, $\text{Te}_x\text{Se}_{1-x}$, does not show any dramatic evolution.

RESULTS AND DISCUSSION

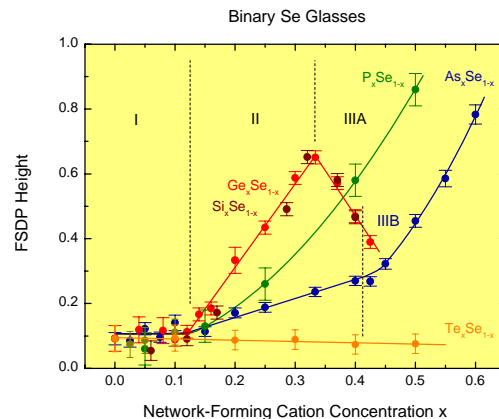


FIG. 2. Amplitude of the FSDP in binary selenide glasses as a function of x . Only neutron diffraction data are plotted.

Region I: Random distribution of the NFC-related structural units at $x \leq 0.10-0.15$. The FSDP amplitude remains almost constant in this region (Fig. 2), while characteristic trends appear in the FSDP position as a function of composition (Fig. 3). In particular, we note a distinct difference in the initial slope, $\partial Q_1/\partial x$, for the Group-IV ($-2.2 \text{ \AA}^{-1} \text{ atom}^{-1}$, $x \leq 0.10-0.15$), Group-V $\text{As}_x\text{Se}_{1-x}$ ($-0.52 \text{ \AA}^{-1} \text{ atom}^{-1}$, $x \leq 0.4$) and Group-VI ($-0.11 \text{ \AA}^{-1} \text{ atom}^{-1}$, $x \leq 0.55$) systems. The invariant FSDP amplitude in this composition range suggests a random distribution of the NFC-related structural units in the disordered selenium network. Direct evidence of the random/non-random NFC distribution is demonstrated in the $\text{Ge}_x\text{Se}_{1-x}$ system. The absence of short Ge-Ge correlations at $\approx 3.0 \text{ \AA}$ below $x \approx 0.10$, characteristic of edge-sharing (ES) $\text{GeSe}_{4/2}$ tetrahedra [4,7], indicates a random distribution of $\text{GeSe}_{4/2}$ units. The short Ge-Ge distances clearly appear at $x \geq 0.14$ indicating an agglomeration of $\text{GeSe}_{4/2}$ into a mixture of corner-sharing (CS) and ES $\text{GeSe}_{4/2}$ tetrahedra. Raman data [12] are also consistent with the edge sharing above $x \approx 0.1$, and recent ^{77}Se NMR results also confirm agglomeration of $\text{GeSe}_{4/2}$ tetrahedra at $x \geq 0.11$ [13]. A non-monotonic change in the entropy of viscous flow at $x \approx 0.1$ [14] and in thermal relaxation above $x \approx 0.12$ [15] correlate with a drastic change in the network topology.

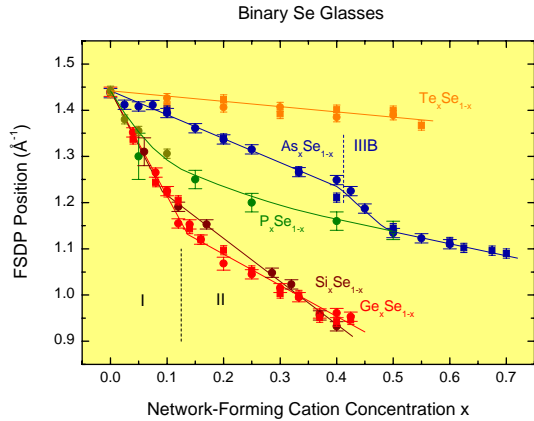


FIG. 3. FSDP position in binary selenide glasses as a function of x . The initial slope of the lines is given in the text. The solid line for $\text{P}_x\text{Se}_{1-x}$ represents calculated Q_1 values (see text for details). The dashed lines show limits for the regions I, II and IIIB ($\text{As}_x\text{Se}_{1-x}$).

The remarkably different slopes for two-, three- and four-fold coordinated guest species reflect the magnitude of changes in the intermediate and short-range order as determined by the real-space functions and spectroscopic data. An empirical equation was found to relate these

initial slopes to the guest n and host n_0 local coordination numbers:

$$\frac{\partial Q_1}{\partial x}(n) = \frac{\partial Q_1}{\partial x}(n_0) \left(\frac{3\pi}{2} \right)^{n-n_0}, \quad (1)$$

where $\partial Q_1/\partial x(n_0)$ is the initial slope for the $\text{Te}_x\text{Se}_{1-x}$ glasses since $n = n_0 = 2$ in this case.

It is interesting to note that the term $(3\pi/2)$ appears for a disordered binary system of hard spheres as a result of chemical ordering and relates the position of the first peak in the Bhatia-Thornton concentration-concentration structure factor $S_{CC}(Q)$ to the sphere diameter d [16]:

$$Q_1^{CC} \cong \frac{3\pi}{2d} \quad (2)$$

Region II: Network formation by NFC-related structural units at $0.10-0.15 \leq x \leq 0.2-0.4$. Above Group-IV and -V atom concentrations of 0.10-0.15, the FSDP amplitude increases dramatically, reaching a maximum for the Group-IV systems at the stoichiometric AsSe_2 composition, $x = 0.33$. In contrast, the FSDP amplitude in the Group-V does not reach a maximum but the rate of increase changes from nearly linear to parabolic at $x \approx 0.2$ (P-Se) and 0.4 (As-Se).

Regions IIIA and IIIB: Homopolar NFC-NFC bonds at $x \geq 0.2-0.4$. The appearance of homopolar NFC-NFC first neighbor correlations in the glass structure dramatically changes the FSDP amplitude. As already mentioned, this effect is different for the Group-IV and -V systems. A sharp decrease in the FSDP amplitude observed in both $\text{Ge}_x\text{Se}_{1-x}$ and $\text{Si}_x\text{Se}_{1-x}$ above the stoichiometric composition $x = 0.33$ (Region IIIA) is related to the change in the structural role played by the Group-IV atoms. They no longer behave as network-forming cations but depolymerize the network as a modifier. In contrast, in the Group-V systems, the network polymerization remains essentially invariant when P-P ($\approx 2.23 \text{ \AA}$) or As-As ($\approx 2.53 \text{ \AA}$) homopolar bonds appear in the network at $x \approx 0.2$ and $x = 0.4$, respectively, (Region IIIB), consistent with ^{31}P NMR, ^{75}As NQR and Raman spectroscopy results [17-19]. The parabolic increase of the FSDP amplitude in this case appears to be related to additional intermediate-range correlations caused by the neighboring phosphorus or arsenic atoms in dimers and/or to a progressive appearance of $\text{P}_4\text{Se}_3/\text{As}_4\text{Se}_3$ cage molecules above $x \approx 0.5$.

The behavior of the P-Se system is more complicated due to multiple phosphorus sites (4- and 3-coordinated) observed at low x in ^{31}P MAS-NMR and Raman spectroscopy studies. Our high-resolution diffraction results in r -space also suggest mixed phosphorus coordination at $x \leq 0.1$. The solid line in Fig. 3, calculated using phosphorus distributions between 4- and

3-coordinated sites and P-P -related structural units derived from NMR, Raman and neutron diffraction data, reproduces the experimental FSDP position as well as the continuous change of $\partial Q_1/\partial x$ from a nearly 4-coordinated to a 3-coordinated value at $x \approx 0.2$.

The observed structural features and trends at the IRO level *do not* correlate with rigidity percolation limits which predict specific changes in the glass network dynamics at $x = 0.2$ for tetrahedral systems and at $x = 0.4$ for trigonal ones. It seems that the network dynamics and static IRO structure are not closely related in case of binary selenide glasses.

Summarizing, we have found that the compositional evolution of the intermediate-range order is closely related to variations in the local order. Consequently, the FSDP reflects multiple changes in the glass network on both the short- and intermediate-range scales: random vs. non-random distribution of the NFC-related structural units, homopolar NFC-NFC bond formation, network-forming vs. modifier-like behavior, the appearance of cage molecules, and the effect of local coordination of the guest atoms, and these changes also correlate with macroscopic properties.

REFERENCES

- [1] A.C. Wright, R.N. Sinclair, and A.J. Leadbetter, *J. Non-Cryst. Solids* **71**, 295 (1985).
- [2] S.C. Moss and D.L. Price, in *Physics of Disordered Materials*, edited by D. Adler, H. Fritzsche, and S.R. Ovshinsky (Plenum, New York, 1985), p. 77.
- [3] M. Arai, R.W. Johnson, D.L. Price, S. Susman, M. Gay, and J.E. Enderby, *J. Non-Cryst. Solids* **83**, 80 (1986).
- [4] I. Petri, P.S. Salmon, and H.E. Fischer, *Phys. Rev. Lett.* **84**, 2413 (2000).
- [5] P.H. Fuoss *et al.*, *Phys. Rev. Lett.* **46**, 1537 (1981); A.C. Barnes *et al.*, *J. Non-Cryst. Solids* **250-252**, 393 (1999).
- [6] L.E. Busse and S.R. Nagel, *Phys. Rev. Lett.* **47**, 1848 (1981); L.E. Busse, *Phys. Rev. B* **29**, 3639 (1984).
- [7] S. Susman, K.J. Volin, D.G. Montague, and D.L. Price, *J. Non-Cryst. Solids* **125**, 168 (1990).
- [8] H. Tsutsu, K. Tamura, and H. Endo, *Solid State Commun.* **52**, 877 (1984).
- [9] M. Guthrie, C.A. Tulk, C.J. Benmore, J. Xu, J.L. Yarger H-K. Mao and R.J. Hemley. *Phys. Rev. Lett.*, **93**, 115502 (2004).
- [10] D.L. Price, M. Misawa, S. Susman, T.I. Morrison, G.K. Shenoy, and M. Grimsditch, *J. Non-Cryst. Solids* **66**, 443 (1984).
- [11] R.W. Johnson, D.L. Price, S. Susman, M. Arai, T.I. Morrison, and G.K. Shenoy, *J. Non-Cryst. Solids* **83**, 251 (1986).
- [12] S. Sugai, *Phys. Rev. B* **35**, 1345 (1987).
- [13] B. Bureau, J. Troles, M. Le Foch, F. Smektala, and J. Lucas, *J. Non-Cryst. Solids* **326&327**, 58 (2003).
- [14] S.V. Nemilov, *Zh. Prikl. Khim.*, **37**, 1020 (1964) [*J. Appl. Chem. USSR*, **37**, 1026 (1964)].
- [15] J.M. Saiter, A. Assou, J. Grenet, and C. Vautier, *Phil. Mag. B* **64**, 33 (1991); P. Cortes, S. Montserrat, J. Ledru, and J.M. Saiter, *J. Non-Cryst. Solids* **235-237**, 522 (1998).
- [16] J. Blétry, *Phil. Mag. B*, **62**, 469 (1990).
- [17] D. Lathrop and H. Eckert, *Phys. Rev. B* **43**, 7279 (1991).
- [18] D.G. Georgiev, M. Mitkova, P. Boolchand, G. Brunklaus, H. Eckert, and M. Micoulaut, *Phys. Rev. B* **64**, 134204 (2001).
- [19] E. Ahn, G.A. Williams, P.C. Taylor, D.G. Georgiev, P. Boolchand, B.E. Schwickert, and R.L. Cappelletti, *J. Non-Cryst. Solids* **299-302**, 958 (2002).

EXPERIMENTS WITH TRANSFORMATION PROCESSES IN AMORPHOUS ICE

Chris A. Tulk¹, Chris J. Benmore², and Dennis D. Klug³

¹ Spallation Neutron Source Project, Oak Ridge National Laboratory, Oak Ridge TN 37831, USA.

² Argonne National Laboratory, Argonne, IL 60439.

³ National Research Council of Canada, Ottawa, Ontario K0A 0R6, Canada.

INTRODUCTION

The non-crystalline solid forms of water have been intensively studied, and these studies have extended back over the entire second half of the twentieth century. Despite this intensive interest some fundamental questions remain, foremost among these is the detailed relationship between these non-crystalline forms and super cooled liquid water and, more specifically, the extent to which transformations in the amorphous forms relate to transformations in the liquid. These non-crystalline ices have been formed by several techniques including vapor deposition, quenching the liquid and pressurization and annealing of crystalline ice at low temperature. At low pressure these have been mostly characterized by a density very similar to low pressure crystalline ice. These forms have become known collectively as low density amorphous ice. The exact relationship among the various amorphous forms at low density remains unclear. At higher pressure and low temperature crystalline ice amorphizes into a form whose density is substantially greater than the other amorphous forms, thus this form has been referred to as high density amorphous ice. This high density amorphous form exhibits a well known transformation to a low density form upon decompression and annealing at ambient pressure and upon recompression. Furthermore, this transformation has often been observed to occur rapidly. Thus the temptation has been to consider all the low density amorphous forms as being nearly identical, and to relate these to the glass formed by rapid low pressure temperature quench of the liquid, and likewise, the high density amorphous form to the glass formed by temperature quenching the liquid at high pressure. By extension then, the transformation between the high density and low density amorphous forms might relate to transformations in the glassy forms and even further into the supercooled liquid regime. And that a two state model of the amorphous-amorphous transformation might be used as a basis to explain the structural transformation processes evidenced in the liquid at higher temperature. Toward further understanding these processes, we ask, what is the detailed structural nature of the amorphous – amorphous transformation process?

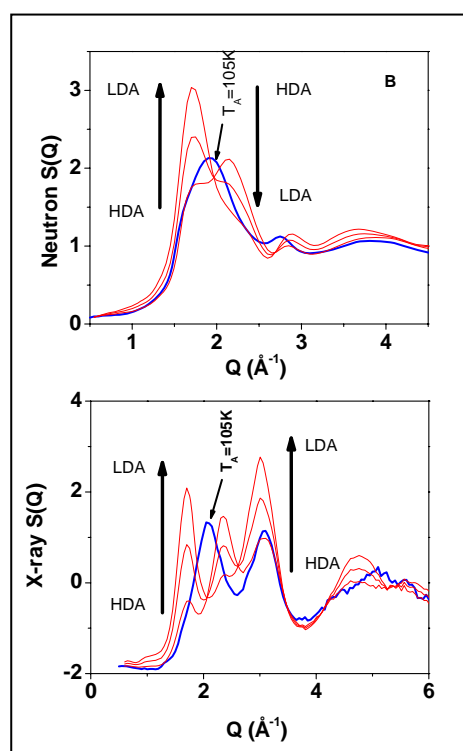


Figure 1, shows various linear combinations ($x S(Q)_{\text{HDA}} + (1-x) S(Q)_{\text{LDA}}$) of the initial and final high density and low density amorphous ice structural factors compared with a measured intermediate relaxed structure factor (blue line) as measured by both x-ray and neutron diffraction. Clearly the two component model fails.

EXPERIMENTAL DETAILS

Over the past several years we have engaged in a systematic series of studies regarding the transformation processes in pressure induced amorphous ice using complementary neutron scattering at IPNS (using the GLAD and SEPD instruments) along side with high energy x-ray diffraction experiments carried out at the APS. In these experiments we have obtained time-of-flight neutron diffraction data, structure factor functions and radial distribution functions as the samples are very carefully annealed at atmospheric pressure and during the transformation from the high density form to the low density form. These experiments were facilitated by the

intensity of the sources combined with the instrument stability and low background levels. As such, several datasets were collected very quickly under each annealing condition giving a snap-shot of the sample structure. Our first set of experiments detailed that the high density structure actually relaxes through a process of continuous network evolution, and since the instantaneous ‘relaxed’ structure is clearly unique, these studies showed that there is no one definitive high density amorphous ice structure, thus calling into question previously held assumptions regarding the simple two component transformation process. (see Fig 1). [1].

RESULTS AND DISCUSSION

Subsequent studies detailed that the network relaxation process involved a continuous ‘unfolding’ of the oxygen atoms that are located between the first and second coordination shells in the amorphous network. During this relaxation process these interstitial oxygen atoms were clearly observed to smoothly move to greater distances from near the first coordination shell and to eventually form a well defined second coordination shell.

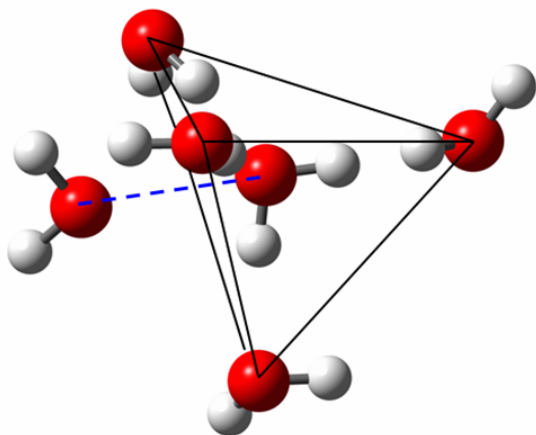


Figure 2. A schematic showing the location of a nearest neighbour interstitial molecule in amorphous ice which defines the local structure. Picture courtesy of Rob Hart.

There was no apparent discontinuity at these longer distances that might indicate the structural process was discontinuous. Despite the fact that the process is exothermic, and once started can take place quickly, it is likely that this smooth transformation sequence of the network structure is independent of the transformation. While this is evident in our real space plots of the data from both neutrons and x-rays [3] it can also be seen empirically in the directly measured reciprocal space data, and the data plotted in Figure 3 [4]. In general the first peak in the structure factor function is representative of the intermediate range ordering. The position of the peak indicates the periodicity of the structural units in the amorphous structure, while the height and width indicated the extent of the ordering within the structure.

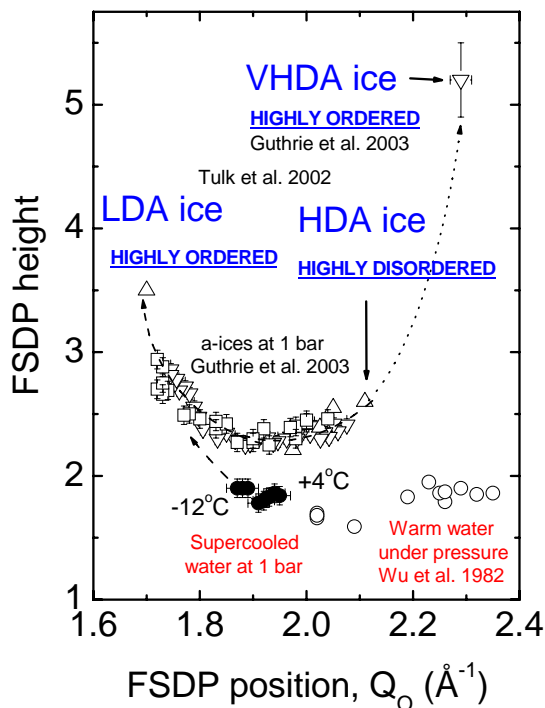


Figure 3. There appears to be two stages to the process, one where the first peak decreases in intensity and broadens followed increasing intensity and sharpening. The peak height vs peak position of the first strong peak in the structure factor of various amorphous ice structures including very high density amorphous ice.

As such, a plot of the peak height vs. the peak width for all the data collected thus far clearly indicates the trend from highly ordered amorphous structure in the highest density form, through a rather disordered amorphous structure traditionally referred to as high density amorphous ice, into the new low density structure again exhibiting considerable ordering.

The next series of experiments focused on the structural relationship with a newly formed amorphous ice that is synthesized by annealing the high density form at elevated temperature, near the transformation to ice VI, while under pressure. This form is known as very high density amorphous ice. Using both neutron and x-ray scattering it became clear that this annealed form exhibited a significantly higher degree of intermediate range ordering, i.e. ordering that extends into the glassy network structure well beyond the first and second nearest neighbor correlations, relative to the unannealed ‘traditional’ high density form. The general picture that emerged was that the highest density network structure (VHDA) exhibited considerable ordering, and that in the high density form (HDA) this ordering was broken down substantially and did not extend much beyond the first few bond lengths, and in the low density form (LDA, produced by heating the sample at atmospheric pressure toward the low pressure crystalline ice form) introduced a different network structure that also exhibited a

substantial level of intermediate range ordering relative to the more disordered high density amorphous form.

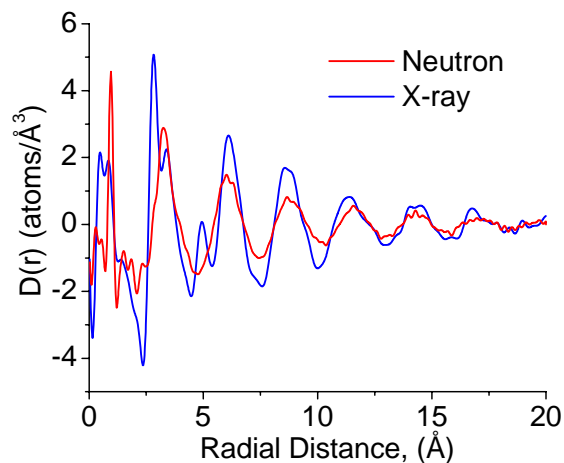


Figure 4. The real space differential distribution functions of very high density amorphous ice including never before seen details of the location of the oxygen ordering in the very high density form.

The net result of these investigations was to call into question the connection between the amorphous forms of ice produced by compression and the glassy forms of liquid water. It is likely that amorphous ice and the transition between the forms is not an extension of the structural process that takes place in the low temperature liquid.

REFERENCES

- [1] Structural studies of several distinct metastable forms of amorphous ice. C.A. Tulk *et al. Science* 297, 1320-1323 (2002)
- [2] M. Guthrie *et al. Phys. Rev. B* 68, (2003) 184110.
- [3] A structural study of very high-density amorphous ice. M. Guthrie, *et al. Chem. Phys. Lett.*, 397 (2004) 335
- [4] J. Urquidi *et al. Molecular Physics*, 2004, 102 (2004) 2007.

COMBINED LEVITATION AND NEUTRON DIFFRACTION AT HIGH TEMPERATURES

J.K.R. Weber¹, J.E. Rix¹, J.A. Tangeman¹, C.J. Benmore², J. Siewenie² and R.T. Hart²

¹Containerless Research, Inc., Evanston, IL 60201 USA

²Argonne National Laboratory, Argonne, IL 60439.

INTRODUCTION

Investigation of the structure of high temperature and metastable liquids is important in the development of new glass and photonic materials and in fundamental studies of liquid state phenomena such as nucleation and liquid phase behavior [1,2]. The application of neutron techniques complements X-ray studies and opens opportunities for studies of oxides, nitrides and other low atomic number elements [3-5].

Neutron-based measurements on high temperature liquids are generally performed using furnaces with vanadium shields that are limited to a maximum temperature of ~1400 K before structural integrity becomes problematic. The use of containerless techniques:

- (i) completely eliminates crucible-derived contamination of melts,
- (ii) expands the temperature range that can be studied,
- (iii) avoids container-induced heterogeneous nucleation of crystals, allowing access to deeply undercooled liquids and metastable states, and
- (iv) accesses pristine, free liquid surfaces.

Recent experiments [6-12] have shown the utility of using containerless techniques in combination with neutrons. The availability of very high flux neutron sources such as the Spallation Neutron Source (SNS) being constructed at Oak Ridge, TN [13] will enable fast measurements on liquids to provide data on structural changes during transient processes.

In this work, an aerodynamic levitator equipped with a pure vanadium levitation nozzle and a 240 watt CO₂ laser was integrated with a neutron beam line. Metal oxides were levitated and studied at temperatures from 300 to 3300 K.

EXPERIMENTAL DETAILS

Neutron diffraction experiments were performed at the Glass Liquids and Amorphous materials Diffractometer (GLAD) at the Intense Pulsed Neutron Source (IPNS), Argonne National Laboratory. Liquid samples were studied using a levitation technique which completely eliminated contact with container surfaces [11, 12].

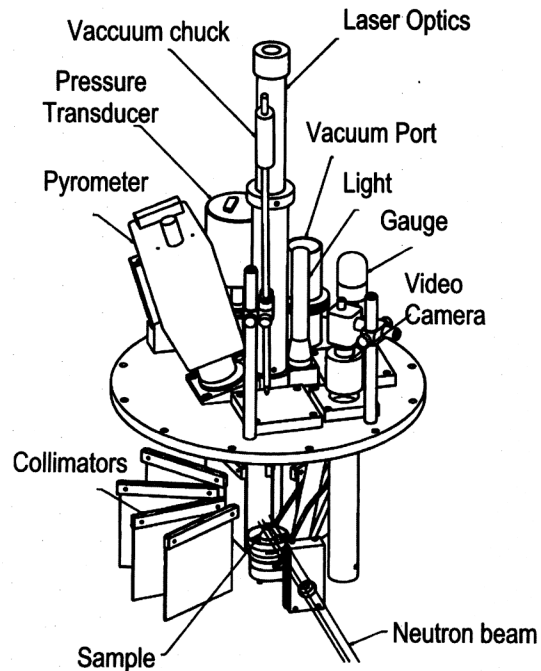


Figure 1. Diagram of levitator layout. Heating was performed using a 240 Watt continuous-wave carbon dioxide laser. The levitation and laser beam heating systems were controlled from a remote computer using a LabView program.

The apparatus is illustrated in Fig. 1 and described in detail elsewhere [11]. Initially, a thick-walled nozzle was used. Later, a thin-walled nozzle with a wall thickness of *ca.* 1 mm in the area intercepted by the neutron beam path was used. The use of a thin-walled nozzle reduced scattering and attenuation of the neutron beam, lowering the errors by a factor of ~2 compared to the nozzle with a 5 mm thick wall [11]. Neutron diffraction experiments were performed in the higher flux downstream sample position at the beamline. The neutron beam was collimated to a rectangular profile 10 mm wide by 13 mm high. Levitation was performed in argon at a total pressure of ~0.5 bar with a beam path length through the gas of approximately 10 cm. Scattered neutrons were detected with a bank of ³He-based detectors that covered a

continuous angular range in 2θ of 3° to 117° in the horizontal plane and $\pm 11^\circ$ from the vertical plane.

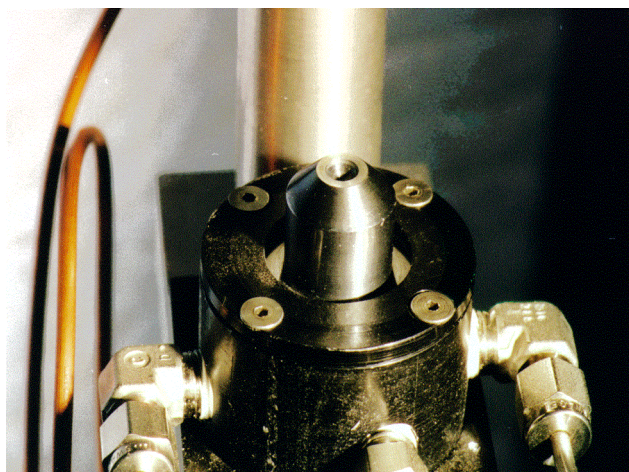


Figure 2. (Top-bottom): Photographs of the vanadium nozzle. The laser beam system set up on GLAD. A video image side-view of a levitated sample.

Data were acquired in one hour sets and combined into single data sets for each composition before analysis. Calibration data were obtained for the levitation nozzles with and without a 5 mm diameter vanadium sphere

placed in the nozzle, a 6 mm diameter vanadium rod, and the chamber with the levitator components removed. The data for the liquids and glasses were corrected for background, absorption, multiple scattering, and inelastic effects using the ISAW software package that was developed for analysis of disordered materials [14].

RESULTS AND DISCUSSION

Levitation of hot solids and liquids was performed at a total pressure of approximately 0.5 bar using a gas flow rate of *ca.* 500 standard cubic centimeters per minute. Liquid samples were levitated for periods of up to 6 hours. Total data acquisition times were up to 22 hours for the calcium aluminate composition, obtained using four different samples. Measurements on liquid YAG and ZrO_2 were limited to approximately 2 hours each. Mass losses from the low vapor pressure samples were negligible. Data from these samples has been published elsewhere [11, 15]. Results obtained for zirconia at temperatures from 25 to $3050^\circ C$ are presented in Figure 3.

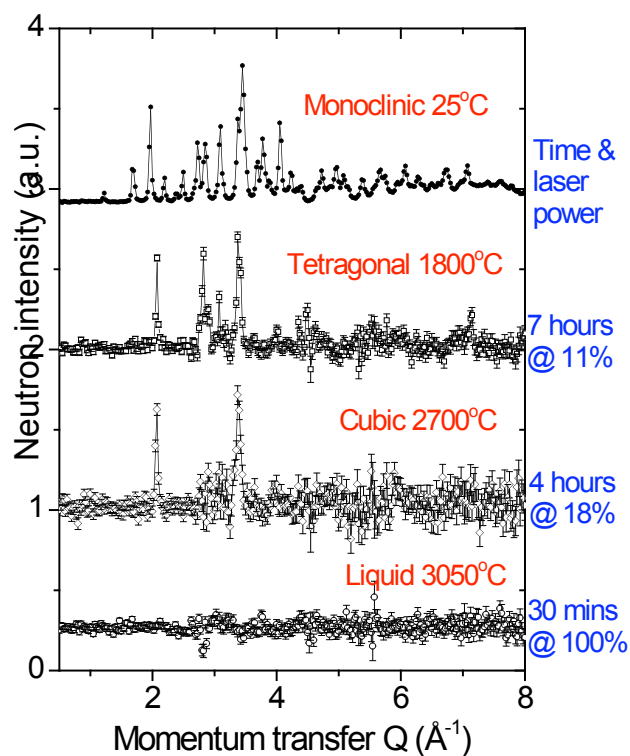


Figure 3. Data from a 3mm diameter (~ 90 mg) ZrO_2 sphere levitated in an argon gas jet, heated using a 240W CO_2 laser beam on GLAD.

Aerodynamic levitation utilizes a very compact levitation device that can be integrated with beamlines. The small levitator size and the use of vanadium nozzles practically eliminated the effects of the sample “holder” from the interpretation of the experimental data. The use of uniaxial laser beam heating resulted in temperature

gradients due to cooling of the underside of the sample by the levitation gas flow. In the case of low viscosity liquids, stirring of the melt by convection effectively distributes heat and decreases gradients to tens of degrees in a 3 mm diameter drop. Experiments performed at Containerless Research, Inc. (Evanston, IL) and at the Advanced Photon Source at Argonne National Laboratory (Argonne, IL) show that a second laser beam can be introduced through the underside of the nozzle *via* the nozzle orifice [16]. The use of underside heating reduces temperature gradients and enables deeper undercooling of the levitated liquid before the onset of crystal nucleation. Further work to optimize two-sided beam heating would expand the range of experiments that can be performed.

The levitation instrument was designed to be integrated with the GLAD beamline. With modifications to the re-entrant well and some ancillary components, the device can also be integrated with beamlines such as the NOMAD [17] instrument that is being constructed at SNS. Ultimately, the high flux beamlines can extend the scientific capabilities of a levitation instrument by enabling fast measurements. Such measurements are necessary to investigate subtle temperature- and composition-dependent effects in fragile liquids, near the approach to the glass transition, or during nucleation of metastable phases. In addition, measurements made using a small collimated neutron beam would enable complete elimination of interactions with the levitation nozzle. Plans are in place to develop a complementary levitation capability for use at an APS beamline.

ACKNOWLEDGEMENTS

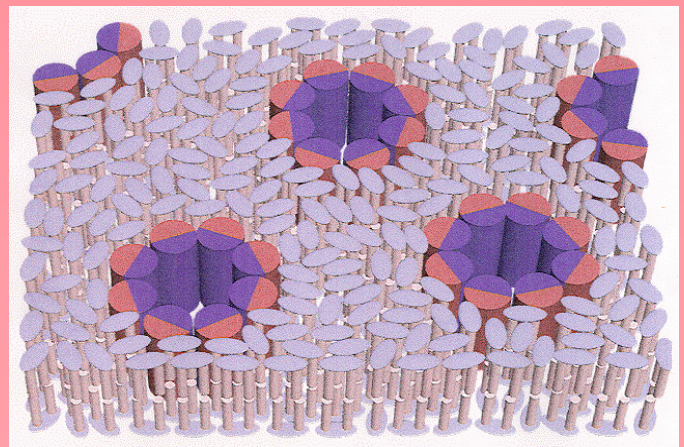
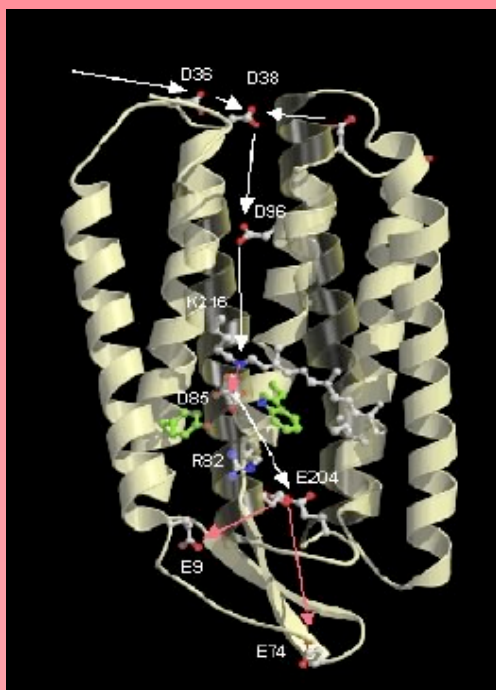
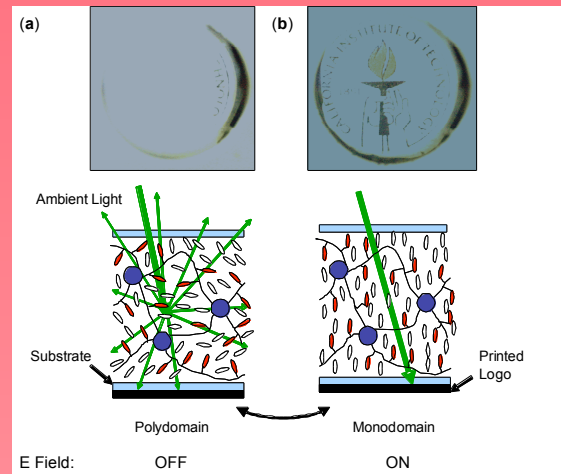
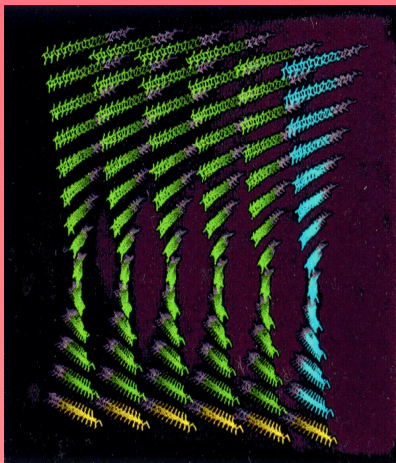
Supported by DOE under contract numbers DE-FG02-01ER86121, Dr. Helen Kerch contract monitor (CRI) and W-31-109-ENG-38 (IPNS). We thank Ken Volin, Rich Vitt, Qiang Mei and Nicole Murphy of IPNS for help with construction and installation of the instrument.

REFERENCES

[1] B.T. Poe, P.F. McMillan, B. Cote, D. Massiot, and J.-P. Coutures, *J.-P. Science*, **259**, 786 (1993).
 [2] J.K.R. Weber and P.C. Nordine, *Microgravity Sci. and Tech.*, **VII**, 279 (1995).
 [3] C.J. Benmore, J.K.R. Weber, J.E. Siewenie and K.J. Hiera, *Appl. Phys. Lett.*, **24**, 4954 (2003).
 [4] J.K.R. Weber, C.J. Benmore, J. Urquidi, J.E. Siewenie and T.S. Key, *Phys. Chem. Chem. Phys.*, **6**, 2480 (2004).
 [5] C.J. Benmore, J.K.R. Weber, J.E. Siewenie, J. Urquidi, J.A. Tangeman, and S. Sampath, *J. Phys. Cond. Matt.*, **15**, 2413 (2003).
 [6] S. Krishnan and D.L. Price, *J. Phys.: Condens. Matt.*, **12**, R145 (2000).

[7] S. Krishnan, J.J. Felten, J.E. Rix, J.K.R. Weber, P.C. Nordine, M.A. Beno, S. Ansell, and D.L. Price, *Rev. Sci. Instrum.*, **68**, 3512 (1997).
 [8] C. Landron, X. Launay, J.C. Rifflet, P. Echegut, Y. Auger, M. Ruffier, J.-P. Coutures, M. Lemonier, M. Gailanou, M. Bessiere, D. Bazin, and H. Dexpert, *Nucl. Instrum. Methods Phys. Res.*, **B124**, 627(1997).
 [9] C. Landron, L. Hennem, J.-P. Coutures, T.E. Jenkins, C. Aletru, G.N. Greaves, A.K. Soper, and G. Derbyshire, *Rev. Sci. Instrum.*, **71**, 1745 (2000).
 [10] C. Landron, L. Hennem, T.E. Jenkins, G.N. Greaves, J.-P. Coutures, and A.K. Soper, *Phys. Rev. Lett.*, **86**, 4839 (2001).
 [11] J.K.R. Weber, C.J. Benmore, J.A. Tangeman, J.E. Siewenie, and K.J. Hiera, *J. Neutron Res.*, **11**, 113 (2003).
 [12] C.J. Benmore, and J.E. Siewenie, *Neutron News*, **15**, 16 (2004).
 [13] T.E. Mason, M. Arai, and K.N. Clausen, *Mat. Res. Bull.*, **28**, 923 (2003).
 [14] J. Tao, C. J. Benmore, T. G. Worlton, J. M. Carpenter, D. Mikkelson, R. Mikkelson, J. Hammonds, A. Chatterjee, "Time-of-Flight Neutron Total Scattering Data Analysis implemented in the software suite *ISAW*," *Nuclear Instruments and Methods*, submitted.
 [15] J.K.R. Weber, J.E. Rix, K.J. Hiera, J.A. Tangeman C.J. Benmore, R. Hart and J. Siewenie. *Phys. Chem. Glasses*. 2005, 46 (4) in press.
 [16] CRI, unpublished research.
 [17] *Conceptual Design Report of a Disordered Materials Diffractometer for the Spallation Neutron Source*, Spallation Neutron Source Document number 101080200-TR002-R00.

Soft Materials and Large Scale Structures



A 3D model of a lipid bilayer structure, showing the arrangement of phospholipids. The model consists of two layers of phospholipids, with the hydrophilic heads facing outwards and the hydrophobic tails facing inwards. The heads are represented by purple and red spheres, and the tails are represented by yellow cylinders.

STRUCTURAL ARREST TRANSITION IN L64/D₂O TRIBLOCK COPOLYMER MICELLAR SOLUTIONS

Wei-Ren Chen^{1,2,3}, Francesco Mallamace^{1,4}, Emiliano Fratini⁵, Piero Baglioni⁵ and Sow-Hsin Chen^{1,*}

1. Department of Nuclear Science and Engineering, Massachusetts Institute of Technology, Cambridge, MA, 02139

2. Department of Chemistry, the University of Tennessee, Knoxville, TN, 37996

3. The NIST Center for Neutron Research, National Institute of Standards and Technology, Gaithersburg, MD, 20899

4. Dipartimento di Fisica e Istituto Nazionale per la Fisica della Materia, Università di Messina, I-98100 Messina, Italy.

5. Department of Chemistry and CSGI (Consorzio Sistemi a Grande Interfase), University of Florence, via della Lastruccia 3, I-50019, Florence, Italy

Abstract

Soft and complex materials, such as proteins in solutions, micellar systems and colloid suspensions, are of great interest in many fields of science and in daily life [1]. There is a common feature shared by all soft matters, namely, structurally they are all characterized by a hierarchical order in the mesoscopic scale. This feature in turn gives rise to a dynamical behavior characterized by multiple relaxations, starting out initially by a short-time Gaussian relaxation and followed with the so-called Boson peak, then by a β relaxation and finally an α relaxation, spanning many different temporal orders of magnitude from picoseconds to seconds [2]. The origin of a large variety of metastable or stable structural orders and phases lies in the nature of the interparticle interaction which depends on the external thermodynamical control parameters including temperature, composition and pressure.

Among the many members of the soft matter family, colloids are a model system because of their unique nature: In general the intercolloidal potential is short ranged (i.e., small if compared with the typical particle sizes) and, in addition, the ratio between the repulsive and the attractive contribution can be easily manipulated. Therefore, with the change of the interparticle interaction, colloids exhibit a rich variety of phase behaviors. The existence of different ordered liquid crystalline structures, the liquid–liquid phase demixing line with a critical point and a percolation transition line is typical of these systems. These phenomena can be traced back to some of the manifestations of the short-range feature of the interaction potential [3].

Among all the different regions of the phase diagram, probably the regions where the structural arrest states (glassy states) are located is the most interesting one. They are observed in many colloidal systems and their vital importance to our daily life is reflected in the following list: glue, shampoo, toothpaste and medical oral gel are all examples of structurally arrested matter. Despite their ubiquity, these structural arrested states are notoriously ill-characterized scientifically: they cannot be categorized as gaseous, liquid or crystalline states, in terms of structure and dynamics. Therefore, although colloidal glass is common in daily life, its scientific investigation is a rather recent development due to lack of its coherent physical picture [4].

In 1984, Götze [5] and Leutheusser [6] simultaneously pointed out a way to describe a discrete transition in a liquid state based on a prediction of the Mode-coupling theory (MCT), originally proposed to explain the so-called high-density effects of the liquid state observed by inelastic neutron scattering and computer simulations around the triple point density [7]. Theoretically for the liquid state, if its external control parameter, such as temperature or volume fraction, exceeds a certain value, a transition, characterized by the increasingly sluggish structural relaxation making the liquid effectively behave like a frozen disordered solids, will be triggered.

The connection between the kinetic glass transition (KGT), or structural arrest transition in a colloidal system with the MCT prediction was immediately realized. MCT makes direct predictions about the density and the single-particle correlators for a colloidal system when its constituent particles interact via a given potential. These calculated correlators can be tested directly by scattering techniques and computer simulations. Experimentally it was found that, for a spherical colloidal system treated as a hard sphere fluid physically, the idea of depicting the long-lived but nonequilibrium state of matter, in terms of the concept of this dynamically arrested state, indeed yields a generic and quantitative understanding of the ergodic-to-nonequilibrium transition [8]. However, there have been some anomalous dynamical observations, which cannot be interpreted in terms of the theory based on the hard sphere potential alone [9].

It is natural to ask whether a more complete picture of the KGT can be obtained by modeling the interparticle potential more accurately. The answer stems from a slight modification of the hard sphere interaction potential and has captivated a great deal of attention lately. Recent MCT calculations show that if a system is characterized by a hard core plus an additional short range attractive interaction — for example, by an adhesive hard sphere system (AHS) — a different structural arrest scenario emerges [10]. In addition to the aforementioned glass state called a ‘repulsive glass’ (RG), as a result of the cage effect, a manifestation of the excluded volume effect due to the existence of the hard core, an ‘attractive glass’ (AG) can form in which the motion of the typical particle is constrained instead by cluster formation with neighboring particles due to the short-range attraction. Furthermore, it is predicted that the additional short-range

attraction provides extra stabilization force to the liquid state and therefore creates a ‘liquid pocket’ at volume fraction surrounded by re-entrant shapes of RG and AG lines and beyond the hard sphere liquid-glass transition limit. Dynamically, MCT predicts the intermediate scattering functions (ISFs) of the ergodic states in the liquid pocket region are characterized by logarithmic decay in the β relaxation in the hydrodynamic region. Of particular interest is the occurrence of an A_3 singularity at which point the glass-to-glass transition line terminates. MCT suggests that the long time dynamics of the two distinct structurally arrested states become identical at and beyond this point.

Our Small Angle Neutron Scattering (SANS) and Photon Correlation Spectroscopy (PCS) measurements results obtained from a micellar system provide compelling evidence of the latest MCT predictions. The micellar system studied in this experiment is prepared by dissolving the Pluronic (BASF AG, Ludwigshafen, Germany) L64 triblock copolymers, used extensively in industrial applications, into D_2O at different weight fractions after suitable purification procedures. L64 is made of polyethylene oxide (PEO) and polypropylene oxide (PPO) and the chemical formula is $(PEO)_{13}(PPO)_{30}(PEO)_{13}$. Above 293 K, the copolymers self-assemble into spherical micelles each with PPO segments packed into a compact core and PEO segments forming a corona around it. The short-range attraction arises from the overlap of PEO chains in the corona regions when two micelles approach one another [11].

The panels A and B shown in Figure 1 give the evidence of the short-range nature of the inter-micellar interaction potential: The intermediate scattering functions (ISFs) measured at $k = 0.00222 \text{ \AA}^{-1}$ and at the two volume fractions ($\phi = 0.525$ and 0.535 respectively) within the ‘liquid pocket’ as a function of temperature. The ISFs measured in the ergodic states indeed exhibit a logarithmic relaxation indicated by a straight-line fit at intermediate time, (the signature of the AHS system), followed by a power-law decay before the final relaxation, in agreement with the predictions of MCT [11-14].

The SANS absolute intensity distribution of a two-phase system (the micelles and the solvent) is given by a three-dimensional Fourier transform of the Debye correlation function $\Gamma(r/\Lambda)$ with characteristic length $\Lambda = \frac{1}{k_{\max}}$, k_{\max} being the interaction peak position of SANS intensity distribution. Therefore, by a simple transformation of variables, the dimensionless, scaled intensity distribution can be put into a unique function of a scaled scattering wave vector y in the following form:

$$\frac{k_{\max}^3 I(k)}{\langle \eta \rangle^2} = \int_0^{\infty} dx 4\pi x^2 j_0(xy) \Gamma(x)$$

where $x = k_{\max} r$, $y = \frac{k}{k_{\max}}$ and $\langle \eta \rangle^2$ is the so-called

invariant of the scattering. Thus, by plotting the scaled intensity as a function of scaled variable y , all the scattering intensity distributions at different temperatures within a single-phase region should collapse into a single master curve. It is shown that the dimensionless physical quantity $\frac{k_{\max}^3 I(k_{\max})}{\langle \eta \rangle^2}$, named as the scaling height, is

proportional to the coordinate number of a reference particle in a given phase; in other words, it contains the information about the local order [11,13]. In this way, the distinct local structures associated with different phases occurring at different temperature ranges can be identified, even for the glassy states where the theoretical representations of the structure factor remain unavailable due to their nonergodicity.

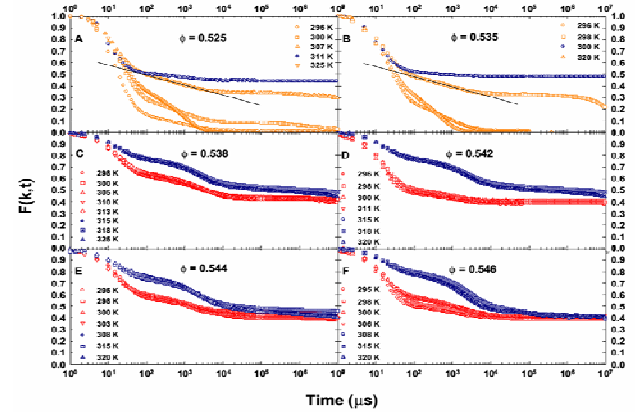


Figure 1. The ISFs measure by PCS for the L64/ D_2O micellar solutions at various volume fractions and temperatures.

Several sets of the scaling plots are shown in Figure 2 and the scaling heights for various phases are given in the associated insets. At volume fraction $\phi = 0.450$, all the scaled intensity distributions are temperature independent and indeed collapse into one single master curve, indicating that the system is in the liquid state, because all the scaled peaks are considerably broader than the resolution function of the instrument. At $\phi = 0.522$, the transition between the ergodic (liquid) state and the nonergodic (AG) state can be driven by varying the temperature. It shows a substantial difference between the local structure peaks of the resolution-limited nonergodic state and a much broader ergodic state peak. Furthermore, it should be noted that the transition shows a reentrant behavior. Increasing $\phi = 0.532$ and 0.536 , the scenario is similar to the previous example: a temperature dependent degree of disorder again characterizes the system. As the temperature rises, the system experiences a liquid-to-glass-to-liquid transition. However, in addition to all the similarities, when the temperature increases above 340K the system is driven into another glassy state. By increasing ϕ to 0.538 , we drive the system into the phase region, where the two glass-forming mechanisms nearly

balance each other. Changing temperature in turn affects the well depth, and a transition from RG (lower temperatures) to AG (higher temperatures) is triggered. We see two distinct sets of resolution-limited peaks, with the one for RG higher than the one for AG. Thus, we can conclude that the RG is better ordered locally than AG. At $\phi = 0.544$, we see that the two sharp peaks merge into one sharp peak independent of temperature, signifying that the local structures of the two glasses become identical. Increasing ϕ further to 0.546, the situation remains the same as in the previous volume fraction. This is proof that the MCT indeed gives accurate predictions. [12-14]

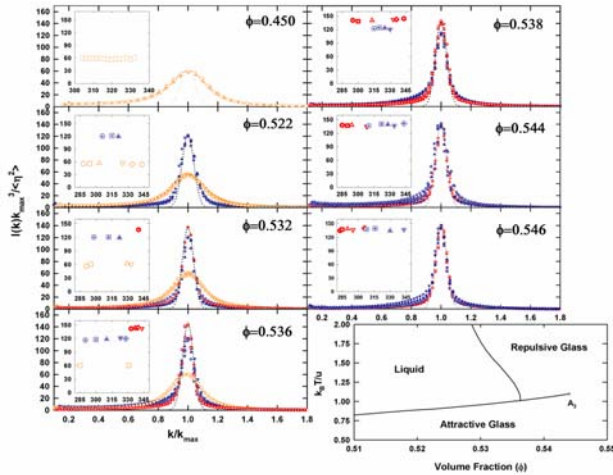


Figure 2. The scaling plots for the SANS intensity distributions obtained from the L64/D₂O micellar solutions at various volume fractions and temperatures and the phase paradigm predicted by MCT for the AHS system.

Panels C and D represent ISFs measured at $\phi = 0.538$ and 0.542. According to MCT, in this volume fraction range, there is a possibility of observing a glass-to-glass transition by varying the effective temperature. By comparing the long time limits (Debye-Waller Factor, DWF) of the ISFs, the two different types of the glasses can be identified by their respective DWFs, $f_k^{AG} \sim 0.5$ and $f_k^{RG} \sim 0.4$. The reason for observing two different values of DWFs can be identified as the different degrees of localization of the density fluctuation having the wavenumber k for the two types of glasses. Panel E gives ISFs measured at $\phi = 0.544$, where according to MCT, the long time limits of the ISFs of the two glasses become identical. In our measurements, the long time limit of the ISF of the AG gradually decreases from 0.5 and gets closer to 0.4, the long time limit of the ISF of RG. Although the DWFs of these two types of glass are almost identical, it is essential to recognize that there is a significant difference between the dynamics of their intermediate time relaxations. Panel F gives ISFs measured at $\phi = 0.546$. At this volume fraction, the long time limit of the ISF of AG approaches close to 0.4, which is the long time limit of the ISF of RG. This indicates that beyond the volume fraction 0.544, the two

glasses merge into a single RG phase. Judging from panels E and F, the experimentally determined volume fraction for the A₃ singularity lies somewhere between $\phi = 0.544$ and 0.546. [12-14]

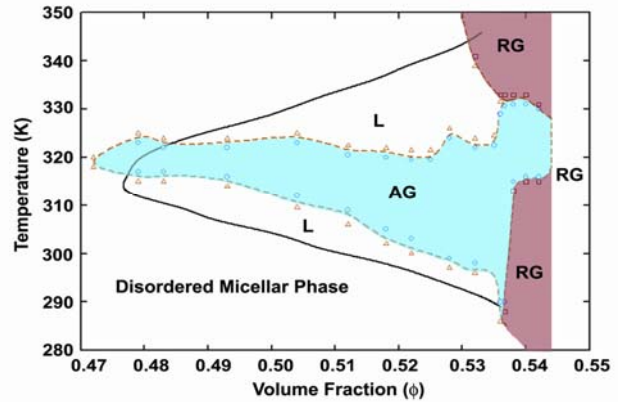


Figure 3. The experimental phase diagram of the L64/D₂O micellar system.

Figure 3 summarizes the essential results of the extensive SANS and PCS data analysis. It contains the known equilibrium, liquid-to-hexagonal crystalline phase boundary (solid curve), the experimentally determined KGT lines (dash curves) and the phase points where parts of the experimental data are taken (symbols). This figure gives several important pieces of information about this system: first, only the metastable AG is observed within the region where the true lowest free energy state is the hexagonal liquid crystalline phase; next, RG only exists in the region where the volume fraction is larger than 0.536. It is interesting to see that there is a pocket of the AG embedded in between two separate RG regions spanning the volume fraction range between 0.536 and 0.544, where the re-entrant glass-to-glass transition is observed. From Figures 1 and 2, the two different glasses become identical in local structure and long time dynamics in hydrodynamic region at $\phi = 0.544$ or greater. Furthermore, judging from the DWF and the peak height of the scaled intensity, the merged identical glassy state is RG. Furthermore, important physical insights need to be addressed for the phase region $0.53 < \phi < 0.54$ and $320 < T < 340$: At high temperature $T \sim 340$ K the dominating glassy mechanism is the cage effect, therefore only RG is observed. Upon cooling the temperature to $T \sim 330$ K, the short range attraction is no longer negligible and effectively makes the cages more compact and simultaneously creates voids allowing micelles to diffuse. Consequently the glass melts by cooling. Further lowering the temperature to around 320K, the spatial inhomogeneity becomes more significant. The transient bonding among micelles become stronger and longer lasting and in turn hinders the micellar diffusion and results in another nonergodic state AG with a different glass forming mechanism [12-14].

REFERENCES

- [1] D.H. Everett, Basic Principles of Colloid Science, Royal Society of Chemistry, Letchworth, UK, 1988.
- [2] W. Kob, in Slow Relaxations and Nonequilibrium dynamics in Condensed Matter, edited by J.-L. Barrat, M. Feigelman, J. Kurchan and J. Dalibard, NATO Advanced Study Institute, 2002.
- [3] K. Dawson, *Curr. Opin. Colloid Interface Sci.* 7 218 2002.
- [4] K. Dawson, ICTP Lecture, Trieste, Italy, 2002.
- [5] U. Bengtzelius *et al*, *J. Phys. C* 17 5915 1984.
- [6] E. Leutheusser, *Phys. Rev. A* 29 863 1984.
- [7] J.-P. Boon and S. Yip, *Molecular hydrodynamics*, McGraw-Hill Inc, 1980.
- [8] For example, see P.N. Pusey and W. van Meegen, *Phys. Rev. Lett.* 59 2083 1987.
- [9] E. Bartsch *et al*, *J. Chem. Phys.* 97 3950 1992.
- [10] K. Dawson *et al*, *Phys. Rev. E* 63 011401 2001.
- [11] W.-R. Chen *et al*, *Phys. Rev. E* 66 021403 2002.
- [12] S.-H. Chen *et al*, *Science* 300 619 2003.
- [13] W.-R. Chen *et al*, *Phys. Rev. E* 68 041402 2003.
- [14] W.-R. Chen *et al*, *J. Phys.: Condens. Matter* 16 S4951 2004.

NANOSCALE EFFECTS ILLUMINATED BY NEUTRON SCATTERING AND REFLECTIVITY

Melissa Holmes, R.S. Krishnan, Michael E. Mackay, Leslie M. Passeno and Anish Tuteja
Department of Chemical Engineering & Materials Science, Michigan State University, East
Lansing, MI 48824

Introduction

We have used neutron scattering to delineate the molecular morphology and phase stability of nano-objects blended with linear polymers. Small angle neutron scattering (SANS) has been an important tool to understand peculiar nanoscale phenomena that we have discovered. For example, we used SANS to show that chemically dissimilar nanoparticles are soluble at large concentration even when the interparticle gap is smaller than the polymer radius of gyration. One would expect phase separation caused by depletion flocculation would occur, [1] yet, this nanoscale system does not follow contemporary rules based on microscopic arguments.

In other research we have used neutron reflectivity to show that nanoparticles will segregate to a hard substrate after thermal or solvent vapor annealing a polymer film. This has important implications since the nanoparticles are found to stabilize the thin (~50 nm) film which will not dewet the substrate. Further, the utility of the films is enhanced since this is an enabling technology for sensors which suffer from dewetting thereby reducing their utility and also allows for nanoparticle self assembly.

We also used SANS to investigate the molecular morphology of linear-dendrimer diblock copolymers in solution. A low molecular weight polystyrene chain swelled the dendrimer without perturbing its native sphere-like conformation. However, at larger linear polymer molecular weights, the linear block manipulated a transition of the dendrimers' morphology from sphere-like to an extended, perhaps cone-like, conformation. Control of this shape and size change has potential for these unique macro-

molecular architectures to function as a novel molecular building block or molecular machine, and is discussed below.

Linear – dendrimer block copolymers [2]

Previous studies of linear-dendrimer diblock copolymers, where a linear chain is connected to the focal point of a dendrimer in solution, have focused on the conformation of the entire system. A full understanding of the system necessitates pinpointing the relative locations and morphology of each block. Figure 1 illustrates three possible linear-dendrimer diblock conformational states for a system where the linear and dendrimer blocks are compatible with each other. Each conformational state pertains to different relative locations of the two blocks. The first state is a knitted coil, where the linear chain weaves in and out of the dendrimer, thus the dendrimer shields or partially shields the linear polymer from the surrounding environment. For this to occur, the dendrimer must have enough free volume to accommodate the linear block. A second hybrid conformation consists of the linear chain wrapping itself around the dendrimer, thus shielding the dendrimer from the surroundings and forming a unimolecular micelle. This encapsulated dendrimer state would occur when the linear block is compatible with the surrounding medium and the dendrimer less compatible, resulting in a core-shell morphology. A third potential molecular arrangement consists of the linear chain completely expelled from the cavities within the dendrimer. This could occur if there is not enough free volume within the dendrimer to contain the entire linear chain and each component has similar solubility in the solvent.

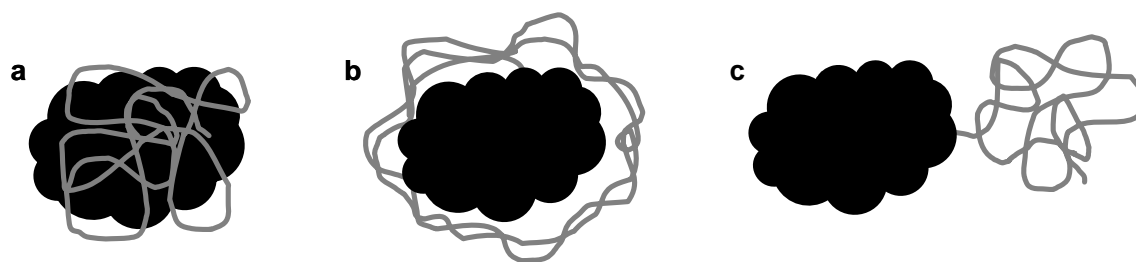


Figure 1. Three potential conformational states of linear-dendrimer diblocks in solution: **a.** knitted coil **b.** encapsulated dendrimer **c.** random coil.

We used SANS to distinguish between these three states of a fourth generation poly (benzyl ether) dendrimer – linear polystyrene (G4-PBE-PS) hybrid block copolymer. Three different molecular weight hybrids were studied; 20kDa, 45kDa and 100kDa, which is the sum of the G4 PBE dendrimer ($M = 3288\text{g/mol}$) and linear chain molecular weights and thus the only difference between the three hybrids is the molecular weight of the linear block. The PS chain was also deuterated (dPS) to allow contrast matching experiments to be performed with SANS and individually visualize each block.

The dendrimers behave as sphere-like objects in both d^6 -benzene and d^8 -THF due to the observed negatively sloped straight line in the Guinier plots for compact objects (Figure 2). It is evident from the Guinier fits in Figure 2 that the dendrimer is larger in d^6 -benzene than in d^8 -THF, with radii values of 1.73 ± 0.03 nm and 1.35 ± 0.04 nm, respectfully.

The dendrimer block conformation within the hybrid block copolymers was determined by dissolving the G4-PBE-dPS diblocks in d^8 -THF, which is a contrast match for the dPS block. These contrast match experiments revealed that the dendrimer block's size and shape is dependent upon the linear block molecular weight. The G4-PBE-dPS-20kDa hybrid has a dendrimer block where the branches adopt a 'sphere-like' shape, Figure 3a, just as the free dendrimer in solution, Figure 2, yet the size of this sphere is approximately 35% larger in the hybrid system ($>2\times$ change in volume). The difference in size between the hybrid's dendrimer block and the free dendrimer in

solution is probably due to the linear chain occupying space within the dendrimer, resulting in swelling and possible development of the knitted coil morphology shown in Figure 1. The two higher molecular weight systems, G4-PBE-dPS-45kDa, Figure 3b, and G4-PBE-dPS-100kDa, Figure 3c, did not show the expanded sphere-like morphology and instead these two systems have dendrimer blocks that are 'rod-like' in shape [3]. According to the cylinder model, the cylinder radius for the 45kDa and 100kDa systems has values of 3.81 ± 0.39 nm and 3.40 ± 0.38 nm, respectively, making the cylinder length of order 0.1 nm, suggesting a disc-like morphology which certainly does not represent the data.

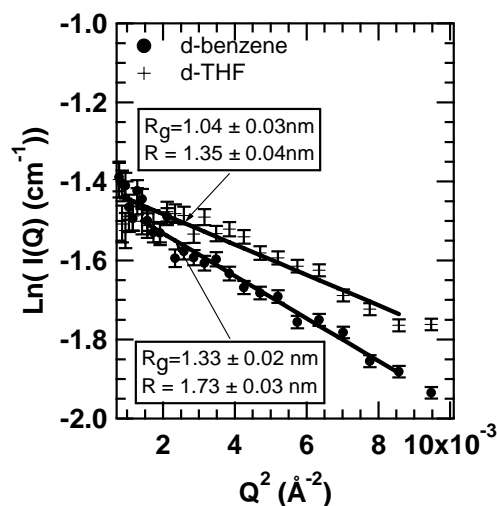


Figure 2. Guinier analysis for PBE G4 dendrons in d^6 -benzene and d^8 -THF at a concentration of 50 mg/mL, data fit for a compact (sphere-like) object.

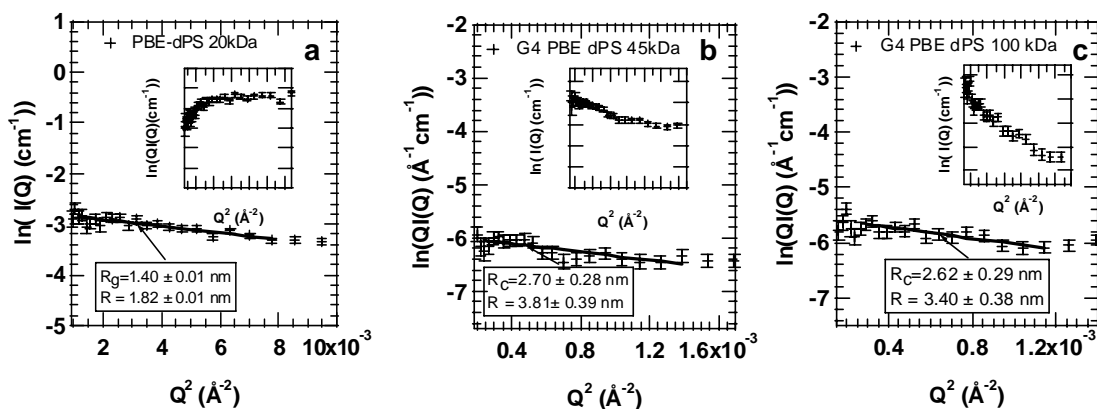


Figure 3. Shape of the dendrimer block as the linear block molecular weight is changed. **a.** Guinier analysis for PBE-dPS-20kDa system in d^8 -THF at a concentration of 50 mg/mL, dendrimer block is scattering as a sphere-like object. Inset is a modified Guinier analysis for a rod-like object, which does not represent the data. **b.** Rod-like Guinier analysis for PBE-dPS-45kDa hybrid in d^8 -THF at a concentration of 50 mg/mL. Inset shows the attempted representation of data to Guinier fit for compact object. **c.** Rod-like Guinier analysis for PBE-dPS-100kDa hybrid in d^8 -THF at 50mg/mL. Inset is the Guinier analysis for a compact-object, which is a poor fit due to curvature.

Rather, it is expected that the data are represented by a cone-like or solid angle form factor [4] and so the random coil conformation demonstrated in Figure 1c may be possible for the higher molecular weights with the caveat that the dendrimer changes shape. Thus, it is hypothesized that, as the linear polymer molecular weight is increased, the dendrimer goes from being swollen with the linear polymer knitting in and out of it to a dendrimer that is collapsed with significant shape change and a linear polymer surrounding it. It is hoped that the relative size of the two blocks can be controlled in a similar manner to have this molecule act as a molecular machine.

Nanoparticle stabilized thin films [5]

We have shown that polystyrene nanoparticles [6] can eliminate dewetting of linear polystyrene films after high temperature annealing. As shown in Figure 4, blends of polystyrene nanoparticle - linear polymer do not dewet, or there is a marked reduction in the dewetting velocity. Indeed, Krishnan et al. [5] found that addition of 1% nanoparticle caused a substantial decrease in

the dewetting velocity although it was not completely eliminated under these conditions.

To probe why this unique phenomenon occurs, we performed neutron reflectivity measurements on a 10 wt% representative sample before and after annealing. The neutron reflectivity measurements were performed at the POSY2 neutron reflectometer at Argonne National Lab. The film was ca 17nm thick and was annealed under vacuum at 140°C prior to the measurement.

Neutron reflectivity data for a 10wt% blend of 25.3kDa protonated nanoparticle blended with 63 kDa deuterated linear polystyrene film (R is the reflectivity) are shown in Figure 5a. The scattering length density profile generated from this model changed more gradually than that for a sharp interface, yet, the plateau for Rq^4 vs. q is a signature for a fairly sharp interface. As seen in Figure 5a it seems that the nanoparticles phase separate to the solid substrate surface since other scattering length density profiles do not adequately represent the data at all.

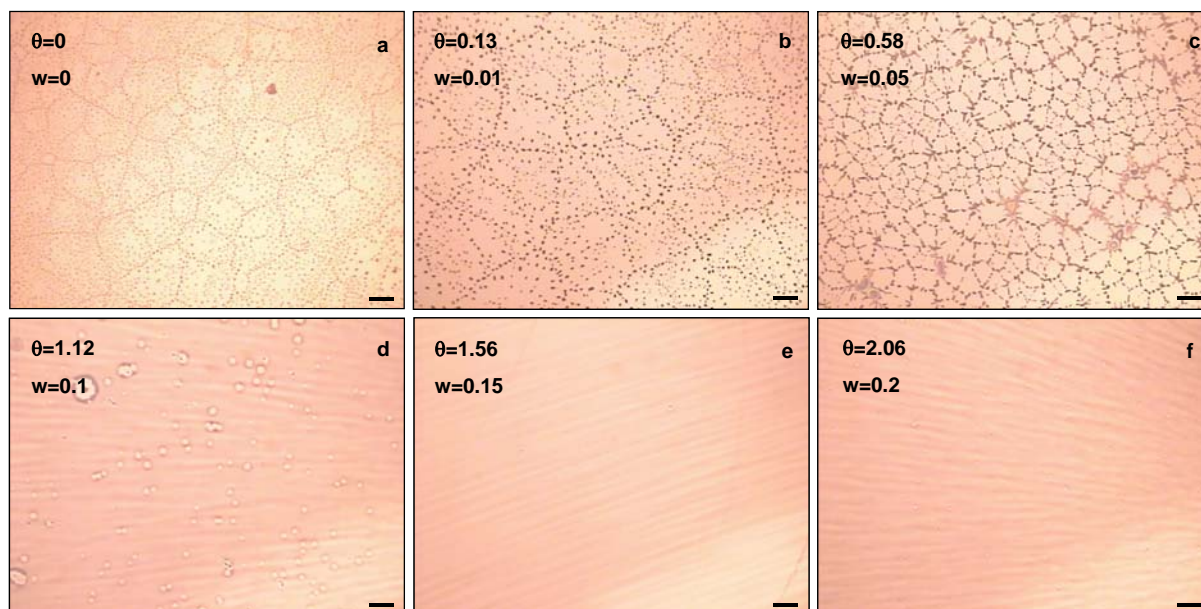


Figure 4. Optical micrographs of blends of linear polystyrene 75kDa with 25.3 kDa nanoparticle. All the films were annealed for time >24hrs in vacuum: **a.** Pure PS, **b.** 1%, **c.** 5%, **d.** 10%, **e.** 15% and **f.** 20% nanoparticle concentration. Note at 0.15-0.20 nanoparticle weight fraction (w), the dewetting is completely eliminated (aerial fraction, $\theta \sim 1.5$ -2.0). Film thicknesses are ca. 40nm and the length of the scale bars are 100 μm .

One can convert this profile to a concentration and this was done as shown in Figure 5b with a scaled representation of the nanoparticle in the lower right-hand corner of the graph. It is clear that the concentration profile changes substantially near the substrate surface and that the concentration profile correlates almost exactly with the nanoparticle size.

The nanoparticle induced stability of thin polymer films shown in Figure 4 thus depends on the aerial coverage of the segregated nanoparticles. The fractional areal coverage (θ) can be determined by a simple mass balance from the following relation

$$\theta = [\Delta/2a] \times \phi$$

where Δ is the film thickness, a , the nanoparticle radius and ϕ , the bulk nanoparticle volume fraction. Once an areal coverage of about a monolayer (Figure 4e) is reached, then film stability is promoted.

It is believed that the linear polymer loses too many conformations near the solid substrate and “entropically pushes” the

nanoparticles to the substrate. Since the nanoparticles can not move past each other above a monolayer surface concentration, an effective solid coating is formed by them shielding unfavorable energetic interactions between the substrate and the linear polymer. Calculations suggest this is true, however, other phenomena such as an induced nano-rough surface formed by the nanoparticles may partly cause the wetting behavior. This is currently being investigated by us.

Fullerenes and their film stabilization effect in solvent atmospheres [7]

One recent application of thin polymer films has been in the field of chemical sensors. Sandia National Laboratories has developed a chemical sensor from an array of surface acoustic wave (SAW) devices onto which a specifically designed polymer is deposited. When the analyte is present in the air, it is absorbed into the polymer film, resulting in a detectable shift in the frequency of the SAW device. The sensor is tested, or

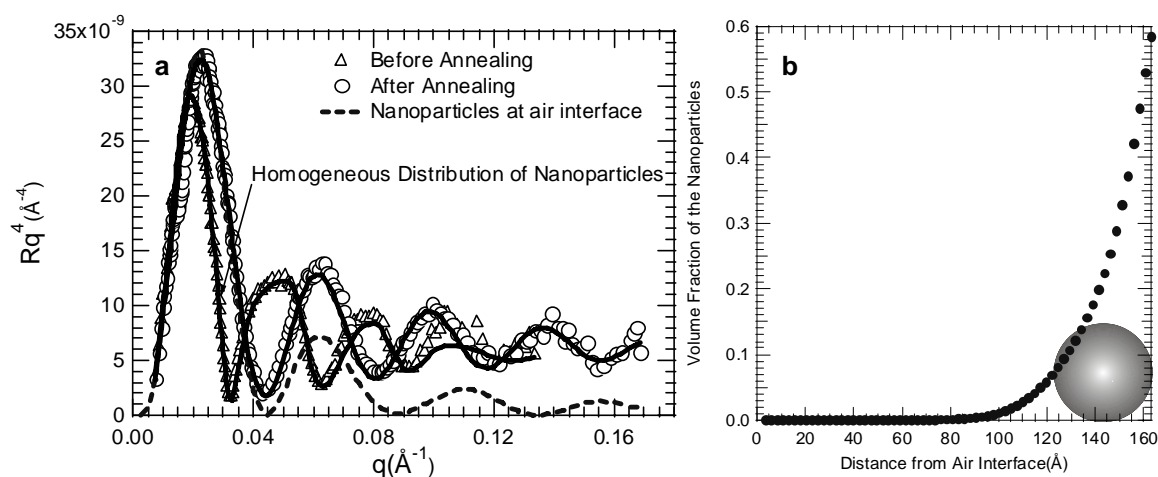


Figure 5. The concentration profile of nanoparticles changes dramatically after high temperature annealing. **a.** Reflectivity multiplied by reflectance wave vector to the fourth power (Rq^4) vs. q for a silanized silicon wafer spin coated with 63 kDa deuterated polystyrene blended with 10wt% 25.3 kDa protonated, tightly crosslinked, polystyrene nanoparticles before and after annealing at 140°C for 2hrs under vacuum. The dotted line represents the reflectivity profile fit if the nanoparticles phase separated to the air interface. The solid lines represent the fits for the before and after annealed films as described in the text. **b.** Nanoparticle concentration determined from the reflectivity data for the nanoparticle after annealing. The nanoparticles are all at the solid substrate as demonstrated by the scaled nanoparticle representation shown in the lower, right-hand corner.

challenged, by blowing various solvent vapors across the polymer films. These vapors include surrogates for aggressive biochemical agents as well as those found ubiquitously in the environment. It has been seen however, that upon exposure of these vapors, the polymer film can dewet from the surface, rendering the sensor useless. We have found, however, that the addition of C_{60} fullerenes to polymer films can inhibit dewetting upon exposure to solvent vapor.

We have found that a polystyrene film with 3 wt% addition of fullerenes demonstrates vastly different behavior than a pure polystyrene film upon exposure to a saturated toluene atmosphere (Figure 6). The pure film breaks up to form holes, which eventually coalesce into droplets after 1 hour of exposure. However, for the filled film after 3 hours of exposure, no dewetting is seen and the film remains uniform. The fullerenes stabilize the film upon vapor annealing just as they have been shown to do upon high temperature annealing. It is believed that the stabilization mechanism may be similar to that proposed by Barnes et al. [8]. Fractal-like fullerene “trees” form at the substrate-film interface influencing the polymer

conformation to produce a change in the molecules’ surface energy. Further, the trees pin the contact lines to inhibit dewetting, allowing any nucleated hole to stop growing and the film remains intact.

To test the hypothesis, neutron reflectivity experiments were performed at POSY2 to determine the location of the nanoparticles in the polymer film. The first experiment consisted of two samples that were prepared by spin-coating a solution of PS with 3 wt% C_{60} relative to PS in toluene onto piranha-cleaned silicon wafers that were 2 inches in diameter and 0.5 mm thick. One of the samples was tested immediately after spin-coating while the other was first exposed to a saturated toluene atmosphere for 3 hours. We find that the fullerenes are near the polymer-substrate interface immediately after spin-coating. Further, the fullerenes stayed at this position after solvent vapor annealing as shown in Figure 7. Detailed modeling (Table 1) revealed that the nanoparticles formed a layer approximately 2 nm thick which is larger than the fullerene diameter (~ 0.7 nm). This model (Substrate Model) agrees fairly well with the data, while inverting the nanoparticle and pure polymer layers’

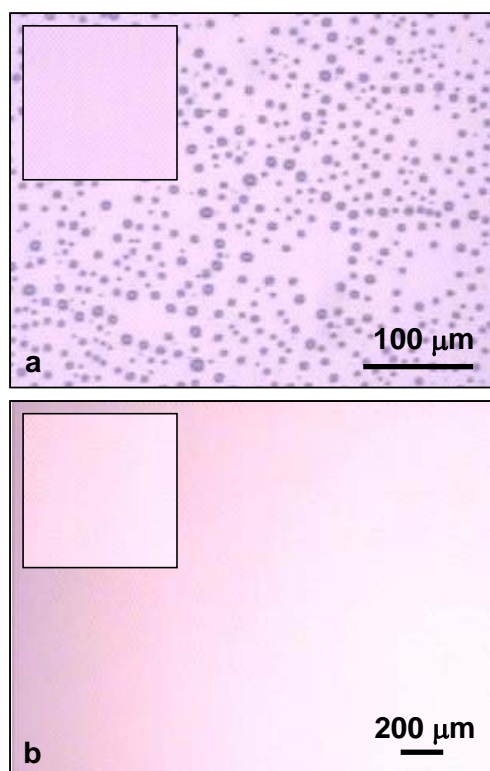


Figure 6. Optical micrographs of spin-cast films on piranha cleaned silicon wafers exposed to a saturated toluene atmosphere. Insets show the film prior to annealing (same scale bar). **a.** Pure polystyrene film after exposure for 50 min. **b.** Polystyrene with 3 wt% fullerenes after exposure for 3 hours. Films are 33 nm thick.

positions (Air Model) or assuming the nanoparticles are homogeneously distributed throughout the film (Homogeneous Model) does not represent the data well. Further, there is no change in the fullerene concentration profile after vapor annealing since the reflectivity profile does not change as seen in Figure 7.

We hypothesize that during the spin coating process, the fullerenes form a gel-like network having ~ 29 vol% fullerenes, relative to the PS, determined from the 2 nm thick layer scattering length density, which shields the substrate from the bulk polymer film. This agrees with the recent work by Luo and Gersappe [9] where they conclude that for smaller, mobile particles, an increase in the local viscosity occurs at the substrate forming area network-like structure, thus inhibiting dewetting. However, it could also be that the

layer nano-roughness also plays a part in promoting wetting which is a current area of active research.

Nanoparticle blends with polymers [10,11]

Our research incorporating both nanotechnology and fluid flow seeks to impart unique behavior in materials to improve both processing and performance. Recently, nanofillers have attracted the interest of a variety of research groups as these materials can cause unusual material property enhancements. These enhancements are induced by the presence of the nanoparticles, their interaction with the host matrix, and also quite critically, by their state of dispersion.

The phase behavior for the dispersion of colloidal particles in a polymer is well established [12], with particle clustering or phase separation occurring, as a result of osmotic pressure differences around the particle, when the polymer molecule becomes larger than the average interparticle gap.

Contrary to the observation in colloid – polymer blends, recent simulations have shown that nanoparticles can slow down the phase separation of two incompatible polymers, suggesting the use of nanoparticles as compatibilizers in polymer blends [13]. There have also been some experimental studies on the dispersion and distribution of nanoparticles in polymer blends, suggesting enhanced miscibility of nanoparticles in polymers. For example, in our previous work we showed that 2.7 nm radius polystyrene nanoparticles [10] could be blended with linear polystyrene to large volume fraction ($\phi \approx 0.5$) without the expected phase separation.

In the present work, we used SANS to study two disparate nanoparticle-polymer systems. First we investigate the effect of the addition of shape persistent polystyrene (PS) nanoparticles (NP), synthesized by intramolecular crosslinking of linear PS [6], to linear PS creating a blend with the simplest enthalpic interactions between the components. This system was thus ideal to

Table 1. Three models of the reflectivity data given in Figure 8 where the fullerene rich layer is next to the silicon wafer (Substrate Model), next to the air interface (Air Model) or homogeneously distributed (Homogeneous Model). The layer thickness and scattering length density (SLD) were optimized in the Substrate Model to achieve the best fit. Modeling was performed with Parratt32 from HMI Berlin.

Model	Layer	Thickness (Å)	SLD (10^6 Å^{-2})
Substrate	1	295	1.41
	2	20	2.66
	wafer	-	2.07
Air	1	20	2.66
	2	295	1.41
	wafer	-	2.07
Homogeneous	1	315	1.49
	wafer	-	2.07

delineate the effect of particle size on the miscibility of the blend. Next, we look at the miscibility of dendritic polyethylene nanoparticles [14] in linear polystyrene. Polystyrene and polyethylene is a classic phase separating system. Thus, these two systems probe the two limits for the enthalpic interactions between the nanoparticles and the linear polymer chain.

The intensity as a function of the wave vector q , obtained from SANS, is shown in Figure 8 for the blends of the dendritic polyethylene nanoparticles with linear polystyrene of two different molecular weights ($M_w = 393 \text{ kDa}$ and $M_w = 75 \text{ kDa}$). For the lower molecular weight linear polystyrene, a power law scattering pattern at low q is evident. Such a power law is a clear indicator of the phase separation in the blend. However, in the case of the higher molecular weight polystyrene, no phase separation occurs, as is evident by the absence of power law scattering at low q . In fact, the scattering profile can be fitted quite well to a polydisperse sphere model, as shown.

A phase diagram was developed from this and other data for various miscible and

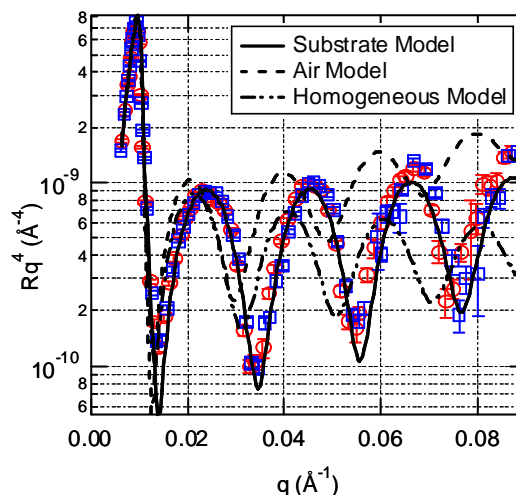


Figure 7. Neutron reflectivity data and model calculations for polystyrene films with 3 wt% fullerenes before (circles) and after (squares) exposure to a saturated toluene vapor. There is no change in the reflectivity profile.

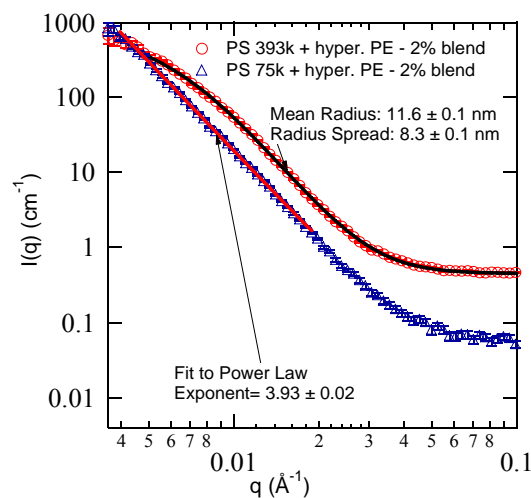


Figure 8. Polyethylene - polystyrene blends can produce a stable system provided the appropriate molecular architecture is used. The figure shows SANS data obtained for the blends of dendritic polyethylene nanoparticles with linear polystyrene of two different molecular weights (75 kDa and 393 kDa). Fractal-like scattering at low wave vector for the lower molecular weight material indicates phase separation which is not present with the higher molecular weight polymer. The mean radius of the dendritic polyethylene is determined to be 11.6 nm with a polydispersity of 8.3 nm which agrees well with electron microscopy results.

immiscible blends observed for both polystyrene nanoparticles in linear polystyrene and dendritic polyethylene nanoparticles in linear polystyrene as shown in Figure 9. The solid line shown in the figure represents the limit where the radius of gyration of the polymer is equal to the radius of the nanoparticle.

Thus, from this figure it is evident that nanoparticles can be dispersed in linear polymers, despite chemical dissimilarity, when the nanoparticle is smaller than the linear polymer. If the particle is larger than the polymer, phase separation occurs, even polystyrene nanoparticles phase separate from linear polystyrene! In addition, from other neutron scattering experiments, we find that the linear polymer becomes distorted on the addition of nanoparticles in the stable systems and is far from its equilibrium conformation. This aspect demonstrates the uniqueness of nanoscale thermodynamics as phase separation is expected (i.e. depletion flocculation) and it is believed that the nanoparticles are stabilized by enthalpic gain [15].

When properly dispersed, addition of nanoparticles was shown for the first time to cause a large reduction (up to 90%) in the melt viscosity of the system [10,11], a result at odds with Einstein's century old prediction [16] and experimental observations of the viscosity increase particles provide to liquids and melts (*i.e.* slurries and suspensions). The above and other quite interesting and unusual nanoscale phenomena including enhancements in the thermal, electrical and mechanical properties of the composite have been discovered, explained and aided by our research work at IPNS.

Conclusion

We have used the neutron scattering facilities at IPNS to conduct a variety of studies as described above. Utility of the neutron scattering and reflectivity instrumentation at Argonne National Laboratory has been invaluable to our research, allowing us to investigate

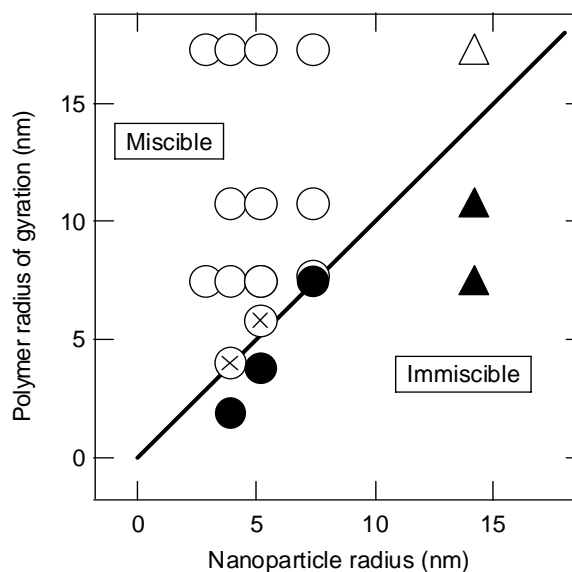


Figure 9. A phase diagram where the filled circles represent data where phase separation was detected and the open circles where miscibility occurs, open circles with an X represent conditions where some agglomeration was detected by SANS, yet, large scale phase separation was not present. Circles denote the crosslinked polystyrene nanoparticle – linear polystyrene system; and triangles, dendritic polyethylene – linear polystyrene system.

phenomena key to national defense and industrial products.

Acknowledgements

Financial support from IPNS for R.S. Krishnan and scattering time at Argonne National Laboratories is greatly appreciated. The help of Dr. P. Thiyagarajan and Mr. Denis Wozniak at IPNS is greatly appreciated. Funding from NSF CTS-0400840, NSF NIRT 0210247, NSF NIRT 0506309, DOE DE-FG02-05ER46211 and ARO W911NF-05-1-0357 is truly appreciated.

References

- [1] W. B. Russel, D. A. Saville, W. R. Schowalter, *Colloidal Dispersions*. Cambridge University Press: Cambridge, 1989; p 525.
- [2] L. M. Passeno, M. E. Mackay, G. L. Baker, R. Vestberg, C. J. Hawker, "Conformational Changes of Linear-Dendrimer Diblock Copolymers in

- Dilute Solution", *Macromolecules in press*.
- [3] J. M. Gallas, K. C. Littrell, S. Seifert, G. W. Zajac, P. Thiyagarajan, "Solution structure of copper ion-induced molecular aggregates of tyrosine melanin", *Biophys. J.* **1999**, 77, 1135-1142.
- [4] R. P. Hjelm, "The Small-Angle Approximation of X-Ray and Neutron Scatter from Rigid Rods of Non-Uniform Cross-Section and Finite Length", *J. Appl. Crystal.* **1985**, 18, 452-460.
- [5] R. S. Krishnan, M. E. Mackay, C. J. Hawker, B. Van Horn, "Influence of molecular architecture on the dewetting of thin polystyrene films", *Langmuir* **2005**, 21, (13), 5770-5776.
- [6] E. Harth, B. VanHorn, V. Y. Lee, D. S. Germack, C. P. Gonzales, R. D. Miller, C. J. Hawker, "A facile approach to architecturally defined nanoparticles via intramolecular chain collapse", *J. Am. Chem. Soc.* **2002**, 124, 8653-8660.
- [7] M. A. Holmes, M. E. Mackay, R. K. Giunta, "Nanoparticles for Dewetting Suppression of Thin Polymer Films used in Chemical Sensors", **submitted**.
- [8] K Barnes, A. Karim, J. Douglas, A. Nakatani, H. Gruell, E. Amis, "Suppression of dewetting in nanoparticle-filled polymer films", *Macromolecules* **2000**, 33, 4177-4185.
- [9] H. B. Luo, D. Gersappe, "Dewetting dynamics of nanofilled polymer thin films", *Macromolecules* **2004**, 37, (15), 5792-5799.
- [10] M. E. Mackay, T. T. Dao, A. Tuteja, D. L. Ho, D. VanHorn, H.-C. Kim, C. J. Hawker, "Nanoscale effects leading to non-Einstein-like decrease in viscosity", *Nature Materials* **2003**, 2, 762-766.
- [11] A. Tuteja, M. E. Mackay, C. J. Hawker, B. V. Horn, "Effect of Ideal, Organic Nanoparticles on the Flow Properties of Linear Polymers: Non-Einstein-like Behavior", *Macromolecules* **2005**, 38, 8000-8011.
- [12] S. Asakura, F. Oosawa, "Interaction between Particles Suspended in Solutions of Macromolecules", *J. Poly. Sci.* **1958**, 33, 183-192.
- [13] V. V. Ginzburg, "Influence of Nanoparticles on Miscibility of Polymer Blends. A Simple Theory", *Macromolecules* **2005**, 38, 2362-2367.
- [14] Z. Guan, P. Cotts, E. McCord, S. McLain, Chain Walking: "A New Strategy to Control Polymer Topology," *Science* **1999**, 283, 2059-2062.
- [15] M. E. Mackay, A. Tuteja, P. M. Duxbury, C. J. Hawker, B. V. Horn, Z. Guan, G. Chen, R. S. Krishnan, "A General Strategy for Nanoparticle Dispersion," *Science* **submitted**.
- [16] A. Einstein, "On the theory of Brownian movement," *Ann. d. Phys. Leipzig* **1906**, 19, 371-381.

SOLVATION AND AGGREGATION OF ASPHALTENES IN MODEL PETROLEUM MIXTURES

Keith L. Gawryś and Peter K. Kilpatrick, Chemical and Biomolecular Engineering, North Carolina State University

Asphaltenes, the portion of crude oil insoluble in *n*-alkanes (such as *n*-heptane or *n*-pentane), are well known for their tendency to associate in solution and adsorb at interfaces, linking the solubility class to petroleum production problems such as pipeline deposition and water-in-crude oil emulsion formation. Asphaltenes are comprised of a polydisperse mixture of chemically heterogeneous species that can vary greatly from one crude oil to another. Asphaltene molecular structure is generally characterized by the presence of fused ring aromatic moieties, small aliphatic side chains, and polar heteroatom-containing functional groups capable of participating in proton donor-acceptor interactions (e.g., carboxylic acids, carbonyls, phenols, pyrroles, and pyridines). See Ref. 1 and 2 for a detailed overview of asphaltene chemical and physical properties. Figure 1 shows a cartoon schematic depicting an asphaltene monomer and a small oligomer formed by the interaction of aromatic groups and/or polar moieties.

Over the past five years, we have used the small-angle neutron diffractometer (SAND) at IPNS to study the roles of chemical composition and solvency on the aggregation and solubility behavior of asphaltenes. In our earliest experiments, small-angle neutron scattering (SANS) studies were performed on more soluble (i.e., “soluble”) and less soluble (i.e., “precipitate”) fractions of “whole” asphaltenes dispersed in model crude oil solvents (e.g., mixtures of deuterated *n*-heptane and toluene)³. Enhancement of polar and π -bonding interactions for the less soluble fractions indicated by elemental analysis results was reflected by the relatively large aggregate sizes for the “precipitate” fractions compared to the “whole” and “soluble” fractions. The “precipitate” fractions

contributed the majority of species responsible for asphaltene aggregation. In another study, SANS measurements were performed on asphaltene solutions in mixtures of heptane-toluene with various concentrations of added resins⁴. In general, the addition of resins to asphaltenes reduced the aggregate size by disrupting the π - π and polar bonding interactions between asphaltene monomers. Interaction of resins with asphaltene aggregates rendered the aggregates less interfacially active and thus reduced emulsion stability. The propensity of asphaltenes to form stable water-in-crude oil emulsions was ultimately related to the extent of asphaltene aggregation and the solvating power of the crude oil media. Asphaltenes maintain a delicate balance among solvency, aggregation, and interfacial activity that is related to the chemical composition of the participating components.

We refer to the separation of asphaltenes into two more and less soluble fractions as a so-called “coarse” fractionation experiment. In later experiments, asphaltenes from three different crude sources (i.e., B6, HO, and CS) were separated on a preparatory-scale into 20 to 30 discrete or “fine” fractions by sequential precipitation in mixtures of heptane and toluene⁵. Coefficients of linear correlation for the chemical composition, solubility, and aggregate size parameters provided a statistical means of determining the properties of the asphaltene fractions that promoted aggregation and precipitation. Table 1 summarizes the coefficients of linear correlation for B6 and HO asphaltene fractions. Aggregation in B6 asphaltenes was most highly correlated to atomic N/C and H/C ratios and was consistent with previous scattering experiments. The relatively high correlation of N/C

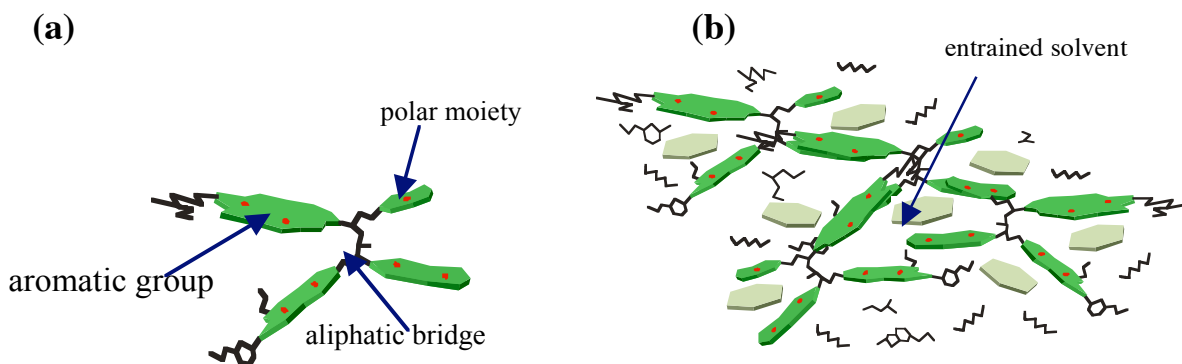


Figure 1. Schematic representations of (a) an asphaltene monomer and (b) an asphaltene tetramer in a mixture of aromatic and aliphatic solvents.

Table 1. Coefficients of linear correlation for chemical composition, solubility, and aggregate size parameters of B6 and HO asphaltenes

B6	δ	H/C	N/C	Na/C	Ca/C	K/C	Mg/C	V/C	Al/C	Fe/C	Ni/C	R _g
δ	1.000											
H/C	-0.332	1.000										
N/C	0.755	-0.381	1.000									
S/C	0.267	-0.157	0.381									
O/C	0.298	-0.082	0.282									
Na/C	0.451	-0.264	0.142	1.000								
Ca/C	0.348	-0.094	0.049	0.893	1.000							
K/C	0.439	-0.172	0.109	0.971	0.966	1.000						
Mg/C	0.350	-0.106	0.059	0.898	0.999	0.968	1.000					
V/C	0.501	-0.332	0.765	-0.334	-0.397	-0.360	-0.391	1.000				
Al/C	0.307	-0.078	0.026	0.884	0.997	0.961	0.996	-0.414	1.000			
Fe/C	0.323	0.050	-0.002	0.770	0.897	0.856	0.893	-0.320	0.902	1.000		
Ni/C	0.366	-0.231	0.651	-0.525	-0.437	-0.486	-0.433	0.875	-0.460	-0.395	1.000	
R _g	0.530	-0.580	0.683	0.115	0.073	0.106	0.080	0.466	0.050	-0.005	0.475	1.000
HO	δ	H/C	N/C	Na/C	Ca/C	K/C	Mg/C	V/C	Al/C	Fe/C	Ni/C	R _g
δ	1.000											
H/C	-0.404	1.000										
N/C	0.416	-0.312	1.000									
Na/C	0.374	-0.219	0.366	1.000								
Ca/C	0.500	-0.025	0.291	0.503	1.000							
K/C	0.362	-0.316	0.406	0.958	0.391	1.000						
Mg/C	0.441	0.014	0.276	0.480	0.995	0.369	1.000					
V/C	0.623	-0.210	0.237	0.536	0.495	0.521	0.443	1.000				
Al/C	0.401	0.056	0.225	0.419	0.981	0.295	0.980	0.430	1.000			
Fe/C	0.209	0.295	0.345	0.108	0.399	-0.016	0.393	0.319	0.395	1.000		
Ni/C	0.780	-0.370	0.279	0.412	0.420	0.423	0.357	0.942	0.342	0.285	1.000	
R _g	0.895	-0.515	0.249	0.410	0.311	0.403	0.242	0.645	0.186	0.167	0.810	1.000

ratio with vanadium and nickel contents in B6 asphaltenes suggests that interactions of chelated porphyrin compounds are important in the asphaltene aggregation mechanism. In fact, vanadium and nickel contents provided the highest correlation to aggregate size and solubility parameter in HO asphaltenes.

Small-angle neutron scattering (SANS) has proven useful for deducing the sizes and morphologies of asphaltene aggregates in solution. Various intra-particle structure factor models have been applied in the past to determine aggregate size parameters from scattering intensity curves of asphaltene solutions, but not all of these models accurately reflected the morphology of the asphaltene aggregates in solution. In another study, we showed that an oblate cylinder model with radius polydispersity best described the shape of asphaltene aggregates⁶. The polydisperse oblate cylinder model provided the lowest reduced χ^2 values of the various geometric models applied and values of the I_0 and R_G parameters that were consistent with Guinier parameters.

The polydisperse radius oblate cylinder model and a small-particle mass-fractal model were used to analyze the SANS scattering curves obtained for 108 asphaltene samples possessing a wide variation in the chemical composition of the asphaltenes and solvent quality⁷. Values of the apparent fractal dimension from the mass-fractal fits appeared to decrease with increasing aggregate size, suggesting that the smallest aggregate formers were more globular with little

surface roughness (i.e., $D \sim 3$) while the largest aggregate formers were more dendritic with higher surface roughness ($D \sim 2.2$ to 2.4). Typical values of the aggregate thickness from the polydisperse cylinder fits ranged from 5 to 32 Å, while the average particle radius ranged from 25 to 125 Å. The polydispersity in the particle radius appeared independent of the particle size and was approximately 30%. Assuming an asphaltene monomer consists of groups of condensed aromatic rings containing polar moieties that are interconnected by aliphatic chains (i.e., the “archipelago” model of asphaltene structure), the asphaltene aggregation mechanism might proceed through a series of localized stacking interactions of aromatic rings. The physical linkage of one ring system to another in a monomer somewhat increases the particle thickness, but significantly expands the aggregate in the radial dimension, where polydispersity in the aggregate size is most evident. Consistent with this presumed means of aggregate growth, the mean “aspect ratio” of these oblate cylindrical aggregates given by R_{avg}/L was observed to increase as aggregate radius of gyration or size increased (Figure 2).

Figure 2. Correlation of particle aspect ratio with average aggregate size parameters obtained from the polydisperse cylinder model for asphaltene fractions in mixtures of d-heptane and d-toluene. Inset shows a schematic representing an asphaltene aggregate of cylindrical shape.

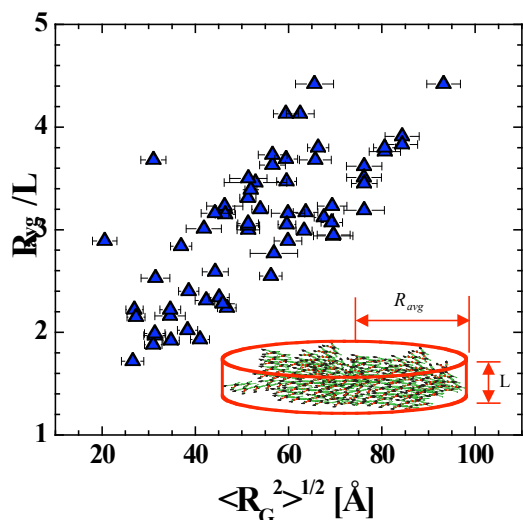


Figure 2. Correlation of particle aspect ratio with average aggregate size parameters obtained from the polydisperse cylinder model for asphaltene fractions in mixtures of *d*-heptane and *d*-toluene. Inset shows a schematic representing an asphaltene aggregate of cylindrical shape.

Discrepancies between average aggregate molecular weight values obtained from two independent methods suggested the need to include solvation effects in the calculations. Assuming that entrained solvent contributed to the coherent scattering of neutrons within the aggregates and effectively modified the scattering contrast between the solute and solvent, we estimated the amount of solvent entrainment in individual samples by forcing parity of the molecular weight calculations. Figure 3 provides estimates of entrained solvent within aggregates for solutions of various asphaltenes (1 % wt.) in mixtures of *d*-heptane

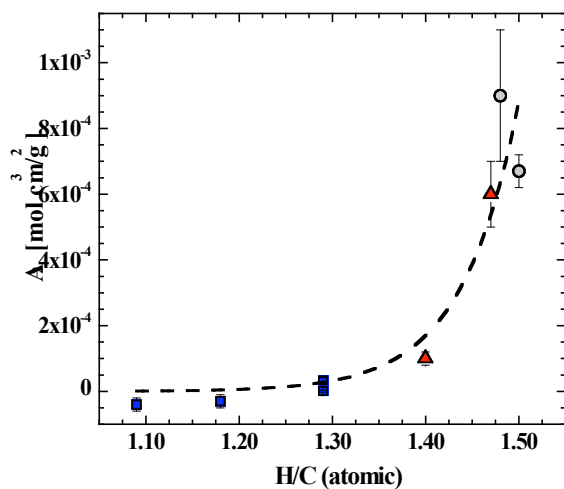


Figure 3. Estimated extent of solvent entrainment within aggregates as a function of aggregate size for asphaltene fractions dispersed in mixtures of *d*-heptane and *d*-toluene.

and *d*-toluene. Solvent entrainment within the aggregates roughly varied from 30 to 50% (v/v). These analysis methods may be extended to the determination of solvent entrainment within asphaltene-stabilized films observed in water-in-oil emulsions and the determination of selective solvent partitioning within asphaltene aggregates.

Changes in the apparent aggregate mass with concentration indicated deviations from ideal solution behavior (i.e., non-interacting asphaltenes plus solvent), which were quantified through the determination of aggregate second virial coefficients (A_2)⁸. A_2 values were previously reported or inferred of source crude, chemical composition, solvent conditions, and the influence of selective

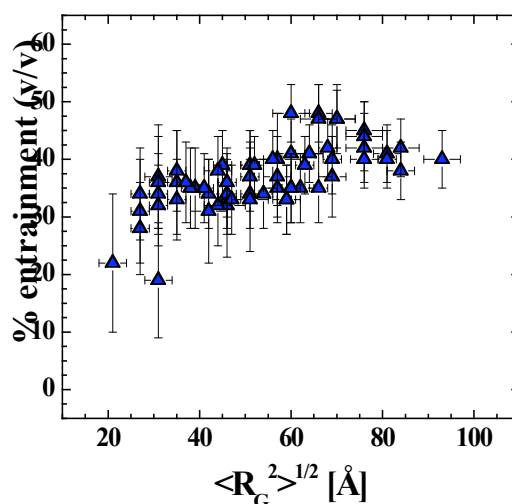


Figure 4. Correlation of second virial coefficients to atomic H/C ratio for (squares) asphaltenes, (circles) resins, and (triangles) mixtures of asphaltenes and resins in *d*-toluene.

solvating agents on asphaltene A_2 values from SANS and VPO experiments studying asphaltenes in toluene and 1,2-dichlorobenzene; however, this study was the first to investigate the roles

Results of the second virial determination for Hondo asphaltenes (0.25 – 4 % w/w) in *d*-toluene and 90:10 *d*-toluene: *d*-methanol (v/v) indicated that the aggregates experienced net repulsive interactions at these solvent conditions with A_2 values on the order of 10^{-5} mol cm^3/g^2 . A negative A_2 value was observed for HO2 asphaltenes in 40:60 *d*-heptane: *d*-toluene at the same concentration range, indicating flocculation (i.e., attractive interactions) of the aggregates. B6 resins effectively reduced the aggregate mass of HO1 asphaltenes in *d*-toluene and increased the magnitude of the observed A_2 values, likely through the disruption of aromatic π -bonding interactions within the aggregates. A_2 values appeared to vary significantly with chemical composition, specifically atomic H/C of

the solute mixture (Figure 4), suggesting that the interactions between asphaltenes, resins, and the d-toluene solvent are strongly dominated by dispersion and π -bonding interactions.

The magnitude of the experimentally measured A_2 values generally under-predicted or agreed with the values of A_2 calculated from an excluded volume model, suggesting that the types of interactions between the solute and solvent are not completely steric repulsive. The structure of asphaltene aggregates is more diffuse than that of a rigid body; thus, energetic interactions of the solute and entrained solvent are significant.

REFERENCES

1. E. Sheu and O. Mullins, eds. **Asphaltenes: Fundamentals and Applications**; Plenum Press: New York, 1995.
2. O. Mullins and E. Sheu, eds. **Structures and Dynamics of Asphaltenes**; Plenum Press: New York, 1995.
3. P. M. Spiecker, K. L. Gawrys, and P. K. Kilpatrick, "Aggregation and solubility behavior of asphaltenes and their subfractions," *Journal of Colloid and Interface Science*, 2003, **267**(1): p. 178-193.
4. P. M. Spiecker, K. L. Gawrys, C. B. Trail, and P. K. Kilpatrick, "Effects of petroleum resins on asphaltene aggregation and water-in-oil emulsion formation," *Colloids and Surfaces A: Physicochemical and Engineering Aspects*, 2003, **220**(1-3): p. 9-27.
5. K. L. Gawrys, G. A. Blankenship, and P. K. Kilpatrick, "On the distribution of chemical properties and aggregation of solubility fractions in asphaltenes," *Energy & Fuels* (accepted for publication).
6. K. L. Gawrys and P. K. Kilpatrick, "Asphaltene aggregates are polydisperse oblate cylinders," *Journal of Colloid and Interface Science*, 2005, **288**(2): p. 325-334.
7. K. L. Gawrys, G. A. Blankenship, and P. K. Kilpatrick, "Solvent entrainment in and flocculation of asphaltene aggregates probed by small-angle neutron scattering," *Langmuir* (submitted).
8. K. L. Gawrys and P. K. Kilpatrick, "Second virial coefficients of asphaltene aggregates in various solvents probed by small-angle neutron scattering," *Energy & Fuels* (submitted).

MECHANISM AND ENERGETICS OF THIRD PHASE FORMATION IN TBP SOLVENT EXTRACTION OF METAL SALTS

Renato Chiarizia, Chemistry Division, Argonne National Laboratory
Pappannan Thiyagarajan, IPNS Division, Argonne National Laboratory

The Problem

Liquid-liquid extraction has played a fundamental role in the development of nuclear science and technology, as the recovery of uranium and plutonium from irradiated fuel and the treatment of liquid nuclear wastes are largely based on solvent extraction separations. However, after several decades of studies and practical applications of liquid-liquid extraction to metal separations, some aspects of this technology remain insufficiently understood, as, for example, the unwanted phenomenon of third phase formation. Third phase formation is observed when, at high metal and/or mineral acid loading of the extractant, the organic phase splits into two liquid phases of different densities. The lighter phase contains most of the diluent and low concentrations of extractant and solutes, while the heavier or “third” phase is a highly concentrated solution of extractant, metal and acid. The splitting of the organic phase is the scourge of solvent extraction practitioners, since plants are designed to operate with two, not three, liquid phases. Furthermore, in the nuclear field, it is essential to avoid the risk of concentrating fissile materials in third phases because of criticality concerns.

Although a few qualitative explanations for third phase formation have appeared in the literature¹⁻³, a thorough physico-chemical description of this phenomenon is still lacking. A primary reason for this deficiency is that studies of metal extraction are usually approached from a metal-centered standpoint using models and procedures appropriated from coordination chemistry. For example, studies of metal solvent extraction are generally performed under the ideal conditions of low concentrations of cations and extractants that generally promote the existence of discrete, mononuclear metal-extractant complexes in the organic phase.

The complexes identified in this way, however, are very unlikely to exist under the conditions met in practice, where the extractant concentration is generally high and the organic phase often approaches saturation with respect to the extracted species. Under these more realistic conditions, the discrete metal-extractant entities familiar to coordination chemistry undergo self-assembly leading to the formation of much larger species, and to phase separation phenomena. We believe that these phenomena can only be understood by complementing the metal-centered approach traditionally followed in coordination chemistry, with a ligand-centered approach in which the major emphasis is on interactions between the molecules of the extractant and between its metal complexes. For this

reason, we have started an investigation of self-assembly phenomena and third phase formation with the goal of achieving a comprehensive description of mechanism and energetics of third phase formation in solvent extraction through a combination of coordination chemistry and concepts and techniques that are common in colloid chemistry.

The most important extractant molecule in nuclear technology as well as in other hydrometallurgical separations of industrial interest is the PUREX extractant tri-*n*-butyl phosphate (TBP) dissolved in an alkane diluent⁴. TBP selectively extracts uranium (VI), thorium (IV) and plutonium (IV) nitrates from nitric acid solutions leaving behind most fission products and the transition elements⁴. We elected to conduct our investigations of third phase formation in this important system for which no prior investigations have addressed the structures formed in the extractant phase at high solute loading.

Phase Diagrams and SANS Measurements

For each system investigated and for each set of experimental conditions, such as, diluent, TBP concentration and aqueous phase acidity, we determined the composition of the various phases in equilibrium before and after the critical point of organic phase splitting. A typical set of distribution data is shown in Figure 1 for the system composed of

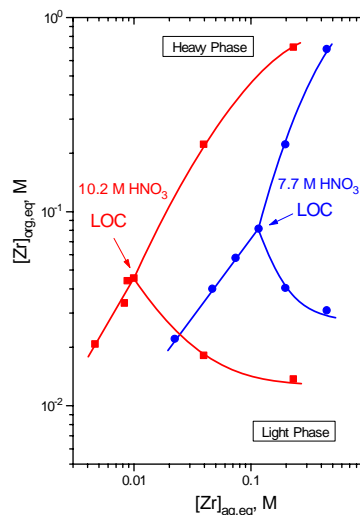


Figure 1. Distribution isotherm and simplified phase diagram for the distribution of $Zr(NO_3)_4$ between 7.7 M HNO_3 (blue circles) or 10.2 M HNO_3 (red squares) and 0.73 M TBP in *n*-octane at 23 ± 0.5 °C.

nitric acid and zirconium nitrate in the aqueous phase

and 0.73 M (20% (v/v)) TBP in *n*-octane.

In the figure, the critical point for each aqueous acidity is indicated as the LOC (limiting organic concentration) condition, i.e., the highest concentration of $\text{Zr}(\text{NO}_3)_4$ that can exist in the TBP phase without third phase formation. The points on the left of the LOC conditions refer to a biphasic system; those on the right refer to a triphasic system where the aqueous phase is in equilibrium with two organic phases, one containing very little solute, the other one containing most of the organic metal salt. The extractant, TBP in this case, also distributes asymmetrically in favor of the heavy phase after reaching the LOC condition. The critical point for phase splitting is a strong function of temperature. Therefore all the experiments were conducted at the constant temperature of 23 ± 0.5 °C.

The key tool in our studies of the aggregates in organic solutions of TBP after extraction of metal nitrates and nitric acid was the technique of small-angle neutron scattering (SANS). By using deuterated diluents, the large difference in the ability of ^1H and ^2H to scatter neutrons assists greatly in defining the size and shapes of structures created as solute molecules spontaneously organize. We applied the SANS technique to investigate third phase formation in the extraction of uranyl, thorium, plutonium and zirconium nitrates by TBP dissolved in *n*-alkanes at concentrations (20-30% (v/v)) representative of the PUREX process⁵⁻¹⁴. The measurements were performed at the time-of-flight small-angle neutron diffractometer (SAND) at IPNS¹⁵. A typical set of SANS data is shown in Figure 2 for the extraction of increasing amounts of $\text{Th}(\text{NO}_3)_4$ by TBP, up to the LOC condition. The data in Figure 2 clearly show a pronounced increase in scattering intensity in the low Q range for increasing amounts of metal nitrate transferred into the organic phase up to the LOC condition. This intensity increase has been the subject of our modeling efforts.

Model Development

We have interpreted the increase in scattering intensity with an increase of the metal concentration in the organic phase by using two different models: particle growth and particle interaction. The particle growth model assumes that any increase in scattering intensity observed in the low Q region arises from an increase in size of non-interacting particles as more metal salt or acid is extracted into the TBP solution. The SANS data for all systems investigated could be fit satisfactorily by using Guinier and modified Guinier analysis for rod-like particles and the form factors of cylinders or ellipsoids of rotation. However, according to this model, the critical LOC condition was always characterized by weight-average TBP aggregation numbers, n_w , that could reach values as large as 50 and higher, indicating the formation of very large cylindrical or ellipsoidal “super-aggregates” with

radius and length values up to ~ 13 and ~ 200 Å, respectively. These results were considered unrealistic, because there are no reports in the literature describing aggregates of this size in organic solutions of TBP. Since TBP third phases are typically formed under conditions in which ideal behavior can no longer be assumed (high solute concentrations), we decided that it was prudent to re-examine our SANS data using a different model.

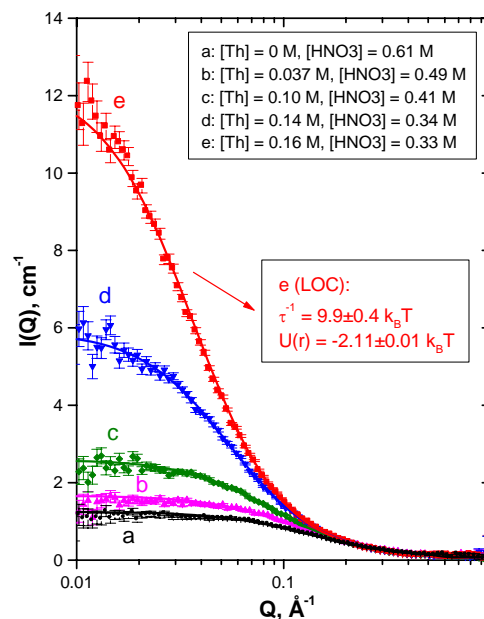


Figure 2. SANS data and best fit curves for the extraction of $\text{Th}(\text{NO}_3)_4$ from 5 M HNO_3 by 0.73 M TBP in *n*-octane at 23 ± 0.5 °C. See text for the fitting procedure.

We concluded that a more realistic picture of the TBP aggregates in solution could be obtained by applying concepts frequently used in colloid chemistry. The links between TBP coordination chemistry and colloid chemistry stem from the facts that: i) all extractants, including TBP, are by definition amphiphiles, i.e., they have both polar and non-polar components in the same molecule; ii) TBP is known to form small reverse micelles in non-polar diluents¹⁶; iii) third phase formation strongly resembles cloud-point phase separation¹⁷. Based on these considerations, we hypothesized that the increase in scattering intensity as the conditions of phase splitting are approached may be better interpreted by using a model based on interactions between small TBP reverse micelles rather than on micellar growth. In this case, success depends on the ability to evaluate the structure factor, $S(Q)$, that describes the correlation between micelles due to intermicellar interactions. A convenient way to calculate short-range interactions between colloidal aggregates is offered by Baxter’s model for hard spheres with surface adhesion (also known as the

“sticky spheres” model)¹⁷⁻¹⁹. Some features of the model, relevant for this work, are shown in Figure 3.

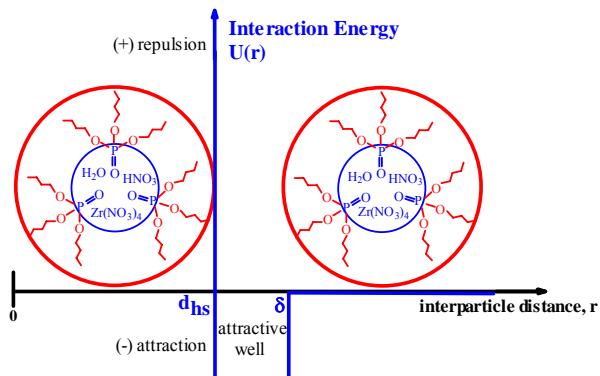


Figure 3. Schematic representation of the interaction between small TBP reverse micelles containing zirconium nitrate, nitric acid and water in their polar core.

In Figure 3, r is the distance between two particles, d_{hs} is the hard sphere diameter, i.e., the distance from the origin below which the particles become incompressible, and $(\delta - d_{hs})$ represents the width of a square-well attraction potential. When the distance between the left rims of two particles equals d_{hs} (i.e., the particles are in contact), the repulsion becomes infinite, while for a distance larger than δ , the attraction between particles vanishes. For a distance larger than d_{hs} but smaller than δ , the particles experience attraction. In this case, it is possible to calculate an approximate value of the potential energy of attraction (negative) between two hard spheres, $U(r)$, expressed in $k_B T$ units (where k_B is the Boltzmann constant), through the equation:

$$U(r) = \lim_{\delta \rightarrow d_{hs}} \ln \left[12 \tau \left(\frac{\delta - d_{hs}}{d_{hs}} \right) \right] \quad \text{for } d_{hs} < r < \delta \quad (1)$$

Use of eq. 1 requires knowledge of the parameter τ . The reciprocal τ , τ^{-1} , also expressed in $k_B T$ units, is the “stickiness parameter” and its value is higher when the adhesion between particles is stronger. The limit in eq. 1 indicates that the calculation of the interparticle attraction potential energy is valid only when the attractive well is extremely narrow, i.e., with a width within 10% of the particle diameter ($(\delta - d_{hs}) / d_{hs} \leq 0.1$). An important advantage of Baxter model approximation is that analytical expressions have been derived for the structure factor $S(Q)$ in terms of the parameter τ ¹⁷⁻¹⁹.

Results and Discussion

To apply the Baxter model to our SANS data, the neutron scattering intensity was expressed as:

$$I(Q) = \eta V_p (\rho_p - \rho_s)^2 P(Q) S(Q) + I_{inc} \quad (2)$$

where η is the solute volume fraction, V_p is the particle volume, ρ_p and ρ_s are the scattering length densities of the extractant and solvent, respectively, $P(Q)$ is the form factor of a sphere having a radius equal to $d_{hs}/2$, $S(Q)$ is the structure factor, and I_{inc} is the incoherent scattering background. The three parameters I_{inc} , d_{hs} and τ were used as independent fit parameters and were optimized using the nonlinear curve fitting features of the Origin™ program (Microcal Software, Inc.). Figure 2 (continuous lines) shows the fit to the SANS data in the figure together with the fit parameters for the LOC sample. Similar results were obtained for all other cases investigated. Figure 4 shows the strong sensitivity of the calculated $I(Q)$ values to small variations in the d_{hs} and τ parameters for one of the thorium nitrate – TBP samples.

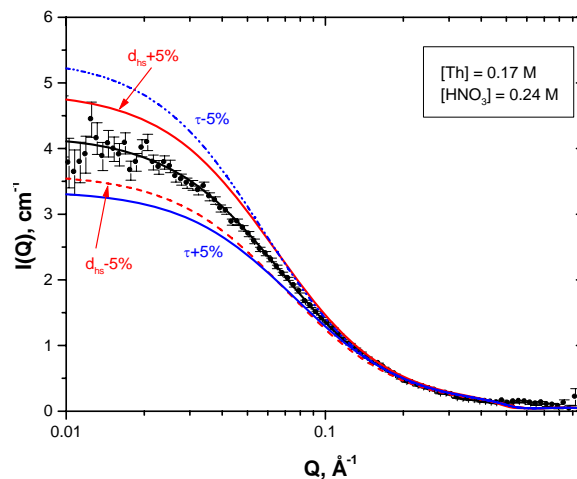


Figure 4. SANS data and $I(Q)$ curves calculated with a $\pm 5\%$ variation of the τ and d_{hs} values for the extraction of $\text{Th}(\text{NO}_3)_4$ from 2.5 M HNO_3 by 0.73 M TBP in n -octane at 23 ± 0.5 °C.

Figure 5 shows the calculated $P(Q)$ and $S(Q)$ curves together with the experimental and calculated $I(Q)$ values for the same sample as in Figure 4. The $S(Q)$ curve exhibits a pronounced maximum at $Q = 0.5 \text{ \AA}^{-1}$. This Q value corresponds to the correlation distance between interacting particles, d , through Bragg’s law in the form $d = 2\pi/Q_{max}$. For all samples and systems investigated, the correlation distance provided by the maximum in the $S(Q)$ curve was systematically about 2 Å shorter than the d_{hs} value, indicating that the two interacting micelles are not completely hard but interpenetrate to some extent. For each sample, the value of the hard-sphere diameter, d_{hs} , obtained from the Baxter model fit of the SANS data, was used to calculate the volume of the spherical scattering particles. From the composition of each sample, it was possible to calculate the volumes of the polar core and of the lipophilic shell of the micelles. Finally, the weight-average TBP aggregation number, n_w , was calculated by dividing the volume of the shell by the molecular volume of TBP.

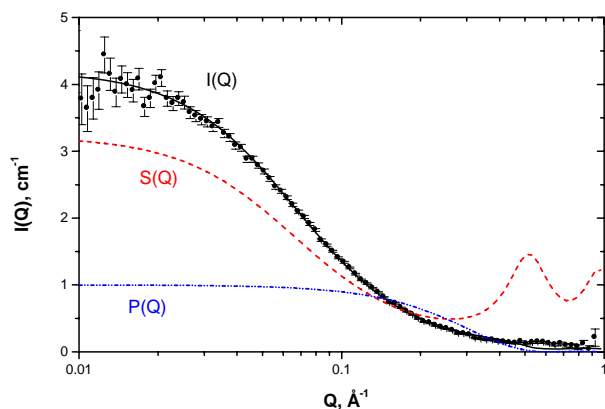


Figure 5. SANS data and $I(Q)$, $P(Q)$ and $S(Q)$ curves calculated for the same sample in Figure 4.

Table 1 collects some representative results from the Baxter model calculation for the LOC samples for the various systems investigated.

The results in Table 1 indicate that according to the particle interaction model, the TBP aggregation number, n_w , remains small, in the 2 to 4 range, up to the point of phase splitting (LOC samples). The d_{hs} values, in the range of 13 to 15 Å, agree with molecular modeling calculations showing that the TBP molecule has a length of 7.1 Å¹⁰. The critical values of the stickiness parameter and intermicellar interaction energy are constants, characteristic of each solvent extraction system (diluent and TBP concentration). Their values are higher in *n*-octane than in *n*-dodecane, a diluent in which phase splitting is achieved more readily. The data in Table 1 also show that in moving from $UO_2(NO_3)_2$ to $Th(NO_3)_4$ and to $Zr(NO_3)_4$, a progressively lower concentration of the salt in the organic phase is required for phase splitting to occur.

At the point of phase splitting, the value of the intermicellar attraction energy is essentially constant ($\sim 2k_B T$) for the various metal nitrates investigated. However, we discovered that the type of metal nitrate determines how rapidly the interaction energy increases upon extraction of increasing amounts of solutes by the TBP solution. More precisely, the derivative of the interaction energy with respect to total nitrate concentration in the organic phase is a function of specific physico-chemical properties of the extracted cation, e.g., charge-to-ionic radius ratio, ionization potential and hydration enthalpy. This is shown in Figure 6, where the derivative of $-U(r)$ with respect to the total nitrate concentration in the organic phase is plotted as a function of the hydration enthalpy of the cations (whose values are available from the literature²⁰).

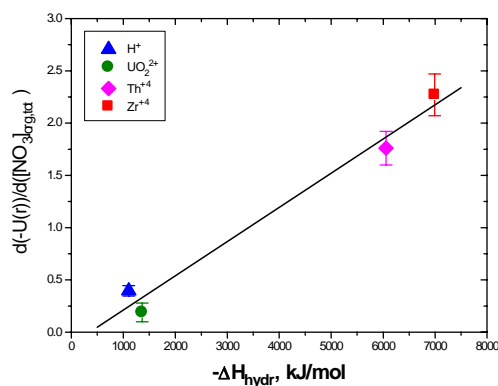


Figure 6. Plot of $d(-U(r))/d([NO_3]_{org,tot})$ vs. the enthalpy of hydration for the extraction of the nitrates of various cations by 0.73 M TBP in *n*-octane at 23 ± 0.5 °C.

Although based on the behavior of only four cations, the data in Figure 6 clearly confirm that when a cation is transferred from an aqueous phase into a 20 % TBP solution in *n*-octane, its effect on promoting third phase formation, as measured by how rapidly the energy of interaction between reverse micelle-like particles reaches the critical value of $\sim 2 k_B T$, strongly depends on its charge and size and other related physico-chemical parameters.

Conclusions

SANS measurements performed at the SAND instrument of IPNS have allowed us to provide an answer to the vexing old question of why the phenomenon of third phase formation in solvent extraction occurs. We have developed a simple model that involves micellization of the extractant and van der Waals interactions between small reverse micelles in the organic phase.

According to this model, the small reverse micelles formed by the extractant in the organic phase are subjected to two contrasting physical forces. Thermal energy, $k_B T$, tends to keep the micelles dispersed in the solvent, while intermicellar attraction causes micellar adhesion. The latter factor becomes stronger as increasing amounts of polar solutes are transferred into the organic phase. As long as these two energies are comparable, the organic phase remains stable. The separation of most of the solute particles in a third phase takes place when the energy of attraction between the particles in solution becomes about twice the average thermal energy.

More research is planned to verify the general validity of the micellization/interaction model of third phase formation by extending our SANS measurements to more complex solvent extraction systems involving other families of extraction reagents and diluents, and other extracted inorganic species. The ultimate goal of our investigations is to provide a more efficient and scientifically sound management of this type of

phenomena through a thorough description of its physical chemistry.

Acknowledgments

We thank K. C. Littrell and D. G. Wozniak (IPNS), M. P. Jensen and P. G. Rickert (CHM), and K. L. Nash and M. Borkowski (formerly of CHM) for participating at various levels in this project.

This work was funded by the U. S. Department of Energy, Office of Basic Energy Science, Division of Chemical Sciences, Biosciences and Geosciences (for the part performed at the Chemistry Division of ANL) and Division of Material Science (for the part performed at IPNS). The submitted manuscript has been created by the University of Chicago as Operator of Argonne National Laboratory ("Argonne") under Contract No. W-31-109-ENG-38 with the U.S. Department of Energy. The U.S. Government retains for itself, and others acting on its behalf, a paid-up, nonexclusive, irrevocable worldwide license in said article to reproduce, prepare derivative works, distribute copies to the public, and perform publicly and display publicly, by or on behalf of the Government.

REFERENCES

- [1] Y. Marcus and A. S. Kertes. *Ion Exchange and Solvent Extraction of Metal Complexes*; Wiley Interscience: New York, NY, 1969, p 715.
- [2] K. Osseo-Asare. In *Metal Separation Technologies Beyond 2000: Integrating Novel Chemistry with Processing*; Liddel, K. C., Chaiko, D. J., Eds.; The Minerals, Metals & Materials Society: Warrendale, PA, 1999, pp 339-346.
- [3] L. Lefrançois, F. Belnet, D. Noel and C. Tondre. *Sep. Sci. Technol.* **1999**, *34*, 755-770.
- [4] A. Naylor and P. D. Wilson. In *Handbook of Solvent Extraction*, T. C. LO, M. H. I. Baird and C. Hanson, Eds.; J. Wiley and Sons: New York., NY, 1983, pp 783-798.
- [5] R. Chiarizia, M. P. Jensen, M. Borkowski, J. R. Ferraro, P. Thiyagarajan and K. C. Littrell. *Sep. Sci. Technol.* **2002**, *38*, 3313-3331.
- [6] M. Borkowski, R. Chiarizia, M. P. Jensen, J. R. Ferraro, P. Thiyagarajan and K. C. Littrell. *Sep. Sci. Technol.* **2002**, *38*, 3333-3351.
- [7] M. P. Jensen, R. Chiarizia, J. R. Ferraro, M. Borkowski, K. L. Nash, P. Thiyagarajan and K. C. Littrell. In *Proceedings of the International Solvent Extraction Conference, ISEC 2002*, K. C. Sole, P. M. Cole, J. S. Preston and D.J. Robinson, Eds., South African Institute of Mining and Metallurgy: Johannesburg, South Africa, 2002, pp 1137-1142.
- [8] R. Chiarizia, M. P. Jensen, M. Borkowski, J. R. Ferraro, P. Thiyagarajan and K. C. Littrell. *Solvent Extr. Ion Exch.* **2003**, *21*, 1-27.
- [9] R. Chiarizia, P. Thiyagarajan, M. P. Jensen, M. Borkowski and K. C. Littrell. In *Proceedings of Hydrometallurgy 2003, Fifth International Conference in Honor of Prof. Ian Ritchie*, C. A. Young, A. M. Alfantazi, C. G. Anderson, D. B. Dreisinger, B. Harris and A. James, Eds., TMS (The Minerals, Metals and Materials Society), Warrendale, PA, 2003, Vol. 1, Leaching and Solution Purification, pp 917-928.
- [10] R. Chiarizia, K. L. Nash, M. P. Jensen, P. Thiyagarajan and K. C. Littrell. *Langmuir*, **2003**, *19*, 9592-9599.
- [11] R. Chiarizia, M. P. Jensen, M. Borkowski, P. Thiyagarajan and K. C. Littrell. *Solvent Extr. Ion Exch.*, **2004**, *22*, 325-351.
- [12] R. Chiarizia, M. P. Jensen, Z. Kolarik, M. Borkowski and P. Thiyagarajan. *Langmuir*, **2004**, *20*, 10798-10808.
- [13] R. Chiarizia, M. P. Jensen, M. Borkowski and K. L. Nash. *A New Interpretation of Third Phase Formation in the Solvent Extraction of Actinides by TBP*, in *Separations for the Nuclear Fuel Cycle in the 21st Century*, G. J. Lumetta, K. L. Nash, S. B. Clark and J. I. Friese, Eds., ACS Symposium Series, American Chemical Society, Washington, DC, 2005, *in press*.
- [14] J. Plaue, A. Guelis, K. Czerwinski, P. Thiyagarajan and R. Chiarizia. *Small-Angle Neutron Scattering Study of Plutonium Third Phase Formation in 30% TBP/HNO₃/Alkane Diluent Systems.*, *Solvent Extr. Ion Exch.*, **2005**, *in press*.
- [15] P. Thiyagarajan, J. E. Epperson, R. K. Crawford, J. M. Carpenter, T. E. Klippert and D. G. Wozniak. *J. Appl. Cryst.* **1997**, *30*, 280-293.
- [16] K. Osseo-Asare. *Adv. Colloid Interface Sci.* **1991**, *37*, 123-173.
- [17] C. Erlinger, L. Belloni, Th. Zemb and C. Madic. *Langmuir*, **1999**, *15*, 2290-2390.
- [18] R. J. Baxter. *J. Chem. Phys.* **1968**, *49*, 2770-2774.
- [19] S. V. G. Menon, V. K. Kelkar and C. Manohar. *Physical Review A*, **1991**, *43*, 1130-1133.
- [20] Y. Marcus. *Ion Properties*. Marcel Dekker, Inc.: New York, NY, 1997.

Table 1. Selected results from Baxter model calculations for LOC samples with 20% TBP in *n*-octane

Extracted Species	[HNO ₃] _{aq} M	LOC M	[HNO ₃] _{org} at LOC M	n _w	d _{hs} , Å	τ ⁻¹ , k _B T	U(r), k _B T
HNO ₃	10.2	/ ^a	0.81 ^a	2.5±0.2	13.6±0.2	6.1±0.1	-1.62±0.02
UO ₂ (NO ₃) ₂	10.0	0.23	0.27 ^b	3.7±0.4	14.7±0.6	7.1±0.1	-1.78±0.01
Th(NO ₃) ₄	5.0	0.16	0.33	3.4±0.4	14.4±0.5	9.9±0.4	-2.11±0.01
Zr(NO ₃) ₄	7.7	0.081	0.62	1.9±0.1	12.4±0.2	9.9±0.1	-2.11±0.01

- a) This sample does not represent a LOC condition: no third phase formation takes place in the extraction of HNO₃ without metal salts under the experimental conditions used;
- b) *n*-dodecane diluent.

MISANS (Modulated Intensity Small Angle Neutron Scattering)*

M. Bleuel[#], E. Lang, J. Lal, ANL, Argonne, IL 60439, U.S.A.
R. Gahler, ILL, Grenoble, France

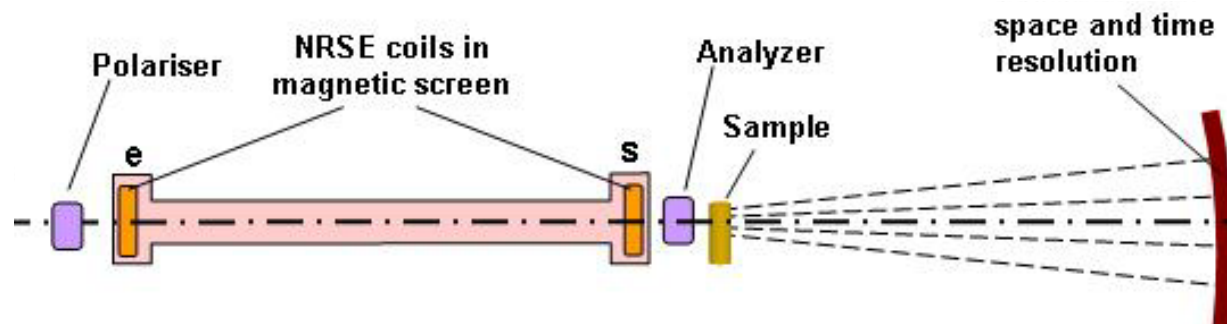


Figure 1: Schematic of the MISANS instrument

Abstract

A new kind of spectrometer will be installed at the SASI beamline at the IPNS which combines small angle and spin echo techniques to determine structure and dynamics of nanostructured samples.

INTRODUCTION

In 2004 a new project was started at the IPNS in order to develop a new kind of neutron instrument. So far there exists no neutron spin echo (NSE) spectrometer on any pulsed source in the world. Since an NSE spectrometer would hugely benefit from the broad wavelength band and the time structure of every neutron pulse [1] several attempts are under development worldwide in order to adapt this technique to a modern pulsed neutron source like the Spallation Neutron Source (SNS). The planned MISANS instrument (see Figure 1) is unique [2]. This technique can be adapted to use the full pulse width of the neutron source and thus has higher neutron utilization than other planned NSE spectrometers. Further, the design includes a full scale small angle detector, which makes this spectrometer a hybrid where both structure and dynamics in samples can be measured. For example, spatial and dynamic information of nanoparticles can be collected with high resolution at the same time. Another unique feature of this technique is that the analyzer is placed before the sample ensuring that the neutrons at the sample are already polarized. This enables the application of external magnetic fields at the sample, to study magnetic samples (e.g. nanomagnets), without the prohibitive loss of intensities encountered in other NSE spectrometers [3]. Furthermore, the MISANS instrument makes strong gains in contrast, as the signal is not affected by spinflip scattering (in conventional NSE spectrometers it is often required to replace the hydrogen in the sample with deuterium).

CONCEPT

MISANS is designed to measure dynamics and structure at the same time. The most likely field of application will be biological, soft matter, and nanomagnetism research. Most samples are mixtures of spinflip and non spinflip scattering atoms, which means that other spinecho techniques, classical with static fields [1], as well as neutron resonance spin echo (NRSE), experience significant intensity losses when measuring such samples, due to the depolarization of beam from spin flip. In addition, as of the date of publication, no other NSE spectrometer provides a polarized beam at the sample as a standard feature, which makes MISANS a perfect tool for the measurement of magnetic dynamics on nanometer scales.

The basic idea of this spectrometer is to simulate the effect of static fields with RF-fields. Figure 2 shows the successful test of one of the MISANS coils in March 2005 [4]. As can be seen in Figure 2, the Larmor-precession frequency increased from 1kHz (static fields) to 3kHz (static fields + RF fields). An intensity modulation of the RF amplitude makes sure that the oscillation is independent from the neutron wavelength.

Parallel to these tests, at the neutron small angle scattering instrument (SASI), Argonne was prepared to install the new components including new focusing solid state collimators, which are new neutron optical components developed for SASI in FY05 and will be useful for other neutron beamlines.

The test of the polarizer for the SASI beamline failed; however, and the component had to be sent back to the vendor for repairs. It was scheduled for return in November 2005.

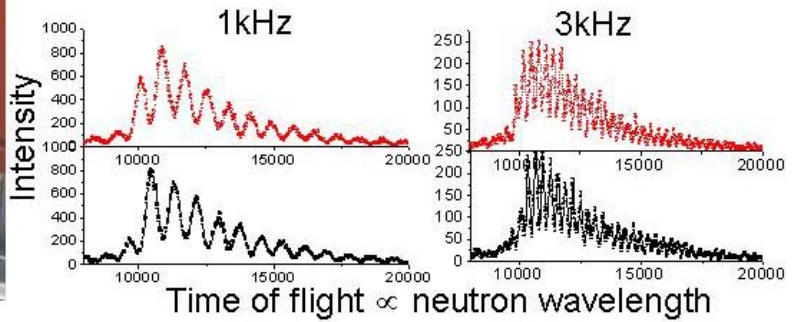


Figure 2: Test of a MISANS coil on the polarized reflectometer Posy1, Argonne

OUTLOOK

In the near future the MISANS instrument will be moved to its final position at the SASI beamline at Argonne. Some benchmark experiments which show the performance of the new instrument are planned, followed by the integration of the instrument into the user mode of SASI. The performance of the beamline will be expanded to be the first polarized SANS beamline on a pulsed source and the first MISANS instrument in the world. An important part of the design was to be able to reverse all changes on the beamline very quickly. It will be possible to unpolarize the beamline within two minutes and gain an intensity factor of two, and to install/uninstall the MISANS coils within a few hours.

REFERENCES

- [1] F. Mezei 'The Application of NSE on pulsed neutron sources', Nuc. Instr. And Meth 164 (1979) 153
- [2] M. Bleuel, K. Littrell, R. Gaehler, J. Lal 'MISANS a method for quasi-elastic small angle neutron scattering experiments', Physica B 356/1-4 (2004) 213-217
- [3] M. Bleuel, F. Demmel, R. Gaehler, R. Golub, K. Habicht, T. Keller, S. Klimko, I. Koeper, S. Longeville, S. Prokudaylo in F. Mezei, C. Pappas (Eds.) Neutron Spin Echo Spectroscopy, Lec. Not. Phys. 601, Springer, Berlin (2002) 176
- [3] M. Bleuel, M. Bröll, E. Lang, K. Littrell, R. Gähler, J. Lal 'First tests of a MIEZE (modulated intensity by Zero effort)-type instrument on a pulsed neutron source', to be published in Physica B (2005)

STRUCTURAL TRANSITIONS OF BLOCK COPOLYMERS IN LIQUID CRYSTAL SOLVENT

Neal R. Scruggs, Rafael Verduzco, Michael D. Kempe, and Julia A. Kornfield

Division of Chemistry and Chemical Engineering, California Institute of Technology, Pasadena, CA 91125

Jyotsana Lal

Intense Pulsed Neutron Source, Argonne National Laboratory, Argonne, IL 60439

Abstract

Triblock copolymers having random coil polymer endblocks and a side-group liquid crystalline polymer (SGLCP) midblock self-assemble in small-molecule liquid crystal (LC) solvent to form physical gels. These gels are optically uniform, thermoreversible, and can be rapidly switched at modest electric fields, making them ideal candidates for printable display technology. An understanding of the gels' nanostructure is gained from small-angle neutron scattering (SANS) from diblock copolymer analogues. The results show that the size of the micellar structures can be varied by molecular design of the SGLCP midblock. It is also demonstrated that the solvent's transition from the nematic LC phase to the isotropic phase is accompanied by a change in solvent quality, causing the micelle cores to swell.

INTRODUCTION

Recently we have developed a new class of materials that use block copolymer self-assembly and the dramatic change in solubility at the nematic-isotropic transition to create thermoreversible nematic gels (Figure 1).^{1, 2} Reversibility makes them ideal for a new paradigm in fabrication of liquid crystal displays (LCDs) in which printing is used to enable continuous production. Their optical uniformity is excellent as a consequence of the self-healing character of self-assembled nanostructure and they exhibit rapid switching speed at moderate threshold electric field (Figure 2).

Triblock copolymers are designed with a side-group liquid crystal polymer (SGLCP) midblock and random coil polymer endblocks. The midblock is well solvated by small-molecule liquid crystal (LC) solvent yielding a single-phase, optically uniform gel. The endblocks are chosen to be a random coil polymer (polystyrene, PS) that readily dissolves in isotropic solvent, but is insoluble in nematic solvent. Thus, the immiscible endblocks associate with one another in the nematic phase to form the gel's physical crosslinks, but become solvated upon transition to the isotropic phase. This change in solubility is the basis for the gels' thermoreversibility; the sol-gel transition is

triggered by the solvent's nematic-isotropic phase transition.

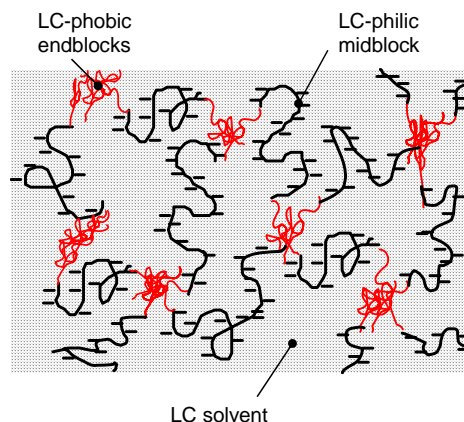


Figure 1. Schematic diagram of a nematic liquid crystalline gel self-assembled from a coil-LC-triblock copolymer. When dissolved in LC solvent, the LC-phobic endblock associate with one another to form the gel's physical crosslinks while the LC-philic midblock forms the network strands, spanning between crosslinks.

Neutron scattering is a central tool in discovering the underlying physics that governs the nanostructure, dynamics, rheology, and optical properties of these new materials. For example, prior small-angle neutron scattering

(SANS) results showed that molecular design of the mesogenic side groups on the midblock strongly alters both the sense and degree of spontaneous anisotropy of the polymer backbone (Figure 3), explaining the shear-induced alignment tendency of PS-SGLCP-PS gels¹ and the mechano-orientational coupling that governs, for example, dramatic banded structures that form in these gels.³

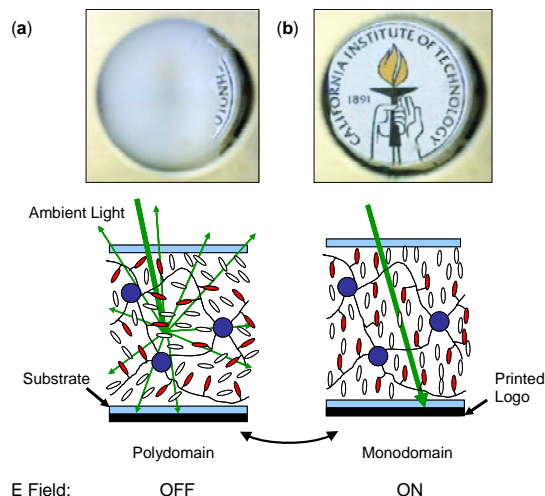


Figure 2. Nematic gels can be switched from (a) a light-scattering, unaligned (polydomain) state to (b) an optically clear, uniformly aligned monodomain using modest electric fields. In this case, 40 V_{rms} is applied to layer of gel 25 μm thick and switching is achieved in under 100 ms. (Reprinted from Kempe et al.¹)

MATERIALS AND METHODS

Linear diblock copolymers having a random coil (polystyrene, PS) polymer block and a SGLCP block are synthesized by attaching LC “mesogens” to the backbone of a readily available precursor polymer (PS-*b*-1,2 polybutadiene). The mesogens are chosen to confer solubility in a common nematic LC (4-pentyl-4'-cyanobiphenyl, 5CB) having T_{NI} = 35 °C (Figure 1). We employ two inherently different mesogens to explore two different types of polymer-LC coupling. In the first type, called “end-on” attachment, the mesogen is connected with its long axis perpendicular to the polymer backbone. In the second type, called “side-on” attachment, the mesogen is connected with its long axis parallel (Figure 4).

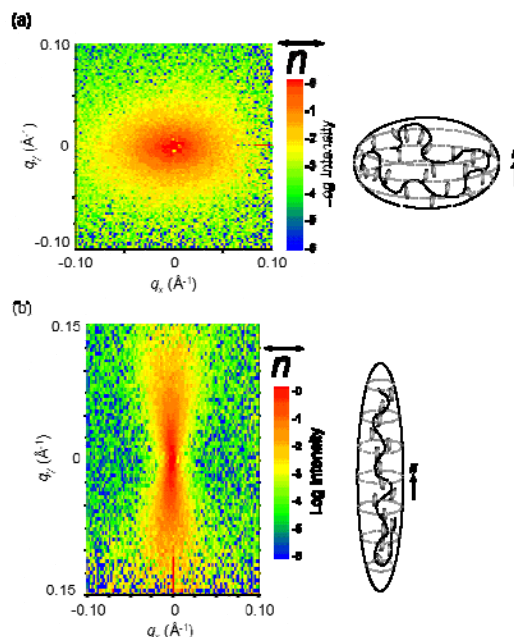


Figure 3. SANS of dilute solutions of side-group liquid crystalline polymers in nematic solvent reveals the coupling of polymer conformation with LC order. (a) When the polymer side-groups are attached perpendicular to the backbone (end-on) the polymer adopts a moderately anisotropic oblate ellipsoid conformation. (b) When the polymer side-groups are attached parallel to the backbone (side-on) the polymer adopts a strongly anisotropic prolate ellipsoid conformation. (Reprinted from Kempe et al.¹)

In order to obtain sufficient contrast, polymers are dissolved in perdeuterated 5CB having a deuterium content of greater than 95%.⁴ Two-dimensional scattering patterns are collected from these solutions on the Small-Angle Scattering Instrument (SASI) at a fixed temperature. Solutions of diblock copolymers are prepared at concentrations of 2, 5, 10, and 20 wt % polymer and scattering patterns collected from the unaligned, polydomain samples. This results in globally isotropic scattering that can be azimuthally averaged for improved signal to noise ratio.

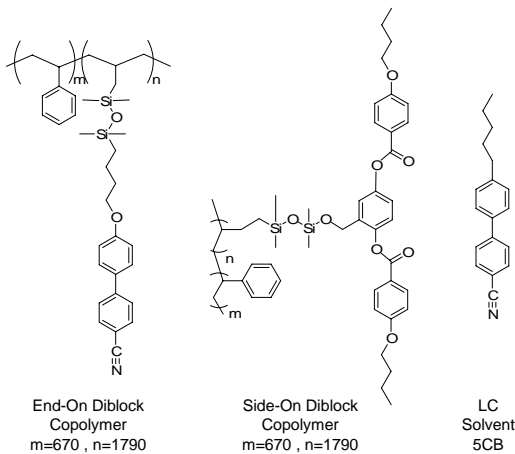


Figure 4. Chemical structures of the coil-LC diblock copolymers and small-molecule LC solvent

CHANGE IN SOLVENT QUALITY CORRELATES WITH CHANGE IN NANOSTRUCTURE

Scattering patterns were collected from solutions of end-on and side-on diblock copolymers at two different temperatures: one in the nematic phase (25 °C) and one in the isotropic phase (37 °C) (Figure 5). The results show a marked change in the self-assembled nanostructure coincident with the isotropization of the LC solvent. Peaks at low values of Q are indicative of micellar structures. The scattered intensity from a solution of spherical, monodisperse block copolymer micelles is written as the product of a constant, K , a structure factor, S , describing inter-particle correlations and a form factor, P , describing intra-particle correlations. In the nematic phase, a strong structure factor peak is observed at low Q in the scattering from end-on diblock solutions at all concentrations (Figure 5a). In the case of side-on polymers (Figure 5b), the structure factor peak is shifted to lower Q beyond the accessible range of the instrument.

The dramatic shift in the position of the structure factor peak from end-on to side-on copolymer indicates that the side-on diblock micelles are spaced much further apart. Prior SANS experiments¹ on SGLCP homopolymers with similar mesogenic structures showed the side-on chains to be highly-elongated as a result of strong coupling of the polymer conformation

to orientational order of the LC solvent (Figure 3). Therefore, the chains in the corona of the side-on polymer micelles are expected to be similarly elongated in the nematic phase creating larger micelles and a greater core-to-core distance.

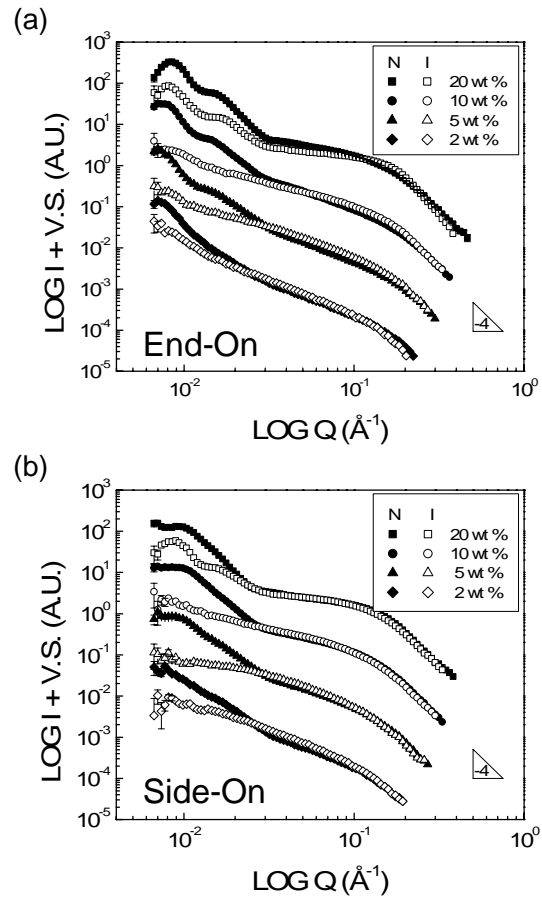


Figure 5. Azimuthally averaged scattering patterns from a concentration series of (a) end-on and (b) side-on diblock copolymers at temperatures in the nematic phase (25 °C, closed symbols) and in the isotropic phase (37 °C, open symbols). Data for each concentration are successively shifted down one order of magnitude for clarity.

A striking observation from the scattering patterns is the persistence of self-assembled micellar structures in the isotropic phase, where 5CB is a good solvent for both blocks. Peaks at low Q , similar to those observed at 25 °C, are clearly observed in the scattering patterns from 20 wt % end-on and side-on samples at 37 °C. The presence of micelles at lower concentrations

in the isotropic phase is evidenced by the scaling of the high- Q intensity with Q^{-4} (the Porod law⁵ scaling for structures containing a sharp interface). Pairwise thermodynamic interactions between PS, SGLCP, and 5CB inferred from the ternary phase diagram of these components⁶ show that self-assembly in the isotropic phase is driven by the slight preference of the solvent for the SGLCP block at polymer concentrations less than approximately 10 wt % and by unfavorable PS-SGLCP interactions at higher concentration (e.g. 20 wt % polymer).

Although self-assembly persists into the isotropic phase, the change in solvent quality that accompanies the nematic-isotropic transition is, nevertheless, apparent. The increased affinity of isotropic 5CB for the PS block results in substantial penetration of solvent into the PS cores and results in a decrease in neutron scattering contrast. Thus, the scattered intensity in the isotropic phase is decreased relative to the nematic.

SUMMARY

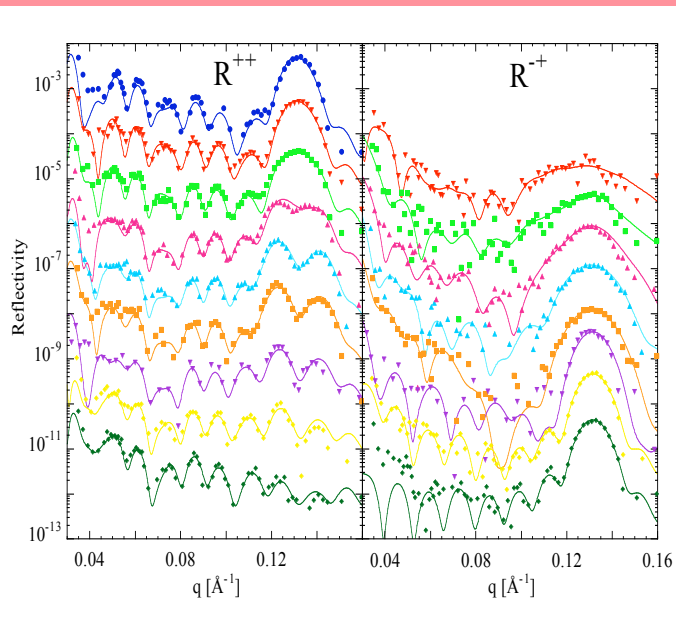
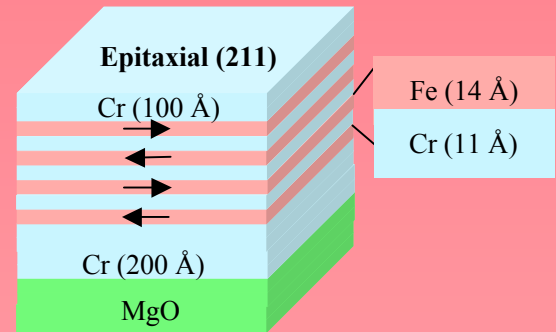
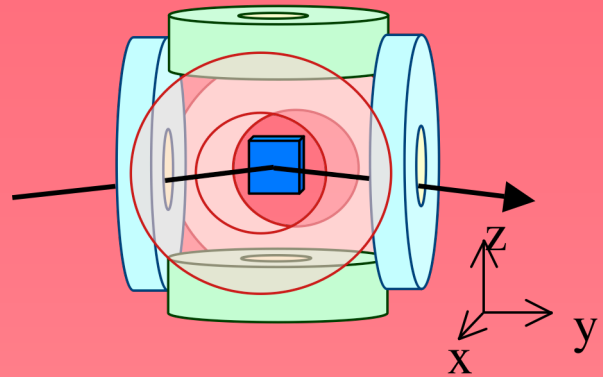
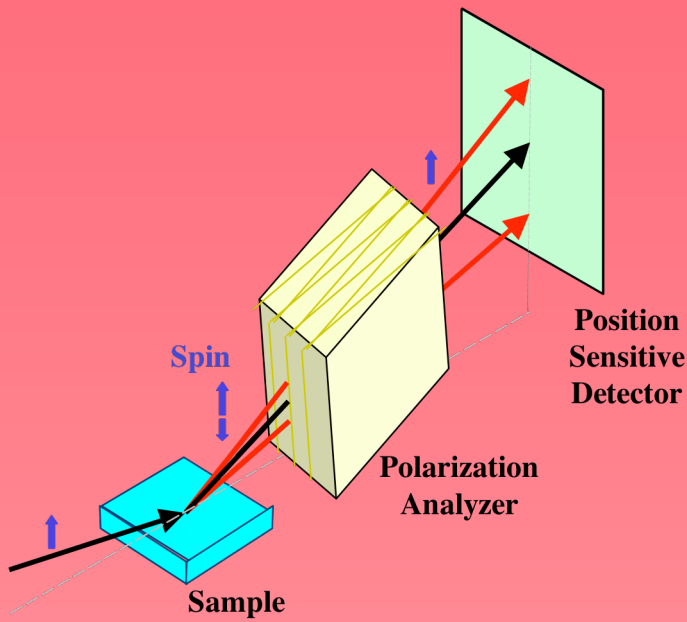
We have designed triblock copolymers to self-assemble in LC solvent to form nematic physical gels having useful electro-optic and mechano-optic properties. SANS from solutions of analogous diblock copolymers gives insight into the underlying nanostructure and demonstrates a discontinuous change in the quality of the LC solvent for the component blocks that is coincident with the nematic to isotropic phase transition. Furthermore, SANS experiments show a marked difference in length scales depending on the structure of the SGLCP midblock, demonstrating the ability to use molecular design to tailor nanostructure.

References

- 1 M. D. Kempe, N. R. Scruggs, R. Verduzco, et al., *Nature Materials* **3**, 177 (2004).
- 2 J. A. Kornfield and M. D. Kempe, United States Patent 6,821,455 (2004)
- 3 R. Verduzco, G. Meng, J. A. Kornfield, et al., Submitted for Publication (2005).
- 4 S. T. Wu, Q. H. Wang, M. D. Kempe, et al., *Journal of Applied Physics* **92**, 7146 (2002).

- 5 J. S. Higgins and H. C. Benoit, *Polymers and Neutron Scattering* (Oxford University Press, New York, NY, 1996).
- 6 N. R. Scruggs, J. A. Kornfield, and J. Lal, Submitted for Publication (2005).

Neutron Reflectometry



0

0.67

0.68

0.69

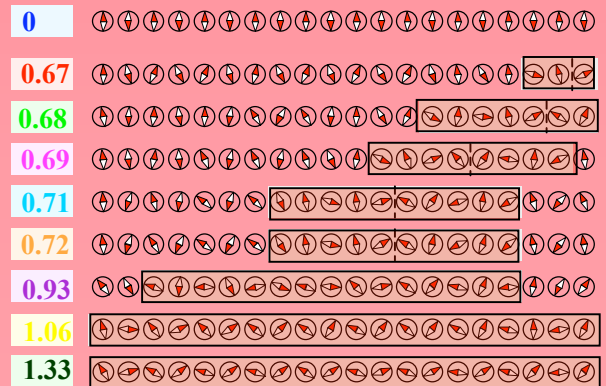
0.71

0.72

0.93

1.06

1.33



MAGNETIC PROFILES IN FERROMAGNETIC/SUPERCONDUCTING SUPERLATTICES

Suzanne G.E. te Velthuis, Axel Hoffmann, MSD/ANL, Argonne, IL 60439, U.S.A.

Jacobo Santamaria, GFMC, Departamento Fisica Aplicada III, Universidad Complutense de Madrid, 28040 Madrid, Spain

The interplay between ferromagnetism and superconductivity has been of longstanding fundamental research interest to scientists, as the competition between these generally mutually exclusive types of long-range order gives rise to a rich variety of physical phenomena. A method of studying these exciting effects is by investigating artificially layered systems, i.e. alternating deposition of superconducting and ferromagnetic thin films on a substrate, which enables a straight-forward combination of the two types of long-range order and allows the study of how they compete at the interface over nanometer length scales. While originally studies focused on low temperature superconductors interchanged with metallic ferromagnets, in recent years the scope has broadened to include superlattices of high T_c superconductors and colossal magnetoresistance oxides. Creating films where both the superconducting as well as the ferromagnetic layers are complex oxide materials with similar crystal structures (Figure 1), allows the creation of epitaxial superlattices, with potentially atomically flat and ordered interfaces.

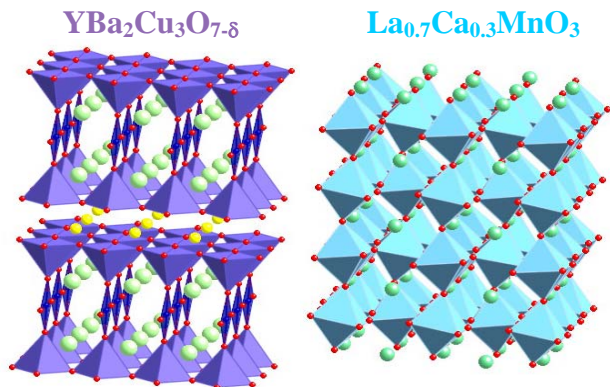


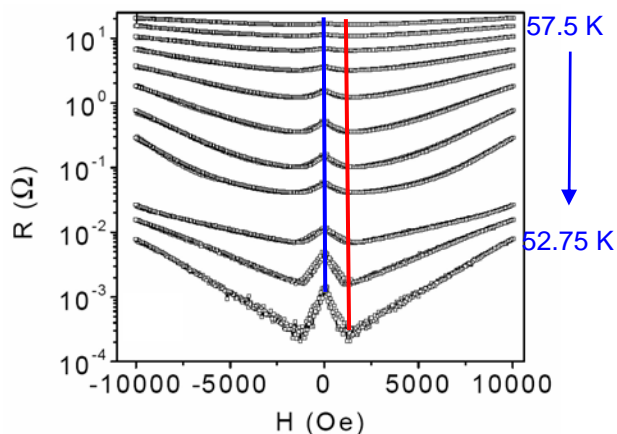
Figure 1: Models of the crystal structure of $\text{YBa}_2\text{Cu}_3\text{O}_{7-\delta}$ and $\text{La}_{0.7}\text{Ca}_{0.3}\text{MnO}_3$

Additionally, owing to their moderate carrier density of $10^{19}-10^{22} \text{ cm}^{-3}$, inhomogeneous charge distributions can be expected within a distance of a few unit cells from an interface. Since the physical properties of these complex oxides depend strongly on the charge carrier doping, this opens up a wide variety of different interactions between dissimilar complex oxides.

Motivated by these arguments the group of Jacobo Santamaria (GFMC, Departamento Fisica Aplicada III, Universidad Complutense de Madrid, 28040 Madrid, Spain) created and started investigating heterostructures of ferromagnetic $\text{La}_{0.7}\text{Ca}_{0.3}\text{MnO}_3$ / superconducting $\text{YBa}_2\text{Cu}_3\text{O}_{7-\delta}$ deposited on SrTiO_3 . The high degree of

spin polarization of the $\text{La}_{0.7}\text{Ca}_{0.3}\text{MnO}_3$ conduction band additionally makes this system a good candidate for the search of novel spin dependent effects, which could lead to the creation of spintronic devices based on magnetoresistance (MR) effects associated with the accumulation and transport of spin polarized electrons. In initial studies of the superconducting properties of series of heterostructures with varying thicknesses of either the $\text{La}_{0.7}\text{Ca}_{0.3}\text{MnO}_3$ or $\text{YBa}_2\text{Cu}_3\text{O}_{7-\delta}$ layers, proximity effects were detected evidenced by a depression of the superconductivity [1,2].

Figure 2: The resistance as a function of field for



decreasing temperature around the onset of superconductivity for a $\text{La}_{0.7}\text{Ca}_{0.3}\text{MnO}_3$ (40 u.c.)/ $\text{YBa}_2\text{Cu}_3\text{O}_{7-\delta}$ (15 u.c.)/ $\text{La}_{0.7}\text{Ca}_{0.3}\text{MnO}_3$ (40 u.c.) trilayer.

More recently, Santamaria's group observed a novel magnetoresistance (MR), in excess of 1000%, for heterostructures with only a limited number of bilayer repetitions [3]. While this effect is reminiscent of the giant magnetoresistance (GMR) effect typically measured in magnetic superlattices [4], the MR discussed here is only observed when $\text{YBa}_2\text{Cu}_3\text{O}_{7-\delta}$ is in the superconducting state. Figure 2 shows the measured resistance as a function of applied field for various temperatures close to the superconducting transition temperature of $\text{YBa}_2\text{Cu}_3\text{O}_{7-\delta}$. For lower temperatures, peaks in the resistance occur at moderate fields. Comparison with SQUID magnetometry measurements of the magnetization showed that the peaks in the resistance occur close to the coercive fields. Additionally, the magnetization curves show an unusual stepped behavior.

In order to explore the reason for this stepped behavior and gain insight into the origin of the magnetoresistive behavior, polarized neutron reflectivity (PNR)

experiments were performed on the POSY1 instrument at IPNS. With these experiments the magnetization of the individual $\text{La}_{0.7}\text{Ca}_{0.3}\text{MnO}_3$ layers was determined as a function of applied magnetic field for various temperatures.

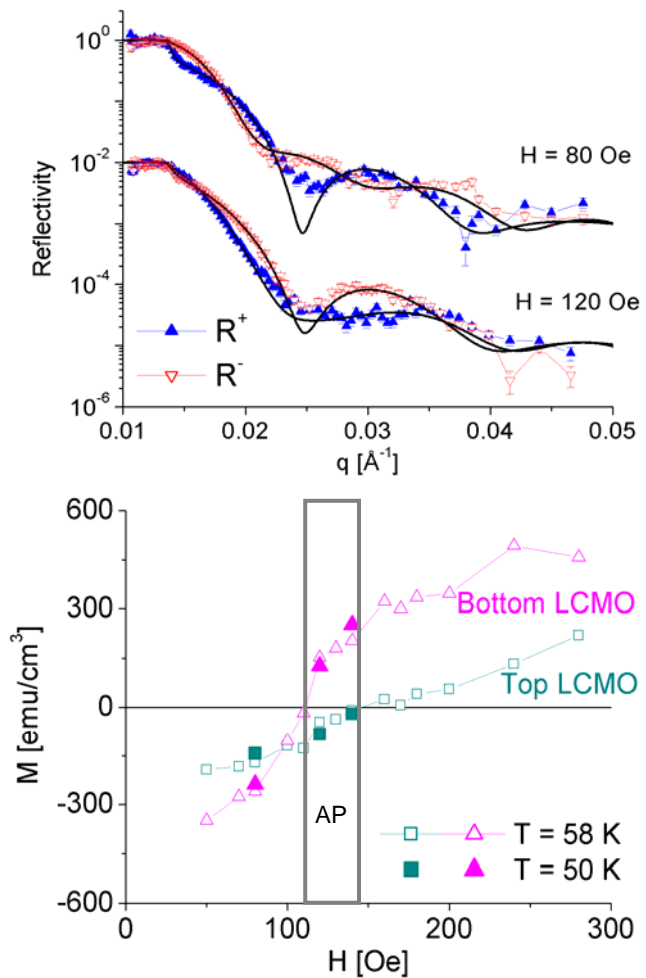


Figure 3: Top: Polarized neutron reflectivity data for the $\text{La}_{0.7}\text{Ca}_{0.3}\text{MnO}_3$ (40 u.c.)/ $\text{YBa}_2\text{Cu}_3\text{O}_{7-\delta}$ (15 u.c.)/ $\text{La}_{0.7}\text{Ca}_{0.3}\text{MnO}_3$ (40 u.c.) trilayer at two applied fields at $T = 58\text{K}$. Bottom: Magnetization of the individual LCMO layers as a function of applied field as determined from the fits of the PNR data. The gray box marks where antiparallel (AP) alignment was detected.

Figure 3 shows how the field dependence of the magnetization of the two $\text{La}_{0.7}\text{Ca}_{0.3}\text{MnO}_3$ layers is quite different. The bottom $\text{La}_{0.7}\text{Ca}_{0.3}\text{MnO}_3$ has a larger magnetization and therefore has a coercive field (where $M=0$) that is lower than that of the top layer. This difference in coercive fields of the two layers, creates a field region where the two layers are aligned antiparallel to each other. Similar results were obtained for a second sample, which had four $\text{La}_{0.7}\text{Ca}_{0.3}\text{MnO}_3$ layers spaced by three $\text{YBa}_2\text{Cu}_3\text{O}_{7-\delta}$ layers, (Figure 4). Here the bottom $\text{La}_{0.7}\text{Ca}_{0.3}\text{MnO}_3$ layer has a larger magnetization and is aligned antiparallel to the other three for a limited field

region. The reason for the variation of the saturation magnetization of the LCMO layers, which causes the variations in switching behavior, was determined with other PNR measurements on similar superlattices [5]. It was found that at the $\text{La}_{0.7}\text{Ca}_{0.3}\text{MnO}_3/\text{YBa}_2\text{Cu}_3\text{O}_{7-\delta}$ interface the magnetization of the $\text{La}_{0.7}\text{Ca}_{0.3}\text{MnO}_3$ was suppressed over a length scale of the order of 1nm, likely due to charge transfer across the interface. This effect would influence the bottom $\text{La}_{0.7}\text{Ca}_{0.3}\text{MnO}_3$ layer less, as it is grown directly on the substrate, therefore it retains a magnetization that is close to that of the bulk material.

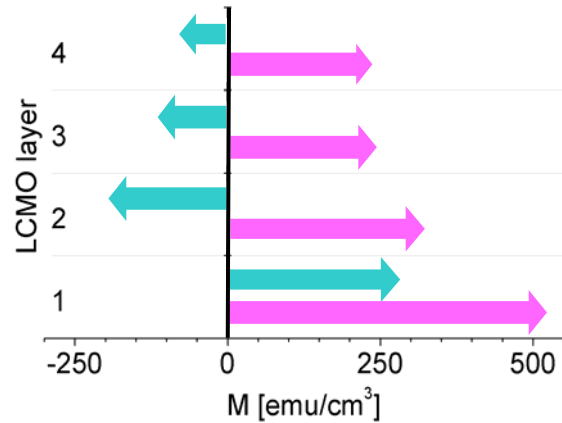


Figure 4: The magnetization of the four LCMO layer in a saturating field (pink) and close to the coercive field (green) determine with polarized neutron reflectivity for a $[\text{La}_{0.7}\text{Ca}_{0.3}\text{MnO}_3$ (40 u.c.)/ $\text{YBa}_2\text{Cu}_3\text{O}_{7-\delta}$ (7 u.c.) $\times 3.5$ superlattice.

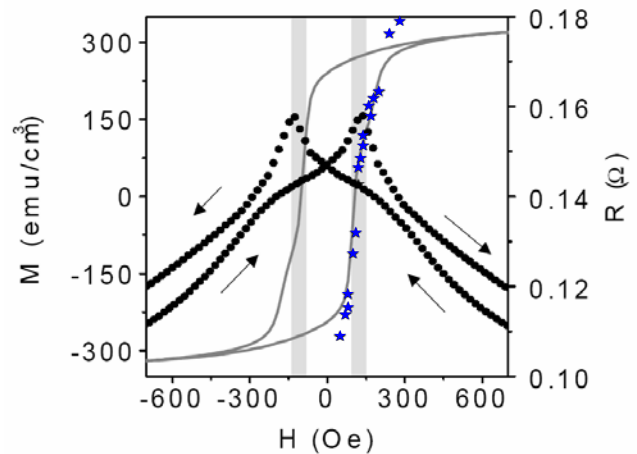


Figure 5: SQUID magnetization M (solid line), resistance R (filled circles) and, PNR magnetization (blue stars) for the $\text{La}_{0.7}\text{Ca}_{0.3}\text{MnO}_3$ (40 u.c.)/ $\text{YBa}_2\text{Cu}_3\text{O}_{7-\delta}$ (15 u.c.)/ $\text{La}_{0.7}\text{Ca}_{0.3}\text{MnO}_3$ (40 u.c.) trilayer as a function of applied field. The gray areas mark where antiparallel alignment was detected, which coincides with the peak in R and step in M .

These results were crucial to the understanding of the MR behavior because it is exactly in the field region

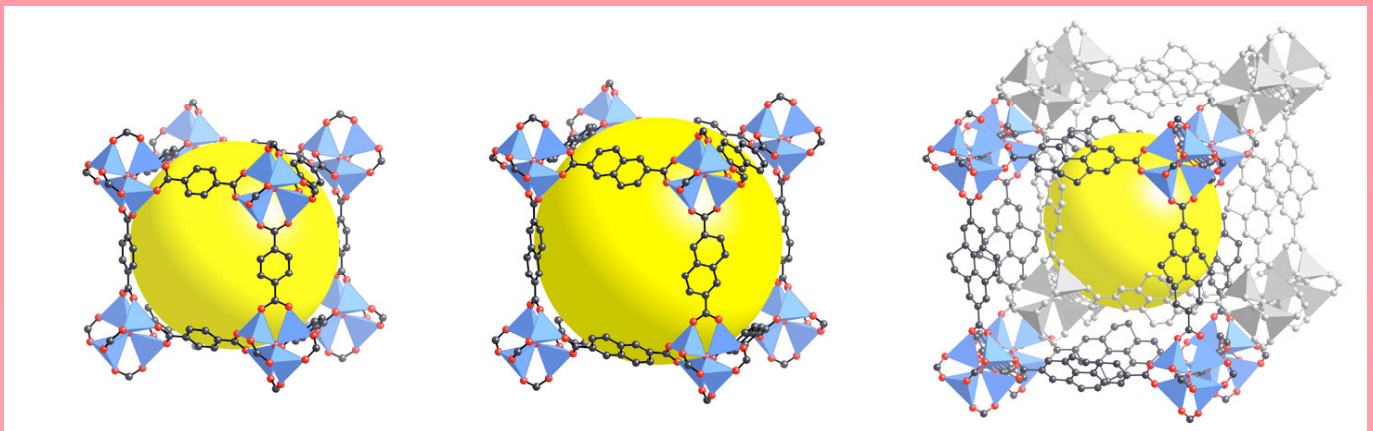
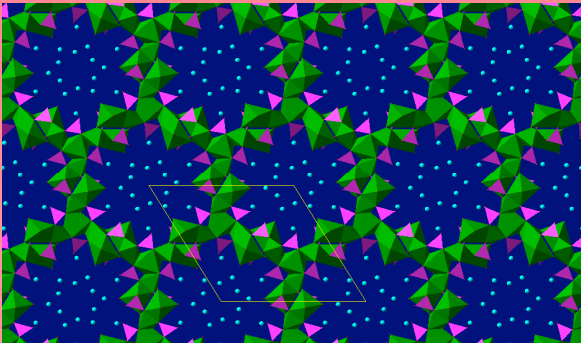
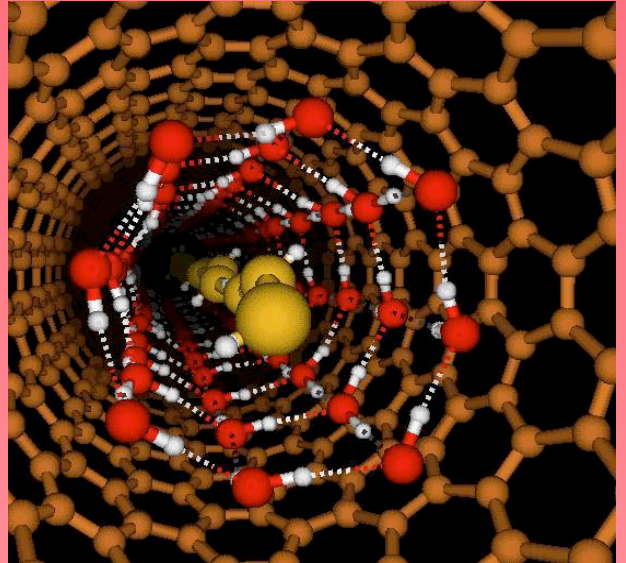
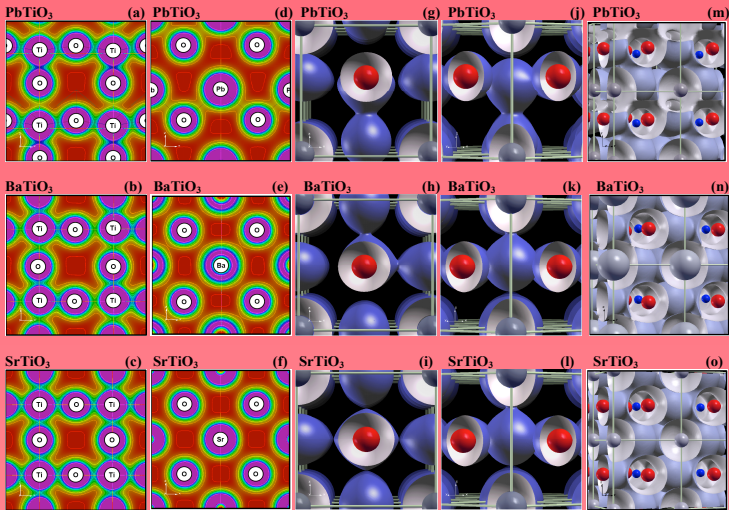
where antiparallel alignment occurs, that the peak in the magnetoresistance is at its maximum (Figure 5). This also means that the ordering temperature for the superconducting YBCO is suppressed more for antiparallel (blue line in Figure 2) than for parallel alignment (red line in Figure 2). Considering only the

proximity effect, the superconductivity depression should be larger with a parallel than with an antiparallel orientation, as has been observed for metallic systems [6]. Our results indicate that spin imbalance [7] in the superconductor due interactions with the ferromagnet is dominating the behavior in these complex oxide films [3].

REFERENCES

- [1] Z. Sefrioui, M. Varela, V. Peña, D. Arias, C. León, J. Santamaría, J. E. Villegas, J. L. Martínez, W. Saldarriaga, and P. Prieto, *Appl. Phys. Lett.* **81**, 4568 (2002).
- [2] Z. Sefrioui, D. Arias, V. Peña, J. E. Villegas, M. Varela, P. Prieto, C. León, J. L. Martinez, and J. Santamaria, *Phys. Rev. B* **67**, 214511 (2003).
- [3] V. Peña, Z. Sefrioui, D. Arias, C. Leon, J. Santamaria, J. L. Martinez, Suzanne G.E. te Velthuis, and Axel Hoffmann, *Phys. Rev. Lett* **94**, 057002 (2005).
- [4] M. N. Baibich, J. M. Broto, A. Fert, F. Nguyen Van Dau, F. Petroff, P. Eitenne, G. Creuzet, A. Friederich, and J. Chazelas, *Phys. Rev. Lett.* **61**, 2472 (1988).
- [5] A. Hoffmann, S. G. E. te Velthuis, Z. Sefrioui, J. Santamaría, M. R. Fitzsimmons, S. Park and M. Varela, *Phys. Rev. B* **72** 140407 (R) (2005).
- [6] J.Y. Gu, C.-Y. You, J. S. Jiang, J. Pearson, Y. B. Bazaliy, and S. D. Bader, *Phys. Rev. Lett.* **89**, 267001 (2002).
- [7] S. Takahashi, H. Imamura, and S. Maekawa, *Phys. Rev. Lett.* **82**, 3911 (1999).

Spectroscopy



WATER IN CARBON NANOTUBES: NEUTRON SPECTROSCOPY AND MD SIMULATIONS

A.I. Kolesnikov[#], C.-K. Loong, N.R. de Souza, P. Thiyagarajan, IPNS, Argonne National Laboratory, Argonne, IL 60439, USA

C.J. Burnham, The University of Houston, Houston, Texas 77204, USA

A.P. Moravsky, MER Corporation, 7960 South Kolb Road, Tucson, AZ 85706, USA

J.-M. Zanotti, LLB (CEA-CNRS), CEA Saclay, 91191 Gif-sur-Yvette Cedex, France

Abstract.

Quasi-one-dimensional water (*nanotube-water*) encapsulated inside carbon nanotubes at different temperatures (4-300 K) and pressures (1-3700 atm) were studied by means of SANS, ND, inelastic and quasielastic neutron scattering in parallel with ‘parallel tempering’ molecular dynamics (MD) simulations. The observed extremely soft dynamics of nanotube-water at low temperatures were consistent with the MD model that includes shell water molecules near the inner wall of the nanotubes plus central water-chain structure. It was found that chain water molecules are responsible for the observed large mean square displacements (~4 times larger than in bulk ice) as a result of their low coordination and weak bonding to the outer shell. Temperature and pressure phase transitions were observed experimentally and supported by the MD simulations.

INTRODUCTION

Water confined in nanoscale one-dimensional channels is of great interest to biology, geology, and materials science. An excellent model for such a system is water in single-walled carbon nanotubes (SWNT), realized by the unique geometry of nanotubes and the weak interaction between the water molecules and carbon atoms. As a result of nanoscale confinement, the physical properties of this quasi one-dimensional water, referred to as *nanotube-water*, are expected to be different from those of the bulk counterparts. Recently, there has been considerable research activity in the theoretical investigation of water molecules confined within nanometer channels in SWNT bundles [1-10]. Molecular dynamics (MD) simulations [5] showed that water in SWNT displays anomalous ice-like behavior in both symmetry and mobility while retaining a liquid-like degree of water-water hydrogen bonding. The results suggested that the confined water is in an intermediate state having both solid- and fluid-like properties.

Some simulations showed that the number of hydrogen bonds within SWNT was reduced relative to conditions

[#] akolesnikov@anl.gov

in bulk water [4,6,7]. Other MD results [1] indicated that water molecules are hydrogen-bonded with four nearest neighbors in a nearly two-dimensional net that is clearly different from the conventional tetrahedral arrangement of water molecules in ice. Series of the MD simulations at different pressures and temperatures [2,8] revealed the existence of a variety of new ice phases, and of a solid-liquid critical point [3], beyond which the distinction between the solid and liquid phases disappears. MD simulations [1] showed also that water molecules inside the SWNT tend to organize themselves into a highly hydrogen-bonded network, i.e., solid-like wrapped-around ice sheets, and the disorder-to-order transition of these ice-sheets can be achieved at ambient pressure by varying the size of the tubes.

To check the validity of the water models used in the simulations, experimental structural and spectroscopic data are required for water in SWNT. Before our study there were no spectroscopic measurements of water in SWNT known in the literature, and there was only one experimental X-ray study [11], where the authors found that a substantial amount of water was absorbed inside SWNT at room temperature and the liquid-like water at 235 K was transformed into a new solid form, ice nanotubes, having the structure proposed in Ref. 2.

Neutron scattering is a preferred method to study the dynamics of water owing to the extraordinarily large scattering cross-section of hydrogen and the straightforward comparison of the experimental data with the results from MD simulations.

Here we present a study of water encapsulated inside SWNT by using small-angle neutron diffraction (SAND diffractometer), inelastic and quasielastic neutron scattering (HRMECS and QENS spectrometers) in parallel with MD simulations, performed recently [12].

EXPERIMENTAL

Sample preparation

The 3.8 g sample of purified SWNT was prepared as follows. The raw SWNT sample was produced by

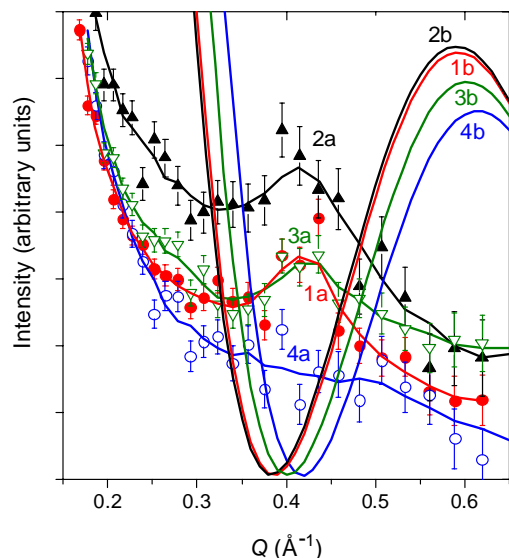


Figure 1. Neutron diffraction patterns ($T=5^{\circ}\text{C}$) around 0.4 \AA^{-1} for dry SWNT (red curve with solid circles) and SWNT with the encapsulated water of different isotopic forms, H_2O (black curve with solid triangles), $\text{H}_2\text{O}:\text{D}_2\text{O}=1:1$ mixture (green curve with open triangles) and D_2O (blue curve with open circles). The calculated form-factors for dry SWNT and for SWNT with the encapsulated water of different isotopic forms, H_2O , $\text{H}_2\text{O}:\text{D}_2\text{O}=1:1$ mixture and D_2O are shown as red, black, green and blue curves without points.

composite anodes. The metal component consisted of Co/Ni catalyst in a 3:1 mixture. The purification of SWNT was achieved by leaching out the metal catalyst with hydrochloric acid followed by oxidation of non-tube carbon components by air at $300\text{--}600^{\circ}\text{C}$, similar to the known procedure [13]. The synthesis and purification procedure yield totally opened nanotubes about $14\pm 1 \text{ \AA}$ in diameter and about $10 \mu\text{m}$ in length as revealed by electron microscopy observation using HRTEM and SEM.

To fill the nanotubes with water, the dry SWNT sample was first exposed in water vapor at 110°C for 2h in an enclosed environment. The excess water adsorbed in the exterior of the nanotubes was then extracted by evaporation at 45°C to the final $\text{H}_2\text{O}/\text{SWNT}$ mass ratio of about 11.5 wt.%.

Small-angle neutron diffraction

To investigate the location of water molecules in the sample we have measured small-angle neutron diffraction at 5°C around momentum transfer 0.4 \AA^{-1} , which corresponds to Bragg reflections on the (01) planes of a two-dimensional hexagonal lattice in SWNT crystalline bundles. The experiments were done for dry SWNT and SWNT with ~ 10 wt.% water of different isotopic forms, H_2O , $\text{H}_2\text{O}:\text{D}_2\text{O}=1:1$ mixture and D_2O . The ND (Fig. 1) shows the (01) peak at

$\sim 0.41 \text{ \AA}^{-1}$ for all samples but the one with D_2O . The intensity of the (01) peak is highest for dry SWNT and SWNT with H_2O . It slightly decreases for the SWNT with isotopic water mixture and vanishes completely for the sample with D_2O (the observed higher background for SWNT containing H_2O is due to large incoherent neutron scattering cross-section for hydrogen atoms). It is well known that ND and X-ray patterns for SWNT are strongly modulated by the form-factor of the sample ‘‘particles’’/tubes. To explain the obtained results we have calculated the form-factor [14] for the SWNT with the used concentration water of different isotopic forms. Around 0.4 \AA^{-1} the calculated form-factors (Fig. 1) have a zero-minimum value for all the samples, and the position of the minimum is at 0.385 \AA^{-1} for SWNT and SWNT with H_2O , at 0.4 \AA^{-1} for SWNT with isotopic water mixture and at 0.41 \AA^{-1} for SWNT with D_2O . The latter position exactly coincides with the position for (01) Bragg peak resulting in its vanishing for the SWNT sample with D_2O . The form-factor simulations for SWNT with water placed outside the tubes (between the tubes in the channels of the nanotubes bundles) produce curves with minimum at Q values below 0.385 \AA^{-1} , that could not explain the observed ND data. This result can be considered as proof that water occupies the space inside the tubes of the SWNT bundles.

Inelastic neutron scattering

The INS data were collected over a wide range of wave vectors Q . The data obtained at small Q values from high incident neutron energies were crucial to the measurements of the vibrational spectra due to the extraordinarily large mean-square displacement of hydrogen, $\langle u_{\text{H}}^2 \rangle$, which severely damps the intensity with increasing Q according to $\sim \exp(-\langle u_{\text{H}}^2 \rangle Q^2)$. The measurements were made on 11.3 wt% water in SWNT, and, in addition, on a dry SWNT sample for background removal and on a bulk ice-Ih for comparison. Figs. 2(A) and 2(C) show the observed generalized vibrational density of states $G(E)$ of nanotube-water at 9 K as compared with those of ice-Ih. In general, the spectra of ice are dominated by low-frequency intermolecular motion (e.g., translational and librational vibrations of water molecules at $0\text{--}40$ and $55\text{--}120 \text{ meV}$, respectively) and high-frequency intramolecular vibrations (e.g., H-O-H bending around 200 meV and O-H stretching modes near 420 meV). The observed stretching mode frequency of nanotube ice (422 meV) is higher than that of ice-Ih (406 meV), which is in good agreement with the MD results of Marti´ and Gordillo [8,9]. The higher O-H stretching frequency arises from the shorter O-H covalent bonds and a longer intermolecular O-O distance, $R_{\text{O-O}}$. The estimated $R_{\text{O-O}}$ of 2.916 \AA for nanotube-water at 9 K, based on the observed O-H stretching frequency and a phenomenological model [15], agrees reasonably well with that ($\sim 2.81 \text{ \AA}$) predicted by our MD simulations (see below). Comparing with the $R_{\text{O-O}}$ (2.76 \AA) of ice-

Ih, the structure of nanotube-water supports a weaker hydrogen-bonded network.

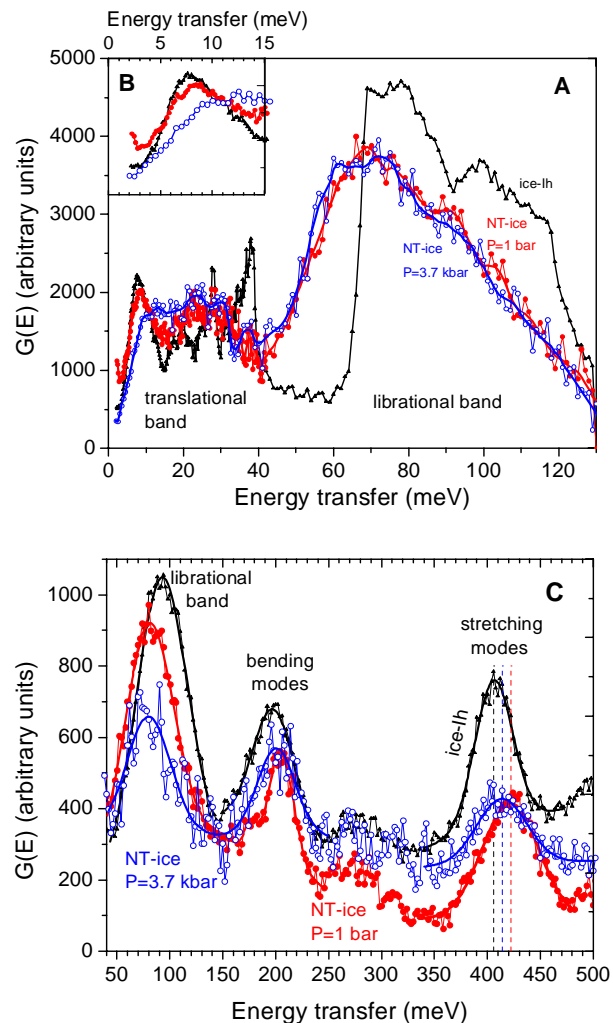


Figure 2. Generalized vibrational density of states, $G(E)$, of nanotube-water and ice-Ih measured at 9 K using the HRMECS spectrometer. The blue shifts of the stretching vibrations (figure C) in conjunction with the red shifts of the intermolecular modes (figure A) with extra spectral density extending to lower energies (insert B) indicate a weakened hydrogen-bonded network in nanotube-water. The $G(E)$ of nanotube-water under high pressure, $P=3.7$ bar at 50 K, shows features similar to that for bulk high-density amorphous ice.

The bending mode of nanotube-water consists of a narrow peak at 205 meV and a shoulder at ~ 176 meV. The latter can be accounted for as the second-order overtone of the librational modes. Thus the peak at 205 meV could be assigned solely to the intramolecular H-O-H bending mode. This value is slightly larger than that for ice Ih (~ 199 meV).

Distinct features reflecting the soft hydrogen bond dynamics unique to nanotube-water are revealed in the intermolecular part of spectra, shown in Fig. 2(A). The librational band shifts to lower energies in comparison

to ice-Ih. The spectral density on the low-energy side broadens and merges with the translational band below 40 meV, which is in sharp contrast to the abrupt cutoff at ~ 67 meV in ice Ih. The half maximum of this band at the low-energy side occurs at 55 meV. The translational band over the 25–40 meV region broadens and lacks the salient feature that was observed for ice-Ih. In nanotube-water the intensity of the high-energy translation-like optical modes (at ~ 36 meV) drops drastically and redistributes to lower frequencies (between 12–25 meV). Moreover, a large excess intensity appears below 5 meV [see Fig. 2(B)].

Applying a high pressure ($P=3.7$ kbar, with He gas as a pressure transmission medium) to nanotube-water results in strong change of the low-energy part of the translation intermolecular band in the $G(E)$ spectrum below 20 meV. The position of the first maximum (acoustical peak) shifted to much higher energy, ~ 10 –11 meV, and the $G(E)$ intensity is strongly decreased at $E < 10$ meV. This spectral transformation is similar to those in high-pressure (and high-density) phases of ice (ice-VI, ice-VIII, high-density amorphous ice, etc). So, nanotube-water under 3.7 kbar pressure should correspond to a dense ice phase.

Quasielastic neutron scattering

The ‘softness’ of nanotube-water was characterized by high-resolution ($\Delta E = 80 \mu\text{eV}$) QENS measurements of the $\langle u_{\text{H}}^2 \rangle$. The integrated intensity of the elastic peak $I(Q)$ was recorded over a wide range of Q at select temperatures as the sample was warmed up from 8 to 300 K. Since the signal arises predominantly from incoherent neutron scattering of hydrogen atoms, the elastic intensity follows the expression of $I(Q) \sim \exp(-\langle u_{\text{H}}^2 \rangle Q^2)$. In the case of bulk water (Fig. 3), $\langle u_{\text{H}}^2 \rangle$ increases steadily with increasing temperature until 273 K where an abrupt increase occurs due to the melting of ice-Ih. The data of bulk ice can be adequately explained by a harmonic potential

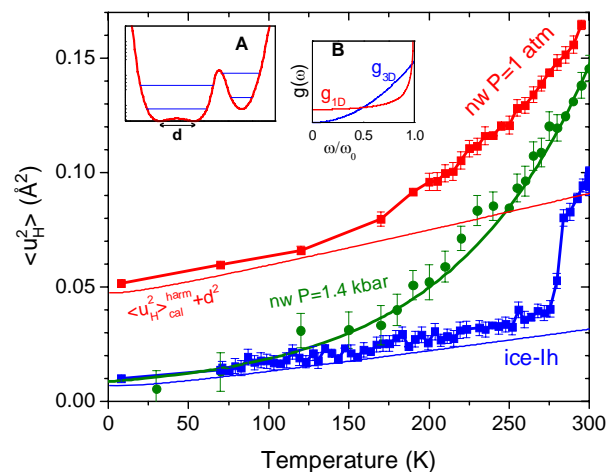


Figure 3. The mean-squared displacements, $\langle u_{\text{H}}^2 \rangle$, of H atoms in nanotube-water measured with the high-resolution ($\Delta E = 80 \mu\text{eV}$) spectrometer QENS as a

function of temperature and pressure, compared to ice-Ih.

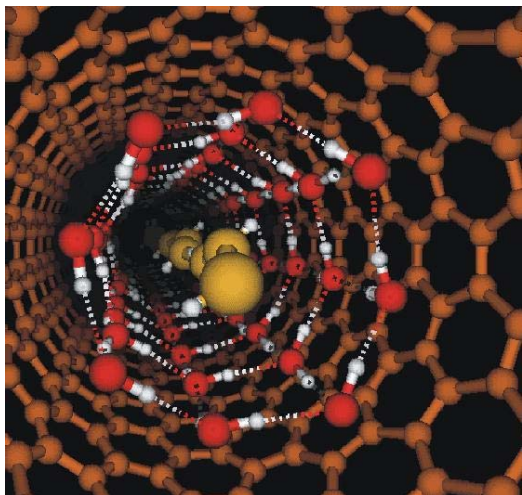


Figure 4. Proposed structure of nanotube water. The interior “chain” water molecules have been colored yellow to distinguish them from the exterior “shell” water molecules (colored red).

corresponding to the measured $G(E)$. The situation for nanotube water is drastically different. The magnitude of $\langle u_H^2 \rangle$ for nanotube-water is about 4 times larger than that for ice-Ih throughout the 8–273 K temperature range. Note that at 8 K $\langle u_H^2 \rangle$ of nanotube-water is already larger than the value for ice-Ih just prior to melting. The $\langle u_H^2 \rangle$ for nanotube-water under pressure $P=1.4$ kbar (green curve in Fig. 3) below 100 K is reduced drastically to values comparable to those in ice-Ih. At higher temperatures it rises very rapidly above the ice-Ih value.

The data imply a strongly anharmonic potential for nanotube-water at ambient pressure. Qualitatively, the data favor a flattened bottom or low-barrier double-well potential with hydrogen delocalized over ~ 0.2 Å distance, as schematically shown in the inset of Fig. 3(A). Such an anharmonic potential can qualitatively account for the observed $\langle u_H^2 \rangle$ up to about 120 K. At higher temperatures, additional fluctuations in terms of hydrogen-bond-breaking diffusion processes have to be included in order to explain the sharp rise of the curve. Another possible scenario is shown in the inset of Fig. 3(B): the large $\langle u_H^2 \rangle$ in quasi 1D nanotube-water may be originated from a finite value of the $g(\omega)$ at low energies in a 1D chain, $g(\omega) \sim (\omega_0^2 - \omega^2)^{-1/2}$, contrary to the $g(\omega) \sim \omega^2$ behavior for the bulk 3D case.

MOLECULAR DYNAMICS SIMULATIONS

MD calculations for water in SWNT were performed using the TTM2-F polarizable flexible water model of Burnham and Xantheas (using smeared charges and

dipoles to model short range electrostatics) [16,17]. This model has been shown to be in excellent agreement with high-level electronic structure data for small water clusters and can also reproduce the bulk behavior of ice and ambient liquid water. The MD simulations consist of a rigid (10,10) carbon nanotube of length 40 Å subjected to periodic boundary conditions and includes NT-water interactions modeled via a Lennard-Jones (L-J) potential [18].

To study the effect of temperature we utilized the parallel capabilities of the Jazz computers cluster at ANL with a ‘parallel tempering’ molecular dynamics (PTMD) algorithm. The PTMD algorithm calculates multiple simultaneous trajectories for the system, where each trajectory is assigned a different temperature, and the occasional swapping of temperatures between neighboring trajectories is employed (in accordance with detailed balance under the Boltzmann distribution), which allowed to locate more efficiently low-lying minima of the nanotubes-water structure compared to conventional MD simulations.

The MD simulations show that a convincing atomic model for the low-temperature nanotube-water structure consists of shell water molecules near the inner wall of the carbon nanotubes, in which the waters are H-bonded together in a square lattice wrapped into a cylinder, plus central water-chain, in which the waters are H-bonded to form a quasi one-dimensional linear chain (see Fig. 4). The soft dynamics of nanotube-water arises mainly from the drastic change in hydrogen-bond connectivity of the central water-chain with an average coordination number of 1.86 (compared to ~ 4 for other known states of water). Because of the loose bonding, the chain-water is very active; the water-shell is more stable, but the mobile chain makes and breaks bonds continuously between parts of the chain and sometimes with the shell-water even at ~ 50 K (see Fig. 5).

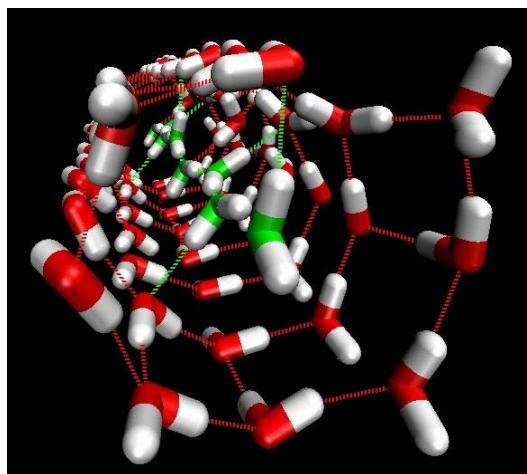


Figure 5. This view of nanotube-water at 50 K shows its strong and weak bonds. The red and white water

exterior shell has ‘permanent’ bonds shown by the red lines. The interior chain is constantly in motion and its green chains represent a snap shoot of the weak bonds.

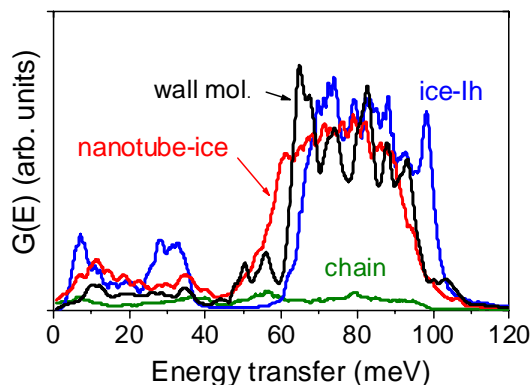


Figure 6. Calculated vibrational spectra for nanotube-water, wall-water molecules alone and chain-water in nanotube-water, compared with ice-Ih.

The MD simulations well describe the observed softening of INS spectra (Fig. 6) and anomalously enhanced thermal motions in the nanotube-water (Fig. 7).

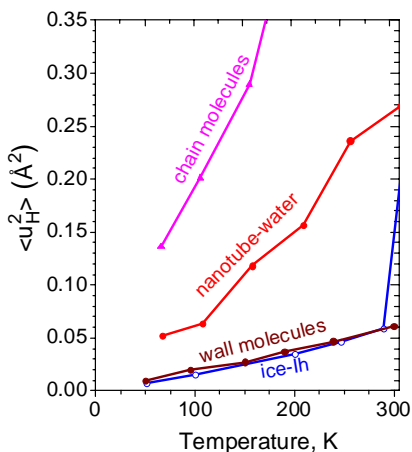


Figure 7. Calculated $\langle u_H^2 \rangle$ for nanotube-water, wall-water molecules alone and chain water in nanotube-water, compared with ice-Ih.

The MD result, in terms of the free energy of water molecules in a cross section of the tube, as shown in Fig. 8, is more revealing. At low densities the water molecules begin to fill the minimum of the L-J well. With increasing density the waters first adhere to the inside of the nanotube wall, which acts to lower the energy barrier along the center of the nanotube, eventually allowing water to occupy the interior region. The interior well is found to be much flatter and more anharmonic than the outer groove and is large enough to allow fairly easy passage of the interior molecules through the nanotube. At 50 and 100 K the chain molecules fluctuate between the central local minima resembling a double-well potential. At elevated

temperatures thermal activation leads to the flattening of the well and hence an additional increase of mobility.

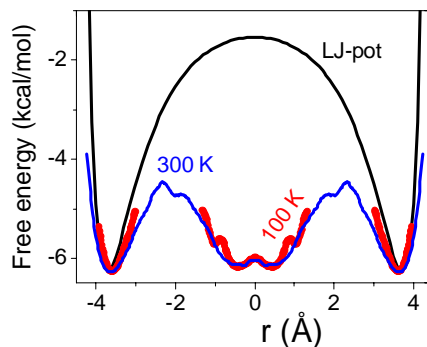


Figure 8. Free energies across the nanotube walls for water molecules in nanotube-water at 100 K (red) and 300 K (blue). The L-J potential (black) provides the minima for the position of individual water molecules initially entering the SWNT.

The PTMD simulations of nanotube-water clearly show the phase transition on heating from high to low density liquid at ~ 200 K (see Fig. 9). Above the phase transition the structure becomes a disordered H-bonded network similar to the bulk liquid. Applying a high pressure results in decreasing the mean-square displacement of nanotube-water at low temperatures, comparable to that in bulk ice. The calculated vibrational density of states of nanotube-water at $P=3.7$ kbar well describe the experimental data and also show a large change in its structure: water becomes more dense (by $\sim 30\%$), like a dense bulk ice (Fig. 10).

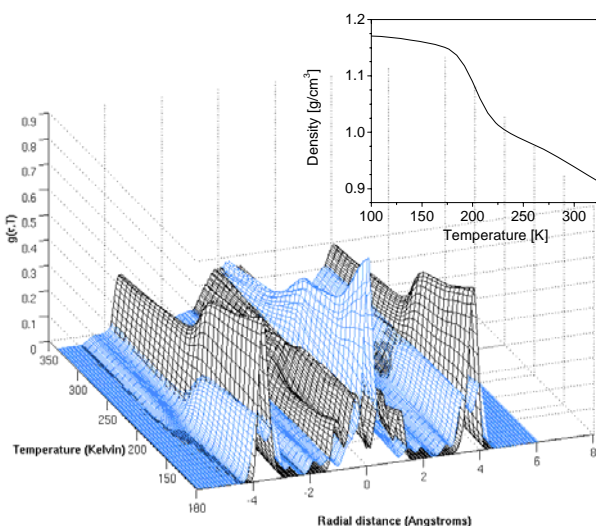


Figure 9. Radial/thermal R_{O-O} distribution function of waters inside SWNT of diameter 14 Å. Black surface: oxygen distribution, blue surface: hydrogen distribution. The central peak in the H-distribution corresponds to the chain of waters running down the center of the nanotube. The two outer peaks in the O-

distribution are from shell molecules. Insert shows the temperature dependence of density for water in SWNT as obtained from MD simulations.

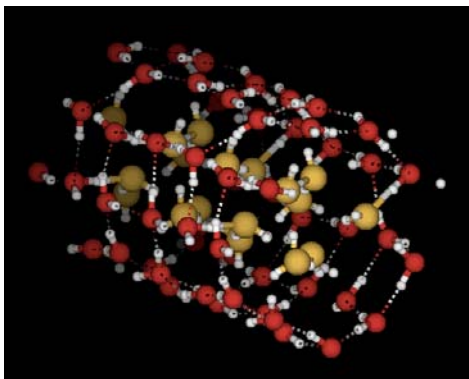


Figure 10. Structure of nanotube-water under 3.7 kbar pressure.

SUMMARY

ND, INS and QENS measurements in parallel with MD simulations clearly showed the entry of water into SWNT and identified an ice-shell plus water-chain structure at low temperatures. The soft dynamics of nanotube-water at low-temperature arises mainly from the drastic change in hydrogen-bond connectivity of the central water chain. The PTMD simulations of nanotube-water clearly show the phase transition on heating from high to low density liquid at ~ 200 K. Above the phase transition the structure becomes a disordered H-bonded network similar to the bulk liquid. An applied pressure suppresses the soft dynamics below ~ 150 K, and water becomes more dense (by $\sim 30\%$), like a dense bulk ice

The work at Argonne National Laboratory was supported by the U.S. Department of Energy, Basic Energy Sciences-Materials Sciences, under Contract No. W-31-109-ENG-38. CJB is thankful for Grant from Argonne Theory Institute for his stay at IPNS. The PTMD calculations were made with a grant of time on the Argonne National Laboratory Jazz computer.

REFERENCES

- [1] W.H. Noon et al., Chem. Phys. Letters 355 (2002) 445.
- [2] K. Koga et al., Nature 412 (2001) 802.
- [3] H.E. Stanley in Introduction to Phase Transitions and Critical Phenomena 2 (Oxford Univ. Press, New York, 1971).
- [4] G. Hummer, J.C. Rasaiah, J.P. Noworyta, Nature 414 (2201) 188.
- [5] R.J. Mashl et al., Nano Letters 3 (2003) 589.
- [6] J. Martí, M.C. Gordillo, Phys. Rev. E 64 (2001) 021504.
- [7] D.J. Mann, M.D. Halls, Phys. Rev. Letters 90 (2003) 195503.
- [8] K. Koga et al., Physica A 314 (2002) 462.
- [9] J. Martí, M.C. Gordillo, Phys. Rev. B 63 (2001) 165430.
- [10] M.C. Gordillo, J. Martí, J. Chem. Phys. 117 (2002) 3425.
- [11] Y. Maniwa et al., J. Phys. Soc. Japan 71 (2002) 2863.
- [12] A.I. Kolesnikov et al., Phys. Rev. Lett. 93 (2004) 035503.
- [13] I.W. Chiang et al., J. Phys. Chem. B 105 (2001) 8297.
- [14] S. Kline, A. Munter, Model CoreShellCylinder <http://www.ncnr.nist.gov/resources/sansmodels/CoreShellCylinder.html> (1999).
- [15] D.D. Klug, E. Whalley, J. Chem. Phys. 81 (1984) 1220.
- [16] C.J. Burnham, S.S. Xantheas, J. Chem. Phys. 116 (2002) 1500.
- [17] C.J. Burnham, S.S. Xantheas, J. Chem. Phys. 116 (2002) 5115.
- [18] J. H. Walther et al., J. Phys. Chem. B 105 (2001) 9980

THE PROTON DENSITY OF STATES STUDY OF DEEPLY SUPERCOOLED WATER NEAR THE SECOND CRITICAL POINT

Sow-Hsin Chen[#], Li Liu, Department of Nuclear Science and Engineering, Massachusetts Institute of Technology, Cambridge, MA, 02139, USA.

Antonio Faraone, NIST Center for Neutron Research, National Institute of Standards and Technology, Gaithersburg, Maryland 20899-8562 and Department of Materials Science and Engineering, University of Maryland, College Park, Maryland 20742-2115, USA.

Alexander. I. Kolesnikov, Intense Pulsed Neutron Source Division, Argonne National Laboratory, Argonne, IL, 60439-4814, U.S.A.

Abstract

Water is essential for all living systems and its properties impact our daily life and environment directly. Hence the counterintuitive behavior in its supercooled state stimulates enormous interests in scientific communities. For example, some thermodynamic response functions and transport coefficients show a tendency to diverge at a singular temperature 228 K at ambient pressure. However, this singular temperature is so-far inaccessible to experiments because water inevitably freezes into ice before reaching it. By confining water in nano-pores of mesoporous silica, we succeeded in entering this unreachable range of supercooled temperatures. Using quasielastic neutron scattering (QENS) method we discovered a series of fragile-to-strong (F-S) dynamic crossover temperatures as a function of pressure in deeply supercooled water under pressure for the first time. Inelastic neutron scattering (INS) method, furthermore, enables us to measure the proton density of states of H₂O and shows evidence that two kinds of liquids co-exist in supercooled water. INS clearly shows that the F-S dynamic crossover is accompanied by the appearance of a well-defined Boson peak at and below the crossover temperature. The crossover temperature can thus be interpreted as a generalized mode-coupling crossover temperature usually referred to as the “kinetic glass transition temperature” in the idealized version of the theory. We present our new experimental findings which shed light on the location of the liquid-liquid transition line and its end point, the much discussed and anticipated second critical point of recent literature.

One of the most intriguing questions related to the unusual properties of supercooled water is whether two critical points may exist in a single component liquid [1]. The anomalies of the thermodynamic quantities become plausible if one postulates the existence of a second low-temperature critical point at about 228 K and at somewhat elevated pressure. Search for the existence of the predicted [2] first-order liquid-liquid

transition line and its end point, the second low-temperature critical point [1] in water, has been hampered by intervention of the homogenous nucleation process, which takes place at 235 K at the ambient pressure. However, by confining water in nano-pores of mesoporous silica MCM-41-S with cylindrical pores of 14 Å diameter, we have been able to study the dynamical behavior of water in a temperature range down to 160 K, without crystallization. Using the high-resolution Quasi-Elastic Neutron Scattering (QENS) method, with Backscattering and Disc-Chopper spectrometers at NIST NCNR [3-4], and Relaxing-Cage Model (RCM) [5] for the spectral analysis, we determine the temperature and pressure dependences of the average translational relaxation time, $\langle\tau_T\rangle$, for the confined supercooled water. The latter essentially gives a measure of the structural relaxation time of the hydrogen-bond cage surrounding a typical water molecule in liquid state.

The behavior of the shear viscosity η or equivalently the structural relaxation time τ of a supercooled liquid approaching its glass transition temperature is called ‘fragile’ when it varies according to the so-called Vogel-Fulcher-Tammann (VFT) law; and the behavior is called ‘strong’ when η or τ obeys Arrhenius law. For water, a fragile liquid at room temperature and at moderately supercooled temperatures, Ito and coworkers [6] proposed that a ‘fragile-to-strong’ transition would occur at around 228 K, based on a thermodynamic argument.

We show in a P-T plane, in Fig. 1, the observed pressure-dependence of the F-S transition temperature, T_L . Also depicted in the figure are the T_H line (homogeneous nucleation line) and TMD line (temperature of maximum density line). One should note that the T_L line has a negative slope, parallel to the TMD line, indicating a lower density for the low temperature phase. This T_L line also approximately tracks the T_H line, and terminates in the upper end when intersecting the T_H line at 1600 bar and 200 K.

Since what we observe experimentally is a dynamic crossover, it is natural to ask whether T_L is related to

[#]sowhsin@mit.edu

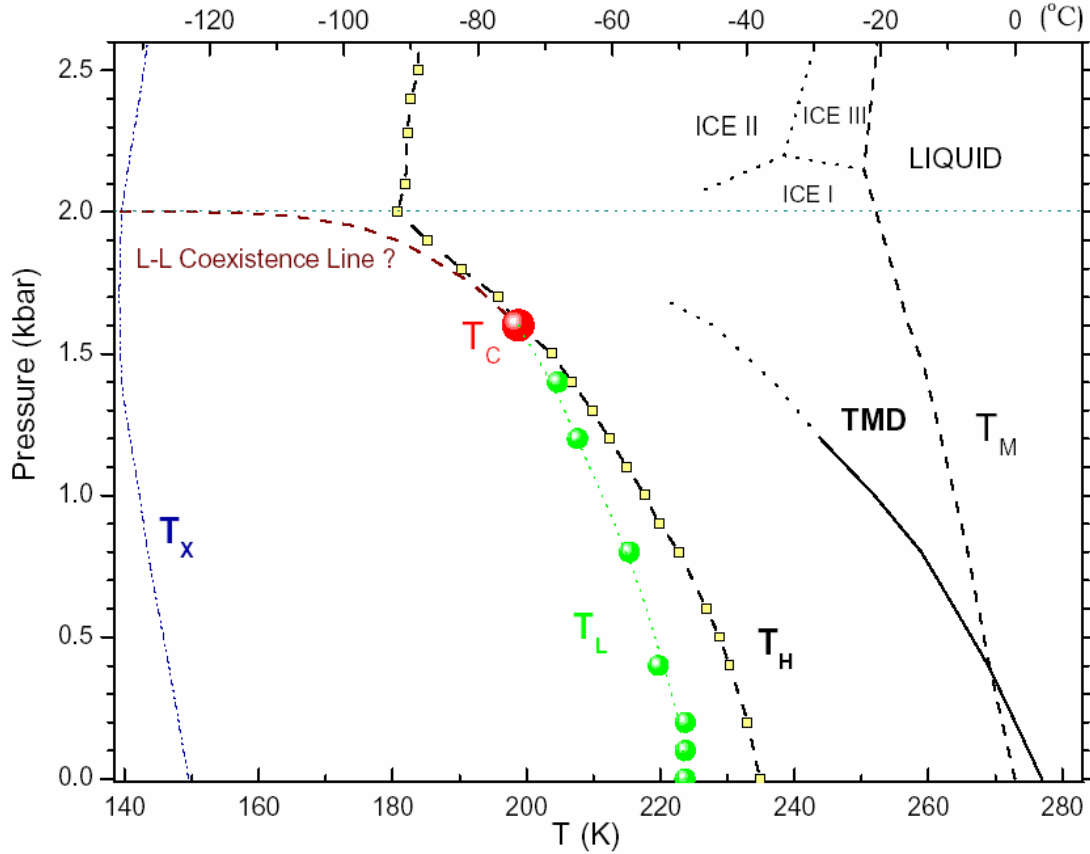


FIG. 1. Summary of the pressure dependence of the fragile-to-strong dynamic crossover temperature, T_L , plotted in the P-T plane (solid circles). Also shown are the homogeneous nucleation temperature line, denoted as T_H , and the temperature of maximum density line, denoted as TMD. Our experiment indicates that the T_L line terminates on the upper end when it crosses the T_H line. Note that we would like to identify this line as the Widom line extrapolated from the predicted liquid-liquid coexistence line in supercooled water [9].

the liquid-liquid transition temperature, and if so, what would the nature of the high-temperature and low-temperature liquids be? According to the inelastic neutron scattering experiments using the High-Resolution Medium-Energy Chopper Spectrometer (HRMECS) at ANL IPNS (see Fig. 2), which measure the librational density of states of water contained in 18 Å pore size MCM-41-S, water remains in a disordered liquid state both above and below the fragile-to-strong transition at ambient pressure. Furthermore, our analysis indicates that the activation energy barrier for initiating the local structural relaxation is $E_A = 4.89$ Kcal/mol for the low-temperature phase. On the other hand, our previous inelastic scattering experiments of the stretch vibrational band of water [7] indicated that the effective activation energy of breaking a hydrogen bond at 258 K (high-temperature phase) is 3.2 Kcal/mol. Combining these two observations, it is then reasonable to conclude that the high-temperature liquid corresponds to the high-density liquid (HDL) where the locally tetrahedrally coordinated hydrogen bond network is not fully developed, while the low-temperature liquid corresponds to the low-density

liquid (LDL) where the more open, locally ice-like hydrogen bond network is fully developed.

On the other hand, Sastry et al [8] suggested in their work of MD simulated liquid silicon that a fragile-to-strong crossover is accompanied by the change of intermediate scattering function (ISF) from a monotonic decay before the crossover to a damped oscillation after. Since the dynamic structure factor, $S(Q,E)$, is the Fourier Transform of the ISF, when the latter function shows an oscillation, it is a clear signature of a Boson peak in $S(Q,E)$. Our recent results from HRMECS (see Fig. 3) which cover the energy range of $S(Q,E)$ between -15 and +15 meV at Q range between 1-2 Å⁻¹, effectively scan the translational bands of the proton density of states. The measured $S(Q,E)$ show appearance of a well-defined Boson peak for temperature ≤ 220 K, near the $T_L = 225$ K at ambient pressure. This result suggests a transition of the structure of water from a fragile liquid to a strong liquid near 225 K.

It is appropriate now to address the possible location of the second critical point [2]. Above the critical

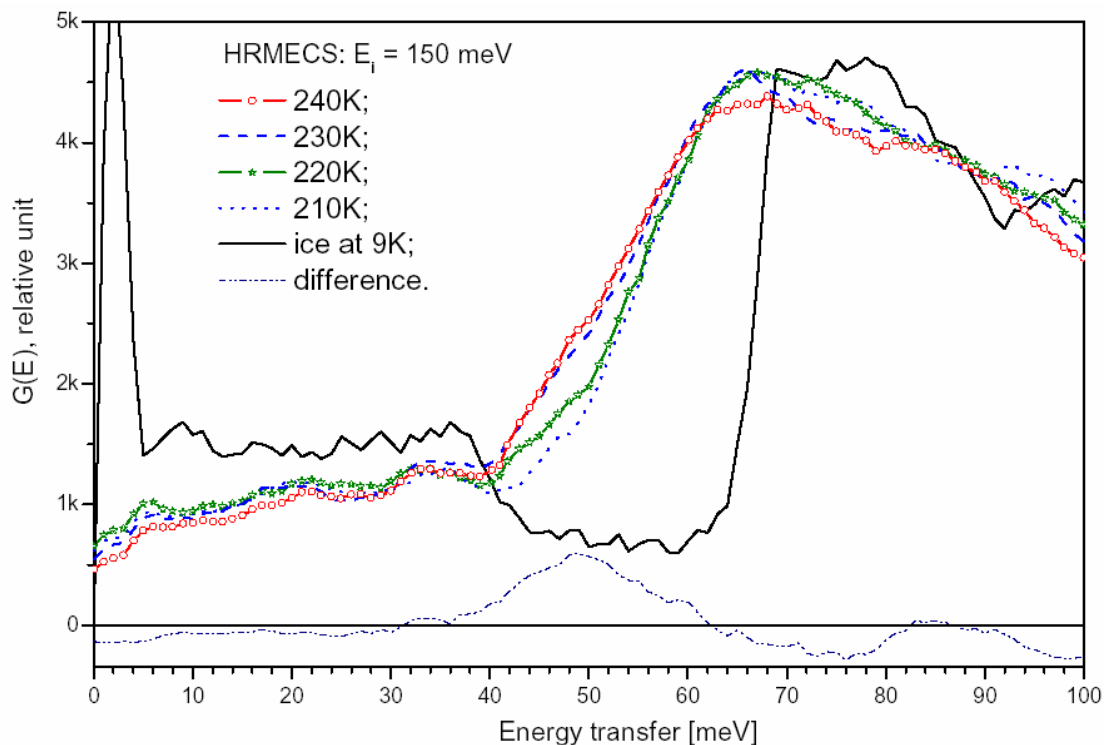


FIG. 2. The generalized librational density of states $G(E)$ (taken with $Q < 2 \text{ \AA}^{-1}$) of ice and confined water (within the energy range from 40 meV to 120 meV) at different temperatures measured with HRMECS spectrometer using incident neutron energy of 150 meV. It should be noted that $G(E)$ of ice (solid line) is characterized by a much steeper leaning edge compared to that of supercooled water in the temperature range from 210 K to 240 K. The broader $G(E)$ of supercooled water confined in MCM-41-S with pore diameter of 18 \AA is seen to be more characteristic of a liquid state. From the behavior of the low-energy cut-off of the librational band around 50 meV, it is obvious that the state of confined water (its hydrogen bond network) is different at temperatures above and below 225 K. The difference between the average spectra above and below 225 K is shown to have a clear peak at around 50 meV (dash-dot line).

temperature T_C and below the critical pressure P_C , we expect to find a one-phase liquid with a density ρ , which is constrained to satisfy an equation of state: $\rho = f(P, T)$. If an experiment is done by varying temperature T at a constant pressure $P < P_C$, ρ will change from a high-density value (corresponding to HDL) at sufficiently high temperature to a low-density value (corresponding to LDL) at sufficiently low temperature. Since the fragile behavior is associated with HDL and the strong behavior with LDL, we should expect to see a clear F-S transition as we lower the temperature at this constant P . Therefore, the cusp-like F-S crossover we observed should then occur when we cross the so-called Widom line in the one-phase region [9]. On the other hand, if the experiment is performed in a pressure range $P > P_C$, corresponding to the two-phase region and crossing the Liquid-Liquid (L-L) coexistence line, the system will consist of a mixture of different proportions of HDL and LDL as one varies T . In this latter case, the $\langle \tau_T \rangle$ vs. $1/T$ plot will not show a clear-cut F-S transition (the transition will be washed out) because the system is in a mixed

state. From this observation, we propose that the lower end point of the liquid-liquid coexistence line, or the upper end point of the Widom line, is the second low-temperature critical point, $P_C = 1500 \pm 200$ bar and $T_C = 200 \pm 10$ K [9].

REFERENCES

- [1] P.G. Debenedetti, H.E. Stanley, *Physics Today* 56 (2003) 40.
- [2] P.H. Poole, F. Sciortino, U. Essmann, H.E. Stanley, *Nature* 360 (1992) 324.
- [3] A. Meyer et al, *Rev. Sci. Instrum.* 74 (2003) 2759.
- [4] J.R.D. Copley, J.C. Cook, *Chem. Phys.* 292 (2003) 477.
- [5] A. Faraone et al, *J. Chem. Phys.* 121 (2004) 10843.
- [6] K. Ito, C.T. Moynihan, C.A. Angell, *Nature* 398 (1999) 492.
- [7] M.A. Ricci, S.-H. Chen, *Phys. Rev. A* 34 (1986) 1714.
- [8] S. Sastry, C.A. Angell, *Nature Materials* 2 (2003) 739.
- [9] L. Liu et al, *Phys. Rev. Lett.* 95 (2005) 117802.

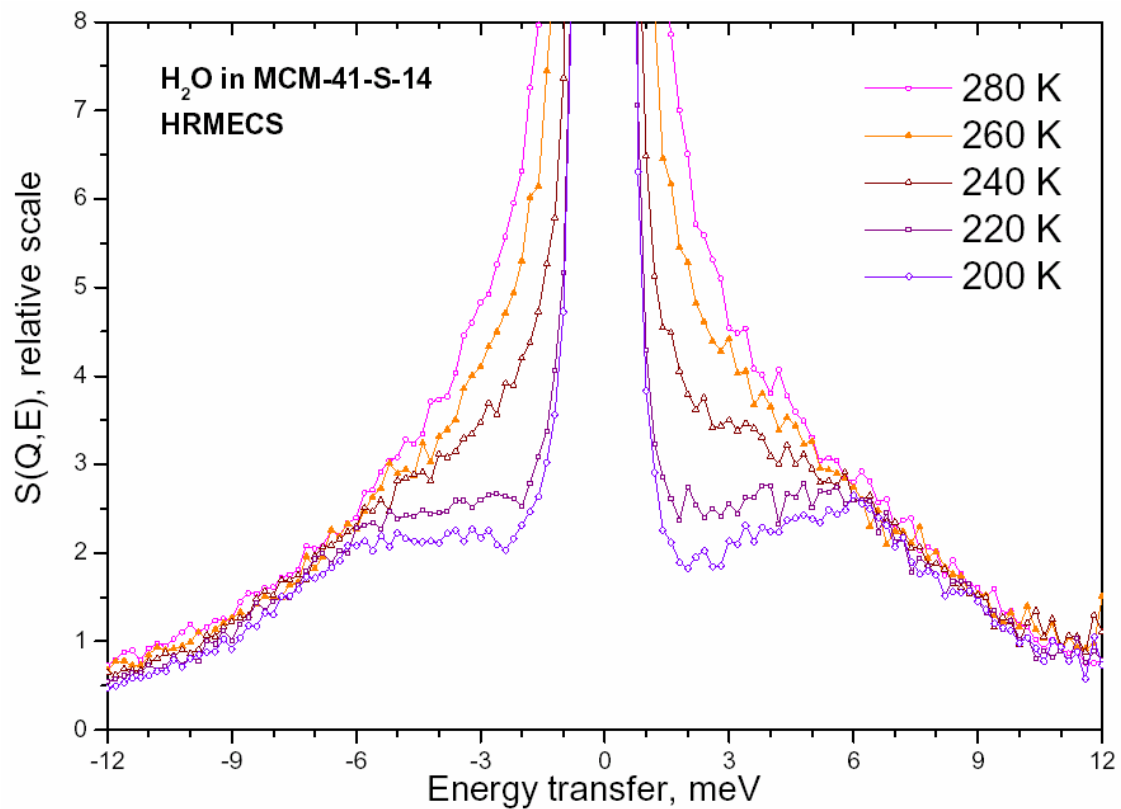


FIG. 3. The low-energy part of the translational band of proton density of states (taken with $Q < 2 \text{ \AA}^{-1}$) of supercooled water confined in MCM-41-S with pore diameter of 14 \AA at different temperatures, measured with the HRMECS spectrometer using incident neutron energy of 15 meV . It should be noted that a well defined Boson peak appears at $\sim 220 \text{ K}$.

PHONON DENSITY OF STATES OF MODEL FERROELECTRICS

N. Choudhury[#], Solid State Physics Division, Bhabha Atomic Research Centre, Trombay, Mumbai
400 085, India

E.J. Walter, Dept. of Physics, College of William and Mary, Williamsburg, Virginia 23187, USA

A.I. Kolesnikov, C.-K. Loong, IPNS Division, Argonne National Laboratory, Argonne, Illinois
60439, USA

Abstract

First principles density functional calculations and inelastic neutron scattering measurements have been used to study the phonon density of states of PbTiO_3 , BaTiO_3 and SrTiO_3 . The phonon spectra of the quantum paraelectric SrTiO_3 is found to be fundamentally distinct from that of ferroelectric PbTiO_3 and BaTiO_3 . A large band gap in SrTiO_3 in the energy range from 70-90 meV is bridged by the Ti-O vibrations in PbTiO_3 and BaTiO_3 . Visualization of the first principles derived charge density distributions help understand the bonding changes in these materials which have an important bearing on their ferroelectric character. While the Pb-O bonds are highly covalent in tetragonal PbTiO_3 , the Ba-O and Sr-O bonds in rhombohedral BaTiO_3 and cubic SrTiO_3 are ionic. There is strong hybridization of the Pb-O bonds in tetragonal PbTiO_3 which were theoretically predicted (R.E. Cohen, Nature, 1992) to be the principal factors responsible for the larger ferroelectricity of PbTiO_3 as compared to BaTiO_3 . The bonding changes in these materials lead to important differences in their observed phonon density of states. The computed phonon density of states is in excellent agreement with the inelastic neutron experiments and enables microscopic interpretations of the observed data.

INTRODUCTION

Ferroelectric materials find important applications as piezoelectric transducers and actuators, pyroelectric arrays, non-volatile memories, dielectrics for microelectronics and wireless communication, non-linear optical applications, medical imaging, etc. These materials have switchable macroscopic polarization and exhibit piezoelectric properties, interconverting electrical and mechanical energies. Ferroelectrics like PbTiO_3 and BaTiO_3 are model systems which have been well studied [1-7] using experimental and theoretical techniques both due to their fundamental interest as well as due to their technological relevance. These perovskite materials have a rich phase diagram and their physical properties are found to be strongly influenced by the crystal structure [1,2]. Studies of the correlations between structural, dynamical and

piezoelectric behavior are crucial to design materials with superior performance.

We have employed first principles *ab initio* theoretical calculations and experimental neutron scattering measurements to understand the phonon density of states and its variations in PbTiO_3 , BaTiO_3 and SrTiO_3 . Our goals are to study how the changes in bonding which lead to different ferroelectric behavior in these materials, manifests in their vibrational properties. Substitution of the A and B sites in these ABO_3 type perovskites, are known to give rise to important differences in their material properties. While BaTiO_3 and PbTiO_3 are ferroelectric, SrTiO_3 is an incipient ferroelectric [7]. The soft modes and phonon instabilities in these materials have an important bearing on their piezoelectric and dielectric properties. While the ferrodistortive modes involve zone center phonon instabilities, the antiferrodistortive phase of SrTiO_3 involves zone boundary phonons related to rotations of the TiO_6 octahedra. Accurate characterization of the phonon modes in the entire Brillouin zone of these perovskites are therefore highly desirable. Unlike Raman and infrared studies, which probe only the long wavelength excitations, inelastic neutron scattering measurements can directly probe the phonon modes in the complete Brillouin zone. While limited single crystal inelastic neutron data of phonon dispersion of PbTiO_3 and BaTiO_3 are available [6], studies of their phonon density of states however were not earlier reported and have formed the focus of the present study.

EXPERIMENTAL AND CALCULATIONS

The inelastic neutron scattering measurements were carried out on the High Resolution Medium Energy Chopper Spectrometer (HRMECS) at the Intense Pulsed Neutron Source of the Argonne National Laboratory. The energy resolution ΔE of the HRMECS spectrometer varies between 2-4% of the incident-neutron energy over the neutron-energy-loss region. Two incident neutron energies were used ($E_i=50$ and 130 meV) to get a good resolution in all ranges of energy transfer. The data were collected in wide range of scattering angles (28 to 132 degrees), which provides large coverage of momentum transfer to insure good averaging of the vibrational spectra over

[#] dynamics@apsara.barc.ernet.in

Tetragonal PbTiO₃

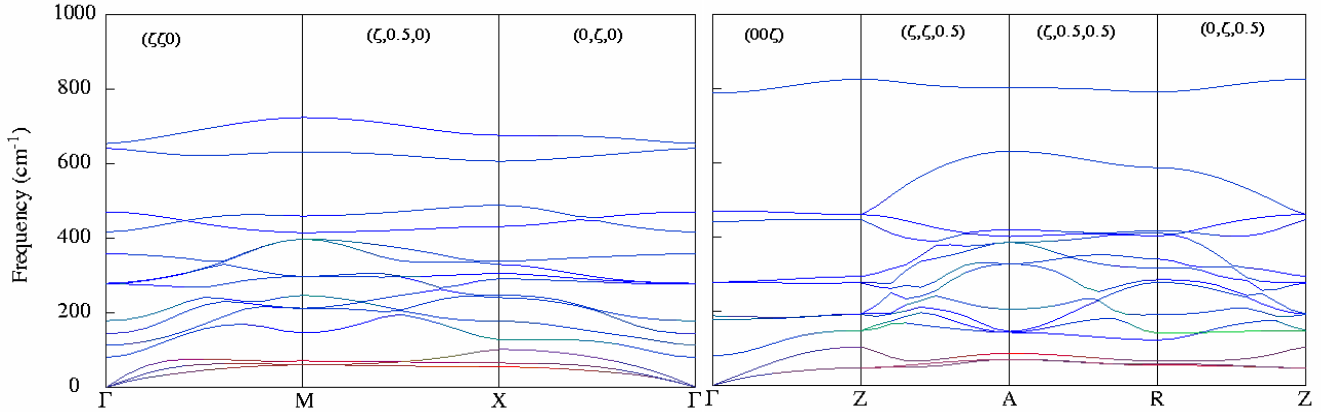


Figure 1. The computed phonon dispersion relation of tetragonal PbTiO₃. The color code corresponds to red (Pb vibrations), green (Ti) and blue (oxygen vibrations).

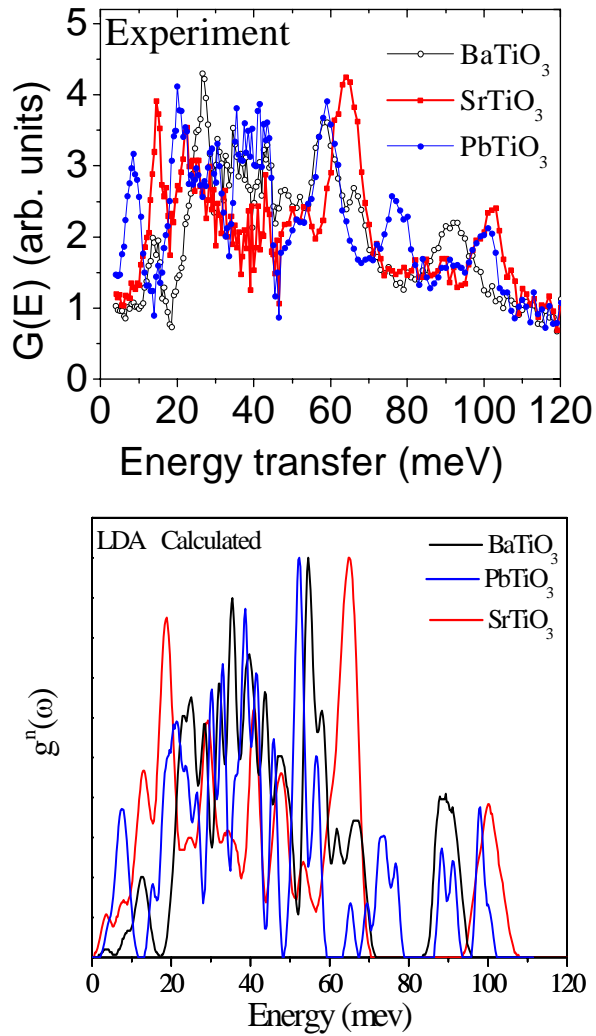


Figure 2. Comparison of the measured inelastic neutron scattering data with the computed neutron weighted density of states.

inverse space. The data were corrected for background scattering by subtracting the results from empty container runs. Measurements of the incoherent scattering from a vanadium standard provided the detector calibration and intensity renormalization. The samples were cooled to 6 K by a closed cycle refrigerator with the sample temperature maintained within 0.1 K throughout a run to minimize multiphonon contributions. Detailed analysis of the inelastic-neutron-scattering data in the incoherent approximation were undertaken for comparison with the lattice dynamics calculations.

First principles density functional theory (DFT) and density functional perturbation theory (DFPT) linear response calculations have been carried out using plane wave basis sets and the code ABINIT [8] within the local density approximation (LDA) for electron exchange and correlation. These studies employ norm conserving pseudopotentials obtained using the code OPIUM [9,10]. The Brillouin zone integrations were carried out with a 6x6x6 \mathbf{k} -point mesh using a plane wave energy cut off of 50 Ha. Exact linear response calculations on a 4x4x4 \mathbf{k} -point grid of wavevectors were undertaken and the force constants derived.

RESULTS AND DISCUSSION

Tetragonal PbTiO₃ (space group P4mm) (Fig. 1) and rhombohedral (R3m) BaTiO₃ are found to be dynamically stable in the entire Brillouin zone. Both PbTiO₃ and BaTiO₃ have a simple cubic high temperature paraelectric phase which transforms to a ferroelectric tetragonal phase around 763 K and 403 K, respectively. Tetragonal PbTiO₃ is a large strain material ($c/a=1.06$) exhibiting ferroelectricity up to high temperatures, and exhibits a single cubic to tetragonal transition; its spontaneous polarization at

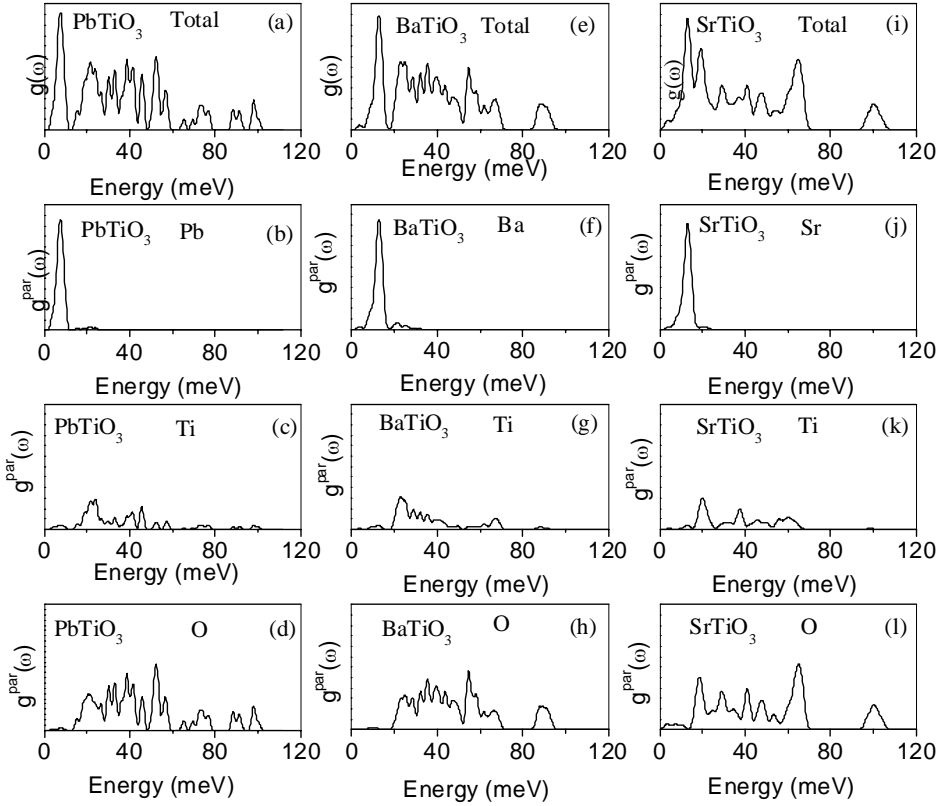


Figure 3. The computed total and partial density of states.

room temperature is almost three times that of BaTiO₃. BaTiO₃ on the other hand has a much smaller strain (1.01) and exhibits successive phase transitions from cubic to tetragonal, orthorhombic and rhombohedral structures with decreasing temperature. SrTiO₃ is a quantum paraelectric with an extremely large dielectric constant. As the temperature is reduced, SrTiO₃ undergoes a transition from the cubic ($Pm\bar{3}m$) to a tetragonal ($I4/mcm$) AFD phase at 105 K, but this transition has a non-polar character and does not affect its dielectric properties. Experimental studies suggest that although SrTiO₃ is paraelectric at low temperatures, it is very close to the ferroelectric threshold with quantum fluctuations of the atomic positions suppressing the ferroelectric instability and leading to a stabilized paraelectric state. Zero pressure LDA calculations of paraelectric cubic SrTiO₃ yield soft zone center and zone boundary R-point soft phonon modes in agreement with earlier studies [7] and these soft modes exhibit strong volume dependence. The phonon density of states which involves averaging over the phonon modes in the entire Brillouin zone is, however, not significantly altered by the changes in volume which significantly affects the dynamical stability. Preliminary LDA calculations on a coarse wavevector mesh of the tetragonal AFD phase suggest that the phonon density of states of the tetragonal

(AFD) and cubic paraelectric phases are overall quite similar.

The computed neutron-weighted phonon density of states $g^n(\omega)$ of tetragonal PbTiO₃, rhombohedral BaTiO₃ and cubic SrTiO₃ are found to be in excellent agreement with the measured inelastic neutron scattering data (Fig. 2). The total one phonon and partial density of states giving the dynamical contributions from various atoms are shown in Fig. 3. The Pb, Ba and Sr vibrations span the low energy 0-20 meV range, while the Ti and O vibrations span the 15-80 and 0-120 meV, respectively. The changes in the phonon spectra in the low energy region involve mainly the Pb, Ba and Sr vibrations.

The hybridization and sharing between the Ti and O are evident from (a-c) and (g-l) in Fig. 4. First principles electronic structure calculations [1] revealed that the hybridization between the titanium $3d$ states and the oxygen $2p$ states is essential for ferroelectricity in PbTiO₃ and BaTiO₃. From Fig. 4 ((d-f) and (m-o)), it can be seen that while the Pb-O bond is covalent, the Ba-O and Sr-O bonds are ionic (note the well connected region of charge between the Pb and O atoms in tetragonal PbTiO₃; in rhombohedral BaTiO₃ they almost connect while in cubic SrTiO₃ they are far from connecting). The computed charge distributions are in good agreement with the observed distributions

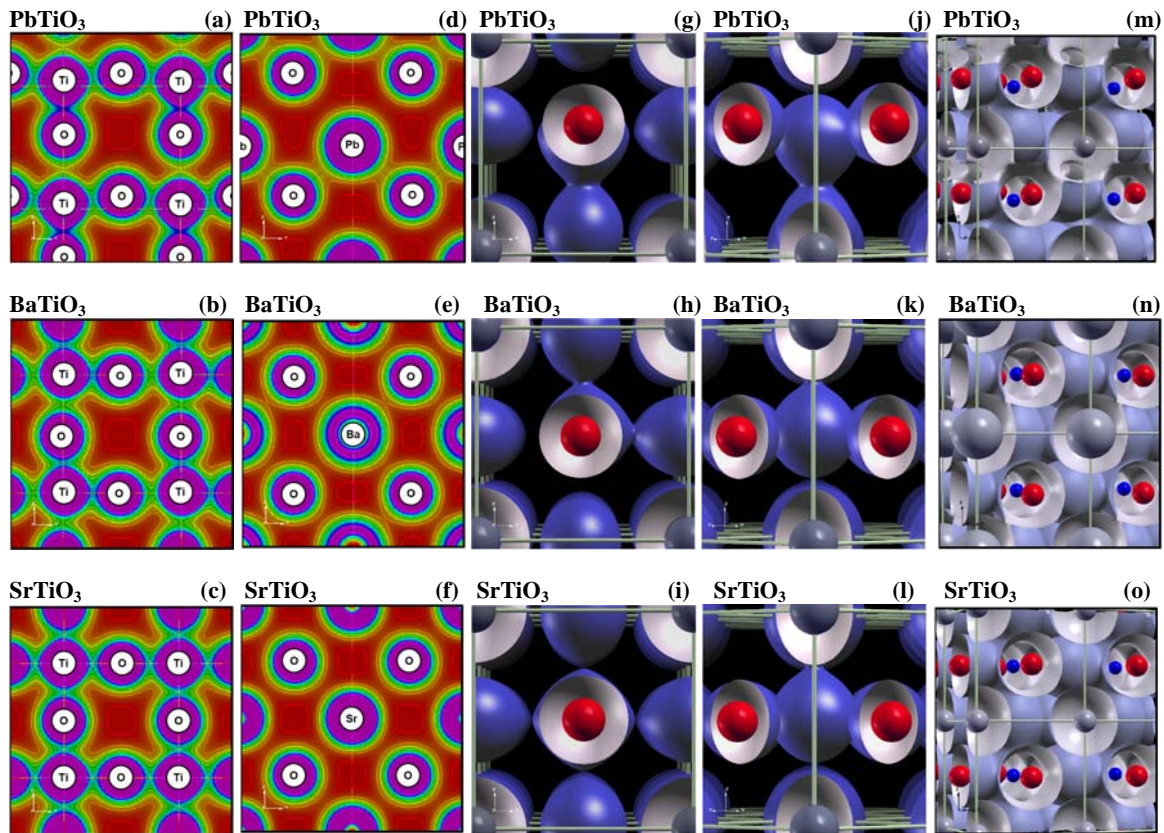


Figure 4. The computed first principles derived charge density distributions and isosurface plots (displayed using the software xcrystden [12]) of tetragonal PbTiO_3 , rhombohedral BaTiO_3 and cubic SrTiO_3 . All densities were computed from the fully relaxed zero pressure LDA structures. The charge density distribution in the $[010]$ Ti-O plane (a-c) and the $[010]$ Pb-O plane (d-f) are shown. In (a-f), the contours range from 0.01 a.u. (red) to 0.2 a.u. (violet), (1 a.u. of charge density = 1.0812×10^{12} C/m³, and gives the number of electrons per unit bohr³ volume). The 0.12 a.u. isosurfaces viewed down $[100]$ and $[110]$ are shown in (g-i) and (j-l), respectively, while the 0.03 a.u. isosurfaces are shown in (m-o). In (g-o), the grey spheres represent the A cation (namely, Pb in PbTiO_3 , Ba in BaTiO_3 and Sr in SrTiO_3), while the blue and red spheres correspond to the titanium and oxygen atoms, respectively.

of tetragonal PbTiO_3 and BaTiO_3 obtained using maximum entropy analysis of synchrotron data [11]. The clear evidence of the Pb-O hybridization (Fig. 4) and the strong covalency of the Pb-O bonds in tetragonal PbTiO_3 which arises from the hybridization of the Pb $6s$ state and O $2p$ state has been theoretically predicted [1] as a key factor of the much larger ferroelectricity of PbTiO_3 as compared to BaTiO_3 . The bonding changes in these materials also manifest in their dynamical properties and lead to important differences in the phonon density of states (Fig. 2).

In conclusion, a combination of first principles calculations and inelastic neutron scattering experiments have been helpful in understanding how the bonding changes in PbTiO_3 , BaTiO_3 and SrTiO_3 manifest in their phonon density of states. The bonding changes have an important bearing on their ferroelectric, piezoelectric and dielectric behavior and systematic investigations on a variety of perovskites may provide microscopic insights about the vibrational signatures of ferroelectric behavior.

REFERENCES

- [1] R.E. Cohen, Nature (London) 358 (1992) 136.
- [2] D. Vanderbilt, Current Opinion in Solid State and Materials Sci. 2 (1997) 701 and references therein.
- [3] A. García, D. Vanderbilt, Phys Rev B54 (1996) 3817; P. Ghosez et al., Phys. Rev. B60 (1999) 836.
- [4] J.D. Freire, R.S. Katiyar, Phys. Rev. B37 (1988) 204 and references therein.
- [5] C.M. Forster, M. Grimsditch, Z. Li, V.G. Karpov, Phys. Rev. Lett. 71 (1993) 1258.
- [6] G. Shirane, Rev. Mod. Phys. 46 (1974) 437; G. Shirane et al., Phys. Rev. Lett. 5 (1967) 234.
- [7] N. Sai, D. Vanderbilt, Phys. Rev. B 62 (2000) 13942.
- [8] X. Gonze et al., Comp. Mat. Sci. 25 (2002) 478 ; <http://www.abinit.org/>
- [9] <http://www.sourceforge.net/>
- [10] A.M. Rappe et al., Phys. Rev. B 41 (1990) 1227.
- [11] Y. Kuroiwa et al., Phys. Rev. Lett. 87 (2001) 217601.
- [12] A. Kokalj, Comp. Mater. Sci. 28 (2003) 155.

MODELING OF NEGATIVE THERMAL EXPANSION IN ZrW_2O_8 , HfW_2O_8 AND $ZrMo_2O_8$ USING LATTICE DYNAMICS AND INELASTIC NEUTRON SCATTERING

R. Mittal, S.L. Chaplot, Solid State Physics Division, Bhabha Atomic Research Centre, Trombay, Mumbai 400 085, India

A.I. Kolesnikov, C.-K. Loong, IPNS, Argonne National Laboratory, Argonne, IL 60439, U.S.A.

Abstract

Isotropic negative thermal expansion (NTE) has been known in cubic ZrW_2O_8 , HfW_2O_8 and $ZrMo_2O_8$ over a wide range of temperature up to 1443 K, 1050 K and 600 K, respectively. Anomalous thermal expansion is also observed in the orthorhombic phase of ZrW_2O_8 and HfW_2O_8 . We have carried out lattice dynamical calculations for cubic as well as orthorhombic phases of ZrW_2O_8 and HfW_2O_8 using a transferable interatomic potential. The calculated phonon spectrum for cubic HfW_2O_8 is in fair agreement with the spectrum measured using HRMECS. Our calculations reproduced the observed anomalous thermal expansion in these compounds. It is found that the softening of low energy modes (below 8 meV) results in a negative thermal expansion.

INTRODUCTION

Negative thermal expansion has been known for a long time in several elemental solids (e.g. Si, Ge, diamond) at low temperatures and other compounds in certain crystallographic directions e.g., quartz and β -eucryptite $LiAlSiO_4$. However, large isotropic negative thermal expansion (NTE) has been known in cubic ZrW_2O_8 , HfW_2O_8 [1,2] (space group $P2_13$, $Z=4$) and $ZrMo_2O_8$ [3] (space group $Pa\bar{3}$, $Z=4$) over a wide range of temperature up to 1443 K, 1050 K and 600 K, respectively. The compounds can be used for the preparation of controlled thermal expansion composites where the NTE material to some extent compensates for the positive thermal expansion of the other component. The structure of AX_2O_8 ($A=Zr, Hf$; $X=W, Mo$) consists of corner linked AO_6 octahedral and XO_4 tetrahedral units.

Neutron diffraction data [4,5] show a cubic to orthorhombic (space group $P2_12_12_1$, $Z=12$) phase transition at pressures around 2.1 kbar and 6 kbar for ZrW_2O_8 and HfW_2O_8 , respectively. However cubic $ZrMo_2O_8$ does not show any phase transition [3] below 6 kbar. An anomalous thermal expansion is also observed in the orthorhombic phase [4,5] of ZrW_2O_8 and HfW_2O_8 . Specific heat [6] measurements for cubic AW_2O_8 ($A=Zr, Hf$) and Raman [7] and inelastic neutron scattering measurements [8] for cubic ZrW_2O_8 are reported.

Some estimates of the Grüneisen parameters are reported [7-9] for AW_2O_8 ($A=Zr, Hf$) on the basis of the

observed NTE and certain assumptions about the energy dependence of the Grüneisen parameters or the phonon density of states. These estimates indicated fairly large negative values of the Grüneisen parameters. We have shown [10-17] via lattice dynamical calculations and high-pressure inelastic neutron scattering experiments that a large softening of several low-energy phonons (up to 8 meV) is mainly responsible for the anomalous thermal expansion in AX_2O_8 ($A=Zr, Hf$; $X=W, Mo$). Here we summarize the results obtained from our studies on these compounds. While complete phonon spectrum measurements on $ZrMo_2O_8$ and HfW_2O_8 were performed at ANL, pressure dependence of the low energy phonon spectrum was measured at ILL, France.

EXPERIMENTAL

The ambient pressure measurements for HfW_2O_8 were carried out using HRMECS. The spectrometer is equipped with a large detector bank covering a wide range (-10° to 140°) of scattering angles. A polycrystalline sample of 25 gm was placed inside a sealed aluminum container. We chose a high incident energy ($E_0=200$ meV) of neutrons, which permitted the data to be collected over a wide range of momentum transfer Q from 4 to 19 \AA^{-1} . This was needed to ensure an effectively uniform sampling of Q wave vectors over the Brillouin zone, according to the requirements of the incoherent approximation [18]. The measurements were performed in the energy loss mode. In order to reduce multi-phonon scattering, the phonon measurements were carried out at low temperatures of 7 K. Background scattering was subtracted from the data by using an empty-container run. Measurements of the elastic incoherent scattering from a vanadium standard provided detector calibration and intensity normalization.

LATTICE DYNAMICAL CALCULATIONS

We used a semiempirical interatomic potential consisting of Coulombic and Born - Mayer type short ranged terms and a van der Waals type attractive interaction between the oxygen atoms. The parameters of the potential are the effective charge and radius of the atoms. A covalent potential is also included between the nearest W and O atoms. The polarizability of the oxygen atom is introduced in the framework of the shell model [10]. The potential reproduces the equilibrium crystal structural parameters and other dynamical properties quite

rmittal@apsara.barc.ernet.in

satisfactorily. The procedure for the thermal expansion calculations is given in our previous publications [10,13].

RESULTS AND DISCUSSION

The experimental and calculated neutron-weighted one-phonon density of states for cubic HfW_2O_8 as shown in Fig. 1 reveal a gap at about 60-90 meV. Agreement between the experimental data and calculations below the gap is good. However, above 90 meV the calculated density of states shows a single peak around 120 meV, whereas the experimental data reveal a three peak structure. The phonons above 90 meV involve W-O stretching vibrations. Their force field is apparently more dispersed than that described by the interatomic potential in the lattice dynamical model. As far as the phonon contribution to the NTE behavior is concerned, only the low energy phonons are involved (as shown below). Therefore the model is able to correctly account for the thermal expansion behavior.

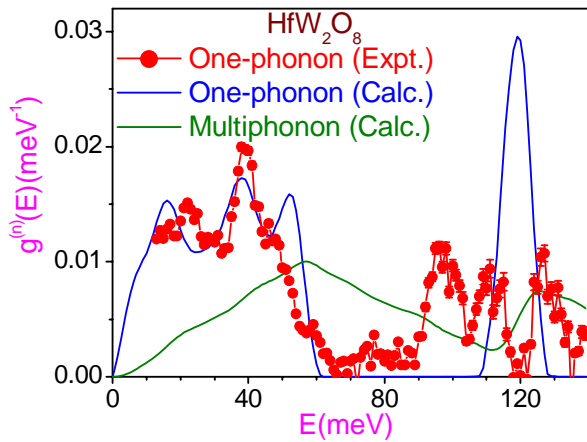


Figure 1. The experimental and calculated neutron-weighted phonon density of states [13] of cubic HfW_2O_8 . In order to account for the experimental resolution broadening in cubic HfW_2O_8 the calculated spectrum have been convoluted with a resolution function of HRMECS spectrometer. The multi-phonon contribution (dash line) has been subtracted from the experimental data of cubic HfW_2O_8 to obtain the experimental one-phonon density of states.

The calculated pressure dependence of the phonon spectrum for ordered cubic AW_2O_8 ($\text{A}=\text{Zr}, \text{Hf}$) (Fig. 2) as well as the calculated Grüneisen parameter (Fig. 3) show that the phonons of energies below 8 meV are most relevant to NTE. Fig. 4 shows the quasiharmonic calculation of the thermal expansion. This reveals a very interesting result, namely, that nearly 40% of the NTE in the cubic phase arises from just the two lowest phonon branches and almost all the NTE is contributed from the modes below 8 meV. The absolute value of thermal expansion coefficient for HfW_2O_8 is smaller in comparison with ZrW_2O_8 . The calculated relative thermal expansion for both the cubic ZrW_2O_8 and HfW_2O_8 is

shown in Fig. 5, which indicates an excellent agreement with the experimental data [1,2,4].

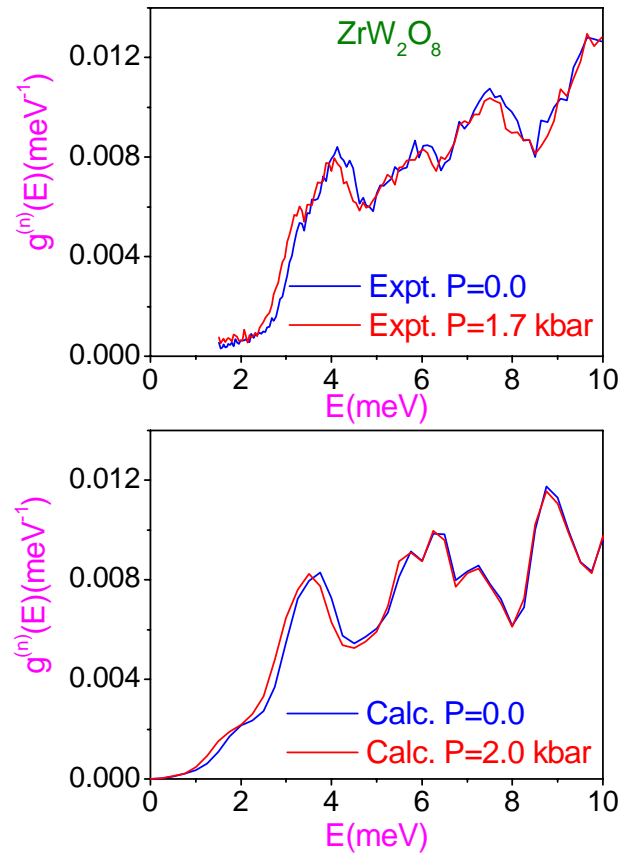


Figure 2. The comparison between the calculated and experimental inelastic neutron scattering spectra for cubic ZrW_2O_8 [14].

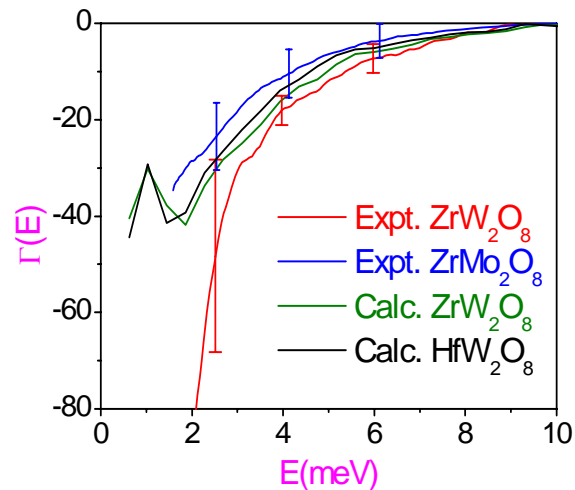


Figure 3. The Grüneisen parameter ($\Gamma(E)$) [10,13-15] averaged over phonons of energy E . The experimental [14,15] values are determined using the neutron data of phonon density of states as a function of pressure.

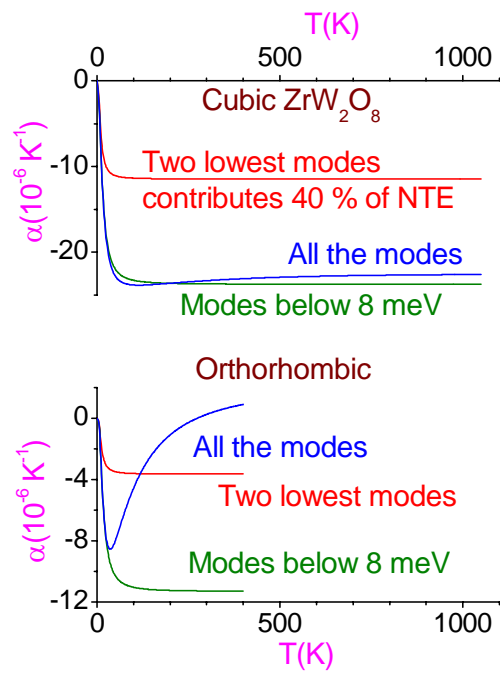


Figure 4. The calculated [10] volume thermal expansion in the cubic and orthorhombic ZrW_2O_8 along with separate contributions from the two lowest phonon branches and all the phonons below 8 meV.

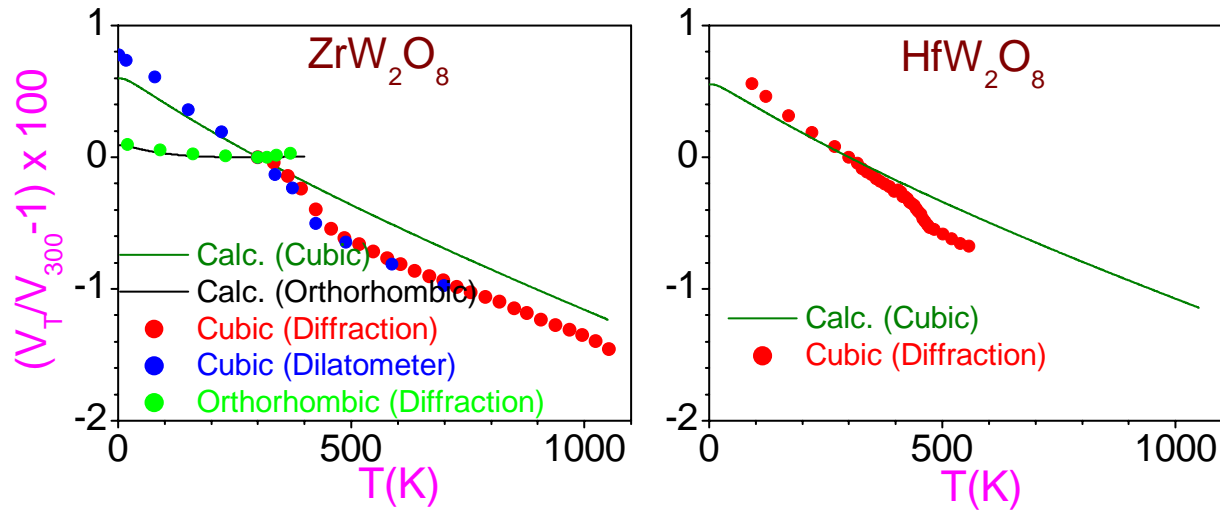


Figure 5. The experimental and calculated [10,13] relative volume thermal expansion for cubic ZrW_2O_8 , HfW_2O_8 and orthorhombic ZrW_2O_8 , $(V_T/V_{300}-1) \times 100\%$, V_T and V_{300} being the cell volumes at temperature T and 300 K, respectively. There is a small sharp drop in volume for cubic phase at about 400 K associated with an order disorder phase transition [1,2]. Experimental data; cubic ZrW_2O_8 [1], cubic HfW_2O_8 [2], orthorhombic ZrW_2O_8 [4].

CONCLUSIONS

Large softening of phonon modes below 8 meV on compression is able to explain the thermal expansion behavior of ZrW_2O_8 , HfW_2O_8 and $ZrMo_2O_8$. The inelastic neutron scattering measurements were useful for validating the lattice dynamical model developed by us. Further experimental characterization of the specific

The thermal expansion of the orthorhombic phase is observed [4] to be anomalous; it is negative below 300 K and positive above 300 K. Above 400 K the orthorhombic phase transforms to cubic phase. The calculation of thermal expansion in the orthorhombic phase of ZrW_2O_8 is compared with the experiments in Fig. 5 which shows a very good agreement. Compared to the cubic phase, the negative thermal expansion contributed by the phonons below 8 meV (Fig. 4) is much reduced, which allows the high energy modes to dominate at high temperatures and yield a net positive expansion above 270 K in calculations.

In order to understand the nature of phonons responsible for NTE we have calculated the partial contributions of the phonons of different energies to the mean square vibrational amplitude of the various atoms at 300 K. The modes up to 1 meV are largely acoustic in nature. For modes between 1 to 4 meV, oxygen atoms constituting the WO_4 tetrahedra have significantly different values of their vibrational amplitudes, which indicates distortions of the tetrahedra. Above 4 meV the amplitude of all the atoms is relatively small. The phonon modes of energy about 4 meV contribute maximum to the negative thermal expansion.

phonons would require single crystal measurements in the entire Brillouin zone.

REFERENCES

- [1] T.A. Mary, J.S .O. Evans, T. Vogt and A.W. Sleight, Science 90 (1996) 272.
- [2] Y. Yamamura, N. Nakajima, T. Tsuji, Phys Rev B 64 (2001) 184109.

- [3] C. Lind, A.P. Wilkinson, Z. Hu, S. Short and J.D. Jorgensen, *Chem. Mater.* 10 (1998) 2335.
- [4] Z. Hu, J.D. Jorgensen, S. Teslic, S. Short, D.N. Argyriou, J.S.O. Evans, A.W. Sleight, *Physica B* 241-243 (1998) 370.
- [5] J.D. Jorgensen, Z. Hu, S. Short, A.W. Sleight, J.S.O. Evans, *Journal of Applied Physics* 89 (2001) 3184.
- [6] Y. Yamamura, N. Nakajima, T. Tsuji, M. Koyano, Y. Iwasa, S. Katayama, K. Saito, M. Sorai, *Phys. Rev. B* 66 (2002) 14301.
- [7] T.R. Ravindran, A.K. Arora, T.A. Mary, *J. Phys.: Condens. Matter* 13 (2001) 11573.
- [8] G. Ernst, C. Broholm, G.R. Kowach, A.P. Ramirez, *Nature (London)* 396 (1998) 147.
- [9] W.I. David, J.S.O. Evans, A.W. Sleight, *Europhys. Lett.* 46 (1999) 661.
- [10] R. Mittal, S.L. Chaplot, *Phys. Rev. B* 60 (1999) 7234.
- [11] S.L. Chaplot, R. Mittal, *Phys. Rev. Lett.* 86 (2001) 4976.
- [12] R. Mittal, S.L. Chaplot, *Solid State Communication* 115 (2000) 319.
- [13] R. Mittal, S.L. Chaplot, A.I. Kolesnikov, C.-K. Loong, T.A. Mary, *Phys. Rev. B* 68 (2003) 54302.
- [14] R. Mittal, S.L. Chaplot, H. Schober, T.A. Mary, *Phys. Rev. Lett.* 86 (2001) 4692.
- [15] R. Mittal, S.L. Chaplot, H. Schober, A.I. Kolesnikov, C.-K. Loong, C. Lind, A.P. Wilkinson, *Phys. Rev. B* 70 (2004) 214303.
- [16] R. Mittal, S.L. Chaplot, N. Choudhury, *Progress in Materials Science* 51 (2006) 211.
- [17] S.L. Chaplot, *Current Science* 88 (2005) 347.
- [18] D.L. Price, K. Skold, in *Methods of experimental physics: Neutron scattering Part A*, edited by K. Skold and D.L. Price (Academic Press, Orlando, 1986), Vol. 23.



Alexander Kolesnikov – HRMECS Instrument Scientist

DYNAMIC MAGNETIC SUSCEPTIBILITY OF $Gd_5Si_2Ge_2$ AND $Gd_4YSi_{1.9}Ge_{2.1}$

C. Vecchini, O. Moze[#], INFN, Dipartimento di Fisica, Università di Modena e Reggio Emilia
Modena, 41100, Italy

A.O. Pecharsky, V.K. Pecharsky, K.A. Gschneidner, Jr, Ames Laboratory and Department of
Materials Science and Engineering, Iowa State University, Ames, Iowa 50011-3020, U.S.A.

A.I. Kolesnikov, IPNS, Argonne National Laboratory, Argonne, IL, 60439-4814, U.S.A.

E. Brück, Van der Waals-Zeeman Institut, Universiteit van Amsterdam, Valckenierstraat 65,
1018XE, Amsterdam, The Netherlands

R. Bewley, ISIS Facility, Rutherford Appleton Laboratory, Didcot, OX11 0QX, UK.

The rare-earth intermetallic compound $Gd_5Si_2Ge_2$ displays a technologically relevant magnetocaloric effect which approaches values of over $36 \text{ Jkg}^{-1}\text{K}^{-1}$ for a magnetic field change of 0 to 5 Tesla near room temperature [1,2]. The aforementioned effect in this material is associated with a first order magnetic transition which takes place simultaneously with a structural phase transition from an orthorhombic low temperature phase (space group Pnma) to a high temperature monoclinic phase (space group P112₁/a) [3]. Alterations in (Si-Ge)-(Si-Ge) covalent bond distances and local environments across the transition are intimately related to the electronic structure of $Gd_5Si_2Ge_2$ [4,5]. The first order transition which gives rise to such a large magnetocaloric effect holds a naturally promising prospective for magnetic refrigeration near ambient temperatures. Exchange interactions between localized Gd moments are an important source of these magnetic phenomena, and details of the exchange interaction are usually investigated by inelastic neutron scattering [6]. From the inelastic neutron scattering cross section, the dynamic magnetic susceptibility (or dynamic magnetic response) can be obtained directly. The latter quantity, which is model independent, is of considerable interest as it can be compared directly with model calculations of the dynamic susceptibility. An unfortunate technical drawback is the very high neutron absorption cross section for the naturally occurring mixture of isotopes in Gd. This cross section can be reduced to values below 1000 barns for incident neutron energies above 250 meV and experience has shown that a reasonable energy resolution, combined with an observable cross section can be obtained with incident neutron energies of this order. Up until now, nothing at all is known about the energy range of the magnetic excitations in $Gd_5Si_2Ge_2$. For this purpose, we have utilized high incident energy neutrons available at IPNS (HRMECS spectrometer) and ISIS (HET spectrometer) in order to overcome this limiting factor for the compound $Gd_4YSi_{1.9}Ge_{2.1}$ and the pure compound [7]. Dilution of one or more of the magnetic sites in this system by a non magnetic ion such as Y is expected to result in modifications of the crystal structure, bulk magnetic

properties and dynamic response of the parent compound.

The temperature dependence of the inelastic neutron spectra at small scattering angles (at these small angles, Q is small and the magnetic form factor approaches its $Q = 0$ value of 1 for the Gd^{3+} ion) for $Gd_5Si_2Ge_2$ and $Gd_4YSi_{1.9}Ge_{2.1}$ are displayed in Fig. 1 and Fig. 2 respectively. In order to verify that any observed excitation is indeed of magnetic origin, the inelastic neutron spectra at 5 K and at similarly small scattering angles were also measured for $Y_5Si_2Ge_2$, which does not order magnetically. The scattering at high angles for this compound is dominated by a relatively small phonon density of states. Even though the structure of this compound is different from the Gd compounds, they are closely related to each other, so that any effective phonon density of states in the Gd and Y compounds are most likely similar to each other.

The dynamic response for $Gd_5Si_2Ge_2$ consists of two excitations extending up to 40 meV. These excitations are magnetic since they do not appear in the response observed for the non-magnetic reference compound, $Y_5Si_2Ge_2$, and they commence a steady collapse into an almost broad response at 265 K. This response is entirely paramagnetic at 310 K which is above the Curie temperature of ~ 270 K for this compound. The observed magnetic response for the diluted compound $Gd_4YSi_{1.9}Ge_{2.1}$ at 7 K is also different from the non-diluted compound, whereby the positions and intensities of the magnetic excitations have decreased markedly with respect to $Gd_5Si_2Ge_2$. The magnetic excitation observed at 20 meV for $Gd_5Si_2Ge_2$ has been considerably scaled down to a lower energy, at just over 15 meV for $Gd_4YSi_{1.9}Ge_{2.1}$, whilst the excitation at 30 meV has suffered a significant reduction in intensity. These data clearly and unambiguously show that the magnetic excitation spectrum in these compounds does not extend beyond 40 meV. The energy range of the magnetic excitations is similar in magnitude to that reported for metallic Gd. A detailed analysis of the inelastic spectra presented here is clearly rendered difficult by Gd ions located in three different crystallographic sites of the low temperature, ferromagnetic orthorhombic phase. Dispersion of the magnetic modes cannot be ruled out, but any further information in this regard must await a detailed single

[#] moze@unimore.it

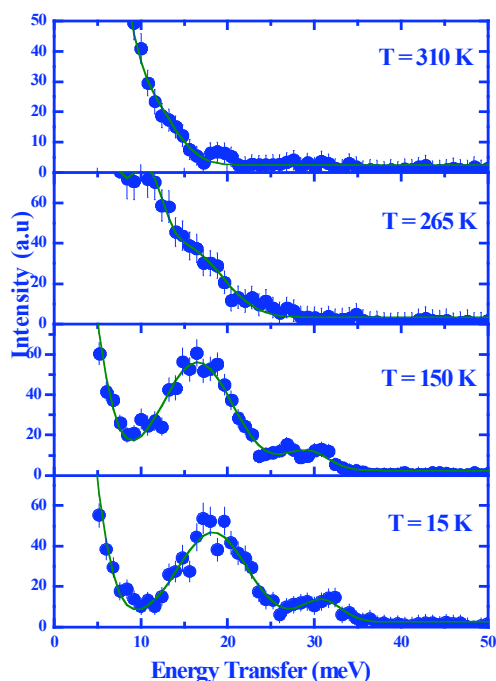


Fig. 1. Low angle detector bank inelastic neutron spectra for $\text{Gd}_5\text{Si}_2\text{Ge}_2$ at 15, 150, 265 and 310K.

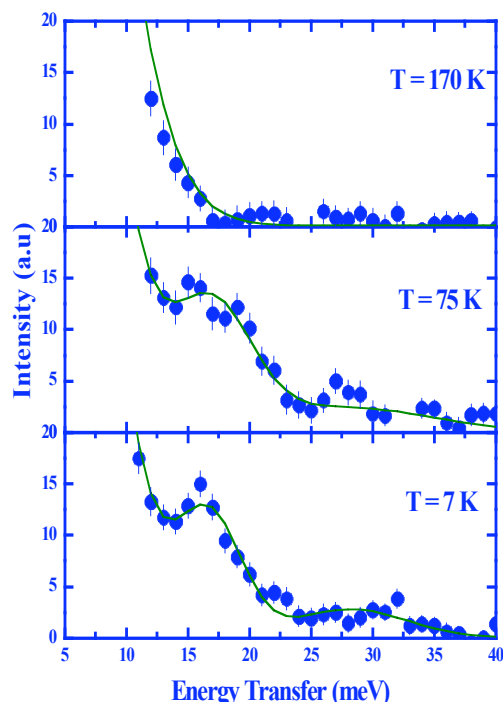


Fig. 2. Low angle detector bank inelastic neutron spectra for $\text{Gd}_4\text{YSi}_{1.9}\text{Ge}_{2.1}$ at 7, 75, and 170K

crystal inelastic neutron scattering investigation. In this regard, model calculations of the dynamic susceptibility incorporating recent first principles band structure calculations [8] for both the monoclinic and orthorhombic structures are highly warranted.

Financial support from the INFM, Sezione D: Magnetismo, Metalli, Superconduttività (Intervento Speciale) is gratefully acknowledged. The Ames Laboratory is operated by Iowa State University for the U.S. Department of Energy (DOE) under contract No. W-7405-ENG-82. This research was supported by the Office of Basic Energy Sciences, Materials Sciences Division of the U.S. DOE (K.A.G, A.O.P. and V.K.P). This research was also supported by the Dutch Technology Foundation STW, the Applied Science Division of NWO and the Technology Programme of the Ministry of Economic Affairs. The work at Argonne National Laboratory was supported by the U.S. Department of Energy, Basic Energy Sciences-Materials Sciences, under Contract No. W-31-109-ENG-38.

REFERENCES

- [1] V.K. Pecharsky and K.A. Gschneidner, Jr, Phys. Rev. Lett. 78 (1997) 4494, and J. Appl. Phys. 70 (1997) 3299.
- [2] A. O. Pecharsky, K. A. Gschneidner, Jr and V. K. Pecharsky, J. Appl. Phys. 93(2003) 4722.
- [3] L. Morellon, P.A. Algarabel, M.R. Ibarra, J. Blasco, B. Garcia-Landa, Z. Arnold, and F. Albertini, Phys. Rev. B 58 (1998) R14721.
- [4] V. K. Pecharsky and K. A. Gschneidner, J. Alloys Comps 260 (1997) 98.
- [5] W. Choe, V.K. Pecharsky, A.O. Pecharsky, K.A. Gschneidner, Jr, V.G. Young, Jr, and G.J. Miller, Phys. Rev. Lett. 84 (2000) 4617.
- [6] P. Tiles, M. Lowenhaupt, K.H.J. Buschow and R.S. Eccleston, J. Mag. Mater. 210 (2000) 196.
- [7] C. Vecchini, O. Moze, A.O. Pecharsky, V.K. Pecharsky, K.A. Gschneidner, Jr, E. Brück, R. Bewley, and A. Kolesnikov, J. Appl. Phys. 95 (2004) 7207.
- [8] B.N. Harmon and V.N. Antonov, J. Appl. Phys. 91 (2002) 9815.

OBSERVATIONS OF WATER-FRAMEWORK INTERACTIONS IN A HYDRATED MICROPOROUS ALUMINUM PHOSPHATE

Huaxin Yang[#], National Laboratory for Condensed Matter Physics, ACS, Beijing, 100080, China

Jichen Li, Department of Physics, The University of Manchester, Manchester, M60 1QD, U.K.

Richard I. Walton[#], Department of Chemistry, Open University, Walton Hall, MK7 6AA, U.K.

Alexander I. Kolesnikov, IPNS Division, ANL, Argonne, IL 60439, U.S.A.

Abstract

HRMECS data have been measured to explain the water-framework interactions in a hydrated microporous aluminum phosphate (AIPO-14). Two O-H stretching modes for bound water in hydrated AIPO-14 were detected, consistent with the model of two types of water present in the material: the tightly bound water bridge pairs of Lewis acidic framework aluminums in a dense region of the structure, while loosely bound water resides in the pores of the solid; the loosely bound water is connected to neighboring water molecules by intermolecular hydrogen bonds.

INTRODUCTION

Host-guest interactions in microporous materials are of the utmost importance in understanding the sorption properties of the solids, which give rise to their widespread commercial applications in, for example, molecular sieving and catalysis. It is often difficult, however, to locate the positions of adsorbed guest molecules in porous solids using crystallographic techniques, due to considerable positional disorder of the adsorbed species. It is therefore necessary to turn to short-range probes to gain insight into the average local atomic arrangement about individual atom types and to allow a picture to be built up of the interactions between sorbed molecules and the inorganic framework of the porous solid. AIPO-14 is a microporous material made up of four-, six-, and eight-rings and has a three-dimensional channel system delimited by the eight-rings [1]. AIPO-14 is very easy to absorb water. We have used various techniques including: thermal analysis, solid-state ²⁷Al MAS NMR and incoherent inelastic neutron scattering studies using TOSCA instrument at ISIS and HRMECS instrument at ANL [2] to deduce information concerning the local structure of the absorbed water molecules in the hydrated solid.

The TOSCA data were recorded over the range 2-500 meV. In this paper we present HRMECS measurements using high-incident neutron energy provided data that are complementary to those performed using TOSCA.

[#] R.I.Walton@open.ac.uk

EXPERIMENTAL SECTION

AIPO-14 was prepared by a method adapted from that of Broach et al. using isopropylamine as the template [2]. Calcination was performed by heating AIPO-14 at 600 °C for 2 h in air. The hydrated form of the material results from standing the calcined solid in moist air. The HRMECS data were collected at T=8 K over a period 21 h from a sample of mass 5.66 g. The data were measured over a wide range of detector angles (5-130°), hence a large coverage of wavevectors, Q . The data obtained at small angles (small Q values) from HRMECS were crucial to the measurement of high-energy spectra due to the large mean-square displacement of hydrogen $\langle u_H^2 \rangle$, which severely damps the intensity with increasing Q , according to $\exp(-\langle u_H^2 \rangle Q^2)$.

RESULTS AND DISCUSSION

Differential scanning calorimetry of the hydrated, microporous aluminum phosphate AIPO-14 shows two distinct water losses between room temperature and 120 °C, indicating the presence of two types of water in the solid. Multiple-quantum magic angle spinning (MQMAS) ²⁷Al NMR shows that, while in dehydrated AIPO-14 all aluminum is found in tetrahedral sites, on hydration a significant proportion of the aluminum increases its coordination number to 6. This accounts for the presence of tightly bound water. The TOSCA studies of such a

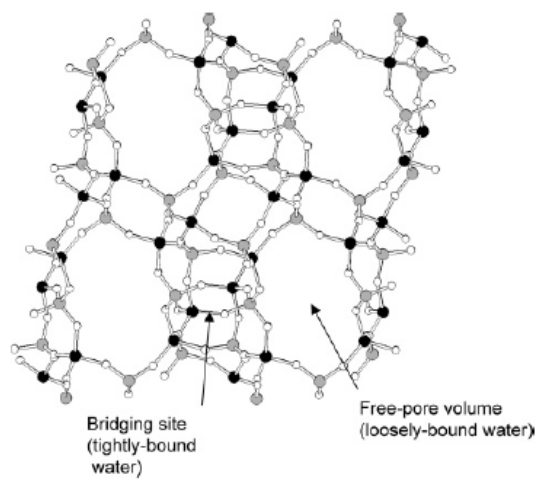


Figure 1. Part of the structure of calcined, dehydrated AIPO-14. Aluminum atoms are gray circles, and phosphorus are black.

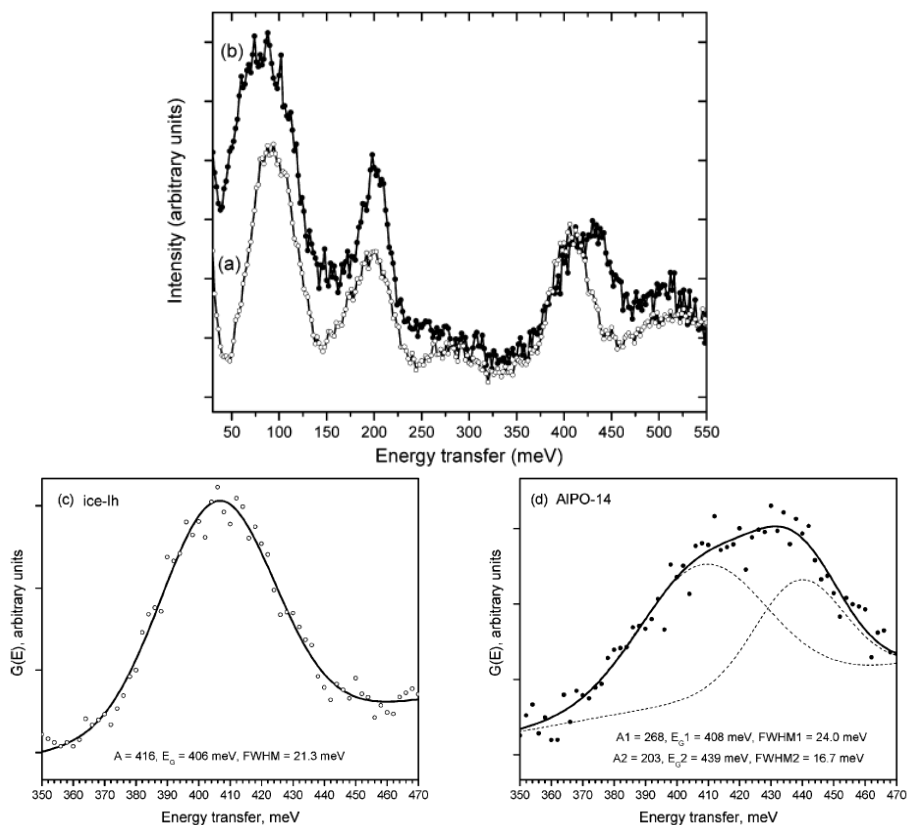


Figure 2. IINS data from (a) ice Ih and (b) calcined, hydrated AIPO-14 measured using incident neutron energy of 600 meV on HRMECS. Gaussian deconvolutions are shown in c and d, respectively, where the fitting parameters are shown (points are the experimental data, and lines are the fitted curves).

system give a spectrum with distinct and sharp librational bands for bound water, significantly different than seen in ice Ih. Using these data, and by consideration of the crystal structure of dehydrated AIPO-14, we propose a model for the hydrated material in which the tightly bound water bridges pairs of Lewis acidic framework aluminums in a dense region of the structure, while loosely bound water resides in the pores of the solid [2].

For a better understanding of the model, Fig. 1 shows part of the structure of calcined, dehydrated AIPO-14 (a projection along c -axis using the atomic coordinates of Broach et al.[1]) with free pore volume and the location of the bridging positions of water indicated.

Further evidence for the presence of two distinct types of water in hydrated AIPO-14 is provided by HRMECS measurement. Figure 2 shows these data for ice Ih and for the hydrated AIPO-14. We note that the sharp libration peaks are actually seen in the region of 50-100 meV, despite the low resolution of these data in this spectral region. More importantly, these data reveal new information in the region around 400 meV. The peak centered at 406 meV (determined by Gaussian fitting, Figure 2c) in ice Ih is attributed to water O-H stretching modes [3]. It has previously been shown that this band is sensitive to the nature of intermolecular hydrogen bonding (for example, its position can vary between different polymorphs of ice [3], or with pressure [4]). For hydrated AIPO-14 this region of the spectrum is more complex than in ice Ih, and two Gaussians can be fitted at 408 and 439 meV, Figure 2d. The former would suggest

the presence of intermolecular hydrogen bonds of a strength similar to those seen in ice Ih, consistent with water present in the pores of the AIPO-14 structure, only weakly interacting with the inorganic framework, but themselves interconnected by hydrogen bonding. The latter suggests water that is more weakly hydrogen-bonded, which is consistent with individual water molecules (i.e., not interconnected to neighboring water molecules by hydrogen bonding), coordinating to the Lewis acidic aluminums in the bridging sites and having weaker hydrogen bonding interactions with framework oxygens.

The IINS data from our hydrated AIPO-14 are of much higher quality than those available in the literature for related systems and demonstrate the utility of the method in probing water confined in microporous solids.

REFERENCES

- [1] R.W. Broach, S.T. Wilson, R.M. Kirchner, Proceedings of the 12th International Zeolite Conference; Materials Research Society: Warrendale, PA, 1999; p. 1715.
- [2] H.X. Yang, R.I. Walton, S. Biedasek, S. Antonijevic and S.Wimperis A.J. Ramirez-Cuesta, J. Li, A.I. Kolesnikov, J. Phys. Chem. B 109 (2005) 4464.
- [3] J. Li, J. Chem. Phys. 105 (1996) 6733.
- [4] D.D. Klug, E. Whalley, J. Chem. Phys. 81 (1984) 1220.

EXPERIMENTAL EVIDENCE OF A LIQUID-LIQUID TRANSITION AT 240 K IN INTERFACIAL WATER

J.-M. Zanotti[#], M.C. Bellissent-Funel, LLB (CEA-CNRS), CEA Saclay,
91191 Gif-sur-Yvette Cedex, France

S.-H. Chen, Department of Nuclear Engineering, MIT, Cambridge, Massachusetts 02139, USA

A.I. Kolesnikov, IPNS, Argonne National Laboratory, Argonne, IL 60439, USA

Abstract

At ambient pressure, bulk liquid water shows an anomalous increase of thermodynamic quantities and apparent divergences of dynamic properties on approaching a temperature T_S of 228 K. At normal pressure, supercooled water spontaneously freezes below the homogeneous nucleation temperature, $T_H = 235$ K. Upon heating, the two forms of Amorphous Solid Water (ASW), LDA (Low Density Amorphous Ice) and HDA (High Density Amorphous Ice), crystallise above $T_X = 150$ K. As a consequence, up to now no experiment has been able to explore the properties of liquid water in this very interesting temperature range between 150 and 235 K. We present nanosecond-time-scale measurements of local rotational and translational dynamics of interfacial, non-crystalline water from 77 to 280 K. These experimental dynamic results are combined with calorimetric, diffraction and inelastic neutron scattering data to show that after exhibiting a glass transition at 165 K, interfacial water experiences a first order liquid-liquid transition at 240 K from a low density to a high density liquid. Here, using interfacial water as a model system, we show that such a liquid-liquid transition between a low and a high density form of liquid water is possible.

transition line (thick dash line) between a high density liquid (HDL) and a low density liquid (LDL).

INTRODUCTION

This study is related to the tremendously active field of water dynamics and the debate on the hypothetical low temperature critical point of water at $T_S = 228$ K [1].

A condition for the existence of this critical point is the presence of a first order transition between a High (HDL) and a Low Density Liquid (LDL), see dashed line in Fig. 1. At normal pressure, supercooled water spontaneously freezes below the homogeneous nucleation temperature, $T_H = 235$ K. Upon heating, the two forms of amorphous solid water, LDA (Low Density Amorphous Ice) and HDA (High Density Amorphous Ice), crystallise above $T_X = 150$ K. As a consequence, up to now no experiment has been able to explore the properties of liquid water in this very interesting temperature range between 150 and 235 K. The coexistence line has actually only been studied using the low temperature amorphous forms of the liquids: High Density Amorphous Ice and Low Density Amorphous Ice.

We have been able to measure for the first time the dynamics of NON-crystalline water from 77 to 280 K and have accessed orientational and translational nanosecond dynamics of water on the surface of a porous Vycor silica glass.

EXPERIMENTAL

Sample preparation

In our study, water is adsorbed as a monolayer on Vycor (Vycor brand porous glass n°7930 is a product of Corning Glass Works), a porous hydrophilic silica glass. A partially hydrated sample was prepared by absorption of water in the vapour phase, until a level of hydration corresponding to a monolayer coverage was obtained (25% hydration).

Thermodynamics

As shown by DSC (Fig. 2) this system experiences a significant phase transition at 240 K. Density change of the interfacial water above and below the transition has been inferred from diffraction data (not shown, 7C2, LLB).

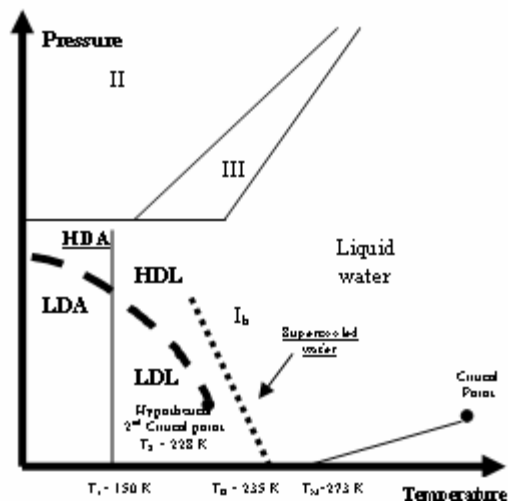


Figure 1. Simplified phase diagram of water, showing the hypothetical 2nd critical point and the related

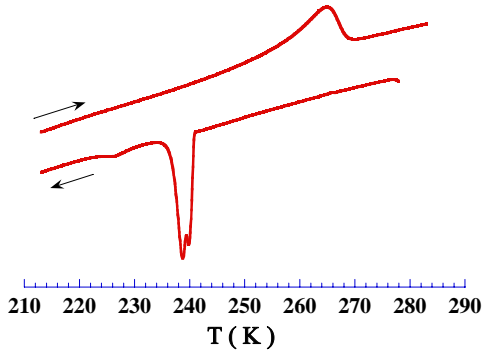


Figure 2. Thermograms (5 K/min) of a monolayer of water at the Vycor hydrophilic surface. Cooling and heating are indicated by arrows.

Inelastic Neutron Scattering

Using HRMECS (ANL/IPNS), we have been able to access over a very broad energy range ranging from 150 to 500 meV, the intramolecular OH water stretching and HOH bending modes.

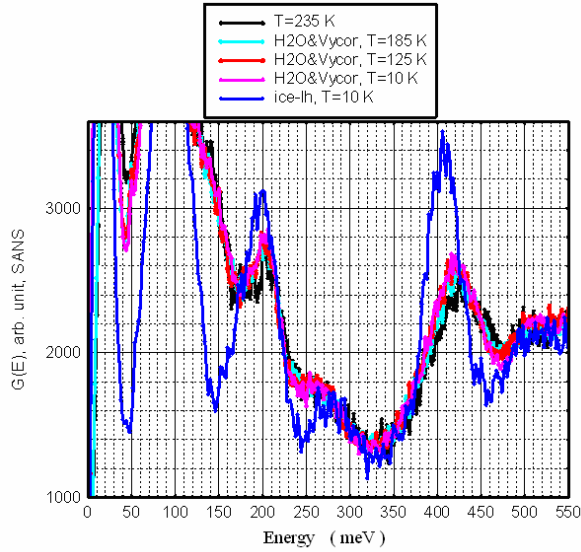


Figure 3. Monolayer of water on Vycor high energy transfer (600 meV incident energy neutrons HRMECS, ANL/IPNS) vibrational density of states as function of temperature from 10 to 235 K; Dry Vycor not subtracted. The intramolecular HOH bending mode and intramolecular OH stretching are clearly detected at 208 meV and 420 meV respectively. Ice-Ih signal is given for comparison.

Compared to the same bands in Ice I-h, the interfacial water intramolecular excitations exhibit at all the temperatures a strong shift towards higher energy (420 meV in bulk and 425 meV interfacial). As shown by IR study of ice VII under pressure [2], a shift of the intramolecular stretching OH towards higher energy is expected to be correlated with a decrease of the H-bond strength. The HRMECS experiment leads to the conclusion that H-bond is weaker in interfacial water than in bulk water.

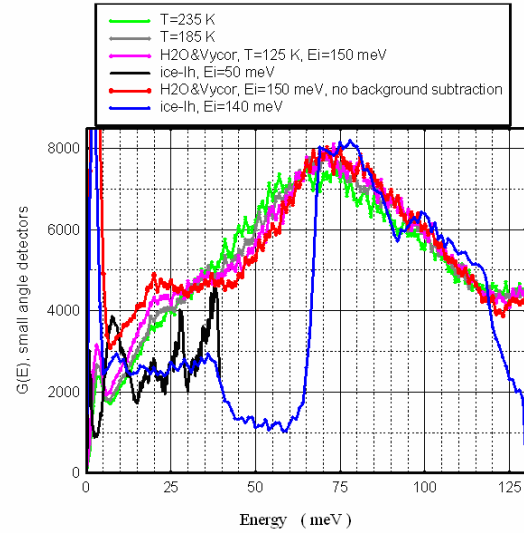


Figure 4. Same as Fig. 3 but with 150 meV incident energy neutrons so as to accurately measure the intermolecular vibrational density of states in the 70 meV range. Ice-Ih signal is given for comparison.

The intermolecular librational band is strongly correlated to the level of disorder in the H-bond network. As compared to the steep rise of the librational band observed in hexagonal ice, the shape of this excitation observed with 150 meV incident neutron energy suggests some high degree of disorder of the interfacial water H-bond structure. As suggested by previous diffraction data, interfacial water is to be described as a glassy-like material.

Quasi-elastic neutron scattering

Incoherent quasi-elastic neutron scattering has been used to probe rotational and translational dynamics of the interfacial water as sensed by the water molecules hydrogen atoms. Measurements in the ns time range have been performed on IN16 backscattering (ILL) while measurements in the 15 ps time scale have been performed on QENS (ANL/IPNS).

Based on incoherent neutron scattering data and subsequent CMD simulations, a picture of the short time (picosecond) local bulk water dynamics is available (Fig. 5). The rotational dynamic structure factor is given by:

$$S_{Rot}(Q, \omega) = A_0(Q)\delta(\omega) + (1 - A_0(Q))L_{Rot}(Q, \omega)$$

$$\text{with } L_{Rot}(Q, \omega) = \frac{1}{\pi} \frac{\tau_1^{-1}}{\tau_1^{-2} + \omega^2} \quad (1)$$

$A_0(Q) = j_0(Qr_{OH})^2$ is the Elastic Incoherent Structure Factor of a hydrogen atom experiencing a rotation over the intramolecular OH distance, r_{OH} (0.98 Å) with a correlation time τ_1 . If a molecule is not H-bonded to any other molecule, it diffuses freely with a translational diffusion coefficient D_t and the dynamic structure factor is:

$$S_{trans}(Q, \omega) = \frac{1}{\pi} \frac{f(Q)}{f(Q)^2 + \omega^2}$$

$$\text{where } f(Q) = \frac{D_t Q^2}{1 + D_t Q^2 \tau_0} \quad (2)$$

This is obeyed until one or more H bonds are formed again. The molecule will remain on this “site” for a residence time τ_0 (of the order of 1 ps at room temperature), before experiencing this cycle again.

A key point is to keep in mind that any transition related to the water translational behavior has to be preceded by a transition related to the water rotational behaviour.

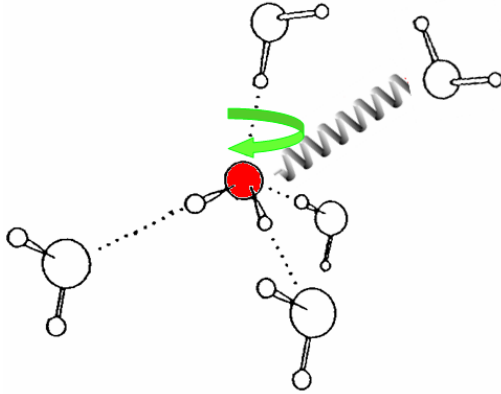


Figure 5. A water molecule is hydrogen bonded on average to three or less neighboring molecules. If due to thermal energy, one hydrogen bond O--H-O moves apart from linearity by more than 25° the bond breaks. When three of the four H-bonds possibly engaged by a molecule are simultaneously broken, the molecule follows a rotational diffusive movement, characterized by a correlation time τ_1 , associated to the H-bond lifetime.

If these rotational and translational dynamics are uncorrelated, the global dynamics of a single water molecule is described by the convolution of Eq.1 and 2:

$$S_{inc}(Q, \omega) = A_0(Q) \cdot S_{trans}(Q, \omega) + \dots \\ (1 - A_0(Q)) S_{Trans}(Q, \omega) \otimes L_{Rot}(Q, \omega) \quad (3)$$

While a detailed line-shape analysis makes it possible to extract all the parameters of the above equation, due to the limited neutron flux on such a high resolution instrument as IN16, such a detailed analysis can only be made at a few temperatures.

A wider temperature range can be explored using an “elastic scan” [3]. Fig. 6 shows selected normalised curves $\ln(S(Q, \omega=0))$ vs Q^2 at various temperatures. The mean square displacements deduced from the low $[0.1 \text{ \AA}^{-1} - 1.0 \text{ \AA}^{-1}]$ and high Q ranges $[1.1 \text{ \AA}^{-1} - 1.9 \text{ \AA}^{-1}]$, denoted $\langle u^2 \rangle_{Trans}$ and $\langle u^2 \rangle_{Rot}$, are associated with the long range translational diffusion and local rotational dynamics, respectively (Fig. 7).

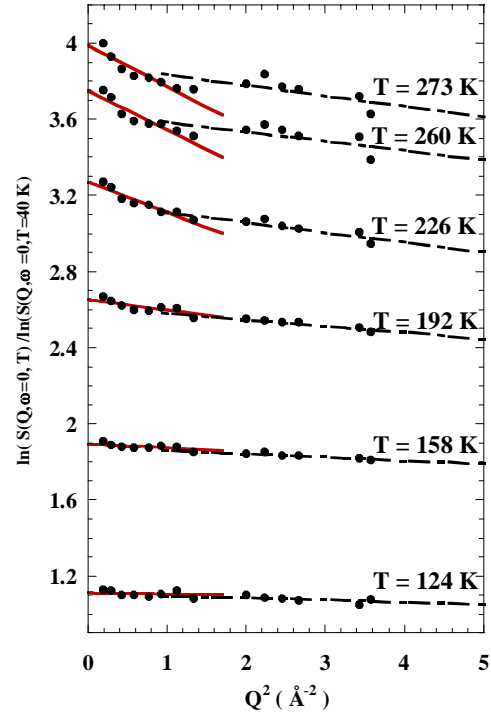


Figure 6. Normalized $\ln S(Q, \omega=0)$ vs Q^2 at selected temperatures in the range 77 - 280 K (IN16, ILL). At high temperature, two distinct linear regions may clearly be defined.

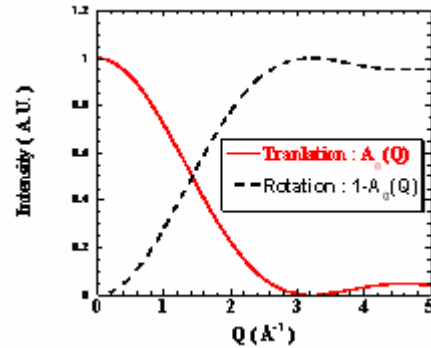


Figure 7. Integrated intensity of both terms of Eq. 3. The translational and rotational contributions to the scattered intensity are strongly Q dependent, making it possible to discriminate between them. From the data in the low Q range $[0.1 \text{ \AA}^{-1} - 1.0 \text{ \AA}^{-1}]$ of Fig. 6, we extract a first characteristic mean square displacement, $\langle u^2 \rangle_{Trans}$, related to the water molecule long range diffusion. From the data in the higher Q range $[1.1 \text{ \AA}^{-1} - 1.9 \text{ \AA}^{-1}]$ we define $\langle u^2 \rangle_{Rot}$, a mean square displacement related to the local molecular reorientations.

We show that on a timescale of 1 nanosecond:

(i) $\langle u^2 \rangle_{Rot}$ significantly increases above 150 K (Fig. 8a). This is the onset of rotational dynamics of the water molecules (glass transition for rotational dynamics to be related to T_x in Fig. 1).

(ii) Below 165 K, interfacial water is a low density amorphous material ($Q_0=Q_0^{\text{LDA}}=1.71 \text{ \AA}^{-1}$, Q_0 is the first peak in $S(Q)$) showing no long range translational dynamics ($\langle u^2 \rangle_{\text{Trans}} \approx 0$, Fig. 8b). Above 165 K, no change is observed in water density (not shown) but translational dynamics becomes possible on a 1 nanosecond timescale, as shown by the $\langle u^2 \rangle_{\text{Trans}}$ non null value. This is a clear signature of a glass transition at 165 K (Fig. 8b).

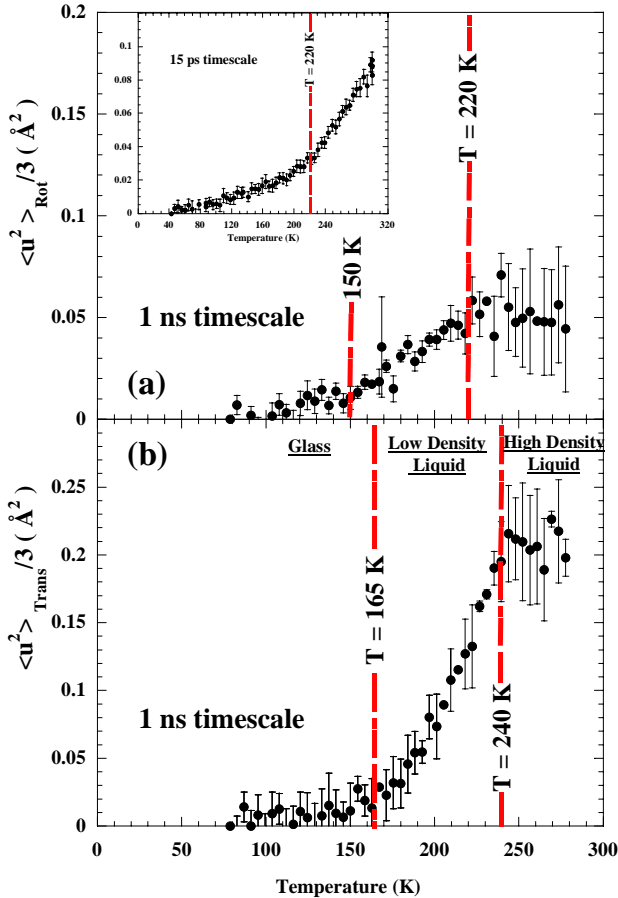


Figure 8. Temperature dependence of rotational and translational mean-square displacements of interfacial water $\langle u^2 \rangle_{\text{Rot}}$ (a) and $\langle u^2 \rangle_{\text{Trans}}$ (b) have been extracted from the two Q ranges defined in Fig. 6. Inset: lower resolution (shorter times) experiment (QENS, ANL/IPNS) confirming the saturation effect observed on IN16 due to the “high density” water fast dynamics above 240 K. The different transitions (see text) detected in water rotational (a) and translational (b) behaviours are noted by red dash lines. As expected in water, where translational dynamics is driven by hydrogen bond life time (i.e. rotational behavior, see Fig. 5), any transition in the long range translational behavior is preceded by a transition in the water molecules rotational behavior.

(iii) At 240 K, this Low Density Liquid (LDL) experiences a transition to a High Density Liquid, HDL

($Q_0=1.86 \text{ \AA}^{-1}$) [4] and rotational and translational correlation times related to $\langle u^2 \rangle_{\text{Trans}}$ and $\langle u^2 \rangle_{\text{Rot}}$ significantly decrease leading to a “saturation” of the signal on IN16 (Fig. 8). An experiment at lower resolution i.e. shorter time (QENS, ANL/IPNS) actually shows that $\langle u^2 \rangle_{\text{Rot}}$ increases (Inset Fig. 8) above 220 K therefore confirming this “saturation” effect.

The existence of a liquid-liquid transition is a key element in discriminating between the different scenarios proposed for the peculiar properties of liquid water. In spite of strong similarities between interfacial water and bulk water (structure, calorimetric $T_g = 165 \text{ K}$) the extrapolation of the interfacial water 240 K liquid-liquid transition to the existence of a liquid-liquid transition in bulk liquid water would be speculative. Nevertheless, the evidences presented here of a liquid-liquid transition involving water is a real breakthrough and is of general interest. Beyond the fundamental interest above, the finding of liquid water at temperatures as low as 165 K is relevant to fields as different as material science (cement technology, nuclear waste confining materials, geology) and biology (dynamics of hydration water).

Acknowledgements: The IPNS QENS and HRMECS experiments were supported by the U.S. Department of Energy, Basic Energy Sciences-Materials Sciences, under Contract No. W-31-109-ENG-38. JMZ and MCBF are also grateful to LLB and ILL for neutron beam time access.

jmzanotti@cea.fr

REFERENCES

- [1] O. Mishima, H.E. Stanley, Nature 396 (1998) 329. H.E. Stanley, in Hydration processes in Biology, Les Houches 1998, edited by M.C. Bellissent-Funel, Nato Science Series – Serie A, vol 305, IOS Press (1999).
- [2] D.D. Klug, E. Whalley, J. Chem. Phys. 81 (1984) 1220.
- [3] This means recording for few minutes the Q dependence of the elastic intensity. In a way similar to the famous X-Ray Debye-Waller effect, the Q dependent Gaussian intensity loss $\exp(-Q^2 \cdot \langle u^2 \rangle)$ can be related to the spatial extension ($\langle u^2 \rangle$) of atoms around their equilibrium position.
- [4] J.-M. Zanotti, M.-C. Bellissent-Funel, S.-H. Chen, Europhys. Lett. 71 (2005) 91.



Lynette Jirik (IPNS) raises sample well on the HRMECS instrument.

HYDROXYL GROUP CONTENT OF BONE MINERAL

M.J. Glimcher, L. Graham, Children's Hospital, Boston and
Harvard Medical School, Boston, MA, 02115

A.I. Kolesnikov, C.-K. Loong, Intense Pulsed Neutron Source Division, Argonne National
Laboratory, Argonne, IL, 60439-4814, U.S.A.

Bone is a nanocomposite whose principal components are collagen (a fibrous protein) and the mineral apatite. Bone apatites are nanocrystals, extremely small compared to the macro-sized crystals of synthetic apatites, and, as a result of their size, poor crystal perfection, and ion substitutions, the bone crystals generate very poor x-ray diffraction patterns, preventing determination of their exact atomic lattice structure. In addition, bone apatite crystals, which are calcium deficient, contain ion substitutions by CO_3 and HPO_4 groups. Further, a significant proportion of the CO_3 and HPO_4 groups which substitute for PO_4 and OH groups (if present) occur both in these lattice positions or on the surface. Surface ions would be functionally quite different from the CO_3 and HPO_4 groups within the lattice positions and presumably have an altered exchange rate with similar ions from solution and therefore an altered ability to participate in some of the physiological functions of bone, such as growth and remodeling and ion homeostasis. The goal of our present experiments is to determine to what extent OH groups occur in bone apatite in lattice positions which are equivalent to those in standard hydroxyapatite and/or in positions on the surface of the crystals. It can

be seen from our recent determination of the dimensions of bone apatite crystals [1] that surface positions constitute a high percentage of the total material.

Our initial neutron scattering studies were done using bone mineral crystals which had been isolated by removal of the collagen matrix by plasma ashing [2]. We later repeated this determination for crystals isolated by hydrazine treatment, in response to work by Taylor et al., who reported significant hydroxyl levels in bone crystals isolated by this method [3]. In both cases, our finding was of very low or absent levels of hydroxyl ions in bone mineral. More recently, our data demonstrates that quantitation of hydroxyl in bone powder using the ~ 85 meV OH libration peak is highly problematic due to the overlap of this peak with that due to loosely bound water. Fig. 1 shows turkey and bovine bone samples with and without prior exposure to high vacuum for one hour immediately prior to analysis. Thus, the OH stretch peak at ~ 445 meV found in hydroxyapatite (Fig. 2) is far more informative for this purpose.

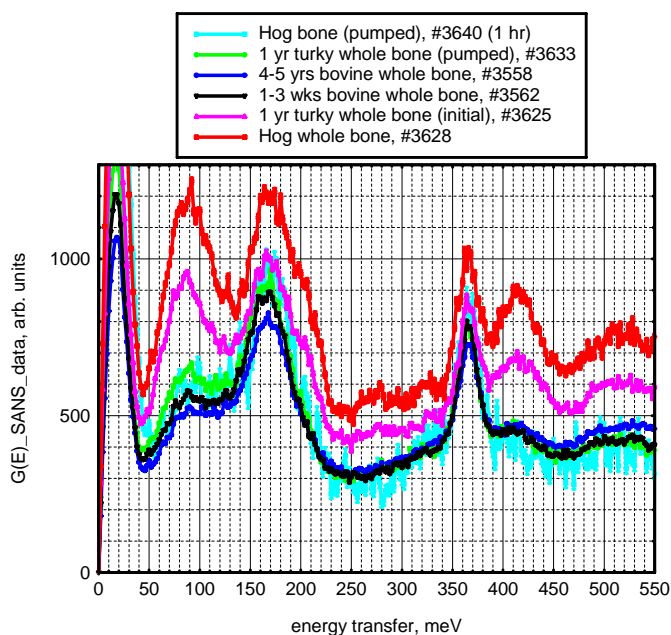


Figure 1. INS spectra for turkey and bovine bone samples with and without prior exposure to high vacuum for one hour immediately prior to analysis.

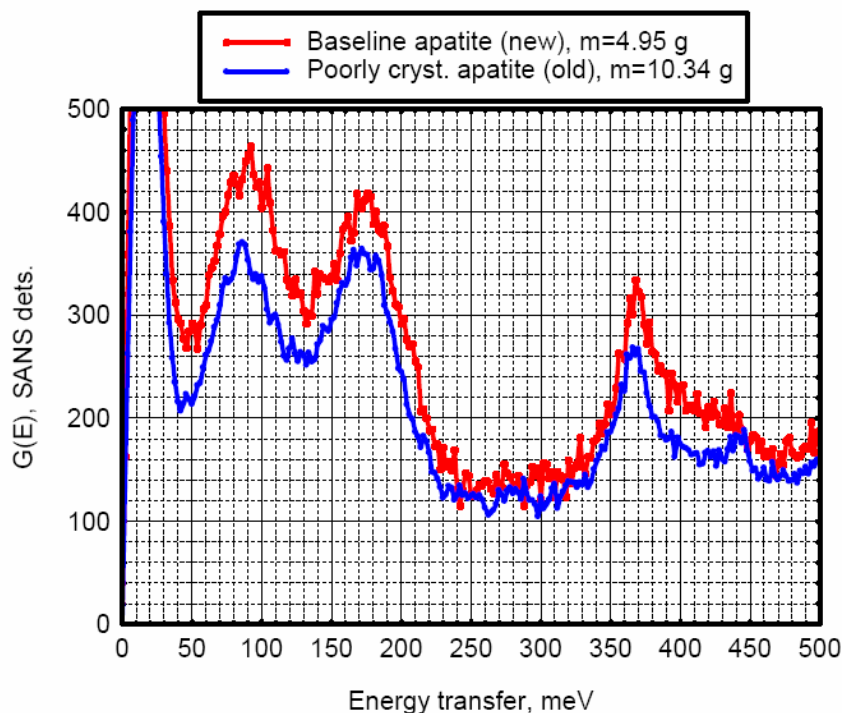


Figure 2. INS spectra for baseline apatite and poorly crystalline apatite samples.

The direction of our work on the OH content of bone mineral was influenced by publication of data from 2D solid-state ^1H - ^{31}P heteronuclear correlation NMR spectroscopy [4]. Our results are apparently inconsistent with the estimate of Cho et al. that bone apatite contains 20% of the amount of hydroxyl groups found in stoichiometric hydroxyapatite, although these authors stress the difficulties involved in quantitation by this technique. We have arranged with this group and others to correlate the results of several analytical methods in a systematic approach to resolving the apparently inconsistent reports concerning levels of OH groups in bone mineral, and the possible effects of animal age, animal species, and sample preparation. In collaboration with Jerome Ackerman and colleagues at the NMR Center at Massachusetts General Hospital and Christian Rey and coworkers at Centre Interuniversitaire de Recherche et D'Ingenierie des Materiaux, Institut National Polytechnique de Toulouse, we are obtaining directly comparable results from analyses by 2D NMR, FTIR, UV Raman, and inelastic neutron scattering of whole bone samples, isolated bone crystals, and synthetic mineral standards. In every case, the samples are from the same source to control for any variations due to biological origin or methods of preparation or storage.

We are also preparing synthetic nanocrystalline apatite of varying hydroxyl content by a method that has shown, in our recent unpublished results, progressively increasing hydroxyl content by quantitative Raman spectroscopy [5]. Two of these samples are shown in Fig. 2. Minimal hydroxyl content is shown in the "baseline" sample (red), as indicated by the absence of detectable OH stretch at 445 meV. A partially hydroxylated sample is also shown (blue). It will thus be possible to prepare a "standard curve" of calibrated, increasingly hydroxylated apatite samples for comparison with bone. Larger amounts of these samples are currently in preparation for hydroxyl quantitation by FTIR, Raman, and 2D NMR spectroscopy to correlate with neutron scattering results.

REFERENCES

- [1] W. Tong, M. Glimcher, J. Katz, L. Kuhn, S. Eppell, *Calcif Tissue Int.* 72 (2003) 592.
- [2] C.-K. Loong, C. Rey, L.T. Kuhn, C. Combes, Y. Wu, S.-H. Chen, M.J. Glimcher, *Bone* 26 (2000) 599.
- [3] M.G. Taylor, S.F. Parker, K. Simkiss, P.C.H. Mitchell, *Phys. Chem. Chem. Phys.* 3 (2001) 1514.
- [4] G. Cho, Y. Wu, J.L. Ackerman, *Science* 300 (2003) 1123.
- [5] G. Penel, G. Leroy, C. Rey, E. Bres, *Calcif Tissue Int.* 63 (1998) 475.

LATTICE VIBRATIONS IN α -URANIUM: NON-LINEARITY, LOCALIZATION, AND IMPURITY STIFFENING

M. E. Manley

Department of Chemical Engineering and Materials Science, University of California, Davis, CA 95616, U.S.A., and

Los Alamos National Laboratory, Los Alamos, NM 87545, U.S.A.

Abstract

Lattice vibrations in crystals are generally described as plane waves with vibrational frequencies determined by fixed interatomic potentials. Recent experiments on α -uranium, however, are showing that these notions do not always apply. First, a large softening of phonon density of states (DOS) has been attributed to thermal changes in the electronic structure, defying the notion of a fixed interatomic potential [1]. Second, evidence shows that significant quantities of intrinsically localized vibrational modes form at high temperatures [2], defying the plane-wave notion. Another common belief is that trace amounts of impurities do not affect the phonon DOS. By contrast, as little as 0.4 atomic-percent carbon dissolved in uranium causes a significant stiffening of the phonon DOS [3]. The present article is aimed at summarizing these surprising results as well as some of their implications.

NON-LINEARITY

Here, the term non-linearity refers to a situation where small perturbations cause large shifts in the excitation spectrum. By this definition the phonons in α -uranium are clearly non-linear, as shown in Figure 1 the phonon DOS softens considerably with small temperature changes. Although thermal softening is an expected consequence of anharmonicity, α -uranium is unusual in that it does not show behavior typically associated with a strongly anharmonic solid. First, the elastic energy of expansion can only account for about 10% of the observed softening [1]. Second, the power-spectrum derived energy exhibits linear scaling with temperature, behavior consistent with classical harmonic vibrations [1]. Finally, the features in the phonon DOS appear to sharpen with increasing temperature, the opposite of what is expected from anharmonic lifetime broadening. Based on these observations it has been concluded that the phonon softening originates with intrinsic temperature dependence in the inter-atomic forces. By extension it has been argued that the softening originates with thermal changes in the electronic structure [1].

The nature of the non-linearity in the lattice dynamics of α -uranium is clearly unconventional; the usual effects associated with phonon softening are not observed. There is, however, another way non-linearity might appear. Non-linear dynamics can lead to the formation of spatially localized dynamical modes [4].

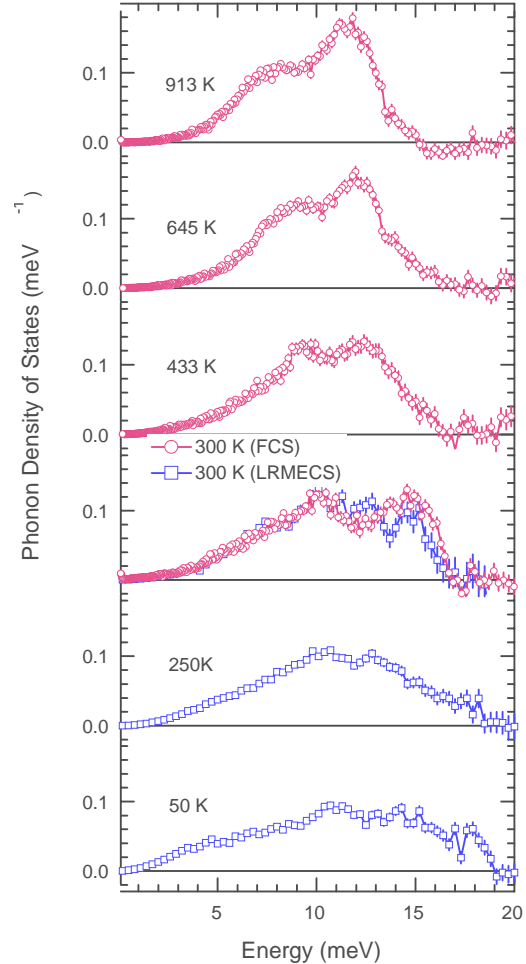


Figure 1: Phonon density of states of α -uranium at several temperatures. High temperature data were collected on the FCS spectrometer at NIST. Low-temperature data were collected on the LRMECS spectrometer at IPNS [1].

INTRINSICALLY LOCALIZED MODES

Recent measurements using both inelastic x-ray scattering (IXS) and inelastic neutron scattering (INS) have revealed that at least some of the phonon softening in α -uranium is associated with a new mode forming [2]. Figure 2 shows how the new 14.3 meV mode appears at high temperatures at a Q -position on the $[01\zeta]$ zone boundary. Also appearing in Figure 2, a phonon branch that sits just below the new mode energy softens with its formation. A more detailed view of the dispersion curves (not shown here) indicates that other branches also soften,

but mainly along the zone boundary [2], and also that intensity is lost in the $[00\zeta]$ longitudinal optic phonon branch [2].

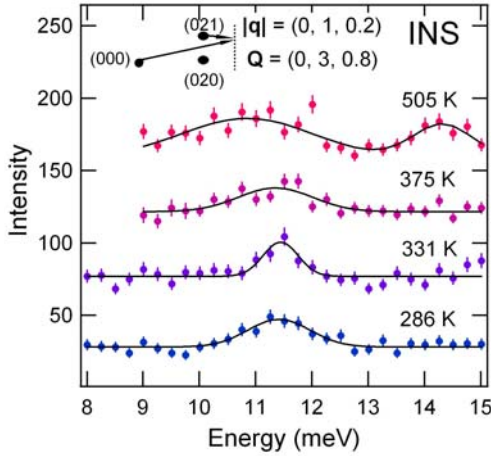


Figure 2: Data showing a new mode emerge near 14 meV at high temperature, together with the softening of the mode at about 11 meV. Data are offset for clarity. The scattering vector, \mathbf{Q} , is in the \mathbf{b} - \mathbf{c} plane. The phonon wave vector, \mathbf{q} , is at a zone boundary. Data was collected using the at the HFIR facility of Oak Ridge National Laboratory [2].

Reference [2] provides detailed arguments supporting the hypothesis that the new mode shown in Figure 2 is an intrinsically localized vibration [4]. In summary, the five main points are:

- (1) The extra modes form without a long-range crystal structure change, indicating that the required symmetry breaking must be local;
- (2) The new modes appear confined to a zone boundary, implying that its spatial periodicity does not extend much beyond the lattice spacing;
- (3) The movements of defects involved in plastic deformation are impeded by the new modes while the long-range elastic moduli are not affected;
- (4) The mode forms in the presence of a strong non-linearity in the dynamical behavior;
- (5) An excess in the heat capacity is found to be consistent with the configurational entropy of having randomly distributed intrinsically localized modes on the lattice.

Many of the effects of the local mode resemble the effects of adding impurities; a reduction in mechanical ductility and the appearance of mixing entropy [2]. This is because, much like impurities, local modes are distinguishable within the crystal and they have associated strain fields. In light of these observations we now turn to the effects of real impurities on the lattice dynamics of uranium.

IMPURITY STIFFENING

Impurity effects were investigated by measuring the phonon DOS on pure uranium and solutions U-0.4% C, U-1.5% Si, and U-0.91% Fe (atomic) using the LRMECS

instrument at IPNS. While all solutes caused a stiffening of the phonons, carbon had the largest per atom effect [3]. Figure 3 shows that the phonon DOS is both stiffened and sharpened by adding just one carbon for every 250 uranium atoms (0.4 atomic %). The magnitudes of the changes were too large to be explained in terms of short-range force constant models. It has been suggested that the stiffening may originate with impurity pinning of collective modes associated with α -uranium's charge density wave transitions [3]. Briefly, charge that was coupled to the phonons is partially localized at impurity sites. The subsequent decoupling leads to both a sharpening and a stiffening of the phonons.

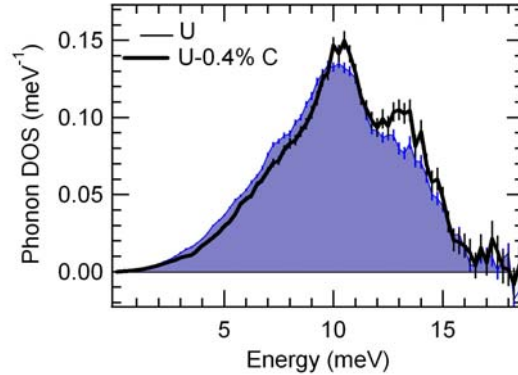


Figure 3: Phonon DOS measured on pure U and U-0.4% C (atomic) using the LRMECS spectrometer at IPNS [3].

While the origin of the large impurity effect remains controversial, the thermodynamic implication is clear. The stiffening for carbon decreases the vibrational entropy by an amount that is four times the configurational entropy increase. The mixing entropy is not only negative but is dominated by vibrations [3].

CONCLUSION

Neutron scattering measurements are revealing a surprising assortment of exotic dynamical phenomena in uranium, forcing us to rethink our basic understanding of phonon physics as well as a number of related problems including thermodynamic stability and mechanical deformation.

REFERENCES

- [1] M. E. Manley, B. Fultz, R. J. McQueeney, C. M. Brown, W. L. Hulst, J. L. Smith, D. J. Thoma, R. Osborn, J. L. Robertson, Phys. Rev. Lett. **86**, 3076 (2001).
- [2] M. E. Manley, M. Yethiraj, H. Sinn, H. M. Volz, A. Alatas, J. C. Lashley, W. L. Hulst, G. H. Lander, and J. L. Smith, Phys. Rev. Lett. in review.
- [3] M. E. Manley, W. L. Hulst, J. C. Cooley, R. E. Hackenberg, D. J. Thoma, M. W. Koby, J. L. Smith, K. Littrell, Phys. Rev. B **72**, 184302 (2005).
- [4] D. K. Campbell, S. Flach, Y. S. Kivshar, Phys. Today **57**, 43 (2004).

INVESTIGATION OF POROUS MATERIALS FOR HYDROGEN STORAGE*

Juergen Eckert, Paul Forster, Anthony K. Cheetham, MRL, University of California, Santa Barbara, CA 93106.

Jesse L. C. Rowsell, Omar M. Yaghi, Department of Chemistry, University of Michigan, Ann Arbor, MI 48109

The problem of hydrogen storage for mobile applications represents a critical step on the road towards realization of a “Hydrogen Economy” and is widely viewed as requiring a fundamental breakthrough in materials research rather than an incremental improvement of known technologies [1]. A wide range of solid materials is being examined for their ability to take up and release the required large amounts of hydrogen. These range from metals or alloys that dissociate H_2 upon adsorption and form solid solutions or compounds, chemical compounds with very high hydrogen content (such as aminoborane) where the release of hydrogen requires a chemical reaction, to highly porous materials which physisorb molecular hydrogen within their cavities. Each class has its own merits and deficiencies, yet neither has given rise to a material that comes even close to satisfying the many criteria delineated by the United States Department of Energy and other national energy agencies [2].

Storage of hydrogen by adsorption in porous materials is in principle very attractive because of the very favorable kinetics for uptake and release. However, the materials must have surface areas of at least $3000\text{m}^2/\text{g}$ and bind hydrogen much more strongly than the weak physisorption on carbons, for example, in order to store

the necessary amount of hydrogen at room temperature under acceptable pressures. Among the subset of highly porous materials, metal-organic frameworks (MOFs) have been identified as potential candidates for this role because of their very large capacities for binding hydrogen, albeit at 77K. Frameworks built from the linking of octahedral $Zn_4O(CO_2-)_6$ clusters with polyaromatic moieties have been shown to have some of the highest porosities known, and we therefore wish to determine if hydrogen binding in these materials is sufficiently strong to reduce operating pressures at room temperature appreciably from that of the compressed H_2 gas.

Our investigation of hydrogen sorption in these materials [3,4] benefits from the fact that the structures of these compounds are well defined, which makes it possible, for example, to relate bulk adsorption measurements to structural features that may be responsible for enhanced hydrogen uptake. The experimental method, which is by far the most sensitive to the chemical environment of adsorbed H_2 is inelastic neutron scattering (INS) spectroscopy of the hindered rotational transitions of the adsorbed H_2 molecules.

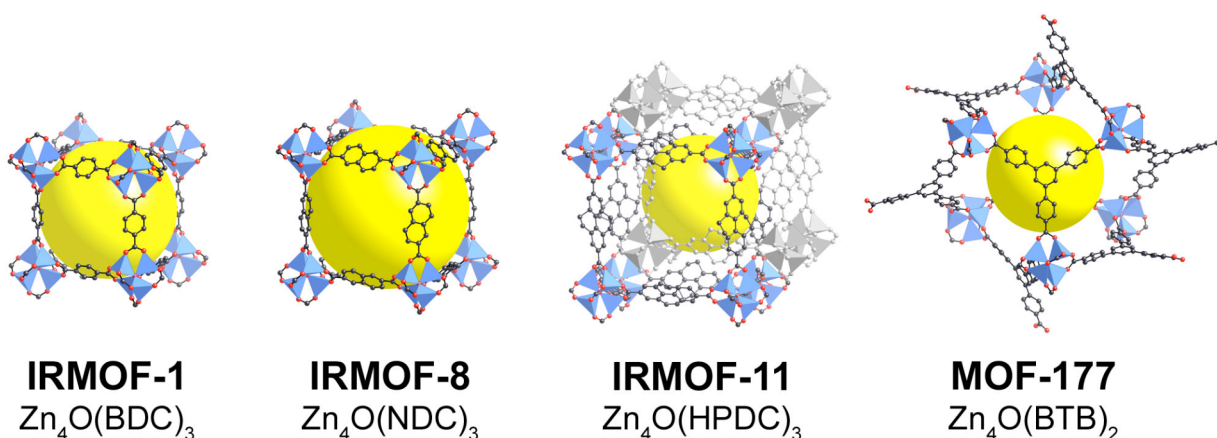


Figure 1. Some of the metal-organic frameworks analyzed in this study. These are members of a group of MOF's constructed by linking octahedral $Zn_4O(CO_2-)_6$ secondary building units with polyaromatic moieties. Included are IRMOF-1 constructed with benzene-1,4-dicarboxylate (BDC), IRMOF-8 from naphthalene-2,6-dicarboxylate (NDC), IRMOF-11 from 4,5,9,10-tetrahydropyrene-2,7-dicarboxylate (HPDC), and MOF-177 from fully deprotonated 1,3,5-tris(4-carboxyphenyl)benzene (= “benzene-1,3,5-tribenzoate”, BTB).

The INS spectra of adsorbed H_2 consist of one set of transitions for the hindered rotor for each binding site. These are interpreted in terms of a model for H_2 rotations with two angular degrees of freedom in a double-minimum potential to extract the height of the barrier to rotation. The extraordinary sensitivity of these measurements is based on the fact the lowest (0-1) and most prominent transition energy depends exponentially on this barrier height. The rotational energy levels of the free hydrogen molecule are given by $BJ(J+1)$, where B is the rotational constant (taken to be 7.35 meV) and J the rotational quantum number. Application of a barrier to rotation drastically changes these level spacings.

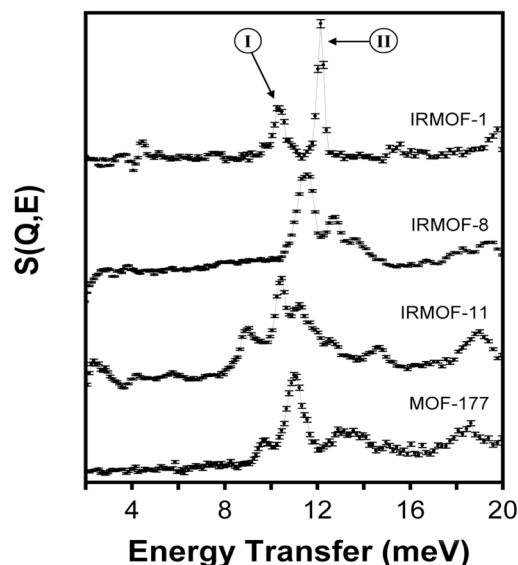
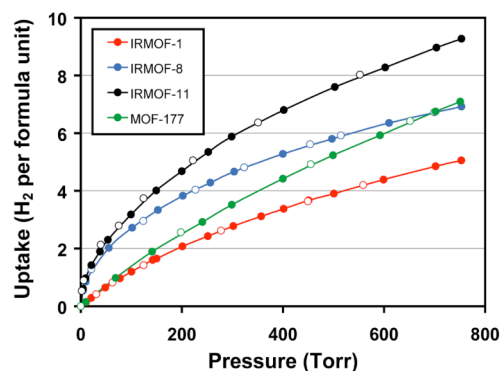


Figure 2. (a) Hydrogen adsorption isotherms [5] measured at 77 K for the MOFs analyzed in this study. Adsorption points shown as filled circles, desorption points as open circles. (b) Inelastic neutron scattering spectra ($T=15K$; QENS spectrometer at IPNS) [4] for each material loaded with 4 H_2 per formula unit. The two 0-1 transitions originally assigned to sites I and II in IRMOF-1 are labeled. Spectra are vertically offset for comparison purposes, the error bars shown are representative of all spectra.

Assignment of the INS spectra [3,4] shown in Fig. 2b for the four Zn_4OL_x based MOF's (Fig. 1) suggests that the favored binding site for H_2 is in the corner pocket of the Zn cluster (I), and that many secondary binding sites (II) exist around this cluster and the organic link. Hydrogen is found to bind more strongly than in carbons on all sites in all these compounds

Although the materials studied here are chemically very similar, their capacities for hydrogen adsorption are rather different. This is apparent when the adsorption isotherms [5] are normalized per formula unit, as shown in Figure 2a. While it is clear that the organic links play important roles in defining pore sizes and providing organic adsorptive sites, they also alter the interaction of H_2 with the cluster due to differences in their electronic structures. This is demonstrated by comparing the INS spectrum of each material at a loading of 4 H_2 molecules per Zn_4OL_x formula unit (Figure 2b) which nominally saturates the cluster binding sites (I). Pronounced frequency shifts are evident for those sites as well as others in going from one material to another, and these variations may then be attributed to the interplay between the Zn cluster and the organic link.

Interaction of hydrogen with these host materials is, however, not nearly as strong as would be required for room temperature use as hydrogen storage materials. For example, the capacity in MOF-5 is only about 0.5 wt % at 10 atm and room temperatures. Considerable progress may be possible with the use of charged frameworks as can be illustrated by a comparison of hydrogen binding in a zeolite and a MOF both containing Cu. INS spectra of H_2 adsorbed at the divalent, extraframework Cu^{2+} cation in zeolite A (Fig. 3) and at the Cu cluster of neutral framework in Cu-BTC [6] (Fig. 4) show rotational bands near 3 meV, and 9 meV, respectively, that may be assigned to sorption at or near Cu. Peaks at higher frequencies in Cu-BTC are again associated with binding sites around the

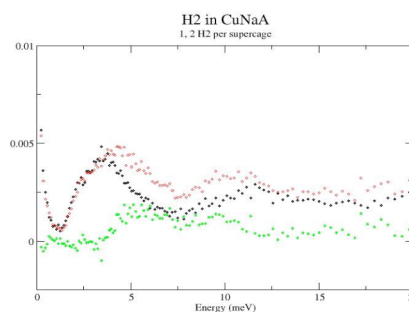


Figure 3. INS spectrum of 1 and 2 Hydrogen molecules per supercage in CuNaA ($T = 15 K$) collected on the QENS spectrometer at IPNS

organic link. Comparison of these results shows that interaction of hydrogen with cationic Cu is considerably

stronger than that with the Cu cluster in Cu-BTC. In fact, we consistently find that mean of the

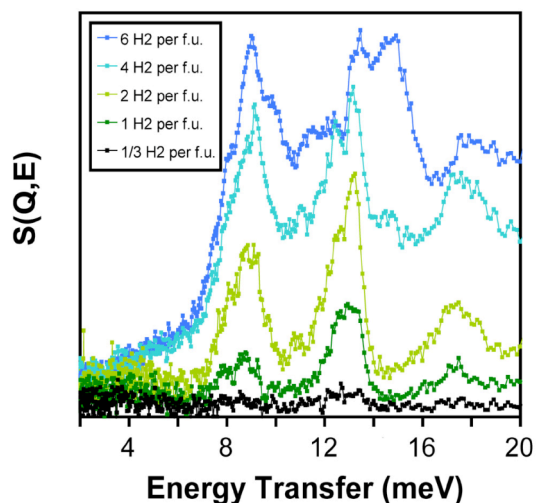


Figure 4. INS spectrum of Hydrogen in Cu-BTC ($T = 15$ K) as a function of loading collected on the QENS spectrometer at IPNS.

rotational bands from adsorbed hydrogen in zeolites is considerably lower than that in MOF's. This suggests that the interaction of hydrogen with the electrostatic field in the zeolite cavity (resulting from the charged framework) as well as the presence of the extra-framework cations significantly enhances the binding of hydrogen in such a material.

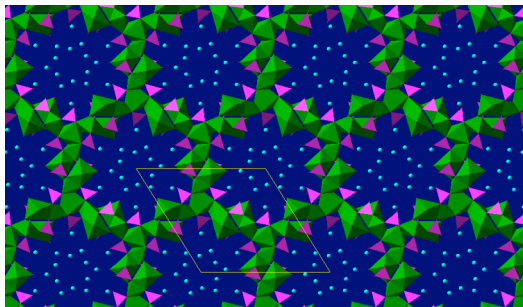


Figure 5. Structure of the Ni phosphate VSB-5 (left). Ni octahedra are shown in green, phosphate tetrahedral in purple. One water ligand per Ni can be removed by evacuation to 325 C to create an unsaturated Ni binding site. [9].

Molecular chemisorption of hydrogen at unsaturated metal binding sites would constitute an even more significant improvement in hydrogen binding in porous materials, and still preserve the favorable adsorption/desorption kinetics of a sorption-based hydrogen storage system. Formation of such metal

dihydrogen complexes was first demonstrated for organometallic compounds by Kubas et al. [7] and was first reported by us [8] to also be possible in porous materials. More recently, we found that in the nanoporous Ni phosphate VSB-5 (Fig. 5) a vacant coordination site at the Ni can be produced by dehydration at 325 C, and that this site strongly binds [9] hydrogen in molecular form (Fig. 6).

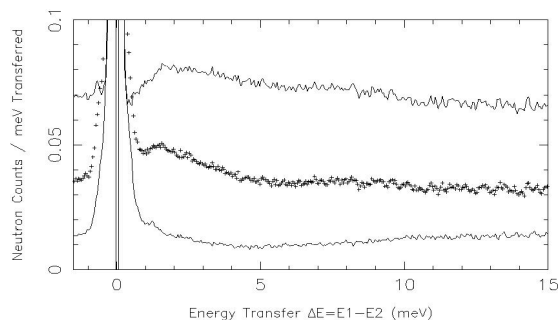


Figure 6. INS spectrum of H₂ in VSB-5 obtained on the QENS spectrometer at IPNS. The peak at 1.5 meV is attributed to molecularly chemisorbed H₂ at the vacant Ni binding site [9].

This approach may be the key to the use of porous materials for hydrogen storage provided that new materials can be synthesized with a much larger number of unsaturated metal binding sites as well as higher surface area. As this may only be possible with transition metals it will be necessary to bind multiple dihydrogen ligands at such sites in order to achieve prescribed gravimetric capacity goals. The existence of such compounds has been theoretically demonstrated and observed in organometallic systems.

Acknowledgments

Funding was provided by the NSF, DOE, and BASF. The work has benefited from the use of facilities at the Intense Pulsed Neutron Source (IPNS), a national user facility funded as such by the Office of Science, U.S. DOE.

REFERENCES

- [1] See, for example, Schlappbach, L. *MRS Bull.* **2002**, 27, 675-676 and other articles in this special issue.
- [2] *Basic Research Needs for the Hydrogen Economy*, United States Department of Energy, report of the Basic Energy Sciences Workshop on Hydrogen Production, Storage, and Use, May 13-15, 2003. <http://www.sc.doe.gov/bes/hydrogen.pdf>.
- [3] Rosi, N. L.; Eckert, J.; Eddaoudi, M.; Vodak, D. T.; Kim, J.; O'Keeffe, M.; Yaghi, O. M. *Science* **2003**, 300, 1127-1129. [2] A. Name and D. Person, *Modern Editor's Journal* 25 (1997) 56.

- [4] Rowsell, J. L. C.; Eckert, J.; Yaghi, O. M. *J. Am Chem Soc.* **2005**, *127*, 14904.
- [5] Rowsell, J. L. C.; Millward, A. R.; Park, K. S.; Yaghi, O. M. *J. Am. Chem. Soc.* **2004**, *126*, 5666-5667
- [6] Chui, S. S.-Y.; Lo, S., M.-F.; Chramant, J. P. H.; Orpen, A. G.; Williams, I. D. *Science* **1999**, *283*, 1148.
- [7] Kubas, G.J.; Ryan, R. R.; Swanson, B. I.; Vergamini, P. J.; Wasserman, H. J. *J Am. Chem. Soc.* **1984**, *106*, 451.
- [8] Mojet, B.; Eckert, J.; van Santen, R.; Albinati A.; Lechner R. J. *Am. Chem. Soc.* **2001**, *123*, 8147.
- [9] Forster, P. M.; Eckert, J.; Chang, J.-S.; Park, S.-E.; Ferey G.; Cheetham A. K.. *J. Am. Chem. Soc.* **2003**, *125*, 1309.



Lynette Jirik (IPNS) with X-ray Neutron School students.

Instrument hardware and software upgrades at IPNS

Thomas Worlton¹, John Hammonds¹, Rodney Porter¹, Julian Tao¹, Dennis Mikkeslon², Ruth Mikkelson²

¹IPNS Controls and Computing Group, ²University of Wisconsin-Stout

Introduction

INS began operation in 1980 and is one of the oldest spallation neutron source facilities in the world. Much of the technology used for the original data acquisition system (DAS) is now obsolete and replacement parts are unavailable. In addition, the software written for collection and reduction of the data was written in Fortran 77 and used features specific to DEC VAX computers for data collection and analysis.

The original DAS hardware communicated through proprietary DEC Qbus protocols, requiring computer control systems supporting the Qbus, and preventing us from easily moving to newer technology in computer hardware and software.

Because of the obsolete technology used for the IPNS DAS, an IPNS DAS/Instrument upgrade project was started in 1996 which is allowing us to replace aging components and eliminate dependence on VAX computers and old interfaces. Due to limited staff and budget and coupling of DAS replacement with instrument expansions, completion of all the upgrades is taking several years. We have now reached the point where more than half of the instruments have been upgraded to the new system and are using new software for instrument control, data acquisition, and data analysis.

The improvement in data quality comes from an increase in signal to noise ratio due to finer grained summation of spectra with proper weighting [1]. The GLAD hardware upgrade will be done as soon as budget permits and is expected to further improve the data. We also expect to upgrade POSY1 this year.

The new DAS hardware [2] is based on open standards such as Ethernet, VME, and VXI, and uses standard Intel-based computing hardware running Linux. Data collection and Ancillary equipment control is based on the Experimental Physics Industrial Control System, EPICS [3].

The software upgrades involve conversion to a new Java-based data reduction, visualization, and analysis software package called the Integrated Spectral Analysis Workbench, ISAW [4]. Java facilitates the use of the software on different computing platforms and ensures ease of use and distribution for many years to come.

Instrument Upgrades

The High Resolution Medium Energy Chopper Spectrometer, HRMECS, was the first IPNS instrument to be upgraded with a new DAS and new software. Upgrades included the reconfiguration of the high-angle detector banks, addition of LPSDs at small angles (-20° to 20°) for better Q-resolution and replacement of detector and data-acquisition

Instrument	DAS Upgrade	Software used
HRMECS	Completed 1998	ISAW
SCD	Completed 2003	ISAW + GSAS
SAND	Completed 2003	ISAW + Igor Pro
SAD/SASI	Completed 2004	ISAW + Igor Pro
GPPD	Completed 2004	ISAW + GSAS
HIPD	Completed 2004	ISAW + GSAS
SEPD	Completed 2005	ISAW + GSAS
POSY1	Scheduled 2006	IDL-based
POSY2	Scheduled 2006	IDL-based
GLAD	Partial 2006	ISAW

HRMECS, HIPD, SCD, SAND, SASI, GPPD, and SEPD have received upgrades in both hardware and software. On GLAD, only the software has been upgraded, but the software upgrade has produced a factor of two improvement in data quality, which permits a significant extension of the usable Q range.

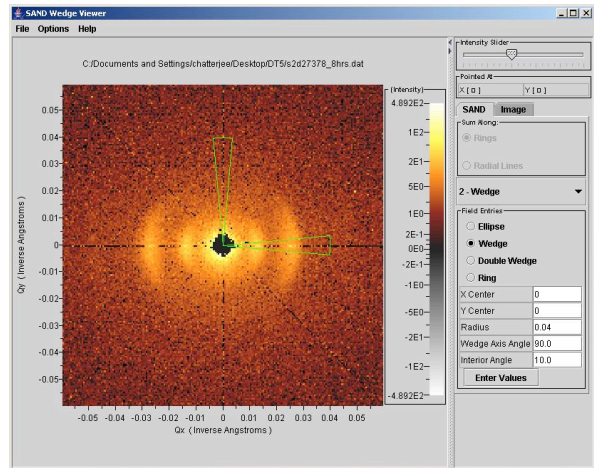


Figure 2 The SAND wedge viewer with two selected wedge regions.

electronics, leading to significant improvements in signal-to-noise ratio and operational flexibilities. The chopper spectrometer data reduction and analysis routines were ported to Java to take advantage of the ISAW visualization and data reduction tools [5].

The Single Crystal Diffractometer, SCD, has been upgraded to include expanded detector coverage and improved spatial resolution, resulting in an increase of two in data rate. A new feature added to ISAW for SCD analysis was form-based wizards for data reduction and analysis. The two SCD wizards used are the Initial Peaks Wizard which produces a crystal

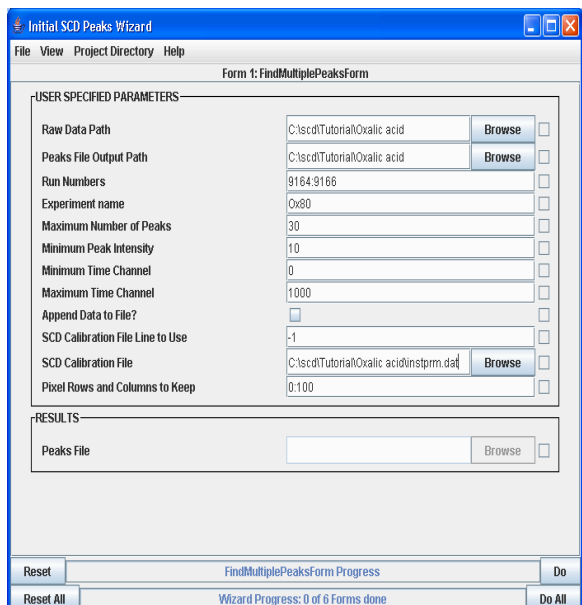


Figure 1 Form 1 of the SCD Initial Peaks Wizard

orientation matrix and the Daily Peaks Wizard which takes advantage of the orientation matrix and finds, indexes and fits all diffraction peaks for each crystal setting [6]. For more details on the SCD upgrade, see the article by A. J. Schultz et al. [7].

Replacement of the DAS electronics on SAND has allowed higher resolution data collection. The addition of a beam stop monitor has enabled the concurrent collection of scattering and transmission run data, reducing data collection time requirements. Since the new DAS systems are based on Linux, the old VAX-based data reduction routines for SAND and SAD would no longer work once the instruments were upgraded. All SAND data reduction is now done through ISAW scripts which simplifies and enhances the user experience. A new ISAW data viewer was developed for SAND which allows selection and integration of wedge, double-wedge, or annular regions of the area detector.

The detector upgrade on SASI (previously SAD) has resulted in a wider Q-range and higher data rates. It has better spatial resolution (about 3mm) and lower gamma efficiency, which allows for optimal discrimination. The detector size has increased from a 20X20 area to 50X50. These improvements produce an overall factor of 8-12 reduction in data collection time. These improvements would not have been possible without the new DAS which can handle much higher data rates.

The General Purpose Powder Diffractometer (GPPD) upgrade included adding neutron guides to increase intensity, and increasing the initial flight path to increase resolution. We also added more position-sensitive detectors for improved measurements at low Q. The longer flight path caused frame overlap and motivated us to add a frame overlap chopper to eliminate very high Q data and allow a clear view of the low Q data. A time shift operator was added to ISAW to shift the overlapped data to its proper time range.

The Special Environment Powder Diffractometer, SEPD, was upgraded after GPPD. Although the two instruments are very similar, we developed new logarithmic time binning methods for SEPD. New scripts and operators were also developed to calibrate SEPD using individual peak fitting instead of Rietveld refinements on the spectrum from each detector segment. This greatly reduced the time needed to complete a calibration.

General ISAW Software Improvements

Many of the improvements to ISAW in the last few years have been made to meet the needs of specific instruments. In addition, the ISAW infrastructure has continued to improve and become more modular. Some changes are being made to facilitate the use of ISAW at other facilities, such as LANSCE, which do not store their data and metadata in the same way as IPNS does. The original ISAW viewers were designed around “DataSets” which are “heavy weight” objects. We subsequently recognized the need to have lower level view components that could be combined in various ways to make complete data viewers. We have developed several new viewer components which can visualize simple arrays. We have also developed some auxiliary routines to retrieve needed metadata from facility and instrument-specific files at IPNS and LANSCE.

The simplest way for scientists to access and extend the power of ISAW is to write scripts and operators, and allow automation of procedures for processing large numbers of files. It is also possible to convert a set of scripts into a wizard with several

forms which may be filled out by the user to process the data. Wizards allow stepping forward or backwards through the set of input forms.

For data types supported by the ISAW scripting language, a graphical user interface element will be automatically generated for each parameter when the script is run. For instance, if an input parameter is specified as one of the supported file types, the dialog box generated by the command interpreter will include a browse button for that parameter.

A recently developed tool to generate operators from public static Java methods should make it much easier for users or developers to add new functionality to ISAW. The operator generator tool will automatically generate the code which will allow the new method to be integrated with ISAW and be accessible from the ISAW menus and script language. Help documentation entered in the forms for this tool will be accessible through the ISAW help menus.

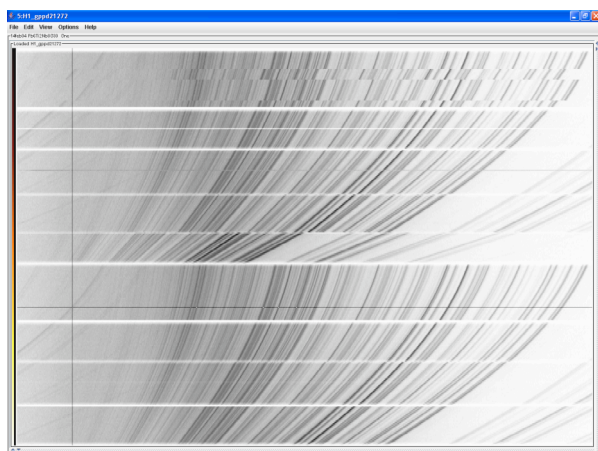


Figure 3. Reverse gray image view of GPPD data after increasing flight path and before correcting for frame overlap. Each row of pixels represents the data from one detector segment. The white horizontal lines represent dead pixels. Peaks due to frame overlap, such as the one under the cross hairs, need to be shifted one pulse period.

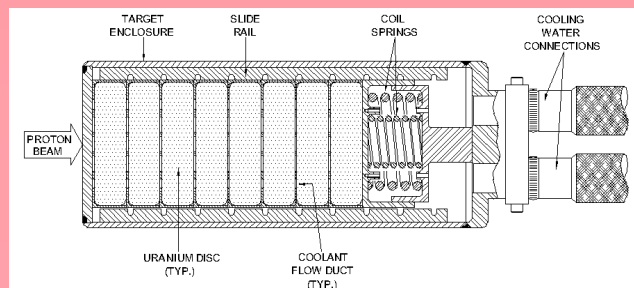
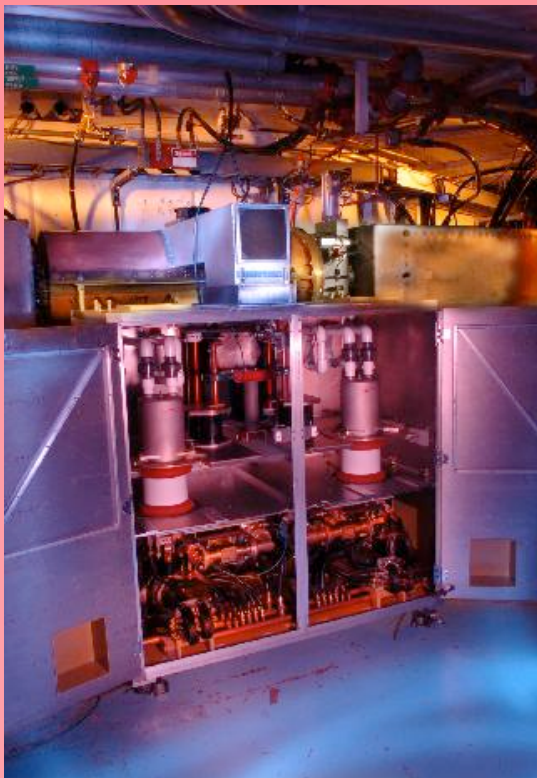
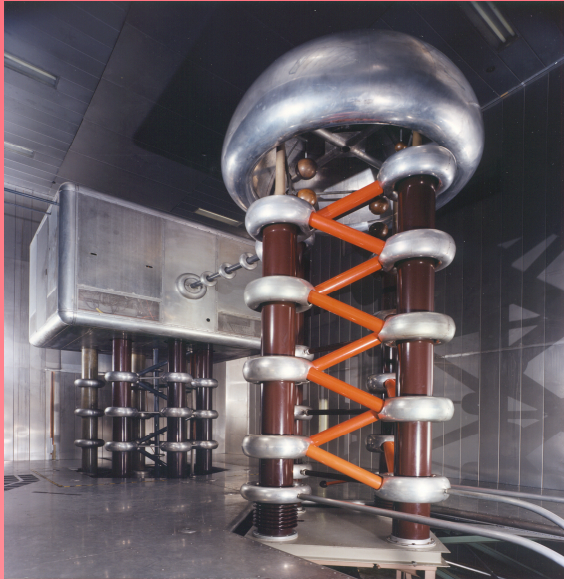
References

- [1] J. Tao, C.J. Benmore, T.G. Worlton, J.M. Carpenter, D. Mikkelson, R. Mikkelson, J. Siewenie, J. Hammonds, A. Chatterjee, "Time-of-Flight neutron total Scattering Data Analysis implemented in the software suite ISAW, submitted to Nuclear Instruments and Methods.
- [2] J.P. Hammonds, R.R. Porter, A. Chatterjee, T.G. Worlton, P.F. Peterson, J.W. Weizeorick, P.M. De

Lurgio, I. Naday, D. J. Mikkelson, R.L. Mikkelson, Developments for the IPNS Data Acquisitions System Upgrade, in NOBUGS 2002, November 4-6, 2002, Abs. no.39, NIST, Gaithersburg, MD,
<http://www.arxiv.org/abs/physics/0210075>

- [3] <http://www.aps.anl.gov/epics/>
- [4] <http://www.pns.anl.gov/computing/isaw/>
- [5] D. Chen, C.-K. Loong, D. Mikkelson, R. Mikkelson, A. Chatterjee., T. Worlton, ICANS-XV Proceedings, Nov. (2000), Vol. 1, pp. 665-70
- [6] D. Mikkelson, A.J. Schultz, R. Mikkelson, T. Worlton, IUCR Commission on Crystallographic Computing Newsletter (2005), No. 5, P. 32, edited by S. Billinge, G. Chapuis, L. Cranswick, R. Lifshitz. Online Newsletter
<http://www.iucr.org/iucr-top/comm/ccom/>
- [7] A.J. Schultz, P.M. De Lurgio, J.P. Hammonds, D.J. Mikkelson, R.L. Mikkelson, M.E. Miller, I. Naday, P.F. Peterson, R.R. Porter, T.G. Worlton, "The upgraded IPNS single crystal diffractometer", ICNS 2005, Sydney, Australia.

3. Accelerator and Target Systems



THE IPNS ACCELERATOR SYSTEM

G.E. McMichael and F.R. Brumwell
IPNS Division, Argonne National Laboratory

Accelerator Description

The IPNS accelerator system consists of an H⁻ ion source, a Cockcroft-Walton preaccelerator, a 50 MeV Alvarez linac, a 450 MeV Rapid Cycling Synchrotron (RCS), transport lines and ancillary subsystems (controls, diagnostics, services). Figure 1 shows the layout of the IPNS accelerator, including linac, RCS and spallation target.

The accelerator normally operates at an average beam current of 14 to 15 uA, delivering pulses of approximately 3×10^{12} protons at 450 MeV to the target, 30 times per second. The preaccelerator and linac centered service in

The Ion Source and Preaccelerator

The H⁻ ion source and associated equipment are housed in the terminal of a 750 kV Cockcroft-Walton preaccelerator (Fig. 2). The H⁻ ion source is a magnetron type in which negative ions are extracted directly from the hydrogen plasma on the surface of the source cathode. The extractor electrode and magnet poles are at terminal ground potential and the source itself, including the pulsed arc supply, pulsed hydrogen gas supply, and cesium supply (cesium greatly increases the H⁻ generation) are pulsed to a negative 20 kV potential. The H⁻ beam is extracted, bent 90° (to remove electrons from

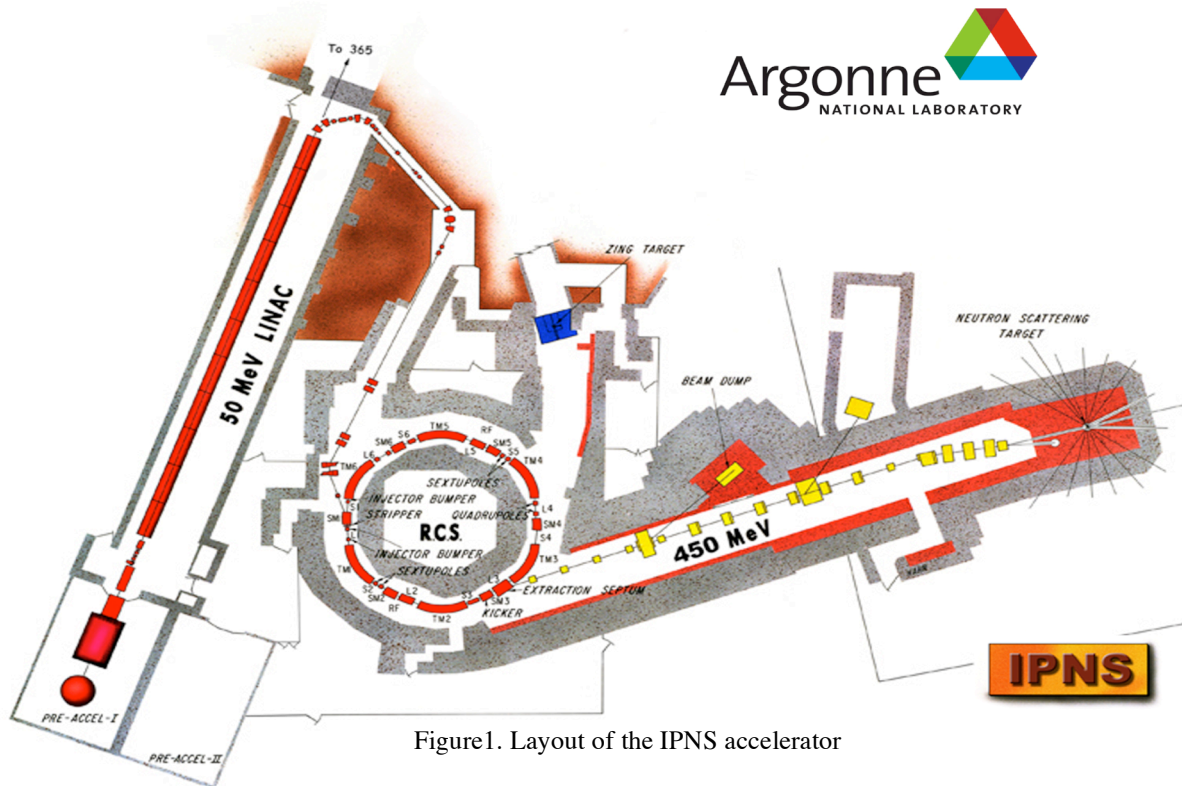


Figure 1. Layout of the IPNS accelerator

1961 and served as the injector to the 12.5 GeV Zero Gradient Synchrotron (ZGS) high-energy physics accelerator until it was shut down in 1979. The RCS was developed and constructed in the mid 1970's as a proposed booster for the ZGS. However, with shutdown of the ZGS imminent, these plans were dropped and instead the RCS was used initially (1977-1980) to provide beam to the ZING experimental target and in 1981, began providing beam to the present IPNS target. In the 25 years since IPNS began operation, over 8.7 billion pulses have been delivered to the target.

the H⁻ beam) by a magnetic dipole, focused by a set of three quadrupole magnets and injected into the high-voltage column of the preaccelerator. The preaccelerator produces approximately 30 mA, 750 keV, 70 microsecond pulses at a repetition rate of up to 30 Hz.

The Low-Energy Beam Transport System (LEBT)

The LEBT is a 4-m line between the preaccelerator and the linac. It contains quadrupole magnets to confine the beam and focus it into the linac, two steering magnets, a



Figure 2. The Cockcroft-Walton generator and 750 kV ion-source terminal.

200-MHz single-gap buncher cavity to improve the capture in the linac, a beam chopper to establish the beam rate, beam diagnostics, and a beam stop (Faraday cup)

The Linac

The linac (Fig. 3) is a copper-clad-steel structure 0.94 m (37 in.) in diameter and 33.5 m (110 ft) long. Along with the preaccelerator and LEBT, it was originally commissioned in 1962 and provided beam for the ZGS accelerator until that facility's shutdown in October 1979. (Its lineage can actually be traced back even further, because the copper-clad steel was some of that produced in the early 1950s for the then-top-secret MTA accelerator at Livermore.) The linac was constructed in seven sections, which are bolted together. It contains 124 drift tubes, each with a dc quadrupole magnet. The magnets are divided into 12 series groups and powered by 12 dc power supplies, located on the service floor. Transistorized shunts are attached to each of the first 58 magnets, allowing remote control of individual magnets. Nominal vacuum level in the linac is $2\text{-}3 \times 10^{-7}$ torr, maintained by four ion, one turbo-molecular and five cryo pumps. The linac is water-cooled with a closed-loop system, which is temperature-regulated to within 0.2°F to keep the cavity tuned during normal operation to $200.070 \text{ MHz} \pm 1 \text{ kHz}$. The 200-MHz pulsed rf power is obtained from a four-stage amplifier; the output stage is a 7835 triode with a normal operating level of 3 MW and a peak-power rating of 5 MW. The 50-MeV beam exiting from the linac is about 1 cm in diameter and the current during the $70\text{-}\mu\text{s}$ pulse is about 10 mA.

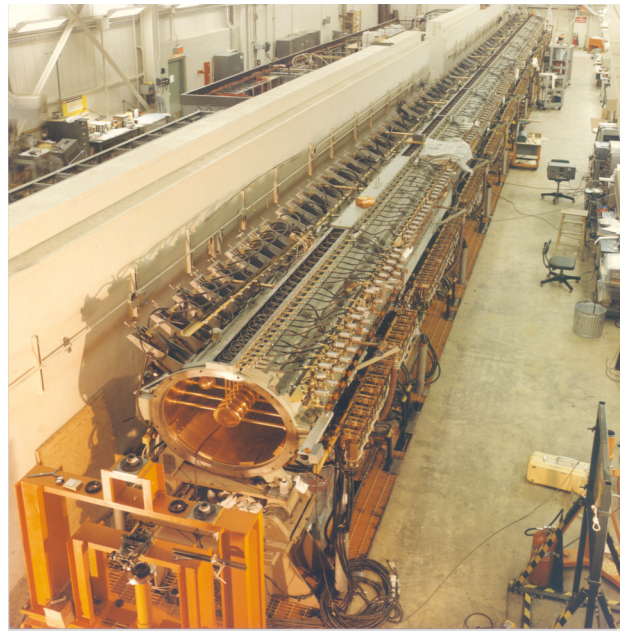


Figure 3. 200 MHz Alvarez linac that accelerates the H⁻ beam to 50 MeV.

The 50-MeV Transport Line

The 50-MeV beamline transports the H⁻ beam from the high-energy end of the linac approximately 38 m (125 ft) to the RCS accelerator. Beam steering and focusing is provided by a total of eight horizontal and two vertical dipole magnets and 16 quadrupole magnets. To avoid excessive gas stripping of the H⁻ beam, the vacuum level in the 50-MeV line is kept below 2×10^{-6} torr. About midway along this beamline, there is a target station where special targets are irradiated to produce short-lived isotopes for subsequent acceleration and physics studies in the ATLAS accelerator, an important physics facility here at ANL.

The Rapid Cycling Synchrotron (RCS)

The RCS was originally designed as a booster for the 12.5-GeV ZGS high-energy physics accelerator, the intent being to provide increased ZGS beam intensity by injecting higher-energy (boosted) particles and taking advantage of the higher space-charge limit that would result. However, since the ZGS could only accept 8 pulses every 4 seconds, 90% of the beam from the RCS would have been available for other uses — specifically, for a pulsed neutron source. Although a 300-MeV beam was extracted toward the ZGS from the RCS in 1977 (two years before the termination of the ZGS program), it was stopped at the ZING experimental target and never injected into the ZGS because, with shutdown imminent, priority was given to exploiting ZGS's uniqueness as the world's only producer of high-energy polarized proton beams.

Over the next four years, the IPNS accelerator took on much of its present form. The extraction point from the RCS was moved to permit beam delivery to the present IPNS target location, and improvements were made to injection and extraction regions. The kicker magnet system, ac and dc septum magnet systems, and the extraction beamline were completed. By May 1981, the RCS was delivering 10- μ A pulses at 300 MeV or 4.5- μ A pulses at 400 MeV to the new neutron Radiation Effects Facility (REF) target.

The RCS is a strong-focusing, combined-function synchrotron. It is a six-period machine with a magnet structure of DOOFDFO and a circumference of 42.95 m. The ring magnets, part of a biased 30-Hz resonant circuit driven from twin solid-state power supplies, generates a magnetic field from 0.28 to 1.0 Tesla so that the beam orbital radius remains constant during the acceleration from 50 to the design maximum of 500 MeV. Two pairs of sextupole magnets, powered by 30-Hz programmable power supplies, provide betatron tune correction and manipulation.

H- stripping injection, pioneered on the Booster I experiment for the ZGS, is accomplished on the RCS with a carbon stripper foil located on the inside radius of a long straight section (L-1) outside the limit of the circulating proton beam. The equilibrium orbit is deformed in the injection region into the foil by a series of three small, pulsed "bumper" magnets. The H- beam is injected through a singlet ring magnet so that at the stripper foil, its path matches the deformed orbit. During injection, the bumper magnet current decays at a controlled exponential rate, moving the closed orbit away from the stripper foil and uniformly filling the horizontal aperture.

The proton beam is accelerated by two ferrite-loaded coaxial cavities. A third rf cavity and amplifier system is being installed and will be commissioned in FY06. It will operate at the 2nd-harmonic of the ring frequency during the initial few milliseconds of the acceleration cycle (to improve capture efficiency) and then will be used to add fundamental voltage during the time when the ring-magnet field is increasing most rapidly.

Moving at 2.2×10^8 m/s (almost 75% of the speed of light), the 450 MeV protons circle the ring in just under 200 ns (2×10^{-7}) just prior to extraction.. The beam is bunched such that it fills just over a third of the circumference, giving a bunch about 70-80 ns long with about a 120 ns gap between head and tail. The accelerated beam is extracted in a single turn by two ferrite-loaded kicker magnets and two septum magnets, one pulsed and one dc. The extracted beam, 450 MeV, 70-80 ns pulse, peak current ~ 12 A, is then transported to the neutron-generating target. The high-energy neutron pulse is correspondingly short, but the moderation process spreads it out a bit, resulting in the few microsecond pulse that is seen at the instruments.

The PTS Transport Line

The PTS transport line (Fig. 4), a 37-m- (120-ft-) long beamline that includes three horizontal (bending), two vertical (steering), and 15 quadrupole (focusing) magnets, transports the beam from the RCS in Building 391 to the neutron-generating target in Building 375.



Figure 4. PTS (Proton Transport System) Beamline between synchrotron and target

Controls and Diagnostics

All of the accelerator operations can be handled by one operator, thanks in part to the control and diagnostics system. Since the early 1990's, the original minicomputer/CAMAC-based data acquisition and control system has been replaced with a system built from the continually-evolving Experimental Physics and Industrial Control System (EPICS) This is a distributed, real-time, control and instrumentation system developed jointly by Argonne (Advanced Photon Source) and other national laboratories/research facilities. The system is customized for the individual needs of the IPNS system.

An EPICS system consists of one or more Input/Output Controllers (IOCs) and one or more Operator Interfaces (OPIs), all connected together via an ethernet. The data collection and control functions are handled by the IOCs and are built up of simple building blocks called records. A set of these records is put into a database to perform a required function. Readout and operator input functions are handled by the OPIs. Any type of display (meter, bar, number, etc.) may be made for any record in any IOC and may be displayed on any OPI.

Since any OPI can get information from any of the IOCs, this new system greatly improves the ease with which the operator can retrieve necessary information. A single OPI can do the whole job of displaying information if necessary, and spare parts for them and the IOCs are readily available. This substantially improves system reliability and minimizes downtime in the event of a failure.

A single CAMAC module remains interfaced to the new system (controlling and monitoring equipment in the 750 kV source terminal); all others have now been replaced with the VME-based IOCs. The IPNS system now includes 15 OCs monitoring approximately 500 analog/digital inputs and with controls for source parameters, beamline and ring magnets etc.

Accelerator Operations

Three performance measures for the IPNS accelerator are operating hours/year, system availability, and current delivered to target. Operating hours on IPNS have historically been funding-limited rather than machine-limited. Figure 5 shows the operating record since the facility began operation in 1981. Government funding for user facilities saw a step increase with the Scientific Facilities Initiative in FY96, allowing IPNS operation to increase over 50% from its low in 1982-84. Funding permitting, IPNS could operate as much as 30 weeks (over 4500 hours of beam-on-target) per year. Although beam current is primarily a machine-limited parameter, it is the engineers' and technicians' repair of faults and improvements to the hardware, and the skill of the operators in "tuning", that has allowed what was initially a 10-12 uA machine to consistently achieve average currents of 14-15 uA.

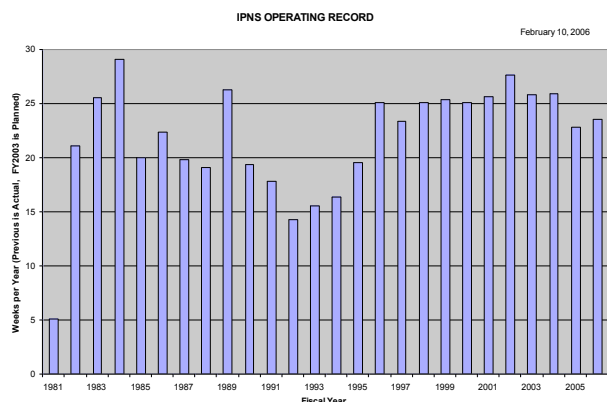


Figure 5. IPNS operation (weeks per year)

System reliability (delivering beam when scheduled) is a very important performance measure from the user's perspective. At the conclusion of each "run" (2-4 week period, during which beam is scheduled to be available to the users 24 hours a day), reliability is calculated as the ratio of hours-available to hours-scheduled. Accelerator reliability and average current since 1981 is plotted in Figure 6, one point for each scheduled run. For the last ten years, rarely has reliability for a single run dropped below 80%, and yearly averages are close to (or exceeding) 95%. During this same period, IPNS target-system reliability has hovered around 99.5% except for approximately once every five years when the target reaches end-of-life and must be replaced. Figure 7 shows the accelerator and target-system reliability yearly-

averages since 1982, and the combined accelerator/target reliability, which is the important parameter for users to IPNS.

Prior to 1983, current was limited by the ion source. Since then, it has been ultimately limited by "beam loss", the fact that as more beam is injected, the fraction of the beam that gets "spilled" in the accelerator reaches some limit (determined usually by radiation levels or local heating of components) that it is not prudent to exceed. As can be seen in Figure 6, the maximum current has been relatively constant for a number of years, as expected because the basic machine parameters have been constant over that period. With the exception of one run in 1991 (where low current was required for target studies) and much of 1994 (where a damaged septum magnet limited operation to about 10 uA), yearly average current has exceeded 14 uA with some runs as high as 16 uA.

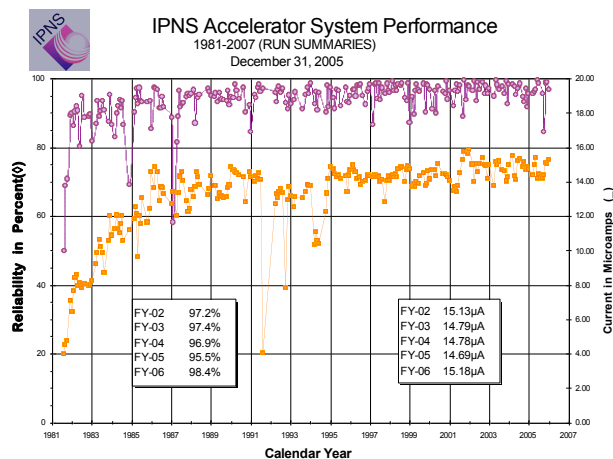


Figure 6. IPNS accelerator system performance (reliability and average current) from turn-on in 1981 to the present. Reliability is calculated as the ratio of beam hours available to beam hours scheduled.

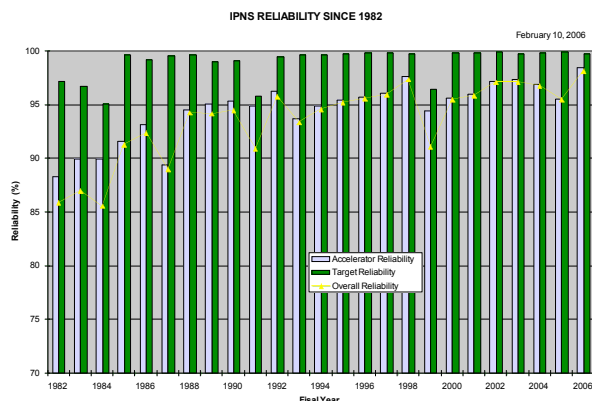


Figure 7. Fiscal-year averages for accelerator and target-system reliability

FABRICATING A NEUTRON GENERATING TARGET USING RECYCLED URANIUM DISCS

C.E. Prokuski, IPNS Division, Argonne National Laboratory

IPNS has historically operated at an availability of over 95%. Reliability is mainly governed by availability of the accelerator; however, overall facility reliability is limited by the weakest link in the chain. Any significant problem with the neutron generating target would directly affect facility reliability and therefore IPNS has a policy that requires that a spare target always be available for service. This article describes the fabrication of a new target, to increase the spare inventory and help to maintain the high reliability of IPNS.

The IPNS neutron-generating target is a passive component, having no mechanical moving parts, that essentially consists of a stainless steel enclosure containing eight depleted uranium discs. See Figure 1. The disc material is called "adjusted uranium". The base material is ^{238}U with 0.2 wt % ^{235}U , and the following minor additions: 450 wt ppm C, 250 wt ppm Fe and 350 wt ppm Si [1]. The discs are clad in a zirconium alloy called Zircaloy II. The two cup-shaped halves of the cladding that cover each disc are circumferentially welded and the cladding is bonded by hot isostatic pressure processing to the uranium core. The cladding is then machined to the final thicknesses of .5 mm on the disc faces and 1.25 mm on the circumferences. The cladding has a twofold purpose. First, it maintains confinement of the radioactive fission and spallation products arising from the impingement of the 450 MeV, 15 μA , 30 Hz pulsed proton beam on the target. Second, the cladding prevents direct contact between the uranium discs and the cooling water circulating through the target. Such contact would cause rapid corrosion of the uranium.

A disc reaches the end of its life when the cladding develops a small breach due to the anisotropic swelling of the uranium during service. See Figure 2. This swelling is characteristic of the orthorhombic crystal structure of the α -phase "adjusted" uranium. The degree of swelling correlates most closely with the number of fissions that have occurred in the material [2]. Three IPNS targets have reached end-of-life, exhibiting a mean lifetime of 260,000 $\mu\text{A}\cdot\text{hrs}$, or about four years given the average proton beam current of 15 μA . When any individual disc experiences clad breach, small amounts of fission and spallation products are released into the cooling water system. A γ radiation monitor sensitive to the 250 keV γ -ray from ^{135}Xe detects the elevated levels and the neutron generating system is shut down, taking the target out of service. Facility safety is not compromised by clad breach. A clad breach is the expected end-of-life event for the target. No more than one disc in any one target has ever been shown to have developed a breach. To date, the only confirmed breaches have occurred in either the first or second discs, at the front of the target where the proton beam enters. This fact is consistent with the expectation that the majority of the proton beam energy is deposited in the first few discs.

NEED FOR DISCS ARISES

The available inventory of uranium discs has dwindled as they have been used up in the previous five targets irradiated at IPNS since 1981. The reason for the IPNS policy that we will always have a spare target

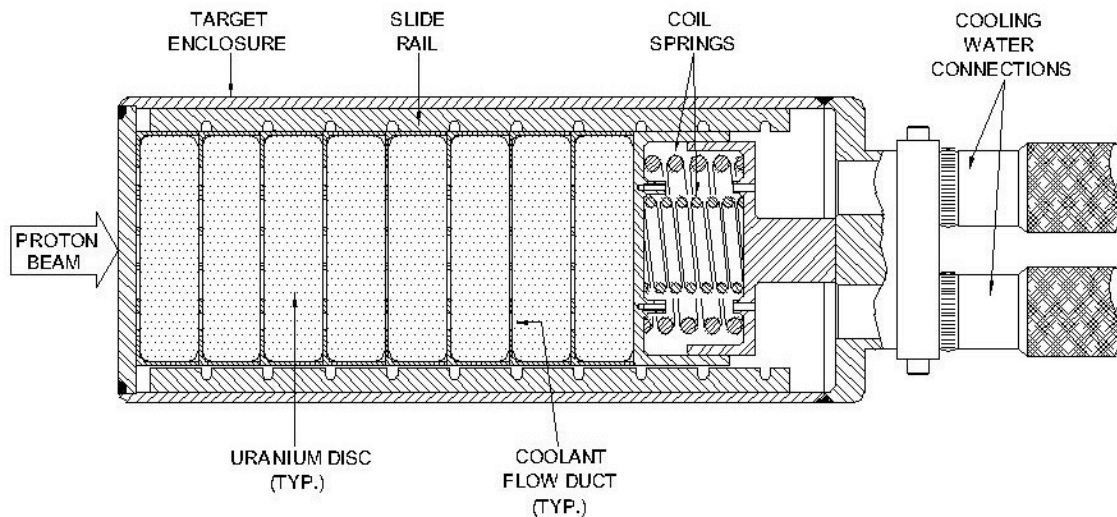


Figure 1: Cross section of IPNS neutron generating target

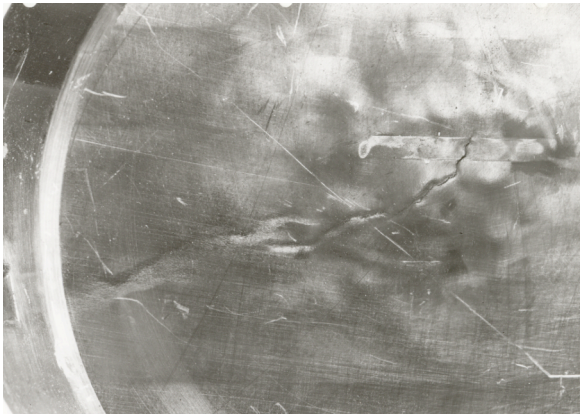


Figure 2: Photo of disc cladding breach

available during operation is that any target could reach end-of-life prematurely. The reduced disc inventory and need for spare targets, together with increasing budgetary austerity, provided the impetus for the development of a creative idea during the year 2000. That idea was the removal of used discs from targets that had reached end-of-life and the construction of a new target containing some of those discs. A calculation was performed to estimate remaining life in the used discs [3] using the following methodology. First, results of a previous calculation from the early years of IPNS were used as input to predict the percentage of target power produced within each disc. The results were normalized to the disc in position 2, which was the disc that was predicted to generate the most power and hence was expected to develop a breach first. Conversion to a fraction, subtraction from 1.0 and multiplication by 100 gave the predicted percent of life remaining for each used disc in the retired targets. Table 1 summarizes the results of the calculation. The percentages refer to expected lifetime compared to the 260,000 $\mu\text{A}\cdot\text{hr}$ mean target lifetime. It is clear from this calculation that the discs near the front (proton beam end) of the target would be expended first and that the discs in the rear would have considerable life remaining. It is important to note that the term “expended” as it is used here refers to the degree of swelling caused by proton beam irradiation, and not to a lessening in the production of neutrons. Even at the end of its life, an “expended” disc of depleted uranium still produces about 14 neutrons for

each proton that collides with a uranium nucleus, as does a new disc.

The estimated radioactivity levels associated with handling of the activated uranium discs, which would result in increased dosage to personnel, were an important factor in the decision of whether to proceed with the project. After an informal cost/benefit analysis was completed, the decision was made to fabricate a target containing discs recovered from retired targets. Funding was allocated and the project began early in the year 2001.

RECOVERY OF USABLE DISCS

The first step in the process was the removal of discs from one of the two remaining retired targets. The retired targets were held in sealed underground storage silos beneath the IPNS experimental hall. The target assembly was prepared by separating the target enclosure from the connected cooling hoses and linkage, a task that was performed in the IPNS experimental hall. Next, the target was transported to one of Argonne National Laboratory’s hot cell facilities. The activated state of the retired target necessitated that the work be done in such a facility.

The target was measured and photographed for reference prior to cutting operations. A series of documentation photographs was also made of the cutting, disc removal, inspection and target assembly processes. The rear end (the end away from proton beam entry) of the target was cut to remove the cooling hose linkage extension using a band-type cutoff saw. Next, a suitable cut location toward the rear end was selected based on minimizing material cross sectional area. The target enclosure was secured with a hold down clamp and the ends were held in place to prevent spring-out as the cuts were made. This was necessary because targets are designed to be under an internal spring compressive force of 670 N (150 lbs.) to prevent vibration of the discs in the cooling water flow of 190 liter/min (50 gal/min) passing through the target. Six cuts to predetermined depths were carefully made sequentially around the circumference of the enclosure, with the body of the enclosure being reclamped for each cut. After full separation, the end restraints were slowly released against the internal spring tension. Internal mechanical components and five of the disc

Table 1: Percentage of remaining disc life in target that has reached end-of-life

		Disc Position							
		1*	2	3	4	5	6	7	8
% Life Remaining →									
		1.9	0.0	10.2	21.8	34.0	61.2	90.3	94.7
* Disc closest to proton beam entry									

were then removed. Figure 3 shows a photo of two removed discs. The three front discs resisted removal and were left in place in the enclosure for disposal, an acceptable situation since there was no plan to use them in the recycled target in any case. Measurements showed the average radiation dose rate from a typical removed disc to be 1.7 mSv/hr (170 mR/hr) at 1 m. The removed discs were visually inspected and identified. The other internal components were also visually inspected for future design reference. The discs that would be used in the recycled target were selected based on the remaining life calculation [3]. The selected discs were segregated in a clean area and a careful cleaning step was performed. The cleaning consisted of immersion in an ultrasonic water bath, rinsing with deionized water and air drying. This step was a precaution against “tramp” contamination that might have been deposited on the discs after removal from the target. Because the hot cell is used for a variety of projects involving cutting and grinding of very radioactive materials, contamination of the discs from non-target sources was possible. Such contamination could result in the unintentional shutdown of the facility after the target was placed in service, as the sensitive radiation detection system could mistake the activity from the contamination for that arising due to a clad breach.

A careful leach test of each selected disc was then performed. This consisted of immersion of the disc in deionized water for a minimum of one hour, followed by analysis of the water for fission or spallation products. This process was repeated a minimum of four times for each disc, with a deionized water rinse occurring between each cycle. Decreasing concentration of a particular activation product with each iteration, or no detection of activation products, confirmed that there were no breaches in the cladding of the discs.

NEW TARGET FABRICATION

Next, new target components were procured and fabricated. The recycled target fabrication process was similar to that used for the previous five IPNS targets, with the exception that the work occurred in the hot cell and consequently required somewhat more preparation and deliberation. All the components in the recycled target were new with the exception of the used discs, since the cost of working with the activated components from the retired targets outweighed the cost of producing new components. Figure 3 shows some of these components. The new parts were assembled and delivered to the hot cell facility.

Both recycled and new discs were stacked inside the target enclosure. The target was filled with six used uranium discs, one new uranium disc, and one tantalum disc, which was located in the rear most position. (Only five used discs were removed from the retired target as part of this project; an earlier retired target, which was opened in 1993 in order to study radiation effects, provided several more usable discs for the recycled target.) The life expectancy of a used disc will be less than that of a new disc, because fission and spallation have occurred in the used disc, and it has been expended (anisotropically swelled) to some extent. The order of disc placement in the recycled target was based on the percentage of life remaining in the disc and the rate at which the disc would be expended in the new location in the recycled target. In general, the placements were arranged to maximize target life by locating the least expended discs in the forward most locations. A refined calculation [4] using MCNPX Monte Carlo simulation predicts that the recycled target will last 90% as long as a target containing all fresh discs.

The target enclosure was welded, inspected and pressure tested. The recycled target was transported to the IPNS experimental hall where the new cooling water hoses and linkages were installed and inspected.



Figure 3: Left: Removed target discs Right: New target components

It was decided to place the recycled target in operation to confirm that it would perform as expected; the operating target that it replaced would then serve as the spare. If the recycled target performed up to expectations, it would be left in place as the operating target.

PERFORMANCE

The recycled target was lowered into the operating position in the moderator/reflector assembly and entered service in January of 2004. The target operated as expected, with no abnormal indications from the cooling water or radiation detection systems. Initial reactions from the instrument staff and users were encouraging, with no apparent deficiency in flux being noticed. A quantitative comparison was necessary to confirm target performance; therefore, neutron flux data from seven of the thirteen IPNS scattering instruments were collected and analyzed. The data were retrieved from the period of August 2003 to December 2003 for the previous target having all original uranium discs, and from the period of February 2004 to June 2004 for the recycled target containing the used discs. Five data points, spaced about thirty days apart, were selected for each target to perform the comparison. Two of three IPNS moderators contain solid methane, and undergo a complete inventory exchange once per week. To minimize effects of moderator variation, all data were collected on days after methane exchanges, a time when methane condition could be expected to be most consistent across all instruments. On each selected day, a multi hour run was chosen. For each run, the total number of neutron counts recorded by the instrument beam monitor was divided by the total number of proton beam arrival pulses sent by the accelerator monitoring circuitry. The results of the comparison are presented in Figure 4. The data are compared as ratios of flux from the recycled target to flux from the previous target. It can be seen that the values of the ratios are near unity. The fact that the ratio is not exactly equal to one could be due to a small change in positional placement of the target in the moderator/reflector assembly, or to variations in neutron production caused by differences in disc location from the previous targets to the recycled target. For all practical purposes, however, the neutronic performance of the recycled target, as measured by this method, is identical to that of the previous target.

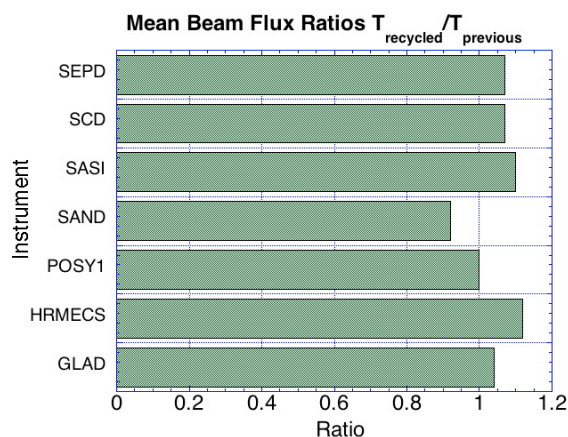


Figure 4: Ratios of mean beam flux from recycled target to mean beam flux from previous target measured at seven IPNS scattering instruments

RESULTS

This project was successful from a performance standpoint and also successful economically, and resulted in enhanced facility reliability. A neutron generating target utilizing partially expended uranium discs has been constructed and placed into service. The neutronic performance of the target is effectively identical to that of a target containing all fresh uranium discs; however, there is roughly a 10% penalty in expected target lifetime. A considerable amount of direct cost, over \$100K, was saved through use of the recycled discs. More important, however, was the deferment for four years of the spending of nearly \$1M for a supply of new uranium discs. This is especially relevant during times of tight budgets. An indirect benefit of this project was the presentation of Argonne National Laboratory's Spirit Award for recycling materials to two individuals who played lead roles on the project, William Ruzicka and Richard Vitt. In addition, Samuel Bodman, the Secretary of Energy, cited this project as an Office of Science Notable Practice in a letter dated July 21, 2005.

REFERENCES

- [1] Safety Analysis Report for the Intense Pulsed Neutron Source Facility for Operation with the Depleted Uranium Target, 2001 revision.
- [2] Uranium Target Failure Correlations, Argonne Intra-Laboratory Memo from T.A. Broome, J. M. Carpenter, M. Holding, dated November 18, 1992.
- [3] Used Target Disc Life Expectancy, IPNS calculation by Jeffery Toeller dated April 12, 2000.
- [4] IPNS Recycled Target Disc Stack Plan, IPNS calculation by Jeffery Toeller dated April 8, 2005.

SUMMARY AND STATUS OF IPNS MODERATORS

P. V. Brod, IPNS Division, Argonne National Laboratory

The history of cold moderator development at IPNS is described in the progress reports of 1991, 1996 and 2001. This report is an update of, from 2001 to present, those reports. IPNS has strived to remain at the forefront of solid methane moderator development and operation. We are currently operating two solid methane moderators and one liquid methane moderator. This configuration has been in use since 1994 when the H moderator was changed from liquid methane to solid methane. The liquid methane moderator, "F," supports six beam lines on two viewing surfaces, is poisoned on both faces and is operated at a temperature of 100 K. The solid methane moderators, "C" and "H," each support three beam lines and are operated at 28K. The H moderator is poisoned while the C moderator is unpoisoned, coupled and of re-entrant geometry. The moderators are arranged in the "wing" geometry relative to the target. Although other materials have been used in the past and new materials considered, methane has remained the moderator material of choice at IPNS.

MODERATOR OPERATION

As during the last reporting period, the reliability and efficiency of the moderators between 2001 and present have been exceptional, with no moderator failures and 100% availability during the scheduled run time. The moderators were replaced in January 2003 to improve flux by coupling the C moderator. The details are described in a later section. Both solid methane

moderators are operated at a temperature of 28K and annealed to 70K every 2-3 days. The anneal process releases stored energy and hydrogen, which, if allowed to, can build to levels that can damage the moderator when the temperature is increased. The methane is replaced every full week of scheduled run operation. The F moderator is a "continuous" system in that the methane is flowing into and out of the moderator in a closed loop. This moderator is operated at 100 K and is in the liquid state. Hydrogen and radiolytic polymerization products accumulate in the system over time, thus the methane charge is replaced on a regular schedule.

FLUX IMPROVEMENTS

In review, the entire moderator/reflector system was replaced in July 2000 due to a failure of the H moderator, which had developed a thermal short. This prevented cooling below 80 K. As a part of the moderator/reflector system replacement, the C solid methane moderator was changed from a horizontal groove design, with cooling on the back of the moderator only, to a vertical groove design with cooling on the front and back. The vertical groove design improved the flux to the POSY instruments by a factor of approximately 1.5. However, the small angle instruments experienced a loss in flux of a magnitude greater than expected and predicted by calculations. In January 2002, the C moderator cooling flow was reconfigured. This change

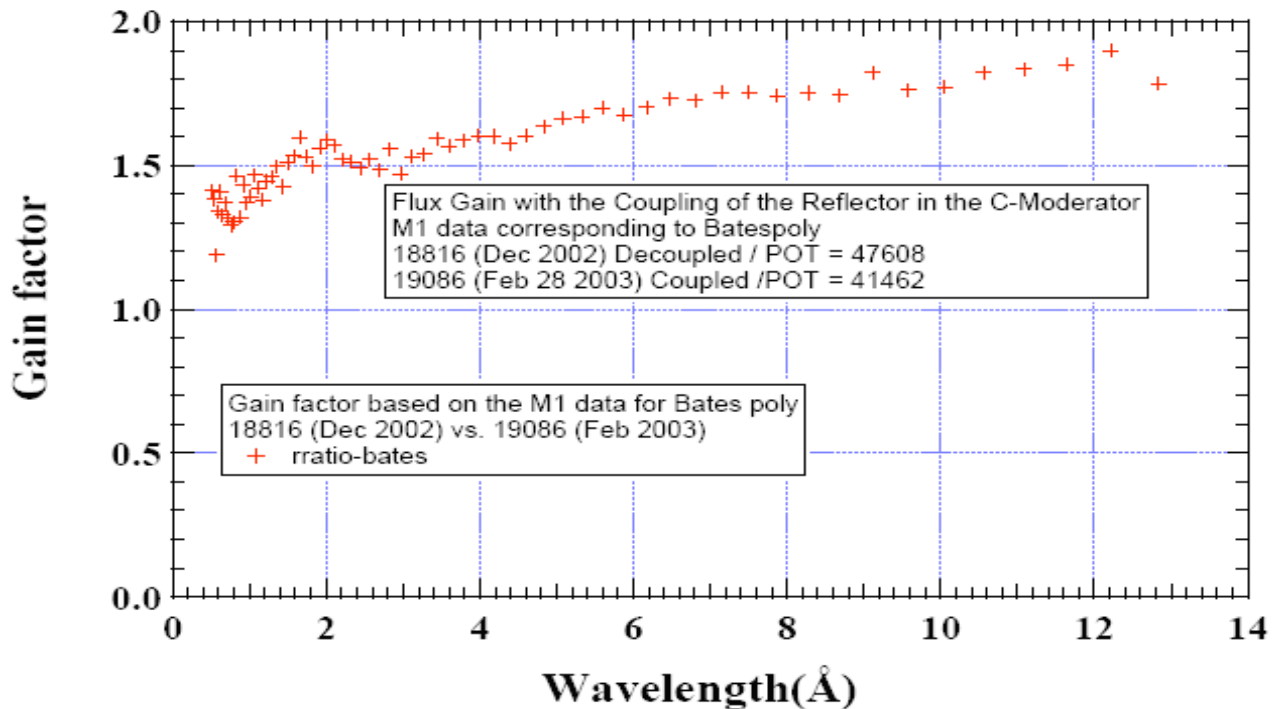


Figure 1: Gain Factor Measured on SAND

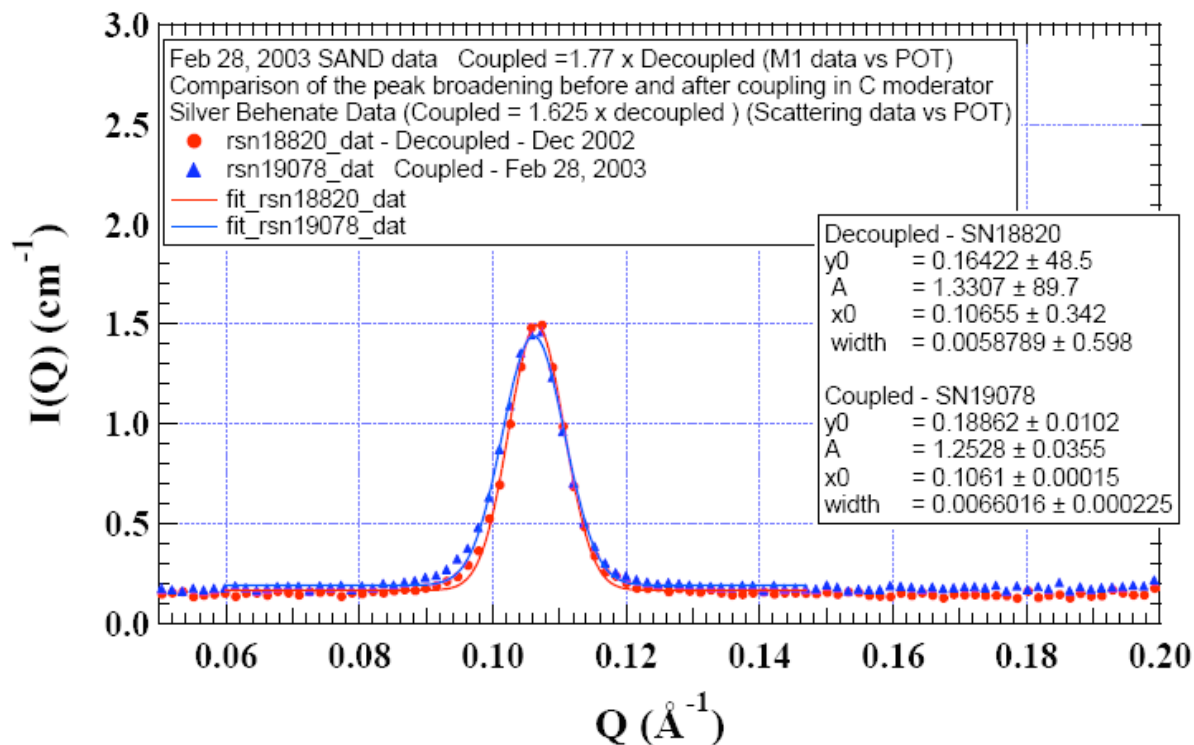


Figure 2: Resolution Effect Measured on SAND

in cooling flow configuration provided ~10% more flux in the long wavelength region to all the C moderator instruments as a result of a lower temperature on the viewed face of the moderator.

In January 2003 we installed a new moderator/reflector system with a coupled C moderator. We were operating with decoupled moderators, which provide increased resolution at the cost of flux. The C moderator instrument personnel reached a consensus that the increased flux of a coupled moderator outweighs the cost in resolution, thus the decision to couple the C moderator was made. We used this opportunity to revert to the horizontal groove design for the C moderator. The moderator was installed without decoupling material. The combination of the horizontal grooves and coupling the moderator resulted in an average gain factor of 1.6 across the spectrum (Figure 1). A marginal effect in δQ resolution (Figure 2) was noted on the SAND diffractometer.

Some effort has been devoted to the prospect of replacing the graphite inner reflector with a beryllium inner reflector. An increase in flux on the order of 10 – 15% is predicted by Monte Carlo simulations. Preliminary cost estimates and a conceptual design have been completed. As the concept stands, the cost of machining beryllium necessitates re-use of the reflector for each moderator installation. This then precludes using the current moderator designs, insulating vacuum connection system and cooling system lines. The final decision has not been made to move forward on this project at the time of this writing.



Figure 3: Inner Reflector Assembly

MODERATOR CONSTRUCTION

Construction and installation of one complete moderator/reflector system with a coupled C moderator was completed. The installation took place in January 2003. A spare reflector (graphite, Figure 3) and moderator system is currently in production. The reflector parts have been fabricated and test-fit together. Parts

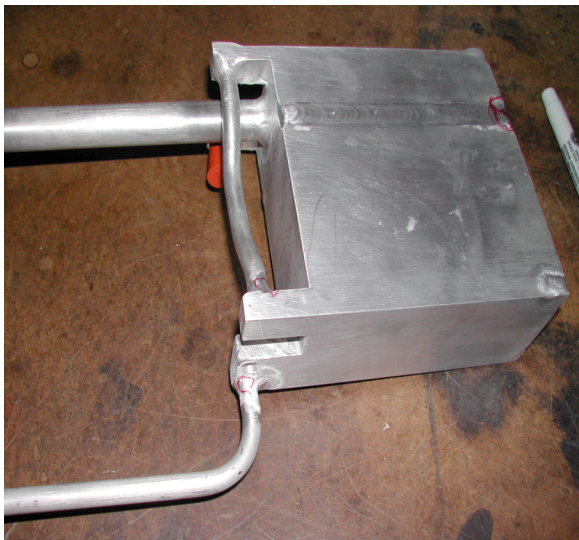


Figure 4. "H" moderator under construction

for the H moderator (Figure 4) have been fabricated and are in the process of being assembled. Parts for the F moderator have been fabricated. The C moderator is being redesigned to incorporate horizontal grooves and cooling on the front face at the bottom of the groove.

STORED ENERGY STUDIES

Studies were performed on the effect of moderator operating temperature and irradiation level on stored energy and hydrogen production in the C and H solid methane moderators. As it was planned to change the moderator/reflector system in January 2003, we took the opportunity to conduct the studies during the last two run cycles of 2002. Although some interesting data were obtained, unfortunately, much of the data were unusable due to periodic stored energy releases initiated by perturbations in the cooling flow. The perturbations in cooling were caused by a problem with a valve on the helium refrigerator. Figure 5 shows a

typical temperature response curve of the C moderator during an anneal, with the pronounced temperature excursion at ~300 seconds into the anneal, due to the release of stored energy. Figure 6 shows the strong effect that operating temperature has on the accumulation rate of stored energy

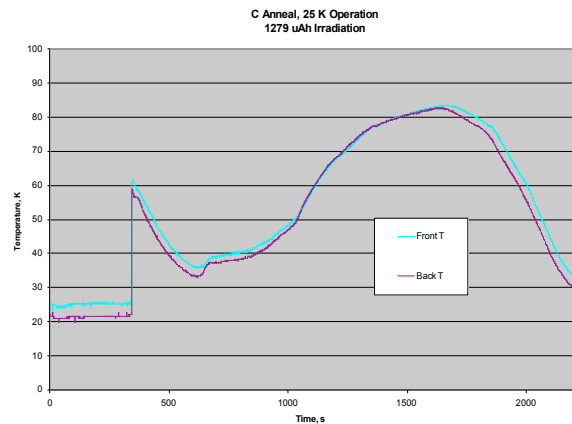


Figure 5. C Moderator temperature response during anneal

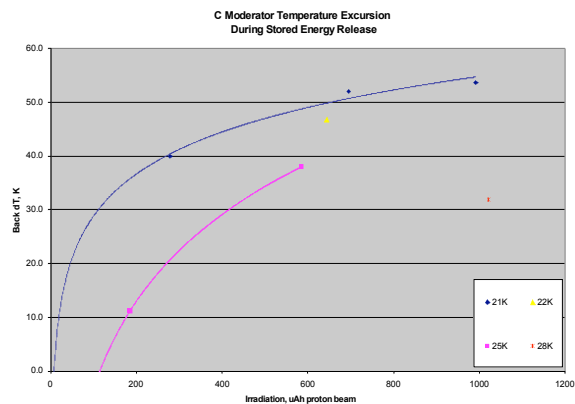


Figure 6. C Moderator anneal excursion temperature vs irradiation time at several temperatures

4. Future Plans



A VERY-COLD NEUTRON SOURCE

B. J. Micklich and J. M. Carpenter, Argonne National Laboratory, Argonne, IL 60439, U.S.A.

Abstract

A group of scientists at the Intense Pulsed Neutron Source has begun studying concepts for a Very-Cold Neutron Source (VCNS). The VCNS would characterize materials over large length and slow time scales, and complement the Long-Wavelength Target Station, a second target station proposed for the Spallation Neutron Source (SNS). The VCNS would be driven by a long-pulse linear accelerator and, using moderators cooled with liquid He-II, produce a neutron spectrum with a peak around 20 Å and a usable neutron flux out to 100 Å. We envision a multi-year research program investigating the scientific applications, instruments, and neutron source technology for VCNS.

INTRODUCTION

The Intense Pulsed Neutron Source has begun studying concepts for a Very-Cold Neutron Source that would support materials characterization on large length scales and slow time scales. The basis of VCNS is a target/moderator system generating a high neutron flux of the coldest practically imaginable spectrum, in an installation providing a large number of beams – a multiple-use very cold neutron scattering facility. This source would be well suited to serve applications in nanoscience, soft materials, fundamental physics, and energy, environmental, and medical sciences as a complement to the Long-Wavelength Target Station, a second target station proposed for the Spallation Neutron Source (SNS). The goal of VCNS is to deliver an intense source of neutrons with peak intensity around 20 Å and usable flux out to 100 Å.

The prospects for developing a VCNS depend on three issues: (i) enumerating scientific applications that would require long-wavelength neutrons, (ii) developing instrumentation that takes advantage of the unique characteristics of the proposed source, and (iii)

constructing a source of sufficient intensity to enable forefront science. Here we discuss the results of a workshop we held to investigate these issues.

VCNS WORKSHOP AT ARGONNE

IPNS held a workshop on Applications of a Very Cold Neutron Source on August 21-24, 2005. The purpose of the workshop was to address topics in neutron sources, instrumentation, and science at a VCNS. Thirty-nine participants from 12 institutions attended the workshop, which began with a description of the VCNS concept and a series of plenary sessions on neutron sources, neutron beam optics, instrumentation, and scientific applications. The participants then formed three working groups in the areas of sources, instruments and beamline components, and scientific applications. The workshop presentations and the reports of the working groups have appeared as a proceedings in an Argonne report. [1] Figure 1 pictures the participants in the workshop.

SCIENTIFIC APPLICATIONS

The workshop participants identified a number of exciting possibilities for research with neutrons having wavelengths longer than 20 Å, including

- addressing problems in fundamental nuclear physics
- answering questions about the fundamental nature of matter
- developing direct-imaging neutron techniques (such as microscopy, tomography, holography, and radiography)
- imaging the motion of proteins and molecular motors within living cells
- characterizing hydrogen transport in storage and photoproduction materials, and
- studying spin dynamics in magnetic nanostructured materials.



Figure 1. Participants in the Workshop on Applications of a Very Cold Neutron Source.

Given the unprecedented high flux of long-wavelength neutrons anticipated from the VCNS, and the superb performance of advanced optical devices, polarizers, and detectors favoring very cold neutrons, the group was enthusiastic about the scientific opportunities and possible breakthroughs in many important areas that are unattainable by present neutron sources including the SNS, but realizable by the VCNS. In each of the areas addressed, the group felt that not only could VCNS dramatically improve current science, but that a VCNS could make possible entire new fields of research.

INSTRUMENTS

The instrument working group felt that VCNS would offer excellent opportunities for developing best-in-class instruments for a variety of instrument types. In some cases this is because properties of long-wavelength neutrons can be exploited in instrument design. In other cases, existing instruments would function better at VCNS simply because of the colder neutron spectrum.

Many neutron optical techniques work better at longer wavelengths, and the extreme absorption of VCNs for certain nuclides combined with low absorption for others allows the design of highly precise optical components similar to light optics. Divergent VCN beams can be focused with high precision at focal lengths in the meter range. The phase shift of neutrons passing through matter is proportional to wavelength, making VCNs an ideal probe for viewing small contrasts. Likewise, the interaction of neutrons with gravitational and magnetic fields scales with $(\text{wavelength})^2$, enabling better design of instruments exploiting these effects. Optics can correct for unwanted effects of gravity in long flight path beamlines. Large-area high resolution detectors commonly used now in x-ray instruments at synchrotron sources could be adapted to neutron science without the need for extensive developments

NEUTRON SOURCE

Because present and near-term proposed sources have the peak of their neutron distribution in the range of 2-4 Å, we need a completely new type of neutron source to deliver neutrons with peak intensity around 20 Å and usable flux out to 100 Å wavelength. Developing a neutron source with the coldest practical spectral temperature means using moderators cooled by liquid helium. We envision these moderators to be in the form of pellets cooled by He II circulating through the spaces between pellets, or as small pellets carried in slurry form.

The slowing-down time of neutrons in candidate moderator materials is on the order of milliseconds. This indicates a long-pulse source such as a linear accelerator to drive the neutron-producing target. Table 1 lists parameters for the accelerator driver, which could be built with current technology.

The target material should be of high Z for neutron production efficiency, able to withstand high proton beam power, and have low neutron absorption. Liquid lead is

the present leading candidate. The community will soon acquire experience with the operation of high-power targets at the Spallation Neutron Source (USA), Japanese Spallation Neutron Source (Japan), and the MEGAPIE target (Switzerland). We expect no serious cavitation problems in the long-pulse source.

Table 1. Accelerator Parameters

Type	Linear accelerator, multiple cavity types
Energy	1 GeV
Pulse Rep. Rate	5 Hz
Pulse width	4 ms
RF frequency	325 MHz / 1300 MHz
Peak current	75 mA
Average current	1.5 mA
beam average power	1500 kW
duty cycle	0.02 (2%)

The principal constraint on the system is the amount of heat that can be removed from the few-K moderator. The main obstacles to solving this problem are the lack of scattering kernel data for the materials, temperatures, and neutron energies of interest, and the lack of thermophysical property data for materials at these extreme low temperatures.

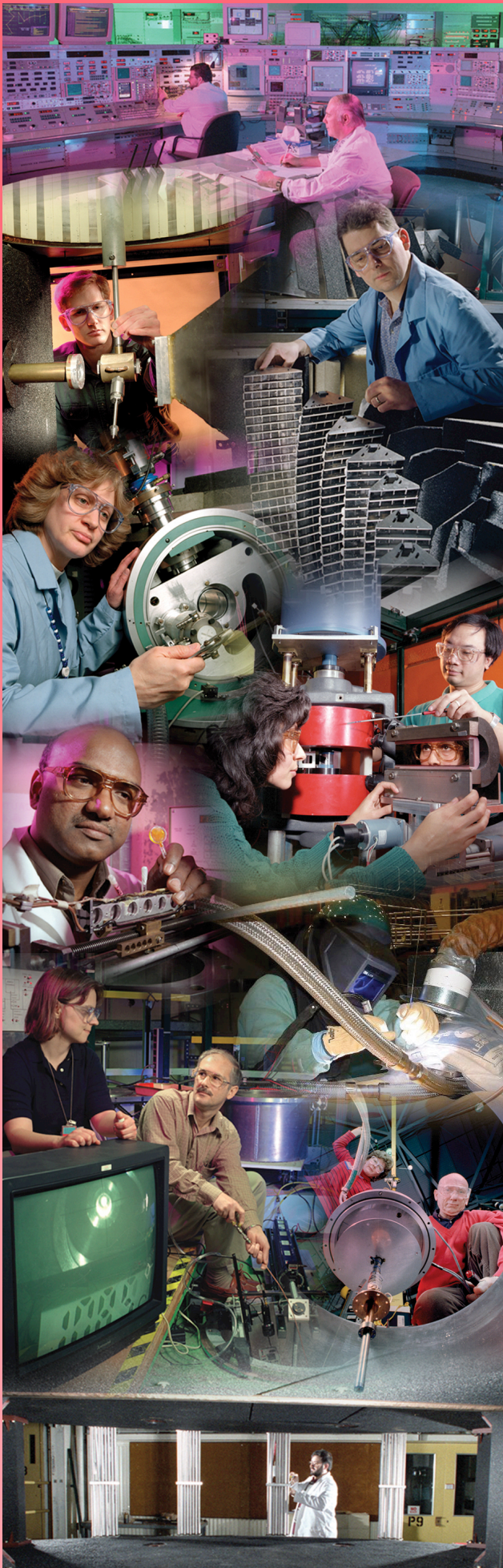
SUMMARY

A large number of developments related to VCN sources are taking place worldwide on the generation and use of ultra-cold neutrons. We feel that many of the key technical issues regarding a VCNS can already be adequately addressed, particularly the design of the accelerator system. The most important need is to develop the neutron scattering kernels necessary to perform more realistic computer simulations and the optimization of instruments to take advantage of the unique characteristics of a VCNS. The science case needs further detailed definition and refinement as a basis for instrument concepts. It is nevertheless clear that the VCNS would enable entire new fields of research and lead to significant advances in nanomaterials, soft matter dynamics, fundamental physics, and applied fields such as energy, environmental, and medical research.

REFERENCES

- [1] B. J. Micklich and J. M. Carpenter, eds., "Proceedings of the Workshop on Applications of a Very Cold Neutron Source," ANL-05/42, Argonne, IL, USA, August 21-24, 2005.

5. User Program and Organization



Organization and User Program

Maria Heinig, IPNS Division, Argonne National Laboratory

PERSONNEL

IPNS is operated by the IPNS Division. The IPNS management team—which includes the Division Director, Deputy Director, Technical Director, ESH/QA Coordinator & Financial Administrator, Operations Manager, Accelerator Facilities Manager and Deputy Manager, Group Leader for Neutron Scattering, and Controls & Computing Manager—provides strategic direction for the organization's mission, vision, values, and goals, and defines the personnel roles and responsibilities to attain these objectives. The management team takes a positive, proactive approach in developing new or revised IPNS strategies and in integrating such strategies into the operational program. These strategies incorporate modes of operation, staffing plans, new instruments, new advanced sources, and external interactions.

IPNS itself has a permanent scientific and technical staff to maintain and run the accelerator, target and moderator systems and instruments (and to pursue development where necessary), as well as to serve the user program. Service personnel, administratively part of other Laboratory organizations, are dedicated to work closely with the IPNS organization to provide support. In addition, at any given time a number of visiting faculty members, post-doctoral appointees, and students spending extended periods at Argonne add a welcome diversity to the in-house neutron scattering community.

NEUTRON SCATTERING INSTRUMENTS

IPNS currently has twelve operating neutron scattering instruments, as well as one not currently in the user program :

- General Purpose Powder Diffractometer (GPPD)
- Glass, Liquid, and Amorphous Materials Diffractometer (GLAD)
- High Intensity Powder Diffractometer (HIPD)
- High-Resolution Medium-Energy Chopper Spectrometer (HRMECS)
- Low-Resolution Medium-Energy Chopper Spectrometer (LRMECS)
- Neutron Reflectometer (POSY II)
- Polarized Neutron Reflectometer (POSY I)
- Quasielastic Neutron Spectrometer (QENS)
- Single Crystal Diffractometer (SCD)
- Small Angle Scattering Instrument (SASI)
- Small Angle Neutron Diffractometer (SAND)
- Special Environment Powder Diffractometer (SEPD)
- Chemical Excitation Spectrometer (CHEX – not currently in user program)

These instruments are the result of a continuous series of developments that began with the early prototypes. Ancillary equipment, available for all of these instruments, includes various capabilities for measurements at high temperature, low temperature, high pressure, and high magnetic field, as well as under various gaseous conditions. A majority of users comes from outside Argonne, representing universities, industrial corporations, and government-sponsored research laboratories throughout the nation and overseas (Fig. 1).

USER PROGRAM

IPNS is by far the most user-oriented of the U.S. Department of Energy's (DOE's) neutron source facilities. IPNS utilizes a team approach to assist neutron users as they plan and perform experiments. For fully supported instruments the team consists of a PhD instrument scientist, a scientific associate, and post doctoral as well as pool-based technical support. This team provides experimental and scientific assistance, as needed through the entire experiment process, from sample preparation and environment and experiment setup, through the collection and evaluation of data. Other services provided for users include helping with travel and lodging arrangements, assisting with site entrance, and providing site-specific IPNS orientation and training. In addition, training and safety-related information are provided to users to facilitate independent future experiments, permitting instrument scientists to work with other new users and thereby expanding the user base of IPNS.

IPNS has attained an enviably high record of reliability – one of the primary requirements for a user facility. Operating reliability is defined as the percentage of scheduled operating time during which the accelerator, target, and moderators are all functioning to deliver useful beams to the instruments. From the beginning, the operating reliability of IPNS has been consistently above 90%, and for the last ten years has been better than 95%. Reliability is especially important for a neutron scattering facility, because the typical experiment lasts only a few days. IPNS's high reliability has made it possible for users to schedule their visits and be assured of collecting data during their scheduled time. In the few cases where extensive accelerator or target downtime, or problems in operation of specific instruments or failure of the user's own equipment has put an experiment in jeopardy, it has often been possible adjust the schedule (for example, by

extending an operating cycle) and provide the running-time needed to complete the experiment. The dedication and skill of the accelerator operators, engineers and technicians and their willingness to respond 24/7 when problems occur have been crucial in maintaining the remarkable level of success.

A majority of users come from outside Argonne, representing universities, industrial corporations, and government-sponsored research laboratories throughout the nation and overseas.

Instrument	Range		Resolution	
	Scattering vector* Q(Å ⁻¹)	Energy (eV)	ΔQ(Å ⁻¹)	Energy (eV)
(Instrument Scientist -phone/Scientific Support)				
Special Environment Powder Diffractometer (R. von Dreele -630-252-8178/J. Fieramosca)	0.5-50	**	0.35%	**
General Purpose Powder Diffractometer (J. Richardson -630-252-3554/E. Maxey)	0.5-100	**	0.25%	**
Single Crystal Diffractometer (A. J. Schultz -630-252-3465/M. Miller)	2-20	**	2%	**
Low-Res. Medium -Energy Chopper Spectrometer (K. Littrell -630-252-3423)	0.1-30	0-0.6	0.02 k _e	0.05 E _e
High-Res. Medium -Energy Chopper Spectrometer (A. Kolesnikov -630-252-3555/L. Jirik)	0.1-30	0-0.8	0.01 k _e	0.02 E _e
Small Angle Scattering Instrument (J. Lal -630-252-6042/E. Lang -630-252-6102)	0.006-0.35	**	0.004	**
Small Angle Neutron Diffractometer (P. Thiyagarajan -630-252-3593/D. Wozniak -630-252-3592)	0.0035-0.8	**	0.001-0.004	**
Neutron Reflectometer (POSY II) (S. Park -630-252-8874)	0.0-0.25	**	0.001	**
Quasielastic Neutron Spectrometer (C. -K. Loong -630-252-5596/R. Ziegler)	0.42-2.59	0-0.1	~0.2	70 μeV§ 0.01 DE
Glass, Liquid and Amorphous Materials Diffractometer ¶ (C. Benmore -630-252-7665/J. Siewenie)	0.2-40	**	~1.0% cot θ	**
High Intensity Powder Diffractometer (J. Richardson -630-252-3554)/E. Maxey	0.5-25 1.8-50	**	1.8-3.5% 0.9%	**

* Scattering vector, $Q = 4\pi \sin \theta / \lambda$, $2\theta =$ scattering angle, $\lambda =$ wavelength

** No energy analysis

¶ Two sample positions

§ Elastic and inelastic resolution

NOT CURRENTLY IN THE USER PROGRAM
Chemical Excitations Spectrometer (CHEX)
Polarized Neutron Reflectometer (POSY I)

November 10, 2005

Calendar Year	82	83	84	85	86	87	88	89	90	91	92	93	94	95	96	97	98	99	00	01	02	03	04	05	TOTAL	
Number of Experiments																										
Proposed:	94	110	210	180	212	223	257	323	330	273	210	248	281	279	320	353	384	328	397	400	385	369	472	453	7091	
EXPERIMENTATORS TO IPNS FOR AT LEAST ONE EXPERIMENT:																										
Nuclear Physics	37	41	49	44	52	55	57	60	61	60	53	48	49	55	58	60	66	65	68	65	54	42	52	66	1317	
Neutron Scattering	8	9	8	7	11	15	18	16	19	15	14	18	13	16	18	29	33	21	21	31	37	41	42	45	505	
Universities	27	33	45	51	79	78	89	94	120	92	62	64	63	83	85	91	97	93	103	98	111	111	137	230	2136	
Industry	5	5	9	7	13	24	20	24	36	18	20	16	15	12	7	6	6	6	10	15	12	7	8	8	309	
Foreign	12	18	39	35	27	24	17	26	18	27	14	25	32	33	33	42	23	23	28	31	29	28	40	48	672	
TOTAL	89	106	150	144	182	196	201	220	254	212	163	171	172	199	201	228	225	208	230	240	243	229	279	397	4939	

IPNS PROGRAM ADVISORY COMMITTEE

The Program Advisory Committee (PAC) meets twice a year to review proposals for beam time at IPNS. The PAC has a majority of non-Argonne members, with its membership chosen to span the diverse types of

scientific experiments typically proposed. Program Advisory Committee Members during the past five years are shown in the following table. Current members of the PAC are identified with an asterisk.

PROGRAM ADVISORY COMMITTEE MEMBERS (2001-2005)

MEMBER'S NAME	AFFILIATION
ELASTIC SUBCOMMITTEE	
Bogdan Dabrowski*	Northern Illinois University
Christina Hoffmann*	ORNL/Spallation Neutron Source
James Jorgensen	Argonne National Laboratory
James Martin*	North Carolina State University
Aaron Krawitz	University of Missouri
James Richardson*	Argonne National Laboratory
Chris Tulk*	ORNL/Spallation Neutron Source
Joseph Zwanziger	Indiana University
INELASTIC SUBCOMMITTEE	
Meigan Aronson	University of Michigan
Doug Abernathy*	ORNL/Spallation Neutron Source
Julia Chan*	Louisiana State University
Brent Fultz*	California Institute of Technology
Stephen Nagler	Oak Ridge National Laboratory
David Price*	CNRS-CRMHT
Frans Trouw*	Los Alamos National Laboratory
SMALL ANGLE DIFFRACTOMETER AND REFLECTOMETER SUBCOMMITTEE	
John Ankner*	ORNL/Spallation Neutron Source
Greg Beaucage*	University of Cincinnati
Michael Fitzsimmons	Los Alamos National Laboratory
Jyotsana Lal*	Argonne National Laboratory
Thomas Russell*	University of Massachusetts
David Tiede*	Argonne National Laboratory

*Current PAC members.

The PAC allocates 75% of the beam time on most instruments to the users, on the basis of proposals submitted by those users. IPNS reserves the remaining 25% for the instrument scientists, who operate, maintain, and improve the instruments and carry out their own scientific programs. Most instruments have been oversubscribed by factors of 2-3 since their commissioning, and no instruments are undersubscribed. For experiments on publishable research accepted by the PAC or done in collaboration with an Argonne instrument scientist, the neutron beam time, complete scientific and technical assistance, and the use of the relevant IPNS instrument, analysis codes, and computing facilities are provided free of charge. Some support is also available to cover travel and lodging for university users who are otherwise unable to arrange this support. Scientists can easily access IPNS computers remotely and complete data analysis from their home institutions. Beam time for proprietary work or for publishable work that is not accepted by the PAC can be purchased under a rate structure that has been established by the DOE.

USER LIAISON

Thomas F. Koetzle of IPNS (tkoetzle@anl.gov) is the IPNS User Liaison, and will pass along user issues or concerns to IPNS management.

APPLICATION FOR BEAM TIME

Proposals for research at IPNS are solicited semiannually for experiments that will be run during the next six month cycle. Programmatic proposals which, if successful, can be granted beamtime for up to two years are also accepted (see below). The PAC meets twice a year to consider these proposals.

WEB-BASED SUBMISSION OF PROPOSALS

A call for proposal is sent to a large subset of the IPNS mailing list twice a year, one month in advance of each deadline. In previous rounds in order to apply for neutron beam time at IPNS, researchers completed a proposal form which was downloaded via the IPNS website. However, for the current round, Round 46, IPNS developed a new online proposal form. To apply for neutron beam time at IPNS, researchers must complete an online IPNS proposal form [Create Proposal Online](#). The first step to becoming a user is to register as an IPNS user and receive a badge number before submitting a proposal. For access to Argonne's facilities use this link: https://beam.aps.anl.gov/pls/apsweb/ufr_main_pkg.usr_start_page by registering, you begin the administrative steps required to gain approval for you to enter the Argonne site and to submit a proposal for IPNS.

Researchers who have already run experiments at IPNS must submit an experiment report on the standard

IPNS Experimental Report form (available via the IPNS web site at <http://www.pns.anl.gov>). Further beam time will not be granted unless reports on all previous experiments have been submitted. Referencing and discussing all previous work at IPNS is extremely useful to the PAC, and can enhance a proposal's prospects for acceptance. Experimental reports will also be accepted by electronic mail to mheinig@anl.gov.

FAST ACCESS PROCEDURE

A procedure has been implemented for providing the opportunity to researchers to perform fast turn-around experiments on the following instruments:

General Purpose Powder Diffractometer (GPPD)

High Intensity Powder Diffractometer (HIPD)

Neutron Reflectometer (POSY II)

Small Angle Scattering Instrument (SASI)

Small Angle Neutron Diffractometer (SAND)

Special Environment Powder Diffractometer (SEPD)

A small fraction of the operating time on each of these instruments will be available on a first-come, first-served basis. This service will be limited to short (less than one day) experiments involving only room-temperature data collection for samples that present no special handling problems. The time allocated to a single user will be limited to allow access for as many different users as possible. For these experiments, researchers may bypass the online proposal submission form, and may instead complete a short, 1-page form, which indicates any potential hazards. Interested users should contact the specific instrument scientist to learn the backlog for each instrument. Data collection on samples shipped to IPNS will be performed when time becomes available; the users need not come in person to IPNS. Raw data can then be accessed on the instrument computer. As with other experiments performed at IPNS, users will be responsible for data analysis.

PROGRAMMATIC PROPOSALS

IPNS will accept Programmatic proposals for many instruments. Programmatic proposals are similar to regular proposals, except that they require a more extensive "scientific background" that justifies access to IPNS instruments for two years. The number of days requested should be for the next cycle only.

Programmatic proposals are identified by the first two words in the abstract ("Programmatic Proposal"). The same form is used for regular and programmatic proposals and the submittal procedure is the same.

The Program Advisory Committee (PAC) evaluates the proposal initially and assigns a Numeric Rating (NR) as for other proposals, and time will be granted based on this rating. For the following three cycles the

Instrument Scientist (IS) or designate will communicate with the PI to assign days based on needs.

Instrument Scientists will review the scientific productivity of programmatic proposals and continued access to instruments will be granted only to productive proposals. Renewals will be considered after 2 years and will require PAC review.

For further information or questions, contact the respective Instrument Scientist (contact information at IPNS website) <http://www.pns.anl.gov/proposalcall/>

ASSISTANCE FOR UNIVERSITY USERS OF IPNS

IPNS does provide limited financial assistance to IPNS users from North American universities.

PURCHASE OF PROPRIETARY BEAM TIME

Beam time for experiments can be purchased under a rate structure approved by the Department of Energy. For proprietary or publishable work that is not of direct interest to the DOE, the full-cost-recovery rate (effective 2005) is ~\$5000 per instrument per day. Researchers may contact IPNS Division Director, Raymond Teller, at 630-252-4999 or rteller@anl.gov for further information.

OTHER IPNS ACTIVITIES

IPNS activities are related to a wide variety of DOE programs, such as fossil energy, energy efficiency, nuclear waste management, and research in the areas of transportation, defense, and biology. Many industrial users have performed experiments at IPNS; some of them have paid for beam time for proprietary research. A significant number of these experiments – collaborations with Argonne and IPNS scientists – result in joint publications.

IPNS and the Neutron Scattering Group in the Argonne Materials Science Division have continued to develop on-site Ph.D. thesis participation programs in collaboration with Argonne's Division of Educational Programs. Faculty advisors have frequently supplemented their trips to Argonne during the academic year with spending summers at Argonne as part of a faculty research program. Some IPNS personnel have served as adjunct faculty for universities throughout the region.

IPNS PERSONNEL – DECEMBER 2005

Specific job responsibilities of IPNS personnel are listed. IPNS instrument responsibility is given in parentheses.

IPNS DIVISION ADMINISTRATION

Ray Teller, Division Director
Jim Richardson, Deputy Division Director
Maria Heinig, User Administrator
Jack Carpenter, Technical Director
Beverly Marzec, Financial Administrator & ESH
Coordinator

NEUTRON SCATTERING

Jim Richardson, Group Leader for Neutron Scattering,
Instrument Scientist for General Purpose
Powder Diffractometer (GPPD)
Chris Benmore, Instrument Scientist for Glass, Liquid
and Amorphous Materials (GLAD)
Nicole Green, Administrative Secretary
Alexander Kolesnikov, Instrument Scientist for High-
Resolution Medium-Energy Chopper
Spectrometer (HRMECS)
Jyotsana Lal, Instrument Scientist for Small Angle
Scattering Instrument (SASI)
Chun Loong, Instrument Scientist for Quasielastic
Neutron Spectrometer (QENS)
Brad Micklich, Radiation Physicist
Art Schultz, Instrument Scientist for Single Crystal and
Powder Diffraction (SCD, HIPD)
Pappannan Thiyagarajan, Instrument Scientist for
Small Angle Diffraction (SAND)
Robert Von Dreele, Instrument Scientist for Special
Environment Powder Diffractometer (SEPD)

POSTDOCTORAL FELLOWS

Markus Bleuel, Small Angle Scattering Instrument
(SASI)
Nicolas de Souza, Quasielastic Neutron Spectrometer
(QENS)
Ashfia Huq, Powder Diffraction (GPPD)
Ryoji Kiyanagi, Special Environment Powder
Diffractometer (SEPD)
Natalie Malikova, Quasielastic Neutron Spectrometer
(QENS)
Sarka Malkova, Small Angle Scattering Instrument
(SASI)
Qiang Mei, Glass, Liquid and Amorphous Materials
Materials (GLAD)

Paula Piccoli, Single Crystal and Powder Diffraction
(SCD)
Sai Vengatesh Pingali, Small Angle Diffraction
(SAND)

CONTROLS AND COMPUTING GROUP

Tom Worlton, Controls & Computing Group Manager
Merle Faber, Computer Support
John Hammonds, Controls and Detectors
Chris Piatak, Controls and Detectors
Rodney Porter, Controls and Detectors
Tom Walsh, Controls and Detectors

NEUTRON OPERATIONS

Chuck Prokuski, Operations Manager
Cathy Riblon, Administrative Secretary
Jonathan Baldwin, Operations
Don Bohringer, Special Term Appointee – Special
Projects
Paul Brod, Moderators and Cryogenics
Phil Calahan, Engineering Support – Design/Drafting
Rich Como, Sample Environments
Joe Fieramosca, Special Environment Powder
Diffractometer (SEPD)
Lynette Jirik, High-Resolution Medium-Energy
Chopper Spectrometer (HRMECS)
Bob Kleb, Special Term Appointee – Engineering and
Design
Ed Lang, Small Angle Scattering Instrument (SASI)
Dave Leach, Operations – Engineering Support
Mark Malek, Operations
Evan Maxey, Powder Diffraction Instrumentation
(GPPD, HIPD)
Martha Miller, Single Crystal Diffractometer (SCD)
Mark Schlueter, Operations
Joan Siewenie, Glass, Liquids and Amorphous
Materials Diffractometer (GLAD)
Jeff Toeller, Neutron Facilities Supervisor
Tony Tafoya, Operations
Rich Vitt, Operations – Engineering Support
Ken Volin, Sample Environments
Michael Wolbing, Moderators and Cryogenics
Denis Wozniak, Small Angle Neutron Diffractometer
(SAND)
Ray Ziegler, Quasielastic Neutron Spectrometer
(QENS)

ACCELERATOR OPERATIONS

Gerry McMichael, Accelerator Facilities Manager
Frank Brumwell, Deputy Accelerator Facilities Mgr.
Maria Gerches, Administrative Secretary
Jerome Ballentine, Electro-mechanical, Vacuum
Tom Beilfus, Electronics, Power Supplies
Bob Bertrand, Operations, Electronics
Bill Brzowski, Engineer, Power Supplies and Magnets
Mike Bucciarelli, Operations, Electronics
Walter Czyz, Special Term Appointee
Jim Davis, Assistant Chief of Operations
Joe Dittrich, Operations, Electronics
Lawrence Donley, Engineer, Linac and Kicker Magnets
Jeff Dooling, Accelerator Physicist, Diagnostics
Arnold Germain, Electro-mechanical, Vacuum
Quentin Hasse, Group Leader - Synchrotron
Larry Johns, Special Term Appointee
Ray Kucera, Electronics, Preaccelerator and Source
Marvin Lien, Engineer, Controls and RF
Mark Middendorf, Engineer, Synchrotron RF
Mark Moser, Operations, Electronics
Dean Peters, Engineer, Vacuum
Don Piatak, Special Term Appointee
John Sendera, Special Term Appointee
Jim Spindler, Assistant Chief of Operations
Vern Stipp, Group Leader - Linac
Bill Sullivan, Assistant Chief of Operations
George Vasilopoulos, Assistant Chief of Operations
Shaoheng Wang, Postdoctoral Fellow, Accelerator
Physics
Charles Whiteford, Operations, Electrical/Mechanical
Jim Zmuda, Electro-mechanical, Vacuum

USER SUPPORT AND TECHNICAL ASSISTANCE FROM OUTSIDE IPNS

MATERIALS SCIENCE DIVISION

Suzanne teVelthuis, Neutron Reflection (POSYI)
Stephan Rosenkranz, Prototype Diffuse Scattering
Diffractometer (Christina)

HEALTH PHYSICS SUPPORT

Mark Delrose, Health Physics Chief Technician
Randy Wilson, Health Physics Technician

IPNS-Sponsored Workshops

Maria Heinig, IPNS Division, Argonne National Laboratory

IPNS activities are related to a wide variety of DOE programs, such as fossil energy, energy efficiency, nuclear waste management, and research in the areas of transportation, defense, and biology. Many industrial users have performed experiments at IPNS; some of them have paid for beam time for proprietary research. A significant number of these experiments – collaborations with Argonne and IPNS scientists – result in joint publications.

IPNS and the Neutron Scattering Group in the Argonne Materials Science Division have continued to develop on-site Ph.D. thesis participation programs in collaboration with Argonne's Division of Educational Programs. Faculty advisors have frequently supplemented their trips to Argonne during the academic year with spending summers at Argonne as part of a faculty research program. Some IPNS personnel have served as adjunct faculty for universities throughout the region.

CONFERENCES AND WORKSHOPS

IPNS has sponsored a variety of conferences and workshops. These events inform and educate the outside community about the usefulness of neutrons across a spectrum of scientific disciplines; additionally, they serve to train newcomers in the neutron scattering applications. The following IPNS sponsored conferences and workshops have been held since 2002.

The International Workshop on “Nanocomposites: Materials, Neutrons and Data Interpretation”, was held on March 28-30, 2002, at the Intense Pulsed Neutron Source Division, Argonne National Laboratory.

The purpose of the workshop was to bring together experts in the fields of nanomaterials synthesis and characterization using a variety of techniques. Its objective was to identify the key nanocomposite systems and their properties and data interpretation schemes for neutron scattering studies.

The Workshop on Neutron Spin Echo Techniques at Pulsed Sources was held on July 15-16, 2002 at the Intense Pulsed Neutron Source Division, Argonne National Laboratory.

At Argonne National Laboratory (ANL) experts from all over the world gathered in July 2002 to discuss the prospects of classical spin echo and new variants of spin echo based on resonance spin echo (NRSE) coils at the future Spallation Neutron Sources like the SNS. At present no Spin Echo based instrument exists at any of the pulsed neutron sources. At the end of the workshop it was agreed that options like MIEZE (modulation of intensity with zero field spin echo) a variant of NRSE, which allow for high resolution energy analysis

could be explored and implemented on a conventional small angle spectrometer at a pulsed source like IPNS at ANL.

The Workshop on the Future of Power Diffraction at the IPNS and SNS was held on November 16-17, 2003. The goals of the workshop were (1) familiarize the science community with the expected performance of the upgraded GPPD at the IPNS, which is expected to be operational in 2003; (2) to consider options for the upgrade of the SEPD at the IPNS; (3) to review progress on the construction of POWGEN3 for the SNS and discuss the science opportunities enabled by its expected performance; (4) to explore the science case for an ultra-high resolution powder diffractometer at the SNS; and (5) to discuss the new data analysis methods that will allow full exploitation of the capabilities of the upgraded GPPD at the IPNS and POWGEN3 at the SNS and develop a strategy for developing the new analysis codes.

The Workshop on Single Crystal Diffuse Scattering at Pulsed Neutron Sources was held on June 16-17, 2003 with thirty participants from Europe and North America.

The goals of this workshop were to assess the range of science to which single-crystal diffuse scattering can make an important contribution, to review current instrumentation, and to discuss the technical challenges that have to be addressed by an optimized diffuse scattering diffractometer. The workshop helped to provide the scientific case for a dedicated SNS instrument. A prototype is currently under construction at IPNS with funding from the DOE. For more details on the workshop click on

The Workshop on Neutron Macromolecular Crystallography at the Spallation Neutron Source was held on October 2-3, 2003.

The primary goal of the workshop had been to exploit the high neutron flux that will become available by 2006 at the Spallation Neutron Source (SNS), and to leverage the strong support and interest of the macromolecular crystallography community.

The Workshop on Applications of a Very Cold Neutron Source was held on August 21-24, 2005.

On August 21-24, 2005 IPNS convened a workshop on the scientific prospects of a Very Cold Neutron Source (VCNS) at Argonne National Laboratory. 39 participants from 12 institutions attended the three-day meeting.

IPNS has begun studying concepts for a Very-Cold Neutron Source (VCNS) that would support materials characterization on large length scales and slow time

scales. The neutron source would be driven by a long-pulse linear accelerator and produce a neutron spectrum with a peak around 20 Å and a usable neutron flux out to 100 Å. A special-purpose installation such as VCNS would better provide for nanoscience and other applications of very cold neutrons than could any existing or proposed facility. A workshop was held on August 21-24 2005 to examine the scientific applications of a VCNS. The workshop concluded that not only could current science in a wide range of fields (such as nanomaterials, soft matter dynamics, material contrast, spintronics, fundamental physics, energy & environmental science, and biological and medical sciences) be improved dramatically by a VCNS, but that a VCNS could make possible entirely new fields of research. While considerable work needs to be done in defining instruments that are suitable for the expected scientific applications and for the use of very cold neutrons in a long-pulse mode, the workshop participants were nonetheless excited about the scientific prospects.

National School on Neutron and X-ray Scattering

In August 1999, IPNS and the Materials Science Division joined with Argonne's Advanced Photon Source (APS) in organizing the nation's first National School on Neutron and X-ray Scattering. The Office of Basic Energy Science of the Department of Energy funded the school, which will continue to be offered

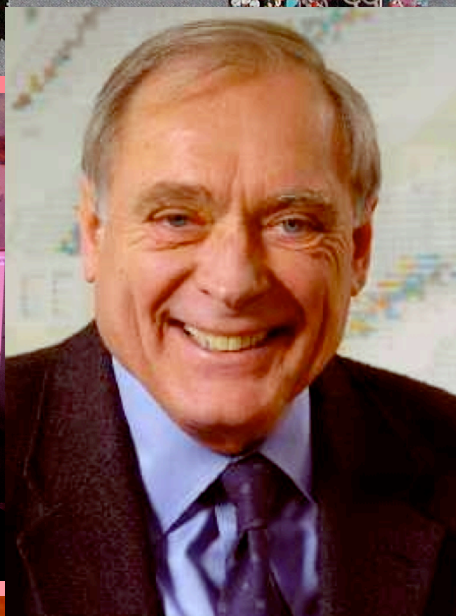
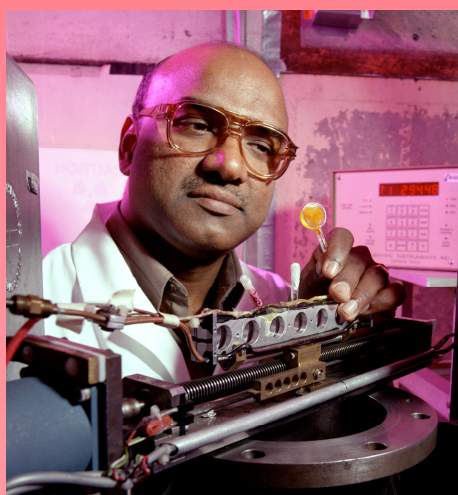
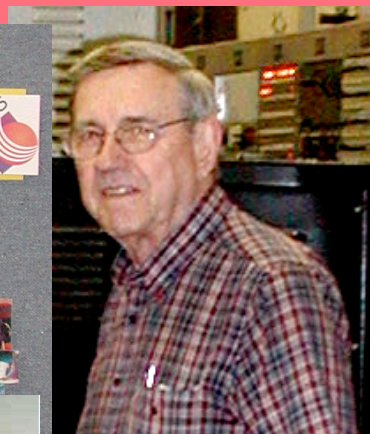
annually each summer. The success of the 1999 session was so overwhelming that DOE provided additional funding to increase its size from 48 to 60 students.

Now in its seventh year the National School on Neutron and X-ray Scattering continues to attract students from nationwide universities. The classes are normally scheduled in the month of August for two weeks.

The main purpose of the National School on Neutron and X-ray Scattering is to educate graduate students attending U.S. universities on the use of major neutron and x-ray facilities. Attendance at the school gives participants an opportunity to learn fundamentals of the interaction of X-rays and neutrons with matter, techniques of synchrotron radiation, and properties and applications of neutron beams. Each year the school dwells on specific scientific or technological areas. For example, the curriculum for 2005 emphasizes materials science, solid state physics and soft matter. The first week of this accelerated program will offer tutorial lectures on the principles of scattering theory and the characteristics of the neutron and X-ray sources. The second week will be devoted to applying scattering methods to condensed matter, both during seminars and in hands-on experiments with instruments at the APS and the IPNS.



6. Awards and Recognitions



IPNS named 'Nuclear Historic Landmark'

by Evelyn Brown

The Intense Pulsed Neutron Source at Argonne was named a Nuclear Historic Landmark by the American Nuclear Society (ANS) at a ceremony May 13, 2002. ANS President Gail H. Marcus presented the plaque to IPNS Division Director Ray Teller and retired Argonne Director Hermann Grunder before a roomful of IPNS employees and retirees.

The award identifies sites or facilities where outstanding physical accomplishments instrumental in the development and implementation of, and the peaceful uses of, nuclear technology took place.

IPNS is the seventh Argonne facility to be named a Nuclear Historic Landmark. Others are Chicago Pile-1 and -5, Experimental Breeder Reactor-I and -II, Experimental Boiling Water Reactor and the Materials Testing Reactor.

Using pulses of neutrons – uncharged particles in the nucleus of atoms – IPNS probes the structures and motions of material ranging from semiconductors to proteins. The research helps scientists understand material behavior.

The neutron source serves chemists, biologists, physicists, engineers and materials scientists. More than 250 scientists use the facility each year, completing approximately 400 experiments and producing 150 publications.

Since its opening in 1981, IPNS has continually guided the neutron-user community. Even after 20 years, it continues to improve its performance – the IPNS provides neutrons to scientists more than 95 percent of time consistently – and is preparing for a new role in the neutron research world.

Building on the success of IPNS, DOE is constructing a \$1.4 billion state-of-the-art neutron research facility called the Spallation Neutron Source (SNS) at Oak Ridge National Laboratory. Scheduled to open in 2006, the SNS will be the world's most intense spallation source for neutron scattering research with beams 40 to 100 times more intense than those at IPNS. Researchers will be able to perform experiments faster and gather data in greater detail.

Argonne is designing and building the first set of experimental instruments for the SNS.

"IPNS has a magnificent role to educate the large number of people moving into neutron research," said Grunder.

SNS will be able to perform 10 times as many experiments as the IPNS and host 2,000 users. In the next five years IPNS will train the growing neutron-user community to use the SNS.



HISTORICAL OCCASION – American Nuclear Society President Gail H. Marcus recently presented a plaque designating the Intense Pulsed Neutron Source a Nuclear Historic Landmark to IPNS Division Director Ray Teller (center) and retired Laboratory Director Hermann Grunder.



Dr. J.M. Carpenter

Carpenter to receive neutron scattering award

ARGONNE, Ill. (April 21, 2006) — Jack Carpenter of the U.S. Department of Energy's Argonne National Laboratory will receive the 2006 Clifford G. Shull Prize from the Neutron Scattering Society of America for his groundbreaking work developing neutron sources and instrumentation.

Carpenter, technical director at Argonne's Intense Pulsed Neutron Source, is receiving the award "for seminal contributions to the development of neutron sources and instrumentation that have had world-wide impact on neutron scattering across a broad range of scientific disciplines, culminating in the optimized design of the Spallation Neutron Source at Oak Ridge."

The Clifford G. Shull Prize in Neutron Science is named in honor of Clifford G. Shull, who shared the Nobel Prize in physics in 1994 with Bertram Brockhouse for pioneering developments in neutron science.

"It is wonderful to have my name associated with Shull," Carpenter said, "and to have my work acknowledged by my community of colleagues."

Carpenter played a pivotal role in developing pulsed neutron sources across the globe, including the founding of IPNS. He pioneered exploitation of the inherent efficiency of the spallation process for producing neutrons, together with the advantages of pulsed operation and time-of-flight measurements to study structure and dynamics of materials. His patented design for the moderator-reflector combination is at the heart of modern pulsed neutron sources.

Carpenter said his data and patented source moderator "that boosted the intensity to interesting levels" helped pave the way to building IPNS. He played a major role in designing and overseeing construction of the IPNS, even using parts from the decommissioned Zero Gradient Synchrotron at Argonne.

Since the IPNS was completed in 1981, Carpenter's technical and strategic skills have been in demand to advise on all subsequent pulsed neutron sources built—the KEK in Japan, ISIS in the United Kingdom and the Lujan Center at Los Alamos National Laboratory, as well as the new generation of pulsed source facilities—AUSTRON in Austria, J-PARC in Japan, ESS in Europe and the soon-to-be-opened Spallation Neutron Source at Oak Ridge National Laboratory.

Carpenter's contributions to developing pulsed-source instrumentation and coupling neutron source performance and instrument design have expanded the use of pulsed neutron sources to a broad range of scientific endeavors.

"When IPNS opened, we established a simple proposal and peer-review system for making the facility available to a widespread community of users, which was later used as a model across the country with other large research facilities," Carpenter said. Previously such facilities were available only to a small, dedicated group of researchers on staff.

The award will be presented during the American Conference on Neutron Scattering, June 18-22, in St. Charles.

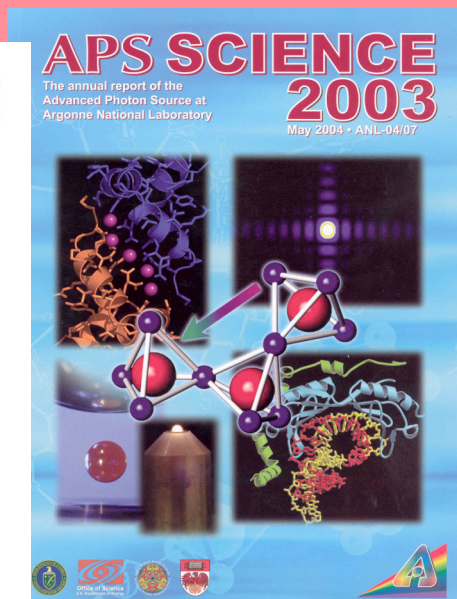
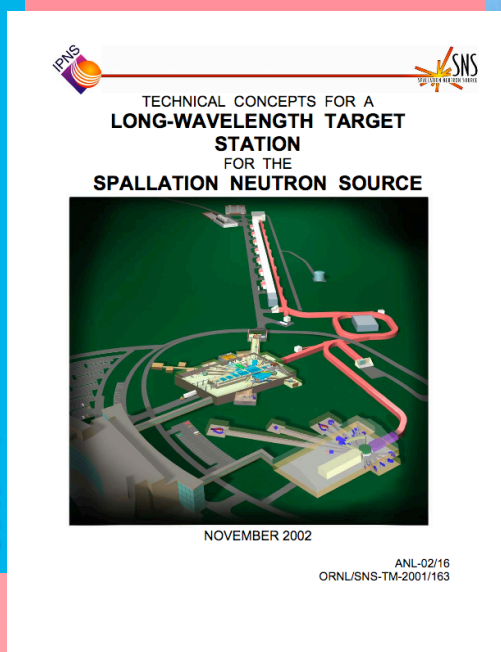
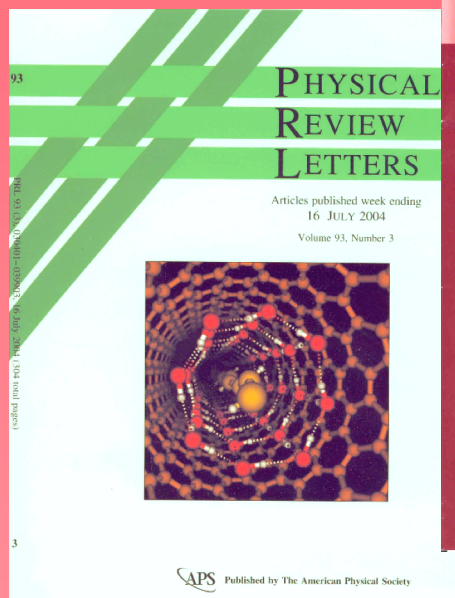
The nation's first national laboratory, Argonne National Laboratory conducts basic and applied scientific research across a wide spectrum of disciplines, ranging from high-energy physics to climatology and biotechnology. Since 1990, Argonne has worked with more than 600 companies and numerous federal agencies and other organizations to help advance America's scientific leadership and prepare the nation for the future. Argonne is managed by the University of Chicago for the U.S. Department of Energy's Office of Science.

Awards and Recognition

Acknowledging employee contributions is essential to operating a program that will continue to be successful. Performance awards may be given to individual employees in recognition of performance achievements, as set forth in the specific award program criteria. IPNS personnel have been nominated for and received numerous awards. Since 2001, the following IPNS personnel have received awards:

- 2001** **U.S. Department of Energy Distinguished Associate Award**
Bruce Brown
- University of Michigan Distinguished Alumnus Award**
Jack Carpenter
- 2002** **University of Chicago Distinguished Performance Award**
Chun Loong
- Argonne Pacesetter Award**
Paul Brod
Roger Blackman, Joe Dittrich, Quentin Hasse, and Charles Whiteford
- 2003** **University of Chicago Outstanding Service Award**
Denis Wozniak
- Argonne Pacesetter Award**
Larry Kurek, Fran Clark, Charles Prokuski and George Vukovich
- 2004** **U.S. Department of Energy Spirit Award**
Bill Ruzicka and Rich Vitt
- American Nuclear Society Outstanding Achievement Award**
Jack Carpenter
- Argonne Pacesetter Award**
Patrick DeLurgio and Martha Miller
Ed Lang
George Vasilopoulos, Jim Davis, Jim Spindler and Bill Sullivan
Joan Siewenie
- 2005** **University of Chicago Outstanding Service Award**
Vern Stipp
- 2006** **University of Chicago Distinguished Performance Award**
Pappannan Thiyagarajan
- University of Chicago Outstanding Service Award**
Beverly Marzec

7. Publications (2001-2006)



D. P. Abraham, J. W. Richardson and S. M. McDeavitt (2001). "Microscopy and Neutron Diffraction Study of a Zirconium-8 wt% Stainless Steel Alloy." J. Mater. Sci. **36**(21): 5143-5154. GPPD

T. Adachi, T. Oku, S. Morita, H. Ohmori, Y. Takizawa, H. M. Shimizu, J. Suzuki, C.-K. Loong, K. C. Littrell and R. Goyette (2002). Development of Neutron Compound Refractive Optics: A Progress Report. ICNS 2001. POSYII

T. Adachi, K. Ikeda, T. Oku, J. Guo, W. Lin, H. Ohmori, T. Morishima, H. M. Shimizu, K. Sakai, J. Suzuki, K. C. Littrell and C.-K. Loong (2003). A Compound Focusing Device for Cold Neutrons. ICANS-XVI. POSYII

T. Adachi, K. Ikeda, T. Oku, J. Guo, W. Lin, H. Ohmori, T. Morishima, H. M. Shimizu, K. Sakai, J. Suzuki, K. C. Littrell and C.-K. Loong (2003). A Compound Focusing Device for Cold Neutrons. ICANS-XVI. POSYII

T. Adachi, K. Ikeda, T. Oku, J. Guo, W. Lin, H. Ohmori, T. Morishima, H. M. Shimizu, K. Sakai, J. Suzuki, K. C. Littrell and C.-K. Loong (2003). A Compound Focusing Device for Cold Neutrons. ICANS-XVI. POSYII

T. Adachi, K. Ikeda, T. Oku, K. Sakai, S. Suzuki, J. Suzuki, H. M. Shimizu, K. C. Littrell, C.-K. Loong, W. Lin, J. Guo, N. Mitsuishi, S. Morita and H. Ohmori (2003). "Recent Progress in the Development of Concave Fresnel Lenses for Neutrons." J. Appl. Crystallog. **36**(Pt. 3): 806-808. POSYII

T. Adachi, K. Ikeda, T. Oku, J. Guo, W. Lin, H. Ohmori, T. Morishima, H. M. Shimizu, K. Sakai, J. Suzuki, K. C.

Littrell and C.-K. Loong (2004). "Possible Application of Compound Fresnel Lens for Neutron Beam Focusing." Physica B **350**: 775-778. POSYII

T. Adachi, K. Ikeda, T. Shinohara, K. Hirota, T. Oku, J. Suzuki, H. Sato, K. Hoshino, J. Guo, W. Lin, H. Ohmori, H. M. Shimizu, K. Sakai, K. C. Littrell and C.-K. Loong (2004). "Development of a Compound Focusing Lens: Improvement of Signal-Noise Ratio." Nucl. Ins. Meth. Phys. Res. A **529**(1-3): 112-115. POSYII

D. T. Adroja, J. G. Park, E. A. Goremychkin, N. Takeda, M. Ishikawa, K. A. McEwen, R. Osborn, A. D. Hillier and B. D. Rainford (2005). "Influence of the Crystal Field Potential on the Superconducting Properties of PrRU4Sb12." Physical B **359**: 983-985. LRMECS

K. Ahn, D. Louca, S. J. Poon and G. J. Shiflet (2003). "Local Structure of Al and Fe Based Metallic Glasses." J. Phys. Cond. Matt. **15**(31): S2357-S2364. GLAD

K. Ahn, D. Louca, M. C. Gao and G. J. Shiflet (2004). "Topological and Chemical Ordering Induced by Ni and Nd in Al₈₇Ni₇Nd₆ Metallic Glass." Phys Rev. B **70**(22). SEPD

A. Alexander, P. D. Battle, J. C. Burley, D. J. Gallon, C. P. Grey and S. H. Kim (2003). "Structural and Magnetic Properties of Li₃RuO₄." J. Mater. Chem.(13): 2612-2616. SEPD

I. Anderson, J. Cook, G. Felcher, T. Gentile, G. Greene, F. Klose, T. Koetzle, E. Lelievre-Berna, A. Parizzi, R. Pynn

and J. Zhao (2005). "Polarized Neutrons for Pulsed Neutron Sources." J. of Neutron Res. **13**(4): 193-223. POSYI

T. M. Anderson, W. A. Neiwert, M. L. Kirk, P. M. B. Piccoli, A. J. Schultz, T. F. Koetzle, D. G. Musaev, K. Morokuma, R. Cao and C. L. Hill (2004). "A Late-transition Metal Oxo Complex: $K_7Na_9[O=Pt^{IV}(H_2O)L_2]$, $L = [PW_9O_{34}]^{9-}$." Science **306**: 2074-2077. SCD

C. Andreani, D. Colognesi, J. Mayers, G. F. Reiter and R. Senesi (2005). "Measurement of Momentum Distribution of Lightatoms and Molecules in Condensed Matter Systems using Inelastic Neutron Scattering." Adv. in Physics **54**(5): 377-469. HRMECS

J. F. Ankner and C. Rehm (2003). "Time-dependent measurements at the SNS Liquids Reflectometer." Physica B **336**: 68-74. POSYII

B. K. Annis, O. Borodin, G. D. Smith, C. J. Benmore, A. K. Soper and J. D. Londono (2001). "The Structure of a Poly(ethylene Oxide) Melt From Neutron Scattering and Molecular Dynamics Simulations." J. Chem. Phys. **23**(115): 10998-11003. GLAD

B. K. Annis, M.-H. Kim, R. Alamo and M. Pyda (2001). "Inelastic Neutron Scattering from Isotactic Polypropylene." J. Polym. Sci. Part B Polymer Phys. **39**: 2852. HRMECS

B. K. Annis, Y. S. Badyal and J. M. Simonson (2004). "Neutron Scattering Determination of the Li^+ Environment in an Aqueous Poly(ethylene Oxide) Solution." J. Phys. Chem. B **108**(8): 2554. GLAD

D. N. Argyriou, J. W. Lynn, R. Osborn, B. Campbell, J. F. Mitchell, U. Ruett, H. N. Bordallo, A. Wildes and C. D. Ling (2002). "Glass Transition in the Polaron Dynamics of Colossal Magnetoresistive Manganites." Phys Rev. Lett. **890**(3): 6401-6401. LRMECS

M. C. Aronson, R. Osborn, R. Chau, M. B. Maple, B. D. Rainford and A. P. Murani (2001). "Magnetic Correlations and the Quantum Critical Point of $UCu_{5-x}Pd_x$, $x=1, 1.5$." Phys Rev. Lett. **8719**(19): 197205-+. LRMECS

R. Aryaeinejad, E. L. Reber, J. K. Jewell, J. D. Cole and M. W. Drigert (2005). "Fission Process and its Application in Fissile Material Identification." Journal of Radioanalytical and Nuclear Chemistry **264**(1): 155-162. INEEL

B. J. Ash, R. W. Siegel and L. S. Schadler (2004). "Mechanical Behavior of Alumina/Poly(methyl methacrylate) Nanocomposites." Macromolecules **37**(4): 1358-1369. SAND

B. Ashok, L. Arleth, R. P. Hjelm, I. Rubinstein and H. Önyüksel (2004). "*In vitro* Characterization of PEGylated Phospholipid Micelles for Improved Drug Solubilization: Effects of PEG Chain Length and PC Incorporation." J. Pharmaceutical Sciences **93**(10): 2476-2487. SAND

M. Avdeev, M. K. Haas, J. D. Jorgensen and R. J. Cava (2002). "Static Disorder from Lone-Pair Electrons in $Bi_{2-x}M_xRu_2O_{7-y}$ ($M=Cu, Co$; $x=0.04$) Pyrochlores." J. Solid State Chem. **169**(1): 24-34. SEPD

M. Avdeev, J. D. Jorgensen, R. A. Ribeiro, S. L. Bud'ko and P. C. Canfield (2003). "Crystal Chemistry of Carbon-Substituted MgB₂." Physica C **387**(3-4): 301-306. SEPD

A. M. Awasthi and S. Sampath (2002). "Thermo-Kinetic Anomalies across Rigidity Threshold in Ge_xSe_{1-x}." Materials Transactions **43**(8): 2046-2049. GLAD

Y. S. Badyal, D. L. Price, M.-L. Saboungi, D. R. Haeffner and S. D. Shastri (2002). "Quantum Effects on the Structure of Water at Constant Temperature and Constant Atomic Density." J. Am. Chem. Phys. **116**(24): 10833-10837. GLAD

Y. S. Badyal, J. M. Simonson, B. Annis and M. D. Londono (2002). "The Hydration Structure of Ni²⁺ in Aqueous Solution by Neutron Diffraction Isotope Substitution: A Case Study on the Effects of Systematic Error." J. Neutron Research **10**(1): 19-29. GLAD

Y. S. Badyal and J. M. Simonson (2003). "The Effects of Temperature on the Hydration Structure around Ni₂₊ in Concentrated Aqueous Solution." J. Chem. Phys. **119**(8): 4413-4418. GLAD

I. Baek, E. B. Iverson and J. M. Carpenter (2001). MCNP Simulations of a Disk Chopper on a Pulsed Neutron Source. ICANS-XV. FACILITY

I. Baek, J. M. Carpenter and E. Iverson (2002). "The Upgrade of Intense Pulsed Neutron Source (IPNS) Through the Change of Coolant and Reflector." Nuclear Instrument and Methods in Physics Research **490**(3): 522-526. FACILITY

I. Baek, E. B. Iverson and J. M. Carpenter (2002). "The Monte Carlo Simulation of Neutron and Scattered by Disk Choppers of Various Composition." Nucl. Instruments and Methods in Phys. Res. A **481**(1-3): 145-153. FACILITY

I. Baek, E. B. Iverson and J. M. Carpenter (2002). "The Monte Carlo Simulation of Neutron Transmitted and Scattered by Disk Choppers of Various Compositions." Nucl. Instruments and Methods in Phys. Res. A **487**(1-3): 422-430. FACILITY

R. Bansil, H. Nie, Y. Li, G. Liao, K. Ludwig, M. Steinhart, C. Konak and J. Lal Structure and Ordering Kinetics of Micelles in Triblock Copolymer Solutions in Selective Solvents. Macromolecular Symposia Proc. 20 Discussion Conf. hosted by Int. Union of Pure and Applied Chemistry, Czech Chemical Society, Prague (2001). SASI

R. Bansil, H. Nie, C. Konak, M. Helmstedt and J. Lal (2002). "Structure and Dynamics of Solutions of a Polystyrene-Polybutadiene Pentablock Copolymer in a Styrene-Selective Solvent." J. of Polymer Sci: Part B Polymer Physics **40**(24): 2807-2816. SASI

R. Bansil, H. Nie, Y. Li, G. Liao, K. Ludwig, M. Steinhart, C. Konak and J. Lal (2002). "Structure and Ordering Kinetics of Micelles in Triblock Copolymer Solutions in Selective Solvents." Macromolecular Symposia **90**: 161-170. SASI

P. S. Barbeau, J. I. Collar, J. Miyamoto and I. Shipsey (2003). "Toward Coherent Neutrino Detection Using Low-

Background Micropattern Gas Detectors." IEEE Transactions on Nuclear Science **50**(5): 1285-1289. GPPD

P. J. Barclay, T. Griffiths, J. McKirdy, J. Kennedy, R. Cooper, N. W. Paton and P. Gray (2003). "Teallach - A Flexible User-Interface Development Environment for Object Database Applications." J. Visual Languages and Computing **14**(1): 47-77. SOFTWARE

P. W. Barnes, M. Avdeev, J. D. Jorgensen, D. G. Hinks, H. Clause and S. Short (2005). "Superconductivity and Cobalt Oxidation State in Metastable $\text{Na}_x\text{CoO}_2 \cdot y\text{H}_2\text{O}$ (x approximate to 1/3; y approximate to 4x)." Phys Rev. B **72**(13): 134515. SEPD

E. D. Bauer, A. D. Christianson, J. M. Lawrence, E. A. Goremychkin, N. O. Moreno, N. J. Curro, F. R. Trouw, J. L. Sarrao, J. D. Thompson, R. J. McQueeney, W. Bao and R. Osborn (2004). "Crystalline Electric Field Excitations in the Heavy Fermion Superconductor CeCoIn_5 ." J. Appl. Phys. **95**(11 pt 2): 7201-7203. LRMECS

J. A. Belot, J. Clark, J. A. Cowan, G. S. Harbison, A. I. Kolesnikov, Y.-S. Kye, A. J. Schultz, C. Silvernail and X. Zhao (2004). "The Shortest Symmetrical O-H...O Hydrogen Bond has a Low-Barrier Double-well Potential." J. Phys. Chem. B **108**(22): 6922-6926. HRMECS, SCD

D. D. Bendejacq, V. Ponsinet and M. Joanicot (2005). "Chemically Tuned Amphiphilic Diblock Copolymers Dispersed in Water: From Colloids to Soluble Macromolecules." Langmuir **21**(5): 1712-1718. SASI

C. J. Benmore, B. Tomberli, P. A. Egelstaff and J. Neuefeind (2001). "Quantum Effects in the Structure of Liquid Benzene at Room Temperature." Molecular Physics **99**(10): 787-794. GLAD

C. J. Benmore, B. Tomberli, J. Neuefeind and P. A. Egelstaff (2002). Isotopic Quantum Correction to Liquid Methanol at -30°C. ICNS 2001, Appl. Phys. A. GLAD

C. J. Benmore, J. K. R. Weber, S. Sampath, J. Siewenie, J. Urquidi and J. A. Tangeman (2003). "A Neutron and X-Ray Diffraction Study of Calcium Aluminate Glasses." J. Phys. Cond. Matt. **15**(31): S2413-S2423. GLAD

C. J. Benmore, J. K. R. Weber, J. Siewenie and K. J. Hiera (2003). "Structure of Neodymium-doped Aluminate and Silica Glasses." Appl. Phys. Lett. **24**: 4954-4956. GLAD

C. Benmore and J. Siewenie (2004). "Polyamorphism and Extreme Environments on GLAD." Neutron News **15**(3): 16-19. GLAD

C. J. Benmore, R. T. Hart, Q. Mei, D. L. Price, J. Yarger, C. A. Tulk and D. D. Klug (2005). "Intermediate Range Ordering in Amorphous and Liquid Water, Si and Ge." Phys Rev. B **72**(13): 132201. GLAD

A. Bentien, B. B. Iversen, J. D. Bryan, G. D. Stucky, A. E. C. Palmqvist, A. J. Schultz and R. W. Henning (2002). "Maximum Entropy Method Analysis of Thermal Motion and Disorder in Thermoelectric Clathrate $\text{Ba}_8\text{Ga}_{16}\text{Si}_{30}$." J. Appl. Phys. **91**(9): 5694-5699. SCD

I. Bernal, M. T. Gonzalez, J. Cetrullo and J. Cai (2001). "Why Are Hexol Clusters so Easily Resolved into Their Antipodes? Part 2. Preparation, Crystal Structural Studies and the Nine Sources of Chirality of Hexol Clusters." Structural Chemistry **12**: 73. SCD

I. Bernal, D. S. Yufit and J. A. K. Howard (2001). "The Structure of $\text{Co}(\text{NH}_3)_6\text{CuCl}_5$ at 10K." Z. Kristallogr. **216**: 413. SCD

S. R. Bhatia, M. Crichton, A. Mourchia, R. K. Prud'homme and J. Lal (2001). "Tuning Interactions Between Novel Polyelectrolyte Micelles." Polymer Preprints **42**(2): 326-327. SASI

L. J. Bie, J. H. Lin, Y. X. Wang and C.-K. Loong (2002). "n=2 Member of the Hexagonal Perovskite-intergrowth Manganate Family $\text{A}_{n+1}\text{Mn}_n\text{O}_{3n+3}$ (Ca_2O)." Inorg. Chem. Comm. **5**(11): 966-970. GPPD

L. J. Bie, Y. X. Wang, J. H. Lin, C. K. Loong, J. W. Richardson, Jr., L. P. You and C. Dong (2003). "Synthesis and Structure of n=5 Member of the $\text{A}_{n+1}\text{Mn}_n\text{O}_{3n+3}$ (A_2O)." Chem. Mat. **15**(2): 516-522. GPPD

M. Bieringer and J. E. Greedan (2002). "Structure and Magnetism in $\text{BaLaMnO}_{4+1-\delta}$ ($\delta = 0.00, 0.10$) and $\text{Ba}_x\text{Sr}_{1-x}\text{LaMnO}_4$. Disappearance of Magnetic Order for $x > 0.30$." J. Mater. Chem. **12**(2): 279-287. SEPD

S. J. L. Billinge Strain Nano-phase Separation Multi-scale Structures and Function of Advanced Materials. Intrinsic Multiscale Structure and Dynamics of Complex Electronic Oxides, eds. S. Shenoy and A. R.

Bishop, (World Scientific, Singapore, 2003): 25-40. SEPD

S. J. L. Billinge, M. Gutmann and E. S. Bozin (2003). "Structural Response to Local Charge Order in Underdoped but Superconducting $\text{La}_{2-x}(\text{SrBa})_x\text{CuO}_4$." Int. J. Mod. Phys. B **17**(18-20): 3640-3647. SEPD

M. Bleuel, M. Broll, E. Lang, K. Littrell, R. Gahler and J. Lal (2005). First tests of RF-flippers for a Neutron Resonance Spin Echo (NRSE) Instrument on a Pulsed Source. Proc. ICANS-XVII 2005, Santa Fe, NM. POSYI

M. Bleuel, K. Littrell, R. Gahler and J. Lal (2005). "MISANS, A Method for Quasi-Elastic Small Angle Neutron Scattering Experiments." Physica B **356**: 213-217. SASI

M. Bleuel, L. B. Lurio, K. Littrell, R. Gahler and J. Lal (2005). "Complementarity of MIEZE-SANS and X-Ray Photon Correlation Spectroscopy (XPCS)." Physica B **356**: 223-228. SASI

P. Blomqvist, R. Wappling, A. Broddefalk, P. Nordblad, S. G. E. teVelthuis and G. P. Felcher (2002). "Structural and Magnetic Properties of bcc Fe/Co (001) Superlattices." J. Magn. Magn. Mater. **248**(1): 75-84. POSYI

P. Blomqvist, M. Kannan, S. Krishnana, S. Srinath and S. G. E. teVelthuis (2004). "Magnetization Processes in Exchange-Biased MnPd/Fe Bilayers Studied by Polarized Neutron Reflectivity." J. of Applied Physics **96**: 6523-6526. POSYI

S. Bobev and K. T. Tait (2004). "Methanol-inhibitor or Promoter of the

Formation of Gas Hydrates from Deuterated Ice?" Amer. Mineralogist **89**(8-9): 1208-1214. HIPD

P. D. Bogdanoff, T. L. Swan-Wood and B. Fultz (2003). "Phonon Entropy of Alloying and Ordering of Cu-Au." Phys Rev. B **68**: 014301-014307. LRMECS

C. H. Booth, J. L. Sarrao, M. F. Hundley, A. L. Cornelius, G. H. Kwei, A. Bianchi, Z. Fisk and J. M. Lawrence (2001). "Local and Average Crystal Structure and Displacements of La^{11}B_6 and EuB_6 as a Function of Temperature." Phys. Rev. B **63**: 224302. GPPD

H. N. Bordallo, L. C. Chapon, J. C. Cook, J. R. D. Copley, E. Goremychkin, S. Kern, S.-H. Lee, T. Yildirim and J. L. Manson (2002). Spin Excitations in 3D Molecular Magnets Probed by Neutron Scattering. ICNS 2001. LRMECS

H. N. Bordallo, L. Chapon, J. L. Manson, C. D. Ling, J. S. Qualls, D. Hall and D. N. Argyriou (2003). "Structural and Magnetic Behavior of a Quasi-1D Antiferromagnetic Chain Compound $\text{Cu}(\text{NCS})_2(\text{Pyz})$." Polyhedron **22**: 2045-2049. SEPD

H. N. Bordallo, L. Chapon, J. L. Manson, J. Hernandez-Velasco, D. Ravot, W. M. Reiff and D. N. Argyriou (2004). "S = 1/2 Ising Behavior in the 2D Molecular Magnet $\text{Fe}(\text{NCS})_2(\text{pyrazine})_2$." Phys Rev. B **69**: 224405-1 - 224405-9. QENS

H. N. Bordallo, K. W. Herwig, B. M. Luther and N. E. Levinger (2004). "Dynamics in DMSO/Water Mixtures by Quasielastic Neutron Scattering." J. Chem. Phys. **121**(24): 12457-12464. QENS

M. Borkowski, R. Chiarizia, M. P. Jensen, J. R. Ferraro, P. Thiyagarajan and K. C. Littrell (2003). "SANS Study of Third Phase Formation in the $\text{Th}(\text{iv})\text{HNO}_3/\text{TBP}-n\text{-Octane}$ System." Separation Sci. Technol. **38**(12-13): 3333-3351. SAND

A. Botti, W. Pyckhout-Hintzen, D. Richter, V. Urban, E. Straube and J. Kohlbrecher (2004). "Silica Filled Elastomers: Polymer Chain and Filler Characterization in the Undeformed State by a SANS-SAXS Approach." Polymer **44**: 7505-7512. SAND

F. Bouquet, R. A. Fisher, N. E. Phillips, D. G. Hinks and J. D. Jorgensen (2001). "Specific Heat of (MgB_2) -B11: Evidence for a Second Energy Cap." Phys. Rev. Lett. **87**04(4): 7001-+. SEPD

F. Bouquet, Y. Wang, R. A. Fisher, D. G. Hinks, J. D. Jorgensen, A. Junod and N. E. Phillips (2001). "Phenomenological Two-gas Model for the Specific Heat of MgB_2 ." Euro. Phys. Lett. **56**(6): 856-862. SEPD

E. S. Božin, V. Petkov, P. W. Barnes, P. M. Woodward, T. Vogt, S. D. Mahanti and S. J. L. Billinge (2004). "Temperature Dependent Total Scattering Structural Study of $\text{CaCu}_3\text{Ti}_4\text{O}_{12}$." J. Phys. Cond. Matt. **16**: S5091-S5102. SEPD

E. S. Božin, V. Petkov, P. W. Barnes, P. M. Woodward, T. Vogt, S. D. Mahanti and S. J. L. Billinge (2004). "Total Scattering Local Structural Study of $\text{CaCu}_3\text{Ti}_4\text{Ti}_4\text{O}_{12}$." J. Phys. Cond. Matt. **16**(44): S5091-S5102. SEPD

A. Bracchi, K. Samwer, J. Almer, P. Thiyagarajan and S. Schneider (2004).

"Separation of Grain Growth and Glass Transition During Structural Evolution of the Bulk Nd₆₀Fe₃₀Al₁₀ Alloy." Phys Rev. B **70**(17): 172105. SAND

A. Bracchi, S. Schneider, P. Thiyagarajan and K. Samwer (2004). Cooling Rate Dependent Microstructure and Magnetic Properties of the Glass Forming Alloy Nd₆₀Fe₃₀Al₁₀. ICM 2004. SAND

J. C. Burley, J. F. Mitchell, S. Short, D. Miller and Y. Tang (2003). "Structural and Magnetic Chemistry of NdBaCo₂O_{5+δ}." J. Solid State Chem. **170**: 339-350. SEPD

J. C. Burley, J. F. Mitchell and S. Short (2004). "Competing Electronic Ground States in La_{1-x}Ca_xCoO₃." Phys Rev. B **69**(5): 054401-1 - 054401-5. SEPD

E. Bychkov, D. L. Price and A. Lapp (2001). "Universal Trend of the Haven Ratio in Glasses: Origin and Structural Evidences from Neutron Diffraction and Small-Angle Neutron Scattering." J. Non-Crystall. Solids **293-295**: 211-219. GLAD

E. Bychkov, M. Fourmentin, M. Miloshova, C. J. Benmore and J. Neufeind (2002). Overconstrained CsCl-Ga₂S₃ Glasses. APS Activity Report 2002 03/21. GLAD

E. Bychkov, D. L. Price, C. J. Benmore and A. C. Hannon (2002). "Ion Transport Regimes in Chalcogenide Glasses: From the Host to the Cation-related Network Connectivity." Solid State Ionics **154-155**(B): 349-359. GLAD

E. Bychkov, M. Fourmentin, M. Miloshova, D. L. Price, C. J. Benmore

and A. Lorriaux (2003). New Structural Features and Trends in the Short-, Intermediate- and Mesoscopic Range Order in Binary Chalcogenide Glasses. Proc. XIIIth Int. Symp on Non-Oxide Glasses, Pardubice, Czech Republic. GLAD

E. Bychkov, C. J. Benmore and D. L. Price (2005). "Compositional Changes of the First Sharp Diffraction Peak in Binary Selenide Glasses." Phys Rev. B **72**(17): 172107-172111. GLAD

C. Cabrillo, M. A. Gonzalez, G. J. Ceullo, F. J. Bermejo, M.-L. Saboungi and D. L. Price (2004). "Microscopic Origin of the Non-Gaussian Behavior of Dynamic Structure Factors of Glassy Matter." Phys Rev. B **69**13(13): 4202-4202. QENS

A. Cady, D. Haskel, J. C. Lang, G. Srajer, P. Chupas, R. Osborn, J. F. Mitchell, N. Hur, S. Park and S. W. Cheong (2005). "Scanning Low-temperature Element-specific Magnetic Microscopy." Rev. Sci. Instr. **76**(6): 63702-63702. LRMECS

J. Cai, X. Hu, X. Feng, L. Ji and I. Bernal (2001). "Structures of Three cis-β2 Isomers of [Co(trien)aminoacido]²⁺ Complexes." Acta Cryst. **57**: 45. SCD

H. Cai, T. Chen, X. Wang, A. J. Schultz, T. F. Koetzle and Z. Xue (2002). "Direct Observation of η²-Imine Formation through β-H Abstraction Between Amide Ligands. Neutron and X-ray Diffraction Structure of a Dihydride Imine Ditantalum Complex." Chem. Commun. **3**: 230-231. SCD

O. Cambon and J. Haines (2003). "Structure-piezoelectric Property

Relationships in α -quartz Isotypes: Design and Characterization of High Performance Piezoelectric Materials." IEEE **7803**(7688): 650-653. SEPD

B. J. Campbell, R. Osborn, D. N. Argyriou, L. Vasiliu-Doloc, J. F. Mitchell, S. K. Sinha, U. Ruett, C. D. Ling, Z. Islam and J. W. Lynn (2002). "Structure of Nanoscale Polaron Correlations in $\text{La}_{1.2}\text{Sr}_{1.8}\text{Mn}_2\text{O}_7$." Phys. Rev. B **6501**(1): 4427-. LRMECS

B. J. Campbell, S. K. Sinha, R. Osborn, S. Rosenkranz, J. F. Mitchell, D. N. Argyriou, L. Vasiliu-Doloc, O. H. Seeck and J. W. Lynn (2003). "Polaronic Zorbital Polarization in a Layered Colossal Magnetoresistive Manganite." Phys. Rev. B **6702**(2): 409-409. LRMECS

B. J. Campbell, D. N. Argyriou, J. F. Mitchell, R. Osborn, B. Ouladdiaf and C. D. Ling (2004). "Enhanced Stability of Charge and Orbital Order in $\text{La}_{0.78}\text{Sr}_{2.22}\text{Mn}_2\text{O}_7$." Phys Rev. B **69**(10): 104403-1 - 104403-6. SEPD

J. M. Carpenter, K. C. Littrell, D. L. Abernathy and E. B. Iverson (2001). "Electronic Time-Focusing of Pulsed-Source Neutron Chopper Data: Binning to Minimize Effects of Proton Pulse and Chopper Opening Time Variations." Nuclear Instruments and Methods in Physics Research A **459**: 221-228. FACILITY

J. M. Carpenter (2002). A Long-Wavelength Target Station for the Spallation Neutron Source. ANS Winter Meeting. FACILITY

J. M. Carpenter (2002). "Time Focusing of Pulsed-Source Crystal Analyzer

Spectrometers. Part I: General Analysis." Nucl. Instruments and Methods in Phys. Res. A **483**(3): 774-783. FACILITY

J. M. Carpenter (2002). "Time Focusing of Pulsed-Source Crystal Analyzer Spectrometers. Part II: Practical Expressions." Nucl. Instrum. & Meth. **A483**(3): 784-806. FACILITY

J. M. Carpenter, B. Micklich and J.-M. Zanotti (2002). Neutron Scattering Measurements from Cryogenic Ammonia: A Progress Report. Proc. 6th Mtg. Collaboration on Advanced Cold Moderators. FACILITY

J. M. Carpenter, M. Agamalian, K. C. Littrell, P. Thiyagarajan and C. Rehm (2003). "Time-of-Flight Implementation of an Ultra-Small-Angle Neutron Scattering Instrument." J. Appl. Crystallog. **36**(Pt 3 (1)): 763-768. SAND

J. M. Carpenter, E. B. Iverson and K. C. Littrell (2003). "Prospects for Solid Ammonia as a Cold Moderator." J. Neutron Research **11**(1-2): 41-49. FACILITY

J. M. Carpenter (2004). Experience with Spallation Neutron Sources. Proc. American Nuclear Society Accelerator Applications Division, Accelerator Applications in a Nuclear Renaissance. FACILITY

J. M. Carpenter and T. E. Mason (2005). "A Long-Wavelength Target Station for the Spallation Neutron Source." Nucl. Ins. Meth. Phys. Res. A **545**(1-2): 1-19. FACILITY

J. M. Carpenter and G. Zsigmond (2005). "Time-Focused Crystal Analyzer

Spectrometer." Phys. Chem. Chem. Phys. **7**: 1250-1254. FACILITY

G. Caruntu, T. A. Kodenkandath and J. B. Wiley (2002). "Neutron Diffraction Study of the Oxychloride Layered Perovskite, (Cu,CI)LaNb₂O₇." Mater. Res. Bulletin **37**: 593-598. SEPD

E. N. Caspi, J. D. Jorgensen, M. V. Lobanov and M. Greenblatt (2003). "Structural Disorder and Magnetic Frustration in ALaMnMoO₆ (A=Ba, Sr) Double Perovskites." Phys Rev. B **67**(13): 4431-4431. SEPD

E. N. Caspi, M. Avdeev, S. Short, J. D. Jorgensen, B. Dabrowski, O. Chmaissem, J. Mais and S. Kolesnik (2004). "Synthesis, Structure, and Properties of Randomly Mixed and Layer-Ordered SrMn_{1-x}GaO_{3-δ} Perovskites." J. Solid State Chem. **177**(4-5): 1456-1470. SEPD

E. N. Caspi, M. Avdeev, S. Short, J. D. Jorgensen, M. V. Lobanov, Z. T. Zeng, M. Greenblatt, P. Thiyagarajan, C. E. Botez and P. W. Stephens (2004). "Structural and Magnetic Phase Diagram of the Two-Electron-Doped (Ca_{1-x}Ce_x)MnO₃ System: Effects of Competition Among Charge, Orbital, and Spin Ordering." Phys Rev. B **69**10(10): 4402-4402. SAND, SEPD

E. N. Caspi, M. Dubman, H. Etedgui, H. Shaked, S. Short and J. D. Jorgensen (2005). Magnetic and Crystallographic Properties of HoCo₃B₂. Strongly Correlated Electron Systems 2004. SEPD

Y. Chai, D. Vicic and M. C. McIntosh (2003). "A Cycloaldol Approach to the

Isobenzofuran Core of the Eunicellin Diterpenes." Org. Lett.: 1039-1042.

K. Chari, J. Kowalczyk and J. Lal (2004). "Conformation of Poly(ethylene oxide) in Polymer-Surfactant Aggregates." J. Phys. Chem. B **108**(9): 2857-2861. SASI

S. Chang, M. H. Jung, H. Nakotte, E. Bruck, J. C. P. Klaasse, M. Mihalik, A. H. Lacerda, K. Prokes, M. S. Torikachvili and A. J. Schultz (2001). "Electronic Properties of UIrGe in High Magnetic Fields." J. Appl. Phys. **89**(11; pt. 2): 7186-7188. SCD

A. Chatterjee, D. Mikkelson, R. Mikkelson, J. Hammonds and T. Worlton (2002). "Remote Access and Display of Neutron Data." Appl. Phys. A **74**: 194-197. SOFTWARE

G. S. Chauhan, L. K. Guleria and S. Mahajan (2001). "A Study in Sorption of Some Metal Ions on Novel Hydrogels Based on Modified Cellulosics and 2-acrylamido-2-methyl Propane Sulphonic Acid." Desalination **141**(3): 325-329.

S.-H. Chen, F. Mallamace, A. Faraone, P. Gambadauro, D. Lombardo and W. R. Chen (2002). "Observation of Re-entrant Kinetic Glass Transition in a Micellar System with Attractive Interaction." Eur. Phys. J. **E9**: 283-286. SAND

S.-H. Chen, W.-R. Chen and F. Mallamace (2003). "The Glass-to-Glass Transition and Its Point in a Copolymer Micellar System." Science **300**: 619-622. SAND

S.-H. Chen, W.-R. Chen and F. Mallamace (2003). "Observation of

Liquid-to-Glass and Glass-to-Glass Transitions in L64/D₂O Triblock Copolymer Micellar System." Molecular Simulation **29**(10-11): 611-618. SAND

S.-H Chen, W. R. Chen, F. Mallamace, M. Broccio and E. Fratini Kinetic Glass Transition in a Copolymer Micellar System with Temperature-Dependent Short-Range Attractive Interaction. Self-Assembly, ed. B. H. Robinson, IOS Press (2003): 269-283. SAND

W. C. Chen, C. Bailey, J. A. Borchers, R. F. C. Farrow, T. R. Gentile, D. Hussey, C. F. Majkrzak, K. V. O'Donovan, N. Remmes, W. M. Snow and A. K. Thompson (2003). "Polarized He-3 Analyzers for Neutron Reflectometry." Physica B **335**(1-4): 196-200. POSYI

W.-R. Chen, S.-H. Chen and F. Mallamace (2002). "Small-Angle Neutron Scattering Study of the Temperature-Dependent Attractive Interaction In Dense L64 Copolymer Micellar Solutions and Its Relation to Kinetic Glass Transition." Phys. Rev. E **66**: 021403-12. SAND

W.-R. Chen, R. Mallamace, C. J. Glinka and S.-H. Chen (2003). "Small-Angle Neutron And Dynamic Light Scattering Studies Of The Liquid-To-Glass And Glass-To-Glass Transitions In Dense L64 Copolymer Micellar Solutions." Phys. Rev. E **E68**: 011402-1-15. SAND

W.-R. Chen, Y. Liu, F. Mallamace, P. Thiyagarajan and S.-H. Chen (2004). "Pressure-Induced Cluster Formation and the Ergodic-to-Non-Ergodic Transitions in Dense Triblock Copolymer Micellar Solutions." J. Phys. Cond. Matt. **16**: S4951-S4974. SAND

W.-R. Chen, Y. Liu, F. Mallamace, P. Thiyagarajan and S.-H. Chen (2004). "Studies of Structural Arrest Transition in L64/D₂O Micellar Solutions." J. Phys.: Condensed Matter **16**(42): S4951-S4974. SAND

B. Cherry, J. W. Zwanziger and B. G. Aitken (2002). "The Structure of GeS₂-P₂S₅ Glasses." J. Phys. Chem. **106**: 11093-11101. GLAD

B. Cherry, J. W. Zwanziger and B. G. Aitken (2004). "Structure and properties of Ge_{2.5}PS_x glasses." Non-Cryst. Solids **333**: 28-36. GLAD

R. Chiarizia, A. W. Herlinger, D. R. McAlister, R. E. Barrans and J. R. Ferraro (2001). "Aggregation of Dialkyl-Substituted Diphosphonic Acids and its Effect on Metal Ion Extraction." Separation Sci. Technol. **36**(5-6): 687-708. SAND

R. Chiarizia, M. P. Jensen, M. Borkowski, J. R. Ferraro, P. Thiyagarajan and K. C. Littrell (2003). "SANS Study of Third Phase Formation in the U(VI)-HNO₃/TBP-*n*-Dodecane System." Separation Sci. Technol. **38**(12-13): 3313-3331. SAND

R. Chiarizia, M. P. Jensen, M. Borkowski, J. R. Ferraro, P. Thiyagarajan and K. C. Littrell (2003). "Third Phase Formation Revisited: The U(VI), HNO₃ - TBP, *n*-Dodecane System." Solvent Extr. Ion Exch. **21**(1): 1-27. SAND

R. Chiarizia, K. L. Nash, M. P. Jensen, P. Thiyagarajan and K. C. Littrell (2003). "Application of the Baxter Model for Hard Spheres with Surface Adhesion to

SANS Data for the U(VI)-HNO₃, TBP-*n*-Dodecane System." Langmuir **19**(23): 9592-9599. SAND

R. Chiarizia, M. P. Jensen, M. Borkowski, P. Thiyagarajan and K. C. Littrell (2004). "Interpretation of Third Phase Formation in the Th(IV)-HNO₃, TBP-*n*-octane System with Baxter's "Sticky Spheres" Model." Solvent Extr. Ion Exch. **22**(3): 325-351. SAND

R. Chiarizia, M. P. Jensen, Z. Kolarik, M. Borkowski and P. Thiyagarajan (2004). "Extraction of Zirconium Nitrite by TBP In *n*-octane: Third Phase Formation According to the "Sicky Spheres" Model." Langmuir **20**(25): 10798-10808. SAND

R. Chiarizia, M. P. Jensen, M. Borkowski and K. L. Nash (2005). A New Interpretation of Third Phase Formation in the Solvent Extraction of Actinides by TBP. Proc. Separations for the Nuclear Fuel Cycle in the 21st Century, Washington, D.C., American Chemical Society. SAND

O. Chmaissem, B. Dabrowski, S. Kolesnik, J. Mais, D. E. Brown, R. Kruk, P. Prior, B. Pyles and J. D. Jorgensen (2001). "Relationship Between Structural Parameters and Neel Temperature in Sr_{1-x}Ca_xMnO₃ (0 ≤ x ≤ 1) and Sr_{1-y}Ba_yMnO₃ (y ≤ 0.2)." Phys. Rev. B **64**(13): 134412-+. SEPD

O. Chmaissem, Y. Eckstein and C. G. Kuper (2001). "Structure and a Bond-Valence-Sum Study of the 1-2-3 Superconductors (Ca_xLa_{1-x})(Ba_{1.75}La_{0.25+x})Cu₃O_y and YBa₂Cu₃O_y." Phys. Rev. B **63**: 4510. SEPD

O. Chmaissem, B. Dabrowski, S. Kolesnik, J. Mais, J. D. Jorgensen and S. Short (2003). "Structural and Magnetic Phase Diagrams of La_{1-x}Sr_xMnO₃ and Pr_{1-y}Sr_yMnO₃." Phys. Rev. B **67**09(9): 094431-1- 094431-13. SEPD

O. Chmaissem, B. Dabrowski, S. Kolesnik, J. Mais, J. D. Jorgensen, S. Short, C. E. Botez and P. W. Stephens (2005). "Effects of A-site Ordering on the Structures and Properties of La_{1-x}Ba_xMnO₃ (x similar to 0.5)." Phys Rev. B **72**(10): 104426. SEPD

O. Chmaissem, B. Dabrowski, S. Kolesnik, S. Short and J. D. Jorgensen (2005). "Nuclear and Magnetic Structural Properties of Ba₂FeMoO₆." Phys Rev. B **71**17(17): 4421-4421. SEPD

A. D. Christianson, J. M. Lawrence, P. G. Pagliuso, J. L. Sarrao, J. D. Thompson, P. S. Riseborough, S. Kern, E. A. Goremychkin and A. H. Lacerda (2002). "Neutron Scattering Study of Crystal Fields in CeRhIn₅." Phys. Rev. B **66**: 193102. LRMECS

A. D. Christianson, E. D. Bauer, J. M. Lawrence, P. S. Riseborough, N. O. Moreno, P. G. Pagliuso, J. L. Sarrao, J. D. Thompson, E. A. Goremychkin, F. R. Trouw, M. P. Hehlen and R. J. McQueeney (2004). "Crystalline Electric Field Effects in CeMIn₅ (M=Co, Rh, Ir): Superconductivity and the Influence of Kondo Spin Fluctuations." Phys Rev. B **70**(13): 4505-4505. LRMECS

A. D. Christianson, J. M. Lawrence, N. O. Moreno, E. D. Bauer, E. A. Goremychkin, C. H. Booth, J. L. Sarro, J. D. Thompson, A. Lobos, A. A. Aligia, C. D. Batista, F. R. Trouw and M. P.

Helen (2005). "Anisotropic Behavior in Intermediate Valence Yb₂M₃Ga₉ (M = Rh, Ir)." Phys Rev. B **72**(8): 1102. LRMECS

A. D. Christianson, J. M. Lawrence, P. S. Riseborough, N. O. Moreno, P. G. Pagliuso, E. D. Bauer, J. L. Sarro, W. Bao, E. A. Goremychkin, S. Kern, F. R. Trouw and M. P. Hehlen (2005). "Crystal Field Effects in CeIrIn₅." J. Neutron Research **13**: 179. LRMECS

M. A. Crichton and S. R. Bhatia (2004). "SANS Study of Poly(styrene)-poly(acrylic acid/ethyl acrylate) Copolymers: Effect of Degree of Hydrolysis of the P(AA/EA) Block." J. Appl. Polymer Science **93**(2): 490-497. SASI

J. K. Christie, M. Guthrie, C. A. Tulk, C. J. Benmore, D. D. Klug, S. N. Taraskin and S. R. Elliott (2005). "Modeling the Atomic Structure of Very High-Density Amorphous Ice." Phys Rev. B **72**(1): 012201. GLAD

H. Chun and I. Bernal (2001). "Conformational Isomers of Neutral Transdinitrocobalt (III) Complexes." Acta Cryst. **57**: 33. SCD

H. Chun and I. Bernal (2001). "Polymorphism in the Crystallization Behavior of Trinitrocobalt Complexes with Tridentate Amine Ligands: Hydrogen Bonding and Syntheses of Racemic and Conglomerate mer-Co(dpt)(NO₂)₃." Crystal Growth and Design **1**: 67. SCD

H. Chun and I. Bernal (2001). "Crystal Structures of Neutral Co(III) Complexes: Common Hydrogen Bonding Patterns Observed in Compounds of Different

Molecular Structures." Crystal Growth and Design **1**: 143. SCD

H. Chun, E. M. Maes, I. Bernal and R. S. Czernuszewics (2001). "Syntheses, Structures and Spectroscopic Characterization of fac- and mer-Co(aepn)(CN)₃ and of Their ¹³CN Analogues [aepn = N-(2-aminoethyl)-1,3-Propanediamine]." Polyhedron **20**: 2597. SCD

R. W. Connatser, H. Belch, L. Jirik, D. J. Leach, F. R. Trouw, J.-M. Zanolli, Y. Ren, R. K. Crawford, J. M. Carpenter, D. L. Price, C.-K. Loong, J. P. Hodges and K. W. Herwig (2003). The QuasiElastic Neutron Spectrometer (QENS) of IPNS: Recent Upgrade and Performance. Proc. ICANS-XVI, Germany. QENS

F. A. Cotton, L. M. Daniels, C. Y. Liu, C. A. Murillo, A. J. Schultz and X. Wang (2002). "How to Make a Major Shift in a Redox Potential: Ligand Control of the Oxidation State of Dimolybdenum Units." Inorg. Chem. **41**(16): 4232-4238. SCD

M. A. Crichton and S. R. Bhatia (2003). "Structure and Intermicellar Interactions in Block, Polyelectrolyte Assemblies." J. Appl. Crystallog. **36**: 652-655. SASI

B. Dabrowski, O. Chmaissem, J. Mais, S. Kolesnik, J. D. Jorgensen and S. Short (2002). Increase of Magnetic Transition Temperatures by Reduction of Local Disorder for Perovskite Manganites. Proc. MRS Spring Meeting (Materials Research Soc., 2002). SEPD

B. Dabrowski, X. Xiong, O. Chmaissem, Z. Bukowski and J. D. Jorgensen (2002). "Structure-Properties Relationships for Manganese

Perovskites." SMART'99 **60**(10): 7006-7017. SEPD

B. Dabrowski, O. Chmaissem, S. Kolesnik, J. Mais and J. D. Jorgensen (2003). "Correlation of Magnetic Transition Temperatures to Disorder for Atomically Arranged Perovskites." Physica C **387**(1-2): 266-271. SEPD

B. Dabrowski, O. Chmaissem, J. Mais, S. Kolesnik, J. D. Jorgensen and S. Short (2003). "Tolerance Factor Rules for $\text{Sr}_{1-x-y}\text{Ca}_x\text{Ba}_y\text{MnO}_3$ Perovskites." J. Solid State Chem. **170**: 154-164. SEPD

B. Dabrowski, P. W. Klamut, O. Chmaissem, S. Kolesnik, M. Maxwell, J. Mais, C. W. Kimball, J. D. Jorgensen and S. Short (2003). Decrease of Ferromagnetic Transition Temperature in Nonstoichiometric $\text{SrRu}_{1-v}\text{O}_3$ Perovskites. Ruthenate and Rutheno-Cuprate Materials: Unconventional Superconductivity, Magnetism and Quantum Phase Transitions. A. V. C. Noce, M. Cuoco and A. Romano (Springer). **603**: 303-311. SEPD

B. Dabrowski, O. Chmaissem, P. W. Klamut, S. Kolesnik, M. Maxwell, J. Mais, Y. Ito, B. D. Armstrong, J. D. Jorgensen and S. Short (2004). "Reduced Ferromagnetic Transition Temperatures in $\text{SrRu}_{1-v}\text{O}_3$ Perovskites from Ru-site Vacancies." Phys Rev. B **70**(July): 014423-1 - 014423-7. SEPD

B. Dabrowski, M. Avdeev, O. Chmaissem, S. Kolesnik, P. W. Klamut, M. Maxwell and J. D. Jorgensen (2005). "Freezing of Octahedral Tilts below the Curie Temperature in $\text{SrRu}_{1-v}\text{O}_3$ Perovskites." Phys Rev. B **71**: 4411-4411. SEPD

B. Dabrowski, E. N. Caspi, S. Kolesnik, O. Chmaissem, J. Mais and J. D. Jorgensen (2005). "Synthesis, Structure, and Magnetic Properties of $\text{SrMn}_{1-x}\text{Ga}_x\text{O}_{3-\delta}$ ($x = 0-0.5$) Perovskites." J. Solid State Chem. **178**: 3453-3460. SEPD

B. Dabrowski, S. Kolesnik, A. Baszczuk, O. Chmaissem, T. Maxwell and J. Mais (2005). "Structural, Transport, and Magnetic Properties of ($R = \text{La, Pr, Nd, Sm, }^{153}\text{Eu, Dy}$)." J. of Solid State Chem. **178**: 629-637. SEPD

B. Dabrowski, S. Kolesnik, O. Chmaissem, T. Maxwell, M. Avdeev, P. W. Barnes and J. D. Jorgensen (2005). "Increase of Ferromagnetic Ordering Temperature by the Minority-band Double-Exchange Interaction in $\text{SrRu}_{1-x}\text{Cr}_x\text{O}_3$." Phys Rev. B **72**(5): Art. No. 054428. SEPD

S. Deemyad, J. S. Schilling, J. D. Jorgensen and D. G. Hinks (2001). "Dependence of the Superconducting Transition Temperature of MgB_2 on Pressure to 20 GPa." Physica C **361**(4): 227-233. SEPD

S. Deemyad, T. Tomita, J. J. Hamlin, B. R. Beckett, J. S. Schilling, D. G. Hinks, J. D. Jorgensen, S. Lee and S. Tajima (2003). "Dependence of the Superconducting Transition Temperature of Single and Polycrystalline MgB_2 on Hydrostatic Pressure." Physica C **385**(1-2): 105-116. SEPD

O. Delaire, T. Swan-Wood and B. Fultz (2004). "Negative Entropy of Mixing for Vanadium-Platinum Solutions." Phys Rev. Lett. **93**: 185704. LRMECS

J. D. Deloach, C. R. Aita and C.-K. Loong (2002). "Growth-Controlled Cubic Zirconia Microstructure in Zirconia-Titania Nanolaminates." J. Vac. Sci. Technol. **20**(5): 1517-1524. POSYII

P. M. DeLurgio, R. T. Klann, C. L. Fink, D. S. McGregor, P. Thiyagarajan and I. Naday (2003). "A Neutron Detector to Monitor the Intensity of Transmitted Neutrons for Small-Angle Neutron Scattering Instruments." 505 1-2: 46-49. SAND

N. R. deSouza, A. Kolesnikov, C.-K. Loong, A. P. Moravsky, R. O. Loutfy and C. J. Burnham (2004). Structure and Dynamics of Water Adsorbed in Carbon Nanotubes: A Joint Neutron-Scattering and Molecular-Dynamics Study. 2004 MRS Fall Meeting, Boston, MA. QENS, HRMECS

M. D. Determan, J. P. Cox, S. Seifert, P. Thiyagarajan and S. K. Mallapragada (2005). "Synthesis and Characterization of Temperature and pH-responsive Pentablock Copolymers." Polymer **46**(18): 6933-6946. SAND

A. C. Dewitt, K. W. Herwig and S. J. Lombardo (2005). "Adsorption and Diffusion Behavior of Ethane and Ethylene in Sol-Gel Derived Microporous Silica." Adsorption **11**(5-6): 491-499. QENS

A. Diama, L. Criswell, H. Mo, H. Traub, K. W. Herwig, F. Y. Hansen and U. G. Volkmann (2002). Fast Diffusive Motions in Tetracosane Monolayers Adsorbed on Graphite. Proc. March Meeting Am. Phys. Soc., Indianapolis, IN. QENS

W. Dmowski, M. Akbas, T. Egami and P. K. Davies (2001). "Structure Refinement of Large Domain Relaxors in the $\text{Pb}(\text{Mg}_{1/3}\text{Ta}_{2/3})\text{O}_3\text{TlZrO}_3$ System." J. Phys. Chem. Solids **63**: 15. SEPD

W. Dmowski, M. Akbas, T. Egami and P. K. Davies (2002). "Structure Refinement of Large Domain Relaxors in the $\text{Pb}(\text{Mg}_{1/3}\text{Ta}_{2/3})\text{O}_3 - \text{TlZrO}_3$ System." J. Phys. Chem. Solids **63**: 15. SEPD

W. Dmowski and K. E. Swider-Lyons (2004). "PDF Analysis - from Atomic Displacements to Nanocrystals." Z. Kristallogr. **219**(3): 136-142. SEPD, GPPD

L. I. Donley, J. C. Dooling and G. E. McMichael (2003). Using Ferrite as a Fast Switch for Improving Rise Time of IPNS Extraction Kicker. Proc. IEEE PAC 2003 Particle Accelerator Conference, Portland, OR. ACCELERATOR

L. I. Donley, J. C. Dooling, G. E. McMichael and V. F. Stipp (2004). Using a Solid State Switch for a 60KV Bouncer to Control Energy Spread During the Beam Pulse. Proc. 2004 LINAC Conference, Lubeck, Germany. ACCELERATOR

J. C. Dooling, F. R. Brumwell, L. I. Donley, G. E. McMichael and V. F. Stipp (2001). "Beam Transmission and Emittance in the IPNS 50 MeV Linac", ed. Peter Lucas (Fermilab, Batavia, 2001). Proc. 2001 Particle Accelerator Conference. ACCELERATOR

J. C. Dooling, L. I. Donley, G. E. McMichael and V. F. Stipp (2002). Diagnostic and Numerical Studies of the IPNS LINAC with a Recently Installed

Buncher Amplifier. Proc. 2002 LINAC Conference, Gyongju, Korea. ACCELERATOR

J. C. Dooling, G. E. McMichael and F. R. Brumwell (2002). Diagnostic Investigation of Tune and Tune Shift in the IPNS RCS. Proc AIP 20th ICFA Advanced Beam Dynamics Workshop. ACCELERATOR

J. C. Dooling, G. E. McMichael and F. R. Brumwell (2002). Plasma Considerations in the IPNS RCS. Proc. Int. Workshop on Two-Stream Instabilities in Particle Accelerator and Storage Rings. ACCELERATOR

J. C. Dooling, F. R. Brumwell, W. S. Czyz, K. C. Harkay, M. K. Lien and G. E. McMichael (2003). Observations of Electrons in the Intense Pulsed Neutron Source (IPNS) Rapid Cycling Synchrotron (RCS). Proc. IEEE PAC 2003 Particle Accelerator Conference, Portland, OR. ACCELERATOR

J. C. Dooling, F. R. Brumwell, L. I. Donley, G. E. McMichael and V. F. Stipp (2004). Beam Analysis Using the IPNS LINAC ESEM. Proc. LINAC 2004 Conference, Lubeck, Germany. ACCELERATOR

J. C. Dooling, F. R. Brumwell, G. E. McMichael and S. Wang (2005). Observations of UHF Oscillations in the IPNS RCS Proton Bunch. Proc. 2005 PAC Conference, Knoxville, TN. ACCELERATOR

K. Dorogov, E. Dumont, N.-N. Ho, L. G. Kuzmina, J.-M. Poblet, A. J. Schultz, J. A. K. Howard, R. Bau, A. Lledos and G. I. Nikonov (2004). "Neutron and X-Ray Diffraction Studies and DFT

Calculations of Asymmetric Bis(silyl) Niobocene Hydrides." Organometallics **23**(12): 2845-2847. SCD

S. Dudoit, R. C. Gendeman and J. Quackenbush (2003). "Open Source Software for the Analysis of Microarray Data." Biotechniques **S**: 45-51. SOFTWARE

D. V. Dyck (2003). "New Heuristic Approach to the Calculation of General Recoupling Coefficients." Computer Physics Communications **151**(3): 354-368. SOFTWARE

K. W. Eberman, B. J. Wuensch and J. D. Jorgensen (2002). "Order-Disorder Transformations Induced by Composition and Temperature Change in $(\text{Sc}_z\text{Yb}_{1-z})_2\text{Ti}_2\text{O}_7$ Pyrochlores, Prospective Fuel Cell Materials." Solid State Ionics **148**(3-4): 521-526. SEPD

J. Eckert, C. Draznieks and A. K. Cheetham (2002). "Direct Observation of Host-Guest Hydrogen Bonding in the Zeolite NaY/Chloroform System by Neutron Scattering." J. Am. Chem. Soc. **124**(2): 170-171. GLAD, QENS

T. Egami (2001). "Inhomogeneous Charge State in HTSC Cuprates and CMR Manganites." Physica C **364-365**: 441.

T. Egami Medium-Range Atomic Correlation from the PDF Analysis. in Semiconductors to Proteins: Beyond the Average Structure, eds. S.J.L. Billinge and M. F. Thorpe, (Plenum Press New York, 2002). GLAD

T. Egami (2002). "Atomistic Mechanism of Relaxor Ferroelectricity." Ferroelectrics **267**: 101-111. SEPD

T. Egami and D. Louca (2002). "Charge Localization in CMR Manganites: Renormalization of Polaron Energy by Stress-Field." Phys. Rev. B **65**: 094422-1 - 094422-8. GLAD, SEPD

T. Egami (2004). "Local Crystallography of Crystals with Disorder." Zeitschrift für Kristallographie **219**(3): 122-129. SEPD, GLAD, GPPD

S. El-Khatib, S. Chang, H. Nakotte, D. Brown, E. Bruck, A. J. Schultz, A. Christianson and A. Lacerda (2003). "Low-Temperature Magnetic Structure of UPdGe." J. Appl. Phys. **93**(10): 8352-8354. SCD

R. Engels, G. Kemmerling, H. Rongen, J. Schelten and R. Cooper (2002). "Comparison of Neutron Scintillation Detectors with a He-3 Proportional Counter for the Spallation Neutron Source (IPNS)." IEEE Trans. of Nucl. Sci. **49**(3): 923-925. QUIP

R. Engels, G. Kemmerling, R. Cooper and J. Schelten (2003). Detection Properties of a Neutron Counter Based on Scintillator, Wavelength Shifter, and Photomultiplier. IEEE NSS Conf. QUIP

J. S. O. Evans, E. B. Brogden, A. L. Thompson and R. L. Cordiner (2002). "Synthesis and Characterisation of the New Oxyselenide $\text{Bi}_2\text{YO}_4\text{Cu}_2\text{Se}_2$." ChemComm: 912-913. SEPD

A. Evdokimov, A. J. K. (Gilboa), T. F. Koetzle, W. T. Klooster, A. J. Schultz, S. Mason, A. Albinati and F. Frolow (2001). "Structures of Furanosides: Geometrical Analysis of Low Temperature X-ray and Neutron Crystal Structures of Five Crystalline Methyl

Pentofuranosides." Acta Cryst. B **57**(Vol. 2): 213-220. SCD

L. R. Falvello, I. Pascual, M. Tomas, E. P. Urriolabeitia and A. Schultz (2001). "Saccharinate as a Versatile Polyfunctional Ligand. Four Distinct Coordination Modes, Misdirected Valence, and a Dominant Aggregate Structure from a Single Reaction System." Inorg. Chem. **40**: 4455-4463. SCD

C. M. Fang, C.-K. Loong, G. A. deWijis and G. deWith (2002). "Phonon Spectrum of ZnAl_2O_4 Spinel from Inelastic Neutron Scattering and First-Principles Calculations." Phys. Rev. B **66**: 144301 - 144307. LRMECS

A. Faraone, E. Fratini, P. Baglioni and S.-H. Chen (2004). "Quasielastic and Inelastic Neutron Scattering on Hydrated Calcium Silicate Pastes." J. Chem. Phys. **121**(7): 3212-3220. QENS

G. P. Felcher and S. G. E. teVelthuis (2001). "Perspectives of Polarized-Neutron Reflectometry: Magnetic Domains and Off-Specular Scattering." Appl. Surf. Sci. **182**(3-4): 209-215. POSY I

G. P. Felcher, S. G. E. teVelthuis, A. Ruhm and W. Donner (2001). "Polarized Neutron Reflectometry: Recent Developments and Perspectives." Physica B **297**(1-4): 87-93. POSY I

G. P. Felcher, S. G. E. teVelthuis, J. Major, H. Dosch, C. Anderson, K. Habicht and T. Keller (2003). Spin-Echo Resolved Grazing Incidence Scattering (SERGIS) of Cold Neutrons. Proc. SPIE Meeting "Advances in Neutron

Scattering Instrumentation" 2002.
POSYI

B. N. Figgis, A. N. Sobolev, A. J. Schultz and P. A. Reynolds (2001). "Tetrachlorobis (N^1 - phenylacetamindino- kN^2) Rehenium (IV) at 11K by X-ray Diffraction and at 20 K by Neutron Diffraction." Acta Cryst. **C57**: 1151-1153. SCD

M. R. Fitzsimmons, S. D. Bader, J. A. Borchers, G. P. Felcher, J. K. Furdyna, A. Hoffmann, J. B. Kortright, I. K. Schuller, T. C. Schulthess, S. K. Sinha, M. F. Toney, D. Weller and S. Wolf (2004). "Neutron Scattering Studies of Nanomagnetism and Artificially Structured Materials." J. Magn. Magn. Mat. **271**(1): 103-146. POSYI

N. Floros, J. T. Rijssenbeek, A. B. Martinson and K. R. Poeppelmeier (2002). "Structural Study of A_2CuTiO_6 ($A=Y, Tb-Lu$) Compounds." Solid State Sci. **4**(11-12): 1495-1498. GPPD

P. M. Forster, J. Eckert, J.-S. Chang, S.-E. Park, G. Ferey and A. K. Cheetham (2003). "Hydrogen Adsorption in Ananoporous Nickel (II) Phosphates." J. Amer. Chem Soc. **125**(5): 1309-1312. QENS

C. A. Foster, D. E. Schechter and J. M. Carpenter (2002). Methane Pellet Moderator Development. 6th Mtg. Collaboration on Advanced Cold Moderators. FACILITY

E. Fratini, S.-H. Chen and P. Baglioni (2003). "Investigation of the Temporal Evolution of Translational Dynamics of Water Molecules in Hydrated Calcium Aliminate Pastes." J. Phys. Chem. B **107**: 10057-10062. QENS

A. Friedrich, G. A. Lager, M. Kunz, B. C. Chakoumakos, J. R. Smyth and A. J. Schultz (2001). "Temperature-dependent Single-crystal Neutron Diffraction Study of Natural Chondrodite and Clinohumites." American Mineralogist **86**(9): 981-989. SCD

A. Gachet and P. Haettenschwiler (2003). "A Jini-Based Software Framework for Developing Distributed Cooperative Decision Support Systems." Software-Practice & Experience **33**(3): 221-258. SOFTWARE

R. Gahler and J. Lal (2003). "Neutron Spin Echo and Pulsed Sources - Prospects of a Future Liaison." Neutron News **14**(1): 8. FACILITY

K. L. Gawryś, P. M. Spiecker and P. K. Kilpatrick (2003). "The Role of Asphaltene Solubility and Chemical Composition on Asphaltene Aggregation." Petroleum Sci. and Tech. **21**(3-4): 461-489. SAND

K. L. Gawryś and P. K. Kilpatrick (2005). "Asphaltenic Aggregates are Polydisperse Oblate Cylinders." J. of Colloid and Interface Sci. **288**: 325-334. SAND

T. R. Gentile, E. Babcock, J. A. Borchers, W. C. Chen, D. Hussey, G. L. Jones, W. T. Lee, C. F. Majkzrak, K. V. O'Donovan, W. M. Snow, X. Tong, S. G. E. teVelthuis, T. G. Walker and H. Yan (2005). "Polarized 3He Spin Filter In Neutron Scattering." Physica B: 96-102. POSYI

W. M. Gibson, A. J. Schultz, H. H. Chen-Mayer, D. F. R. Mildner, T.

Gnaupel-Herold, M. E. Miller, H. J. Prask, R. Vitt, R. Youngman and J. M. Carpenter (2002). "Polycapillary Focusing Optic for Small Sample Neutron Crystallography." J. Appl. Crystallog. **35**: 677-683. SCD

W. M. Gibson, A. J. Schultz, J. W. Richardson, Jr., J. M. Carpenter, D. F. R. Mildner, H. H. Chen-Mayer, M. E. Miller, E. R. Maxey and R. Youngman (2004). "Convergent Beam Neutron Crystallography." J. Appl. Crystallog. **37**(pt. 5): 778-785. SCD, GPPD

E. P. Gilbert, L. Auvray and J. Lal (2001). "Structure of Polyelectrolyte Chains Confined in Nanoporous Glass." Macromolecules **34**: 4942-4948. SASI

E. P. Gilbert (2002). "Modulated Structure Formation in Demixing Paraffin Blends." Appl. Phys. A **74**: S339-S341. SASI

E. P. Gilbert, D. Sutton, A. Nelson, N. Terrill, C. Martin, J. Lal and E. Lang (2005). Phase Separation in the Organic Solid State: The Influence of Quenching Protocol in Unstable n0Alkaline Blends. Proc. Molecular Crystals and Liquid Crystals, Sydney, Australia. SASI

M. R. Gittings, L. Cipelletti, V. Trappe, D. A. Weitz, M. In and J. Lal (2001). "The Effect of Solvent and Ions on the Structure and Rheological Properties of Gaur Solutions." J. Phys. Chem. A **105**(40): 9310-9315. SASI

I. Glagolenko, K. Carney, S. Kern, E. Goremychkin, T. J. Udovic and J. R. D. Copley (2002). Quantitative Analysis of UH3 in U Metal and UO2 Matrices by Neutron Vibrational Spectroscopy. ICNS 2001. LRMECS

I. Y. Glagolenko, K. P. Carney, S. Kern and E. A. Goremychkin (2002). "Quantitative Determination of Zirconium Hydride in a Zirconium Oxide Matrix by Neutron Vibrational Spectroscopy." J. Appl. Spectroscopy **56**(7): 942-947. LRMECS

B. Glorieux, M. L. Saboungi and J. E. Engerby (2001). "Electronic Conduction in Liquid Boron." Europhysics Letters **56**(1): 81-85. QENS

A. Goldbach, M.-L. Saboungi, L. E. Iton and D. L. Price (2001). "Approach to Band Gap Alignment in Confined Semiconductors." J. Chem. Phys. **115**(24): 11254-11260.

G. B. Gonzalez, J. B. Cohen, J. H. Hwang, T. O. Mason, J. P. Hodges and J. D. Jorgensen (2001). "Neutron Diffraction Study on the Defect Structure of Indium-tin-oxide." J. Appl. Phys. **89**(5): 2550-2555. SEPD

G. B. Gonzalez, T. O. Mason, J. P. Quintana, O. Warschkow, D. E. Ellis, J.-H. Hwang, J. P. Hodges and J. D. Jorgensen (2004). "Defect Structures of Bulk and Nano-Indium-Tin Oxide (ITO)." J. of Applied Physics **96**(7): 3912-3920. SEPD

E. A. Goremychkin, R. Osborn, B. D. Rainford, T. A. Costi, A. P. Murani, C. A. Scott and P. J. C. King (2002). "Magnetic Correlations and the Anisotropic Kondo Effect in $Ce_{1-x}La_xAl_3$." Phys Rev. Lett. **89**14(14): 147201. LRMECS

E. A. Goremychkin, R. Osborn, E. D. Bauer, M. B. Maple, N. A. Frederick, W. M. Yuhasz, F. M. Woodward and J. W.

Lynn (2004). "Crystal Field Potential of $\text{PrOs}_4\text{Sb}_{12}$: Consequences for Superconductivity." Phys Rev. Lett. **93**(15): 7003-7003. LRMECS

R. K. B. Gover, R. Kanno, B. J. Mitchell and J. W. Richardson Jr. (2001). "The Role of Nickel Content on the Structure and Electrochemical Properties of $\text{Li}(\text{Ni}_y\text{Co}_{1-y})\text{O}_2$." J. Power Sources **97**(8): 316-320. GPPD

H. A. Graf (2003). "Single-Crystal Neutron Diffractometry --- Recent Developments and Trends." Zeitschrift für Kristallographie **218**(2): 75-83. SCD

D. H. Gregory, P. M. O'Meara, A. G. Gordon, J. P. Hodges, S. Short and J. D. Jorgensen (2002). "Structure of Lithium Nitride and Transition Metal Doped Derivatives, $\text{Li}_{3-x-y}\text{M}_x\text{N}$ (M=Ni,Cu): A Powder Neutron Diffraction Study." Chem. Mat. **14**(5): 2063-2070. SEPD

L. A. Groat, B. C. Chakoumakos, D. H. Grouwer, C. M. Hoffman, H. Morell, C. A. Fyfe and A. J. Schultz (2003). "The Amblygonite (LiAlPO_4F) -Montebrasite (LiAlPO_4OH) Solid Solution: A Combined Powder and Single-crystal Neutron Diffraction and Solid-state Li-6." Amer. Mineralogist **88**(1): 195-210. SCD

P. C. Guschl, J. U. Otaigbe and L. C.-K (2004). "Investigation of Phase Behavior During Melt Processing of Novel-Inorganic-organic Polymer Hybrid Material." Polymer Engineering and Science **44**(9): 1692-1701. QENS

M. Guthrie, C. A. Tulk, C. J. Benmore, J. E. Siewenie, J. L. Yarger, H.-K. Mao and R. J. Henley (2003). Formation of a

Dense Octahedral Glass. APS Activity Report 2003, ANL 04/16. GLAD

M. Guthrie, J. Urquidi, C. A. Tulk, C. J. Benmore, D. D. Klug and J. Neufeind (2003). "A Direct Observation of Two Distinct Structural Regimes in the HDA to LDA Ice Transformation." Phys. Rev. B **68**: 184110. GLAD

M. Guthrie, C. A. Tulk, C. J. Benmore and D. D. Klug (2004). "A Structural Study of Very High-Density Amorphous Ice." Chem. Phys. Letters **397**: 335. GLAD

M. Guthrie, C. A. Tulk, C. J. Benmore, J. Xu, J. L. Yarger, H.-K. Mao and R. J. Hemley (2004). "The Formation and Structure of a Dense Octahedral Glass." Phys. Rev. Lett. **93**(115): 115502-1 - 115502-4. GLAD

M. Guthrie, J. Urquidi, C. A. Tulk, C. J. Benmore, D. D. Klug and J. Neufeind (2005). "Direct Structural Measurements of Relaxation Processes during Transformations in Amorphous Ice." Phys Rev. B **68**(18): 184110-184115. GLAD

M. G. Gutmann, E. S. Bozin, S. J. L. Billinge, N. A. Babushkina, L. M. Belova, A. R. Kaul and O. Y. Gorbenko (2002). "Temperature Evolution of the Local Atomic Structure in Oxygen Isotope Substituted $\text{Pr}_{0.525}\text{La}_{0.175}\text{Ca}_{0.3}\text{MnO}_3$." Appl. Phys. A **74**: 892. GPPD

M. K. Haas, R. J. Cava, M. Avdeev and J. D. Jorgensen (2002). "Robust Paramagnetism in $\text{Bi}_{2-x}\text{M}_x\text{Ru}_2\text{O}_7$ (M=Mn, Fe, Co, Ni, Cu) Pyrochlore." Phys. Rev. B **66**: 094429-1 - 094429-7. SEPD

J. Haines, O. Cambon, E. Philippot, L. Chapon and S. Hull (2002). "A Neutron Diffraction Study of the Thermal Stability of the α -Quartz-Type Structure in Germanium Dioxide." J. Solid State Chem. **166**: 434-441. SEPD

I. F. Hakem and J. Lal (2002). "Evidence of Solvent-Dependent Complexation in Non-Ionic Polymer/Salt Systems." Appl. Phys. A **74**(Part 1 Suppl. S): S531-S533. SASI

I. F. Hakem and J. Lal (2003). "Polyelectrolyte-like Behavior of Poly(ethylene-oxide) Solutions with Added Monovalent Salt." Europhysics Lett. **64**(2): 204-210. SASI

I. F. Hakem and J. Lal (2004). "Competition between Ion-dipole and Hydrogen Bonding Interactions in a Model Polymer System." Neutron News. SASI

I. F. Hakem and J. Lal (2004). "Interactions of PEO with Monovalent Electrolytes in Solvents of Different Hydrogen Bonding Capacities - Part I Highlight of Science on SAD." Neutron News **15**(3): 27-31. SASI

I. F. Hakem, J. Lal and M. R. Bockstaller (2004). "Binding of Monovalent Ions to PEO in Solutions- Relevant Parameters and Structural Transitions." Macromolecules **37**(22): 8431-8440. SAND, SASI

C. K. Hall and J. Genzer (2004). "Box Length Search Algorithm for Molecular Simulation of Systems Containing Periodic Structures." J. Chem. Phys. **120**(4): 2049-2055. SOFTWARE

Y. Halpern, V. Thieu, R. W. Henning, X. Wang and A. J. Schultz (2001). "Time-resolved In Situ Neutron Diffraction Studies of Gas Hydrate: Transformation of Structure II (sII) to Structure I (sI)." J. Amer. Chem. Soc. **123**(51): 12826-12831. HIPD

M. S. Haluska and S. T. Mixture (2004). "Crystal Structure Refinements of the Three-Layer Aurivillius Ceramics $\text{Bi}_2\text{Sr}_{1-x}\text{A}_x\text{Nb}_2\text{TiO}_{12}$ (A=Ca, Ba, X = 0, 0.5, 1) Using Combined X-Ray and Neutron Powder Diffractions." J. Solid State Chem. **177**(6): 1965. SEPD, GPPD

K. Han, J. D. Embury, P. F. Miceli, G. Felcher, R. Goyette, G. T. Kiehne and J. Ketterson (2003). "Internal Stresses in Wires for High Field Magnets." Proc. MegagaussVII, VIII Int. Conf. on Megagauss Magnetic Fields and Applications. POSYI

K. Han, A. C. Lawson, J. T. Wood, J. D. Embury, R. B. VonDreele and J. W. Richardson, Jr. (2004). "Internal Stresses in Cold-Deformed Cu-Ag and Cu-Nb Wires." Philosophical Magazine **84**(24): 2579-2593. GPPD

S. B. Han, J. Y. Lv, X. F. Lu, J. Peng, X. J. Li, D. F. Chen, Y. J. Xue, J. H. Li and Z. B. Hu (2005). "The Effect of Zr Addition on the Formation and Structural Properties of 3:29 Compounds in the Fe-Nd-Ti-Zr Systems." J. of Phys. and Cond. Mat. **17**: 6007-6014. SEPD

S.-W. Han, J. Farmer, P. F. Miceli, G. Felcher, R. Goyette, G. T. Kiehne and J. Ketterson (2003). "Distribution of Vortices in Nb/Al Multilayers Studied by Spin-Polarized Neutron Reflectivity and Magnetization." Phys. Rev. B **336**(1-2): 162-172. POSYI

S.-W. Han, J. S. Gardner and C. H. Booth (2004). "Structural Properties of the Geometrically Frustrated Pyrochlore $Tb_2Ti_7O_7$." Phys Rev. B - Cond. Mat. **69**(2): 24416-1-7. SEPD

M. R. Harpham, B. M. Ladanyi, N. E. Levinger and K. W. Herwig (2004). "Water Motion in Reverse Micelles Studied by Quasielastic Neutron Scattering and Molecular Dynamics Simulations." J. Chem. Phys. **121**(16): 7855-7868. QENS

R. T. Hart, M. A. Anspach, B. J. Kraft, J. W. Zwanziger, P. J. Santo, B. Stein, J. Jacob and P. Thiyagarajan (2002). "Optical Implications of Crystallite Symmetry and Structure and Texture in Potassium Niobate Tellurite Glass Ceramics." J. Chem. Mat. **14**(10): 4422-4429. GLAD

R. Hart, J. W. Zwanziger and P. L. Lee (2004). "The Crystalline Phase of $(K_2O)_{15}(Nb_2O_5)_{15}(TeO_2)_{70}$ Glass Ceramic is a polymorph of $K_2Te_4O_9$." J. Non-Cryst. Solids **337**: 48-53. GLAD

R. T. Hart, C. J. Benmore, J. Neufeind, S. Kohara, B. Tomberli and P. A. Egelstaff (2005). "Temperature Dependence of Isotopic Quantum Effects in Water." Phys. Rev. Letters **94**(4): 047801. GLAD

M. Hartman and R. Berliner (2004). "An Investigation of the Crystalline Structure of Ettringite using Neutron Powder Diffraction." Bulletin of the American Physical Society **49**(1): B14. SEPD

M. R. Hartman and R. Berliner (2005). "In Situ Neutron Powder Diffraction Investigation of the Hydration of

tricalcium Aluminate in the Presence of Gypsum." J. Solid State Chem. **178**: 3265-3273. SEPD

M. R. Hartman and R. Berliner (2005). "Investigation of the Structure of Ettringite by Time-of-Flight Neutron Powder Diffraction Techniques." Cement and Concrete Research **36**: 364-370. SEPD

A. K. Heilman, Y. Y. Xue, B. Lorenz, B. J. Campbell, J. Cmaidalka, R. L. Meng, Y. S. Wang and C. W. Chu (2002). "Distinct Insulating State Below the Curie Point in $Pr_{0.7}Ba_{0.3}MnO_3$." Phys. Rev. B **65**(21): 214423-1 - 214423-5. SEPD

K. Hense, E. Gratz, H. Nowotny and A. Hoser (2004). "Lattice Dynamics and the Interaction with the Crystal Electric Field in $NdCu_2$." J. Phys. Cond. Mat. **16**: 5751-5768. LRMECS

B. Hertweck, E. Libowitzky and A. J. Schultz (2003). "The Hydrogen Bond System of Mn-leonite: Neutron Diffraction Results in Comparison with IR Spectroscopic Data." Z. Kristallogr. **218**(6): 403-412. SCD

P. Herve, M. Destarac, J.-F. Berret, J. Lal, J. Oberdisse and I. Grillo (2002). "Novel Core-Shell Structure for Collids Made of Neutral/Polyelectrolyte Diblock Copolymers and Oppositely Charged Surfactants." Europhysics Lett. **58**(6): 912-918. SASI

D. G. Hinks, H. Claus and J. D. Jorgensen (2001). "The Complex Nature of Superconductivity in MgB_2 as Revealed by the Reduced Total Isotope Effect." Nature **411**: 457-460. SEPD

D. G. Hinks, J. D. Jorgensen, H. Zheng and S. Short (2002). "Synthesis and Stoichiometry of MgB_2 ." Physica C **382**(2-3): 166-176. SEPD

Y. Hirano, I. Guedes, M. Grimsditch, C.-K. Loong, N. Wakabayashi and L. A. Boatner (2002). "A Brillouin-Scattering Study of the Elastic Constants of $ErVO_4$." J. Amer. Ceram. Soc. **85**(4): 1001-1003. HRMECS

Y. Hirano, S. Skanthakumar, N. Wakabayashi, C.-K. Loong and L. A. Boatner (2002). "The Lattice and Magnetic Properties of $ErVO_4$ and $ErPO_4$." Phys. Rev. B **66**(2): 4424 - 4424. HRMECS

Y. Hirano, N. Wakabayashi, L. C.-K and L. A. Boatner (2003). "Jahn-Teller Effects in the Mixed Vanadate/Phosphate Crystals $TbV_{1-x}P_xO_4$ ($0 \leq x \leq 0.32$)." Phys Rev. B **67**01(1): 014423-1 -014423-7. GPPD

N. Ho, R. Bau, C. Plecnik, S. G. Shore, X. Wang and A. J. Schultz (2002). "A Neutron Diffraction Study of $Cp_2Ti\{(\mu-H)_2BC_8H_{14}\}$." J. Organomet. Chem **654**(1-2): 216-220. SCD

A. Hoffman, S. G. E. t. Velthuis, Z. Sefrioui, J. Santamaria, M. R. Fitzsimmons, S. Park and M. Varela (2005). "Suppressed Magnetization in $La_{0.7}Ca_{0.3}MnO_3/YBa_2Cu_3O_{7-\delta}$ Superlattices." Cond. Mat. **2**: 507123. POSYI

D. Holland, M. E. Smith, I. J. F. Poplett, J. A. Johnson, M. F. Thomas and J. Bland (2001). "Tin Germanate Glasses." J. Non-Crystall. Solids **293-295**: 175-181. GLAD

D. Holland, A. P. Howes, R. Dupree, J. A. Johnson and C. E. Johnson (2003). "Site Symmetry in Binary and Ternary Tin Silicate Glasses - ^{29}Si and ^{119}Sn Nuclear Magnetic Resonance." J. Phys. Cond. Matt. **15**: S2457-S2472. GLAD

M. A. Holmes, M. E. Mackay, R. S. Krishnan, R. K. Giunta, C. J. Hawker and M. Malkoch (2004). "Stabilization of Thin Polymer Films with Nanoparticles for Use in Chemical and Biological Sensors." Polymeric Materials: Science and Engineering **90**: 692-693. POSYII

U. Hoppe, R. Kranold, D. Stachel, A. Barz and C. J. Benmore (2004). "Structural Role of Water in a Sodium Phosphate Glass by Neutron Diffraction." Zeitschrift fuer Naturforschung A **12**: 879. GLAD

X.-J. Hu, K. Littrell, S. Ji, D. G. Pickles and W. M. Risen (2001). "Characterization of Silica-Polymer Aerogel Composites by Small-Angle Neutron Scattering and Transmission Electron Microscopy." J. Non-Crystall. Solids **288**(1-3): 184-190. SAND

X. Hu, R. Biehl, R. K. Prud'homme, M. Monkenbusch and J. Lal (2004). "Fluctuations of Bare Membranes and their Modification on Incorporation of Polymers Having Equally Spaced Anchors." Physica B-Condensed Matter **350**(1-3): 217-219. SASI

Q. R. Huang, P. L. Dubin, J. Lal, C. N. Moorefield and G. R. Newkome (2005). "Small Angle Neutron Scattering Studies of Charged Carboxyl-Terminated Dendrimers in Solutions." Langmuir **21**(7): 2737-2742. SASI

D. Hussey, S. Fan, B. Neff, C. Bailey, W. M. Snow, D. Rich, A. K. Thompson, T. R. Gentile, S. G. E. teVelthuis and G. P. Felcher (2002). Simultaneous Polarization Analysis of Zeeman Splitting in Polarized Neutron Reflectometry using a Polarized ^3He Neutron Spin Filter. ICNS 2001. POSYI

Y. Idemoto, Y. Hawakawa, N. Koura, J. W. Richardson Jr., C.-K. Loong and K. Takeuchi (2002). "Effect of Heat Treatment for Crystal Structure and Ferroelectric Properties of $\text{Sr}_{1-x}\text{Bi}_{2+x}\text{Ta}_2\text{O}_{9-\delta}$ ($x=0, 0.2$)."
J. Ceramic Soc. of Japan **110**(9): 859-866. GPPD

Y. Idemoto, T. Miyahara, N. Koura, T. Kijima and H. Ishiura (2003). "Crystal Structure and Ferroelectric Property of $(\text{Bi},\text{La})_4(\text{Ti},\text{Si})_3\text{O}_{12}$ as a Bulk Ferroelectric Material." Solid State Comm. **128**(6-7): 255-259. GPPD

Y. Idemoto, M. Matsuzawa, N. Koura, K. Takeuchi, J. W. Richardson, Jr. and C. K. Loong (2004). "Effects of Excess Oxygen Content on the Hole-carrying CuO_2 -Layers in $\text{Ti}_2(\text{Ba}_{1-x}\text{Sr}_x)_2\text{Ca}_2\text{Cu}_3\text{O}_y$ Superconducting Oxides." Solid State Communications **131**(8): 513-517. GPPD

Y. Idemoto, H. Yoshikoshi, N. Koura, K. Takeuchi, J. W. Richardson, Jr. and C. K. Loong (2004). "Relation Between the Crystal Structure, Physical Properties and Ferroelectric Properties of $\text{PbZr}_x\text{Ti}_{1-x}\text{O}_3$ ($x=0.40, 0.45, 0.53$) Ferroelectric Material by Heat Treatment." J. Ceramic Society of Japan **112**(1): 40-45. GPPD

Y. Idemoto, N. Yokoyama, N. Koura, J. W. Richardson Jr. and C.-K. Loong (2005). "Relation Between the Crystal Structure and Ferroelectric Properties of

$\text{Bi}_{4-x}\text{La}_x\text{Ti}_3\text{O}_{12-\delta}$ ($x=0.50, y=0; x=0.75, y=0; x=0.75, y=0.15$) Ferroelectric Material by Heat Treatment." Mat. Tech. **23**(3): 182-190. GPPD

B. J. Ingram, G. B. González, T. O. Mason, D. Y. Shahriari, A. Barnabe, D. Ko and K. R. Poeppelmeier (2004). "Transport and Defect Mechanisms in Cuprous Delafossites. Part I: A Comparison of Hydrothermal and Standard Solid-State Synthesis In CuAlO_2 ." Chem. Mater. **16**: 5616-5622. SEPD

B. J. Ingram, B. J. Harder, N. W. Hrabec, T. O. Mason and K. R. Poeppelmeier (2004). "Transport and Defect Mechanisms in Cuprous Delafossites. Part 2: CuScO_2 and CuYO_2 ." Chem. Mater. **16**: 5623-5629. SEPD

E. B. Iverson and J. M. Carpenter (2003). Kinetics of Irradiated Liquid Hydrogen. ICANS-XVI. FACILITY

E. B. Iverson, B. J. Micklich, D. V. Baxter, R. G. Cooper, P. D. Ferguson, D. W. Freeman, F. X. Gallmeier, S. E. Hammonds, I. Popova and C. M. Lavelle (2005). Neutron Beam Characterization for the Spallation Neutron Source Commissioning. Proc. 17th Meeting of the International Collaboration on Advanced Neutron Sources, Santa Fe, NM. FACILITY

W. Jauch and J. Peters (2001). "Correction for Thermal Diffuse Scattering in Single-Crystal Time-of-Flight Neutron Diffraction: First Application." J. Appl. Crystallog. **34**: 493-495. SCD

W. Jauch and A. Palmer (2002). "Reconsideration of the Wavelength-

Dependence of Extinction: A Gamma-Ray Case." Acta Crystallog. **A58**: 448-450. QUIP

W. Jauch, M. Reehuis and A. J. Schultz (2004). "Gamma-Ray and Neutron Diffraction Studies of CoF₂: Magnetostriction, Electron Density and Magnetic Moments." Acta Crystallog. **60**: 51-57. SCD

M. P. Jensen, R. Chiarizia and V. Urban (2001). "Investigation of the Aggregation of the Neodymium Complexes of Dialkyl-phosphoric, -Oxothiophosphinic and -Dithiophosphinic Acids in Toluene." Solvent Extr. Ion Exch. **19**: 865-884. SAND

M. P. Jensen, R. Chiarizia, J. R. Ferraro, M. Borkowski, K. L. Nash, P. Thiyagarajan and K. C. Littrell (2002). New Insights in Third Phase Formation in the U(VI)-HNO₃, TBP-Alkane System. Proc. Int. Solvent Extraction Conf. ISEC 2002, eds. K. C. Sole, P. M. Cole, J. S. Preston and D. J. Robinson, South African Institute of Mining and Metallurgy, Johannesburg. SAND

H. S. Jeon and P. S. Dixit (2001). "Dewetting of Thin Polymer Films." Bull. Am. Phys. Soc. **46**(1): 396. SAND

H. S. Jeon, P. S. Dixit, H. Yim and M. Kent (2002). "Interfacial Structure and Properties in Polystyrene/Epoxy Bilayer Films." J. Polymer Sci. B **40**(23): 2653-2660. SAND

H. S. Jeon (2004). Structure Within Thin Polymer Nanocomposite Films. High Performance Structures And Materials. C. A. Brebbia, WIT Press: Section 3. POSYII

H. S. Jeon and D. H. Weinkauff (2004). "Characterization of Thin Polymer-Like Films Formed By Plasma Polymerization Of MMA: A Neutron Reflectivity Study." J. Polym. Sci., Part B: Polymer Physics **42**: 2522. POSYII

I.-K. Jeong, T. W. Darling, M. J. Graf, T. Proffen, R. H. Heffner, Y. Lee, T. Vogt and J. D. Jorgensen (2004). "Role of the Lattice in the $\gamma \rightarrow \alpha$ Phase Transitions: A High-Pressure Neutron and X-ray Diffraction Study." Phys. Rev. Lett. **92**(10): 105702-1 - 105702-4. SEPD

J. A. Johnson, D. Holland, J. Bland, C. E. Johnson and M. F. Thomas (2003). "Cation Coordination in Oxychloride Glasses." J. Phys. Cond. Matt. **15**: 755-764. GLAD

J. A. Johnson, D. Holland, J. Urquidi, I. A. Gee, C. J. Benmore and C. E. Johnson (2003). "Structure of Oxychloride Glasses by Neutron and X-Ray 'Difference' and XPS." J. Phys. Cond. Matt. **15**(27): 4679-4693. GLAD

G. L. Jones, J. Baker, W. C. Chen, B. Collet, J. Cowan, M. F. Dias, T. R. Gentile, C. Hoffman, T. F. Koetzle, W. T. Lee, K. Littrell, M. Miller, A. J. Schultz, W. M. Snow, X. Tong, H. Yan and A. Yue (2005). "Continuously Operating Compact ³He-based Neutron Spin Filter." Physica B **356**(1-4): 86-90. SCD

J. D. Jorgensen, O. Chmaissem, H. Shaked, S. Short, P. W. Klamut, B. Dabrowski and J. L. Tallon (2001). "Magnetic Ordering in the Superconducting Weak Ferromagnets RuSr₂EuCu₂O₈ and RuSr₂EuCu₂O₈ - art. no. 054440." Phys. Rev. B **63**(5): 054440-1 - 054444-5. SEPD

J. D. Jorgensen, D. G. Hinks and S. Short (2001). "Lattice Properties of MgB₂ Versus Temperature and Pressure." Phys. Rev. B **63**(22): 224522-1 - 224522-5. SEPD

J. D. Jorgensen, Z. Hu, S. Short, A. W. Sleight and J. S. O. Evans (2001). "Pressure-Induced Cubic-to-Orthorhombic Phase Transformation in the Negative Thermal Expansion Material HfW₂O₈." J. Appl. Phys. **89**(6): 3184-3188. SEPD

J. D. Jorgensen, M. Avdeev, D. G. Hinks, J. C. Burley and S. Short (2003). "Crystal Structure of the Sodium Cobaltate Deuterate Superconductor Na_xCoO₂·4xD₂O (x=1/3)." Phys Rev. B **68**(21): 214517-1 - 214517-10. SEPD

J. D. Jorgensen, M. Avdeev, D. G. Hinks, P. W. Barnes and S. Short (2005). "Thermal Expansion and Compressibility in Superconducting Na_xCoO₂·4xD₂O (x{approx}1/3): Evidence for Pressure-induced Charge Redistribution." Phys Rev. B **72**(22): 224515. SEPD

J. Ju, J. Lin, G. Li, T. Yang, H. Li, F. Liao, L. C.-K and L. You (2003). "Aluminoborate-Based Molecular Sieves with 18-Octahedral-Atom Tunnels." Angewandte Chemie **42**: 5607-5610. GPPD

P. Juhas, I. Grinberg, A. M. Rappe, W. Dmowski, T. Egami and P. K. Davis (2004). "Correlations Between the Structure and Dielectric Properties of Pb(Sc_{2/3}W_{1/3})O₃ - Pb (Ti/Zr)O₃ Relaxors." Phys Rev. B **69**(21): Art No. 214101. SEPD

M. Kamal and A. K. Srivastava (2001). "Styrene-co-acrylonitrile and Poly (arsenicacrylate) Based Interpenetrating Polymer Network: Synthesis and Characterization." Reactive and Functional Polymers **49**(1): 55-65. SAND

M. Karabulut, G. K. Marasinghe, C. S. Ray, G. D. Waddill, D. E. Day, Y. S. Badyal, M.-L. Saboungi, S. Shastri and D. Haefner (2002). "A High Energy X-ray and Neutron Scattering Study of Iron Phosphate Glasses Containing Uranium." J. Appl. Phys. **87**(5): 2185-2193. GLAD

V. Y. Kazimirov, D. Louca, V. Ponnambalam, S. J. Poon and T. Proffen (2005). "Structural Model for Amorphous Steels Based on Crystalline Approximants." Phys. Rev. Lett. **72**(5). SEPD

D. Kelley and D. Louca (2005). "Evidence for incomplete martensitic transformation in Ni_{0.62}Al_{0.38} by neutron scattering." Scripta Mat. **53**(5): 475-480. GPPD

M. D. Kempe, J. A. Kornfield and J. Lal (2005). "Chain Anisotropy of Side Group Liquid Crystal Polymers in Nematic Solvents." Macromolecules **37**(23): 8730-8738. SASI

M. D. Kempe, N. R. Scruggs, R. Verduzco, J. Lal and J. A. Kornfield (2004). "Self-Assembled Liquid-Crystalline Gels Designed from the Bottom Up." Nature Materials **3**(3): 177-182. SASI

P. Khalifah, R. Osborn, Q. Huang, H. W. Zandbergen, R. Jin, Y. Liu, D. Mandrus and R. J. Cava (2002). "Orbital Ordering

Transition in $\text{La}_4\text{Ru}_2\text{O}_{10}$." Science **297**(5590): 2237-2240. LRMECS

H. Kim, M. M. Olmstead, J. Y. Chan, P. C. Canfield, I. R. Fisher, R. W. Henning, A. J. Schultz and A. M. Kauzlarich (2001). "Structure and Physical Properties of the New Pseudo-binary Intermetallic Compound $\text{Ti}_{11}(\text{Sb},\text{Sn})_8$." J. Solid State Chem. **157**: 225-232. SCD

J.-S. Kim, J. T. Vaughey, C. S. Johnson and M. M. Thackeray (2003). "Significance of the Tetrahedral A Site on the Electrochemical Performance of Substituted $\text{Li}_{1.05}\text{M}_{0.05}\text{Mn}_{1.90}\text{O}_4$ Spinel Electrodes (M= Li, Mg, An, Al) in Lithium Cells." J. Electrochemical Soc. **150**(11): A1498-A1502. SEPD

B. J. Kirby, J. A. Borchers, J. J. Rhyne, S. G. E. teVelthuis, A. Hoffman, K. V. O'Donovan, T. Wojtowicz, X. Liu, W. L. Kim and J. K. Furdyna (2004). "Annealing-Dependent Magnetic Depth Profile in $\text{Ga}_{1-x}\text{Mn}_x\text{As}$." Phys Rev. B **69**(4): 081307. POSYI

A. Kisliuk, Y. Ding, J. Hwang, J. S. Lee, B. K. Annis, M. D. Foster and A. P. Sokolov (2002). "Influence of Molecular Architecture on Fast and Segmental Dynamics and the Glass Transition in Polybutadiene." J. Polymer Sci. B **40**: 2431-2439. QENS

T. Klimczuk, M. Avdeev, J. D. Jorgensen and R. J. Cava (2005). "Effect of B-11 Substitution on the Superconductivity of MgCNi_3 ." Phys Rev. B **71**18(18): 4512. SEPD

F. Klose and W. T. Lee (2002). Optimization of the SNS Magnetism Reflectometer Design Using Monte Carlo Simulations. ICNS 2001. SNS

D. Ko, K. R. Poeppelmeier, D. R. Kammler, G. B. Gonzalez, T. O. Mason, D. L. Williamson, D. L. Young and T. J. Coutts (2002). "Cation Distribution of the Transparent Conducting Spinel Oxide Solution $\text{Cd}_{1+x}\text{In}_{2-2x}\text{Sn}_x\text{O}_4$." J. Solid State Chem. **163**(1): 259-266. SEPD

T. F. Koetzle and A. J. Schultz (2005). "Single-Crystal Neutron Diffraction: A Valuable Tool for Probing Bond Activation in Transition Metal σ Complexes." Top. Catal. **32**(3-4): 251-255. SCD

T. F. Koetzle, A. J. Schultz, R. Henning, A. Albinati, W. T. Klooster, B. E. Eichler and P. P. Power (2005). "Neutron Diffraction Analysis of the First Stable Hydride Derivative of a Divalent Group 14 Metal." C. R. Chemie **8**: 1487-1490. SCD

S. Kohara and K. Suzuya (2002). "Intermediate-Range Order of Vitreous Silica Studied by High-Energy X-Ray Diffraction, Neutron Diffraction and Reverse Monte Carlo Modelling." Phys. Chem. Glasses **43C**: 51-54. GLAD

S. Kohara, K. Suzuya, K. Takeuchi, C.-K. Loong, M. Grimsditch, J. K. R. Weber, J. A. Tangeman and T. S. Key (2004). "Glass Formation at the Limits of Insufficient Network Formers." Science **303**: 1649-1652. GLAD

S. Kolesnik, B. Dabrowski, O. Chmaissem, Z. Bukowski and J. Mais (2001). "First-Order Antiferromagnetic and Structural Transition in Sr-rich $\text{Pr}_{1-x}\text{Sr}_x\text{MnO}_3$." J. Appl. Phys. **89**(11): 7407-7409. SEPD

S. Kolesnik, B. Dabrowski, J. Mais, D. E. Brown, R. Feng, O. Chmaissem, R. Kruk and C. W. Kimball (2003).

"Magnetic Phase Diagram of Cubic Perovskites $\text{SrMn}_{1-x}\text{Fe}_x\text{O}_3$." Phys Rev. B **67**: 144402-1 - 144402-7. SEPD

L. A. Kovbasyuk, O. Y. Vassilyeva, V. N. Kozozay, H. Chun, I. Bernal, J. Reedijk, G. vanAlbada and B. W. Skelton (2001).

"Triethanolamine Copper Chloride Prepared from Zerovalent Metal: Another Polymorph of a Known Cu(II) Compound or a Mixed-Valence Complex with All-Trigonal Bipyramidal Copper?" Crystal Engineering **4**: 201. SCD

H. Koyanaka, K. Takeuchi and C.-K. Loong (2005). "Gold Recovery from Parts-Per-Trillion-Level Aqueous Solutions by a Nanostructured Mn_2O_3 Adsorbent." Sept. Purif. Technol. **43**(1): 9-15.

J. Kraineva, C. Nicolini, P. Thiyagarajan, E. Kondrashkina and R. Winter (2006).

"Incorporation of α -chymotrypsin into the 3D Channels of Bicontinuous Cubic Lipid mesophases." BBA Proteins & Proteomics **1764**: 424-433. SAND

V. V. Krishnamurthy, P. Mani, G. J. Mankey, S. Srinath and S. G. E. teVelthuis (2005). "Growth and Magnetic Properties of Epitaxial Au/Fe/Au and Au/Fe/Ag Films on $\alpha\text{-Al}_2\text{O}_3$." JMMM(286): 432-436. POSYI

R. S. Krishnan, M. E. Mackay and C. J. Hawker (2004). "Influence of Organic Nanoparticles on Dewetting of Thin Polystyrene Films." Polymeric Materials: Science and Engineering **91**: 925-926. POSYII

X. Kuang, X. Jing, C.-K. Loong, E. E. Lachowski, J. M. S. Skakle and A. R. West (2002). "A New Hexagonal 12-Layer Perovskite-Related Structure with Lanthanide Oxygen Octahedral and Titanate Octahedral and Tetrahedral Layers: $\text{Ba}_6\text{R}_2\text{Ti}_4\text{O}_{17}$ (R= Nd and Y)." Chem. Mat. **14**(10): 4359-4363. GPPD

A. A. Kundig, J. F. Loffler, W. L. Johnson, P. J. Uggowtizer and P. Thiyagarajan (2001). "Influence of Decomposition on the Thermal Stability of Undercooled Zr-Ti-Cu-Ni-Al Alloys." Scripta Materialia **44**(8-9): 1269-1273. SAND

G. A. Lager, G. A. Swayze, C.-K. Loong, F. J. Rotella, J. W. Richardson, Jr. and R. E. Stoffregen (2001). "Neutron Spectroscopic Study of Synthetic Alunite and Oxonium." Canadian Mineralogist **39**: 1131-1138. GPPD, HRMECS

J. Lal (2002). "Interaction between Polymer and Surfactant Mesophases." J. Neutron Research **10**(3-4): 137-141. SASI

J. Lal, E. P. Gilbert and L. Auvray (2002). "Confinement of Neutral and Charged Polymer Chains in Nanoporous Glass." Physica A: Statistical Mechanics and its Applications **304**(1-2): 244-248. SASI

J. Lal and I. F. Hakem (2004). "Unusual Behavior of Poly(ethylene-oxide) in Aqueous Mixtures." Eur. Phys. J. **15**: 217-223. SASI

E. Lang and J. Lal (2005). "Interactions of PEO with Monovalent Electrolytes in Solvents of Different Hydrogen Bonding Capacities - Part II Future

Developments on SAD." Neutron News. SASI

E. Lang and J. Lal (2005). Upgrades to SASI at IPNS. Proc. ICANS-XVII, Santa Fe, NM. SASI

J. M. Lawrence, P. S. Riseborough, C. H. Booth, J. L. Sarrao, J. D. Thompson and R. Osborn (2001). "Slow Crossover in YbXCu_4 (X = AgCd, In, Mg, Tl, Zn) Intermediate-Valence Compounds - art. no. 054427." Phys. Rev. B **6305**(5): 4427. LRMECS

A. C. Lawson (2001). "An Improved Lindemann Melting Rule." Philosophical Mag. B **81**: 255. GPPD

A. C. Lawson, J. A. Roberts, B. Martinez and J. W. Richardson, Jr. (2002). "Invar Effect in Pu-Ga Alloys." Phil. Mag. B **82**(18): 1837-1845. GPPD

A. C. Lawson, J. A. Roberts, G. Martinez, J. W. Richardson, H. Ledbetter and A. Migliori (2003). "Applying the Two-State Invar Model to Delta-Phase Plutonium." J. Minerals Metals & Materials Soc. **55**(9): 31-33. GPPD

L. Lazar, J. S. Jiang, G. P. Felcher, A. Inomata and S. D. Bader (2001). "Oscillatory Exchange Bias in Fe/Cr Double Superlattices." J.M.M.M. **223**(3): 299-303. POSY I

S.-H. Lee, D. Louca, H. Ueda, S. Park, T. J. Sato, M. Isobe, Y. Ueda, S. Rosenkranz, P. Zschack, J. Iniguez, Y. Qiu and R. Osborn (2004). "Orbital and Spin Chains in ZnV_2O_4 ." Phys. Rev. Lett. **93**(15): 156407. LRMECS

W.-T. Lee, X.-L. Wang, J. L. Robertson, F. Klose and C. Rehm (2002). IDEAS - A Monte Carlo Simulation Package for Neutron Scattering Instrumentation. ICNS 2001. POSYI

W.-T. Lee, S. G. E. teVelthuis, G. P. Felcher, F. Klose, T. Gredig and E. D. Dahlberg (2002). "Ferromagnetic Domain Distribution in Thin Films during Magnetization Reversal." Phys. Rev. B **6522**(22): 4417-4417. POSYI

W. T. Lee, F. Klose, H. Q. Yin and B. Toperverg (2003). Measuring Lateral Magnetic Structures in Thin Films Using Time-of-Flight Polarized Neutron Reflectometry. Polarized Neutrons in Condensed Matter Investigations Workshop 2002, Juelich, Germany, Physica B. POSYI

Y. C. Lee, D. L. Price, L. A. Curtis, M. A. Ratner and D. F. Shriver (2001). "Structure of the Ambient Temperature Alkali Metal Molten Salt $\text{AlCl}_3/\text{LiSCN}$." J. Chem. Phys. **114**(10): 4591-4594. GLAD

E. A. Leon-Escamilla and J. D. Corbett (2001). "Hydrogen Impurity Effects. $\text{A}_5\text{Tt}_3\text{Z}$ Intermetallic Compounds between A = Ca, Sr, Ba, Eu, Yb and Tt = Sn, Pb with Cr_5B_3 -like Structures that are Stabilized by Hydride or Fluoride (Z)." Inorg. Chem. **40**: 1226-1233. SCD

E. A. Leon-Escamilla and J. D. Corbett (2001). "Hydrogen Impurity Effects. A_5Tt_3 Intermetallic Compounds between A = Ca, Sr, Ba, Eu and Tt = Si, Ge, Sn with Cr_5B_3 -like Structures that are Stable Both as Binary and as Ternary Hydride and Fluoride Phases." J. Solid State Chem. **159**: 149-162. SCD

J. C. Li and A. I. Kolesnikov (2002). "Neutron Spectroscopic Investigation of Dynamics of Water Ice." J. Molecular Liquids **100**: 1-39. HRMECS

J. C. Li, R. Aswani, X. L. Gao, D. Keen and A. I. Kolesnikov (2003). Supercritical Water Manipulates the Structures of Porous Materials and Nano-scale Particles. Proc. NATO ASI, Turkey. HRMECS

J. C. Li, Y. Wang, S. L. Dong, P. Zhang and A. I. Kolesnikov (2003). "Defect Hydrogen Vibrations in Various Phases Deuterium Ice." J. Chem. Phys. **119**(6): 3332-3335. ISIS

J. C. Li, R. Aswani, X. L. Gao, S. King and A. I. Kolesnikov (2004). Using Supercritical Water Manipulates the Structures of Porous Materials and Nano-Scale Particles. NATO-ASI. S. I. Guceri, Y. Gogotsi and V. Kuzentsov. Dordrecht, Netherlands, Kluwer Academic Book Publishers, (Dordrecht, Netherlands, 2004). **169**: 157-162. SAND

K. Li, L. Guo, Z. Liang, P. Thiyagarajan and Q. Wang (2005). "Oligo (*p*-phenyleneethynylene) Based Coil-rod-coil Triblock Copolymer: Synthesis and Controlled Self-Organization in Solution." J. Pol. Sci: Part A **43**: 6007-6019. SAND

Y. Li, A. I. Kolesnikov, J. W. Richardson Jr., C. Zuo, T. H. Lee and U. Balachandran (2004). "Structure, Proton Incorporation and Transport Properties of Ceramic Proton Conductor $Ba(Ce_{0.7}Zr_{0.2}Yb_{0.1})O_{3-\delta}$." Proc. 2004 MRS Fall Meeting. HRMECS, GPPD

Y. Li, E. R. Maxey, J. W. Richardson, Jr. and B. Ma (2004). "Structural and Chemical Evolution of Fe-Co-O Based Ceramics under Reduction/Oxidation - An In-Situ Neutron Diffraction Study." Mat. Sci. and Eng. B **106**(1): 6-26. GPPD

Y. Li, E. R. Maxey and J. W. Richardson Jr. (2005). "Structural Behaviors of Oxygen Permeable $SrFe_{0.2}Co_{0.8}O_x$ Ceramic Membranes with and without pO_2 Gradients." J. of the American Ceramic Soc. **88**(5): 1244-1252. GPPD

Z. F. Li, G. B. Li, J. L. Sun, L. P. You, C.-K. Loong, Y. X. Wang, F. H. Liao and J. H. Lin (2005). "Synthesis and Characterization of a Ruddlesden-Popper Compound: Sr_3FeMoO_{10} ." J. Solid State Chem. **178**(11): 3315-3322. GPPD

Y. Lin, A. Böker, J. He, K. Sill, H. Xiang, C. Abetz, X. Li, J. Wang, T. Emrick, S. Long, Q. Wang, A. Balazs and T. P. Russell (2005). "Self-directed Assembly of Nanoparticle/Copolymer Mixtures." Nature **434**: 55-59. SAND

Y. Lin, A. Böker, J. T. Russell, S. Long, P. Carl, H. Zettl, J. He, K. Sill, R. Tangirala, T. Emrick, K. Littrell, P. Thiyagarajan, D. Cookson, A. Fery, Q. Wang and T. P. Russell (2005). "Self-assembly and Cross-linking of Bionanoparticles at Liquid-Liquid Interfaces." Angew. Chem. Int. **44**: 2420-2426. SAND

C. D. Ling, J. J. Neumeier and D. N. Argyriou (2001). "Observation of Antiferromagnetism in Marokite $CaMn_2O_4$." J. Solid State Chem. **160**(1): 167-173. SEPD

K. C. Littrell, P. Thiyagarajan, J. M. Carpenter and P. A. Seeger (2002). Design of a TOF-SANS Instrument for the Proposed Long Wavelength Target Station at the Spallation Neutron Source. ICNS 2001. SAND

K. C. Littrell, N. R. Khalli, M. Campbell, G. Sandi and P. Thiyagarajan (2002). "Pore Structure of Activated Carbon Adsorbents Prepared from Paper Mill Sludge." Appl. Phys. A **74**(2): S1403-S1405. SAND

K. C. Littrell, J. W. Richardson, J. M. Carpenter and B. S. Brown (2002). "Present Status and Perspectives on Neutron Scattering Instrumentation Development at IPNS." Physica B **311**(1-2): 112-116. FACILITY

K. C. Littrell (2004). "A Comparison of Different Methods for Improving Flux and Resolution on SANS Instruments." Nucl. Ins. Meth. **529**: 22-27. SAND

K. C. Littrell and W. T. Lee (2004). A Method for Polarization Control and Analysis on Bonse-Hart Double-Crystal USANS Instrument. Polarized Neutrons and Synchrotron X-rays for Magnetism Conference. SAND

G. Liu, X. Yan, Z. Lu, S. A. Curda and J. Lal (2005). "One-Pot Synthesis of Block Copolymer Coated Cobalt NanoCrystals." Chem. Mater. **17**(20): 4985-4991. SASI

Z. Liu, J. Xu, H. P. Scott, Q. Williams, H. K. Mao and R. J. Hemley (2004). "Moissanite (SiC) as Windows and Anvils for High Pressure Infrared Spectroscopy." Rev. Sci. Instrum. **75**(5): 026-029. GLAD

M. V. Lobanov, M. Greenblatt, E. N. Caspi, J. D. Jorgensen, D. V. Sheptyakov, B. H. Toby, C. E. Botez and P. W. Stephens (2004). "Crystal and Magnetic Structure of the $\text{Ca}_3\text{Mn}_2\text{O}_7$ Ruddlesden-Popper Phase: Neutron and Synchrotron X-ray Diffraction Study." J. Phys. Cond. Matt. **16**(20): 5339-5348. SEPD

F. LoCelso, A. Triolo, F. Triolo, P. Thiyagarajan, H. Amenitsch, M. Steinhart, M. Kriechbaum, J. M. DeSimone and R. Triolo (2003). "A Combined Small-Angle Neutron and X-ray Scattering Study of Block Copolymers Micellization in Supercritical Carbon Dioxide." J. Appl. Crystallog. **36**(3): 660-663. SAND

C.-K. Loong, P. Thiyagarajan and A. I. Kolesnikov (2004). "Neutron-Scattering Characterization of Nanostructured Materials Relevant to Biotechnology." Nanotechnology **15**(Sp. Iss SI): S664-S671. QENS, SAND, HRMECS

C.-K. Loong (2005). Complementary of Spallation and Reactor Neutron Sources: Techniques and Scientific Applications. Proc. of the 2nd CCAST Workshop on Application of Spallation Neutron Source, Beijing, China. FACILITY

C.-K. Loong and H. Koyanaka (2005). "Harvesting Precious Metals and Removing Contaminants from Natural Waters - Can Neutrons Benefit Industrial Researchers in Japan?" J. Neutron Research **13**: 15-19. SAND, GPPD, HRMECS

C.-K. Loong and M. Ozawa (2005). "Mass-Fractal-Like Microstructure and Proton Disorder in Nanostructured

Pseudoboehmite: A Neutron-Scattering Study." J. Electroanalytical Chem. **584**(1): 5-8. SAND

C.-K. Loong, M. Ozawa, K. Takeuchi, K. Ui and N. Koura (2005). "Neutron Studies of Rare Earth-Modified Zirconia Catalyst And Yttrium-Doped Barium Cerate Proton-Conducting Ceramic Membranes." J. Alloys and Compounds **408-412**: 1065-1070. GPPD, SAND, HRMECS

C. K. Loong (2005). Separation and Storage of Hydrogen by Novel Materials: Neutron-Scattering Studies and Relevancy to Hydrogen Economy. Proc. of the 2nd CCAST Workshop on Applications of Spallation Neutron Sources, Beijing, China. GPPD, QENS

D. Louca (2001). Jahn-Teller Effects in Transition Metal Oxides. Vibronic Interactions: Jahn-Teller Effect in Crystals and Molecules, ed. M. D. Kaplan and G. O. Zimmerman (Kluwer Academic Publishers, Netherlands): 141-151. SED

D. Louca, T. Egami, W. Dmowski and J. F. Mitchell (2001). "Structural Effect on Colossal Magnetoresistivity in Manganites: Bond vs. Band." Phys. Rev. B **64**: 180403-1 - 180403-4. GLAD, GPPD

D. Louca (2002). "Crossover Dynamics with Low-energy Excitations in Jahn-Teller Co Perovskites." J. Superconductivity: Incorporating Novel Magnetism **15**(6): 591-594. LRMECS, GLAD

D. Louca (2002). "Lattice Effects in Solids Under Hydrostatic Pressure by Neutron Pair Density Function Analysis."

J. Phys. Chem. Solids **64**(2): 343-355. SEPD

D. Louca (2003). "Dynamics of Phase Transitions in $\text{La}_{1-x}\text{Sr}_x\text{CoO}_3$." Physica B **329**(Part 2): 835-836. LRMECS

D. Louca (2003). Jahn-Teller Effects in Transition Metal Oxides. in Vibronic Interactions: Jahn-Teller Effects in Crystals and Molecules, ed. M. D. Kaplan and G. O. Zimmerman (Kluwer Academic Publishers, Netherlands 2001) SEPD

D. Louca (2003). "Lattice Effects in Solids Under Hydrostatic Pressure by Neutron Pair Density Function Analysis." J. Phys. Chem. Solids **64**(2): 343-355. SEPD

D. Louca and J. L. Sarrao (2003). "Dynamical Disorder of Spin-Induced Jahn-Teller Orbitals with the Metal-Insulator Transition in Cobaltates." Phys. Rev. Lett. **91**: 155501. SEPD

D. Louca (2004). "Complexity of the Phase Transition in $\text{La}_{1-x}\text{Sr}_x\text{CoO}_3$." Z. Kristallographic **219**(148). GLAD, LRMECS, SEPD

D. Louca, K. Ahn, A. K. Soper, S. J. Poon and G. J. Shiflet (2005). Phase Transitions in $\text{Al}_{87}\text{Ni}_7\text{Nd}_6$. Proc. MRS Symposium. SEPD

D. Louca, S.-H. Lee and Y. Ueda (2005). "Lattice Distortions in ZnV_2O_4 Frustrated Spinel." Physica B: accepted. SEPD

K. Lu, J. Jacob, P. Thiyagarajan, V. P. Conticello and D. G. Lynn (2003). "Exploiting Amyloid Fibril Lamination for

Nanotube Self-Assembly." J. Amer. Chem. Soc. **125**(21): 6391-6393. SAND

C. Lupu, J.-G. Mao, J. W. Rabalais, A. M. Guloy and J. W. Richardson, Jr. (2003). "X-ray and Neutron Diffraction Studies on $\text{Li}_{17}\text{Sn}_4$." Chem. Mat. **42**(12): 3765-3771. GPPD

B. Ma, N. I. Victory, U. Balachandran, B. J. Mitchell and J. W. Richardson, Jr. (2002). "Study of the Mixed-Conducting $\text{SrFeCo}_{0.5}\text{O}_y$ System." J. Am. Ceramic Soc. **85**(11): 2641-2645. GPPD

P. Macchi, A. J. Schultz, F. K. Larsen and B. B. Iversen (2001). "Experimental and Theoretical Electron Density Study of the Peroxo Function in Oxoperoxo(pyridine-2,6-dicarboxylato)(hexamethylphosphoramide)molybdenum(VI): Implications for Olefin Epoxidation by Peroxo Transition Metal Complexes." J. Phys. Chem. A **105**: 9231-9242. SCD

P. A. Maggard and J. D. Corbett (2004). "Two-Dimensional Metallic Chain Compounds $\text{Y}_5\text{M}_2\text{Te}_2$ (M = Fe, Co, Ni) that are Related to Gd_3MnI_3 . The Hydride Derivative $\text{Y}_5\text{Ni}_2\text{Te}_2\text{D}_{0.4}$." Inorganic Chemistry **43**: 2556-2563. SCD

A. Maira-Vidal, M. A. Gonzalez, C. Cabrillo, F. J. Bermejo, M. Jimenez-Ruiz, M.-L. Saboungi, T. Otomo, F. Fayon, E. Enciso and D. L. Price (2003). "Neutron Scattering on a Re-entrant Binary Liquid Mixture." Chemical Physics **292**(2-3): 273-281. GLAD

A. Maira-Vidal, M. A. Gonzalez, M. Jimenez-Ruiz, F. J. Bermejo, D. L. Price, M. L. Saboungi, R. F. Perea and C. Cabrillo (2004). "Unconventional

Density Dependence of the Stochastic Dynamics in an Organic Liquid." Phys. Rev. E **7002**(2): Pt. 1 1501 - 1501. QENS

J. Major, H. Dosch, G. P. Felcher, K. Habicht, T. Keller, S. G. E. teVelthuis, A. Vorobiev and M. Wahl (2003). "Combining of Neutron Spin Echo and Reflectivity: A New Technique for Probing Surface and Interface Order." Physica B **336**(1-2): 8-15. POSYI

H. Maletta, C. Rehm, F. Klose, M. Fieber-Erdmann and E. Holub-Krappe (2002). "Anomalous Effects of Hydrogen Absorption in Nb Films." J. Magn. Magn. Mater. **240**(1-2): 475-477. POSYII

H. Maletta, C. Rehm, F. Klose, M. Fieber-Erdmann and E. Holub-Krappe (2002). "Anomalous Layer Expansion in Thin Films During Hydrogen Absorption." Phys. Rev. B **65**(11): article no.113404. POSYII

F. Mallamace, M. Broccio, A. Faraone, W.-R. Chen and S.-H. Chen (2004). "Glassy States In Attractive Micellar Systems." Physica A **339**: 92-100. SAND

M. E. Manley, B. Fultz, R. J. McQueeney, C. M. Brown, W. L. Hulst, J. L. Smith, D. J. Thoma, R. Osborn and J. L. Robertson (2001). "Large Harmonic Softening of the Phonon Density of States of Uranium." Phys. Rev. Lett. **86**(14): 3076-3079. LRMECS

M. E. Manley, R. J. McQueeney, B. Fultz, R. Osborn, G. H. Kwei and P. D. Bogdanoff (2002). "Vibrational and Electronic Entropy of Beta-Cerium and Gamma-Cerium Measured by Inelastic

Neutron Scattering." Phys. Rev. B **6514**(14): 4111. LRMECS

M. E. Manley, B. Fultz, T. Swan-Wood, O. Delaire, R. J. McQueeney, E. A. Goremychkin, J. C. Cooley, W. L. Hulst, J. C. Lashley, R. Osborn and J. L. Smith (2003). "No Role for Phonon Entropy in the fcc->fcc Volume Collapse Transition in $Ce_{0.9}Th_{0.1}$." Phys Rev. B **67**(1): 4103-4103. LRMECS

M. E. Manley, W. L. Hulst, J. C. Cooley, R. E. Hackenberg, D. J. Thoma, M. W. Koby, J. L. Smith and K. Littrell (2005). "Vibration Dominated Negative Mixing Entropy for C Impurities in fN -uranium." Phys Rev. B **72**: 184302. LRMECS

J. L. Manson, H. N. Bordallo, J. W. Lynn, R. Feyerherm, A. Loose, L. Chapon and D. N. Argyriou (2002). Magnetic Ordering and Spin Excitations in $Mn(N(CN)_2)_2(py_2)$. ICNS 2001. QENS

J. L. Manson, L. C. Chapon, H. N. Bordallo, R. Geyerherm, D. N. Argyriou and A. Loose (2003). "Spin Ordering in the Mixed-Ligand Antiferromagnet $Mn(Dca)_2(pyrazine)$." J. Magnetism and Magnetic Mat. **260**(3): 462-466. QENS

J. L. Manson, J. G. Lecher, J. Y. Gu, U. Geiser, J. A. Schlueter, R. Henning, X. P. Wang, A. J. Schultz, H. J. Koo and M. H. Whangbo (2003). " $Cu(HCO_2)_2L$ {L = pyrazine, 4,4'-bipyridine}: Employing the Formate Anion as a Building Block in Three-Dimensional Coordination Polymers." Dalton Transactions **14**: 2905-2911. SCD

G. Mao, M.-L. Saboungi, D. L. Price, Y. S. Badyal and H. E. Fishcer (2001). "Lithium Environment in PEO-LiClO₄

Polymer Electrolyte." Europhysics Letters **54**(3): 347-353. GLAD

G. Mao, S. Sukumaran, M.-L. Saboungi and P. Thiyagarajan (2001). "PEO-PPO-PEO Block Copolymer Micelles in Aqueous Electrolyte Solutions: Effect of Carbonate Anions and Temperature on the Micellar Structure and Interaction." Macromolecules **34**: 4666. SAND

G. Mao, M.-L. Saboungi, D. L. Price, M. Armand, F. Mezei and S. Pouget (2002). " α -Relaxation in PEO-LiTFSI Polymer Electrolytes." Macromolecules **35**: 415-419. QENS

J. D. Martin, S. J. Goettler, N. Fosse and L. Iton (2002). "Designing Intermediate Range Order in Amorphous Materials." Nature **419**: 381-384. GLAD

R. A. Martin, P. S. Salmon, C. J. Benmore, H. E. Fischer and G. J. Cuello (2003). "Structure of Lanthanum and Cerium Phosphate Glasses by the Method of Isomorphic Substitution in Neutron Diffraction." Phys Rev. B **68**(5): 054203-1 - 054203-11. GLAD

M. M. Martinez-Iñesta, I. Peral, T. Proffen and R. F. Lobo (2004). "A Pair Distribution Function Analysis of Zeolite Beta." Elsevier Science **77**: 55-66. GLAD

T. O. Mason, G. B. Gonzalez, D. R. Kammler, N. Mansourian-Hadavi and B. J. Ingram (2002). "Defect Chemistry and Physical Properties of Transparent Conducting Oxides in the CdO-In₂O₃-SnO₂ System." Thin Solid Films **411**(1): 106-114. SEPD

T. O. Mason, G. B. Gonzalez, J.-H. Hwang and D. R. Kammler (2003). "Point Defects and Related Properties of Highly Co-Doped Bixbyite In_2O_3 ." Phys. Chem. Chem. Phys. **5**(11): 2183-2189. SEPD

T. Matsuura, R. Kanno, R. Gover, Y. Kawamoto, T. Kamiyama and B. J. Mitchell (2003). "Synthesis, Structure and Physical Properties of $\text{Li}_x\text{Na}_{1-x}\text{NiO}_2$." Solid State Ionics **152**(Part A): 303-309. GPPD

S. E. McLain, C. J. Benmore and J. F. C. Turner (2002). "The Structure of Liquid Fluorosulfuric Acid Investigated by Neutron Diffraction." J. Chem. Phys. **117**(8): 3816-3821. GLAD

S. E. McLain, C. J. Benmore, J. E. Siewenie, J. Urquidi and J. F. C. Turner (2003). On the Structure of Liquid Hydrogen Fluoride. APS Activity Report 2003, ANL-04/16. GLAD

S. E. McLain, J. E. Siewenie, C. J. Benmore and J. F. C. Turner (2003). "On the Structure of Boron Trifluoride in Liquid and Supercritical Phase Investigated by Neutron Diffraction." J. Chem. Phys. **119**(13): 6671-6679. GLAD

S. E. McLain, C. J. Benmore, J. Siewenie, J. J. Molaison and J. F. C. Turner (2004). "On The Temperature Variation Of Structure Of Liquid Anhydrous Hydrogen Fluoride." J. Chem. Phys. **121**(13): 6448-6455. GLAD

S. E. McLain, C. J. Benmore, J. E. Siewenie, J. Urquidi and J. F. C. Turner (2004). "On The Structure Of Liquid

Hydrogen Fluoride." Angewandte Chemie **43**: 1951-1955. GLAD

S. E. McLain (2004) Structural Studies of Superacidic Systems Using Neutron and High Energy X-Ray Diffraction Doctor of Philosophy Degree, University of Tennessee. GLAD

G. E. McMichael (2005). A Tale of Three Facilities - Accelerator Operators at ANL. Proc. Workshop on Accelerator Operations 2005, Batavia, IL. ACCELERATOR

P. F. McMillan, M. Wilson and M. C. Wilding (2003). "Polyamorphism in Aluminate Liquids." J. Phys. Cond. Matt. **15**: 6105-6121. GLAD

R. J. McQueeney, M. E. Manley, R. Osborn, B. Fultz, G. H. Kwei and P. D. Bogdanoff (2001). "Unexpected Similarity of the Dynamic Magnetic Susceptibilities of Gamma-Cerium and Beta-Cerium." Philosophical Mag. B **81**(7): 675-687. LRMECS

R. J. McQueeney, J. L. Sarrao, P. G. Pagliuso, P. W. Stephens and R. Osborn (2001). "Mixed Lattice and Electronic States in High-Temperature Superconductors." Phys. Rev. Lett. **87**(7): 7001+. LRMECS

R. J. McQueeney, J. L. Sarrao, P. G. Pagliuso, P. W. Stephens and R. Osborn (2002). New Oxygen Lattice Modes in the Metallic Region of $\text{La}_{2-x}\text{Sr}_x\text{CuO}_4$. ICNS 2001. LRMECS

Q. Mei, P. Ghalsasi, C. J. Benmore and J. L. Yarger (2003). The Glacial State of Triphenyl Phosphite. APS Activity Report 2003, ANL 04/16. GLAD

Q. Mei, P. Ghalsasi, C. J. Benmore and J. L. Yarger (2004). "The Local Structure of Triphenyl Phosphite Studied Using Spallation Neutron and High Energy X-ray Diffraction." J. Phys. Chem. B **108**: 20076. GLAD

Q. Mei, P. Ghalsasi, C. Benmore and J. L. Yarger (2005). "The Glacial State of Triphenyl Phosphate." J. Chem. Phys. B. **108**: 1951-1955. GLAD

Q. Mei and S. W. Martin (2005). "Structural Investigation of $\text{Ag}_2\text{S} + \text{GeS}_2 + \text{B}_2\text{S}_3$ Glasses Using Neutron Diffraction." Phys. and Chem. of Glass **46**(1): 51-57. GLAD

B. J. Micklich and E. B. Iverson (2003). Calculation of Pulse Shapes for Reentrant Moderators. Nuclear Mathematical and Computational Sciences: A Century in Review, A Century Anew, Gatlinburg, TN. FACILITY

B. J. Micklich, E. B. Iverson and J. M. Carpenter (2003). Comparison of Calculated and Measured Neutron Intensities for the IPNS Cryogenic Methane Moderators. Proc. ICANS-XVI, Germany. QENS, GPPD, SEPD

B. J. Micklich, J. M. Carpenter and J.-M. Zanotti (2005). Neutron Scattering Measurements on Cryogenic Ammonia. Proc. 17th Meeting of the International Collaboration on Advanced Neutron Sources, Santa Fe, NM. FACILITY

B. J. Micklich and P. D. Ferguson (2005). Radionuclide Inventory Calculations for Spallation Neutron Sources. Proc. 17th Meeting of the International Collaboration on Advanced

Neutron Sources, Santa Fe, NM. FACILITY

B. J. Micklich, E. B. Iverson, D. W. Freeman, R. G. Cooper, P. D. Ferguson, F. X. Gallmeier, S. E. Hammonds, I. Popova, D. V. Baxter and C. M. Lavelle (2005). Spectral Intensity Benchmarking on IPNS Beamlines. Proc. 17th Meeting of the International Collaboration on Advanced Neutron Sources, Santa Fe, NM. FACILITY

M. E. Middendorf, F. R. Brumwell, J. C. Dooling, M. K. Lien and G. E. McMichael (2001). The IPNS RCS RF System Third Cavity Upgrade. Proc. 2001 Particle Accelerator Conference. ACCELERATOR

D. J. Mikkelsen, A. J. Schultz, R. Mikkelsen and T. G. Worlton (2005). "Visualization and Analysis of Single Crystal Time-of-Flight Neutron Scattering Data using ISAW." Int. Union Crystallogr.(5): 32-39. SCD

J. E. Milburn, J. F. Mitchell and S. Short (2001). "Impact of Oxygen Partial Pressure on the Ruddlesden-Popper Series $\text{Nd}_{2-2x}\text{Sr}_{1+2x}\text{Mn}_2\text{O}_7$: Oxygen Vacancy Formation and Ordering." Chem. Mat. **13**: 1957-1966. SEPD

D. F. R. Mildner, M. Arif and S. A. Werner (2001). "Neutron Transmission through Pyrolytic Graphite Monochromators." J. Appl. Crystallog. **34**: 258-262. SCD

D. F. R. Mildner and J. M. Carpenter (2002). "Time Uncertainty for Guided Long Wavelength Neutrons on a Pulsed Source." Nucl. Instrum. & Meth. **A484**(1-3): 486-493. FACILITY

D. F. R. Mildner, H. H. Chen-Mayer and W. M. Gibson (2002). "Focusing Neutrons with Tapered Capillary Optics." J. Appl. Phys. **92**(11): 6911-6917. FACILITY

D. F. R. Mildner, H. H. Chen-Mayer, W. M. Gibson and A. J. Schultz (2002). Advances in Neutron Scattering Instrumentation. Proc. SPIE Conf., Seattle, WA. SCD

D. F. R. Mildner, H. H. Chen-Mayer, W. M. Gibson, T. Gnaupel-Herold, M. E. Miller, H. J. Prask, A. J. Schultz, R. Vitt and R. Youngman (2002). "A Monolithic Polycapillary Focusing Optic for Polychromatic Neutron Diffraction Applications." Rev. of Sci. Inst. **73**(5): 1985-1993. SCD

B. J. Mitchell, J. W. Richardson, Jr., C. D. Murphy, B. Ma, U. Balachandran, J. P. Hodges and J. D. Jorgensen (2002). "Phase Stability of $\text{SrFeCo}_{0.5}\text{O}_y$ Under Synthesis and Annealing Conditions." J. European Ceramic Soc. **22**(5): 661-671. GPPD, SEPD

B. J. Mitchell, R. C. Rogan, J. W. Richardson, Jr., B. Ma and U. Balachandran (2002). "Stability of the Cubic Perovskite $\text{SrFe}_{0.8}\text{Co}_{0.2}\text{O}_{3-\delta}$." Solid State Ionics **146**(3-4): 313-321. GPPD

J. F. Mitchell, D. N. Argyriou, A. Berger, K. E. Gray, R. Osborn and U. Welp (2001). "Spin, Charge and Lattice States in Layered Magnetoresistive Oxides." J. Phys. Chem. B **105**(44): 10731-10745. LRMECS

J. F. Mitchell, J. Burley and S. Short (2003). "Crystal and Magnetic Structure of $\text{NdBaCo}_2\text{O}_{5+\delta}$: Spin States in a Perovskite-Derived, Mixed-Valent

Cobalite." J. Appl. Phys. **93**(10): 7364-7366. SEPD

K. Mitchell, F. Q. Huang, E. N. Caspi, A. D. McFarland, C. L. Haynes, R. C. Somers, J. D. Jorgensen, R. P. V. Duyne and J. A. Ibers (2004). "Syntheses Structure and Selected Physical Properties of CsLnMnSe_3 (Ln = Sm, Gd, Tb, Dy, Ho, Er, Tm, Yb, Y) and AYbZnQ_3 (A = Rb, Cs; Q = S, Se, Te)." Inorganic Chemistry **43**(3): 1082-1089. SEPD

R. Mittal, S. L. Chaplot, A. I. Kolesnikov, C.-K. Loong, O. D. Jaykumar and S. K. Kulshreshtra (2002). "Inelastic Neutron Scattering, Lattice Dynamics and Synchrotron X-ray Diffraction Study of FePO_4 ." Phys Rev. B **66**: 174304-1 - 174304-7. HRMECS

R. Mittal, S. L. Chaplot, A. I. Kolesnikov, C.-K. Loong and T. A. Mary (2003). Negative Thermal Expansion in HfW_2O_8 . Proc. Int. Conf. on Phonons in Condensed Materials, eds. S. P. Sanyal and R. K. Singh. HRMECS

R. Mittal, S. L. Chaplot, A. I. Kolesnikov, C. K. Loong and T. A. Mary (2003). "Inelastic Neutron Scattering and Lattice Dynamical Calculation of Negative Thermal Expansion in HfW_2O_8 ." Phys. Rev. B **68**(5): 054302-1 - 054302-7. HRMECS

R. Mittal, S. L. Chaplot, A. I. Kolesnikov, L. C.-K, O. D. Jayakumar and S. K. Kulshreshtha (2004). "Inelastic Neutron Scattering and Lattice Dynamics of GaPO_4 ." Pramana J Phys. **63**(2): 405-408. HRMECS

R. Mittal, S. L. Chaplot, A. I. Kolesnikov, C.-K. Loong and T. A. Mary (2004).

Negative Thermal Expansion in HfW₂O₈. Phonons in Condensed Matter. Proc. International Conf. on Phonons in Condensed Matter (Phonons 2K3), eds. S. P. Sanyal and R. K. Singh, Allied Publishers Pvt. Ltd., New Delhi, 2004. HRMECS

R. Mittal, S. L. Chaplot, H. Schober, A. I. Kolesnikov, C.-K. Loong and A. P. Wilkinson (2004). "Negative Thermal Expansion in Cubic ZrMo₂O₈: Inelastic Neutron Scattering and Lattice Dynamical Studies." Phys Rev. B **70**: 214303-1 - 214303-6. HRMECS

D. Morgan, J. Dong, J. Jacob, K. Lu, R. P. Apkarian, P. Thiyagarajan and D. Lynn (2002). "Metal Switch for Amyloid Formation: Insight into the Structure of the Nucleus." J. Am. Chem. Soc. **124**(43): 12644-12645. SAND

B. V. Mork, T. D. Tilley, A. J. Schultz and J. A. Cowan (2004). "Silylene Hydride Complexes of Molybdenum with Silicon-Hydrogen Interactions. Neutron Structure of (n⁵-C₅Me₅)(Me₂PCH₂CH₂PMe₂)Mo(H)(SiEt₂)." J. Am. Chem. Soc. **126**(33): 10428-10449. SCD

M. L. Morrison, W. Dmowski, T. W. Wilson, P. K. Liaw, C. T. Liu, J. W. Richardson Jr., E. R. Maxey, R. A. Buchanan, C. Fan, H. Choo, T. Egami and W. D. Porter (2005). Pair Distribution Function Analyses of Structural Relaxation in a Zr-based Bulk Metallic Glass. Proc. 2004 MRS Fall Meeting, Boston. GPPD

E. G. Moshopoulou, Z. Fisk, J. L. Sarrao and J. D. Thompson (2001). "Crystal Growth and Intergrowth Structure of the New Heavy Fermion Materials CeIrIn₅

and CeRhIn₅." J. Solid State Chem. **158**: 25-33.

M. R. Moura, A. P. Ayala, I. Guedes, C.-K. Loong and L. A. Boatner (2004). "Phonon Spectra of Terbium-Doped Lutetium Orthophosphates." J. Appl. Phys. **96**(11): 6344-6347. HRMECS

L. E. Muzzy, M. Avdeev, G. Lawes, M. K. Haas, H. W. Zandbergen, A. P. Ramirez, J. D. Jorgensen and R. J. Cava (2002). "Structure and Superconductivity in Zr-Stabilized, Nonstoichiometric Molybdenum Diboride." Physica C **382**: 153-165. SEPD

K. Nakamura, K. T. Park, A. J. Freeman and J. D. Jorgensen (2001). "Magnetic and Electronic Structures of Superconducting RuSr₂GdCu₂O₈." Phys. Rev. B **63**(2): 024507. SEPD

R. A. Narayanan (2003). "Chemical Order, Molecular Clusters, and Topological Transitions in Chalcogenide Network Glasses." Phys Rev. B **68**(21): 212201-1 - 212201-4. GLAD

R. A. Narayanan and J. W. Zwanziger (2003). "The Glass Forming Ability of Tellurites: A Rigid Polytope Approach." J. Non-Crystalline Solids **316**: 273-280. GLAD

D. G. Narehood, N. Grube, R. M. Dimeo, D. W. Brown and P. E. Sokol (2003). "Inelastic Neutron Scattering of H₂ in Xerogel." J. Low Temp. Phys. **132**(3-4): 223-237. LRMECS

J. Neuefeind, C. J. Benmore, B. Tomberli and P. A. Egelstaff (2002). "Experimental Determination of the Electron Density of Liquid H₂O and

D₂O." J. Phys. Conds. Mat. **14**(23): L429-L433. GLAD

J. J. Neumeier, T. Tomita, M. Debessai, J. S. Schilling, P. W. Barnes, D. G. Hinks and J. D. Jorgensen (2005). "Negative Thermal Expansion of MgB₂ in the Superconducting State and Anomalous Behavior of the Bulk Gruneisen Function." Phys Rev. B **72**(22): 220505. SEPD

C. Nicolini, R. Winter and P. Thiyagarajan (2004). "Small-Scale Composition Fluctuations and Micro-Domain Formation in Lipid Raft Models as Revealed by Small-Angle Neutron Scattering." Phys. Chem. Chem. Phys. **6**(24): 5331-5334. SAND

H. Nie, M. Li, C. Bansil, C. Konak, M. Helmstedt and J. Lal (2004). "Structure and Dynamics of a Pentablock Copolymer of Polystyrene-polybutadiene in a Butadiene-Selective Solvent." Polymer **45**(26): 8791-8799. SASI

H. S. C. O'Neill, S. A. T. Redfern, S. Kesson and S. Short (2003). "An In Situ Neutron Diffraction Study of Cation Disorder in Synthetic Qandilite Mg₂TiO₄ at High Temperatures." Amer. Mineralogist **88**(5-6): 860-865. SEPD

R. Osborn, E. A. Goremychkin, A. I. Kolenikov and D. G. Hinks (2001). "Phonon Density of States in MgB₂." Phys. Rev. Lett. **87**01(1): 017005-1 - 017005-4. HRMECS

M. V. Ovchinnikov, C. Wang, A. J. Schultz, I. A. Guzel and R. J. Angelici (2002). "Metal Control of the Reaction Site in Reactions of $[(\eta^5\text{-C}_5\text{H}_3)_2(\text{SiMe}_2)_2]\text{M}_2(\text{CO})_4(\mu\text{-H})^+$ (M = Fe, Ru, Os) with Nucleophilic Amines."

Organometallics **21**(15): 3292-3296. SCD

J. Overgaard, B. Schiott, F. K. Larsen and B. B. Iverson (2001). "The Charge Density Distribution in a Model Compound of the Catalytic Triad in Serin Proteases." Chem. Eur.: 3756-3767. SCD

M. Ozawa, M. Winterer, C.-K. Loong and S. Suzuki (2003). "Local Structure Stability of Cu-Al₂O₃ NO_x Removal Catalyst." Materials Science Research International **9**(1): 114-116. SAND

A. A. Parizzi, W.-T. Lee and F. Klose (2002). "Modeling the Neutron Spin-Flip Process Inside a Time-of-Flight Spin Resonance Energy Filter." Appl. Phys. A **A74**(1): S1498-S1501. POSYI

A. A. Parizzi, W.-T. Lee and F. Klose (2002). Possibilities for Polarized Pulsed Neutron Instrumentation Based on the Time-of-Flight Spin Resonance Energy Filter. ICNS 2001. POSYI

A. Parizzi, W.-T. Lee, G. P. Felcher and F. Klose (2003). "Decoupled Moderators - Do We Always Need Them? or: A New Approach for Pulse Shaping." J. Neutron Research **11**: 51-60. POSYI

V. Peña, Z. Sefrioui, D. Arias, C. Leon, J. Santamaria, J. L. Martinez, S. G. E. teVelthuis and A. Hoffman (2005). "Giant Magnetoresistance in Ferromagnet/Superconductor Superlattices." Phys. Rev. Letters **94**: 057002. POSYI

J. Peters (2003). "The 'Seed-Skewness' Integration Methods Generalized for Three-Dimensional Bragg Peaks." J. Appl. Crystallog. **36**: 1475-1479. SCD

P. F. Peterson, E. S. Bozin, T. Proffen and S. J. L. Billinge (2003). "Improved Measures of Quality for the Atomic Pair Distribution Function." J. Appl. Crystallog. **36**(Part 1): 53-64. GLAD, SEPD

Z. S. Petrovic, Y. J. Cho, I. Javni, S. Magonov, N. Yerina, D. W. Schaefer, J. Ilavsky and A. Waddon (2004). "Effect of Silica Nanoparticles on Morphology of Segmented Polyurethanes." Polymer **45**(12): 4285-4295. SAND

J. Pletsil, C. Konak, X. Hu and J. Lal (2005). "SANS Study of Comicellization of Diblock Copolymers in a Selective Constant." Macromolecular Chem. & Phys. **207**: 231-241. SASI

D. L. Price and Y. Ren (2001). "Neutron Scattering Study of H₂ Adsorption in Single-Walled Carbon Nanotubes." Appl. Phys. Lett. **79**(22): 3684-3686. QENS

D. L. Price, M.-L. Saboungi and F. J. Bermejo (2003). "Dynamical Aspects of Disorder in Condensed Matter." Reports on Progress in Physics **66**(4): 407-480. QENS, HRMECS

T. Proffen and S. J. L. Billinge (2002). "Probing the Local Structure of Doped Manganites Using the Atomic Pair Distribution Function." Appl. Phys. A **74**: S1770-S1772. SEPD

T. Proffen, S. J. L. Billinge, T. Egami and D. Louca (2003). "Structural Analysis of Complex Materials Using the Atomic Pair Distribution Function - A Practical Guide." Z. Kristallogr. **218**: 132-143. GLAD, SEPD

X. Qiu, S. J. L. Billinge, C. R. Kmetz and J. F. Mitchell (2004). "Evidence for Nano-scale Inhomogeneities in Bilayer Manganites in the Mn⁴⁺ Rich Region: 0.54 ≤ q x ≤ 0.80." J. Phys. Chem. Solids **65**(8-9): 1423-1429. GPPD, SEPD, GLAD

X. Qiu, E. S. Bozin, P. Juhas, T. Proffen and S. J. L. Billinge (2004). "Reciprocal-Space Instrumental Effects on the Real-Space Neutron Atomic Pair Distribution Function." J. Appl. Crystallography **37**: 110-116. SEPD, GPPD

A. P. Radlinski, M. Mastalerz, A. L. Hinde, M. Hainbuchner, H. Rauch, M. Baron, L. Fan and P. Thiyagarajan (2001). Non-Invasive Measurements of Pore Size Distribution in Coal Pellets Using X-Ray and Neutron Techniques - Draft. Proc. Int. Coalbed Methane Symposium. SAND

A. P. Radlinski and A. L. Hinde (2002). "Small Angle Neutron Scattering And Petroleum Geology." Neutron News **13**(2): 11-17. SAND

A. P. Radlinski, D. E. Edwards, A. L. Hinde, R. Davenport and J. M. Kennard (2003). "Hydrocarbon Generation and Expulsion from Early Cretaceous Source Rocks in the Browse Basin, North West Shelf, Australia: A Small Angle Scattering and Pyrolysis Study." Geoscience Australia Report: 216. SAND

A. P. Radlinski, J. M. Kennard, D. S. Edwards, A. L. Hinde and R. Davenport (2004). "Hydrocarbon Generation and Expulsion From Early Cretaceous Source Rocks In The Browse Basin, North West Shelf, Australia: A Small Angle Neutron Scattering Study."

Australian Association of Petroleum Production and Exploration Journal: 151-180. SAND

A. P. Radlinski, M. Mastalerz, A. L. Hinde, A. Hainbuchner, H. Rauch, M. Baron, J. S. Lin, L. Fan and P. Thiyagarajan (2004). "Application of SAXS and SANS in Evaluation of Porosity, Pore Size Distribution and Surface Area of Coal." Intl. J. Coal Geology **59**(3-4): 245-271. SAND

A. Raudino, F. LoCelso, A. Triolo and R. Triolo (2004). "Pressure-Induced Formation of Diblock Copolymer "Micelles" in Supercritical Fluids. A Combined Study by Small Angle Scattering Experiments and Mean-Field Theory. I. The Critical Micellization Density Concept." J. Chem. Phys. **120**(7): 3489-3498. SAND

A. Raudino, F. LoCelso, A. Triolo and R. Triolo (2004). "Pressure-Induced Formation of Diblock Copolymer "Micelles" in Supercritical Fluids. A Combined Study by Small Angle Scattering Experiments and Mean-Field Theory. II. Kinetics of the Unimer-Aggregate Transition." J. Chem. Phys. **120**(7): 3499-3507. SAND

S. A. T. Redfern (2002). "Neutron Powder Diffraction of Minerals at High Pressures and Temperatures: Some Recent Technical Developments and Scientific Applications." Eur. J. Mineral **14**: 251-261. SEPD

C. Rehm, H. Maletta, M. Fieber-Erdmann, E. Holub-Krappe and F. Klose (2002). "Anomalous Layer Expansion in Thin Niobium Films During Hydrogen Absorption." Phys Rev. B **65**: 113404-1 - 113404-4. POSYII

D. Renusch, M. Grimsditch, J. D. Jorgensen and J. P. Hodges (2001). "Pressure Dependence of Cr³⁺ Fluorescence in Theta-Alumina." Oxidation of Metals **56**(3-4): 299-311. SEPD

P. A. Reynolds, E. P. Gilbert and J. W. White (2001). "High Internal Phase Water-in-Oil Emulsions and Related Microemulsions Studied by Small Angle Neutron Scattering: The Distribution of Surfactant." J. Phys. Chem. B **105**: 6925-6932. SASI

J. T. Rijssenbeek, S. Malo, V. Caignaert and K. R. Poeppelmeier (2002). "Site and Oxidation State Specificity Yielding Dimensional Control in Perovskite Ruthenates." J. Am. Chem. Soc. **124**: 2090-2091. GPPD

J. T. Rijssenbeek, T. Saito, S. Malo, M. Azuma, M. Takano and K. R. Poeppelmeier (2004). "Effect of Explicit Cationic Size and Valence Constraints on the Phase Stability of 1:2 B-site Ordered Perovskite Ruthenates." J. Am. Chem. Soc. **127**: 675-681. GPPD

G. Rinehart and G. McMichael (2001). EPICS Upgrade of IPNS Accelerator Control and Data Acquisition System. Proc. 2001 Particle Accelerator Conference. ACCELERATOR

K. Rogacki, B. Dabrowski, O. Chmaissem and J. D. Jorgensen (2001). "Increase of the Superconducting T_c Irreversibility Fields, and Critical Currents in Tetragonal YBaSrCu_{3-x}Mo_xO_{7+d}." art. no. 054501." Phys. Rev. B **63**05(5): 4501+. SEPD

R. Rogan, B. J. Mitchell, J. W. Richardson, Jr., B. Ma, U. Balachandran, J. P. Hodges and J. D. Jorgensen (2002). "Stability of the Cubic Perovskite $\text{SrFe}_{0.8}\text{Co}_{0.2}\text{O}_{3-\delta}$ where $(0.35 \leq \delta \leq 0.57)$." Solid State Ionics **146**: 313-321. GPPD

S. Rosenkranz, R. Osborn, L. Vasiliu-Doloc, J. W. Lynn, S. K. Sinha and J. F. Mitchell (2002). "Spin Correlations and Magnetoresistance in the Bilayer Manganite $\text{La}_{1.2}\text{Sr}_{1.8}\text{Mn}_2\text{O}_7$." Physica B **312**: 763-765. LRMECS

J. L. C. Rowsell, J. Eckert and O. M. Yaghi (2005). "Characterization of H_2 Binding Sites in Prototypical Metal-Organic Frameworks by Inelastic Neutron Scattering." J. of Am. Chem. Soc. **127**(42): 14904-14910. QENS

J. T. Russell, Q. Wang, S. Long, A. Boker, H. Zettl, A. Fery, P. Carl, P. Thiyagarajan, K. Littrell, D. Cookson, Y. Lin, K. Sill, R. Tangirala, T. Emrick and T. P. Russell (2005). "Self Assembly and Cross-Linking of Bionanoparticles at Liquid-Liquid Interfaces." Angewandte Chemie **44**(16): 2420-2426. SAND

D. Y. Ryu, D. J. Lee, J. K. Kim, K. A. Lavery, T. P. Russell, Y. S. Han, C. H. Lee and P. Thiyagarajan (2003). "Effect on Hydrostatic Pressure on Closed-Loop Phase Behavior of Block Copolymers." Phys Rev. Lett. **90**(23): 5501/1-2355/4. SAND

M.-L. Saboungi, J. Enderby, B. Glorieux, H. Schnyders, Z. Sungaila, S. Krishnan and D. L. Price (2002). "What is New on the Levitation Front?" J. Non-Crystall. Solids **312**: 294-298. GLAD

M.-L. Saboungi and D. L. Price Dyanmic Disorder in Crystalline Intermetallic Compounds. in Intermetallic Compounds: Principles and Practice ed. J. H. Westbrook and R. L. Fleischer, Volume 3: Progress (Wiley & Sons, Chichester, UK, 2002): 245-261. QENS

M.-L. Saboungi and D. L. Price Effects of Mobile Species. in Intermetallic Compounds: Vol. 3 Principles and Practice, eds. J. H. Westbrook and R. L. Fleischer, John Wiley & Sons, Ltd. (2002): 245-261. QENS

M.-L. Saboungi, D. L. Price, G. M. Mao, R. Fernandez-Perea, O. Borodin, G. D. Smith, M. Armand and W. S. Howells (2002). "Coherent Neutron Scattering from PEO and a PEO-based Polymer Electrolyte." Solid State Ionics **147**(2-4): 225-236. GLAD

K. Sakai, T. Adachi, T. Oku, K. Ikeda, T. Morishima, H. M. Shimizu, M. Furusaka, T. Ino, S. Sato, Y. Kiyonagi, N. Sakamoto, T. Sakuma, J. Suzuki, K. Littrell, C.-K. Loong, R. Goyette, S. Hosoya and M. Ishii (2003). Recent Development of a Position-Sensitive Scintillator Detector Employing Wavelength-Shifting Cross-Fiber. ICANS-XVI. POSYII, QUIP

K. Sakai, T. Adachi, T. Oku, K. Ikeda, T. Morishima, H. M. Shimizu, M. Furusaka, T. Ino, S. Sato, Y. Kiyonagi, N. Sakamoto, T. Sakuma, J. Suzuki, K. Littrell, C.-K. Loong and R. Goyette (2004). Recent Development of Position Sensitive Neutron Detectors Employing Wavelength-Shifting Cross-Fiber. 3rd European Conference on Neutron Scattering, Montpellier, France. POSYII, QUIP

K. Sakai, K. Hirota, T. Adachi, K. Ikeda, T. Morishima, H. M. Shimizu, M. Furusaka, S. Sato, Y. Kiyonagi, N. Sakamoto, T. Sakuma, O. T. J. Suzuki, K. Littrell, C.-K. Loong, J. B. Czirr and T. K. McKnight (2004). "Development of Position-Sensitive Neutron Detector Based on Scintillator." Nucl. Ins. Meth. in Phys. Res. A **529**(1-3): 301-306. POSYII, QUIP

N. Sakamoto, Y. Kiyonagi, S. Sato, H. Sagehashi, M. Furusaka, J. Suzuki, K. C. Littrell, C. K. Loong, A. Gorin, I. Manuilov, A. Ryazantsev, K. Kuroda, K. Sakai, F. Tokanai, T. Adachi, T. Oku, K. Ikeda, H. Miyaska, S. Suzuki, K. Morimoto and H. M. Shimizu (2003). "Development of a High-Resolution Scintillator-Based Area Detector for Neutrons." J. Appl. Crystallog. **36**: 820-825. POSYII, QUIP

P. S. Salmon (2002). "Order Within Disorder." Nature Materials **1**: 87-88. GLAD

S. Sampath, C. J. Benmore, K. Z. Lantzky, J. Neufeind, D. L. Price and J. L. Yarger (2003). "Intermediate-Range Order in Permanently Densified GeO₂ Glass." Phys Rev. Lett. **90**(11): 115502. GLAD

S. Sampath, K. M. Lantzky, C. J. Benmore, J. Neufeind, J. E. Siewenie, P. A. Egelstaff and J. L. Yarger (2003). "Structural Quantum Isotope Effects in Amorphous Beryllium Hydride." J. Chem. Phys. **119**(23): 12499-12502. GLAD

C. K. Sams, F. Somoza, I. Bernal and H. Toftlund (2001). "Coordination Chemistry of Transition Metal Complexes of a Novel Pentadentate

Ligand." Inorg. Chem. Acta **318**: 45. SCD

O. Sanli and G. Asman (2004). "Release of Diclofenac through Gluteraldehyde Crosslinked Poly(vinyl alcohol)/Poly(acrylic acid) Alloy Membranes." J. Appl. Polymer Science **91**(1): 72-77. SAND

B. Saruhan, A. Flores-Renteria, K. Fritscher, U. Schulz, M. Keshmiri and T. Troczynski Sintering Inhibition in Nanostructured EB-PVD-TBCs by Applying Liquid-Phase-Infiltration. Euro Ceramics VIII Key Engineering Materials Trans Tech Publications, Switzerland, (2004). **264-268**: 713-718. SAND

B. Saruhan, A. Flores-Renteria, A. Kulkarni, F. DeCarlo and J. Ilavsky (2004). Characterization of Y₂O₃-Doped La₂Zr₂O₇ based EB-PVD Thermal Barrier Coatings using X-ray Microtomography (CMT) and Small Angle Neutron Scattering (SANS). 28th Cocoa Beach Conf. on Advanced Ceramics and Coatings, Cocoa Beach, FL 2004, The American Ceramic Society, Westerville, USA. SAND

P. M. Saville and J. W. White (2001). "Polymeric Surfactant Structure." Chin. J. Polym. Sci. **19**(2): 135-145. SAND

R. E. Schaak, M. Avdeev, W. L. Lee, L. G. Lawes, H. W. Zandbergen, J. D. Jorgensen, N. P. Ong, A. P. Ramirez and R. J. Cava (2004). "Formation of Transition Metal Boride and Carbide Perovskites Related to Superconducting MgCNi₃." J. Solid State Chem. **177**(4-5): 1244-1251. SEPD

D. W. Schaefer and M. M. Agamalian (2004). "Ultra-Small-Angle Neutron

Scattering: A New Tool for Materials Research." Current Opinion in Solid State & Materials Science **8**(1): 39-47. SAND

D. W. Schaefer, G. Beaucage, D. A. Loy, K. J. Shea and J. S. Lin (2004). "Structure of Arylene-Bridged Polysilsesquioxane Xerogels and Aerogels." Chemistry of Materials **16**(8): 1402-1410. SAND

J. Schelten, R. Engels, U. Clemens and G. Kemmerling (2003). Neutron Detection Experiments with Ionisation Counter and ^6Li Converter. Proc. IEEE Nuclear Science Symposium & Medical Imaging Conference 2003, Portland. QUIP

J. Schelten, R. Engels, U. Clemens and G. Kemmerling (2004). "Neutron Detection Experiments with Ionisation Counter and ^6Li Converter." IEEE **7803**(8257): 655-659. QUIP

J. S. Schilling, J. D. Jorgensen, D. G. Hinks, S. Deemyad, J. Hamlin, C. W. Looney and T. Tomita (2002). Hydrostatic Pressure Dependence of the Superconducting and Structural Properties of MgB_2 . in Studies of High Temperature Superconductors, ed. A. V. Narlikar, (Nova Science Publ., New York, 2002). **38**: 321-338. SEPD

J. E. Schirber, B. Morosin, G. H. Kwei, T. Yildirim, J. E. Fischer and J. D. Jorgensen (2001). "Superconductivity in the Polymeric Phase of $\text{Na}_2\text{CsC}_{60}$." Physica C **353**(3-4): 207-212. SEPD

R. Schmidt, K. E. Gray, D. G. Hinks, J. F. Zasadzinski, M. Avdeev, J. D. Jorgensen and J. C. Burley (2003). "Retention of Two-Band

Superconductivity in Highly Carbon-Doped MgB_2 ." Phys. Rev. B **6806**(6): 508-508. SEPD

S. Schneider, A. Bracchi, K. Samwer, M. Seibt and P. Thiyagarajan (2002). "Microstructure-Controlled Magnetic Properties of the Bulk Glass-Forming Alloy $\text{Nd}_{60}\text{Fe}_{30}\text{Al}_{10}$." Appl. Phys. Lett. **80**(10): 1749-1751. SAND

A. J. Schultz, R. W. Henning, M. A. Hitchman and H. Stratemeier (2003). "Influence of Pressure and Temperature on the Crystal Structure of Deuterated Ammonium Copper Tutton Salt, $(\text{ND}_4)_2[\text{Cu}(\text{D}_2\text{O})_6](\text{SO}_4)_2$." Cryst. Growth Des. **3**(3): 403-407. HIPD

A. J. Schultz, T. F. Koetzle, J. A. Cowan, M. E. Miller and X. Wang (2004). "Single Crystal Analyses of the Structure and Bonding in Transition-Metal σ -Complexes." Neutron News **15**(3): 23-26. SCD

A. J. Schultz, P. Thiyagarajan, J. P. Hodges, C. Rehm, D. A. A. Myles, P. Langan and A. D. Mesecar (2005). "Conceptual Design of the Next Generation Macromolecular Neutron Diffractometer (MaNDi) for the SNS." J. Appl. Crystallog. **38**: 964-974. SNS

A. J. Schultz, A. J. Cowan, M. A. Hitchman and H. Stratemeier (2005). "Single Crystal Neutron Diffraction Study at 20 K of Zn-doped (3.4%) $(\text{ND}_4)_2[\text{Cu}(\text{D}_2\text{O})_6](\text{SO}_4)_2$." Acta Crystallog. **61**(5): M234-M236. SCD

U. Schulz, B. Saruhan, K. Fritscher and C. Leyens (2004). "Review On Advanced EB-PVD Ceramic Top Coats For TBC Applications." Int. J. Appl. Ceram. Technol. **1**(4): 302-315. SAND

A. Serquis, A. Caneiro, A. Basset, S. Short, J. P. Hodges and J. D. Jorgensen (2001). "Oxygen Content, Thermodynamic Stability and Superconductivity of the (Hg, Re)-1201 Compound." Phys. Rev. B **63**(1): 14508-14517. SEPD

K. Seol, A. D. Krawitz, J. W. Richardson Jr. and C. M. Weisbrook (2005). "Effects of WC Size and Amount on the Thermal Residual Stress in WC-Ni Composites." Mater. Sci. Eng. **398**(1-2): 15-21. GPPD

A. Serquis, L. Morales, A. Caneiro, A. Basset, S. Short, J. P. Hodges and J. D. Jorgensen (2001). "Synthesis Methods and Characterization of (Hg,Re)-1201." Physica C **349**(3-4): 305-316. SEPD

S.-I. Shamoto (2002). "Double Honeycomb Lattice Superconductors." Recent Res. Devel. Physics **3**: 287-304. GPPD

S.-I. Shamoto, K. Takeuchi, S. Yamanaka and T. Kajitani (2004). "Structural Study on Na_xHfNCl System." Physica C **402**: 283-292. GPPD

P. K. Sharma and S. R. Bhatia (2004). "Effect of Anti-Inflammatories on Pluronic® F127: Micellar Assembly, Gelation and Partitioning." International Journal of Pharmaceutics **278**: 361-377. SASI

P. K. Sharma and S. R. Bhatia (2004). The Effect of Drugs on Pluronic® F127 Structure. Proc. IEEE/NEBC. SASI

P. K. Sharma, J. E. Matthew and S. R. Bhatia (2005). "Structure and Assembly of PEO-PPO-PEO Copolymers in

Mammalian Cell Culture Media." J. of Bio. Sci. Poly. **16**: 1139-1151. SAND

D. V. Sheptyakov, A. M. Abakumov, E. V. Antipov, A. M. Balagurov, S. J. L. Billinge, P. Fischer, L. Keller, M. V. Lobanov, B. P. Pavlyuk, V. Y. Pomjakushin and M. G. Rozova (2002). "Crystal and Magnetic Structures of New Layered Oxides $\text{A}_2\text{GaMnO}_{5+\gamma}$ (A=Ca,Sr)." Appl. Phys. A **74**: S1734-S1736. GPPD

B. Sieve, X. Z. Chen, R. Henning, P. Brazis, C. R. Kannewurf, J. A. Cowen, A. J. Schultz and M. G. Kanatzidis (2001). "Cubic Aluminum Silicides $\text{RE}_8\text{Ru}_{12}\text{Al}_{49}\text{Si}_9(\text{Al}_x\text{Si}_{12-x})$ (RE=Pr,Sm) from Liquid Aluminum. Empty (Si,Al)(12) Cuboctahedral Clusters and Assignment of the Al/Si Distribution with Neutron Diffraction." J. Amer. Chem. Soc. **123**(29): 7040-7047. SCD

C. M. Silvernail, X. G. Zhao, M. Dvorak, A. I. Kolesnikov, A. J. Schultz, G. S. Harbison and J. A. Belot (2004). "Theoretical and Spectroscopic investigation of Strong, Intramolecular Hydrogen Bonds in beta-cyano-alpha, gamma-diketones." Abstracts of Papers of Amer. Chem. Soc. **227**(U1460). HRMECS, SCD

D. Singh, K. C. Goretta, J. W. Richardson, Jr. and A. R. deArellano-Lopez (2002). "Interfacial Sliding Stress in $\text{Si}_3\text{N}_4/\text{BN}$ Fibrous Monoliths." Scripta Materialia **46**(10): 747-751. GPPD

H. Sinn, B. Glorieux, L. Hennet, A. Alatas, M. Hu, E. E. Alp, F. J. Bermejo, D. L. Price and M.-L. Saboungi (2003). "Microscopic Dynamics of Liquid Aluminum Oxide." Science **299**(5615): 2047-2049. QENS

R. P. Slater and R. K. B. Gover (2002). "Synthesis and Structure of the Perovskite Oxide Carbonate $Ba_4ScCu_2O_{7-x}(CO_3)_y$ ($x \sim 0.3$, $y \sim 0.9$); A New Example of Ordering in the Small Cation Sites." Mater. Res. Bulletin **37**(3): 485-493. GPPD

L. J. Smith, D. L. Price, Z. Chowdhuri, J. W. Brady and M. L. Saboungi (2004). "Molecular Dynamics of Glucose in Solution: A Quasielastic Neutron Scattering Study." J. Chem. Phys. **120**(8): 3527-3530. QENS

A. K. Soper, C. A. Tulk, C. J. Benmore, K. M. Lantzky, J. Urquidi and D. D. Klug (2002). "Enhanced: Water and Ice." Science **297**(5585): 1288-1289. GLAD

S. A. Speakman and S. T. Misture (2001). "In-Situ X-Ray and Neutron Diffraction Study of $Ba_2In_2O_5$." Materials Science Forum **378**: 336. GPPD

S. A. Speakman, J. W. Richardson Jr., B. J. Mitchell and S. T. Misture (2002). "In-Situ Diffraction Study of $Ba_2In_2O_5$." Solid State Ionics **149**(3-4): 247-259. GPPD

P. M. Spiecker, K. L. Gawrys and P. K. Kilpatrick (2003). "Aggregation and Solubility Behavior of Asphaltenes and their Subfractions." J. Colloid and Interface Sci. **267**(1): 178-193. SAND

P. M. Spiecker, K. L. Gawrys, C. L. Trail and P. K. Kilpatrick (2003). "Effects of Petroleum Resins on Asphaltene Aggregation and Water-in-oil Emulsion Formation." Colloids and Surfaces A **220**(1-3): 9-27. SAND

S. Srinath, P. Vavassori, M. T. Rekveldt, R. E. Cook and G. P. Felcher (2004). "Magnetization Reversal in an Obliquely Oriented Metal Evaporated Tape." J. Magn. Magn. Mat. **279**(2-3): 440-447. POSYI

J. L. Stanford, A. J. Ryan and Y. Yang (2001). "Reactive Processing of Acrylic-polyurea Interpenetrating Networks: Reactionkinetic Studies." Polymer International **50**(9): 1035-1045.

I. M. Steele, J. J. Pluth and J. W. Richardson, Jr. (2001). "Progressive Changes in Positive Active Material Over the Lifetime of Lead-Acid Battery." J. Power Sources **95**(1-2): 79-84. GPPD

A. Subbiah, D. Pyle, A. Rowland, J. Huang, R. A. Narayanan, P. Thiyagarajan, J. Zon and A. Clearfield (2005). "A Family of Microporous Materials Formed by Sn(IV) Phosphate Nanoparticles." J. Am. Chem. Soc. **127**(31): 10826-10827. SAND

N. Sukumar, P. Langan, F. S. Matthews, L. H. Jones, P. Thiyagarajan, B. P. Schoenborn and V. L. Davidson (2005). "A Preliminary Time-of-Flight Neutron Diffraction Study on Amicyanin from *Paracoccus Denitrificans*." Acta Crystallog. **61**(5): 640-642. PCS-LANL

S. K. Sukumaran, G. Beaucage, J. E. Mark and B. Viers (2005). "Neutron Scattering from Equilibrium-swollen Networks." The European Physical Journal E - Soft Matter **18**(1): 29-36. SAND

K. Suzuya, K. Itoh, A. Kajinami and C. K. Loong (2004). "The Structure of Binary Zinc Phosphate Glasses." J.

Non-Crystalline Solids **345-346**: 80-87.
GLAD

G. Tae, J. A. Kornfield, J. Hubbell and J. Lal (2002). "Ordering Transitions of Fluorocarbon Ended Poly(ethylene Glycol): Rheology and SANS." Macromolecules **35**(11): 4448-4457.
SASI

K. Takeuchi, A. Nishijima, K. Ui, N. Koura and C.-K. Loong (2005). "Corrosion behavior of Fe-Cr Alloys in Li_2CO_3 - K_2CO_3 ." J. Electrochem. Soc. **152**(9): B364-B368. GPPD

C. Talon, F. J. Bermejo, C. Cabrilo, G. J. Ceullo, M. A. Gonzalez, J. W. Richardson, A. Criado, M. A. Ramos, S. Vieira, F. L. Cumbreira and L. M. Gonzalez (2002). "Chemical Isomerism as a Key to Explore Free-Energy Landscapes in Disorderd Matter." Phys. Rev. Lett. **88**11(11): 5506-5506. GPPD

U. Talon, L. J. Smith, J. W. Brady, B. A. Lewis, J. R. D. Copley, D. L. Price and M. L. Saboungi (2004). "Dynamics of Water Molecules in Glucose Solutions." J. Phys. Chem. **108**(16): 5120-5126.
QENS

C. N. Tam, J. Cowan, A. J. Schultz, V. G. Young, Jr., F. R. Trouw and A. G. Sykes (2003). "Neutron and X-ray Diffraction, Inelastic Neutron Scattering and Solid State ^{13}C NMR Investigations of Polymorphic *p*-Chlorophenylformamide: Absence of Proton Transfer along the Intermolecular N-H...O Hydrogen Bond." J. Phys. Chem. B **107**(31): 7601-7606. SCD, QENS

C. N. Tam, F. R. Trouw and L. E. Iton (2004). "Inelastic Neutron Scattering Study of the Activation of Molecular

Hydrogen in Silver-Exchanged a Zeolite: First Step in the Reduction to Metallic Silver at Low Temperature." J. Phys. Chem. A **108**(21): 4737-4743. QENS

S. Tamura, K. Takeuchi, G. M. Mao, R. Csencsits, L. X. Fan, T. Otomo and M.-L. Saboungi (2003). "Colloidal Silver Iodide: Synthesis by a Reverse Micelle Method and Investigation by a Small-Angle Neutron Scattering Study." J. Electroanalytical Chem. **559**: 103-109.
SAND

R. Tanaka, J. E. Hunt, R. E. Winans, P. Thiyagarajan, S. Sato and T. Takanohaski (2003). "Aggregates Structure Analysis of Petroleum Asphaltene with Small-Angles Neutron Scattering." Energy & Fuels **17**(1): 127-134. SAND

R. G. Teller, J. W. Richardson, Jr. and J. M. Carpenter (2004). "The Intense Pulsed Neutron Source at Argonne National Laboratory." Neutron News **15**(3): 9-13. FACILITY

S. G. E. teVelthuis, G. P. Felcher, P. Blomquist and R. Wappling (2001). "Neutron Spin Rotation in Magnetic Mirror." J. Phys. Conds. Mat. **13**(24): 5577-5583. POSY I

S. G. E. teVelthuis, J. S. Jiang, S. D. Bader and G. P. Felcher (2002). "Spin Flop Transition in a Finite Antiferromagnet: Evolution of the Magnetic Structure." Phys Rev. Lett. **89**12(12): 127203-127204. POSYI

S. G. E. teVelthuis, G. P. Felcher, S. Kim and I. K. Schuller (2002). Magnetic Profiles and Coupling in Fe/Cr (110) Superlattices. ICNS 2001. POSYI

P. Thiyagarajan and L. Fan (2002). Influence of Carbonate Ions on the Micellization Behavior in Triblock Copolymer Solutions. ICNS 2001. SAND

P. Thiyagarajan (2003). Characterization of Materials of Industrial Importance using Small Angle Scattering Techniques. Proc. 12th Int. Conf. on Small Angle Scattering (SAS 2002). SAND

M. F. Thorpe, V. A. Levashov, M. Lei and S. J. L. Billinge Notes on the Analysis of Data for Pair Distribution Functions eds. S. J. L. Billinge and M. F. Thorpe in. From Semiconductors to Proteins: Beyond the Average Structure, (Kluwer/Plenum, New York, 2002: 105-128. SEPD, GPPD, GLAD

B. H. Toby, R. B. VonDreele and A. C. Larson (2003). "CIF Applications. XIV. Reporting of Rietveld Results using pdCIF: GSAS2CIF." J. Appl. Crystallog. **36**: 1290-1294. SOFTWARE

B. Tomberli, P. A. Egelstaff, C. J. Benmore and J. Neufeind (2001). "Isotopic Effects in the Structure of Liquid Methanol. II. Experimental Data in Fourier Space." J. Phys. Conds. Mat. **13**: 11421-11434. GLAD

B. Tomberli, P. A. Egelstaff, C. J. Benmore and J. Neufeind (2001). "Isotopic Quantum Effects in the Structure of Liquid Methanol. I. Experiments with High Energy Photon Diffraction." J. Phys. Conds. Mat. **13**: 11405-11420. GLAD

B. L. Tomberli, C. J. Benmore, P. A. Egelstaff and J. Neufeind (2001). "Temperature Dependence of Structural

Quantum Effects in Liquid Methanol." Euro. Phys. Lett. **55**: 341-347. GLAD

B. Tomberli, C. J. Benmore, J. Neufeind and P. A. Egelstaff (2002). "Isotopic Quantum Effects in the Structure of Liquid Ethanol." Canadian J. Phys. **80**(9): 1059-1068. GLAD

T. Tomita, J. J. Hamlin, J. S. Schilling, D. G. Hinks and J. D. Jorgensen (2001). "Dependence of T-c on Hydrostatic Pressure in Superconducting MgB₂." Phys. Rev. B **6409**(9): 2505-+. SEPD

R. Traiphol, D. W. Smith, Jr. and D. Perahia (2002). "Surface Ordering in Thin Films of Liquid Crystalline Polymers Containing Fluorinated and Protonated Segments: Neutron Reflectometry Study." J. Polymer Sci. Phys. **40**(24): 2817-2824. POSYII

A. Triolo, F. L. Celso, F. Triolo, H. Amenitsch, M. Steinhart, P. Thiyagarajan, S. Wells, J. M. DeSimone and R. Triolo (2002). "Kinetics of Block-copolymer Aggregation in Super Critical CO₂." J. Non-Crystall. Solids **307-310**: 725-730. SAND

J. S. Tse, V. P. Shpakov, V. R. Belosludov, F. Trouw, Y. P. Handa and W. Press (2001). "Coupling of Localized Guest Vibrations with the Lattice Modes in Clathrate Hydrates." Euro. Phys. Lett. **54**(3): 354-360.

J. S. Tse, D. D. Klug, M. Guthrie, C. A. Tulk, C. J. Benmore and J. Urquidi (2005). "Investigation of the Intermediate- and High-Density Forms of Amorphous Ice by Molecular Dynamics Calculations and Diffraction Experiments." Phys Rev. B **71**(21): 214107. GLAD

C. A. Tulk and D. D. Klug (2001). "Formation of Amorphous Ice by Careful Annealing of Ice XII." Phys. Rev. B **63**: 212201-1 – 212201-4. GLAD

C. A. Tulk, C. J. Benmore, J. Urquidi, D. D. Klug, J. Neuefeind, B. Tomberli and P. A. Egelstaff (2002). "Structural Studies of Several Distinct Meta-stable Forms of Amorphous Ice." Science **297**: 1320-1323. GLAD

C. A. Tulk, C. J. Benmore, D. D. Klug, J. Urquidi, J. Neuefeind and B. Tomberli (2003). "Another Look at Water and Ice." Science **299**: 44-45. GLAD

J. F. C. Turner, S. E. McLain, T. H. Free, C. J. Benmore and J. E. Siewenie (2002). On Sample Containment for High-Energy X-Ray Scattering Studies of Hydrogen Fluoride. APS Activity Report 2002 ANL-03/21. GLAD

J. F. C. Turner, S. E. McLain, T. H. Free, C. J. Benmore, K. W. Herwig and J. E. Siewenie (2003). "On Sample Containment for Neutron and High Energy X-Ray Scattering Studies of Hydrogen Fluoride And Related Molecular Species." Review of Scientific Instruments **74**(10): 4410-4417. GLAD

J. Urquidi, C. J. Benmore, J. Neuefeind and B. Tomberli (2003). "ISOMER-X: A New Program for the Analysis of High Energy X-Ray Diffraction Data." J. Appl. Crystallog. **36**: 368. GLAD

J. Urquidi, C. J. Benmore, J. Neuefeind, B. Tomberli, C. A. Tulk, M. Guthrie, P. A. Egelstaff and D. D. Klug (2003). "Isotopic Quantum Effects on the Structure of Low Density Amorphous

Ice." J. Phys. Cond. Matt. **15**: 3657-3664. GLAD

J. Urquidi, C. J. Benmore, P. A. Egelstaff, M. Guthrie, S. E. McLain, C. A. Tulk, D. D. Klug and J. F. C. Turner (2004). "A Structural Comparison of Supercooled Water and Intermediate Density Amorphous Ices." Molecular Physics **102**(19-20): 2007-2013. GLAD

D. A. VanderGriend, S. Malo, S. J. Barry, N. M. Dabbousch, K. R. Poeppelmeier and V. S. Dravid (2001). "La₃Cu₂VO₉: A Surprising Variation of the YAIO₃ Structure-Type with 2D Copper Clusters of Embedded Triangles." J. Solid State Chem. **163**: 259-266.

T. Varga (2005) Synthesis and Characterization of some Low and Negative Thermal Expansion Materials A Dissertation Presented to The Academic Faculty, Georgia Institute of Technology. SEPD

L. Vasiliu-Doloc, R. Osborn, S. Rosenkranz, J. Mesot, J. F. Mitchell and S. K. Sinha (2001). "Polaron Ordering in Ferromagnetic Colossal Magnetoresistive Oxides." Int. J. Mod. Phys. **14**: 13711-3718.

L. Vasiliu-Doloc, R. Osborn, S. Rosenkranz, J. Mesot, J. F. Mitchell, S. K. Sinha, O. H. Seeck, J. W. Lynn and Z. Islam (2001). "Neutron and X-ray Evidence of Charge Melting in Ferromagnetic Layered Colossal Magnetoresistance Manganites." J. Appl. Phys. **89**(11 pt. 2): 6840-6845. LRMECS

C. Vecchini, O. Moze, A. O. Pecharsky, V. K. Perchatsky, K. A. Gshneidner, Jr.,

E. Bruck, R. Bewley and A. I. Kolesnikov (2004). "Dynamic Magnetic Susceptibility of $Gd_5Si_{1.9}Ge_2$ and $Gd_4YSi_{1.9}Ge_{2.1}$." J. Appl. Phys. **95**(11): 7207-7209. HRMECS

G. M. Veith, M. Greenblatt, M. Croft, K. V. Ramanujachary, J. Hattrick-Simpers, S. E. Lofland and I. Nowik (2005). "Synthesis and Characterization of $Sr_3FeMo_{0.88}$: An Oxygen Deficient 2D Analogue of the Double Perovskite Sr_2FeMoO_6 ." Chem. Mater. **17**: 2562-2567. GPPD

D. A. Vivic, T. J. Anderson, J. A. Cowan and A. J. Schultz (2004). "Synthesis, Structure, and Reactivity of a Dinuclear Metal Complex with Linear M-H-M Bonding." J. Am. Chem. Soc. **126**: 8132-8133. SCD

K. Vijayan, D. E. Discher and J. Lal (2005). "Interactions of Membrane-active Peptides with Thick, Neutral, Nonzwitterionic Bilayers." J. Phys. Chem. **109**(30): 14356-14364. SASI

B. D. Vogt, R. A. Pai, H. J. Lee, R. C. Hedden, C. L. Soles, W. L. Wu, E. K. Lin, B. J. Bauer and J. J. Watkins (2005). "Characterization of Ordered Mesoporous Silica Films Using Small-angle Neutron Scattering and X-ray Porosimetry." Chem. Materials **17**(6): 1398-1408. SAND

B. F. Wang, R. A. Fisher, D. G. Hinks, J. D. Jorgensen, A. Junod and N. E. Phillips (2001). "Phenomenological Two-gap Model for the specific Heat of MgB_2 ." Euro. Phys. Lett. **56**(6): 856-862. SEPD

D. Wang, J. Lal, D. Moses, G. C. Bazan and A. J. Heeger (2001). "Small Angle

Neutron Scattering (SANS) Studies of a Conjugated Polyelectrolyte in Aqueous Solution." Chem. Phys. Lett. **348**(5-6): 411-415. SASI

D. Wang, D. Moses, G. C. Bazan, A. J. Heeger and J. Lal (2001). "Conformation of a Conjugated Polyelectrolyte in Aqueous Solution: Small Angle Neutron Scattering." J. Macromolecular Sci. **38**(12): 1175-1189. SASI

L.-C. Wang, H.-Y. Jang, T.-G. Baik, A. L. Luis, Y. Roh, V. Lynch, A. J. Schultz, X. Wang and M. J. Krische (2002). "Diastereoselective Cycloreductions and Cycloadditions Catalyzed by $Co(dpm)_2$ Silane (dpm = 2,2,6,6-tetramethylheptane-3,5-dionate): Mechanism, Scope and Partitioning of Reaction Manifolds. Bifurcation of Hydrometallative and Anion Radical Pathways." J. Am. Chem. Soc. **124**: 9448-9453. SCD

X. Wang, A. J. Schultz and Y. Halpern (2002). "Kinetics of Methane Hydrate Formation from Polycrystalline Deuterated Ice." J. Phys. Chem. A **106**: 7304-7309. HIPD

X. D. Wang, J. D. Pless, D. A. V. Griend, P. C. Stair, K. R. Poeppelmeier, Z. B. Hu and J. D. Jorgensen (2004). "Vanadium and Molybdenum Disorder in $M_{2.5}VMoO_8$ (M = Mg, Mn, and Zn) Determined with Neutron Powder Diffraction and Phase Formation Studies of $Mg_{2.5+x}V_{1+2x}Mo_{1-2x}O_8$." J. of Alloys Compd. **379**(1-2): 87-94. SEPD

X.-L. Wang, Y. D. Wang and J. W. Richardson, Jr. (2002). "Experimental Error Due to Displacement of Sample in Time-of-Flight Neutron Diffractometry."

J. Appl. Crystallog. **35**(5): 533-537.
GPPD

X.-L. Wang, J. H. Schneibel, Y. D. Wang and J. W. Richardson Jr. (2003). "Annealing Induced Structural Changes and Microcracking in Mo-Mo₃Si." Mat. Res. Soc. Sym. Proc. **753**(BB): 5.40.1-5.40.6. GPPD

X. L. Wang, Y. D. Wang, A. D. Stoica, D. J. Horton, H. Tian, P. K. Liaw, H. Choo, J. W. Richardson Jr. and E. Maxey (2005). "Inter- and Intragranular Stresses In Cyclically Deformed 316 Stainless Steel." Mat. Sci. Eng. **399**(1-2): 114-119. GPPD

Y. Wang, A. I. Kolesnikov, S. L. Dong and J. C. Li (2003). "Neutron Scattering Studies of the Phase Transitions in High Pressure Ices During Annealing." Can. J. Phys./Rev. Can. Phys. **81**(1-2): 401-407. ISIS

Y. D. Wang, X.-L. Wang, A. D. Stoica and J. W. Richardson, Jr. (2002). "Measurement of Grain-Orientation-Dependent Stress and Stored Energy Using Spallation Neutron Source." Mat. Sci. Forum **408-412**: 179-184. GPPD

Y. D. Wang, X. L. Wang, A. D. Stoica, Y. H. Sha, X. Zhao and J. W. Richardson, Jr. (2002). "Development of Grain-Orientation-Dependent Residual Stresses in Interstitial-Free Steel after Deformation." Mat. Sci. Forum **408-412**: 119-124. GPPD

Y. D. Wang, H. B. Tian, A. D. Stoica, X. L. Wang, P. K. Liaw and J. W. Richardson Jr. (2003). "Development of Large Grain-Orientation-Dependent-Residual Stresses in a Cyclically-

Deformed Alloy." Nature Materials **2**(2): 101-106. GPPD

Y. D. Wang, X.-L. Wang, A. D. Stoica, J. W. Richardson, Jr. and R. L. Peng (2003). "Determination of the Stress Orientation Distribution Function Using Pulsed Neutron Sources." J. Appl. Crystallog. **36**(1): 14-22. GPPD

Y. X. Wang, J. H. Lin, Y. Du, R. W. Qin, B. Han and C.-K. Loong (2002). "A Hexagonal Perovskite-Intergrowth Compound La₂Ca₂MnO₇." Angew Chem Int. Edit **39**(15): 2730-2732. GPPD

Y.-X. Wang, L.-J. Bie, Y. Du, J.-H. Lin, C.-K. Loong, J. W. Richardson, Jr. and L.-P. You (2004). "Hexagonal Perovskite-Intergrowth Manganates: Ln₂Ca₂MnO₇ (Ln = La, Nd and Sm)." J. Solid State Chem. **177**: 65-72. GPPD

J. K. R. Weber, C.-K. Loong, K. Takeuchi, K. Suzuya, J. A. Tangeman and T. S. Key (2002). "Neutron Diffraction Measurements of the Structure of an Orthosilicate Glass Mg₂SiO₄." Phys. Chem. Glasses **42**: 68-70. GLAD

J. K. R. Weber, C. J. Benmore, J. A. Tangeman, J. Siewenie and K. J. Hieria (2003). "Structure of Binary CaO-Al₂O₃ and SrO-Al₂O₃ Liquids by Combined Levitation-Neutron Diffraction." J. Neutron Research **11**(3): 113-121. GLAD

R. Weber, C. J. Benmore, J. Siewenie, J. Urquidi, T. S. Key and P. C. Nordine (2004). "Structure and Bonding in a Single- and two-phase Alumina-based Glasses." Phys. Chem. Chem. Phys. **6**: 2480-2483. GLAD

C. E. Webster, C. L. Gross, D. M. Young, G. S. Girolami, A. J. Schultz, M. B. Hall and J. Eckert (2005). "Electronic and Steric Effects on Molecular Dihydrogen Activation in $[CP^*OsH_4(L)]^+$, $L=PPh_3$, $AsPh_3$, and PCy_3 ." Journal of American Chem. Society **127**: 15091-15101. SCD

U. Welp, S. G. E. teVelthuis, G. P. Felcher, T. Gredig and E. D. Dahlberg (2003). Domain Formation in Exchange Biased Co/CoO Bilayers. Proc. 46th Annual Conf. on Magn. & Magn. Mater. POSYI

R. Wen, S. S. Massoud and I. Bernal (2001). "The Phenomenon of Conglomerate Crystallization. Part 54. The Crystallization Modes of Five New [trans-(3,2,3-Tet)Co(III)X₂]Y (X=NO₂, CN, NCS)." J. Coord. Chem. **53**: 249. SCD

H. R. Wenk, L. Cont, Y. Xie, L. Lutterotti, L. Ratschbacher and J. Richardson (2001). "Reitveld Texture analysis of Dabie Shan Eclogite from TOF Neutron Diffraction Spectra." J. Appl. Crystallog. **34**(Part 4): 442-453. GPPD

H.-R. Wenk Texture and Anisotropy. Plastic Deformation of Minerals and Rocks, eds. S.-Y. Karato and H.-R. Wenk, Reviews in Mineralogy and Geochemistry, Mineral Soc. America: 291-329. GPPD

H.-R. Wenk and P. VanHoutte (2004). "Texture and Anisotropy." Reports on Progress in Physics **67**: 1367-1428. GPPD

M. Wilding, J. Tangeman, C. Benmore and S. Sampath (2002). Studying the Structure of Magnesium Silicate

Glasses by High-Energy X-Ray Diffraction. APS Activity Report 2002 ANL-03/21. GLAD

M. C. Wilding, C. J. Benmore and P. F. McMillan (2002). "A Neutron Diffraction Study of Yttrium-Aluminate Glasses." J. Non-Crystall. Solids **297**: 143-155. GLAD

M. C. Wilding, C. J. Benmore, J. A. Tangeman and S. Sampath (2004). "Coordination Changes in Magnesium Silicate Glasses." Europhysics Lett. **67**(2): 212-218. GLAD

M. C. Wilding, C. J. Benmore, J. A. Tangeman and S. Sampath (2004). "Evidence of Different Structures in Magnesium Silicate Liquids: Coordination Changes in Forsterite- to Enstatite-Composition Glasses." Chem. Geology **213**: 281. GLAD

M. C. Wilding, M. Wilson and P. F. McMillan (2005). "X-ray and Neutron Diffraction Studies and MD Simulation of Atomic Configurations in Polyamorphic Y₂O₃-Al₂O₃ Systems." Philosophical Transactions: Mathematical, Physical and Engineering Sciences **363**(1827): 589-607. GLAD

B. Wolle (2003). "Static Analysis of Java Applications - Are Lines-of-Code Metric and Halstead Length Suitable?" Wirtschaftsinformatik **45**(1): 29-40. SOFTWARE

T. G. Worlton, A. Chatterjee, J. Hammonds, P. F. Peterson, D. Mikkelson and R. Mikkelson (2003). Distributing Data from Advanced Neutron Sources. ICANS-XVI. SOFTWARE

T. G. Worlton, C. Bouzek, A. Chatterjee, J. P. Hammonds, D. J. Mikkelsen, R. Mikkelsen, M. Miller, P. F. Peterson and B. Serum (2004). "New Software for Neutron Scattering Data Visualization." Neutron News **15**(3): 14-15. SOFTWARE

G. Wu, J. J. Neumeier, C. D. Ling and D. N. Argyriou (2002). "Temperature Evolution of the Crystal Structure of $\text{La}_{2-x}\text{Sr}_x\text{NiO}_4$ ($x= 1/4$ and $1/3$) as Revealed Through Neutron Powder Diffraction." Phys. Rev. B **65**(17): 174113-1 - 174113-8. SEPD

G. H. Wu, J. Majewski, C. Ege, K. Kjaer, M. Weygand, J. Lal and K. Y. C. Lee (2004). "Interaction of Poloxamer with Model Lipid Membranes." Biophysical J. **86**(1): 378A Part 2 Suppl. S. SASI

S. Wu, H. Li, P. Chen and K. Y. Lam (2004). "Modeling Investigation of Hydrogel Volume Transition." Macromolecular Theory and Simulations **13**(1): 13-29. SOFTWARE

B. J. Wuensch and K. W. Eberman (2003). Oxygen-Ion Conductivity, Disorder and Bonding in Pyrochlore Fuel-cell Materials as a Function of Composition. Proc. Second Int. Conf. on Mass and Charge Transport in Inorganic Materials - Fundamentals to Devices (CIMTEC 2002). SEPD

Y. Xie, H.-R. Wenk and S. Matthies (2003). "Plagioclase Preferred Orientation by TOF Neutron Diffraction and SEM-EBSD." Tectonophysics **370**: 269-286. GPPD

J. Xu, Y. Ding, S. D. Jacobsen, H. K. Mao, R. J. Hemley, J. Zhang, J. Qian, C. Pantea, S. Vogel and Y. Zhao (2004).

"Powder Neutron Diffraction of Wüstite (FeO) to 12 GPa Using Large Moissanite Anvils." High Pressure Research **24**: 247-253. SEPD

T. Yaita, A. W. Herlinger, P. Thiyagarajan and M. P. Jensen (2004). "Influence of Extractant Aggregation on the Extraction of Trivalent f-Element Cations by a Tetraalkyldiglycolamide." Solvent Extraction and Ion Exchange **22**(4): 553-571. SAND

B.-S. Yang, J. Lal, J. Kohn, J. S. Huang, W. B. Russel and R. K. Prud'homme (2001). "Interaction of Surfactant Lamellar Phase and a Strictly Alternating Comblike Amphiphilic Polymer Based on PEG." Langmuir **17**(21): 6692-6698. SASI

B.-S. Yang, J. Lal, M. Mihailescu, M. Monkenbusch, D. Richter, J. S. Huang, W. B. Russel and R. K. Prud'homme (2001). Dynamics of Hydrophobically Modified Polymer Doped Surfactant Bilayers: A Neutron Spin-Echo Study. In Lecture Notes in Physics: Neutron Spin Echo Spectroscopy, Springer-Verlag, New York 2001. SASI

B.-S. Yang, J. Lal, P. Richetti, C. M. Marques, W. B. Russel and R. K. Prud'homme (2001). "Interaction of Hydrophobically Modified Polymers and Surfactant Lamellar Phase." Langmuir **17**(19): 5834-5841. SASI

B.-S. Yang, J. Lal, M. Mihailescu, M. Monkenbusch, D. Richter, J. S. Huang, W. B. Russel and R. K. Prud'homme (2002). "Dynamics of Hydrophobically Modified Doped Surfactant Bilayers: A Neutron Spin-Echo Study." Langmuir **18**: 6-13. SASI

H. Yang, R. I. Walton, S. Biedasek, S. Antonijevic, S. Wimperis, A. J. Ramirez-Cuesta, J. Li and A. I. Kolesnikov (2004). "Experimental Observations of Water-Framework Interactions in a Hydrated Microporous Aluminum Phosphate." J. Phys. Chem. B **109**: 4464-4469. HRMECS

H. Yang, R. I. Walton, S. Biedasek, S. Antonijevic, S. Wimperis, A. J. Ramirez-Cuesta, J. Li and A. I. Kolesnikov (2005). "Experimental Observations of Water-framework Interactions in a Hydrated Microporous Aluminum Phosphate." J. Phys. Chem. B **109**: 4464-4469. HRMECS

Y. Yang, M. C. Cheng, X. Hu, R. Goyette, L. J. Lee and M. Ferrari (2005). "Low Pressure Carbon Dioxide Enhanced Polymer Self-Diffusion Below the Glass Transition Temperature." submitted. POSYII

Y. Yang and L. J. Lee (2005). Gas-Assisted Low Temperature Bonding of Polymeric Micro/Nanostructures. Proc. SPE ANTEC.

Y. Yang and L. J. Lee (2005). Subcritical CO₂ Assisted Polymer Surface Engineering at Low Temperature. Proc. 2004 MRS.

H. Yim, M. Kent, H. S. Jeon and G. Smith (2002). "Study of the Interfacial Structure in Epoxy Bilayer Films Using Neutron Reflection." J. Polymer Sci. B **40**: 1709. POSYII

K. L. Yu, C. H. Lee, J. C. A. Huang, H. C. Su and G. P. Felcher (2002). "Determination of Depth Profiles of Ni₈₀Fe₂₀ Thin Films on Mo Buffered Al₂O₃(1-100) Substrates with and

without a Co Interlayer by Polarized Neutron and X-ray Reflectivity Methods." Chinese J. Phys. **40**(6): 616-623. POSYI

K.-L. Yu, M.-Z. Lin, C.-H. Lee, Z. A. Ku, J. C. A. Huang and S. G. E. teVelthuis (2003). "Polarized Neutron and X-ray Reflectivity Study the Structure and Exchange Coupling of the Permalloy (Ni₈₀Fe₂₀)/Cr/permalloy Trilayers." Physica **B336**: 151-156. POSYI

J.-M. Zanotti, L. J. Smith, D. L. Price and M.-L. Saboungi (2004). "Influence of Confinement on Polymer-electrolyte Relaxational Dynamics." Mat. Res. Soc. Symp. **790**: 9.2.1 - 9.2.10. QENS

J.-M. Zanotti, M.-C. Bellissent-Funel and S.-H. Chen (2005). "Experimental Evidence of a Liquid-Liquid Transition in Interfacial Water." Eur. Phys. Lett. **71**: 1-7. QENS

J.-M. Zanotti, M.-C. Bellissent-Funel and S.-H. Chen (2005). "Water Dynamics in the "No-Man's Land" Temperature Regime." Europhys.: accepted. QENS

J.-M. Zanotti, L. J. Smith, D. L. Price and M.-L. Saboungi (2005). "Inelastic Neutron Scattering as a Probe of Dynamics Under Confinement. The Case of a PEO Polymer Melt." Annales de Chimie **30**(4): 353-364. QENS

J. Zhang and N. A. Peppas (2001). "Molecular Interactions in Poly(methacrylic acid)/Poly (N-isopropyl acrylamide) Interpenetrating Polymer Networks." J. Appl. Polymer Sci. **82**(5): 1077-1082. SAND

Y. Zhang, A. P. Wilkinson, G. S. Nolas, P. L. Lee and J. P. Hodges (2003).

"Strategies for Solving Neighboring Element Problems: A Case Study Using Resonant X-Ray Diffraction and Pulsed Neutron Diffraction to Examine $\text{Sr}_8\text{Ga}_{16}\text{Ge}_{30}$." J. Appl. Crystallog. **36**: 1182-1189. SEPD

Z. Zhang, R. A. Lukaszew, C. Cionca, X. Pan, R. Clarke, M. Yeadon, A. Zambano, D. Walko, E. Dufresne and S. G. E. teVelthuis (2004). "Correlated Structural and Magnetization Reversal Studies on Epitaxial Ni Films Grown with Molecular Beam Epitaxy and with Sputtering." J. Vac. Sci. Technol. A. **22**: 1868. POSYI

Z. Zhao, P. Mani, W. T. Lee and G. J. Mankey (2004). "Magnetic properties of uniaxial synthetic antiferromagnetic films." J. Appl. Phys. **95**: 7157. POSYI

Y. Q. Zhao, S. S. Dong, A. M. Jamieson, X. S. Hu, J. Lal, S. Nazarenko and S. J. Rowan (2005). "Rheological properties and conformation of a side-chain liquid crystal polysiloxane dissolved in a nematic solvent." Macromolecules **38**(12): 5205-5213. SASI

Z. Zhao, P. Mani, G. J. Mankey, G. Gubbiotti, F. Spizzo, S. Tacchi, W. T. Lee, C. T. Yu and M. J. Pechan (2005). "Magnetic properties of uniaxial synthetic antiferromagnets for spin-valve applications." Phys Rev. B **71**: 104417. POSYI

J. Zhou, Y. S. Kye, A. I. Kolesnikov and G. S. Harbison (2005). The Origins of Isotopomeric Polymorphism. Proc. International Conference Science of Isotopes, Bath, UK. HRMECS

M. A. Zhuravleva, X. Z. Chen, X. Wang, A. J. Schultz, J. Ireland, C. K.

Kannewurf and M. G. Kanatzidis (2002). "X-Ray and Neutron Structure Determination and Magnetic Properties of New Quaternary Phases $\text{RE}_{0.67}\text{Ni}_2\text{Ga}_{5+n-x}\text{Ge}_x$ and $\text{RE}_{0.67}\text{Ni}_2\text{Ga}_{5+n-x}\text{Si}_x$ ($n = 0, 1$; RE = Y, Sm, Gd, Tb, Dy, Ho, Er, Tm) Synthesized in Liquid Ga." Chem. Mat. **14**(7): 3066-3081. SCD

M. A. Zhuravleva, X. Wang, A. J. Schultz, T. Bakas and M. G. Kanatzidis (2002). "Isolation of the New Cubic Phases $\text{RE}_4\text{FeGa}_{12-x}\text{Ge}_x$ (RE = Sm, Tb; $x=2.5$) from Molten Gallium: Single Crystal Neutron Diffraction Study of the Ga/Ge Distribution." Inorg. Chem. **41**(23): 6056-6061. SCD

M. A. Zhuravleva, R. J. Pcionek, X. Wang, A. J. Schultz and M. G. Kanatzidis (2003). "REMGa₃Ge and RE₃Ni₃Ga₈Ge₃ (M=Ni, Co; RE=Rare-Earth Element): New Intermetallics Synthesized in Liquid Gallium. X-Ray, Electron and Neutron Structure Determination and Magnetism." Inorganic Chemistry Communications **42**(20): 6412-6424. SCD

Y. Zimenkov, V. P. Conticello, L. Guo and P. Thiyagarajan (2004). "Rational Design of a Nanoscale Helical Scaffold Derived from Self-Assembly of a Dimeric Coiled Coil Motif." Tetrahedron **6W0**: 7237-7246. SAND

A. Zirkel, S. M. Gruner, V. Urban and P. Thiyagarajan (2002). "Small-angle Neutron Scattering Investigation of the Q-dependence of the Flory-Huggins Interaction Parameter in a Binary Polymer Blend." Macromolecules **35**(19): 7375-7386. SAND

T. Adachi, K. Ikeda, T. Oku, J. Guo, W. Lin, H. Ohmori, T. Morishima, H. M. Shimizu, K. Sakai, J. Suzuki, K. C.

Littrell and C.-K. Loong (2003). A Compound Focusing Device for Cold Neutrons. ICANS-XVI. POSYII

G. Zsigmond, K. Lieutenant, S. Manoshin, H. N. Bordallo, J. D. M. Champion, J. Peters, J. M. Carpenter and F. Mezei (2004). "A Survey of Simulations of Complex Neutronic Systems by VITESS." Nucl. Ins. Meth. in Phys. Res. **529**(1-3): 218-222. FACILITY

G. Zsigmond and J. Carpenter (2005). "A Numerical Analysis of Time Focusing of Crystal Analyzer Spectrometers on Pulsed Sources." Nucl. Ins. Meth. Phys. Res. A - Accelerators Spectrometers Detectors and Assoc. Equip. **550**(1-2): 359-378. FACILITY, QENS

Acknowledgements

This progress report was prepared by the staff of Argonne's Intense Pulsed Neutron Source Division.

Editor:

Catherine Riblon

Assistant Editor

Beverly Marzec

Scientific Editor

James W. Richardson, Jr.

Publications

Nicole Green

Graphics Support

Merlyn Faber
Matthew Kwiatkowski

Photographer

George Joch

Additional photos contributed by IPNS personnel.

Disclaimer

This report was prepared as an account of work sponsored by an agency of the United States Government. Neither the United States Government nor any agency thereof, nor UChicago Argonne, LLC nor any of their employees or officers, makes any warranty, express or implied, or assumes any legal liability or responsibility for the accuracy, completeness, or usefulness of any information, apparatus, product, or process disclosed, or represents that its use would not infringe privately owned rights. Reference herein to any specific commercial product, process, or service by trade name, trademark, manufacturer, or otherwise, does not necessarily constitute or imply its endorsement, recommendation, or favoring by the United States Government or any agency thereof. The views and opinions of document authors expressed herein do not necessarily state or reflect those of the United States Government or any agency thereof, Argonne National Laboratory, or UChicago Argonne, LLC.

Argonne National Laboratory is owned by the United States Government and operated by UChicago Argonne, LLC under the provisions of a contract with the Department of Energy.